KfK 3880/2
December 1984

Fifth International Meeting on Thermal Nuclear Reactor Safety

Held at Karlsruhe Sept. 9–13, 1984

Proceedings Vol 2

Nuclear Research Center
Karlsruhe

KfK 3880/2 B

FIFTH INTERNATIONAL MEETING ON THERMAL NUCLEAR REACTOR SAFETY

held at KARLSRUHE, September 9 - 13, 1984

VOLUME 2

Compiled by G. Bork and H. Rininsland
Karlsruhe Nuclear Research Center
Project Nuclear Safety

Available from
Kernforschungszentrum Karlsruhe GmbH
Literaturabteilung
Postfach 3640 · D-7500 Karlsruhe 1

Printed in the Federal Republic of Germany

ISSN 0303-4003

Foreword

The 5th International Meeting on Thermal Nuclear Reactor Safety was held in Karlsruhe on September 9-13, 1984; it was attended by some 500 scientists and engineers from 25 countries. The conference was jointly sponsored by the European Nuclear Society (ENS), the American Nuclear Society (ANS), the Canadian Nuclear Society (CNS) and the Japan Atomic Energy Society (JAES). The meeting was further endorsed by, and organized in cooperation with, the Nuclear Energy Agency (NEA) of the Organization for Economic Cooperation and Development, the International Atomic Energy Agency (IAEA), and the Commission of the European Communities (CEC). Host organizations were the Kerntechnische Gesellschaft (KTG) and the Kernforschungszentrum Karlsruhe (KfK). The meeting was the fifth in a series of international meetings in the same subject areas with ANS and ENS as primary sponsors.

The Karlsruhe reactor safety meeting was held to reflect on the present status of engineered safety systems in nuclear power plants and to represent the findings of international safety research.

Seven invited experts of international reputation outlined the present state of the art in survey lectures. Moreover, more than 200 technical and scientific papers selected from 280 submitted papers, dealt with recent findings in reactor safety technology and research in the following areas: safety systems and functions optimization; man machine interface and emergency response; code development and verification; system and component behavior; fuel behavior during severe accidents; core debris and core concrete interaction; fission product behavior; containment response; probabilistic risk assessment. We wish to thank all speakers for their valuable contributions.

The meeting was concluded by a panel discussion on "Progress and Trends in Reactor Safety Technology and Research - What Has Been Achieved to Date? - What Remains to Be Done?"

It is not possible to acknowledge individually all persons who contributed to the meeting. We are greatly indebted to H.H. Hennies, President of the German Kerntechnische Gesellschaft (KTG), and J.M. Hendrie, President of the American Nuclear Society (ANS) who served as General Chairmen, and to A. Birkhofer as Chairman of the Technical Program Committee. Many thanks are due to the members of the Steering Committee, the Technical Program Committee, the Review Committee and the Organizing Committee.

The 6th International Meeting on Thermal Nuclear Reactor Safety was announced to take place in February 1986 at San Diego, California.

Volume 1

Chapter 1

Opening Addresses and Invited Papers (Plenary Sessions)

Chapter 2
Safety Related Operation Experience

Chapter 3

System and Component Behavior

Chapter 6
Fuel Behavior during Severe Accidents

Chapter 8
Containment Response

LIST OF AUTHORS

Chapter 5
Man Machine Interface and Emergency Response

SAFETY PARAMETER DISPLAY SYSTEM FUNCTIONS ARE INTEGRATED PARTS OF THE KWU KONVOI PROCESS INFORMATION SYSTEM (SPDS Functions are parts of the KWU-PRINS)

W. Aleite and K. H. Geyer

Kraftwerk Union AG
Erlangen, FR GERMANY

ABSTRACT

As a consequence of the TMI accident it is US practice for Safety Parameter Display Systems (SPDS) to be required by the NRC for old fashioned control rooms. In Germany the extended Safety Systems with their highly developed "Leittechnik" (I&C) and the human factors oriented control room design using "Kleinwartentechnik" (miniaturized control room equipment) meant that there was no urgent requirement for backfitting of control room equipment.

For many years however the desirablity of having flexible overview as well as extended detail information with pictorial and abstraction features and easy and quick access throughout the large-size control rooms in German plants has been recognized. Developments over the last years now make it possibile to add on extensive computer driven VDU-sytems to the three German KONVOI NPPs (Isar II, Emsland and Neckarwestheim II) thereby creating the Process Information System "PRINS".
The new system is driven by multiple computers at different locations controlling about 30 full-graphic, high resolution Video Display Units. They are arranged singly and in three "mxn - Information Panels" distributed about the control room and present all thinkable kinds of display formats with more than 1000 separate pictures.
The display of only single "Safety Parameters" or even complete "Safety Goal Information" on single or multiple VDUs in parallel is only one aspect of this computerized part of the entire integrated Information System.

INTRODUCTION

Following the TMI accident one of the "lessons learned" resulted in the NRC requirement for computerized operator aids such as the Safety Parameter Display System to allow better accident handling in plants with old fashioned control rooms - and also for plants where only limited numbers of protective actions are automated.

For these reasons, control rooms in German plants did not require any urgent alteration or backfitting. The German Reactor Safety Commission (RSK ≙ ACRS) did, however, recommend the consideration of long-term improvements to information on saturation pressure/temperature, coolant outlet temperature, reactor vessel water level and primary system status with the aid of VDUs. Also quicker access to the contents of the Operating Manual and still higher (!) automation of protective tasks were recommended.

The plants operating in Germany already have very advanced Safety Systems and high-level intelligence Leittechnik [1, 2, 3, 4] for normal as well as accident situations.
They have human factors oriented "Kleinwartentechnik" - control rooms which feature miniaturized hardware on control panels and boards with extensive use made of mimic diagrams.

There has, nevertheless, been for many years a strong desire to optimize the information (and control) capabilities. This information capability includes the following:
- paramount plant status and trend information
- control/protection system status and action information
- transient management and optimization of operation
- maintenance monitoring and directing.

PRINS FEATURES

Ongoing developments in computer based video display systems now permit the design of an overall information system of high diversity, based on 20 years of NPP research, development and design, construction, extensive commissioning and long-term operating experience with different types of NPPs: the Process Information System (PRINS) [5].
The system consists of all information equipment already included in the "Kleinwarten type" control rooms of NPPs in operation in conjuction with a new computer driven information system with multiple Video Display Units distributed around the control room.
This new part of the system (Fig. 1) will be applied to the three KONVOI Plants Isar II, Emsland and Neckarwestheim II and to Brokdorf NPP. There are to be some simplified forerunners installed in the NPPs Biblis, Grohnde and Philippsburg II, two ofthese plants scheduled for backfitting to the same status as the KONVOI versions at a later date.

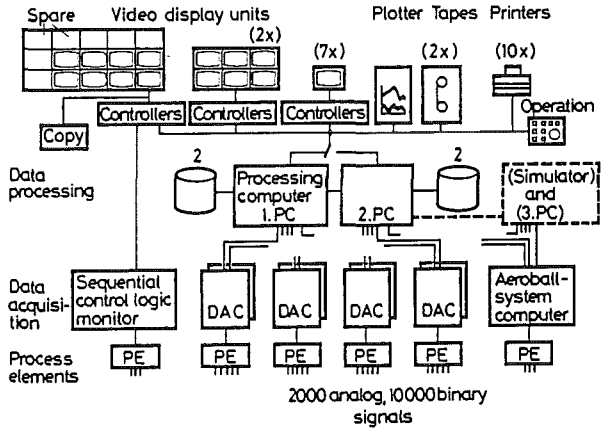

Figure 1: Computerized part of the KWU KONVOI Process Information System PRINS

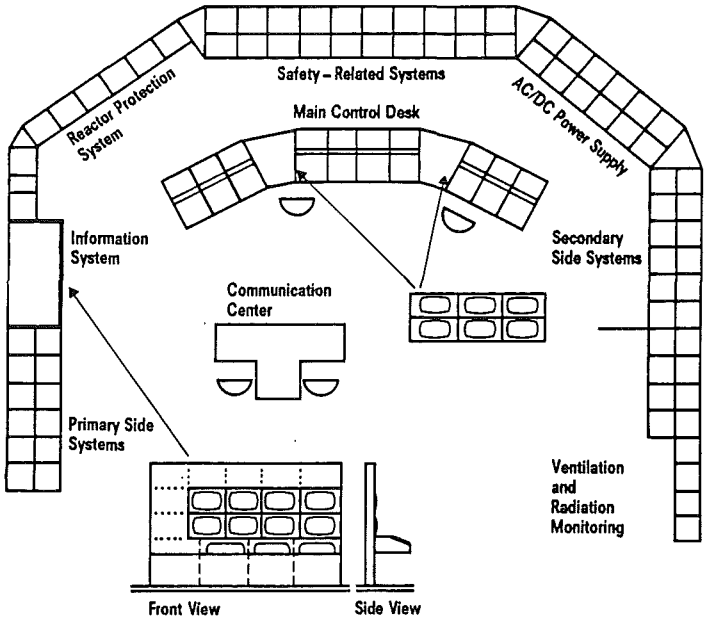

Figure 2: KWU KONVOI Main Control Room cross section

Four distributed data acquisition computers - located in the four rooms of the redundant Leittechnik equipment - sample about 2000 analog (1+5 sec scanning) and 10 000/16 000 binary (10 ms resolution) signals and transmit them all to both of the data processing computers.
These "host computers" feed 30 VDU-controllers (32 bit and with high computational capability) and a number of other recording devices.
The 30 VDUs are located in the Main Control Room (Fig. 2), either singly or in mxn-arrangements at three locations. Two of these locations are in front of the two plant operators and the third of these (with scope for extension) is to the left of the reactor operator: this is the "Information Panel".
The VDUs have full graphic features with up to 7 independent logic planes, high resolution, high repetition frequency and a refresh time of about a second. Best estimate call-up time for a format is about 2 to 3 seconds, highly sophisticated formats requiring a little longer. There are numerous display formats (Fig. 3) used to generate and store about 1000 separate pictures with widely varying complexity and content. "Single" as well as "picture group" calls together with "hierarchical" and "proximity search" capabilities permit rapid access to the most interesting picture (set) at the right moment. (Fig. 4)
The engineering and programming activities for this system have already taken and still will take several hundred man-years. Simulator based qualification and plant operation will need further work and shall contribute to the perfection of the system which is designed to be highly flexible so as to allow for changes and extensions and also for backfitting of simplified versions to plants already in operation.

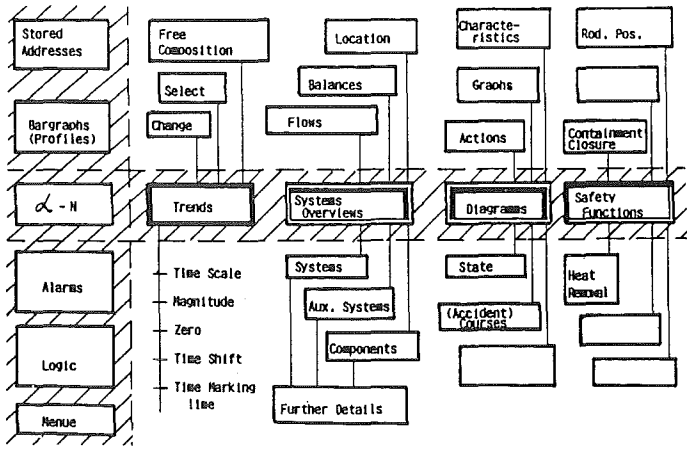

Figure 3: KWU - KONVOI - PRINS Display Formats

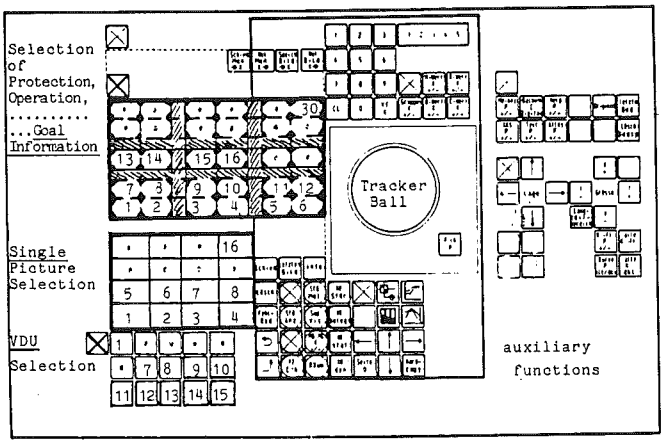

Figure 4: First proposal for the KWU KONVOI PRINS keyboard

PRINS SPECIAL DISPLAY FEATURES

A number of essential differences between PRINS and previous systems follow, together with the main system properties:

- minimization of alphanumeric information by transforming this into pictorial display formats up to a high abstraction level
- display of several formats in parallel to form superpictures or arrays of different formats (e. g. trend logs displayed vertically using VDU columns, overviews with related detail information,system pictures to complement logic or trend logs
- sufficient space available for monitoring of different complexes by using more than one display unit for information and easy shifting of important information to prefered locations and of unimportant information to "parking positions"
- possibility of high abstraction levels for display formats for expert use and interpretation as well as system and equipment oriented information levels for operators or maintenance specialists.
- mini-picture menues (pictograms) displayed to assist in the selection of further helpful information
- the full extent of plant information is used for all kinds of overview or detail formats
- large computational capacity for preprocessing and signal reduction as well as iteration for strategy optimization

OPERATIONAL TASKS OF PRINS

The flexibility and scope of the PRINS allows experts as well as the operators to perform the following tasks in an adequate manner:

1. optimum plant operation
   - optimizing efficiency by parametric studies
   - minimizing the severity of operational transients and scheduled changes
   - generating data for later analysis of experience gained

2. monitoring status and trend of systems and components to detect small deviations at an early stage (and thereby prevent these deviations from increasing in size) by:
   - comparison of redundant information
   - verification of consistency in complementary information
   - monitoring of overview and detail information at the same time and for different locations (e.g. during tests and maintenance work).
   - comparing information at different levels of abstraction
3. to alert operators to increasing abormalities by providing mini picture menues (pictogram sets) to assist in rapid and uncomplicated selection of more relevant formats or format arrays (displaying possible complementary information so as to give the required information scope).

4. to be guided by adequate display of the relevant parts of the operating manual, continuously updated with actual plant data and intentionally reduced to the extent which is of interest in the present state of the plant:
   - control and safety system functions in power operation
   - safety functions secured and/or protective goals reached with considered allocation of appropriate priority levels (set of formats)
   - well-known operational occurrences identified and displayed
   - proposals for alternative strategies with manual actions in operational or accident situations (including communication for external help) made by showing different possibilities for how to proceed (success paths).

SAFETY PARAMETER DISPLAY FUNCTIONS

Bearing all the above features of PRINS in mind, it is evident that it is an ideal system for displaying the status of "Safety Parameters" or even complete information on how to reach and observe "Safety Goals", particularly during such accident handling which can only be taught by theoretical training or training on simulators:
Here the entire concept of accident handling is of importance!

In KWU NPPs highly automated and reliable mechanical and Leittechnik systems first transfer to and hold the plant in a safe status in the case of design basis events and accidents. Increasing deviations from normal status first activate the optimized automatic Controls, then the more reliable Limitations - with their early and soft but intelligent countermeasures - and finally the Protection and Safety Systems - with their simple but very higly reliable measures.
There is a 30 min time limit specified for these automatic actions in severe accidents (and in most cases the measures are even valid for a number of hours). This means that the operating crew has time to make long-term decisions - and to take external advise where necessary.
But there are no objections to act earlier - if the crew is very sure to be on the "right way". For in our opinion sophisticated information systems of the PRINS type make it possible to reduce the length of the above mentioned automatic accident handling period in a number of cases. This can, however, not be interpreted as a requirement nor does it imply that further operator aids, such as computer driven pictorial information, have no advantages or are of no assistance.
On the contrary, additional systems are extremely effective!
The basis of the recommended strategy for accident handling laid down in the Operating Manual is as follows: supervision of performance of the automatic actions at first, followed by monitoring of about 10 "Safety Goals" (a specified fraction of the total of about 100 "Information Goals")and finally deciding the necessary manual actions with careful consideration of the feedback effects of these.
"Safety Goals" are here understood as tasks which must be sustained for plant compliance with basic safety criteria. They are not event or accident-specific. The information for one safety goal may be displayed by between one and eight Pictures. Here the benefit of an integrated Info-System is obvious, as this not only shows the ultimate permitted limit, but also has the capability and space to show trends, margins to limits, priority of conflicting parameter combinations and also to display diverse information about the same event. A further feature here is that this system is not restricted to use in accident situations: during normal operation plant surveillance and operational aids train the operating crew and inform them about and familiarize them with the system .

INFORMATION EXAMPLES

KWU specialists in conjuction with customer personnel have specified about one hundred "Information Goals" across the entire plant and for all occasions. These include the "Safety Goals" mentioned previously.
Each of these goals gives paramount information about its special aspects. It has been attempted to concentrate the information as much as possible in each VDU-format (Fig. 5-10). But there is only limited space available while keeping this information readable and easily intelligible including advice on rapid access to complementary information ("proximity search").

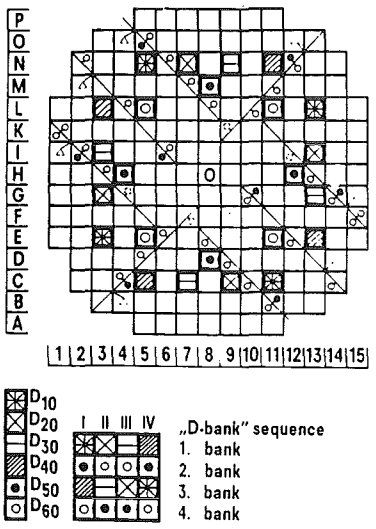

Figure 5: Core cross section showing e.g. the "D-Bank" insertion sequence.

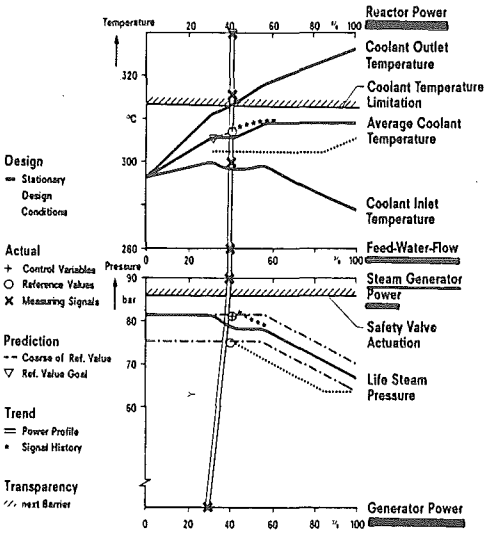

Figure 6: Actualized "Part Load Diagram" with plant power flow profile

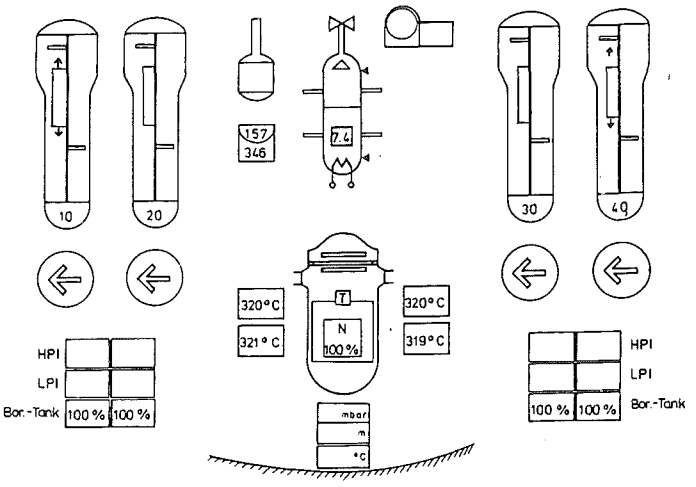

Figure 7: Coolant inventory and heat transfer information

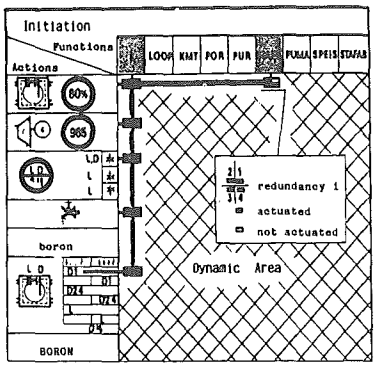

Figure 10: Dynamic Action Status of some (Reactor) Limitation Systems

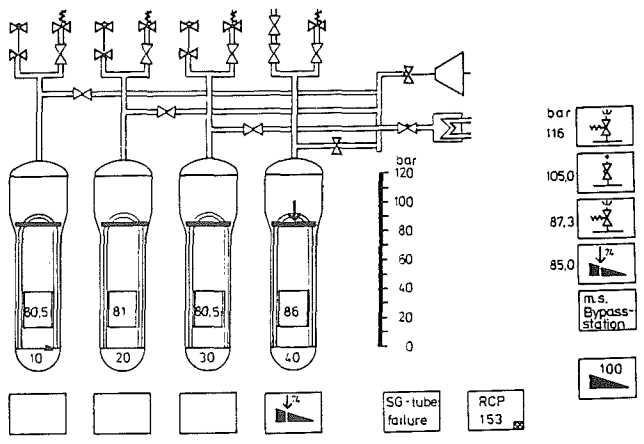

Figure 9: Information about the secondary heat sink

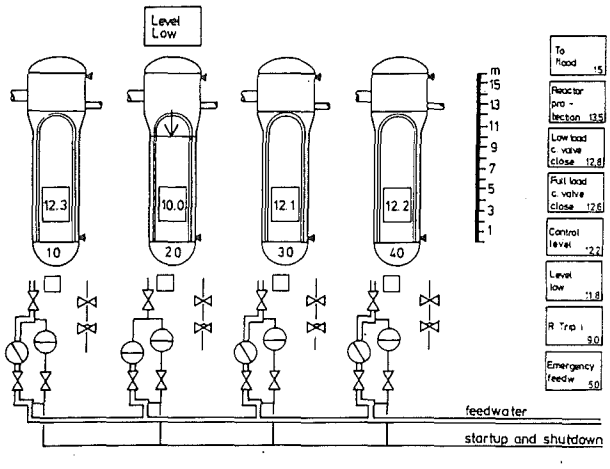

Figure 8:

Status and actions about Steam Generator Feeding

The call for presentation of an information goal is given by a functional pushbutton on the keyboard. The selected VDU then shows the one representive or the "pictogram set" for this info-goal on the selected VDU. (a possible - unrealistic - combination of a set of 8 pictures is shown in Fig. 11, another artificial (!) combination given in Fig 12).

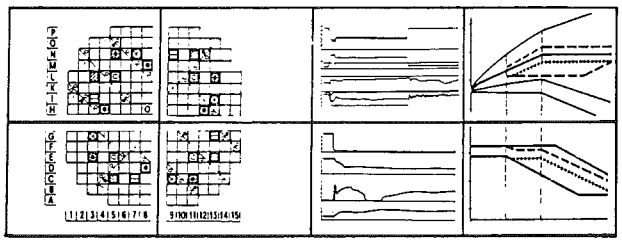

Figure 11:

Examples of "Pictogram-set proposals for certain "Information-Goals"

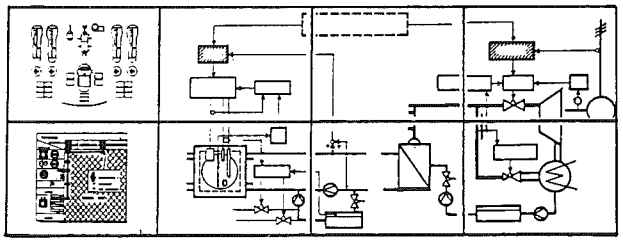

Figure 12:

The operators recognize these simplified pictograms which bear no alphanumeric descriptions (!), and they select those pictures which they think could be of assistance on free screens, arranging them in their order of selection or "shifting" them later on to match their momentary needs.
This information may also include procedural advice, displaying "success paths" with all appropriate data on actual status and associated limits, so contributing to the process of knowledge based behaviour in accidental situations as intended by the introduction of Safety Parameter Display systems.

References:

[1] ORTH, K., "Protected decay heat removal Systems", Thermal Reactor Safety (Proc. ANS/ENS Topical Meeting Knoxville, 1980).

[2] ALEITE, W., "Improved safety and availablity by limitation systems", Nuclear Power Reactor Safety (Proc. ENS/ANS Int. Topical Meeting Brussels, 1978).

[3] ALEITE, W., BOCK, H.W., FISCHER, H.D., "(Protection) limitation systems", Thermal Reactor Safety (Proc. ANS/ENS Topical Meeting Knoxville, 1980).

[4] ALEITE, W., "Defense in Depth by Leittechnique Systems with graded Intelligence" Nuclear Power Plant Control and Instrumentation (Proc. IAEA-Int. Symposium Munich, 1983).

[5] ALEITE, W., BOCK, H.W., RUBBEL, E., "Video Display Units in Nuclear Power Plant Main Control Rooms: The Process Information System KWU-PRINS". SIEMENS Research and Development Reports Vol. 13 (1984) Nr.3 Springer-Verlag 1984.

MAN-MACHINE INTERFACE ENHANCEMENT UNDERTAKEN BY EDF TO MINIMIZE HUMAN ERRORS

R. MARCILLE

Electricité de France / SPT

75384 PARIS FRANCE

ABSTRACT

The analysis of operator's behaviour during incidents has highlighted the need of improving the interface between operators and systems. EDF decided to implement in all his PWR units a safety panel to assist operating teams for : detecting the events by identification of parameters which actuated protective actions and initiated safety actions - assisting the diagnosis by selecting a procedure - assisting in application of the procedure - assisting the safety engineer to apply a state oriented supervision - giving informations to the crisis teams.

To complete the safety panel, EDF decided to improve 900 MW PWR control rooms as follows : - critical review by consultant, - test of various proposals on a full scale mock up, and operators approval, - definition of redesign principles conducting to exchange of support platen and new distribution of instruments and controls.

Such works are to be performed during refuelling outages, without extension of their duration.

INTRODUCTION

The analysis of incidents and accidents which have occurred at nuclear power plants in France and elsewhere has highlighted the need for improvements in a number of areas related to post accident operations ; for example :

- Better organization of post accident operations
- Improvement in the form and content of operating procedures
- More effective assistance for operators through the provision of safety panels
- and better control room design.

OPERATION ORGANIZATION

To understand the French Philosophy of safety panel, it's necessary to say some words about the first two topics.

Three types of actors are involved in operation organization :

- The team of operators with its shift supervisor in charge of applying procedures. They perform all the operation steps and act according to four stages :

  . Detection of events,

  . Confirmation of automatic actions,

  . Event diagnosis and selection of the procedure to be applied,

  . Application of operating procedures.

- The safety engineer, called for to the control room upon detection of an event, watches the trend of the NSSS parameters, thanks to a surveillance logic diagram independant of the event. Under definite state criteria, he can :

  . Request from operators additional actions to be performed without either disturbing or forsaking altogether the procedure under way.

  . Ask the operators to abandon the procedure under way and to apply an emergency procedure with a view to safeguard the core and limit radioactive releases through all the means at their disposal, irrespective of the future facility availability. While the operators are performing the emergency procedure, the safety engineer goes on monitoring the trend of the main parameters through specific means and according to determined criteria.

- Crisis teams, made-up of top-level specialists, they can be summoned by the plant superintendant within a few hour's time. These specialists divide into two teams :

  . A local crisis team that joins the technical support center of the damaged plant,

  . A national crisis team that convenes in Paris.

The safety panel is aimed at assisting in their tasks these three types of actors.

THE SAFETY PANEL ARCHITECTURE

The safety panel includes :

- A computer with data collection and input devices for processing and transmission to three data communication terminals for each of the three actors.

These systems are not redundant and are not indispensable to operators.

Nevertheless, two important functions are duplicated by redundant means for the operators :

- A serie of annunciators directly connected to the plant protective relay circuitry, displays the status of the main safety functions and components.

- A microprocessor directly connected to the temperature and pressure sensors indicates core outlet maximum temperature and subcooling margin.

Two terminals are located in the control room :

- one for the operators, close to the main board where the NSSS is controlled ;

- the second one for the safety engineer, deliberately located in a corner of the room because the safety engineer has not to check what the operators are doing.

SAFETY PANEL UTILIZATION BY OPERATORS

If an event occurs, the first stage for the operators is to understand : what is happening and whay is the status of the plan ?

The first goal of the safety panel is then to point out very clearly to the operators the time sequence of the failures which initiated safety actions.

Upon detection of a cause or an order for action, a picture is automatically displayed on the operator terminal.

It sets forth :

- the identification of the physical parameters, which actuated the protective action and the time of the occurrence.

- The safety action or actions initiated on each of the trains. Such picture is updated as successive protective systems are called upon.

In a second stage, the operators must check that the automatic systems have operated satisfactorily. They are helped by the previous picture which gave after a delay, the account of the right or wrong execution of each protective action.

Should the account prove fautly execution, they can call synoptic pictures of the safeguard systems on a second screen.

This picture displays : the component's position and their possible discrepancy with respect to a reference position. The operators can then try to remedy the defects in the automatic system by triggering individual actuators from the control room or by requesting local control operations to be carried out.

In the third stage, a distinctive picture set up in the form of a logic diagram helps the operators in selecting the procedure to be applied.

For each logigram test based on values of physical parameters, such assistance is implemented through proposal of an answer that the operator must validate by consulting the normal control devices. These diagrams are exactely the same as in the diagnosis procedures.

In the last stage, the operator's safety panel screens are therefore used to present displays designed to help the operators to implement the redrafted post incident procedures.

These new procedures resort to utilize some diagrams X, Y. Such diagrams are rarely used, then the safety panel assists operators by displaying pictures using the same figures as the procedures.

The display includes the current operating point as well as the position of the operating point during the previous 30 minutes and its expected position over the next ten minutes.

For exemple, the plot of pressurizer level v subcooling margin has a green zone permitting the operator to reduce safety injection and a red zone requiring safety injection to be increased.

Similar displays are available showing primary pressure v temperature permitting to cool down or to heat the primary circuit.

The safety panel aids also in the application of surveillance procedures, for instance effective core cooling through residual heat removal system.

SAFETY PANEL : UTILIZATION BY SAFETY ENGINEER

In the same way as for operators, the safety panel displays pictures in the form of logic diagrams to assist the safety engineer in performing his state oriented surveillance procedures :

- during performance of event-oriented procedures,

- during performance of the emergency procedure.

SAFETY PANEL IN THE ON-SITE TECHNICAL SUPPORT CENTER

On site, the crisis team in the technical support center has at its disposal its own safety panel terminal giving access to all the displays available on the safety engineer and operator terminals as well as a set of 40 curves giving a 30 minute time history of trends in the main NSSS parameters.

In the future it is expected that the National Technical Support Center will also have a display of the main parameters and their progress over time. This possibility is currently being investigated.

SAFETY PANEL : SCHEDULE AND VALIDATION

Tests and validation programs have been performed to verify the consistency of the logic used in the first two stages (event detection and confirmation that automatic actions have operated properly).

Further, functional validation using a simulator is scheduled for the end of 1984. This will aim to validate panel performance during the other two stages : fault diagnosis (third stage) and assistance with the application of post-incident procedures (fourth stage).

EDF's thirty-four 900 MWe PWR's and its four simulators will be equipped with the safety panels by the end of 1985. It is possible to proceed with installation of the panels before completion of the validation tests because final adjustements will essentially consist in alterations to the software. Meanwhile, operators are to be trained in post-accident operations on simulators which are to be equipped with safety panels identical to those which will be installed at the plants themselves.

CONTROL ROOM IMPROVEMENT

To complete the creation of the safety panel, EDF has undertaken a study to improve 900 MW PWR Control room.

EDF engaged a consultant to perform a general ergonomic diagnosis of the control room. This review began in October 1980 and the main results, in April 1981 were :

- No upsetting of the control room, because, in the initial lay out of the desks and boards, the standardization and functional regrouping has been complied with.
- Necessity of studying enhancements of the panels and desks to :
  - . Make easier the recognition of controls
  - . Reduce risks of mistakes
  - . Have a better relationship between controls
  - . Have a better general integration
- And for that, building a full scale mock-up permitting to submit the improvements to many operators.

In May 1982, after definition of the set of principles and rules, the mock up of the new control room was terminated and all the improvements were approved by many operators and ergonomists.

The main principles and rules observed are described now.

- The generalization of functional regrouping methodology consists in colored zones containing various functionally linked controls and instrumentation with a general title, framed by a thick line, with secondary zones framed by thinner lines, with if necessary its own title. To each functional zone one of ten colors was assigned, i.e., three shades of blue, green and beige, plus a general sand colored background. These colors do not represent any special coding system. They are intented to make it easier to distinguish one zone from the other ones.

- The functional distinctions made in the horizontal platen are carried over to the vertical platen as much as possible, by extending lines and colors, to integrate horizontal and vertical controls.
Without chart-recorders, all controls are positioned in a functional zone.

- Standardized distribution defines functional hierarchy. Direct analog controls are placed on the right and on a lower position of the analog setpoint device.
Status lights are positioned up and near the associated switches. Controls relative to situation risk are positioned in the upper part of the plates.

- The shape and size coding defines control function

  . Pumps, air-compressors, fans, that is to say all running machines have round labels.

  . Valves have rectangular labels.

- The label's color are green and orange for safety train A and B and white for non-safety train A.

- Inside some functional colored zones, to improve relationship between controls, the controls are placed as a mimic in the good positions "open" or "run". To improve the functional understanding of the system, some grey symbols are included in the mimic. These symbols figure passive components like tanks and heaters.

- To have a better understanding of the labels, we limit the number of words used as strictly necessary, sometimes no word is necessary on a control label because the title of the zone is self supporting.

Applying such principles requies the shifting of the components, essentially within the same platen and, consequently, the removal of all the components, exchange of support plate and new installation of the components.

Such works are to be performed during planned shutdowns for refuelling without extension of their duration. For that purpose, a strict scheduling must be worked out to prioritize modifications of platens, according to the status of the unit and the technical specifications.

A module remains inoperable from the start of the work and till the mandatory requalifications of its last components have been completed.

For each platen, the modification implementation is recorded in a document including :

- Functional contrainsts of each of the systems pertaining to it.

- Provisional operating instructions used as substitutes to the normal ones while the platen is out of service.

- The procedure of requalification for all the components, standard procedures for the components to be found in great number, particular procedure specific to each particular component.

It took four weeks to carry out the first modification on Unit 3 of DAMPIERRE Nuclear Plant, with complete fuel unloading in August 1983.

It took only ten days to carry out the second modification on Unit 4 of the same plant, in April 1984.

Planned modifications will affect :

- In 1984 : 4 units in operation, one simulator, 4 units under construction.

- In 1985 and 1986 : 8 units in operation and one simulator.

- and in 1987, the last 4 units in operation and the last simulator.

INTERNATIONAL RESEARCH AND INFORMATION DISSEMINATION IN THE FIELD OF HUMAN FACTORS OF NUCLEAR POWER

Part 1: NORDIC COOPERATION IN THE FIELD OF HUMAN RELIABILITY

Björn Wahlström

Technical Research Centre of Finland
Electrical Engineering Laboratory
Espoo, Finland

ABSTRACT

The safety of nuclear power is in many way relying on the condition that human actions are carried through timely and without errors. Investigations indicate that human errors are the main, or an important contributing cause, for more than half of the incidents occurring. This fact makes it important to try to understand the mechanisms behind the human errors and to investigate possibilities for decreasing their likelihood. A Nordic cooperation was started 1977 in this field and the present phase of the project will be completed in 1985. The work is divided into the following fields

- human reliability in test and maintenance
- safety oriented work organizations
- design of information and control systems
- new approaches for information presentation
- experimental validation of man-machine interfaces
- planning and evaluation of operator training

In the paper a brief description of the project is given and some preliminary results are presented in more detail.

1. INTRODUCTION

Extended Nordic cooperation was started in 1977 in the field of nuclear safety. This cooperation is partly financed from project funds of the Nordic Council of Ministers and partly from national funds in Denmark, Finland, Norway and Sweden. The safety programme was originally divided into five program areas of which one was Human reliability. The first phase of the program was finished in 1981 and was followed up with a second phase which is due for completion in 1985.

The first phase (cf./1/) of the work was divided into the following projects

- a system and job analysis
- control room design
- human reliability
- operator training

The second phase is based on the findings of the first phase, however some of the investigations are carried through into more detail. The findings included the following:

- Human errors committed outside the control room have a large share as causes for unsafe conditions at nuclear power plants. Errors made during test and calibration activities can also introduce common mode failures in cases where several redundant systems are made unoperational at the same time.
- Another important cause for common mode failures could be the work organization when routines are badly structured or have been allowed to deteriorate. Maintaining the efficiency of a safety oriented organization for handling safety threats is thus a challenge for the nuclear industry.
- The design process leading to an automation concept for a nuclear power plant and to the lay-out of the control room is an important phase. Errors made in this process can cause serious deficiencies in the man-machine interface. The management of the design process and the use of computer aided design methods have potential benefits for improving the quality of design.
- The present methods for information presentation in the control rooms of nuclear power plants are based on conventional approaches regardless of the used technology. The advent of cost efficient computers makes it however possible to base the man-machine interface on completely new approaches.
- It is necessary to validate experimentally the systems proposed for the man-machine interface in nuclear power plants before they are ready for full scale implementations. The problems are then to establish the performance measures and to collect and analyze the data from the experiments.
- Human error data can be collected during simulator training and that information can be used to improve the feedback given to the trainees. In addition the diagnosing of complicated transients is a critical task influencing the safety of a nuclear power plant and is therefore a task to which emphasis should be given during the training.

2. PRELIMINARY RESULTS FROM THE CURRENT NORDIC PROJECT

2.1 TEST AND MAINTENANCE ACTIVITIES

The goal of the project was to investigate the possibilities
- to select an optimal test interval for standby components
- to identify important risk contributions of human errors during test and calibration.

Detailed descriptions of actual test and maintenance practices and of ten selected incidents have been worked out as a part of the project.

The results indicate that there is a risk of decreased availability for standby systems as a consequence of a too frequent testing /2/. There also seems to be need for tests aimed at a more accurate identification of different time dependent fault mechanisms.

The work on test and maintenance is also concerned with:
- relationships between probabilistic risk assessment (PRA) and risk

management - i.e., which human risk contributions can be expected to be covered by a pre-construction PRA as well as which contributions will have to fall under a risk management (RM) program during the operational phase of the plant. This creates the need for a well-documented PRA for use during RM.
- deriving requirements for and developing tools for the identification of potential human risk contributions. For well-structured activities - such as test and calibration - the Work Analysis /3/ method was generated and used.
- providing aids for risk management in the form of systematic post-event analyses of incidents involving human malfunctions as a feedback mechanism from actual operating experience.

2.2 WORK ORGANIZATION

The goal of the project has been to develop an understanding of how the work organization will influence the safety of a nuclear power plant. The subproject has been divided into the following main tasks

- the establishment of an organizational theory
- collection of case stories
- development of checklists for the search for organizational deficiencies.

The basis resources of an organization are the value system, the decision making and executive system, and the information system (cf. /4/. The value system has an influence both on how the organization is prioritizing different goals and on how the individuals are responding to those goals. Many of the human erros made in connection with power plant operation can be shown to be due to organizational deficiencies. An important class of the organizational deficiencies are associated to different limitations in the information system. The checklist developed are intended to make it possible for the organization to maintain its efficiency by a regular review of organizational factors.

2.3 THE DESIGN PROCESS

The goal of the project is to assess how the design quality could be improved and how computers could be used as design aids. The project is divided into the following tasks

- an assessment of present design practices
- the conceptualization of an idealized design process
- assessment of the use of computer aided design methods
- implementation of a demonstration system

The reults indicate several benefits from the use of computers during the design process for the construction and verification of the design data base (cf. /5/). The computerized methods should certainly be used for all new designs, and it seems even beneficial to computerize parts of the design data base as a retrofitting for old plants. The project also is investigating the flow of information during the design process i.e. when and by whom it will be generated and who will be using it. In documenting the design it is important

to describe the link between the requirements and the technical solutions.

2.4 COMPUTERIZED OPERATOR SUPPORT

The goal of project is to establish a basis for the design of computer-based decision aids for supporting the monitoring and supervisory control of complex technical systems such as nuclear power plants, chemical plants, etc.

At the conceptual level, work is being carried out on the establishment of a design and evaluation basis for the allocation of the decision tasks between the operating staff and the computer - especially in situations that affect availability and safety. This requires studies of the strategies as well as structure and forms of knowledge utilized by the operators in coping with the system.

On the experimental side, the Generic Nuclear Plant (GNP) /6/ facility has been created to carry out experiments related to these conceptul problems. One of the areas dealt with is the assessment of a display approach utilizing mass and energy pictures based on a multilevel flow modelling (MFM) method /7/. This results in a consistent functional representation of the plant and, among other things, leads to a systematic identification of control tasks, information requirements, etc.

2.5 EXPERIMENTAL VALIDATION

The goal of the project is to use simulators in order to access different proposals for suggested man-machine interfaces.

The validation of new solutions for man-machine interfaces has to rely on a careful design of experiments. It was thus necessary to develop experimental methods and experimental equipment as a part of the project. The following four phases should therefore included:

- analysis of proposed concepts and definition of performance measures
- training of persons for the experiment
- experimentation and data collection
- analysis of collected data

The results indicate that the analysis of data may become very time consuming and efforts should therefore be made to analyse tha raw data by means of computers. The approach in using the multilevel flow models has been assessed as a part of the project /8/.

2.6 OPERATOR TRAINING

The goals of the project is to develop methods for

- collection of data on human errors during

simulator training
- training for diagnosing complicated events.

The full scope training simulators in Finland and Sweden will be used during the project.

Results indicate that it is possible to collect data on human errors committed in the control room and their causes. The method also has the benefit of providing additional training feed back to the trainees.

Diagnosing of plant events is very complicated task. Results from experiments indicates that different fault finding strategies are utilized in different situations. The teaching of explicit search rules for identifying faults has a potential for improving diagnosing performance. The project is also trying to identify such rules as they are used by skilled operators.

3. CONCLUSIONS

The Nordic cooperation in the human reliability field is presently in its final reporting phase. When it has been completed a total of about 40 persons years will have been spent on the projects.

The results will point the way to improving the human factors aspects associated with the various phases of a nuclear plants life cycle i.e. design, operation, maintenance, modification etc. The final reports of the projects will be available from the participating organizations

- Risø National Laboratory, Roskilde, Denmark
- Technical Research Centre of Finland, Espoo, Finland
- Institute for Energy Technology, Halden, Norway
- Swedish State Power Board, Stockholm, Sweden
- Swedish Nuclear Power Inspectorate, Stockholm, Sweden.

REFERENCES

/1/ B. Wahlström, J. Rasmussen: Noredic cooperation in the field of human factors in nuclear power plants IAEA-CN-42/247, Nuclear Power Experience, IAEA Vienna 1983.

/2/ L. Norros, B. Wahlström: Human errors in ensuring the operability of standby systems; a working paper based on a study of diesel generator failures, VTT Research Notes, to appear 1984.

/3/ J. Rasmussen, O.M. Pedersen: Formalized search strategies for human risk contributions, RISØ-M-2351, Risø National Laboratory, July 1982.

/4/ J. Lindqvist, B. Rydnest, B. Stene: Safety oriented organization and human reliability, First international symposium on human factors in organizational design and management, 21. - 24.8.1984, Honolulu.

/5/ R. Heinonen, J. Ranta, B. Wahlström: A conceptual framework for the design of complex automation systems, IFAC 9th World Congress, Budapest, 1984.

/6/ M. Lind: GNP-a power plant model for man-machine experiments RISØ N-23-82, Risø National Laboratory, 1982.

/7/ M. Lind: Some experiences in application of the multilevel flow modelling method RISØ N-12-83, Risø National Laboratory, June 1983.

/8/ E. Hollnagel, G. Hunt, N. Praetorius, S. Yoshimura: Report from the pilot experiment on multilevel flow modelling displays using the GNP-simulator, HWR-114, OECD Halden Reactor Project, February 1984.

Part 2: RECENT DEVELOPMENT IN DESIGNING AND VALIDATING EMERGENCY OPERATING PROCEDURES AND TRAINING OPERATORS IN THEIR USE

G. Mancini, Joint Research Centre CEC,
Ispra, Italy

B. Wahlström, Tecnical Research Centre of
Finland, Espoo, Finland

On behalf of the NEA/CSNI Principal Working Group on
Operating Experience and Human Factors.

ABSTRACT

The written control room procedures used during nuclear power plant operation is one of important component contributing to the safety of the plant. The approach for the emergency operating procedures (EOPs) has until recently been to write detailed procedures for a number of events. This event-oriented approach has however its drawbacks and new approaches have been suggested. The paper describes a survey of approaches to EOPs used in different NEA countries, prepared by the CSNI PWG on operating experience and human factors.

INTRODUCTION

Operator actions during a reactor incident can be decisive to regaining control of the plant, or to minimizing any consequent damage and risk to the public. In recent years, with the increasing recognition of the importance of the human factor in safety, the content and form of the procedures provided to operators to cope with emergency situations have come under increasing scrutiny.

The content of the procedures relies on the best estimate for how the plant will behave under adverse conditions and the difficulty is then to write procedures which are applicable to all the situations relevant. The form of the procedures, their layout and readability are also important because such factors will influence the way they are used by the operators.

This paper describes a recent review of various new approaches being considered to the design and validation of emergency operating procedures (EOPs), and to training operators in making the best possible use of them. The study was conducted by a special NEA Task Force of experts, which was set up early in 1983 under CSNI Principal Working Group No. 1 (Operating Experience and Human Factors). In 1983 the Task Force compiled and assessed descriptions of EOP-related practices in eleven NEA countries: Belgium, Finland, France, Federal Republic of Germany, Italy, Japan, Netherlands, Spain, Sweden, United

Kingdom and United States. The study showed up the particular importance of several factors in procedure design, in particular the significant additional guidance provided by new types of procedures keyed to accident symptoms, critical safety functions or operating conditions rather than simply specific sequences of events. Additional conclusions from this review are described in the following sections.

COMPARATIVE ANALYSIS OF THE CURRENT FORM AND USE OF EOPs

For most countries, it is impossible to identify one unique "national" philosophy underlying the design and intended use of EOPs,as several reactor types are used, which are supplied by different vendors and exploited by different utilities. The Task Force nonetheless tried to identify some important features in the various EOP approaches developed recently.

Recent guides for EOP preparation exist (or are in preparation) in several countries. A number of quidelines have been published in both France and the United States. Generic technical guidelines are also being developed by Nuclear Steam Supply System (NSSS) vendors and owners' groups. Utilities in Spain, Sweden, Netherlands, Belgium and Japan tend to use NSSS vendors' guidelines, when applicable.

Operating procedures must be authorised by licensing authorities in the Netherlands and Switzerland (at least for the most important EOPs), and in the Federal Republic of Germany. In the other nations surveyd, the writing, approval, backfitting and modification of EOPs are internal utility matters. However, the regulatory authorities must be kept informed of the most important modifications, and they can suggest changes if felt necessary. The process by which EOPs are modified generally involves different hierarchical levels, according to how important the alterations are.

VALIDATION OF CONTENT OF EOPs

In order to ensure the effectiveness of EOPs under real emergency conditions, the EOPs should be both verified and validated (that is, demonstrated not only to be free of errors, but also to accomplish the ultimate goal). In verifying and validating procedures, all other factors which can affect total preparedness for situations (e.g. organisation and training of operators, new instrumentation, etc.) should be evaluated as well as the EOP design itself.

Use of simulators seems essential in validating procedures, and should include simulation of real accidents which have occurred, two-phase thermal-hydraulics and random failures, in order to test the continued applicability of the EOP and relevance of the contingency actions. The design of experimental matrices for EOP validation (conditions on parameters under which the EOPs are tested) should also be studied for use in optimising EOPs.

Validation carried out on full scope training simulators seems to be a viable approach as reported from some of the countries. The validation of EOPs to be used in situations behind the design basis accidents (DBAs) will however require a further development of the reactor accident codes.

HUMAN FACTOR CONSIDERATION IN PREPARING EOPs

Psycholinguistic approaches and typographical arrangements are specially considered in the various guidelines for preparing EOPs mentioned above. Several principles based on human factors considerations are common to these different sets of guidelines:

- Instructions should be short and simple, with a precise use of conditional and logic statements;
- Explanations of the reasons for operator actions are not included in the EOP itself (but in associated technical background documents);
- The EOPs are sometimes presented in a multiple column format, including a column for notes and contingency actions;
- Flow charts and diagrams are used.

In most countries, computers are normally used only to record the chronological sequence of events during an emergency. No utility has introduced computer-assisted presentation of EOP text. A few advanced applications of computers are being developed, and it seems likely that the use of computers will increase in the future both for the preparation of procedures and for their presentation to the operators.

DIFFERENT APPROACHES TO EOP DESIGN

Whilst the now-classical "event-oriented" approaches to EOP design have long been used in most countries, "non-event-oriented" approaches have recently been intensively studied and developed, and are now in the process of being introduced in France and the United States. The "event-oriented" procedures are in principle written one procedure for each of the events considered. The selection of the correct procedure is usually guided by a graphic decision tree aiding the operator to diagnose the event. The "non-event-oriented" approach has been introduced as a remedy to some of the problems observed with the "event-oriented" approach.

The "non-event-oriented" approaches include the "symptom" and "function" oriented approaches developed in the United States, and the "state" approach under study in France. The classical "event-oriented" approach and the new approached can be described as

(1) event-oriented approach: at an early stage of the transient, the operators should identify what type of event has occurred on the basis of the information given by the instrument measurements and take remedial action as defined in the procedure;

(2) non-event-oriented approaches:
- symptom-oriented approach the procedure defines a set of symptoms which are an indication that something abnormal has occurred. The operator can then take remedial action according to the procedure and additional information collected without knowing exactly what type of event occurred;

- function-oriented approach the procedure defines a limited set of safety related functions (Core cooling, subcriticality etc.) which have to be maintained during the operation and how these could be restored if put in danger;

- state-approach the procedure defines a set of critical state variables and how the operators should take actions to return the plant state from an unsafe region to a more stable state.

DEFICIENCIES OF EVENT-ORIENTED PROCEDURES

It has been recognised that the event-oriented EOPs cannot fully cope with the operational needs in the case of an unforeseen incident because

- event-oriented procedures can cover only a limited number of plant malfunctions,

- human errors in diagnosing the event or controling it could render the operator stuck in an incorrect procedure.

The non-event-oriented approaches are directed to more general safety goals and could therefore cover also cases with multiple plant malfunctions. One non-event-oriented procedure is also applicable to several events which makes the practical handling of the procedures more easy. The event-oriented approach is crucially dependent on the correctness of the initial diagnose of the event. The non-event-oriented approach tends to give more guidance and time for the diagnose and the resulting procedures tend to be more robust for human errors.

The gravity in the impact of possible deficiencies of event-oriented procedures depends on the reactor type, the degree of plant automation or operation methods.

In spite of the deficiencies with the event-oriented procedures they will offer however an optimal sequence of remedial actions when the event has been diagnosed with sufficient accuracy. This will probably at least with respect to easily diagnosed events lead to some kind of mix between both approaches.

LATEST APPROACHES IN FRANCE AND THE UNITED STATES

The Task Force reviewed in some detail two newly-developed approaches to overcoming these deficiensies; the function-oriented procedures of the Westinghouse owners' group (United States), and the physical state-oriented procedures of EdF (France).

One similarity between these approaches is that efforts are being made to maintain the compatibility of new procedures with the existing EOPs, so that the new approach does not pose any drastic changes to operators' tasks. To ensure this, the existing procedures are improved, taking account of human factors, and then the new procedures based on new concepts or methods are added to extend the events which the EOPs can cope with.

The new approaches facilitate the detection of operators' errors, and also include optimal recovery actions for such errors. Operators can thus take appropriate actions for these human errors without knowing the actual causes of the event.

Whilst the objectives and the final results of approaches seem equivalent, there are important differences in the logic applied. In the Westinghouse approach, the six most significant "Critical Safety Functions" (CSFs), are monitored in sequences with the help of status trees prepared for each CSF.

On the other hand, in the French state-oriented procedures, a physical state of the plant at any time is defined in terms of a matrix of all the plant parameters being monitored and the availability of the safety system functions. Operating procedures are provided for each of these states in the matrix (called the "U1 grid"). The French approach does not specifically stipulate the contingency actions to take if additional events take place, because as the state evolves, different operating procedures corresponding to the new state are called into play. The U1 procedures are used until the plant reaches a stable state.

CONCLUSIONS

In spite of the differencies in the use of the EOPs in the different countries surveyed it seems to be a broad consensus on their importance and the main principles of their use. It is important to assess the EOPs not in isolation but as a part of the whole work situation, where the control room, staffing principles, training, other operational support and documentations also play important roles.

With respect to the development of EOPs one could note that:

- procedures are now assessed from both technical and human-factors point of view;

- the need to introduce non-event-oriented procedures is well understood; however, the necessary preliminary step to do so are not yet well established in all countries.

The approch for assessment and validation will in different countries take a course which is depending on

- used approaches for control room design (non-computer based or computer based)
- the organisation of the operating crew and their responsibilities
- the role and influence of regulatory bodies in the preparation of EOPs
- simulators available for the validation of EOPs
- used training methods for the introduction of new procedures
- new plant constructions

EOPs is continued in the next future, within the CSNI principal working group activities, by application to some real cases.

SIMULATOR MODELLING OF THE PWR

K. Hartel

Technical University of Brno
Faculty of Mechanical Engineering
Department of Thermodynamics and Nuclear Energetics
Tr. Obrancu miru 65, 662 42 Brno
Czechoslovakia

ABSTRACT

The project of the mathematical modelling of physical processes in the PWR for the 1st Czechoslovak full scope simulator of the nuclear power plant is given. The mathematical models formation issues from the formulation of basic laws and equations of nuclear physics, thermodynamics and mechanics of liquid. Numerical analysis of this problem leads to the choise of one-step explicit difference schemes for the numerical solution of differential parts of the mathematical model. The special programme system SIMULACE enables numerical simulation of plant transients in the PWR in real time including simple incorporating other simulator models of the nuclear power plant.

INTRODUCTION

The problem of the mathematical modelling of a nuclear power plant components for a full scope simulator purposes is specific by the existence of great number of physical quantities to be modelled, the requirement of modelling a wide spectrum of operational regimes and the necessity of achieving the operational level of the simulation precision at the securing of the simulation in real time.

The necessity of the full scope simulator for nuclear power plants with WWER 440 reactors in the Czechoslovakia has been given by the present state and the outlooks of the further development of the Czechoslovak nuclear power complex. Specifications of the WWER 440 reactor: thermal power 1375 MW, electrical power 440 MW, number of control rods 37, number of fuel assemblies 349, number of pins per assembly 126, concentration of fresh fuel 1.6-3.6% U 235, coolant borated water, operating pressure 12.25 MPa, coolant flow 9000 kgs^{-1}, coolant temperature at inlet 276^{o}C, coolant temperature at outlet 296^{o}C, number of circuits 6.

The 1st Czechoslovak simulator for nuclear power plants with WWER 440 reactors is built in Brno and its operating is planned in the 2nd half of 1984. Principal application spheres of this simulator are all phases of granting the operational licences to the relevant worker groups of nuclear power plants. Specifications of the computer system of that full scope simulator: 2 our own digital computers RPP 16 (main memory 128 kbyte, disk store 15 Mbyte) complimented with special analog system.

FORMATION OF THE MATHEMATICAL MODEL OF THE REACTOR

The stage of the mathematical model formation of the PWR represents the adequate application of conservation laws for mass, momentum and energy, equation of state, equations of neutron and xenon balances, initial and boundary conditions and relevant constituing relations on the problem to be solved. In a general case, is the complete mathematical model of the PWR represented by a system of nonlinear partial differential, integrodifferential and nondifferential equations and relations conditions, which must form, from the point of the solution possibility, a closed system of equations. Hence it is not real, and for the simulator requirements advantageous, to simulate numerically in real time that model of the PWR without a adequate simplification.

For our own full scope simulator the approximation of the reactor core by means of a system mutually not reacting channels appears to be sufficient with a simplified geometric configuration is used /3/. The simulation of the physical behavior of the entire reactor core is obtained by means of a suitably celected parametric calculation, related to the physical model simplified in this way.

STRUCTURE OF THE REACTOR CORE MODEL

By the application of general formulations of fundamental laws and relations of the continuum mechanics and nuclear physics on the considered physical model (a one-dimensional channel consisting of n-section), while respecting the simplifing assumptions, we can obtain the following system of equations of the mathematical model:

from the substantial form of the conservation law for mass we then have for the coolant (the index c):

$$\frac{\partial(\rho_c S_c)}{\partial \tau} + \frac{\partial G_c}{\partial z} = 0 \tag{1}$$

where ρ (kgm^{-3}) is the mass density, S (m^2) the cross section, τ (s) the time, G (kgs^{-1}) the mass flow rate, z (m) the Cartesian coordinate of the channel;

the substantial form of the conservation law for momentum leads for the coolant to:

$$\frac{\partial G_c}{\partial \tau} = \left(\sum_{j=1}^{n} \frac{l_j}{S_{c,j}}\right)^{-1} \left\{-g \sum_{j=1}^{n} \rho_{c,j} h_j + (p_{c,j} - p_{c,j+1}) - G_c^2 (\operatorname{sgn} G_c) \times \right.$$
$$\left. \times \sum_{j=1}^{n} \left[\left(\lambda_{fr,j} \frac{l_j}{d_j} + \zeta_j\right) \frac{1}{2\rho_{c,j} S_{c,j}^2}\right] - G_c^2 \frac{\mu_c}{2\rho_{c,n} S_{c,n}^2} \left[1 - \left(\frac{S_{c,n}}{S_{c,1}}\right)^2\right] \right\} \tag{2}$$

where l (m) is the lenght, h (m) the height, p (Pa) the pressure, λ_{fr} (-) the friction coefficient, d (m) the diameter, ζ (-) the coefficient of local losses, μ (-) the velocity parameter, index j is the index of the j-th channel section, n denotes the total number of channel sections;

from the conservation law for energy we obtain for the fuel (the index f):

$$\frac{\partial T_f}{\partial \tau} = \frac{1}{c_f \rho_f} \left[\operatorname{div}(\lambda_f \operatorname{grad} T_f) + q_{v,f}\right] \tag{3.1}$$

where T (K) is the temperature, c ($Jkg^{-1}K^{-1}$) the specific heat capacity, ρ (kgm^{-3}) the mass density, λ ($Wm^{-1}K^{-1}$) the termal conductivity, q_v (Wm^{-3}) the heat power source;

and then have for the coolant:

$$\frac{\partial T_c}{\partial \tau} + w_c \frac{\partial T_c}{\partial z} = \frac{1}{c_c \rho_c} \left[\operatorname{div} (\lambda_c \operatorname{grad} T_c) + q_s \frac{O_s}{S_c} \right] \tag{3.2}$$

where in addition w (ms^{-1}) is the velocity, z (m) the Cartesian coordinate of the channel, q_s (Wm^{-2}) the heat flux density to the coolant, O_s (m) the wetted circuit, S (m^2) the cross section;

the equation of state reduces for the fuel:

$$\rho_f = \text{const} \tag{4.1}$$

and gives for the coolant:

$$\rho_c = \rho_c (p_c, T_c) \tag{4.2}$$

where as function ρ_c is used the polynomical function;

the equation of the neutron balance gives:

$$\begin{aligned} \frac{dn}{d\tau} &= \frac{\varrho - \beta}{\Lambda} n + \sum_{i=1}^{m} \dot{\lambda}_i C_i \\ \frac{dC_i}{d\tau} &= \frac{\beta_i}{\Lambda} n - \dot{\lambda}_i C_i \end{aligned} \tag{5}$$

where n (m^{-3}) is the neutron density, ϱ (-) the reactivity, β (-) the portion of delayded neutrons, Λ (s) the mean time of the instantaneous neutron origin, $\dot{\lambda}$ (s^{-1}) the decay constant, C (m^{-3}) the nucleus concentration, the index i is the index of the i-th group of delayded slow neutrons, m denotes the total number of delayded neutron groups;

the equation of the xenon balance leads to:

$$\begin{aligned} \frac{dC_I}{d\tau} &= \dot{\rho}_I \Sigma_f \Phi - \dot{\lambda}_I C_I \\ \frac{dC_{Xe}}{d\tau} &= \dot{\rho}_{Xe} \Sigma_f \Phi - \dot{\lambda}_{Xe} C_{Xe} - \sigma_{Xe} \Phi C_{Xe} \end{aligned} \tag{6}$$

where $\dot{\rho}$ (-) is the relative yield, Σ_f (m^{-1}) the total macroscopic cross section for fission, Φ ($m^{-2}s^{-1}$) the particle flux density of neutrons, indexes I and Xe refer to I 135 and Xe 135;

the conditions of uniqueness:
these determine geometric, physical, initial and limiting peculiarities of the problem to be solved.

MATHEMATICAL APPROXIMATION OF THE PWR MODEL

In regard to the different character and numerical peculiarities of the mathematical model equations, the next stage of the model formation is the selection of a suitable mathematical approximation.

For energy equations of the fuel (3.1) and of the coolant (3.2), the approximation has been selected by the quasistationary method, the basic idea of which is the assumption of a weak time dependence of the space component of the thermal fields solution within a certain, limited time interval. For the modification of time depending equations of the short termed kinetics of a nuclear reactor (5), the approximation by the method of the singular pertrubation analysis has been used, which with the help of the inner and outer asymptotic solution development eliminates the numerical stiffness of the initial system of differential equations.

After the above mentioned mathematical approximations, the mathematical model of the PWR is formed by 9 submodels (Fig. 1), consisting of the sequence of differential sections (the system of linear and nonlinear ordinary differential equations of the 1st order), and nondifferential sections (the systems of algebraic relations and logic conditions).

PROGRAMME SYSTEM

Before the final classifying of formed mathematical models of individual components of the nuclear power plant (reactor, steam generator, turbine, etc.) in the software of own nuclear simulator, their accouracy is checked, and the selection of the advantageous numerical methods is carried out. For this purpose, the special programme simulation system SIMULACE has been assembled and debuged /3/, which after a simple incorporation of these mathematical models enables their real time simulation by the selected numerical method from a system of 5 programmed one-step explicite methods (the Euler's of the 1st order, the Runge-Kuttov's of the 2nd order, the Heune's of the 3rd order, the Gill's of the 4th order and the Merson's of 5th order).

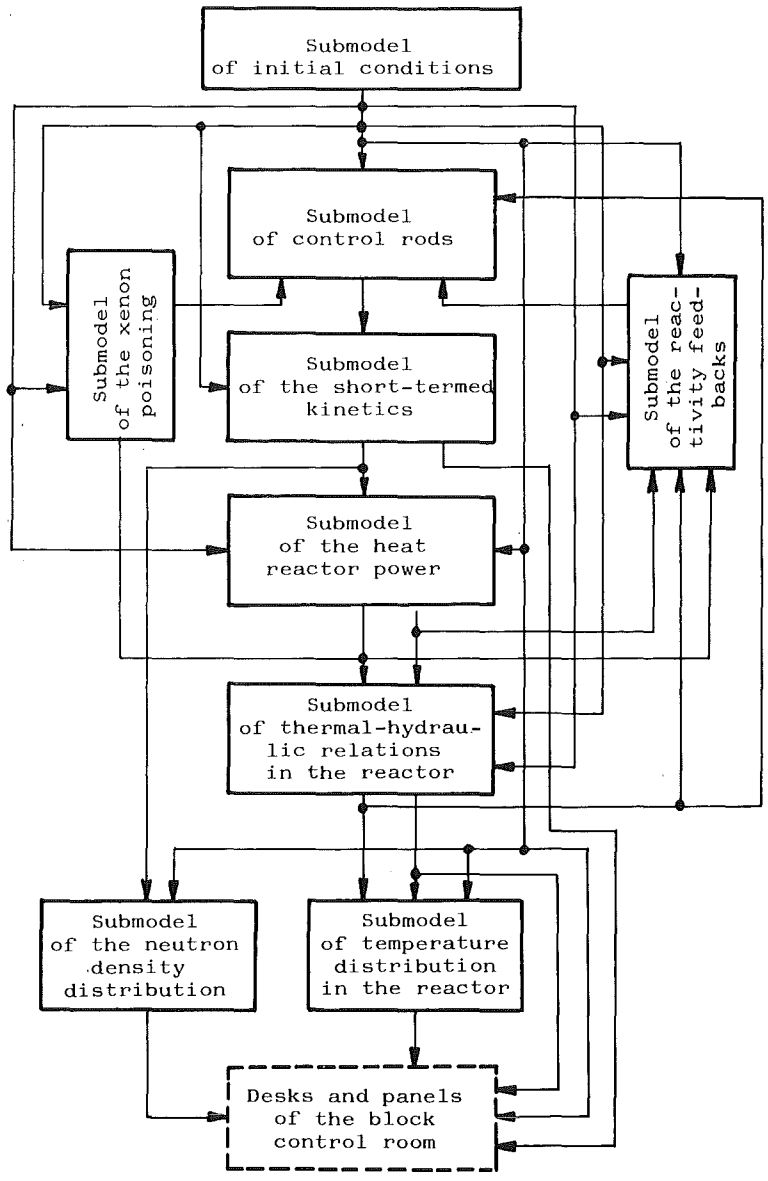

Fig. 1 Strukture of the reactor model

NUMERICAL RESULTS

The correctness selected approaches to the problems solution of the simulator mathematical modelling of anticipated and abnormal plant transients in PWRs of the type WWER 440 has been tested by the numerical simulation of 38 different, stationary and nonstationary, operational regimes. The simulation calculation was made by the Euler´s explicite metod with the different steps of the numerical integration of differential parts of individual mathematical submodels.

The results of the numerical simulation of one group of nonstationary operational regimes, caused by the failures of the main circulation pumps with the subsequent operation of the automatic reactor power regulator are enclosed in Fig. 2 and Fig. 3. Values of represented parameters of the reactor are relatived to the nominal parameters. Used symbols: N_R the heat power, G_c the mass flow rate, t_{c1} the coolant temperature at inlet, t_{c2} the coolant temperature at outlet, p_{c2} the coolant pressure at outlet, the index 0 refers to nominal value of the parameter.

CONCLUSIONS

The carried out comparison of obtained results to the experimental results accomplished at the nuclear power plant V1 at Jaslovske Bohunice /4/ and 3-D calculations for the nuclear power plant V2 /6/ have shown for the full scope simulator purposes the sufficient agreement of the reactor fundamental parameters, whilst achieving simultaneously the simulation in the real time (the time factor of about 0.3).

The profound theoretical analysis of the solved problems enables realisation of the full scope nuclear simulator on the available computer equipment.

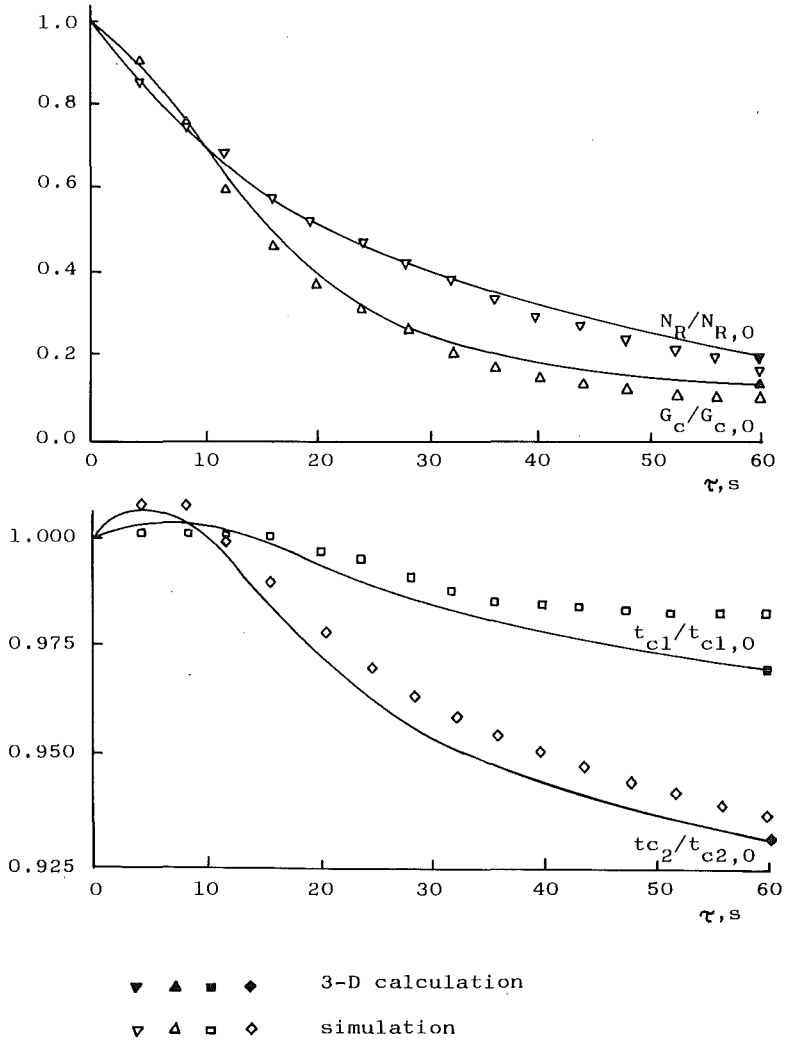

Fig. 2 Results of the plant transient simulation in the PWR of the type WWER 440 - failure of all circulation pumps with the subsequent operation of the automatic reactor power regulator

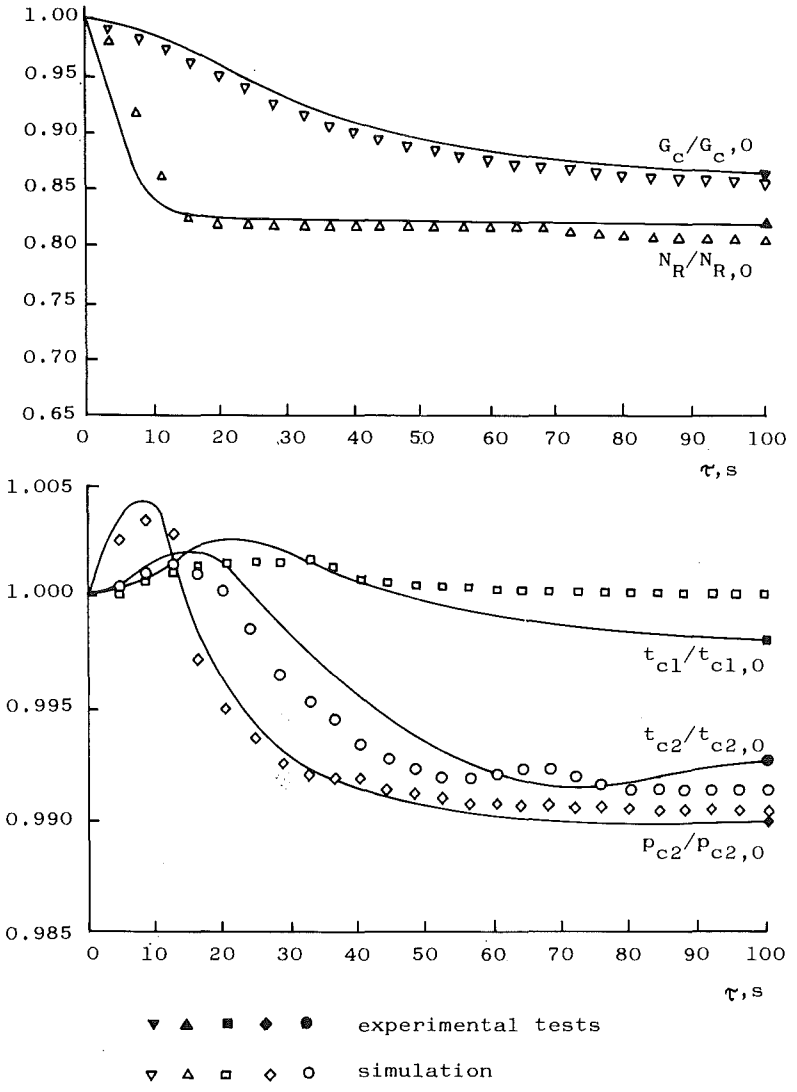

Fig. 3 Results of the plant transients simulation in the PWR of the type WWER 440 - failure of one circulation pump with the subsequent operation of the automatic reactor power regulator

REFERENCES

/1/ I. M. Berman, Power Plant Simulators and Operator Training, Power Engineering, Vol.85, No.1, (1981).

/2/ H. Finnemann and W. Gundlach, Space-time kinetics code IQSBOX for PWR and BWR, Atomkernenergie, Vol.37, No.3, (1981).

/3/ K. Hartel, Mathematical Modelling Physical Processes in Nuclear Reactors, Report T.U. Brno, in Czech, (1982).

/4/ S. Kacmary, J. Ricany, Experiences from the Energy Rise od the 1st and 2nd Bloocks of the Nuclear Power Plant V1, Report VUJE, in Czech, (1980).

/5/ Relap4/Mod5 - A computer Code Program for Transient Thermal--Hydraulic Analysis of Nuclear Reactors and Related System, ANCR-NUREG-1335, (1976).

/6/ Safety report for the Nuclear Power Plant V2, Report EGU Prag, in Czech, (1979).

/7/ Y. Zvirin, Experimental and Analytical Investigation of a PWR Natural Circulation Loop, EPRINT-1364-SR, (1980).

SIMULATION FOR NUCLEAR REACTOR TECHNOLOGY

J.D.Lewins

University of Cambridge
Cambridge CB4 1PZ, England

ABSTRACT

Rapid developments in digital computers have allowed nuclear reactor simulators to take an important role in the nuclear power design and operating industry. The Cambridge international meeting on nuclear reactor simulators clarified national attitudes to simulator use in areas of design, training, accident study and licensing. Papers given to the meeting were useful in making a first approach to a philosophy for the methododlogy of simulator design and their verification and validation.

INTRODUCTION

The Institution of Nuclear Engineers organised an international conference entitled Simulation for Nuclear Reactor Technology at Cambridge, 9-11 April 1984. It was attended by over 150 specialists for many countries and the material covered in the four sessions will be of interest to those concerned with thermal reactor safety in many aspects.

REACTOR DESIGN AND ANALYSIS

The simulation of reactors for design purposes has gone beyond the original concept of static reactor physics coupled with elementary neutron kinetics, to a full-scope simulation of reactors so as to display their dynamic behaviour. At first sight, there is a difference of requirement between the present United Kingdom single-phase gas-cooled reactors and the greater challenge of LWRs with their emphasis on two-phase flow. Dr Wulff and his co-authors from the US Brookhaven Laboratory outlined their special simulation developments on the AD10 processor for BWR technology and A.D.Alley and co-workers from General Electric offered similar insights into the Liquid Metal dynamic simulators. Yet it was clear that the difference between such studies and simulation in gas-cooled systems is actually less marked since the latter, being steam-raising plant, imply that the simulation of boiler dynamics is as much a part of the overall plant representation as the reactor core. What was interesting then in Professor Jeffries' case study of boiler dynamics was the illustration of a different approach to two-phase flow problems using a linearized technique and employing the United Kingdom (UK) Central Electricity Generating Board (CEGB) suite of programs, DYMEL.

Two further papers in this session dealt with the problem of two-phase flow simulation. The first was from Belgium's Mol Centre, with de Greef giving an efficient description of both pressurizer and heat exchanger of a PWR in terms of their common-form equations. The second was one of a pair of papers from Canada on the PHWR-CANDU system in which Dr Kahn described the simulation

study, rig verification and design changes brought about in the 660 MW(e) design. The simulation study revealed an unexpected coolant oscillation, with potential consequences of downgrading reactor power. An experimental rig confirmed both the problem and the efficacy of the design modification to correct the situation. It was brought out in the discussion of this paper how difficult it had been to convince management of the seriousness of the simulation study when analysis by existing codes had apparently not shown any such divergent oscillations. It was a human part of the story to hear that previous studies had indeed predicted such oscillations but these had been attributed to "machine error" and patched out of the programs. When the analyst has justifiable and sufficient faith in his programs to reject such a "fix", we can indeed say that simulation for design and analysis has come of age.

Underlying the particular illustrations of reactor design simulation, valuable as they were, is a more difficult question of the purpose of such simulation and the methodology by which a simulator might be verified and accepted. Such questions were addressed again during the conference and in relation to accident studies and the philosophy of training.

TRAINING AND OPERATIONS

Dr Stammers, an industrial pyschologist, set the scene for a study of simulators in training and operations. He pointed out that it is as important to study the effectiveness of simulators for their psychological role as their physical accuracy. The point was further illustrated by papers from the head of the CEGB Nuclear Power Training Centre (Peter Myerscough), a paper by Scoland of the Westinghouse Corporation (presented by Walsh) and by M.Felignes from Electricité de France. It is evident that all utilities now see a major role for full-scope simulators in training although some variance remains in respect of a different emphasis on plant specific and plant generic models.

This difference, between specific or generic, was tackled several times in the meeting. Part of such discussion showed that there was considerably more PWR operating experience originating in the UK than the role of the Sizewell Inquiry into the proposed first CEGB PWR might suggest, in that the Royal Navy has experience of operating some 20 small PWR submarines and indeed was able to contribute considerably to the meeting in respect of training based upon simulators.

A reflective and philosophical paper, pointing out a number of weaknesses in so-called full-scope simulators, was given by Eugene Thames. He contrasted the nature of the TMI-II accident with its long-term development over a critical period of at least 48 hours with the limited ability of present simulators to do more than illustrate a specific accident condition and the immediate action that operators might take to correct for it. In reality, accidents of a serious nature can have long and slow developing histories. Thames asked the critical question, whether such a training of operators in unreal simulated conditions was satisfactory.

A paper from the CEGB's Wylfa station (the largest commissioned Magnox reactor) discussed a special purpose simulator and its role in providing for the correct choice of emergency cooling.

SIMULATION METHODS, LANGUAGES AND TECHNIQUES

In one sense, the conference had already focussed on an underlying technical problem, the simulation of two-phase flow. Papers on the second day brought attention to another problem: the difficulty of securing stable numerical behaviour over adequate time intervals arising from the "stiff" nature of the coupling of the various physical components from prompt neutron behaviour to slow graphite temperature transients.

Budd's paper from the CEGB gave a practical solution to this problem in what he called "local eigenvalue protection" though this approach was not without dispute. Two interesting papers from Scotland (where the South of Scotland Electricity Board is commissioning the Hunterston-B AGR with a full-scope simulator) carried solutions to these problems through to a working result.

We were also able to hear of applications of simulators to assist operations, in Dr Horne's paper on the essential systems integrity monitor and an account of Finnish work by Hanninen and Miettinen for primary circuit accidents in a training reactor.

General discussion in the Conference raised two points in which national practices differed. There was some puzzlement from North America that UK practioners should not use modern purpose-written simulator languages for digital computing work but expressed a preference for FORTRAN. The UK philosophy seemed to put more emphasis on the need to maintain the program during the necessary plant life of the simulator (say up to 40 years for the station it represents) and the need for clear structure in the programming. Surely this is true, in the sense that CPU power and computer speed are unlikely to be overriding limitations as the years bring further rapid advances in computer hardware. Good programming in this context is far more a matter of good structure, to make it apparent what the program is actually doing, than clever tricks to speed the simulation.

Both sides, however, accepted the desirability of using fundamental physics rather than empirical fitting, particularly where the simulator is to be used to extrapolate into unverifiable accident conditions. There was much less agreement on the methodology of validation for full-scope simualtors. Essentially, one must ask what the purpose of the simulator is. Is it then proper to represent a "best estimate" model and determine how the reactor will most probably behave in an accident, or to employ what might be called a "best accident" model to include pessimism that allows for the dangerous accident to be that which departs from "best estimate" behaviour?

FUTURE OF NUCLEAR REACTOR SIMULATION

Discussion was stimulated by Wachtel's paper, giving the US Nuclear Regulatory Commission's view of developments of the role of simulators in licensing. The first thing we have to absorb is that the purpose of such simulators is, now, not training but operator licensing. Wachtel anticipated that in about three years it would be mandatory to test a reactor operator on a simulator, but he was careful to avoid the term "plant-specific" and used "plant-referenced" instead; no one can build a lawyer-proof 'one-to-one' scale simulator.

CONCLUSION

Major points that arose from the meeting included: firstly, the need to identify the purpose of the simulator and, in many cases, the lack of critical study of whether existing simulators met such a specific purpose. Secondly, there was the challenging problem of two-phase flow simulation with its continuing basis of empiricism in heat-transfer correlations. There remained a divergence of views on how to deal with "stiffness" in speeding machine convergence and an even bigger uncertainty in just how to go about verification and validation of simulators. It remained an unanswered question perhaps, what objective criteria can be written into a purchasing contract.

Proceedings of the Conference (ISBN 0 521 27785 4) are published by the Cambridge University Press for the Institution of Nuclear Engineers (ed D.G.Walton).

EMERGENCY PLANNING AND PREPAREDNESS IN EC COUNTRIES

T. Eckered

Nuclear Safety Board of the Swedish Utilities
Box 5864 S-102 48 STOCKHOLM Sweden

W. Essler

Commission of the European Communities
Rue de la Loi 200 B-1049 BRUSSELS Belgium

ABSTRACT

The TMI-2 accident in March 1979 became a starting point for a reconsidering of the levels of ambition for Emergency Planning and Preparedness (EPP) in many countries. At the same time that accident lead to new and deepened studies of the basis for accident analyses and for emergency preparedness.

Many existing or planned EPP measures are based on assumptions concerning accident sequences, release of radioactivity and accident consequences which in many cases are far too pessimistic. A higher level of ambition for EPP measures based on these assumptions does therefore not seem to be justified.

The present criteria and practices for EPP in the EC countries have recently been brought together in studies made (or under preparation) for the Commission of the European Community. Some results of these studies will be presented and proposals will be given for a harmonized approach to EPP, with special attention to the needs of EC countries.

INTRODUCTION

In many countries the accident at the TMI-2 reactor at the end of March 1979 became a starting point for studies and action in the area of Emergency Planning and Preparedness. Mostly, safety authorities started to question the efficiency and appropriateness of the existing measures but at the same time as the TMI-2 accident underlined the need for revisions of procedures for Emergency Planning and Preparedness (EPP) it also created a new basis of knowledge for judging what EPP were needed. Unfortunately, the new information and knowledge have emerged slower than the need for it. The pressure for improvement of EPP, which was both a technical and a political pressure, came so soon that the new information which should be the basis for the changes was not yet available.

Countries of the European Community have been cautious in their implementation of new requests for EPP measures which has given them the opportunity to learn from what has been tried in other countries and to study needs and consequences more in detail.

THE TECHNICAL AND NON-TECHNICAL BASIS FOR EMERGENCY PLANNING AND PREPAREDNESS

Nuclear facilities are designed, constructed and operated in such ways that the probability for a serious accident is extremely small.

However, general safety and political considerations and the experience of incidents during nuclear power reactor operation justify effective emergency planning and preparedness programmes. It is much more difficult to say on what level of ambition the effective EPP programme should be placed.

Two entirely different technical approaches could be chosen. The first is to rely on extreme conservatism. In that case "a model accident" should be assumed independent of its probabilities. That "worst possible accident" should then be used for defining what emergency measures would be needed. Probably you would then get an EPP programme which would be fit for handling more difficult situations than would ever occur. The other approach would be to start from a best estimate of a range of possible accidents. That would quite naturally lead to EPP programmes being much less ambitious and more flexible than in the former case. You could anyhow show that they would be sufficient for all reactor accidents which would reasonably occur. In both these approaches you would get an EPP programme which would be much more ambitious than corresponding programmes for any other - or at least almost every other - activity in society of comparable risks.

Technical approaches, as described above, are of course the only possible for establishing the basis for the choice of technical EPP measures - and most of those are technical. At the same time it is self-evident that political considerations and political decisions lie behind all EPP programmes.

When considering the technical and non-technical basis for the choice of a general "EPP ambition level" and of different EPP measures, the following aspects are important:

- Risk scenarios
- Protective actions
- Sensitivity of emergency planning assumptions
- Costs and benefits of different protective actions.

It is evident that with the existing knowledge several different risk scenarios can be chosen to describe not only a "best estimate accident" in nuclear power reactors but also to describe "the worst possible accident". The choice of a risk scenario is decisive for the consequence picture of the assumed accident. It is also evident from recent studies and experiments that previous

analyses of core-melt accidents have over-estimated the consequenses of many accident sequences, including a core-melt. Most interesting, anyhow, is that estimated radioactive releases from a severe accident probably have been too high. The uncertainty is the degree to which it has been overstated. Ongoing work will remove that uncertainty, but probably not entirely until some years from now.

In July 1984 the ANS Topical Meeting "Fission Product Behaviour and Source Term Research" gave a picture of the many ongoing international research activities concerning severe accidents. In our view it was evident that there is now a widespread agreement on the technical questions:

- Reactor containments can resist severe accident sequences better than assumed in the WASH-1400 study
- Some of the most violent sequences can be excluded for physical reasons
- Fission products from the reactor core are captured in the reactor more efficiently than assumed earlier and source terms will therefore be smaller

However,

- There are accident sequences which will decrease the efficiency of the containment, and
- The source terms and the activity released to the environment will thus depend on what kind of nuclear power plant is involved.

An illustrative comparison of the impact of a "WASH-1400 accident" and an accident with smaller release factors has been made at EPRI:

IMPACT OF SMALLER RELEASE FACTORS RELATIVE TO WASH-1400
(Iodine and particulates considered)

	WASH-1400	1/5	1/10
Number of early injuries	1	0.032	0.002
Number of latent cancer fatalities	1	0.35	0.22
Area interdicted more than 10 years	1	0.11	0.037

It is evident that a reduction of the estimated releases by a factor of ten, or even less, would markedly affect the basis for present EPP programmes. The EPP areas which are of special interest in this situation are

- The size of the emergency planning zone (EPZ)
- The conditions mandating evacuation or sheltering of the public or parts of it
- Public alerting and warning systems requirements
- The possible distribution and use of stable iodine tablets.

There is a choice of suitable protective actions when a release has occurred or when there is a threat of a release.

Very few studies of the cost effectiveness of different counter-measures to a nuclear accident have been performed. Even studies of the cost of counter-measures are rare.

Some counter-measures could a priori be considered to be cost effective because there are no realistic alternatives to them. These are:

- Emergency planning
- Simple personnel protection measures
- Control of access to contaminated areas

A second category of counter-measures, when judged on a cost-benefit basis, is sheltering. Sheltering can be done in existing buildings, where great parts of the population will stay already when an emergency situation is declared. The costs for sheltering will be low as long as it is imposed for relatively short periods of time. Also risks and harm associated with it will be low.

Others of the counter-measures should be subject to more detailed cost-effectiveness considerations. These are:

- Evacuation
- Distribution of stable iodine tablets
- The size of emergency planning zones (EPZ)
- Installation of warning- and alarm systems
- Bans on food consumption
- Decontamination of land.

Recent studies show clearly that the cost-effectiveness of the distribution of iodine tablets can be strongly questioned. Also in the United States and in Sweden where preplanned stockpiling and predistribution of those have been applied, safety authorities are reconsidering their attitudes.

The most important "protective action" for the health of the public is not included in Emergency Planning and Preparedness. It is the safety functions of the nuclear installations, determined by design, construction, operation and management, which will be the primary contribution to the protection. This is self-evident, but must anyhow be underlined in any discussion about EPP. Planning for emergencies will seldom produce plans which can be applied word by word on a real emergency, but good planning will produce an ability

for correct, improvised actions in an emergency. Therefore, planning as such might be one of the most effective protective actions.

THE PRESENT SITUATION IN THE EC COUNTRIES

The EC countries and also some other countries have answered a questionnaire from the Commission of the European Communities on off-site emergency planning and preparedness. The questionnaire covered the following items:

- The planning basis, i.e. the kind of accident conditions considered
- Organization and responsibilities
- Emergency facilities and functions
- Emergency response measures and means
- Accident assessment
- Training, drills and exercises
- Records keeping
- Guidelines and criteria for emergency measures.

The answers to this questionnaire are at present being brought together into a summary report describing national positions and practices.

The "Emergency Reference Levels" (ERLs) used in different countries (also non-EC countries) are given in the tables below. It must be noted that a policy applied in some countries is that general ERLs should not be used, but that the need for counter-measures should be judged from case to case depending on available information. In some countries the ERLs are recommended values, in others they are mandatory. In for instance the UK and the FRG ERLs are defined as ranges. If predicted dose equivalents exceed the lower level, implementation of the counter-measure is desirable, but not essential. There is also a higher level at which counter-measures are expected to be introduced whatever the circumstances.

EMERGENCY REFERENCE LEVELS FOR EVACUATION

Country	Whole Body (rem)	Thyroid (rem)
CEC Guideline	10-50	30-150
Canada	1-5	15-75
Finland	10	20[1]
FRG	25/>100[8]	>500/[2][8]
Italy	15[3], 25[4]	25
Japan	5	
Luxembourg	1-5	15
Netherlands	5[5], 15[6]	10[5], 30[6]
Sweden	10[4]	
Switzerland	30	
UK	10/50[8]	30/150[8]
USA[7]	1[1], 5[6]	5[1], 25[6]

1) for children
2) 100 rem is ERL for iodine tablet administration
3) for children and pregnant women
4) for adults except pregnant women
5) for children
6) for adults
7) from inhalation
8) see comments in the text about low and high levels

EMERGENCY REFERENCE LEVELS FOR SHELTERING

Country	Whole Body (rem)
CEC Guideline	0.5-2.5
Canada	0.05-0.5
France	0.5
FRG	<25[4]
Japan	1[1], 5[2]
Sweden	1-10
Switzerland	10[1], 30[2]
UK	0.5/2.5

1) sheltering only
2) sheltering and evacuation
3) see comments in the text about low and high levels
4) sheltering is desirable up to 25 rem, above that it is necessary

The "CEC Guideline" in the two tables above refers to the ERLs proposed as broad dose ranges in a CEC guide "Radiological Protection Criteria for controlling doses to the public in the event of accidental releases of radioactive material" (V/5290/82 EN, July 1982).

Emergency Planning Zones (EPZs) can be defined as the areas around a nuclear installation for which planning is recommended to ensure that prompt and effective actions can be taken to protect the public in the event of an accident. The EPZs required in some countries are given in the table below.

EMERGENCY PLANNING ZONES (expressed in radius from the site)

FINLAND	5 km	-	not densely populated areas
	20 km	-	evacuation planning
	100 km	-	general planning
FRANCE	5 km	-	evacuation planning
	10 km	-	sheltering
FRG	$\leq$10 km	-	evacuation planning, warning systems installed, iodine tablets available etcetera
	$\leq$25 km	-	warning systems and monitoring points defined
NETHERLANDS	5 km	-	early warning systems and evacuation planning
	20 km	-	monitoring
SPAIN	10 km	-	evacuation planning
	30 km	-	foodstuff control
SWEDEN	2 km	-	no new dwelling houses allowed; limitations on other activities
	2-15 km	-	evacuation planning, warning systems installed, iodide tablets distributed to households and institutions
	$\approx$ 50 km	-	monitoring prepared
SWITZERLAND	3-5 km	-	warning systems installed, sheltering
	20 km	-	2 hours warning, sheltering
	$\geq$20 km	-	foodstuff control
UK	$\leq$3 km	-	evacuation and distribution of iodine tablets
	$\leq$40 km	-	monitoring prepared
USA	16 km	-	sheltering and evacuation planning
	80 km	-	foodstuff control

The CEC has set up a working party on transfrontier emergency planning. Its terms of reference are:

- to collect information on existing bilateral contacts and agreements between Member States on transfrontier emergency planning and on experience gained therefrom;

- on the basis of the information thus obtained to draw up a report setting out the most important aspects of emergency planning which require to be covered by bilateral agreements between Member States.

Bilateral agreements have been made between EC Countries concerning reactors situated close to borders involving Belgium, Denmark, France, FRG, Luxembourg and the Netherlands. There are also agreements between EC and non-EC countries. Between the Nordic Countries there are agreements on consultations before decisions about border installations and on mutual assistance. The IAEA is preparing a multilateral agreement on mutual assistance in accident situations.

AN APPROACH TO HARMONIZATION

The distribution of risk around a nuclear installation depends on population density, land use and similar parameters, but of course not on whether a national border passes close to the installation. The emergency preparedness in one country at one side of the border could differ from that on the other side, and the protection of the public could then be of different quality on different sides of the border. Attitudes to emergency preparedness are so similar in the EC countries that this situation would probably not occur. Further harmonization of criteria and practices in the EC countries will decrease the risk that divergencies in EPP in two neighbour EC countries should cause public anxiety.

There are areas where harmonization between countries might be difficult due to differences in administrative or organizational patterns, like

- Organization and responsibilities
- Emergency facilities and functions
- Monitoring during and after an acccident.

On the other hand, these areas are not those in which the greatest advantages of harmonization could be found.

There are other areas, however, where harmonization is more needed and could be more easily achieved, like

- Emergency Assessment and Notification
- Communications: Organization, Procedures
- Emergency Planning Zones
- Evacuation

- Other Counter-Measures than Evacuation
- Training, Retraining and Emergency Exercises
- Public Information.

On the other hand some of the areas where harmonization could be achieved ought to be treated with caution because the basis for decisions is still insufficient. Decisions about changes of the EPP situation, which have far-reaching consequences, ought to be avoided for the time being in the areas:

- Action levels
- Emergency Planning Zones
- Evacuation organization
- The use of stable iodine tablets.

More specifically a number of recommendations can be given in areas where harmonization is possible:

* Emergency Reference Levels (ERLs) should to be used as criteria for decisions during at least the first phase of an accident concerning
  - sheltering
  - distribution of stable iodine tablets (or ordering of consumption of previously distributed tablets)
  - evacuation.

* An ERL should never be used as the one and only criterion for a decision about iodine tablet consumption, evacuation or any other far-reaching counter-measure. These decisions should be founded on all available information about the accident situation to the extent that it is practically possible to take the information into account.

* When defining Emergency Action Levels (or "Criteria") for the use of the nuclear utility, a clear distinction should be made between those intended to put the site emergency plan into function and those intended for a general off-site emergency.

* The characteristics of Emergency Planning Zones are very much dependent on assumptions about accident sequences, source terms and release behaviour. Taking into account the rapid reconsideration of these elements in the total risk scenarios, changes of present EPZs should be avoided during the few more years before the less Conservative assumptions for these elements have been confirmed.

* A decision about evacuation of any population should be taken only if such an evacuation has been preplanned or if time is available for careful planning, or if other counter-measures are judged to be definitely inadequate.

* Plans should be established to cope with possible unplanned and spontaneous evacuation by parts of the population.

* Sheltering in buildings where members of the public live, work or dwell should be considered as a first choice of countermeasure.

* Distribution of stable iodine tablets (normally potassium iodide) should not be made in advance of an accident to households in the vicinity of a nuclear installation.

* An agreement should be set up between the EC countries on how mutual aid in an emergency situation in one country should be organized. The agreement should cover, inter alia:

  - Assistance from experts travelling to the site of the accident or working from their home country

  - Equipment and materials to be sent to the site

  - communication means to be used between the EC countries during the emergency situation

  - Financial and legal arrangements for the support given, both as concerns personnel and equipment.

The basis for harmonization is of course a common assessment of what is important and what is not for achieving a sufficient protection of the public. Therefore, a general recommendation is that the ongoing work to verify best estimate values and sufficient safety margins for parameters forming the basis for EPP should be encouraged and followed closely. Until the results of this work are available - which will be within some years from now - EPP efforts should be concentrated on measures which have a low sensitivity to variations in assumptions of accident parameters. Furthermore, priority should not be given to measures of which the possible benefits are small compared to the costs and where the existing planning and preparedness could be judged to be sufficient in the short term.

***

The views presented in this report are those of the authors.

BRUCE NUCLEAR GENERATING STATION 'A' OPERATIONAL REVIEW FOR LOSS OF COOLANT ACCIDENT WITH FUEL FAILURE SCENARIO

Dr. Salah Hassanien (P.Eng.)

Ontario Hydro, Bruce NGS 'A' Operations
Box 3000, Tiverton, Ontario, CANADA N0G 2T0

ABSTRACT

Bruce Nuclear Generating Station 'A' is a four 826 MWe CANDU (PHWR) unit station with a single Negative Pressure Containment System.

The Operations staff carried out a review to re-assess the operations required to maintain the accident unit and the unaffected units, in a safe shutdown state for an extended period of time following a major Loss Of Coolant Accident with fuel failures. Prime considerations were; safe unit shutdown, fuel cooling, containment of radioactivity, essential systems availability, accessibility and reliability, personnel evacuation and operating and emergency procedures following such an accident.

The review identified design and procedural modifications required to enhance the capability of the station systems and staff to control the consequences of such a major accident.

INTRODUCTION

This work describes the rationale and the process which was undertaken by the operating staff at Bruce Nuclear Generating Station 'A' (Bruce NGS 'A') to review the operability and the actions required to maintain the accident unit and the non-accident units, in a safe shutdown state for an extended period of time (ie, 6 months) after a Loss Of Coolant Accident (LOCA) with fuel failures. The same rationale and process can be adapted to assess the essential systems operation and the operating procedures required to enhance the capabilities of any nuclear generating station to control the consequences of such a major nuclear accident.

Bruce NGS 'A' is owned and operated by Ontario Hydro in the county of Bruce on the eastern shore of Lake Huron, Ontario, Canada. The station has four Pressurized Heavy Water Reactor (PHWR) units of the CANDU type designed by Atomic Energy of Canada Limited (AECL) with a unit maximum continuous rating (gross) of 826 MW electrical equivalent [1]. There is a single Negative Pressure Containment System (NPC) for all the four reactor units, the fuelling duct, central fuelling area, pressure relief ducts, pressure relief manifold and vacuum building, all interconnected together (Figure 1). The Emergency Coolant Injection System (ECI) is designed to refill the Heat Transport system and keep it refilled after a Loss Of Coolant Accident (LOCA). The ECI System is common to all four units. The present ECI System design is being upgraded by the addition of a high pressure injection capability. The new high pressure ECI will be commissioned in 1984 and 1985. Figure 2 shows the flow diagram of the present ECI System.

In 1980 the design groups at AECL and Ontario Hydro re-evaluated their assumptions for the radioactivity released from the reactor core to the vault atmosphere and Heat Transport System following a Loss Of Coolant Accident with fuel failure, using very conservative assumptions. Consequently, predictions could be made on the resultant releases of radioactive nuclides from the fuel and their transport and distribution in various plant systems. The design groups then calculated the radiation fields within and around the station and assessed the effects of these fields on the integrity of the material, systems and equipment under prolonged exposure conditions following a major LOCA. Existing shielding provisions were also evaluated as well as provisions for monitoring radiation after such an accident. This work constituted the design review for the station [2].

On the basis of the data from the design review, the operational staff undertook a detailed review on the operations necessary to maintain the accident unit in a safe shutdown state for a prolonged period of time (ie, more than 6 months following the accident). Also, because of the fact that there is a single Negative Pressure Containment (NPC) System and a single Emergency Coolant Injection (ECI) System, the non-accident units would have to be shutdown in a controlled manner within a few hours after the accident and be maintained in a safe shutdown state until both NPC and ECI Systems are repoised.

On the basis of both the design and the operations review, several design modifications and modifications to existing operating procedures were recommended. Interim and permanent solutions were reviewed jointly by the design groups, engineering and operations staff for effectiveness, cost and implementation. The implementation of most of these solutions was completed resulting in a greatly enhanced capability of the station systems, equipment and personnel to effectively control the consequences of such a major accident.

RATIONALE

In order to deal with the consequences of the postulated accident, ie, major LOCA with fuel failure, operations staff should ensure the following:

1. That capability of the station systems to perform the following functions:

   a) to automatically shutdown the accident unit and to shutdown in a controlled manner the unaffected units, and to maintain excess negative reactivity for an extended period of time;

   b) to maintain fuel cooling and heat sinks for extended periods of time;

   c) to contain radioactive nuclides;

   d) to supply water, air and power to essential systems.

2. That the station emergency procedures and the operating procedure cover, in detail, all the actions required after the accident to maintain the units in a safe state, to ensure public safety requirements are met, and to minimize radiation exposure to operating personnel. Also, to cover evacuation of non-essential personnel and the continuation of the essential personnel, ie, Control Room Operators, to perform maintenance requirements and sampling of essential systems.

3. To ensure that there are adequate shielding provisions so as no exposure limits are exceeded for operating personnel during and after the accident.

4. That the requirements for Post-LOCA radiation monitoring are met [3]. These requirements ensure that all releases to the environment are monitored and controlled. Also, they ensure that the exposure to the operating staff or the public will not exceed any regulatory limits.

SYSTEMS REVIEW

The design review assessed the systems on the basis of component and material integrity under acute and prolonged radiation exposure conditions. Operations assessed the systems in term of whether they will be required to operate after an accident and to ensure the reliability of these systems.

The systems were reviewed with respect to:

1. The System Function

   Whether the system is required to shutdown, maintain fuel cooling, contain radioactivity, maintain a heat sink, maintain spent fuel cooling, provide an essential supply of air, power or water.

   Whether the system is required to operate immediately after the accident or not.

   Whether the system will be required to operate for a short or a long duration following the accident.

2. System Status After the Accident

   Whether the system is fired, poised, shutdown or continuing to operate. For example, Shutdown System 1 will be automatically fired and will not be required to be repoised again. The Emergency Cooling Injection recovery will be automatically started and will be required to operate continuously.

3. The Effect of the Accident on the System

   For example, the containment systems and the Emergency Coolant Injection System will contain highly radioactive atmosphere or water.

4. System Accessibility

For systems to be sampled and maintained, it is important that they be accessible to Operators in terms of radiation fields. The system will be fully accessible if the fields around it are less than 200 mrem/h. The system will be partially accessible for maintenance if the fields do not exceed 2 rem/h. In this case, high hazard procedures will be in effect to carry out the required maintenance.

5. System Component Redundancy

The majority of the systems, particularly safety and safety related systems, have been designed with some component redundancy to ensure high system reliability. For example, to maintain long term cooling of the spent fuel, the Primary Spent Fuel Bay Cooling System has 3 pumps and 3 heat exchangers, only two of each are required for the system to be fully operational.

6. Back Up Systems to Essential Systems

For each of the essential systems, the back up and/or alternative systems were fully assessed for accessibility, operability and maintainability.

7. Common Services Reliability

The reliability of the systems required to supply power, water and air to the essential systems and to the station services such as power to instruments and lights, breathing, service and instrument air were assessed to ensure continuing supply of common services on the same basis as safety and safety related systems.

8. Maintenance Call-Ups and Sampling

All necessary call-ups service or maintenance call-ups and sampling requirements for each system were evaluated in terms of need, frequency and the required field operation. The objective of this was to reduce field actions to the minimum to avoid unnecessary radiation exposure. All sampling with the exception of the samples required for operator action will be suspended.

This review resulted in 22 recommendations for design changes, mostly to increase shielding or to change some systems operations from local to remote operation, or to relocate some component of a system to a more accessible area in terms of radiation fields following a LOCA.

PROCEDURES REVIEW

Following a LOCA, the protective systems in the accident units will operate automatically. There are other actions required from the Control Room and field operators as well as other station personnel. The short term actions are:

1. To ensure that the emergency is announced and that restricted areas are identified.

2. To ensure that all the emergency procedures for personnel assembly and accounting, Search and Rescue are active.

3. To ensure that in-Site and off-Site emergency procedures are active.

4. To start up two standby generators to ensure added security of back up power supply.

5. To terminate all fuelling and safety system testing on the unaffected units.

6. To terminate any D_2O transfer from the affected unit if it is in progress to conserve D_2O supply.

7. To shutdown all the other three unaffected units as soon as possible following the accident in a controlled manner by load reduction.

8. To put all the unaffected units in a guaranteed shutdown state (moderator overpoisoned and Heat Transport System is cooled).

9. To restrict access to areas of high radiation fields and suspend all unnecessary field actions.

10. To dispatch survey teams to measure radiation fields in the station and outside.

11. To evacuate all the non-essential personnel via routes previously identified where radiation fields after survey are less than 200 mrem/h.

Following the short term actions to bring the accident and non-affected units to a safe stable state and to ensure safety of station personnel and the public, the operators will concentrate on maintaining the safe state of the units and minimizing any releases to outside the station. The operators will have the services of a large resource pool of management and technical experts. Some ad hoc solutions may be devised to deal with specific problems and/or component breakdown of a system.

A thorough review of all the procedures in the Abnormal Incidents Manual and essential systems Operating Manuals [4], Radiation Protection Procedures [5], in-Site and off-Site emergency plans [6] was carried out. Only minor modifications to the existing procedures were required and these were issued. The procedure for a major LOCA in the Abnormal Incidents Manual was expanded to reflect the information from this operational review.

SHIELDING REVIEW

The overall objectives of the review of the adequacy of existing shielding for Post-LOCA were:

1. To permit continuous occupancy of the main Control Room. Hence, additional shielding was installed in the vicinity of the Control Room to limit the dose to less than 10 mrem/hr at any time after the accident. This ensures that the potential radiation dose uptake of a Control Room operator is less than 3 rem/quarter of a year.

2. To allow safe evacuation of non-essential personnel from the station. The ECI recovery phase will start 15 minutes after the accident, during which time personnel will be at or on route to their assembly areas. Evacuation from the assembly areas will be via designated routes where the dose rate will be less than 200 mrem/h . Evacuation will take 20 - 30 minutes.

3. To facilitate any field operation that is required after the accident. Hence, shielding adequacy depends on where and when the action will take place.

The radiation fields in the station were estimated and mapped in the design reviews for the postulated accident. The unshielded radiation shine from the Emergency Cooling Injection (ECI) header was unacceptably high during the recovery phase, ie, recirculating the emergency core cooling water through the reactor core. While it was considered that the source term is highly conservative, the shielding calculations were based on dose rates occurring half an hour after recovery starts, since these are the highest probable rates. Generally, the dose rate will drop by a factor of 3 after about 3 hours due to decay of short lived radioactive nuclides, and by factors of 4 and 7 after one day and one week from the accident respectively. In addition, after the installation and commissioning of the High Pressure ECI header the dose rate will be reduced by a factor of three due to the increased thickness of the header.

One of the most important recommendations of both the design and operational reviews was to erect shielding around the existing ECI header. The shielding on both sides of the header was constructed of 20 cm of heavy concrete blocks on the north side and 60 cm standard concrete blocks on the south side of the ECI header. (Figures 3 and 4)

RADIATION MONITORING REVIEW

The Design Group, with input from Operations, prepared a detailed list of the Post-LOCA Radiation Monitoring functional requirements. The main requirements were:

1. Performance and control monitoring of all the gaseous and liquid effluents from the station to the environment.

2. Control monitoring of all penetrations of the containment envelope which would provide a pathway to the environment.

3. Environmental monitoring outside the station.

4. Warning system for hazardous areas within the station.

5. Personnel radiation monitoring, dose control and contamination control within the station.

Performance monitoring is required to ensure that the regulatory limits on allowable releases under accident conditions are not exceeded.

Control monitoring is required to provide the operator with adequate and timely warning so that control action can be taken to ensure that regulatory limits will not be exceeded. Operations assessed the existing Radiation Monitoring Systems in terms of:

1. Meeting the functional requirements.

2. Ability to measure the Post-LOCA radioactivity level or operate in the Post-LOCA environment.

3. Manual operation, sampling, maintenance of the Monitoring System.

4. Adequacy of personnel radiation monitoring and warning equipment and dose control.

5. Equipment and procedures for contamination control.

The review pointed out some deficiencies, particularly with respect to monitoring the noble gases which will be released through the contaminated exhaust system stack at amounts exceeding the range of the measuring instrumentation. Some relocation of existing monitors was also recommended to reduce the background radiation to the instrument and improve accessibility to the instruments. Other procedural changes were also recommended.

ACKNOWLEDGEMENT

The author wishes to acknowledge the contributions of the following individuals and departments:

1. Y. Sirota, Technical Supervisor, Reliability, Bruce NGS 'A', Ontario Hydro.
2. S. Abercrombie, Assistant Technical Supervisor, Bruce NGS 'B', Ontario Hydro.
3. Radioactivity Management and Environmental Protection Department, Ontario Hydro.
4. Nuclear Studies and Safety Department, Ontario Hydro.
5. Nuclear Safety Studies, Ontario Hydro.
6. Bruce Engineering Department, Ontario Hydro.
7. Atomic Energy of Canada Limited Engineering Company.

Special thanks for their support and encouragement to:

1. H.L. Austman, Station Manager, Darlington NGS, Ontario Hydro.
2. R. Coutts, Station Manager, Bruce NGS 'A', Ontario Hydro.
3. A.J. Young, Production Manager, Bruce NGS 'A', Ontario Hydro.
4. E.P. Horton, Director, Nuclear Generation Division, Ontario Hydro.
5. W.J. Penn, Manager, Nuclear Studies and Safety Department, Ontario Hydro.

REFERENCES

1. Bruce Nuclear Generating Station 'A' Safety Report Vol. 1,2,3, Revision 2, 1979 and Revision 3, 1984, prepared by Power Projects, Atomic Energy of Canada Limited.

2. Bruce NGS 'A' Design and Operations Review to Assess the Effects of a Loss Of Coolant Accident With Fuel Failures, Report No. 81012, January 1981, prepared by Ontario Hydro, Nuclear Studies and Safety Department and Bruce NGS 'A' Operations. (Property of Ontario Hydro.)

3. A Review of the Adequacy of Bruce NGS 'A' Radiation Monitoring Systems in the Event of a LOCA With Fuel Failure. Addendum to Report 81012. (Property of Ontario Hydro.) May 1984, Ontario Hydro Nuclear Studies and Safety Department.

4. Bruce NGS 'A' Abnormal Incidents Manual, Revision 3, December 1984. (Property of Ontario Hydro.)

5. Bruce NGS 'A' Radiation Protection Procedures Revision (Property of Ontario Hydro.)

6. Site Emergency Plan, Revision 2, 1980. (Property of Ontario Hydro.)

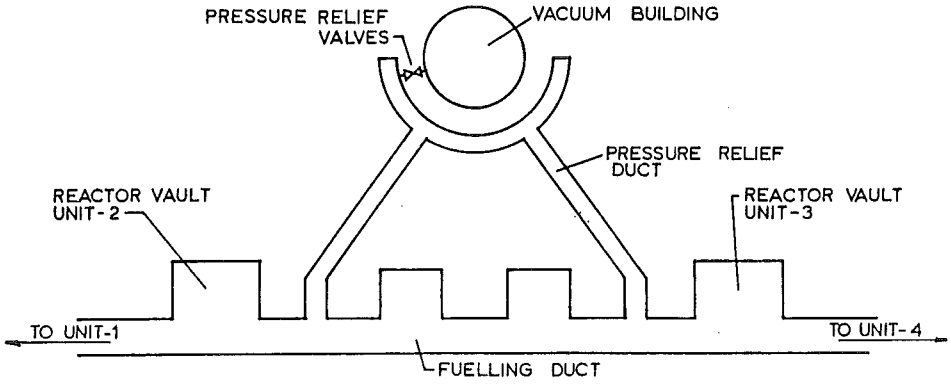

FIG. 1
CONTAINMENT SYSTEM ENVELOPE

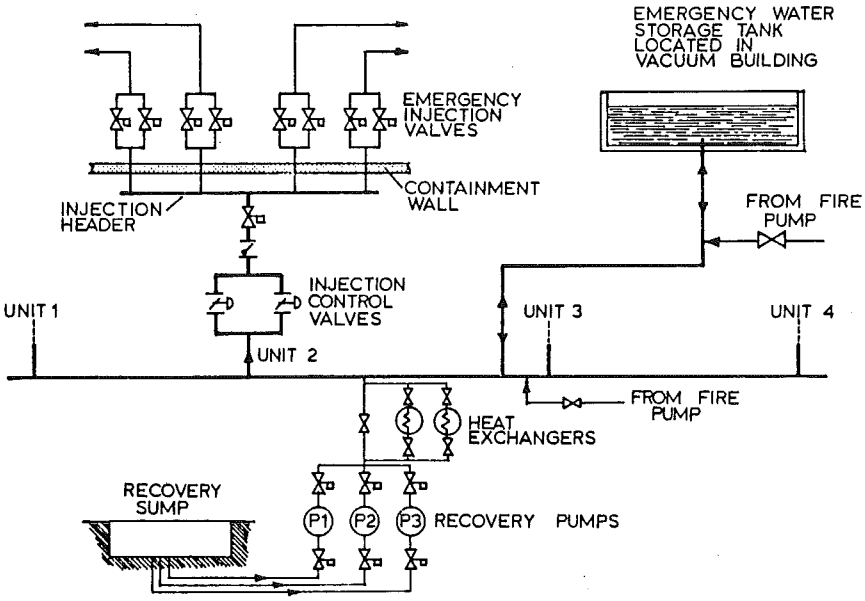

FIG. 2
EMERGENCY COOLING INJECTION

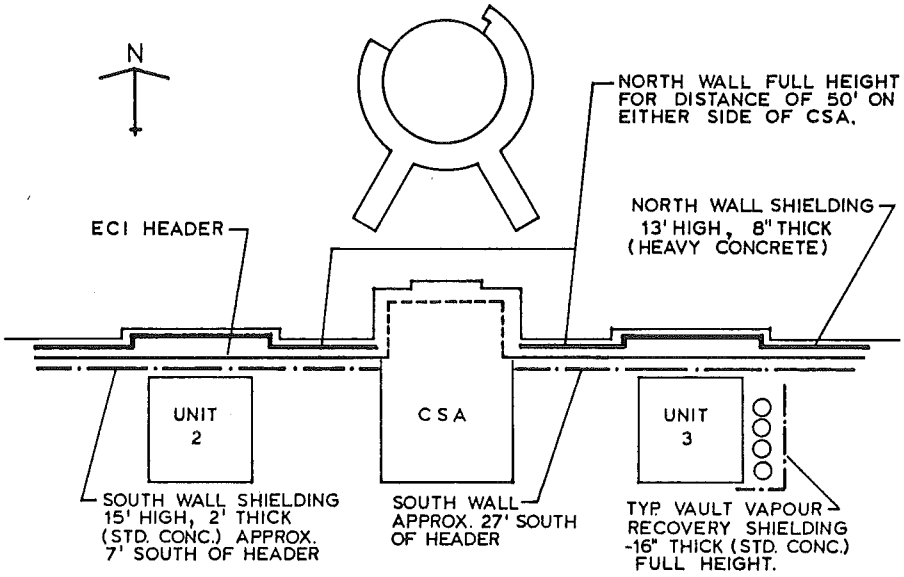

FIG. 3
PLAN VIEW SHOWING ECI HEADER SHIELDING/VAULT VAPOUR RECOVERY SHIELDING

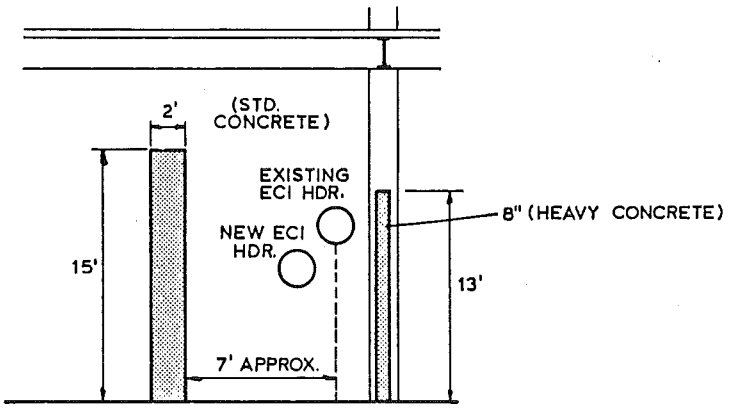

FIG. 4
PROFILE OF ECI HEADER SHIELDING / TYPICAL IN UNIT AREA

HEAT TRANSPORT INVENTORY MONITORING FOR CANDU-PHW REACTORS

E. Hussein, J.C. Luxat

Ontario Hydro
Toronto, Ontario, Canada M5G 1X6

ABSTRACT

A computer-based D_2O coolant inventory monitoring system proposed for implementation on the digital computer controllers at Ontario Hydro's CANDU generating units is discussed. By monitoring process parameters and utilizing probabilistically-based decision algorithms, timely indication of any significant loss of D_2O inventory will be provided to the operator. The monitoring is performed in a co-ordinated manner such that D_2O losses from either the heat transport system or the inventory control system can be detected.

INTRODUCTION

At Ontario Hydro's CANDU generating units a great deal of attention is paid to detecting heavy water coolant losses from the heat transport system and the interfacing inventory control system. Presently, local indicators such as pressurizer and D_2O storage tank levels and moisture detectors are used to detect coolant losses. However, it is desireable to have an indication of the global, rather than the local, coolant inventory in order to account for coolant redistribution between different system components and to avoid any ambiguity that may result from conflicting local indicators. This paper discusses a system that has been proposed at Ontario Hydro for estimating the total mass inventory of the heat transport system. This system is useful as an operator-aid for diagnosing the status of the heat transport system. The function of this inventory monitoring system is similar to that of the coolant level measurement in light water reactors, where also a direct evaluation of the available coolant inventory is provided.

CANDU HEAT TRANSPORT SYSTEM

Figure 1 shows a simplified heat transport circuit of a typical CANDU unit, in this example a unit at the Darlington Nuclear Generating Station

which is under construction. The heat transport system main circuit consists of two figure-of-eight loops. Each loop contains two pumps, two steam generators, two reactor inlet headers, two reactor outlet headers and inlet and outlet feeders for each of 240 fuel channels. Within a loop there are two flow passes through the reactor core such that the coolant flows in opposite directions in adjacent channels.

Each loop removes heat from half of the 480 channels in the reactor core. Heavy water is fed to each of the fuel channels through individual inlet feeder pipes and from each fuel channel through individual outlet feeder pipes to the horizontal reactor outlet headers. Each reactor outlet header is connected to a steam generator which is in turn connected to the suction of a heat transport pump. Each pump delivers heavy water to the corresponding inlet header.

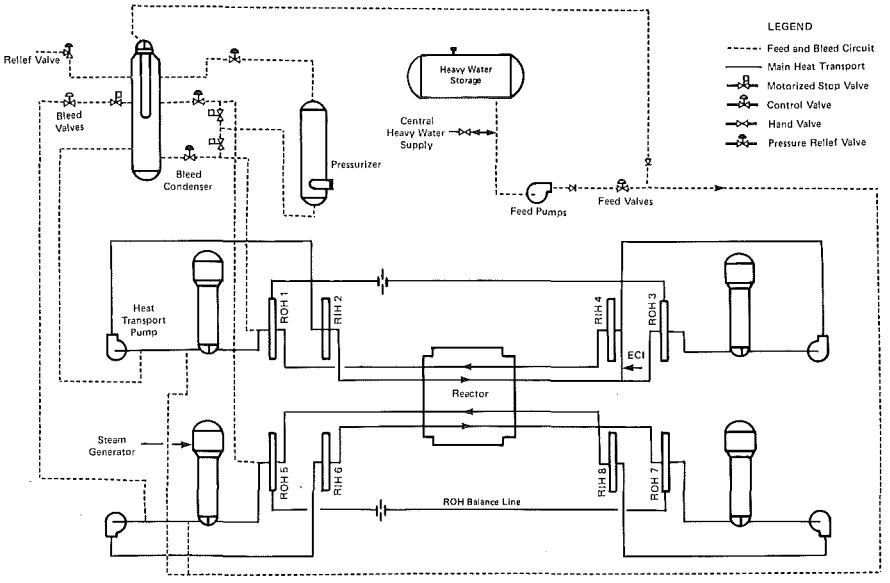

FIGURE 1
A Typical CANDU Heat Transport System – Simplified Flow Sheet

Interfacing with the main heat transport circuit is the heat transport pressure and inventory control system which contains the pressurizer, bleed condenser, D_2O storage tank and a feed and bleed circuit connecting to the heat transport system. When the reactor is at power, pressure is controlled by the pressurizer with inventory being adjusted by the feed and bleed circuit. The bleed condenser can receive steam bleed from the pressurizer and liquid bleed and relief from the heat transport system.

Other systems that interface with the main heat transport circuit have not been shown in Figure 1. These systems are not described here since they do not directly affect the heat transport inventory in the main circuit.

In order to provide reliable control and monitoring of the heat transport system, many process parameters are measured at different locations in the main heat transport circuit and the pressure and inventory control system. Pressure, temperature and liquid level (where appropriate) are among the measurements obtained from different components in the HT system. These measurements are input to unit dual computer control system; used for direct digital control of reactor power regulation and a number of process parameters, as well as for alarm annunciation and data display.

MONITORING APPROACH

The availability of many measured process parameter measurements in the computer control system has motivated the development of computer based systems for monitoring the coolant inventory. This eliminates the need to install either new measurement loops or a data link facility to the control computers. The pressure-tube design of the CANDU system does not permit the use of a single parameter that can directly reflect the global coolant inventory of the heat transport system. This is in contrast to light water reactors where measurement of the coolant level in the pressure vessel can provide a direct indication of the heat transport inventory.

Although the main objective is to monitor the coolant inventory inside the main heat transport circuit, it is desirable to monitor the D_2O inventory in the interfacing pressure and inventory control system. The status of the latter system provides a direct indication of the amount of coolant leaving or entering the main heat transport circuit. The proposed monitoring approach can be systematically presented as shown in Figure 2. External monitoring is provided by estimating the available coolant inventory in the interfacing inventory control system, termed the ex-loop. Coolant inventory changes in the main heat transport circuit (termed the in-loop) are compensated by feed or bleed from the ex-loop, and monitoring the latter provides indirect monitoring of the former. Reliance on monitoring the ex-loop inventory might not be sufficient, particularly when a loss of inventory occurs in the ex-loop itself (analogous to the TMI event where inventory loss occured via the pressurizer relief valve). Therefore, it is desireable to provide direct monitoring of the in-loop inventory. Since the in-loop and ex-loop are interconnected, monitoring both systems accounts for any mass exchange between them and provides an overall indication of the status of the HT system. The following Sections discuss the methods proposed for monitoring the coolant inventory in the ex-loop and the in-loop.

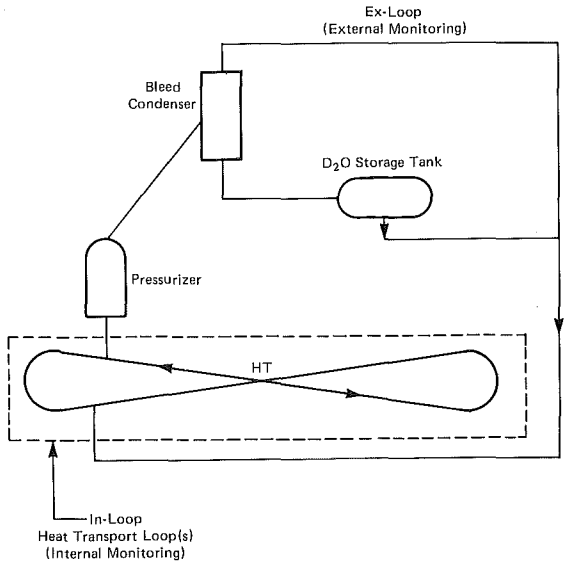

FIGURE 2
Internal and External Monitoring of the
Heat Transport System

EX-LOOP MONITORING

The ex-loop inventory is comprised of the coolant in the pressurizer, bleed condenser and D_2O storage tank. For each of these major components, pressure, temperature and liquid level measurements are available. This enables direct estimation of the ex-loop inventory as follows:

$$M_{ex\text{-}loop} = \sum_{k=1}^{3} Vol_k\,(L_k)/v_k\,(P_k, T_k), \qquad (1)$$

where the subscript k refers to one of the three components considered, Vol is the liquid volume of the components estimated using the liquid level measurement, L, and v is the specific volume of the coolant evaluated using the pressure, P, and temperature, T, measurements.

Equation (1), in addition to providing a simple and a straightforward method of estimating the ex-loop inventory, gives a global indication of the status of the ex-loop that accounts for coolant distribution among the different components. This, of course, is better than relying on a single-component measurement, (either the pressurizer or D_2O storage tank levels), to determine the status of the loop.

INTERNAL MONITORING: THE INTEGRAL METHOD

Analogous to the method used for monitoring the ex-loop inventory, the in-loop inventory can be provided by estimating the mass available in individual components in the HT-loops, with the sum (integral) giving the total in-loop inventory. In each of the figure-of-eight loops, one can identify the following components: the reactor channels and feeders, inlet headers, outlet headers, steam generators and HT pumps. The in-loop mass inventory can be then evaluated using the expression:

$$M_{in\text{-}loop} = \sum_{i=1}^{2} \sum_{j=1}^{N} Vol_{ij} / v_{ij} (P_{ij}, T_{ij}), \qquad (2)$$

where i refers to the figure-of-eight loop considered, usually two loops, j refers to the particular component in the loop, N is the total number of components per loop, Vol is the component volume and v is the specific volume of the component estimated using the measured component pressure, P, and temperature, T. Since two-phase flow (boiling) regions can be encountered near the exit of the reactor channels, particular attention is given in the calculations to account for the vapour content. One should also note that the 120 reactor channels and feeders in a flow pass through the core are considered as a single lumped component.

As evident from equation (2), thermodynamic relationships are required for the subcooled and saturated specific volumes, as well as for the enthalpies employed in the two-phase flow calculations. Also computer storage has to be allocated for the signal processing of the measurements associated with the components. These factors make this method demanding in terms of computer resources and reduces its suitability for adoption in operating reactor units where computer resources are usually limited. Because of the summation process involved, the method is called the integral method to distinguish it from the differential method presented, in the next Section, which is designed to minimize computer resources. Additional details on the integral method are reported elsewhere [1].

INTERNAL MONITORING: DIFFERENTIAL METHOD

This monitoring method takes advantage of the fact that inlet feeder mass flow rate measurements for selected reactor channels are available to the control computers. The average value of these measurements in a flow pass provides an estimation of the inlet flow rate. Flow measurements in a closed loop can be then utilized to check the continuity of mass flow around the loop and provide indication of loss of coolant from the loop. Also, the deviation of the flow measurements from the nominal flow rate at the given operating conditions can give an indication of the status of the heat transport loop. These monitoring methods are discussed in more detail later in the Section, after discussing the prospect of utilizing a flow-related measurement that is also available to the control computers.

Recent LOFT experiments [2] indicated that changes in heat transport pump power and consequently pump-motor current, can be utilized in

monitoring coolant inventory. The pump-motor current is a measurement that is available to the control computer and is taken as an indicator of the mass flow rate through the pump. A significant inventory loss would result in a decrease in the coolant mass flowing through the pump and consequently a reduction of the load on the pump-motor which is directly reflected by the motor current. The pump-motor currents in the heat transport system are treated in the inventory monitoring process in a fashion similar to that employed for flow rate measurements.

The first check applied in the differential method is based on a continuity principle which implies that the mass flow rate between two flow monitoring stations in a loop should be equal if no mass addition or reduction is introduced in the section between the two stations. A loss of flow in that section would then result in a difference in the flow measurements equivalent to the rate of loss. The second check used in the monitoring process is called the "expected" mass delivery. If a specific mass flow rate is expected at a given flow monitoring station at given operating conditions, and a lower flow rate is measured, then this indicates a loss of flow upstream the monitoring station. The nominal loop flow rate is used as the expected value and it is evaluated independently as a weak function of the reactor operating power level.

Using the inlet feeders as the flow monitoring stations for the mass flow measurements and the heat transport pumps as the monitoring stations for the pump-motor current measurements and applying the continuity and the expected mass delivery checks discussed above, a computer algorithm is developed and reported in detail elsewhere [3].

In addition to the simplicity of the differential method, it also provides information regarding the location at which the loss occurs relative to the monitoring stations. The differential nature of the process makes it more susceptible to measurement noise, as compared to the integral method. The effect of noisy measurements is to raise the value of the threshold loss rate in the in-loop above which the loss can be confirmed with a high degree of confidence by the detection algorithm. However, given the fact that coolant losses in the in-loop are directly compensated by feed from the ex-loop, monitoring the latter provides coverage for the small loss rate not covered by the in-loop differential monitoring. Here, one should re-emphasize the importance of the in-loop monitoring for detecting losses in the ex-loop that result in coolant flow out of the main heat transport circuit. A loss such as this is detected only by the in-loop monitoring. The integral monitoring method provides a system that is less susceptible to measurement noise and consequently capable of detecting smaller in-loop losses. On the other hand, the differential method is simpler and is less demanding of computer resources. Therefore it can be more easily implemented in an operating unit.

THE LOSS DETECTION PROCEDURE

The main purpose of the inventory monitoring system is to determine whether a decrease in available coolant inventory has occurred. The procedure used to detect any signficant decrease in coolant inventory is summarized in Figure 3 and discussed below.

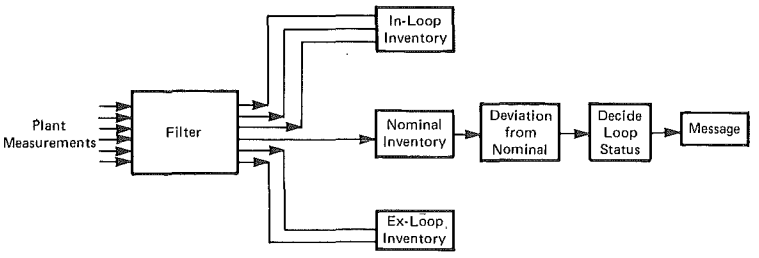

FIGURE 3
Inventory Monitoring System

In an on-line monitoring system fluctuations in the measured data with time are expected. These observed fluctuations generally are a result of internal and external random noise that cannot be controlled. Therefore, it is important to filter or smooth out the measurements before utilizing them in any decision making process. The filtering process has been implemented as a simple first order digital filter, using the exponentially weighted moving average [1] given by:

$$\bar{z}_t = \lambda z_t + (1 - \lambda)\, \bar{z}_{t-\Delta t} \qquad (3)$$

where z_t is a measurement obtained at time t and $\bar{z}_t$ refers to the filtered value, Δt is the time interval and λ is a filtering parameter appropriately chosen to provide acceptable smoothing of the measurements. This simple filtering process can be applied to all the measurements without requiring the storage of a long train of the history of the measurement as is the case for most smoothing digital filters.

The filtered measurements are then utilized in the inventory monitoring calculations discussed in the previous Section, resulting in an estimation of the inventories in the ex-loop, M_{ex}, and the in-loop, M_{in}, as well as their rates of changes, $\dot{M}_{ex}$ and $\dot{M}_{in}$, respectively.

Note that if the integral monitoring method is used M_{in} would be obtained directly while a simple differentiation process would result in an estimate of the rate $\dot{M}_{in}$. On the other hand, the differential method would result in an estimate of $\dot{M}_{in}$, from the flow rate measurements, and then a simple integration process can be used to obtain the mass in the loop, M_{in}. The pump-motor current values in the differential method do not directly result in an estimate of the mass inventory, rather they provide an indicator that is proportional to the available mass. This indicator is utilized in the loss detection process in the same fashion as a mass inventory estimate.

The estimated mass and rate of change of inventories are utilized to detect any deviation from the nominal state at the given operating conditions. Let us designate the nominal mass in a loop by M_o and the corresponding rate of change by $\dot{M}_o$, (the latter is usually equal to zero at steady state operation but can have non zero values during reactor warmup

or cooldown). Detection of a deviation from the nominal state is confirmed by a sustained deviation of the estimated parameters from their nominal values. This deviation can be estimated by the relationship

$$\sigma_t^2 = \theta (M_t - M_o)^2 + (1 - \theta)\, \sigma_{t-\Delta t}^2 , \qquad (4)$$

where σ^2 is a deviation (variance) parameter and θ is an arbitrary weighting parameter. Note that relationship (4) is analogous to the moving average process of equation (3), and consequently σ_t^2 is a moving average estimate of the deviation from nominal. Similarly, estimation of $\dot{\sigma}_t^2$, the deviation of the rate of change from nominal is also obtained. Based on the values σ_t^2 and $\dot{\sigma}_t^2$ a decision is made regarding the status of the loop considered (ex- or in-loop) at time t. Since σ_t^2 and $\dot{\sigma}_t^2$ are moving average values, the decision taken is based on the history of the system, rather than an individual instaneous measurement. The estimated deviation values can be used in a simple decision making algorithm that detects deviation from the nominal state if the deviation exceeds a prescribed threshold value. Alternatively, one may use a more elaborate algorithm based on probabilistic considerations; such as the one proposed in reference [1] or one of the discrimination and classification methods described by Hand [4]. The output of the decision algorithm is an unambiguous indication regarding the status of both the ex-loop and the in-loop that can be displayed to the operator in a timely manner.

ASSESSMENT OF MONITORING SYSTEM

The inventory monitoring system discussed above has not yet been implemented or tested in actual operating conditions. However, in order to assess its capabilities, a series of "simulated" plant conditions are considered, as summarized in Table I. One of the test simulations was a small break loss of coolant with a discharge flow rate of 20 kg/s. This discharge rate is within the capacity of a single D_2O feed pump. The results of this simulation were employed as plant measurements, after adding artificial white noise to simulate plant noise. As shown in Figure 4, the inventory monitoring system confirmed the inventory loss after 50 s from the start of the event and alarmed against coolant loss in the ex-loop. At a further 100 s in the transient the in-loop monitoring initiated warning of an inventory loss in the heat transport loops and 100 s later it confirmed the loss and issued an alarm. The delay in the in-loop response is due to the coolant make-up provided by the ex-loop.

A condition that can cause apparent loss of mass inventory in the in-loop is coolant voiding that may be caused by an increase in the reactor power or a reduction in heat transport pressure. In this case the inventory monitoring system indicates an increase in the ex-loop and a decrease in the in-loop inventory. In the case of ex-loop inventory loss due, for example, to a pressurizer valve stuck open, the increase in the ex-loop inventory caused by the insurge to the pressurizer from the in-loop would be detected together with the subsequent loss in in-loop mass.

TABLE I

RESPONSE OF INVENTORY MONITORING SYSTEM
FOR VARIOUS UPSET AND OPERATING CONDITIONS

Event	Time of Confirming Inventory Loss, s Ex-Loop	In-Loop
20 kg/s break at Reactor Inlet Header at full power	A @ 50	L @ 150 A @ 250
In-loop Voiding (t depends on voiding rate)	H @ t	L @ t
Pressurizer Valve Stuck Open (t depends on valve opening)	H @ t	L @ t
Operational Transients: - reactor shutdown - system warmup - system cooldown - reactor trip	Nominal inventory is adjusted given the reactor power or system temperature. Legitimate inventory changes are accommodated and only genuine inventory losses are detected.	
Maintenance Cooling Monitoring of reactor channel temperatures is used to alert against channel boiling		

A @ t reads: Alarm after t seconds following event initiation
L @ t reads: Low inventory detected after t seconds
H @ t reads: High inventory detected after t seconds

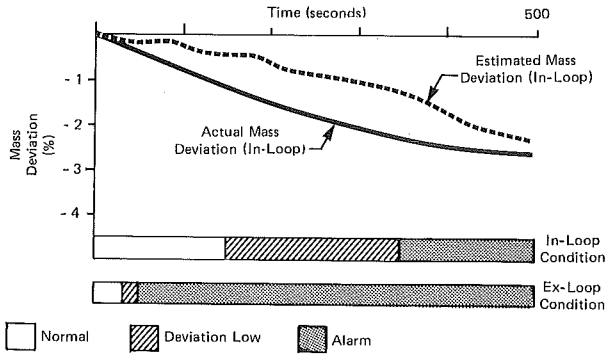

FIGURE 4
Inventory Monitoring Response to Small Loss of Heat Transport Inventory

During operational transients such as reactor shutdown, system cooldown/warmup or a reactor trip, the heat transport mass inventory changes occur due to the coolant density change. These changes are accommodated in the monitoring process by appropriate automatic adjustment of the nominal inventories. Since the detection process is based on deviation from the nominal state the monitoring system exhibits an immunity to generating spurious alarms during these operating transients.

During maintenance outage the heat transport system may be depressurized with low coolant forced circulation. For these conditions the monitoring methods reported here would not be applicable. However, the main concern then is to ensure that adequate fuel cooling is available to prevent boiling in any reactor channel. Therefore, a special algorithm is invoked to monitor channel temperatures, which are then used to alert against potential channel boiling.

CONCLUSIONS

A system for monitoring the heat transport mass inventory in Ontario Hydro's CANDU reactors has been described. The system utilizes measurements available in the unit control computers and provides the operator with unambiguous global indication of the status of the heat transport system at different operating conditions. Through the use of this monitoring system, ambiguities that may arise due to reliance on local inventory indicators can be avoided. The proposed system has not been implemented yet in an operating unit but is being considered for application in the Darlington generating station, as well as some of the other operating units.

REFERENCES

[1] Hussein, E. and J.C. Luxat, "A Study of a Heat Transport Inventory Monitoring Program for Darlington NGS A", presented at the Ninth CNS Simulation Symposium on Reactor Dynamics and Plant Control, Mississauga, Ontario, 1982.

[2] McCreey, G.E., J.H. Linberger and J.E. Kaske, "Primary Pump Power as a Measure of Fluid Density During Bubbly Two-Phase Flow", Second Int Topical Meeting on Reactor Thermal-Hydraulics, Santa Barbara, California, 1983.

[3] Hussein, E. and J.C. Luxat, "A Flow-Based Method for Monitoring Mass Inventory in Heat Transport Loops", presented at the Tenth CNS Simulation Symposium on Reactor Dynamics and Plant Control, St John, New Brunswick, 1984.

[4] Hand, D.J., "Discrimination and Classfication", J. Wiley & Sons, Chichester, 1981.

LOGIC FLOWGRAPH MODEL FOR DISTURBANCE ANALYSIS OF A PWR PRESSURIZER SYSTEM

by

S. Guarro[+] and D. Okrent[++]

+Lawrence Livermore National Laboratory
P.O. Box 808, L-140
Livermore, CA 94550

++School of Engineering and Applied Science
University of California Los Angeles
Los Angeles, CA 90024

ABSTRACT

The Logic Flowgraph Methodology (LFM) has been developed as a synthetic simulation language for process reliability or disturbance analysis applications. A Disturbance Analysis System (DAS) using the LFM models can store the necessary information concerning a given process in an efficient way, and automatically construct in real time the diagnostic tree(s) showing the root cause(s) of occurring disturbances.

A comprehensive LFM model for a PWR pressurizer system is presented and discussed, and the latest version of the LFM tree synthesis routine, optimized to achieve reduction of computer memory usage, is used to show the LFM diagnoses of selected hypothetic disturbances.

INTRODUCTION

In order to implement diagnostic capabilities, a Disturbance Analysis System (DAS) must utilize process models that are at the same time compact and rich in information content.

The models used in the first prototype DASs were developed in the form of cause-consequence diagrams or cause-consequence trees. Both techniques use the same type of binary representation and logic gates employed by fault trees, and are similar to the latter in terms of modeling capabilities. The quite large dimensions of the models resulting from the early attempts to apply these types of representation to whole scale plant systems was indicated by many analysts as a severe hindrance in the development of DASs with extensive diagnostic capabilities.

LFM OVERVIEW

LFM is a new methodology intended to provide a more efficient way of constructing process models for use in diagnosis oriented disturbance analysis systems. At the foundation of this method is the derivation of graph models for the processes to be analyzed. As in the "digraph method"[1] the LFM models include the fundamental units of nodes and edges, which are used to represent respectively process variables and causality relations. In LFM, however, special sets of symbols and representation rules are also used, in order to allow a fully automated fault-tree or diagnostic analysis of complex processes. From the point of view of their general structure, the LFM models are formed by the interconnection of two important and distinct networks, namely, the

causality network, which expresses the fundamental physical relations of direct cause and effect existing in a process, and the condition network, which represents in a formally defined and organized way the conditions whose occurrence may change or modify the course of causality flow in the causality network.

A detailed description of the LFM representation rules can be found in References 2 and 3, while a more synthetic account is given in Reference 4. We use here the simple scheme of Fig. 1 to show an example of some essential LFM features. In this figure the U and V nodes represent continuous variables. These are process variables or parameters that can vary over a continuous range, reduced in LFM to 5 discretized states (0 = normal, $\pm$ 1 = moderate deviations in positive or negative direction, $\pm$ 10 = large deviations). The C node on the other hand represents a truly binary process variable or parameter. U and V are shown to be linked by a causality connection expressed by a causality edge and by a multiple gain box (MGB). The +1 gain value in the MGB signifies that the connection is normally one of direct proportionality from U to V. However, the graph also shows through the diamond shaped text box (TB) that the binary variable C may have a conditioning influence on the relation between U and V. More specifically, when the condition expressed by the equality $C = \overline{1}$ is verified, U has no longer any influence on the value(s) to be taken by V. This type of formal representation is very effective in showing how binary variables, usually associated with primary level faults or with the action of engineered protection devices, can affect the causality relations that link process continuous variables and parameters to one another. LFM is also advantageous in that it condenses in one model the representation of both process success and failure logics, including the effect of feedback and feedforward actions.

After being derived and stored in their condensed-information format, the LFM models can be routinely analyzed by computer to produce fault tree structures for reliability analysis purposes. By additional utilization of the instrument signals coming from the actual process modeled, the same computer routine can be employed in a DAS to produce diagnostic trees for the identification of the root cause(s) of an existing disturbance. This procedure is well suited for DAS implementation since it does not require any analyst's or operator's mediation and can thus be performed on-line. Tests performed on LFM utilization in disturbance analysis showed that a diagnosis can be obtained by the DAS computer one second or less from the start of a disturbance.

PRESSURIZER MODEL

The pressurizer, together with the control and protection devices attached to it, constitutes an essential system in a PWR plant. The complexity of the functions it must perform, in keeping the primary system pressure within the working range and in allowing for the volumetric expansion and contraction of the primary coolant mass, makes the development of a reasonably complete LFM pressurizer model a quite challenging task, one that can seriously test the method capabilities. We review briefly the controls and protections that are typically employed in such a system.

The following devices can intervene in regulating the pressure for control and/or safety purposes: a) safety valves (safety), b) power operated relief valves (PORVs)(control/safety), c) proportional sprays (control), d) proportional heaters (control), e) backup heaters (control).

Pressurizer level, on the other hand, is regulated by properly adjusting the charging flowrate from the chemical and volume control system (CVCS). This can be done by controlling the speed of a positive displacement pump or by throttling a valve on the discharge line of a centrifugal pump (when this alternative charging mode is being used.

In the derivation of the LFM model, the modeled range of pressure and level is the one between the high and low pressure trip set-points and above the low level trip set-point, which deliberately limits the modeling effort to transients before the occurrence of reactor shutdown.

Within the selected pressure range, it was necessary to arrive at a definition of the discrete penta-valued set needed in LFM for representation of the pressurizer pressure (PP) "continuous variable." Figure 2 illustrates the choice that was made in regard to this. In the selected scheme, the PORV setpoint determines the boundary between the +1 and +10 values, whereas the midpoint between the backup heater energizing and de-energizing set-points is used as a boundary between the -1 and -10 values. The separations between the 0 and +1 values, and between the -1 and 0 values, correspond to the start-point of the spray flow demand program ramp, and to the midpoint of the proportional heater demand program ramp respectively. Different choices are possible. The set-up just illustrated, however, provide a sufficiently balanced representation of the "normal" and "upset" conditions within the modeled range.

Figure 3 shows two portions of the pressurizer model that was ultimately developed. Section a represents some of the principal thermal-hydraulic interactions with the paths of the protective and control actions affecting the pressurizer pressure and pressurizer level parameters. Section d shows the details of the level control system. The remaining portions of the model can be found in Reference 3 together with the necessary aids for its detailed interpretation. It is important to notice that, due to the considerable complexity of the physical reality to be represented, it is necessary to break down physical interactions into fundamental composing parts. For instance, the driving mechanisms for variation in the system pressure PP are assumed to be either produced by a direct outflow of steam (SOF) or by volumetric effects (VPE) that cause steam compression or expansion and which are induced by variations in the water level. In addition, pressure changes may be induced by changes in the balance exchange flow (BEF) between the water and steam phases in the pressurizer. BEF normally acts as a corrective agent on either of the other two variables just mentioned above, but is also capable of directly inducing variations in PP. The BEF variable is driven by the combined action of the proportional sprays (variable PSF), the proportional heaters (variable PHA) and backup heaters (variable BHA), and is also influenced by other factors such as the pressurizer pressure itself and the degree of pressurizer water subcooling (variable PWS). To describe the complete interactions between these variables the "special input box" (SIB) operators S1 and S2 are used together with the other LFM standard operators. These are equivalent to multi-state decision tables representing the correspondence between BEF and its input variables PHA, PSF, and BHA. The assumptions for modeling this correspondence derive from knowledge of the relative capacities of the heaters and sprays.

DIAGNOSTIC AND RECOVERY TREES

References 2 and 3 illustrate how the computer program TRIC (Tree Instantaneous Constructor) implements the LFM modeling "grammar" and a complete set of "tracing rules" to allow derivation of logic trees from the flowgraph models. To derive a fault or success tree, TRIC only needs as input a definition of the tree top event in the form (variable) = (value) (for example: V = + 10). If the program is run on-line on a process computer (as would be the case in a DAS application) process instrumentation readings will also be used as inputs, to only allow derivation of tree branches corresponding to the actual events (among all those that could in theory produce the top event). When this latter procedure is used to determine the causes of a process upset, the tree produced by the LFM automated analysis is called a "diagnostic tree."

Diagnostic trees for two different disturbances are presented here. The first hypothesized disturbance is one that affects the PLCS (pressurizer level control

system). While the PLCS is in the centrifugal pump regulating valve mode (control option CO = $\bar{0}$), it is assumed that a drift in the level controller setpoint causes a transient to be initiated, resulting in a moderate lowering of the pressurizer level (PLD = -1). When the disturbance is well under way, different observable variables are affected and assume perturbed values. Figure 4 shows the diagnostic tree developed by TRIC when taking the event PLD = -1 as the top-event and the "observed" values of the other variables just mentioned as "boundary conditions" for the given disturbance. These observable conditions are marked by a dot in Fig. 3 for identification by the reader. It should, however, be understood that other observable conditions, utilized to exclude non-active tree branches from the diagnostic derivation, do not appear in the diagnostic tree itself.

The second hypothetical disturbance with which the pressurizer model was tested is a transient in which a stuck-open power-operated relief valve (RVUO = $\bar{1}$) causes the pressurizer pressure to fall low (in the LFM -10 range). Secondary effects of this are the actuation of the proportional and backup heaters and the disactivation of the sprays, in an attempt by the PPCS (pressurizer pressure control system) to contrast the course of the transient and arrest the observed decrease in the system pressure. The top event PP = -10 was analyzed by TRIC with the use of the appropriate boundary conditions given by the observable events resulting from the occurrence, and the resulting diagnostic tree is shown in Figure 5.

It is worthwhile to notice that the significant part of the tree, in terms of disturbance diagnosis, is the one on the right side under the SOF = +10 event, and shows the disturbance root cause RVUO = $\bar{1}$. The left side (event BEF = +1, etc.) only describes conditions that result from, or accompany, the disturbance, and which are to be shown for a better comprehension of the actual occurrence.

It was mentioned before that LFM permits the derivation of both fault and success trees from the same flowgraph. The ability to derive success trees can be advantageously used in disturbance analysis to identify recovery actions after a disturbance has been identified and diagnosed. For example, to obtain from TRIC a "recovery tree" for the disturbance just discussed above, one may set the top variable PP equal to 0 (which is the "default", unperturbed LFM value for any continuous variable), and adjust accordingly the values of the other observable values on which PP may have direct or indirect influence. Thus the values of the variables BHA and PHA have to be modified into 0's for consistency with the new value assumed for PP. All the other observable variable values produced by the disturbance are, however, kept as boundary conditions. The LFM routine can then identify possible actions that may suppress the undesired effects of the disturbance root cause(s). The tree obtained in this fashion is partially shown in Figure 6. The actual tree derived by TRIC includes development of events like VPE = 0 and BEF = 0, which are only of secondary interest and therefore not shown here. The desired recovery action can be seen at the low left end of the tree, indicated by the event BVS = $\bar{1}$ (which means: PORV block valve secured), 'ANDED' with the primary branch containing the fault event RVUO = $\bar{1}$.

The example given above demonstrates the feasibility "in principle" of the use of LFM-derived success trees to identify needed recovery action. Different strategies can be envisioned to make this process as efficient as possible, so that for instance the LFM routine could automatically avoid the development of "useless" branches such as the ones omitted from the tree in Figure 6, and could also expressly emphasize the identified "recovery action" in some way appropriate for ready interpretation by the operator.

As a factor relevant to the actual on-line applicability of LFM in disturbance analysis, it is noted that, throughout the testing done with the pressurizer model, the developed fault or success trees were produced by the TRIC code in times of the order of 1 sec on an IBM 370/3033 computer.

CONCLUSIONS

This paper has discussed the application of a new approach called the Logic Flowgraph Methodology to a fairly complex system, for the purpose of automatically producing fault or success trees. The computer routine based on LFM is presently operational and capable of performing this task, be it for reliability or disturbance analysis applications. The routine itself requires about 160K of computer memory on an IBM 370/3033. The most recent version has been partially optimized to reduce array storage. As a result, the pressurizer model discussed here requires only an additional 160K. The previous code version required the same amount of array memory for a system model, presented in Reference 4, which had less than 1/3 the number of LFM modeling elements.

Since in the area of reliability and risk analysis many proven and consolidated methods exist and are routinely used, the major emphasis of research for LFM implementation was placed in the disturbance analysis - automatic diagnosis and recovery identification area. We think that the results presented and discussed in the previous sections are promising, and confirm the potential of the method for disturbance analysis applications. Of course, before real implementation, it would be necessary to further test the methodology and the models with real on-line, rather than simulated, disturbances.

Open to definition remain the possible different strategies by which a user may want to utilize the methodology within the scope of an integrated disturbance analysis system. The choice of such strategies is expected to be influenced by contingent practical considerations regarding a specific application area, rather than by aprioristic theoretical arguments.

It is finally noted that for a user, LFM involves in a sense the learning of a new "language." In practical application to complex systems, it will also require intimate knowledge of these systems. Consequently, the skills of trained practitioners will be needed for successful utilization.

REFERENCES

1. S. A. Lapp, G. J. Powers: "Computer Aided Synthesis of Fault-Trees", IEEE Trans. on Reliability, April 1977.

2. S. Guarro, D. Okrent: "The Logic Flowgraph: A New Approach to Process Failure Modeling and Diagnosis for Disturbance Analysis Applications", Ph.D Dissertation, UCLA, June 1983.

3. S. Guarro, D. Okrent: "The Logic Flowgraph: A New Approach to Process Failure Modeling and Diagnosis for Disturbance Analysis Applications", UCLA - ENG report, to be published.

4. S. Guarro, D. Okrent: "Logic Flowgraph Methodology for use in Disturbance, Reliability and Risk Analysis", Proc. of 7th Intl. Conf. on Structural Mechanics in Reactor Technology, Chicago, IL, August 1983.

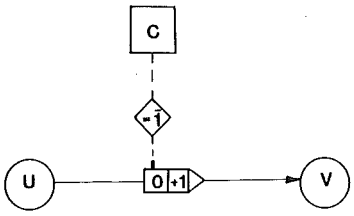

Fig. 1 Example of LFM Representation

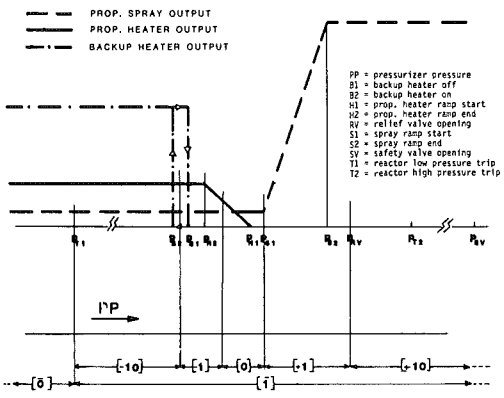

Fig. 2 Discretization of Pressurizer Pressure (PP) Range

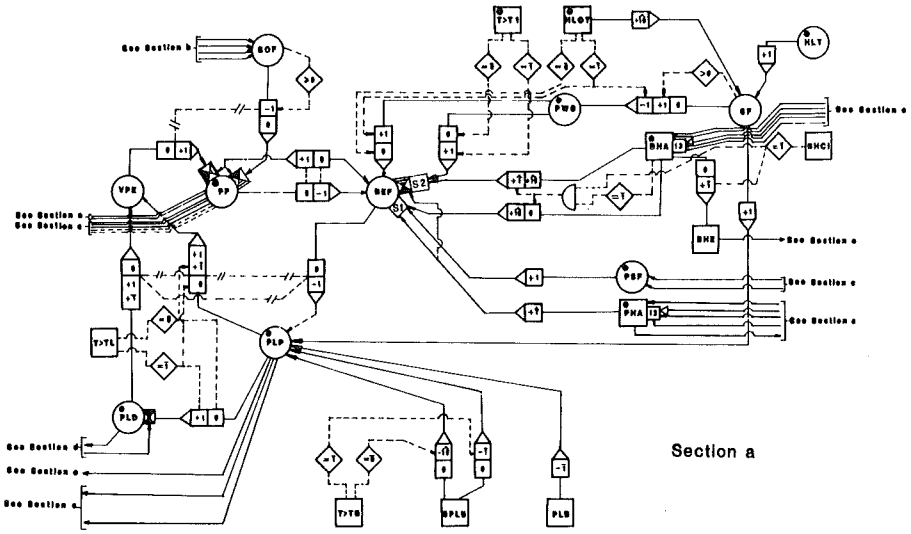

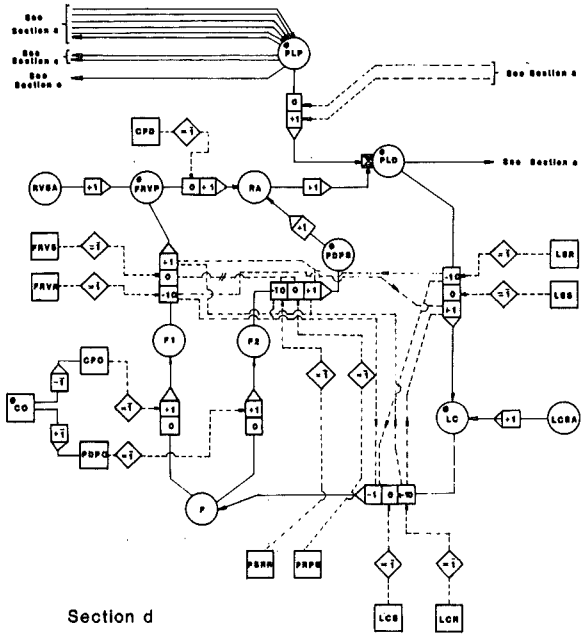

Fig. 3 LFM Pressurizer Model

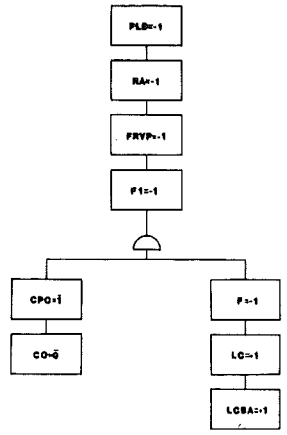

Fig. 4

Pressurizer Level Diagnostic Tree

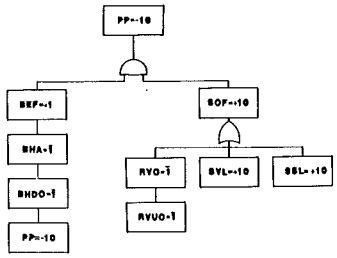

Fig. 5

Pressurizer Pressure Diagnostic Tree

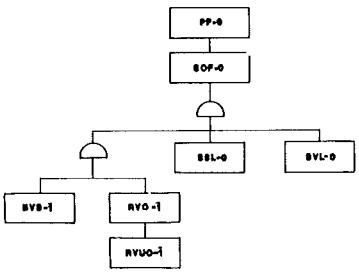

Fig. 6

Pressurizer Pressure Recovery Tree

A SYMPTOM BASED DECISION TREE APPROACH TO BOILING WATER REACTOR EMERGENCY OPERATING PROCEDURES

Ronald C. Knobel

Knobel & Associates, Inc.
P.O. Box 114
Long Beach, North Carolina 28461, U.S.A.

ABSTRACT

This paper will describe a Decision Tree approach to development of Boiling Water Reactor Emergency Operating Procedures for use by operators during emergencies. This approach utilizes the symptom based Emergency Procedure Guidelines approved for implementation by the United States Nuclear Regulatory Commission.

Included in the paper, as background, is a discussion of the relative merits of the event based Emergency Operating Procedures currently in use at United States Boiling Water Reactor plants. The body of the paper is devoted to a discussion of the Decision Tree Approach to Emergency Operating Procedures soon to be implemented at two United States Boiling Water Reactor plants, why this approach solves many of the problems with procedures identified in the post accident reviews of Three Mile Island procedures, and why only now is this approach both desirable and feasible. The paper will also discuss how nuclear plant simulators were involved in the development of the Emergency Operating Procedure decision trees, and in the verification and validation of these procedures.

TEXT

The symptom based Emergency Procedure Guidelines deviate from ANS 3.2/ N18.7-1976 Section 5.3.9 in that they do not provide operator actions for events such as Loss of All Feedwater. Rather, the symptom based guidelines provide operator actions for decreasing reactor water level, one cause of which might be loss of all feedwater. Thus, the operator responds to restore reactor water level regardless of the cause of the decrease with whatever equipment may be functional.

Since all United States Boiling Water Reactor Nuclear Plants (BWR) currently have procedures designed to satisfy the requirements of ANS 3.2/ N18.7-1976 Section 5.3.9 and will soon be implementing these symptom based Emergency Procedure Guidelines, Revision 3 dated December 8, 1982, currently NRC approved for implementation, a dilemma faces them. How to integrate procedures developed from symptom based guidelines into an existing procedure

structure that supposedly, by listing conceivable symptoms, enables the operator to diagnose an event (or event combination), extract the correct procedure (or procedures for multiple events), and decide which is the most important procedure so that its immediate actions are taken first before some other important procedures immediate actions are taken.

It should be noted that ANS 3.2/N18.7-1976 Section 5.3.9 does not address emergency procedure actions in multiple event situations. Section 5.3.9 does state that "when immediate operator actions are required to prevent or mitigate the consequences of a serious condition, procedures should require that those actions be implemented promptly". If the serious condition is a result of multiple events, a situation will face the operator of trying to decide which is the lead procedure and which are the follow on procedures so that the immediate actions may be taken in the correct sequence. This is practically impossible for many reasons, not the least of which is that the operator can not remember them all nor would he probably get the right sequence in a multiple event emergency, since he has been trained for single events.

Shortly after the accident at Three Mile Island (TMI), the NRC formed the Bulletins & Orders Task Force (B&OTF). This task force was responsible for reviewing and directing the TMI related staff activities. In conducting this activity, the B&OTF concentrated its efforts on, among other things, the evaluation of Generic Operator Guidelines and the review of Plant Emergency Operating Procedures. One of the recommendations from the B&OTF was as follows: The Emergency Operating Procedures presently in use at operating BWR Plants should be restructured and reformated on a "symptom" basis, as opposed to the more "event-specific" basis on which these procedures have evolved. The Symptom-Based Emergency Procedures would be categorized according to general plant symptoms, such as Loss-of-Coolant Inventory Accidents (LOCA) as opposed to several separate existing associated procedures such as LOCA Inside Containment, LOCA Outside Containment, and Loss of Normal Feedwater. The Loss-of-Coolant Inventory Procedure would include the essential features of those existing procedures associated with LOCA Inside Containment, LOCA Outside Containment, and Loss of Normal Feedwater, but would make use of the fact that the initial operator responses for the latter procedures are similar.

The Essex Corporation of Alexandria, Virginia made a study of the TMI Emergency Operating Procedures and had the following comments: The procedures were deficient in content and format; inconsistencies existed between the procedure action statement and actual equipment nomenclatures; instructions and action seldom indicated system response; an excessive burden was placed on operator memory; no charts or graphs on parameter response were provided; confusion existed as to which procedure applied; and the procedures were deficient in diagnostic information.

Since TMI is a pressurized water reactor and the findings might be considered by some to be not applicable to BWR, a review of a typical US-BWR's Emergency Operating Procedures as developed in accordance with the ANS 3.2/N18.7-1976 Section 5.3.9 would reveal the following (using the same evaluation criteria that Essex Corporation used on TMI).

- The procedures are event oriented.
- They do not contain guidance on which procedure applies or is the lead procedure in multiple event conditions.
- They rely excessively on operator memory.
- System response is seldom indicated.
- Diagnostic information is presented in a generally long list of symptoms at the beginning of each event procedure.

- They contain many cross-references to other procedures.
- They contain few charts or graphs.
- Usability with multiple failures is poor.
- Operator awareness of total plant conditions would be questionable when multiple event conditions required use of the procedures.

As indicated in ANS 3.2/N18.7-1976 Section 5.3.9, it is extremely difficult to distinguish between procedures prepared for the purpose of correcting off-normal conditions which in themselves do not constitute actual emergency situations, (but which conceivably can degenerate into true emergencies in the absence of positive corrective action), and procedures required for coping with true emergencies that have already occurred. For the purposes of the Emergency Procedure Guidelines, the potential emergency conditions that are considered are those conditions that threaten the integrity of the reactor core or primary and secondary containment, or could threaten to cause harm to plant personnel and to the public. The following categories of events (or event combinations) are considered as examples of potential emergencies:

- Loss of coolant from identified and unidentified sources, from small loss to design basis-accident loss.
- Reactor transients and excursions.
- Failure of vital equipment.
- Loss or degradation of vital power sources.
- Abnormally high radiation levels.
- Excessive release of radioactive liquid or gaseous effuent.
- Malfunction of reactivity control system.
- Loss of containment integrity.
- Conditions that require the use of standby liquid poison systems.

Any and all of these conditions may require immediate actions to be taken by the operator to prevent further degradation and consequent automatic or manual reactor scram. Thus a possible approach would be, indeed the one taken and described in this paper, to extract from all the Emergency Operating Procedures required by ANS 3.2/N18.7-1976 those actions to be taken prior to reactor scram and assemble them into Abnormal Operating Procedures, and those actions to be taken after scram and assemble them into the Emergency Operating Procedures. This approach allows the Emergency Procedure Guideline symptom based instructions required prior to scram to be integrated with the Abnormal Operating Procedures and the Emergency Procedure Guideline symptom based instructions after scram to be integrated with the other procedural actions into the required Emergency Operating Procedures. In the event that the reactor is scrammed automatically or manually, due to a potential danger, the entry condition to the Emergency Operating Procedures would be REACTOR SCRAM. From this point, the Reactor Operator would follow a predetermined sequence of steps which specify immediate actions for operation of controls or confirmation of automatic actions that are required to stop the degradation of conditions and mitigate their consequences. The steps which the operator performs include the following:

- The verification of automatic actions.
- Assurance that the reactor is in a safe shutdown condition.
- Determination that the reactor coolant system pressure boundary is intact.
- Confirmation of the availability of adequate power sources.
- Confirmation that containment and exhaust systems are operating properly in order to prevent uncontrolled release of radioactivity.
- Notification of plant and off-site personnel of the nature of the emergency.

A further advance in the development of symptom based Emergency Operating Procedures exists in the decision tree format used by the National Aeronautics and Space Administration (NASA) in the formulation of the Emergency Operating Procedures for the space shuttle. This concept, translated into the BWR Emergency Operating Procedures here described is depicted (in example step form) in Figure 1.

As shown, several key decisions are made immediately by the operator (note that these decisions are consistent with the Emergency Procedure Guidelines).

- Is Reactor Power less than 3% (no represents a condition that could threaten the integrity of the reactor core).
- Is Drywell Pressure less than 1.8 psig (no represents a condition that could threaten the integrity of the Primary Containment).
- Is Auxiliary Power available from Startup Auxiliary Transformers (no represents a condition that could threaten core, containment, and public).
- Is Reactor Vessel level above -30 inches (no represents a condition that could threaten the integrity of the reactor core).
- Was the Mode Switch in run prior to Scram (a decision which dictates the actions to be taken in the startup mode where violent transients are not expected).

Appropriate actions are presented on the other Paths indicated, Path 1, Path 2, Path 4, Path 5. While not evident here, ALL Paths have the same initial key decisions so that no matter which Path the operator picks up at the time of scram, he will be led to the correct Path for his conditions.

The five Paths consist of operator actions keyed from decisions on availability of plant systems, verification of appropriate automatic actions, with the steps themselves being prioritized on each Path in the same manner that the initial key decisions prioritize for the operator which Path to be on. The Paths are immediate actions and cover roughly one half to one hour of time into the emergency. After that, as Figure 1 depicts, the operator is led to an End Path Manual which contains, among other things, the subsequent actions from all the deposed event based Emergency Operating Procedures required by ANS 3.2/N18.7-1976 Section 5.3.9. The immediate action Flow Chart Paths generally cover operator actions for the following groupings of events: (Refer to Figure 1)

Path 1 - Malfunction of Reactivity Control System
Path 2 - Transients from Low Power (Mode Switch in Startup)
Path 3 - Transients from High Power (Mode Switch in Run)
Path 4 - Loss of Coolant, Failure of Vital Power Source, Failure of Vital Equipment, Abnormally High Radiation
Path 5 - Loss of Coolant, Loss of Primary Containment Cooling, Excessive Radioactive Release, Abnormally High Radiation

Advantages of the symptom based Emergency Operating Procedures in Flow Chart Path format are;

- Immediate operator actions visible and prioritized in Flow Chart Path form.
- Reduced reliance on operator memory since all immediate actions are visible at all times.
- All Flow Chart Paths guide the operator to the correct procedure, in proper priority of actions.

FIGURE 1

PATH 3

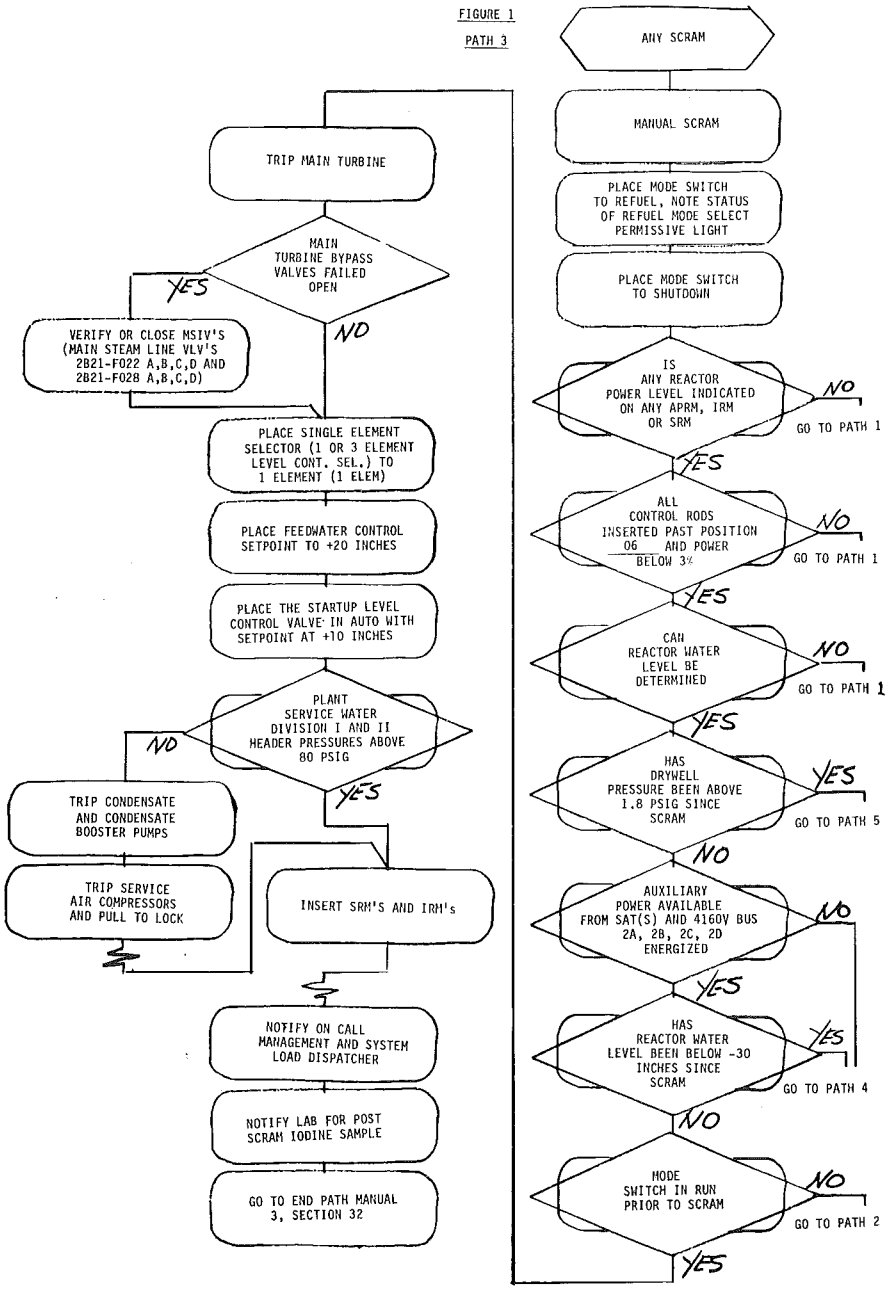

- Removes confusion as to which procedure applies; only one exists and operator is automatically led to it.
- Improves awareness of total plant conditions since many decision diagnostic steps are present.
- Improves decision making process since operator is now constantly keyed to be aware of plant conditions.
- Improves training for emergencies since symptoms are basis, multiple event emergencies can be practiced which were not possible before.

The basis for the Flow Chart Paths, briefly mentioned previously to stop the degradation of plant conditions, is accomplished by use of Key Parameters (see Figure 1). The Key Parameters (these key decisions are symptom evaluations) set the overall priority of operator actions, are identical on each Flow Chart Path, and their evaluation basis is as follows:

- Verify reactor nuclear shutdown or take steps as indicated on Flow Chart Path 1 to affect nuclear shutdown of the reactor while attempting to gain control of reactor water level and pressure.
- Verify the absence of a threat to the Primary Containment or take steps as indicated on Flow Chart Path 5, once reactor nuclear shutdown is verified or accomplished, to initiate containment control systems while attempting to gain control of reactor water level and pressure.
- Verify the absence of a threat to adequate core cooling possibly caused by failure of high pressure injection systems, total loss of AC power (inclusive of partial losses), break outside primary containment, stuck open relief valves (SORV) or take steps as indicated on Flow Chart Path 4 once reactor nuclear shutdown is verified or accomplished and the absence of a threat to the primary containment is verified.
- Determine the state (or states) of expected plant transient response by identifying the position of the reactor mode switch prior to scram (more violent transients are expected from the run mode than from the startup mode) and the operator actions are prioritized by this on Flow Chart Paths 2 and 3.

Thus, the operator has made an immediate determination of the state of the plant. He has determined whether a malfunction has occurred to the reactivity control systems, whether a malfunction or rupture has occurred inside the primary containment, whether AC power is available and whether a rupture outside primary containment or a stuck open relief valve has occurred, or whether he has merely sustained a transient scram from high or low power level.

It should also be noted at this point that the wording of the Key Parameters results in insuring that the operator remains on the proper Flow Chart Path once he has been led there by his symptom (Key Parameter) evaluations. Indeed, at this point the question of what operator action is to be taken if a Key Parameter changes state after the operator has made his initial evaluation, becomes appropriate. The answer lies in the following example: A scram has occurred, the Flow Chart Paths entered, the initial evaluation of Key Parameters has led the operator to Flow Chart Path 3 (transient trips from high power) and while taking actions, drywell pressure increases above 2 psig. What action should be taken? The operator is trained to respond to a change in a Key Parameter, which he constantly monitors for changes after Flow Chart Path entry, by returning to the top of the Flow Chart Path he is on and re-evaluate all of his Key Parameters since a change in any one may result in a change in a higher priority Key Parameter. Thus for this example, he would

be re-routed from Flow Chart Path 3 to Flow Chart Path 5. A review of Figure 1 and the Key Parameter (and its hierarchical position) associated with High Drywell Pressure will reveal that once on Flow Chart Path 5, the operator is not permitted access to any other Flow Chart Path, but is led to the End Path Manual for Flow Chart Path 5 after completion of the immediate actions even if other Key Parameters were to change (loss of AC power, for instance, operator action steps are contained on Flow Chart Path 5). The Key Parameter of Reactor Nuclear Shutdown will not change once it is verified or is achieved following the scram entry conditions.

Once the evaluation of Key Parameters has resulted in Flow Chart Path selection, the operator encounters additional Key Parameters which require the same return to the top of the Flow Chart Path for re-evaluation of ALL Key Parameters, but which do not result in a Flow Chart Path change, unless a consequent result occurs, i.e., if Closed Cooling Water to the Drywell is lost, and the reactor is hot, Drywell Pressure will increase causing its associated Key Parameter to change causing a Flow Chart Path change due to High Drywell Pressure, not due to the Loss of Closed Cooling Water. Other of these Key Parameters are associated with Plant Service Water, Control Air, and Fires.

The purpose of addressing support systems availability (calling their significant parameter out as a Key Parameter ensures that the operator remains constantly aware of their operability status) on the Flow Chart Paths are as follows:

- They enable operation of other systems, e.g., Plant Service Water enables operation of the Reactor Feedwater Pumps (lube oil is cooled by service water).
- They enable other systems to control other Key Parameters, e.g., Closed Cooling Water to the Drywell enables the removal of heat from the Drywell controlling both temperature and pressure.
- They force the operator to get ahead of the plant by monitoring their operability. Under current procedures, he is behind the plant. Something must first fail to be recognizeable as requiring operator attention or action to be taken (in the accident sense that is, as opposed to normal operations).
- They of themselves are symptoms of plant degradation and represent a potential source of damage to plant equipment that may be necessary for accident mitigation and as such are worthy of operator vigilance, especially during accidents.
- Their availability or non-availability result in the establishment of the various decision tree paths, e.g., since air is a cheap and convenient mode of operation of such valves as are associated with the condensate demineralizers on some BWR's, the non-availability of air means the non-availability of the condensate demineralizer and consequent temporary loss of the condensate and feedwater systems.

With existing event based procedures, these support system procedures are generally included in the Emergency Procedures category (Loss of All Plant Service Water could certainly be looked upon as an emergency). The operator's attention to this particular Emergency Procedure would vary from a high degree of attention if its loss was the first event that occurred to a low degree of operator attention if its loss were to occur during some event combination sequence like the following: Load Reject Scram, Bypass Valves Fail Open, MSIV Closure, and consequent Loss of All Feedwater, and then the annunciator alarms indicating Loss of All Plant Service Water. The operator's attention is not going to be instantly focused on this annunciator. In fact, he might not

recognize its receipt at all, as it would be another of the many annunciator alarms he is already receiving. Indeed, the probability exists that for this transient event combination (one that has a fair probability of occurrence) damage would most certainly be sustained by plant equipment that received cooling water from the Plant Service Water system. However, if one argues that all of this equipment has its own protective trips, then not the least that could occur in the above situation would be the operator completely missing the need to execute another Emergency Procedure with its own immediate actions. If one carries this examination a little further, since the operators currently are required to memorize and execute Emergency Procedures immediate actions from their memory, the various operator crews (typically 5 or 6 shift crews of operators) would probably execute the required immediate action steps in different sequences since individual memory is a poor determinant of commonality of action under high stress emergency conditions. Thus, besides the concept behind the Flow Chart Paths of stopping the degradation of plant conditions, the making visible to the operator the immediate actions reduces the uncertainty associated with reliance on his memory. It also requires that he monitor system status not currently required, thereby reducing the potential for equipment damage. Perhaps most important, by making his required immediate actions visible reduces the potential for error due either to failure to recognize that procedural action is required or once recognized, taking immediate action based upon reliance on memory alone and commiting errors of omission.

As previously mentioned, the basis of the Flow Chart Paths (the immediate action) is to stop the degradation of the event combination in progress. As such, the restoration of the support systems (Closed Cooling Water for instance) is not carried out on the Flow Chart Paths, it is however, accomplished in the End Path Manual which the operator enters upon completion of the immediate actions. Thus, on the Flow Chart Paths, the operator verifies system availability, or if indicated loss is apparent, attempts to start the standby components, and if unsuccessful, putting the system in a known configuration by taking immediate action to trip equipment serviced by the lost support system. In the case of Plant Service Water, this would mean a trip of the feedwater and condensate pumps, placing reliance on other high pressure injection systems, or should they be unable to maintain Reactor Water Level above a desired level, the Flow Chart Paths (as does the EPG) would direct the operator to blow down the reactor and start his low pressure injection systems.

As the operator(s) complete a decision tree on a given Flow Chart Path, they will be led to an End Path procedure in the End Path Manual provided for actions subsequent to those immediate actions the operator has completed on the Flow Charts. Each End Path procedure is specifically developed for each possible decision tree on the Flow Charts.

Currently in the United States, Carolina Power and Light at its Brunswick Nuclear Station and Georgia Power at its Hatch Nuclear Station have either implemented or are currently developing the Flow Chart Path approach described herein. Philadelphia Electric and Boston Edison are either developing or have implemented other Flow Chart Path approaches. While the various Flow Chart Path techniques may vary, and the actions contained on the various Flow Chart Paths may also vary, what is significant in this effort by the above mentioned utilities is their efforts to improve the operator responses to degraded emergency operating situations by use of Flow Chart decision trees.

Emergency Operating Procedures Verification

Emergency Operating Procedures Verification consists of ensuring that the Emergency Operating Procedures (Flow Chart Paths and End Path Manuals) are technically correct (accurately reflecting the Plant Specific Technical Guidelines), that they are written correctly and that controls and instrumentation called out in the Emergency Operating Procedures actually exist and verbatim nomenclature has been used. Emergency Operating Procedure verification is performed prior to the start of operator training. This process identifies any deviation from the Plant Specific Technical Guidelines, describes any analysis performed to determine the safety significance of the deviation, and provides a technical justification for the plant specific approach, as required.

Since verification will be completed prior to initial Emergency Operating Procedures implementation, any discrepancies found during verification will also be completely resolved prior to approval and implementation of Rev 0 of the Emergency Operating Procedures. Note that verification is a two-phase process. Phase 1 is performed prior to start of operator training and covers the entire set of Emergency Operating Procedures. Phase 2 is the verification of individual revisions entered during training resulting from the validation program.

Emergency Operating Procedure Validation

Emergency Operating Procedure Validation ensures that the language and level of information presentation in the Flow Chart Paths and End Path Manuals are compatible with the qualifications, training and experience of the operating staff, and that there is a high level of assurance that the procedures will work, i.e., the procedures guide the operator in mitigating transients and accidents. Emergency Operating Procedure Validation is performed in parallel with operator training.

Many man-weeks are spent in the plant specific simulator, with participation by Shift Technical Advisors and reactor operators, developing and validating the Flow Chart Paths decision trees (utilizing multiple-event scenarios extensively) before operator training begins. This work is fully documented including a list of multiple-event scenarios run and significant results. During operator training (over approximately a 1 year period), many additional man-weeks will be spent in the simulator with evaluation of operator response and operator feedback included in the validation of the Flow Chart Paths decision trees.

Actual plant walk-throughs are conducted on a case basis to ensure that the simulator represents the plant correctly and that in-plant name plates are used for proper nomenclature of equipment. Extensive table-top reviews are performed during development, especially utilizing the Shift Technical Advisor/ reactor operator member of the development team, and a record of problems and resolutions is kept. Additionally, initial operator training is conducted in classroom table-top use of the Flow Chart Paths and End Path Manuals, and operator feedback recorded. Note that simulator scenarios are chosen randomly until all possible Paths down the Emergency Operating Flow Chart Paths are followed, thus ensuring complete coverage.

Documentation includes records of operator comments, changes made as a result, exam results, simulator records, and operator simulator performance records.

FLOW CHART SYMBOLS

There are several types of symbols on each chart. Refer to Figure 1.

Decision or Question Symbol

This block always contains a question which must be answered yes or no. The question will concern a specific parameter, setpoint, switch position, or system condition (symptoms),

Information Symbol

This block contains information which may be useful to help the operator diagnose the event combination that has occurred or is occurring.

Performance or Action Symbol

This block contains a specific action or command which the operator should perform. It will consist of a verification of automatic action or a command to take action such as "verify certain pumps in service", "place system in service" or "remove specific equipment from service".

Path to Path Arrow Symbol

These symbols aid the operator in finding the correct entry point into another Flow Chart Path when directed there from a path. These arrows have unique shapes which are designed to aid in rapidly locating the entry point when changing from one Flow Chart Path to another.

Flow Chart Path to End Path Procedure Arrow Symbol

These symbols direct the operator from the Flow Chart Path he has completed to the correct section of the End Path Manual. The symbols contain the numbers that correspond to the appropriate section of the End Path Manual.

In summary, the paper discusses the relative merits of the event based Emergency Operating Procedures currently in use at United States Boiling Water Reactor plants. The body of the paper is devoted to a discussion of the Decision Tree approach to Emergency Operating Procedures soon to be implemented at two United States Boiling Water Reactor plants and why this approach solves many of the problems with procedures identified in the post accident reviews of Three Mile Island procedures. The decision tree Flow Chart format is possible now because of the development of symptom based Emergency Procedure Guidelines. It is desirable to enhance the visibility of procedural guidance for improved operator usability.

The paper also discusses how nuclear plant simulators were involved in the development of the Emergency Operating Procedure decision trees, and in the validation of these procedures.

RECENT RESULTS FROM THE U.S. SEVERE ACCIDENT SEQUENCE ANALYSIS (SASA) PROGRAM

Robert T. Curtis and Bharat B. Agrawal

U.S. Nuclear Regulatory Commission
Washington, D.C. 20555

ABSTRACT

The SASA program provides deterministic analysis of risk dominant sequences to evaluate sources of uncertainty, the effectiveness of accident management strategies and the utility of changes to plant configuration or procedures. It is an integral part of the U.S. program to reduce risk from severe accidents. Detailed analysis which include a review of BWR ATWS sequences, a study of the effectiveness of feed and bleed and studies of plant recovery after core damage is presented. The paper presents results from these studies and their safety implications.

INTRODUCTION

The accident at Three Mile Island (TMI) led to the reorientation of Nuclear Regulatory Commission (NRC) research priorities and the development of a severe accident research program. Part of this program is the Severe Accident Sequence Analysis (SASA) program. The SASA program seeks to improve the understanding of reactor accidents in order to develop better strategies to prevent, manage and mitigate severe accidents. Insights into safety issues are gained by applying best-estimate state-of-the-art methods of analysis to investigate in detail the progression of events in risk dominant accident sequences and, thereby develop guides to evaluate possible operator procedures. The studies concentrate on both the initiating events through early core damage and the later phases of the accident, i.e., core melt, fission product release and transport through containment failure. Significant attention is directed at the identification of alternatives which might terminate the accident and lead to recovery.

The SASA program selects the risk dominant sequences for each plant from appropriate probabilistic risk assessment (PRA) programs such as the Accident Sequence Evaluation Program (ASEP),[1] the Interim Reliability Evaluation Program (IREP) and the Reactor Safety Study Methodology Applications Program (RSSMAP). These risk-dominant sequences provide the framework for calculation and analyses of complex accident sequences in which critical equipment performance and operator actions are simulated. The SASA program is contributing to the development

of probabilistic methods by supporting ASEP with deterministic, best estimate analyses of severe accidents using the available state-of-the-art thermal hydraulic, phenomenological, fission product behavior and consequence codes.

The ongoing SASA program studies presented here are: accident sequence analysis for BWR anticipated transient without scram (ATWS) and a study of the effectiveness of feed and bleed for decay heat removal in PWRs.

DESCRIPTION AND RESULTS OF THE ATWS STUDY

The goals of this study are to (a) make realistic determination of the time-dependent progression of events from the initiating event through core uncovery, meltdown and containment degradation (b) investigate appropriate operator actions and their timings to prevent containment failure and/or core damage and (c) determine if operator actions contained in emergency operating procedures are adequate to manage the accident and determine what information and operator actions are needed to mitigate accident consequences.

The dominant sequence for the ATWS is the Main Steam Isolation Valve (MSIV) closure followed by failure to scram. The MSIV closure was chosen because of its relatively high frequency and severe challenge to heat removal and containment integrity systems.

An ATWS preliminary study[2] has been completed using the BWR-LACP code developed at Oak Ridge National Laboratory. A simulation working session in conjunction with the Human Factors program showed that with training, the operators can effectively shutdown the core by:

a. Lowering and maintaining the indicated water level at the top of the core.
b. Manual Insertion of Control rods.
c. Injection of Sodium Pentaborate Solution.

With the MSIVs shut, all steam generated by the at-power reactor is conveyed into the pressure suppression pool (PSP) via safety relief valves (SRVs) as shown in Figure 1. The MSIVs require about 4 sec to close. As the valves close, automatic reactor scram fails and reactor vessel pressure increases, causing void collapse in the core and thereby inserting positive reactivity. Core power increases rapidly, causing high pressure and the opening of all reactor vessel relief valves. The recirculation pumps trip on high reactor vessel pressure [1120 psig (7.82 MPa)] about 5 s after the beginning of MSIV closure, converting core flow from forced to natural circulation. The reduced core flow immediately causes an increased temperature of the water moderator in the core and consequently, increased voids and negative reactivity. Reactor power decreases and some of the SRVs close, stabilizine reactor vessel pressure at the relief valve setpoint [about 1120 psig (7.82 MPa)]. Feedwater flow reaches zero shortly thereafter since the steam supply to the feedwater turbines is lost when the MSIVs are shut.

Without feedwater (FW) the reactor vessel (RV) water level decreases until the High Pressure Coolant Injection (HPCI) and Reactor Core Isolation

Cooling (RCIC) pumps are automatically actuated. The HPCI and RCIC pumps act as FW pumps and that their combined rate of injection determines the reactor power. The term "reactor power" implies the steaming rate from the RV expressed as a percentage of the steaming rate at normal full operation. All of the steam produced in the RV is discharged through the SRVs to be condensed in the PSP. During the first 15 minutes of ATWS, the PSP temperature is increasing from 90°F to 190°F. When the PSP level increases 7 in. the HPCI pump suction is automatically shifted from condensate storage tanks to the PSP. The increasing PSP temperature challenges the ability of the HPCI system to keep pumping since the HPCI turbine lubrication oil is cooled by the water being pumped and the operating limit for the lubrication oil is 140°F.

After HPCI system failure, the total vessel injection is insufficient to replace the water inventory loss with the core critical and generating 28% thermal power (Figure 2). Upon receipt of the low water level signal the low pressure coolant injection (LPCI) and core spray pumps start but do not immediately inject, since the vessel is still pressurized. The vessel water level continues to decrease, reaching the top of the active fuel (TAF) before automatic depressurization system (ADS) actuation. The ADS actuation opens six SRVs and initiates a rapid depressurization of the RV. The rapid loss of vessel water inventory completely uncovers the core within one minute. With the core uncovered the thermal power subsides to the decay heat level. When vessel pressure decreases to below 418 psia at 20 min., the condensate booster pumps (CBPs), begin pumping water to the RV. The LPCI and the Core Spray pumps begin injection within 10 sec. of the CBP flow and recovers the core in about 20 sec.

The recovery of RV water level provides enough moderator for the core to sustain criticality. Continued increase in water level causes power excursion by building excess positive reactivity. The increasing power and pressure is broken when pressure reaches the relief valve set points and all SRVs open, limiting vessel pressure to the neighborhood of 1100 psia. Whenever the RV pressure is above 418 psia there is no injection by the low pressure systems. The combined RCIC and control rod drive hydraulic systems (CRDHS) injection of 700 gpm is insufficient to prevent a steady decrease in vessel water level. When the vessel pressure decreases to below 418 psia the CBPs and LPECCS pumps are again able to inject. This cycle of vessel depressurization and power excursion and repressurization of the RV is repeated until the drywell failure due to overpressurization in 37 min.

The progression of MSIV-closure initiated ATWS accident sequence in which operator actions play a dominant role is discussed here. The control room operators would recognize the initiation of an ATWS by the existence of a combination of scram signals and continued indication of reactor power on the average power range monitors. The effective means for the operator to insert negative reactivity is by the standby liquid control systems (SLCS). This system is designed to permit sodium pentaborate solution into the RV at a rate of 56 gpm. At an injection rate of 56 gpm it would take about 80 min. to pump the total volume of 4550 gals. of sodium pentaborate solution from the storage tank into the RV. The reactor can thus be brought to hot shutdown.

The BWR Owners Group emergency procedure guidelines (EPGs) instruct the operator to reduce vessel injection as necessary to lower the downcomer water level to the top of the core. The core thermal power is about 9% with the downcomer water level lowered to the TAF and with the RV fully pressurized. Accordingly the EPGs specify that the operator should restore the RV water level to the normal operating level after the amount of sodium pentaborate required for hot shutdown has been injected.

The Commission has approved the Final Rule on ATWS, unanimously supporting the following provisions for BWRs:

a. Each BWR must have an alternate rod injection (ARI) system that is independent and diverse from the reactor trip system (RTS).

b. Each new BWR must have an automatic SLCS with flow capacity of 86 gpm of 13 weight percent of sodium pentaborate solution. This applies to plants granted a construction permit after August 1, 1984 and for plants granted a construction permit prior to August 1, 1984 that have already been designed and build to include this feature.

c. Each BWR must provide diverse means of recirculation pump trip (RPT) automatically under conditions indicative of an ATWS. This safety feature will result in a reduction of reactor power from 100 percent to 30 percent following a transient (failure to scram). This proposed requirement has already been implemented on all operational BWRs.

The Commissioners agreed that the new systems should not have to be fully safety grade but should have some quality assurance and testing requirements. Utilities will have 6 months as of August 1, 1984 to submit to NRC a proposed schedule for meeting the above requirements. NRC officals expect that most plants will meet the requirements within 3 years.

A more detailed analysis of system thermal hydraulic and core neutronic conditions up to core damage and containment failure for ATWS are presently underway using the RELAP5, RAMONA-3B and SCDAP codes. RELAP5 results will be benchmarked using RAMONA-3B with 3-D neutronics capability coupled with non-homogenous, nonequilibrium thermal hydraulics.

DESCRIPTION AND RESULTS OF THE FEED AND BLEED STUDY

The SASA program recently completed an analysis of shutdown decay heat removal using feed and bleed techniques for PWR in support of Unresolved Safety Issues A-45.[3] The accident sequences considered are loss of feedwater induced by loss of offsite power (LOSP), and loss of feedwater (LOFW) transients. The feed and bleed process refers to the direct removal of decay heat from the primary system utilizing the high pressure injection system and the pressure relief system. The TRAC-PF1 code was used in this analysis to enhance our understanding of the capability of PWRs to remove decay heat using feed and bleed in accidents in which all secondary cooling has been lost. The PWR plants analyzed are: Zion (W), Oconee-1 (B&W), and Calvert Cliffs (CE).

During the extensive LOFW studies for the Oconee-1, Calvert Cliffs-1, and Zion-1 reactors, it was determined that a limited number of plant features are most important in defining accident signatures and the outcome of recovery techniques. The recovery techniques examined were feed only (the ECC systems inject coolant at the power operated relief valve (PORV) setpoint) and feed and bleed (the PORV is locked open and the ECC systems inject coolant at an increased rate because system pressure is decreased).

The primary plant feature determining event timing for the primary heatup rate are the reactor trip time and steam-generator-secondary inventory. The primary plant features determining the timing and success of feed and feed-and-bleed cooling operations are the PORV capacity and the ECC system flow characteristics. These significant plant parameters are tabulated in Table I.

TABLE I

KEY PLANT CHARACTERISTICS

	Oconee	Calvert Cliffs	Zion
Steady State power (MWt)	2584	2700	3250
Total SG secondary inventory (kg)	35,000	124,700	173,840
Number of PORVs	One	Two	Two
Rated PORV capacity (kg/s)	12.8	38.7	53.0
ECC flow (kg/s) at PORV setpoint	27.2	8.3	15.6

Comparing the base case transients (Table II), Oconee had the shortest heatup time, which was two to three times faster than that of Calvert Cliffs or Zion. The base transients showed that the LOSP event had a significantly slower heatup time than the LOFW event. In the LOFW event, the reactor does not trip immediately and the reactor coolant pumps continue to operate. These two effects increase heatup rates.

All three plants were successful in the feed mode in stabilizing reactor conditions; however, the timing window of success was different. For both Oconee and Zion, the feed mode was successful if initiated as late as the loss of core-subcooling margin. The high-head flow-injection capability of the HPI systems in these plants makes this possible. However, for Calvert Cliffs, with its high-head low-flow safety injection (SI) capability, feed cooling must be established by steam-generator dryout. Although this requires that feed be initiated earlier (at steam-generator dryout vs. at loss of core subcooling), the actual time delay is at least 20 min from the start of the initiating transient (LOSP, LOFW). This is at about the same time that the loss of core subcooling occurs in Oconee for the LOFW event. For Zion, with the greater steam-generator inventory, the loss of core subcooling would occur after 30 min for the LOFW event. Delayed reactor trip times of up to a minute from the initial loss of feedwater were considered in this analyses.

TABLE II

	Oconee	Calvert Cliffs	Zion
S.G. time to dryout - LOFW event (min)	3.3	20.8	51.3
S.G. time to dryout - LOSP event (min)	10.0	58.3	69.5
Core heatup begins - LOFW event (min)	36.7	70.0	104.7
Core heatup begins - LOSP event (min)	50.0	133.3	138.3

The feed-and-bleed mode can be used successfully in all instances where the feed mode has been determined to be successful: for Oconee and Zion, up to the time of loss of core subcooling; for Calvert Cliffs, up to the time of steam-generator dryout. If feed is initiated later than these times, significant core voiding may have occurred already, with the possibility of fuel/cladding damage. If feed is initiated after possible core voiding, the PORV should not be locked open until core subcooling has been reestablished since locking open the PORV under partially voided core conditions could hinder water-level recovery.

For each of the three plants examined, using detailed thermal-hydraulic studies it was found that there was a span of time within which a feed-and-bleed procedure could be applied successfully to effect a transition from reactor trip to hot standby. For the transition from reactor trip to hot standby, success is defined as the attainment of a stable primary system having the following three characteristics. First, the primary system pressure is above the actuation pressures for both the low pressure injection (LPI) system and accumulators. Second, the primary system and vessel mass inventories are stable or increasing. Third, the cladding temperatures are near primary liquid saturation temperatures with no departure from nucleate boiling. For the transition from reactor trip to hot shutdown, success is defined as the completion of a controlled primary-system depressurization and cooldown to achieve conditions permitting long-term cooling using either the residual heat-removal system or the LPI system taking suction from the containment sump. Figure 3 denotes success or failure criteria as follows:

S1: Success in transition from reactor trip to hot standby (accomplishment of the first success criterion).

F1: Failure in transition from reactor trip to hot standby (failure of the first success criterion).

S2: Success in transition from reactor trip to hot shutdown (accomplishment of the second success criterion).

F2: Failure in transition from reactor trip to hot shutdown (failure of the second success criterion).

Although the viability of a feed-and-bleed operation has been determined for three specific plants, the objective of TAP A-45 is to eventually identify all plants for which feed-and-bleed procedures can be successfully applied.

The SASA program will continue to analyze dominant sequences derived from risk assessment studies for specific plant designs to evaluate areas of uncertainty, to access prevention and mitigation of core melt during severe accidents. Major phenomenological test programs will be used to produce data that can be used to evaluate SASA results.

REFERENCES:

1. A. M. Kolaczkowski et al., Interim report on Accident Sequence Likelihood Reassessment (Accident Sequence Evaluation Program), February 1983.

2. R. M. Harrington et al., ATWS at Browns Ferry Unit One - Accident Sequence Analysis, NUREG/CR-3470, July 1984.

3. B. E. Boyack et al., Los Alamos PWR Decay-Heat-Removal Studies Summary Results and Conclusions (to be published).

Codes:

BWR-LACP: AN ORNL developed simulation program for BWR Accident Analyses to provide plotted studies of the plant response to operator actions.

HECTR: Integrated analysis of hydrogen burns in containment.

RELAP: Integrated analysis of thermal hydraulics of the reactor primary and secondary cooling systems.

TRAC: A multidimensional analysis method to investigate two phase thermal hydraulics behavior of the primary and secondary reactor coolant systems.

RAMONA-3B: A BWR core and systems transients analysis code with 3-D neutron kinetics.

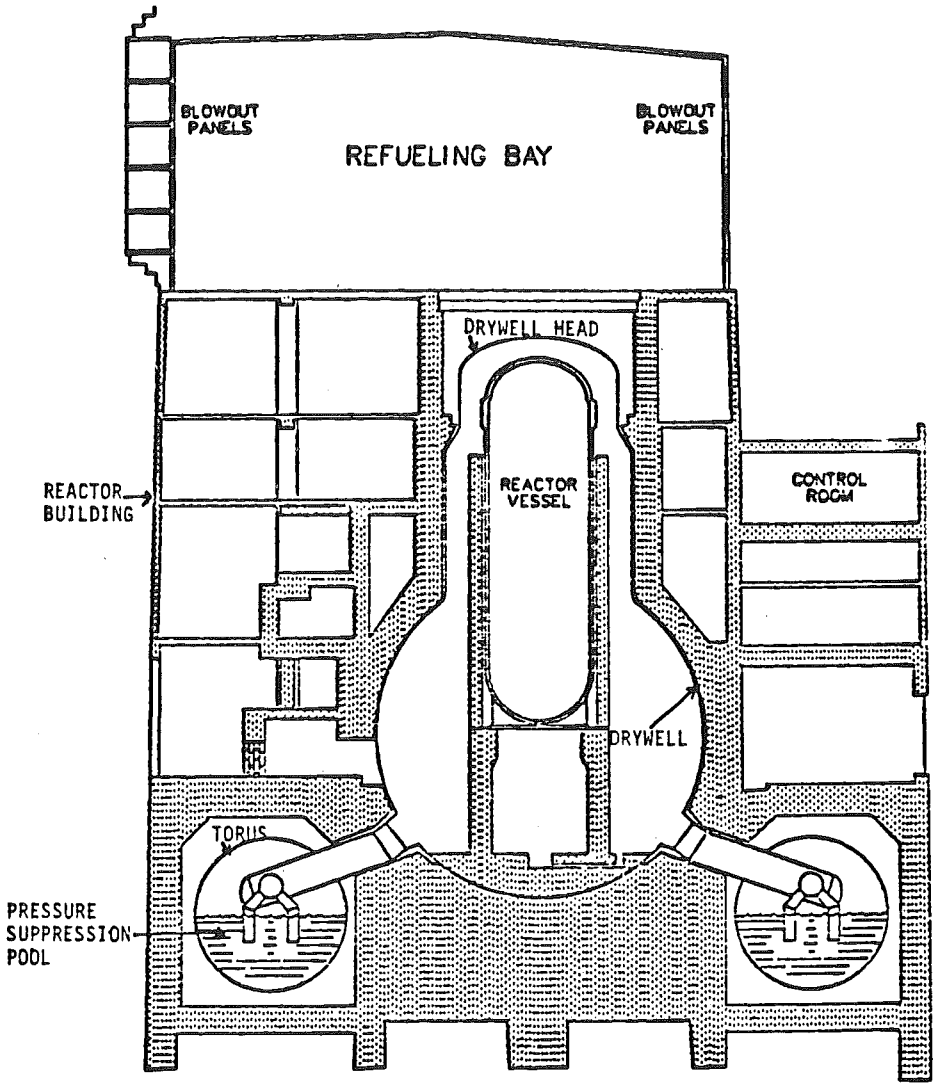

FIGURE 1 BWR MK I CONTAINMENT SYSTEM

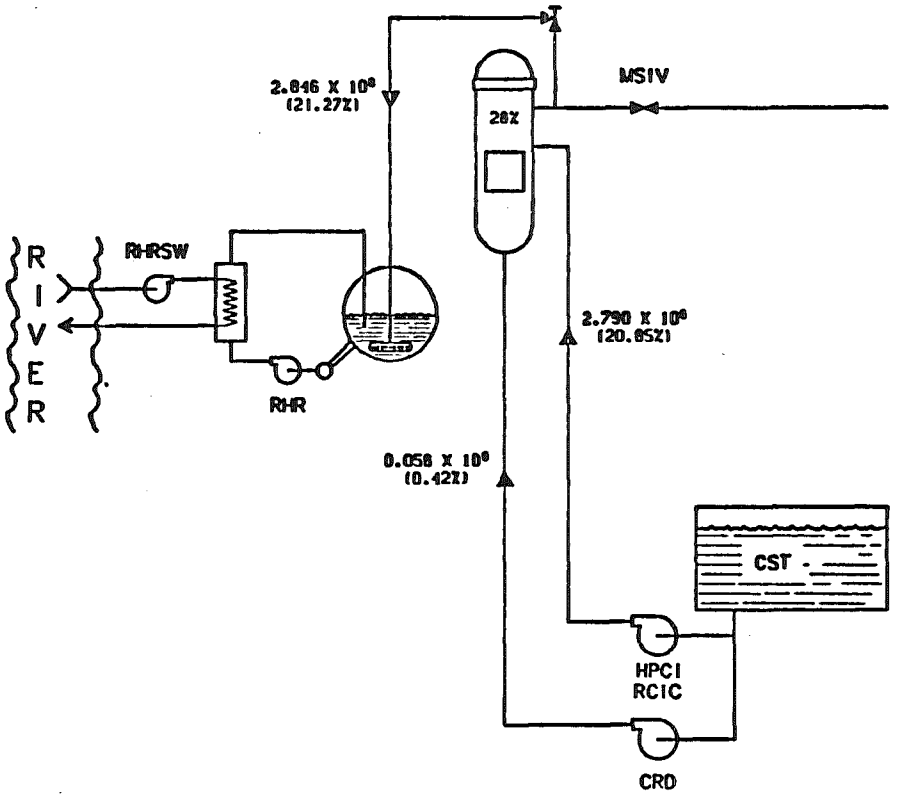

Fig. 2 Plant operation after failure of scram in the MSIV closure — initiated ATWS accident sequence.

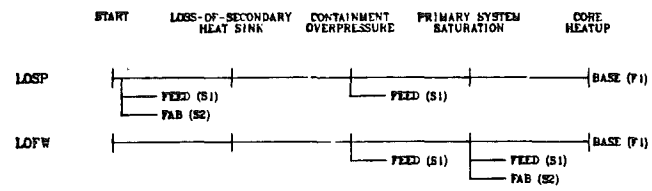

Oconee-1 success/failure chart.

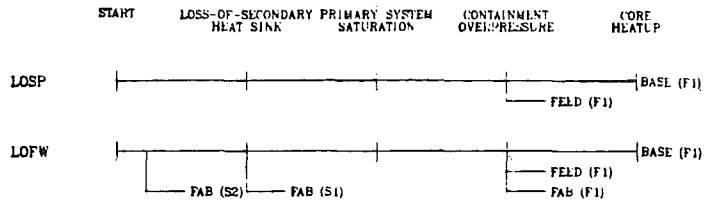

Calvert Cliffs-1 success/failure chart.

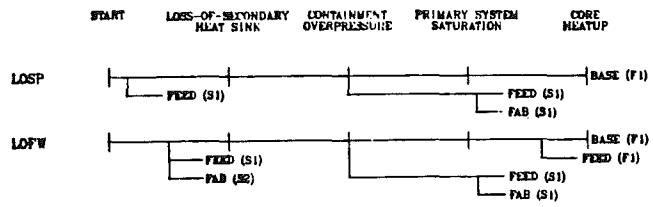

Zion-1 success/failure chart.

Figure 3

FAB = FEED & BLEED

PRECALCULATED DOSES FOR EMERGENCY RESPONSE

Timothy S. Margulies and James A. Martin, Jr.

U.S. Nuclear Regulatory Commission
Washington, D.C. 20555, U.S.A.

Roger M. Blond
Science Applications, Inc.
McLean, Virginia 22102, U.S.A.

Thomas W. Eagles
Johns Hopkins University
Baltimore, Maryland 21218, U.S.A.

ABSTRACT

A set of precalculated doses for the PWR (Pressurized Water Reactor) accident categories of the U.S. Reactor Safety Study (WASH-1400) have been published recently by the U.S. Nuclear Regulatory Commission (NRC). This paper summarizes the information in the publication. Whole body and thyroid doses are presented for a selected set of weather cases. For each weather case these calculations were performed for various times and distances including three different exposure pathways--cloud (plume) shine, ground shine and inhalation. During an emergency this information can be useful since it is immediately available for projecting offsite radiological doses based on reactor accident sequence information in the absence of plant measurements of emission rates (source terms). It can be used for emergency drill scenario development as well.

INTRODUCTION

In the event of a radiological emergency at a nuclear power plant it would be necessary to obtain an early projection of doses that members of the public might receive in the event of a release of radioactivity. All nuclear power plants in the United States are required to develop and maintain dose projection capabilities[1]. Various methods are available to obtain such estimates. This paper summarizes one such method of projection, recently published by the NRC[2], which is based on precalculated doses and dose rates for a set of postulated accident sequences. Doses and dose rates were calculated for each of the postulated releases and for each of the meteorological conditions and sheltering

cases chosen. The CRAC (Calculations of Reactor Accident Consequences) code[3,4,5] was used to generate the dose and dose rate information.

ACCIDENT CATEGORIES

Essentially four core melt/containment failure combinations can occur and are addressed in the dose calculations:

- o Core melt followed by containment failure;
- o Containment failure followed by core melt;
- o Simultaneous failure of all cooling modes, with core melt and containment failure occurring almost simultaneously; and
- o Containment bypass scenarios, where releases from the core travel through open plumbing paths to the atmosphere.

For each of these cases, a spectrum of releases and timings of releases can occur.

The spectrum of accidents considered is that represented by the so called PWR (Pressurized Water Reactor) accident sequences of the Reactor Safety Study (RSS)[3]. These accidents encompass a full range of postulated degraded core and core-melt accidents ranging from simple cladding failure, where the plant containment systems remain essentially intact, and for which the releases of radioactivity to the atmosphere would be relatively small, to extremely severe accidents for which large fractions of the core inventory of radionuclides are postulated to be released to the atmosphere. The release categories are designated PWR 1 through PWR 9. The most severe accident class, PWR 1, is comprised of two parts, PWR 1A and PWR 1B to cover the possible outcomes of a ground level release or a high energy release for which an elevated puff would be expected.

The estimated release fractions and timings of possible releases for the RSS accident categories have been questioned by some experts and major research efforts are underway to re-assess accident source terms. Since the PWR 1 and 2 sequences would involve very rapid releases and very high release fractions, revised (reduced) source terms, if any, should be encompassed within the PWR 1-8 or BWR 1-5 accident categories. If more than minor interpolation is required for newer source terms, these calculations should be revised or supplemented in the future[6]. It should be known that during an actual emergency it would be a very tenuous speculation to accurately predict the eventual release of radioactivity to the environment even if the accident sequences were known perfectly.

ATMOSPHERIC TRANSPORT AND METEOROLOGICAL CONDITIONS

The possibility of a variety of meteorological conditions during a release to the atmosphere and subsequent transport away from the release point provides the potential for a wide range of off-site consequences for each postulated release. This continuous spectrum was approximated by discrete meteorological conditions. Plots of doses are labeled, for example, according to windspeed, atmospheric stability class and occurrence of rainfall.

The atmospheric transport in CRAC is calculated by a Gaussian plume model whose vertical and horizontal dispersion parameters are functions of atmospheric stability class. The Pasquill-Gifford-Turner atmospheric dispersion classification scheme (denoted by the letters A through F) is used to relate types of atmospheric turbulent dispersion to easily observed conditions of the atmosphere: windspeed, day or night conditions and cloud cover[7,8]. Refer to Table 1. A few examples will illustrate how the information in Table 1 can be used to determine a stability class. First, read footnote 1 in Table 1: for heavy cloud cover, the Pasquill-Gifford stability class is D, or neutral stability. Further, for moderate to high windspeeds, the stability class is also D for the most part (see bottom line of Table 1). Indeed, D stability is the most prevalent stability class. Now note the area of the table below the dashed line. here, higher windspeeds would prevail and the stability class would be neutral (D) under most conditions, day or night. However, given strong sunlight and moderate windspeeds better dispersion than "normal: would be expected, and the stability class would be B or C. Additionally, given 5-10 mph windpseed and a cloudless night, poorer than average dispersion would be expected (E stability). Low windspeed conditions can induce either greater or less than normal (D stability) disperson. Observe the area above the dashed line in Table 1. For low windspeeds, dispersion would be greater than normal during the day and less than normal during the night. A long, narrow, concentrated plume is often observed in the late afternoon on a calm sunny evening, or on a cool calm, starry night (e.g., Class F stability). For emergency response purposes considering all other variables and uncertainties, the information in Table 1 can be simplified and summarized as shown in Table 2.

Due to the particulate material in the cloud rainfall could significantly alter the consequences of an accidental release. Ground level dose rates in the wake of a plume could be orders of magnitude greater with rainfall, as compared to transport in dry weather. Thus, dose calculations for dry and wet weather cases were made. One assumption used for the rainfall cases is important to note: it was assumed that rainfall was continuous and steady throughout the transport time at all "downwind" locations. Interception of rainfall after transport in dry weather was not included here, although it can be considered in the CRAC code. Other assumptions of note were: plumes (puffs) were depleted exponentially with travel time, ground runoff was ignored, and plume depletion and ground deposition were the same for all stability classes, for rain cases. Other assumptions inherent in the metorological models used for the calculations are presented in the report.

Extreme care must be exercised in using and interpreting the information in the graphs especially at larger distances. It is clear that should an actual release of sufficient magnitude ever occur, a reasonably accurate dose assessment would require monitoring teams to locate the release(s)[9]. Considering the high dose rates necessary for a Protective Action Guide (PAG)[9] to be realized, the major offsite monitoring problems would involve finding and tracking a release[10]. Considering further the facts that windspeeds average 5 to 10 miles per hour, and that a two hour release could be ten to twenty miles long over areas where the wind directions could be considerably different, aircraft would be the preferred method for plume tracking where at all possible[11]. The wind directions at the release point may not be adequate to project atmospheric transport to distances of more than a few miles, especially in complex terrain.

DOSE CALCULATIONS

Projected doses to the whole body and thyroid were calculated for a selected set of weather conditions and release categories, (PWR 1 through 9) as shown in Table 3 for a 2550 megawatt reactor. These dose calculations are documented in NUREG-1062[2].

The individual in accident/weather scenarios 1 through 14 is unshielded, that is, the individual is not in a brick building, or basement, or other enclosure which could reduce the received dose. These calculations (i.e., cases 1 through 14) are "projected doses" and can provide a perspective on "dose savings" to be afforded by various protective measures. Several sheltering cases, i.e., 15 through 19, with and without the occurrence of rain are included for additional perspective. Shielding factors for these cases are 0.75 for the cloud pathway and 0.33 for the ground.

Doses were calculated for three pathways: inhalation, external gamma irradiation form the plume (cloud) and external gamma irradiation from radionuclides deposited on the ground. Four graphs showing calculated doses at distances between 1 and 100 miles along the track of plume (puff) are displayed for each of the postulated accident/meterological conditions. Information in the graphs can be used to discern both dose rate and pathway contributions to doses. For illustrative purposes see Figure 1, taken from NUREG-1062.

Inputs to CRAC included a specification of the inventory of radionuclides and activities released to the atmosphere, the characteristics of the release and meteorological conditions following the accident. A finite cloud dosimetry model in CRAC was used for the cloud external gamma dose calculations. Standard wet and dry deposition models were used to transfer non-noble gaseous material from the atmosphere to the ground for the ground exposure dose calculations.

The calculations of whole body dose are very sensitive to the assumption of the length of time one remains in the vicinity of contaminated ground. Therefore, three time periods were used in the total dose versus distance calculations (i.e., 4-hour, 24 hour and 7 day). The cloud, ground and inhaled components of the total dose are explicitly plotted (on the right hand side of each figure) using the 24-hour ground exposure time assumption. The external gamma dose from the passing cloud is assumed to happen "instantaneously." Inhalation of radionuclides occurs over a very short time period ("instantaneously") and the dose builds up over time since the body continues to be irradiated for extended time periods by those inhaled radionclides which remain in the body; i.e., which are not immediately exhaled. The dose commitment from inhaled radionuclides is calculated over an individual's lifespan.

DISCUSSION AND CONCLUSION

In an actual emergency response situation it would be useful to base dose projections on actual radiological measurements as quickly as possible. However, for many postulated severe accident scenarios major radionuclide emmissions would bypass at least some engineered safety features and routinely monitored release paths. For such cases precalculated dose projections could be immediately available when a real time dose projection model could not be used and field measurements are absent. These dose projections are keyed on essentially two questions. First, what are the source term characteristics (or what are the conditions of the core/containment?) Second, what are the weather conditions? The dose information can be useful during emergency drills, in the emergency planning process and in the very early stages of an emergency response situation. These calculations can be especially useful during a response situation before a release occurs for purposes of contingency planning based on an assessment of the possible outcomes of the actual accident sequence.

All in all, then, these dose and dose rate calculations can be useful for emergency planning and in the early phases of an emergency response. However, in the post-release phase of an emergency response the best dose projections would be based on actual data obtained from radiological monitoring and the knowledge of plant system performance at the time.

Table 1: Relation of Stability Classes to Weather Conditions

A--Extremely unstable conditions
B--Moderately unstable conditions
C--Slightly unstable conditions
D--Neutral conditions[1]
E--Slightly stable conditions
F--Moderately stable conditions

Approximate Surface wind Speed		Daytime insolation[2]			Nighttime conditions	
					Thin overcast or 4/8 cloudiness[3]	3/8 cloudiness
m/sec[4]	mph[4]					
2	5	A	A-B	B		
2	5	A-B	B	C	E	F
4	10	B	B-C	C	D	E
6	15	C	C-D	D	D	D
6	15	C	D	D	D	D

1. Applicable to heavy overcast, day or night (D, or neutral stability).
2. Insolation is proportional to the amount of solar energy reaching the surface of the earth.
3. The degree of cloudiness is defined as that fraction of the sky above the local apparent horizon which is covered by clouds.
4. m/sec = meters per second; mph = miles per hour.

Table 2: Weather Classification Scheme for Emergency Response Purposes

Atmospheric Condition	Stability Class
Windspeed 10 mph or greater, or heavy cloud cover anytime	D
Low windspeed and few clouds -	
Daytime	B-C
nighttime	E-F
Very low windspeed, high noon, bright summer day	A

Table 3: ACCIDENT SCENARIOS FOR PRECALCULATED DOSES

Case #	Stability Class	Wind Speed (mph)	Rain/Shelter Combinations	
1	A	3	No Rain	No Sheltering
2	A	9	No Rain	No Sheltering
3	D	2	No Rain	No Sheltering
4	D	6	No Rain	No Sheltering
5	D	16	No Rain	No Sheltering
6	E	2	No Rain	No Sheltering
7	E	9	No Rain	No Sheltering
8	F	1	No Rain	No Sheltering
9	F	3	No Rain	No Sheltering
10	D	2	Rain	No Sheltering
11	D	6	Rain	No Sheltering
12	D	16	Rain	No Sheltering
13	E	2	Rain	No Sheltering
14	E	9	Rain	No Sheltering
15	A	3	No Rain	Sheltering
16	D	6	No Rain	Sheltering
17	D	16	No Rain	Sheltering
18	F	1	No Rain	Sheltering
19	D	6	Rain	Sheltering

Shielding Factors for Sheltering Cases: Cloud (0.75); Ground (0.37).

REFERENCES

1. U.S. Nuclear Regulatory Commission, "Criteria for Preparation and Evaluation of Radiological Emergency Response Plans and Preparedness in Support of Nuclear Power Plants," NUREG-0654 (FEMA-REP-1), January 1980.

2. T. S. Margulies and J. A. Martin, Jr., "Dose Calculations for Severe LWR Accident Scenarios," U.S. Nuclear Regulatory Commission, NUREG-1062, May 1984.

3. U.S. Nuclear Regulatory Commission, "Reactor Safety Study, An Assessment of Accident Risks in U.S. Commercial Nuclear Power Plants," WASH-1400, NUREG-75/014, October 1975.

4. T. S. Margulies and L.C. Kohlenstein, "Calculation of Potential Radiological Effects from an Accidental Release at the Three Mile Island Nuclear Generating Station", Johns Hopkins University Applied Physics Laboratory Report, CPE-7902, April 3, 1979.

5. T.S. Margulies and T.W. Eagles, "Accident Consequence Calculations for Calvert Cliffs Nuclear Power Plant," Volume I: Projected Whole Body Doses; Volume II: Projected Thyroid Doses; Draft report prepared by Johns Hopkins University Applied Physics Laboratory for the State of Maryland, Department of Natural Resources, Power Plant Siting Program, October 1979.

6. R. M. Blond, M. Taylor, T. Margulies, M. Cunningham, P. Baranowsky, R. Denning, and P. Cybulskis, "The Development of Severe Reactor Accident Source Terms: 1957-1981," U.S. Nuclear Regulatory Commission, NUREG-0773, November 1982.

7. D. Slade, et al., "Meteorology and Atomic Energy - 1968," TID-24190, NTIS, U.S. Department of Commerce, Springfield, VA 22151.

8. D. Bruce Turner, "Workshop of Atmospheric Dispersion Estimates," U.S. Environmental Protection Agency, Office of Air Programs, Research Triangle Park, NC 27711. (Rev. 1970)

9. U.S. Environmental Protection Agency, "Manual of Protective Action Guides and Protective Actions for Nuclear Incidents," EPA-520/1-75-001 (September 1975), Revised June 1980.

10. J. A. Martin, Jr., "Perspectives on the Role of Radiological Monitoring in an Emergency, Trans. Am. Nucl. Soc., Nol. 34, pp. 727-729, June 1980.

11. U.S. NRC and U.S. EPA, "Planning Basis for the Development of State and Local Government Radiological Emergency Response Plans in Support of Light Water Nuclear Power Plants," NUREG--396 and EPA 520/1-78-016. U.S. Nuclear Regulatory Commission, December 1978.

PWR #5
CASE 4

Stability Class: D
Windspeed: 6 mph

Rain: No
Sheltering: None

WHOLE BODY DOSE

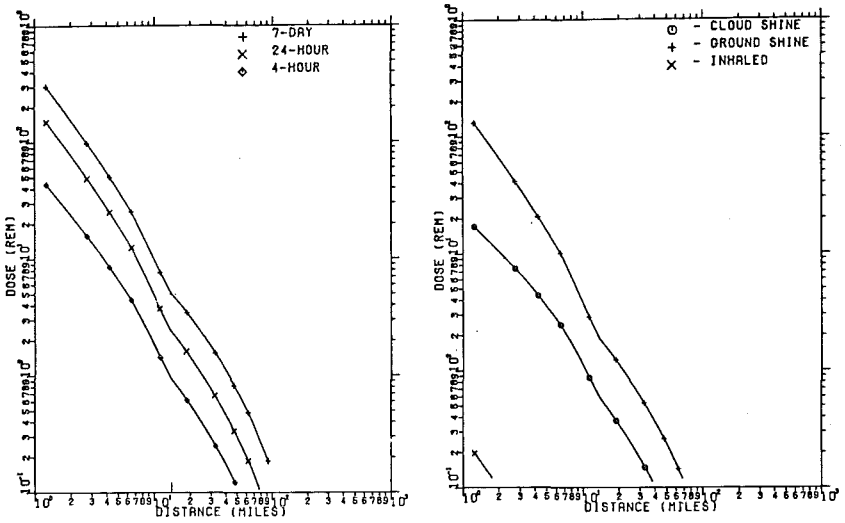

THYROID DOSE

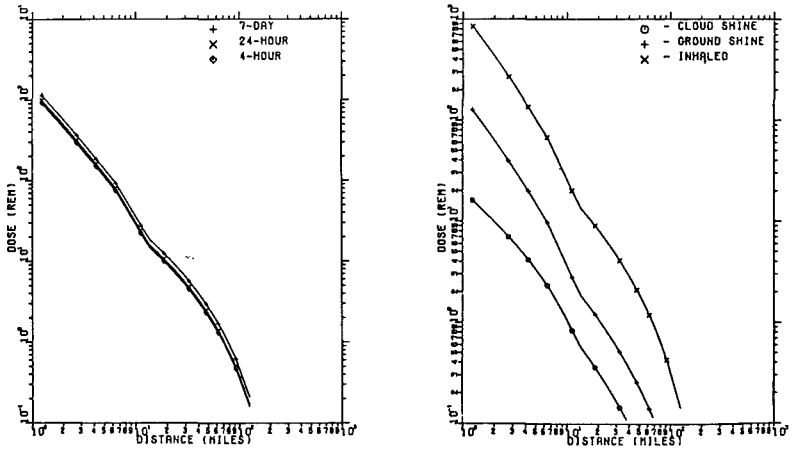

Figure 1: Calculated Doses Versus Distance (from NUREG-1062)

PHYSICAL STATE APPROACH TO PWR EMERGENCY OPERATING PROCEDURES : RECENT DEVELOPMENTS IN FRANCE

H.SUREAU
Service Etudes et Projets Thermiques et Nucléaires
Electricité de France
12 - 14 Avenue DUTRIEVOZ
69628 VILLEURBANNE CEDEX
FRANCE

J.MESNAGE
Société FRAMATOME
1 Place de la Coupole
92080 PARIS LA DEFENSE
FRANCE

ABSTRACT

It is well known that the event oriented procedures do not cover every possible accident with any number of instrument or system failures. Their effectiveness depends on an accurate initial accident diagnosis. This EDF-FRAMATOME Joint development lead to a set of seven unique state oriented procedures (used with a permanent diagnostic procedure based on permanent state criteria) which cover every possible single or multi-event accident. These procedures use an accurate and dependable water level measurement instrumentation along with the existing instrumentation and are not more complicated than the usual event oriented procedures.

INTRODUCTION

The post-accident procedures presently used by the operators in the french PWR's are based on a diagnosis of the accident-initiating incident and on a predetermined succession of events in the most probable sequences.

It is now well-known that this "event" oriented approach does not allow all conceivable accident situations to be taken into account nor the diagnosis to be reviewed and updated should the system deviate from the pattern predicted by the first diagnosis, but the lack of direct knowledge of primary inventary requires this predetermined approach.

FIRST DEVELOPMENT TO IMPROVE EMERGENCY OPERATING PROCEDURES

To improve the present emergency procedures on the 900 MW plants, a new set of two procedures has been added :

- an ultimate one which is already based on physical states - U1 -,
- a permanent monitoring post-incident procedure - SPI - (Surveillance Post-Incidentelle).

The U1 procedure acts like a "safety net" and defines the required actions as a function of the state of the reactor and the available systems. It is used when the normal emergency operating procedures are no longer valid.

Criteria used to call for U1 are checked through a Permanent Monitoring post-Incident Procedure (SPI).

SPI includes a control of the primary system status, steam generators secondary side status and availability, containment status and safety systems availability (high and low pressure safety injection, emergency feedwater and containment spray system).

This continuous post-incident supervision is carried out by the safety and Radioprotection Engineer (ISR - Ingénieur de Sûreté et Radioprotection) who is called into the control room within five minutes after every scram signal and who acts completely independently of the operator's crew.

SPI allows ISR to confirm the main safety actions dictated by the "event oriented" procedures being applied, or to decide to use ultimate one U1.

Once the operator uses U1, no provision is made to go back to the "event oriented procedure". He keeps using U1 until the plant is in a safe state.

Unfortunately, due to the lack of reactor vessel instrumentation, the degradation of the primary coolant inventory is detected relatively late. Consequently, corrective actions are not taken in a progressive way. So, there is a gap between design accidental situations (covered by event oriented procedures) and ultimate degraded situations (covered by U1 procedure) for which no document is presently suitable.

Picture 1 shows the present distribution of the different documents between the operator's crew and the ISR after an incident on French 900 MW plants.

FIGURE 1 : PRESENT DISTRIBUTION OF DOCUMENTS IN CONTROL ROOM
FRENCH 900 MW PLANT

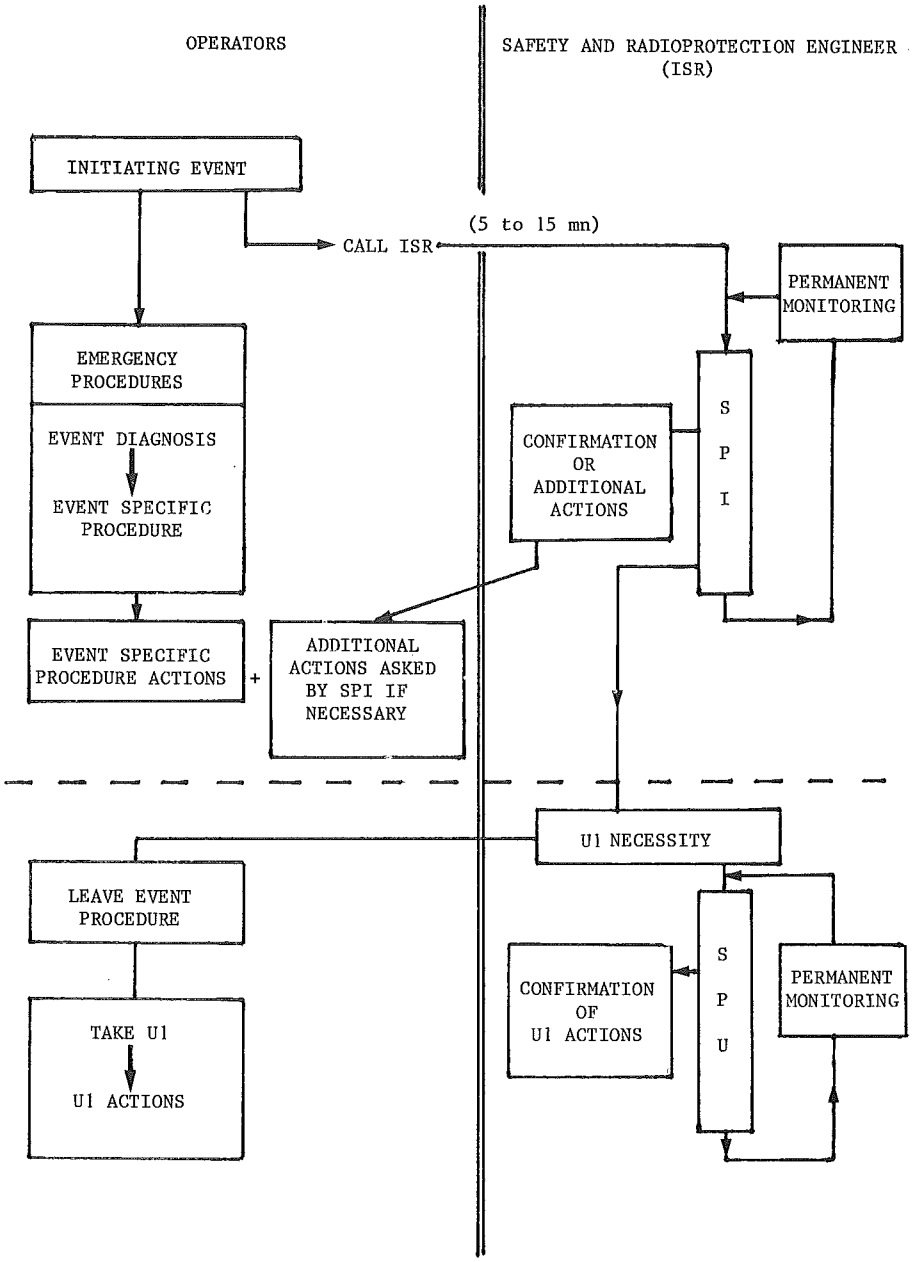

RECENT DEVELOPMENT IN THE EMERGENCY OPERATING PROCEDURES

A reliable reactor vessel water level instrumentation is going to be installed on each french 1300 MW plant.

This detection is based on a pressure differential measure, corrected for the accidental containment conditions (high containment temperature). Therefore, the primary system coolant inventory can be closely and continuously monitored. Work has been carried on to achieve a more systematic application of the state approach with this additional instrumentation.

OBJECTIVES AND METHOD OF RECENT DEVELOPMENT ON PHYSICAL STATES APPROACH

This work is still based on the same principle as U1 namely the relation "state $\longrightarrow$ actions".

The two main objectives are as follow :

- to give a permanent diagnosis of the whole system to insure that at each moment the right action is taken in order to correctly restaure the situation of the plant,
- to generalize this approach to cover the presently existing gap between design calculated situations and ultimate one with proper operating documents.

Briefly, these goals have been sucessfuly reached using the following method :

Operating objectives have been defined. They are decay heat evacuation control, primary coolant inventory control, subcriticality control for the primary side, secondary inventory coolant control and integrity for the secondary side, integrity control for containment and availability and restoration for safety systems.

All the available plant informations are gathered to characterize primary, secondary containment and circuits status.

When possible, measurements of a same physical "reality" are correlated to give a best reliability in the diagnosis.

Consequently the use of two measurements need an intervalidation treatment to eliminate some erratic or faulty measurement.

FIGURE 2 : DEFINITION OF PRIMARY DEGRADATION STATE

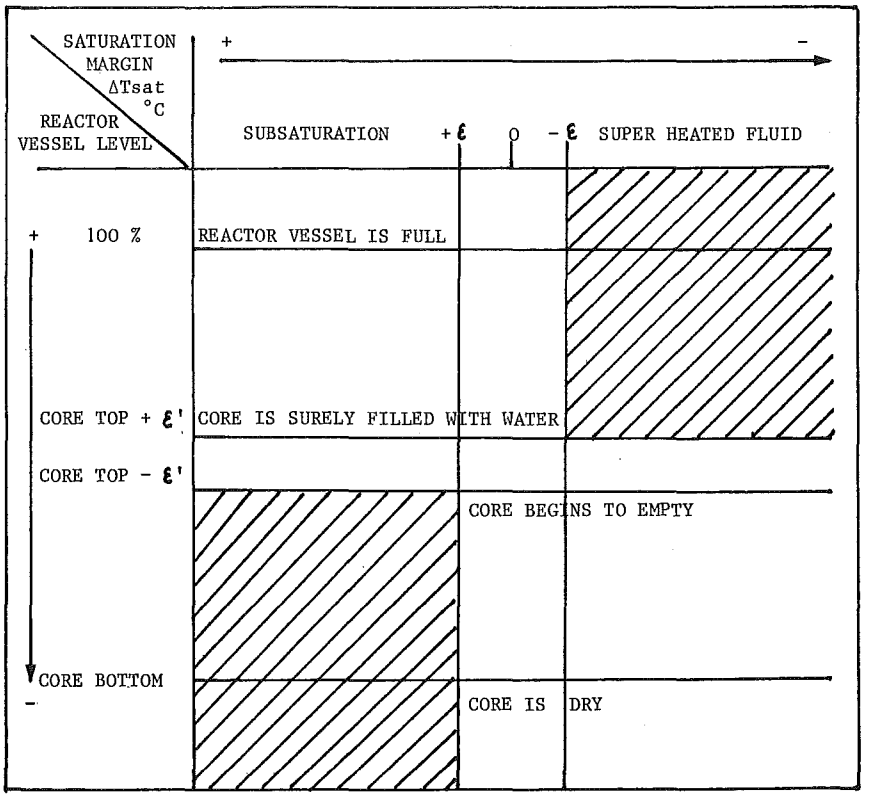

REFERENCES

$\varepsilon - \varepsilon'$ = measurement errors

= PHYSICALLY IMPOSSIBLE AREAS

Figure 2 shows the way to identify the state of primary degradation by the use of saturation margin and reactor vessel ΔP measurements and the physically impossible areas which need this treatment.

The conjunction of all the different possible primary, secondary and containment status and the availability of the safety systems leads to a large number of configurations.

But all these physically different configurations of the plant can be gathered in a limited number of plant states requiring the same recovery actions for the predefinite operating objectives.

Then the only work to do for each state is to define precisely :
- the priority on the operating objectives,
- and the right actions which allow to control these objectives.

The picture n°3 summarizes this method.

For the states oriented approach, the challenge is not to find the appropriate actions to call for in the different plant states, but to give a suitable presentation of the operating documents to the operators.

STATES APPROACH DOCUMENTS ORGANISATION

The goal is to have a limited number of procedures, each being unlengthy and simple to use but yet covering every possible accident with a reasonable number of failures (instrument and/or systems failures).

In a first step of this work, each operating objective was handled apart. Recovery actions for each objective were collected on a same document.

Then these recovery actions documents had to be gathered, following the defined operating objectives priorities, in a suitable manner to be used by operators.

FIGURE 3 : METHOD USED FOR RECENT DEVELOPMENT ON PHYSICAL STATES APPROACH

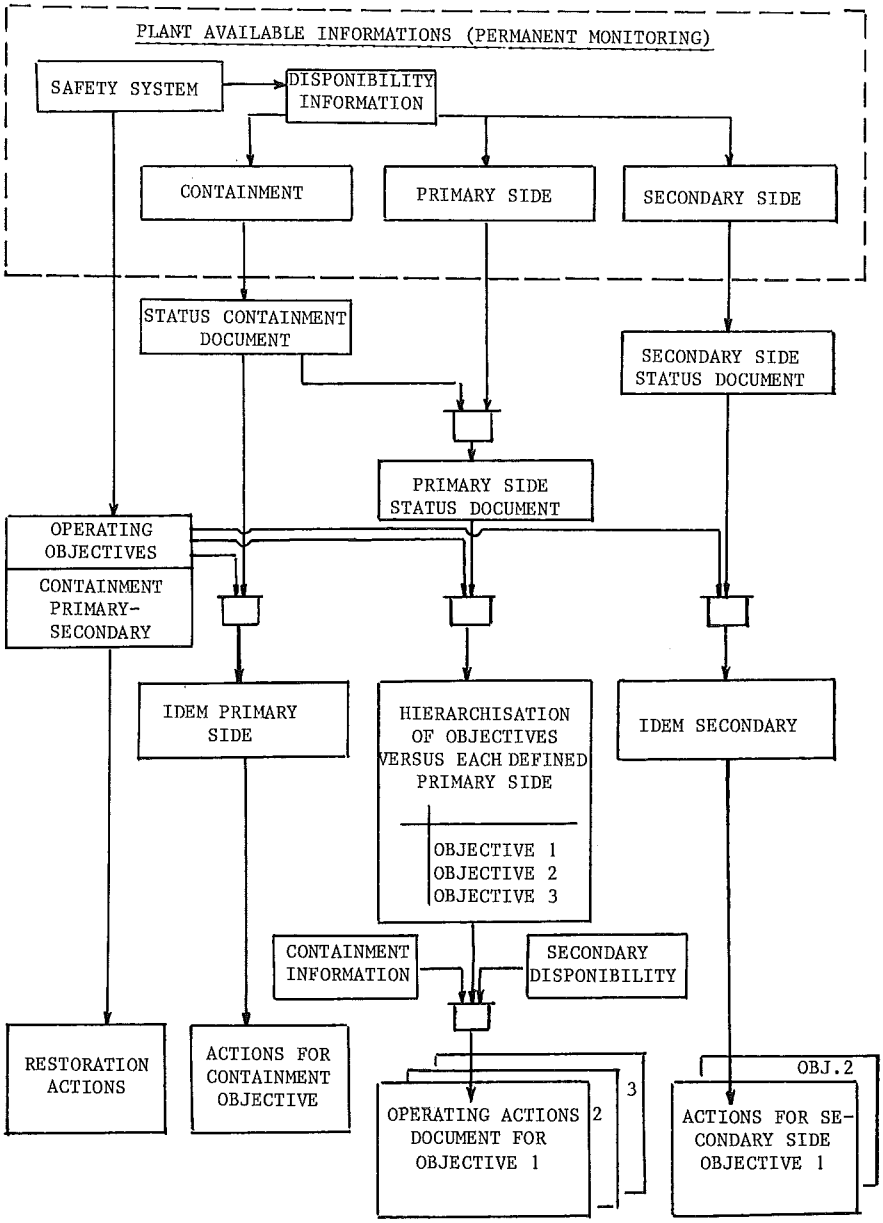

The state oriented approach documents have been split into a set of seven sequential accidental primary operating guidelines, one sequential secondary operating guideline and one sequential containment operating guideline :

- Each of these seven primary guidelines clearly includes its own operating objective and its own specific means. They are self carrying and they are ranged in increasing order of plant degradation.

  The right primary procedure is chosen by the mean of a permanent diagnosis procedure based on a permanent state criteria checking. Once one of the procedure is chosen, the operator may only change it for higher plant degradation procedure (to avoid switching back and forth between procedures).

  Usually, for most simple accident without further degradation or failure, the same self-checking procedure is used throughout the transient.

- The secondary one allows to control or restore the secondary objectives Steam generator (S.G) water inventory and S.G integrity and to carry out the cooling down or the temperature stabilisation actions which are eventually asked from the primary operating guideline.

- The containment procedure allows to control or restore the containment integrity and to give information to elaborate the primary diagnosis (degraded containment or not).

THe figure 4 shows how these documents are chained.

CONCLUSION

The recent development in the symptom oriented procedure allows an extensive covering of all the plant states, enables progressives actions or anticipates them so that there is no important core degradation.

The diagnosis is continuously checked from states criteria and allows to go to an another procedure if the situation becomes wrong.

All these operational documents (verification, diagnosis and symptom oriented operating procedures) are based upon the present definition of operator crew and ISR functions in control room.

This approach will be applied on the new french 1500 MW plant (N4). A decision will be taken for the application on the 1300 MW plant at the end of this year, the training delay of the actual operating crew beeing the most important factor of this decision. (It seems to be possible to anticipate this application on the 1300 MW by 1990).

FIGURE 4 : "PHYSICAL STATES" OPERATIONAL DOCUMENTS

ENTRY CRITERIA

REACTOR TRIP SIGNAL

OR SAFETY INJECTION SIGNAL

ORGANISATION

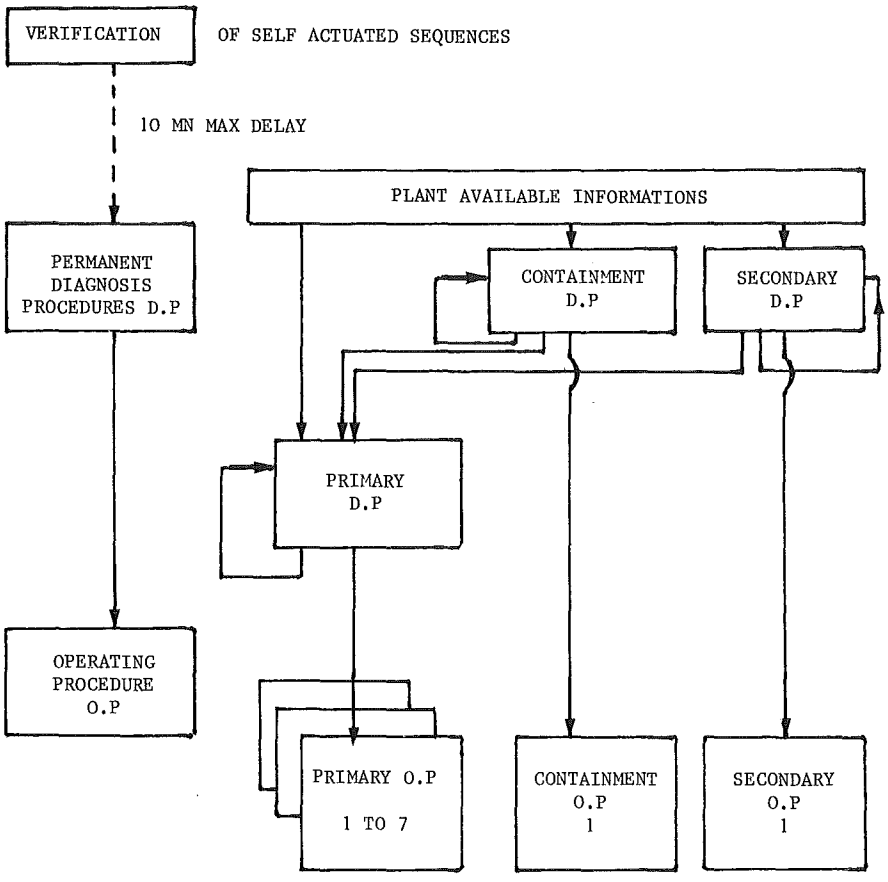

VALIDATION OF EVENT ORIENTED PROCEDURES

A. BRUNET and T. MESLIN

Electricité de France / SPT
75384 PARIS FRANCE

ABSTRACT

One of the most important "post-TMI" action carried out by EDF is the re-writing of the incident and accident procedures.

These new procedures are based on simple initiating events and consist of two different and complementary documents.

- An operating rule : Technical and theorical contents.

- An operating procedure : Practical and operational contents.

As far as the design of the new operating procedures is concerned, many tests were performed on simulator and revealed the main basic requirements such as :

- To separate and coordinate operations on the primary and secondary circuits.

- To separate operating and surveillance tasks.

- To use a suitable vocabulary.

The re-writing of the new documents was realized by engineers working in nuclear power plants.

Each new event oriented procedure is then validated as often as possible on site, otherwise on simulator.

The validation is indispensable :

It guarantees the applicability of the procedure and makes the operators more confident and more efficient.

Particularly, the validations on site increase significantly our knowledge of the physical transients as well as the human behaviour.

HISTORY

In the aftermath of the accident which occurred in 1979 at the Three Mile Island plant, EDF started a number of "post-TMI" actions. One of which aims to verify the technical contents and review the format of event oriented procedures defining the course to be followed in the event of an incident or an accident.

These new procedures are composed of two documents :

- The operating rule : supplied by both the vendor and the EDF's Construction Department as a basic detailled and theorical document giving all technical justifications allowing to write the operating procedure.

- The operating procedure : written by the Operating Department itself, is the action document used by the operators during the transient.

EDF's Operating Department has undertaken work covering the presentation of these operating procedures.

The aim in this case is to improve the efficiency of teams in case of incident or accident conditions and consequently, the safety level.

ELABORATION

The first step was to propose new formats.

Several groups of persons worked in parallel to this end, each one following their own methodological approach. They submitted their own proposal.

The second step, undertaken on operation simulators, led to the implementation of a comparative assessment of the different proposed models.

The goal of the simulation was to compare the effectiveness of the different designs of procedures :

. to cope the same situation,

. to distribute the work among the operators.

Conclusions drawn from the following observations concerned :

- the procedure strategy : guidance for action,

- handling of the procedure (pages turned, reference to earlier passages, reference to a general framework, use of index-cards, etc...),

- operator's movements in the control room,

- communication between operators,

It should be underlined that sixty-seven tests were carried out during this comparative assessment.

It was found that the new procedures were easier to use than the old ones, and that the greatest effectiveness was obtained with a team organized as follow :

- a shift supervisor (who has an overall view of the installation) assuming the coordination,
- an operator performing action on the primary circuit,
- an assistant operator performing action on the secondary circuit.

In addition, the contents should be adapted to the purpose and it is essential to tell operators what they are supposed to do (and not to do) in relation to normal operating conditions.

IMPLEMENTATION SCHEDULE

The re-writing of the new operating procedures began in January 1981 on the basis of the results of the assessment mentioned above.

Writing tasks were distributed among all 900 MWe power plants with a standard writing guide.

This re-writing of operating procedures which necessitated the participation of 40 engineers (part-time) working in the various 900 MWe sites, was completed in July 1984.

VALIDATION

To guarantee the applicability of the new procedures, they must be all validated.

As often as possible, the new documents are validated on site, particularly in the case of the loss of electrical supplies.

When it is not possible, the validation is carried out on simulator.

A procedure validation is split into two steps :

First, a shift team which is not aware of the selected accident makes a diagnosis and applies the selected operating procedure. Three "technical" observers follow each operator's actions during the simulation phase. More particularly, an ergonomic expert is responsible for noting stages during which the coordination and the presentation of the instructions raise a difficulty.

The traditional parameters recording facilities are supplemented with :

- fast recorders to collect main data,

- a plotting table giving the trend of primary pressure as a function of temperature.

The session is recorded on video-tape in order to review the significant sequences.

The second step consists in analysing the results of the test. The shift team and the observers meet at the end of the simulation exercise to collect the operators' impressions and hear the observers' remarks. The observed results lead to correct temporarily the procedure. The synthesis of these results will later serve to improve it.

The first validation campaign on simulator started in November, 1983 and the second took place in April, 1984. Each series of tests requires the participation of seventy people to validate twenty procedures.

The initial conclusions drawn from these validations show that the operators are much more confident with these new procedures, consequently, the global efficiency has risen. For instance, when a steam generator tube breaks, the operators are able to stop the safety injection after 45 minutes, whereas, using the old procedures, almost one hour was necessary.

Several validations on site were carried out among which the most important are two tests performed on plants in operation :

- Loss of the main electrical supply (400 KV) and missed "houseloading" performed on DAMPIERRE EN BURLY unit n° 3, December 4th, 1982.

- Station blackout with two emergency diesel generators in operation performed on DAMPIERRE EN BURLY unit n° 3, August 17th, 1983. (See the paper N° 149 : Station Blackout : A test on a plant at power - Lessons learned for Safety Studies - by T. MESLIN - A. CARNINO - B. PAYEN - A. CAHUZAC).

Most of the others loss of electrical supplies were performed on plants which were in hot shut-down conditions, particularly :

- Station blackout with only one diesel generator in operation performed on CRUAS unit n° 1, December 3rd and 4th, 1982.

- Loss of 125 V DC power performed on CRUAS unit n° 3, October 12th, 1983.

Those validations increase significantly our knowledge of the physical behaviour of the PWR system in case of incident as well as our knowledge of the operator's behaviour under disturbed situation.

OPERATORS' TRAINING

Fortunatly, incidents and accidents occur seldom. Therefore, the operating incident procedures are rarely used.

Consequently, the operators must be motivated and trained to carry out the procedures by specific training courses "placing them in the situation" on simulators and by on job training programs.

FUTURE DEVELOPMENTS

Now, the next validation campaign on simulator relates to the following items :

- Validation of a new supervision procedure.

This procedure is used by the safety engineer permanently during the transient. It guarantees the control of the safe resolution of the incident and if necessary proposes complementary actions (see paper n° 513 : Man-machine interface enhancement undertaken by EDF to minimize human errors - by R. MARCILLE).

- Study and validation of diagnosis procedures extent :

The diagnosis of the event and the choice of the associated procedure can be quickly executed by the use of logical diagrams taking into account the various alarms as well as the symptoms.

- Validation of beyond design procedures.

- More realistic scenarios including shift turnover and long term simulation.

- Elaboration of a quantitative method in order to evaluate comparatively the different procedures validated on simulator.

CONCLUSION

It appears that the validations of new operating procedures, particularly on site, make our operators more confident and efficient, guarantee the technical contents of it, increasing significantly the safe operating of our nuclear power plants in case of unusual event.

Chapter 6
Fuel Behavior during Severe Accidents

STATUS OF THE JOINT PROGRAM OF SEVERE FUEL DAMAGE RESEARCH OF THE USNRC AND FOREIGN PARTNERS

R. W. Wright, M. Silberberg, and G. P. Marino

Fuel Systems Research Branch
Office of Nuclear Regulatory Research
U.S. Nuclear Regulatory Commission

ABSTRACT

The Severe Fuel Damage research program is an integrated program of large-scale integral tests in the PBF and NRU test reactors, separate-effects phenomenological experiments in the ACRR test reactor and in the laboratory, and corollarly analysis and model development on in-vessel fuel and fission-product behavior under severe-accident conditions. The purpose of the program is to provide a data base and validated analytical models for safety assessment and regulatory decisions for LWR accidents beyond the design basis. The SFD program partners with the USNRC include Belgium, Canada, the Federal Republic of Germany, Italy, Japan, Korea, the Netherlands, the United Kingdom, and the U.S. Electric Power Research Institute (EPRI).

PROGRAM BACKGROUND

The U.S. Nuclear Regulatory Commission (NRC) in conjunction with its foreign partners has established a research program on Severe Fuel Damage (SFD) in order to develop a data base and validated analytical models for use in assessing the consequences of LWR accidents that involve severe core damage. This program is a major part of the more comprehensive NRC Severe Accident Research Program (SARP), described in NUREG-0900, which was established after the accident at TMI-2 to furnish the Commission with a technical basis for policy decisions for severe LWR accidents that exceed the design basis.[1] Currently, Belgium, the Federal Republic of Germany, Italy, Japan, Korea, the Netherlands, the United Kingdom, and the U.S. Electric Power Research Institute (EPRI) are participating members in the Severe Fuel Damage research program, and discussions on possible participation in the program are proceeding with other countries.

General applications of the program results are to: regulatory decisions for accidents that exceed the design basis; source-term reassessment; planning for severe-accident management, training, and emergency response; furnishing information to the public and to other government units during the course of a severe accident; and knowledge of what actually happened in the TMI-2 accident. Specific applications of the program results are to: the assessment and reduction of the uncertainties in safety and risk assessment; the development and the validation testing of mechanistic accident-analysis codes for in-vessel

severe-accident behavior; and the benchmarking of advanced fast-running risk-assessment codes such as MELCOR.

Regulatory decisions regarding radiological source terms are usually based on estimates of the upper bound to the source-term uncertainty range. Thus, reductions in the uncertainty range can have regulatory implications comparable to reductions in the best-estimate values, and thus are very significant.

The technical issues addressed by the program are as follows: What are the fission-product and aerosol release rates from the core during the course of a severe accident, including the timing and chemical form, and what are the magnitudes of the fission-product and aerosol attenuation within the reactor vessel and the primary system? These are major questions in determining the accident radiological source term. What are the hydrogen release rates from the core? This is a major question in assessing containment integrity. What are the physical and chemical states of the core and the temperature distributions during the risk-significant severe accident sequences, including the progression of core melt and the attack on reactor structure and the reactor vessel? What are the conditions at reactor vessel failure, including the mode of vessel failure and the spatial mass and temperature distributions of the molten and solid core debris? This information on the state of the core and the core temperature distributions forms a necessary basis for reliability modeling severe-accident consequences. What are the characteristics of the severely damaged core debris in different accident sequences? This is a primary unknown in determining the coolability limits of severely damaged cores by reflooding to terminate an accident.

Severe accident safety assessment and risk assessment require models and safety analysis codes that cover the range of the risk-significant accident sequences and the ranges of the parameters of the governing phenomena, and a data base for model development and validation. An integrated research program with a number of elements is required to obtain this wide range of needed information. The integrated Severe Fuel Damage research program includes integral in-pile tests for multiple-effect interactions at large scale in the PBF and the NRU test reactors and at small scale in the ACRR test reactor; separate-effect phenomenological experiments, both in-pile in the ACRR test reactor and out-of-pile, for model development and model validation testing and to cover the relevant accident parameter range; and analytical model and core development and validation. Two complementary mechanistic severe-accident fuel behavior codes are being developed as part of this program, the Severe Core Damage Analysis Package (SCDAP), and the Melt Progression Model (MELPROG). It is the validated models and codes that are used in the assessment of severe-accident consequences and uncertainties

and in benchmarking risk-assessment codes, and not the experimental data directly.

Because of recent developments, there has been redirection of the Severe Fuel Damage research program. These developments include: (1) results of the consequence studies for dominant-risk accident sequences in the NRC source-term reassessment program that will be reported in BMI-2104, [2] (2) results of the Quantitative Uncertainty Estimation for the Source Term (QUEST) in the same

program that will be reported in SAND 84-0410, [3] and (3) the general increase in knowledge of the governing phenomena and the consequences of severe accidents obtained in the last two years. The QUEST work has shown that, at least for the SURRY TMLB' accident sequence that was studied in detail, the uncertainty in the suspended aerosol activity in the containment is about a factor of 100. This uncertainty was found to result primarily and in about equal amounts from uncertainties in the in-vessel fission product release rates and from uncertainties in the in-vessel progression of core melt that affect both the probability of early containment failure and the fission-product release itself. In-vessel melt progression determines the melt mass and temperature distribution and the mode and timing of vessel failure that in large part determine the hydrogen generation and the fission-product release and aerosol generation. The major goals of the program redirection are: (1) data and models on in-vessel fission-product release rates, chemical form, and attenuation, and aerosol formation and transport under in-vessel conditions up to full fuel-melt temperatues; and (2) models and confirmatory data on in-vessel melt progression up to vessel failure, the melt mass and temperature distribution, and the mode and timing of vessel failure, which are incorporated in the MELPROG melt-progression analysis code.

IN-PILE INTEGRAL TESTS

A major part of the Severe Fuel Damage research program is the series of four large integral (multi-effect) SFD tests in the PBF test reactor on core behavior under core-uncovery accident conditions at temperatures up to about 2500K. These tests are performed with 0.9 meter long, 32-rod bundles of test fuel and at 68 bars pressure. They use either fresh or pre-irradiated fuel that has been preconditioned by a week's operation at full power, in part to build up a short-lived fission-product inventory in the test fuel, and with a pre-test shutdown for build-up of a prototypic cesium-iodine ratio. Fission-product release, hydrogen generation, and temperature distributions in the fuel and the gas phase are measured during the test transients. The resultant fuel-damage conditions are determined by post-test neutron radiography and tomography and by post-irradiation examination (PIE).

The fresh-fuel SFD Scoping Test in PBF used an unprototypically-high steam flow rate and slow heatup with resulting high oxidation, and was quenched from high temperature by reflooding. The fresh-fuel SFD 1-1 test used the low steam flow and rapid heat-up characteristic of core-uncovery transients in small-break loss-of-coolant accidents (LOCAs) in a PWR and was not qenched. The SFD 1-3 and 1-4 tests are also for core-uncovery conditions without quench, and use pre-irradiated fuel that has also been preconditioned at power prior to the test transient for build-up of a short-lived fission-product inventory. These tests will also have improved fission product diagnostics. Two silver-indium-cadmium control rods will be added to the test fuel bundle in test SFD 1-4 along with on-line aerosol diagnostics. The first three of the PBF SFD tests have been performed, and the test series will be completed with the performance of test SFD 1-4 in February 1985.

These integral Severe Fuel Damage tests in PBF have produced a sub-stantial amount of data for determining and modeling the governing

phenomena under core-uncovery accident conditions. Significant integral data have been obtained on the rapid oxidation heating transient, with the resultant generation of large quantities of hydrogen, fuel liquification (dissolution in molten unoxidized metallic zircalloy) and relocation downward, damaged fuel characterization, and fission-product release, transport, and deposition.

Large-scale in-pile integral tests are being continued in the Canadian NRU reactor at Chalk River, which can accommodate bundles of 3.6 meter long full-length PWR fuel rods. Full length tests are important for the validation testing of the SCDAP and MELPROG codes, particularly for clad oxidation and the resulting hydrogen generation where length scaling from the shorter PBF and ACRR test results has uncertainties.

Four integral full-length Severe Fuel Damage tests in NRU are currently planned. High temperature tests HT-1 and HT-2 will provide full length validation testing up to 2100K and 2500K, respectively, of the SCDAP and MELPROG models, particularly for rapid oxidation and hydrogen generation. These fresh-fuel tests will be performed in 1985. The third planned full-length NRU test, called H-max and planned for 1986, is to determine the maximum zircalloy oxidation and hydrogen generation possible during a core uncovery accident, that includes the effect of adverse operator action as at TMI-2. The fourth planned NRU test, THE Source Term (ST) test, is a possible full-length integral high-temperature, melt-progression, and fission-product-release test for code validation that would use pre-irradiated fuel. A preparatory test in NRU for the SFD series, test MT-6, has given excellent data on clad ballooning.

A series of small-scale integral (multi-effect) Severe Fuel Damage experiments is also being performed in the ACRR test reactor on the governing mechanisms involved in the development of fuel damage, fuel liquification, debris relocation, and melt progression under core-uncovery accident conditions. These experiments use visual diagnostics (cinematography) to give time-continuous data on the development of fuel damage and melt progression and on surface temperatures, as well as direct measurement by pulse Raman spectroscopy of hydrogen generation inside the test-fuel bundle. The purpose of these Debris Formation (DF) experiments is to provide detailed time-continuous data for the validation testing of the models in SCDAP and MELPROG, and for the development of advanced versions of these codes. These experiments use 0.5m long 9-or-12 rod bundles of test fuel in flowing steam, and are modeled to represent the behavior of a 0.5m long central section in reactor core in core-uncovery accidents. In the initial series of four experiments with fresh-fuel, the first three cover the conditions of low, medium, and high clad oxidation at the time of melting of the unoxidized cladding (with resulting variations in fuel liquification), and a silver-indium-cadmium control rod and additional aerosol-diagnostics instrumentation are added for the fourth. The first of these experiments has already been performed, and the four-test series will be completed in 1985.

Two later follow-on DFI experiments (Debris Formation Irradiated) are planned with pre-irradiated test fuel. The primary purpose of these experiments is to provide integral data on fission-product release and aerosol generation during the progression through two of the higher-risk accident

sequences. Such results are needed to supplement the data from the new separate-effects experiments in ACRR on fission-product release rates under specific well-defined fuel and environmental conditions, as well as the data from laboratory separate-effects experiments. Irradiated fuel is different mechanically from fresh fuel, and these two experiments will also provide irradiated-fuel data on the development of fuel damage and melt progression. These two DFI experiments are currently scheduled for 1986.

A third DFI experiment in which the fuel is quenched by reflooding is also under consideration. The primary purpose of this experiment would be to determine the puff release of both hydrogen and fission-products that were quite high in the PBF Scoping Test which also was quenched. Data would also be obtained on the characteristics of the core debris that results from accident recovery by core reflooding, as at TMI-2. This would be used for assessment of the limits on degraded core coolability using debris-coolability models which themselves are undergoing validation testing in separate-effects experiments in the Severe Fuel Damage research program.

SEPARATE-EFFECTS PHENOMENOLOGICAL EXPERIMENTS

Separate-effects experiments in the Severe Fuel Damage research program include in-pile experiments in ACRR on in-vessel fission-product release rates and core-debris coolability limits, and out-of-pile laboratory experiments by our German program partners at KfK and also in the United States on the thermodynamics, the kinetics, and the metallurgy of the reactions between UO_2, zircalloy, and steam.

The purpose of the planned new separate-effects Source Term ST) experiments in ACRR, which are a major part of the redirection of the Severe Fuel Damage research program, is to provide a data base on fission-product release rates, chemical form, and aerosol formation, including the non-volatiles, for the most significant range of in-vessel severe-accident conditions up to full fuel melt temperatures. Such data are needed to reduce major uncertainties in current source-term calculations. These ST experiments impose clearly defined conditions of temperature ramps or isothermal plateaus upon the fission-heated test fuel which is in rod or particulate debris form, in some cases with pre-oxidized clad. About eight tests are currently planned. Important test variables are the states of fuel liquification, pressure, temperature, rod debris geometry, and a check on mass-transport limitation of the fission-product release rates. The data from these ST special-effects experiments will be supplemented by results of the two small DFI integral tests in ACRR that provide fission-product release and aerosol data for the progression through the succession of states in two severe-accident sequences. The ST experiments will start in about a year and will extend over a two-year period.

Separate-effects experiment in ACRR on the dry-out limits on Damaged Core Coolability (DCC) are also being performed. The purpose of these experiments is to validate for LWR-specific conditions the advanced debris coolability models that have been developed in LMFBR safety research. The LWR specific

conditions for which validation is needed are the full pressure range to 170 bars, deep debris beds, the relatively more coarse (than LMFBR) LWR core debris, and inlet coolant flow. The first two DCC tests with relatively coarse simulated LWR debris gave, a significantly smaller increase in the dry-out bed specific power with increasing pressure than that in the standard Lipinski 1-D dry out model, particularly for the finer debris.[4] The third DCC test with a vertically-stratified debris bed and variable (from zero) inlet flow is scheduled for mid 1985. The laboratory experiments and analysis at KfK on debris-bed coolability are closely coordinated with and complement the ACRR experiments and analysis.

A major part of the out-of-pile separate-effects experiments associated with the Severe Fuel Damage research program is the research at KfK. In addition to the work on the thermodynamics, kinetics, and the metallurgy of the reactions between UO_2, zircalloy, and steam, this work includes pioneering integral laboratory experiments on the development of severe fuel damage. Laboratory experiments on zircalloy oxidation kinetics and the viscosity of liquified fuel are being performed in the United States, along with related laboratory experiments on fission-product release from irradiated fuel that are not considered to be a part of the Severe Fuel Damage research program.

TMI-CORE DEBRIS EXAMINATION

Examination of the TMI-2 core debris is providing valuable and unique benchmark data on fuel behavior under severe-accident conditions that are an important complement to the Severe Fuel Damage research program.

ANALYSIS AND CODE DEVELOPMENT

In addition to analysis of the experimental results of the Severe Fuel Damage research program and the development of models of the governing processes, two mechanistic code packages are under development and validation testing for use in severe accident safety assessment and the benchmarking of risk-assessment codes. These two code packages have different capabilities and different applications, and thus are complementary, not duplicative.

The Severe Core Damage Analysis Package, SCDAP, treats the state of the core during the earlier stages of core-uncovery transients in detailed pin geometry, and is particularly useful for analysis of recovered accidents like TMI-2. SCDAP includes oxidation and hydrogen generation, fuel liquification, fission-product release, and debris formation and coolability following reflood quenching. The Melt Progression model, MELPROG, treats the in-vessel progression of core melt, liquification, and relocation in core-uncovery accidents through the attack on the reactor internal structure and the reactor vessel. Included are the mode of vessel failure and the initial conditions for melt entry into the reactor cavity and the containment. Modeling to allow analysis of BWRs as well as PWRs will soon be added to both codes. Both also have fission-product release and transport modules that incorporate the modeling of the TRAP/MELT fission-product and aerosol transport code. Incorporated into MELPROG is a special fission-product module, VICTORIA, that

will accommodate the results of current and future research on fission-product release and that also includes the TRAP/MELT transport methodology. Both SCDAP and MELPROG are being linked to appropriate thermal-hydraulic codes to include analysis of this important aspect of in-vessel severe-accident behavior. Because of the internal structure of the codes as well as for other reasons, SCDAP will be linked with the RELAP5 thermal-hydraulic code and MELPROG will be linked with TRAC.

Development has been completed on the MOD 1 version of SCDAP and on the MOD 0 version of MELPROG. SCDAP MOD 1 has been tested against PBF data and has been used in TMI-2 analysis. The integration of SCDAP/MOD 1 with the RELAP5/MOD 2 thermal-hydraulic code and the TRAP/MELT fission-product and aerosol transport code has also been completed. While use of the MOD 0 version of MELPROG has begun, there are currently few experimental data available for assessment of governing models in the code. This assessment will depend on the future experimental results from the Severe Fuel Damage research program. The MOD 1 version of MELPROG that incorporates the VICTORIA fission-product and aerosol release and transport module will be completed late in 1985. Advanced MOD 2 versions of SCDAP/RELAP5 and TRAC/MELPROG that include BWR capability will be available in late 1986. These versions of the codes will have undergone validation testing against experimental results from the Severe Fuel Damage research program.

The SCDAP/RELAP5 and the TRAC/MELPROG codes in their MOD 2 versions will provide advanced and partially validated tools for the mechanistic analysis of in-vessel melt-progression and fission-product behavior in severe LWR accidents. They will provide capability for direct detailed analysis of accidents and experiments, and for benchmarking the advanced new risk-assessment code MELCOR and other advanced codes that are developed for risk assessment. These codes as validated also become the embodiment of the results of the Severe Fuel Damage experimental program.

References

1. "Nuclear Power Plant Severe Accident Research Plan," NUREG-0900 (1983)

2. "Radionuclide Release Under Specific LWR Accident Conditions," BMI-2104 (to be published)

3. "Uncertainty in Radionulcide Release Under Specific LWR Accident Conditions," SAND84-0410 (to be published)

4. R. J. Lipinski, "A Model of Boiling and Dryout in Particle Beds," NUREG/CR-2648 (1984)

ASSESSMENT OF SCDAP BY ANALYSIS OF IN-PILE EXPERIMENTS; POWER BURST FACILITY - SEVERE FUEL DAMAGE SCOPING TEST

J N Lillington

AEE Winfrith
Dorchester
Dorset
England

ABSTRACT

The paper presents severe fuel damage analysis using the SCDAP code [1]. Phenomena modelled include heat transfer, the Zircaloy-steam reaction, fuel and clad relocation, and bundle collapse. The main objective is to describe a comparison of a SCDAP prediction of the Scoping Test with experimental results. Particular emphasis will be paid to the main interesting feature, the mechanism behind the spontaneous clad temperature excursion involving extensive oxidation of the Zircaloy. The paper concludes with an assessment of the SCDAP models, on the basis of the experimental comparison.

INTRODUCTION

This paper presents calculations on the PBF SFD-ST experiment, performed at INEL EG&G Idaho Falls, using the USNRC sponsored code SCDAP. At an early stage in the SCDAP development assessment of the Scoping Test provided insight into the adequacy of the fundamental modelling, eg the boiling and radiation heat transfer models, and this led to significant improvements in subsequent versions of the code. This provides a sound basis for investigating the other main phenomena, clad oxidation, fuel motion phenomena etc, in future model assessment.

The Scoping Test predictions given in this paper are based on best estimate input data, using the version of the code obtained in September 1983, from EG&G, termed SCDAP/MOD0/RELEASE3 and in general incorporating only the minimum changes that were necessary for conversion of the code from the CDC to CRAY computers. There are three exceptions, described later, but no attempt has been made to tune the models to fit experiment.

The experiment was characterised by a very slow heat up from saturation temperatures of 550K to superheats between 500K and 1500K depending on axial location. At about 200 mins a rapid temperature excursion occurred over most of the superheated region associated with the exothermic Zircaloy oxidation reaction. The mechanism of this rapid transient presents an interesting question. Did it result from:

(1) a flame propagation downwards;

(2) deterioration of local heat transfer conditions resulting from the observed flow reduction; which might have been caused by hydrogen back pressure in the separator?

It is not possible to assess the first mechanism using SCDAP but the conditions necessary for the second are predictable using the code, and are discussed below.

PROBLEM SPECIFICATION FOR THE SCOPING TEST

The input data for the calculation were mainly derived from the EG&G Quick Look Report [2], together with some reference to test cases supplied by EG&G, and [1]. In the analysis in the QLR, zero time was taken to be 23-00 hours on 28/10/82. The initial conditions in the SCDAP calculation are based on conditions existing 10 minutes after this time. To avoid confusion all times quoted will be relative to zero time in the experiment.

The test geometry is shown in Figure 1. In the SCDAP calculation the fuel rods are grouped into components 1, 2, 3 according to different radial power levels [2] with the shroud, see description below, as component 4. In the finite difference discretisation the heated length 0.91m was divided into 8 equal length axial cells.

The definition of the fission bundle power is probably uncertain to within 10% [2]. In the calculations here the axial profile taken is that recommended in the TRAC comparison in the QLR. The profile is skewed downwards to allow for partial uncover of the core but only a single profile is used for the calculation. There is considerable uncertainty concerning this parameter. Good steady state calculations were established between 32 and 54 mins with the fission power at 42kW, rising slowly to a peak ~ 98kW just prior to the temperature excursion.

The energy loss to the bypass was estimated from bypass thermocouples. For the SCDAP calculation a heat transfer coefficient of $4 kWm^{-2}K^{-1}$ was taken for heat flow to the bypass which is consistent with the value used in the thermal-hydraulic model for heat transfer to subcooled liquid. A sink temperature of 540K was assumed; this value is 'hard-wired' into the code, but it is consistent with estimates from the bypass thermocouples.

For the thermal hydraulic calculation the inlet flow history was taken from QLR. The flow was constant at 16.2 g/s over most of the heat up, but during the temperature excursion reduced by about 25%. This flow reduction thought to be caused by back pressure, eg due to hydrogen production, is not predictable within the limits of the simplified thermal-hydraulic model used here [3] and has to be prescribed as input data. Radiation view factors and path lengths are required and the values used were supplied by EG&G [4].

The shroud was taken to be composed of six material layers in the following order from outside, outer Zr shroud wall, gas gap, additional Zr shroud wall, Zr saddle, ZrO_2 insulator and inner Zr liner. The material information was based on data supplied in [1], [2].

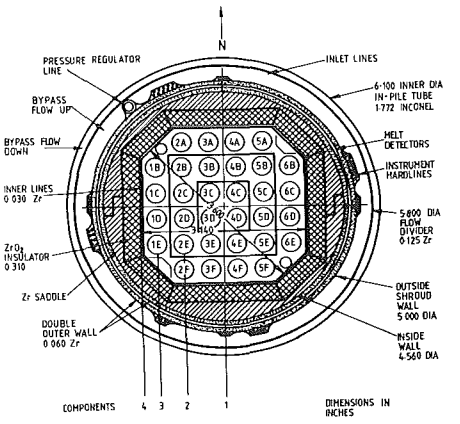

FIG 1 SECTION THROUGH THE PBF SFD TEST TRAIN AND COMPONENTS FOR SCDAP CALCULATION

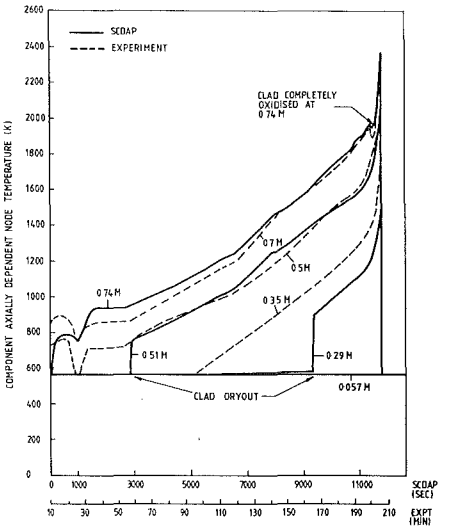

FIG 2 COMPARISON OF SCDAP PREDICTION OF COMPONENT 1 CLAD SURFACE TEMPERATURES WITH EXPERIMENTAL RESULTS

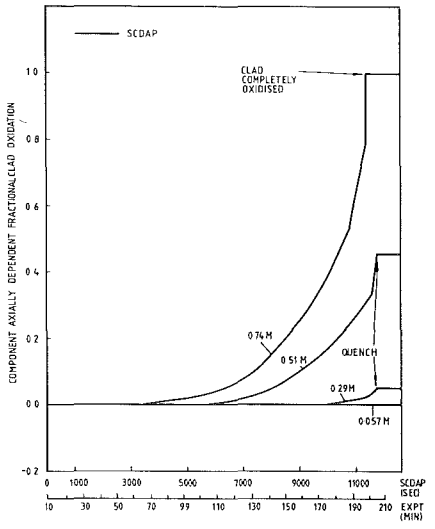

FIG 3 SCDAP PREDICTION OF COMPONENT 1 ROD FRACTIONAL CLAD OXIDATION

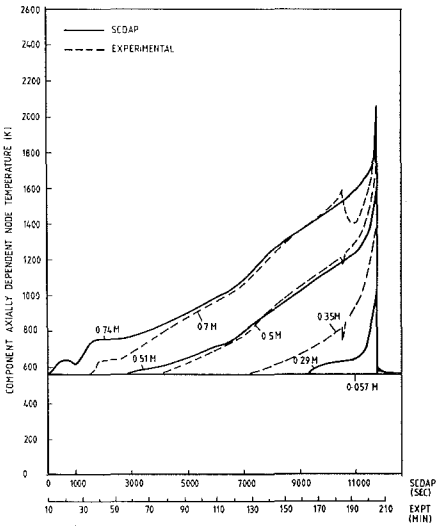

FIG 4 COMPARISON OF SCDAP PREDICTION OF INNER SHROUD SURFACE TEMPERATURES WITH EXPERIMENTAL RESULTS

In addition to the data, three model changes were included in SCDAP. The first was to allow the timestep for coupling the thermal-hydraulic and structure calculations to vary with time. Here a 10 sec timestep was used up to 143 mins and 1 sec timestep for the remainder of the transient. Secondly a correction was made to ensure flow was conserved when ballooning occurred. Thirdly the treatment of the heat transfer at the steam-mixture interface was improved. The original treatment caused heat loss when the interface crossed an axial mesh boundary.

PHENOMENA PREDICTED BY SCDAP

After the steady state hold between 32 and 54 mins, and once dry-out had occurred, the clad temperatures rose steadily at rates between about 0.08 - 0.14 K/s until just prior to the temperature excursion, as shown in Figure 2. The steep increase in clad temperature at dry-out is partly due to the coarse axial mesh in the structure and partly because the assumption of thermal equilibrium implies 100% voidage at dryout.

In the rods in all three components the maximum clad swelling occurred at 0.74m, the level of peak clad temperature. Localised ballooning occurred first in the rods in component 3 at 77 mins with the clad temperature ~ 1042K, and within 3 minutes the rods in components 1 and 2 exhibited similar behaviour. The rods in all components ruptured at hoop strains ~6% between 87 and 93 minutes at temperatures ~ 1090K. Indeed in this calculation the rods in all three components exhibited very similar behaviour at similar times and unless otherwise stated the exact times quoted for the onset of various phenomena will refer to component 1 rods.

It can be seen from Figure 3 that the clad in the upper regions was already oxidising rapidly prior to 190 mins, the start of the flow run down. A small inflection was predicted in the clad temperature at 0.74 m at 200 mins which coincided with complete oxidation of the clad at this elevation. Increase in the temperature rise rates began at all elevations between 194 mins and 200 mins as the flow reduced from 16.2 g/s to 15.39 g/s. After 200 mins the flow reduced from 15.39 g/s to a minimum of 12.15 g/s and this was accompanied by a steep temperature excursion at all elevations. It should be noted that this was even true above 0.74 m, despite the fact that during the period from 200 mins the clad had completely oxidised in this region.

By the time of bundle quench, Figure 3 shows that at nodes half way up the bundle, about 50% of the clad thickness had oxidised. Below 0.17 m the clad was unaffected.

Figure 4 shows the temperatures for the inner shroud. Similar temperatures rise rate increases as seen in the rod profiles are seen for the shroud during the flow run down. In this calculation the shroud was not significantly oxidised. At 0.74 m at the position of peak clad temperature, only about 30% of the inner liner of the shroud had oxidised by the time the bundle was quenched.

In this reference calculation no fuel relocation in the balloon occurred and there was no melting of the Zircaloy or eutectic formation.

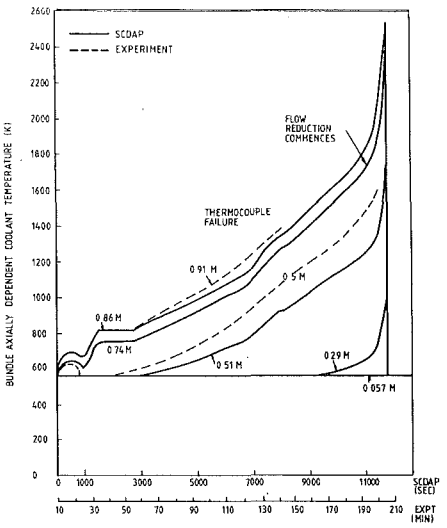

FIG 5 COMPARISON OF SCDAP PREDICTION OF COOLANT TEMPERATURES WITH EXPERIMENTAL RESULTS

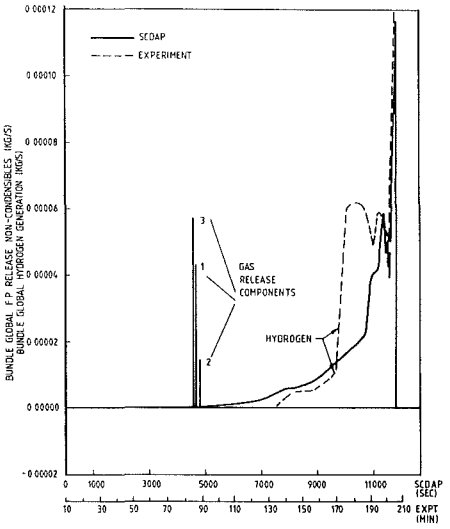

FIG 6 SCDAP PREDICTIONS OF FISSION GAS RELEASE AND HYDROGEN RELEASE IN COMPARISON WITH EXPERIMENT

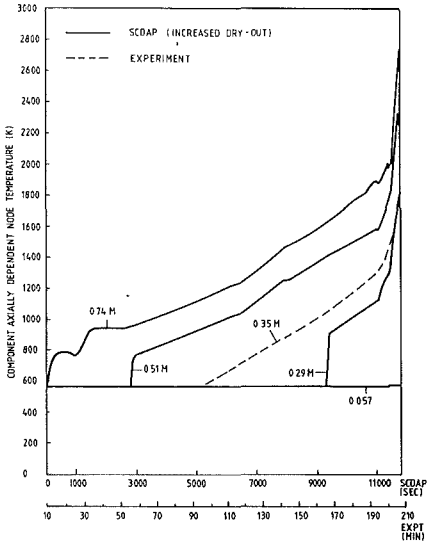

FIG 7 COMPARISON OF SCDAP PREDICTION OF COMPONENT 1 CLAD SURFACE TEMPERATURES, AFTER INCREASED DRY-OUT, WITH EXPERIMENTAL RESULTS

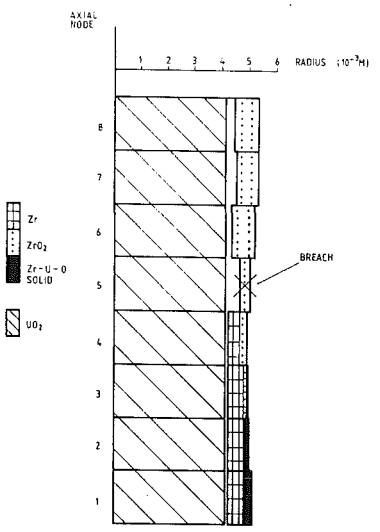

FIG 8 ZIRCONIUM MOTION IN COMPONENT 1 IMMEDIATELY PRIOR TO SCRAM AS PREDICTED IN THE SCDAP CALCULATION WITH INCREASED DRY-OUT

COMPARISON WITH EXPERIMENT

Figures 2 and 4 show some discrepancy between calculation and experiment during the earlier part of the transient. These mainly result from the poor description of dryout in the SCDAP model. For this reason and because no phenomena (eg ballooning or oxidation) occur until the bundle becomes more uncovered, by which time the agreement is better, no attempt has been made to optimise the thermal-hydraulic conditions during this initial period.

The onset of the temperature excursion is well predicted by the calculation in comparison with experiment. In the experimental results a small inflection is observed at 0.7 m at about 200 mins which coincides with the termination of oxidation at this elevation in the calculation. This is good evidence to suggest that in the experiment a significant portion of the clad in upper region regions oxidised prior to the excursion.

The peak temperature predicted in the reference calculation at 0.74 m was about 2370K, against the experimental maximum of about 2400K. At 0.5m the corresponding temperatures were 2000K and 2400K respectively. At the lowest elevation the SCDAP calculated peak temperatures in the reference calculation only reached about 1400K whereas it appears from the experimental data that most of the clad reached high temperatures and oxidised. The 25% reduction in inlet flow applied to the SCDAP calculation did not cause the bundle to dry out. For this reason in the calculation a significant proportion of the lower fuel clad and shroud liner did not oxidise at all.

However from the experimental data there is evidence from the neutron detector signals that the bundle dried out during the temperature excursion [5]. Further from the P.I.E. [6] it has been deduced that about 7.7% of the fuel bundle material (2.4% UO_2 and 5.3% Zircaloy clad) relocated to the bottom third of the bundle. Analytic calculations suggest that if this material fell into the water then it would constitute a significant heat source quite apart from any resulting increase in the nuclear heat in this region, and this would have contributed to increased dryout. In its final state the lower region consisted of rod stubs with previously molten material between most of the rods. There was considerable reduction in flow area. This would tend to cause flow reduction and increased dryout also. Much higher temperatures would have been predicted in the reference calculation if these effects had been simulated. This is demonstrated in the next section by a sensitivity calculation.

The agreement between the SCDAP calculated and measured shroud inner liner temperatures is good up to 180 mins, when the shroud failed in the upper regions of the bundle. At this time the SCDAP calculation predicts the inner shroud clad is only about 10% oxidised at the peak temperature elevation, so even if shroud failure models had been included in the calculation it is unlikely that the shroud would have ruptured at this stage. After this time the SCDAP calculation consequently under-estimates the heat lost to the bypass in the upper regions, resulting in higher predicted temperatures.

The predicted coolant/pin surface temperature gradients are greater than measured see Figures 2 and 5. A possible explanation for this, given in [2], is that the thermocouples reading the steam temperatures could be reading high as a consequence of direct radiation from the rods. This is not confirmed or denied here. The overall temperature rise is reasonably predicted but the temperatures at 0.5 m are overpredicted. This points to a discrepancy in the

axial power profile between calculation and experiment. The use of single profile throughout the calculation is clearly simplistic.

Figure 6 shows that oxidation started to occur earlier in the calculation than in the experiment. However the hydrogen release rate between 175 mins and 190 mins was much higher in the experiment than in the calculation indicating rather more oxidation in the experiment than was predicted. The shroud ruptured during this period in the experiment and more Zircaloy would have been exposed to steam. The general shape of the experimental and calculated releases is similar, but just prior to the scram the maximum rate of hydrogen release was measured at 0.89 g/s, against 0.12 g/s predicted. The total amount of hydrogen released during the experiment was estimated at 375 g against 100 g predicted. However the complete oxidation of the Zircaloy in the fuel bundle and shroud inner liner, and oxidation of portions of the rig such as the fall-back barrier and Zircaloy saddles (not currently modelled in SCDAP) is required to account for all the hydrogen measured in the test. The presence of metallic Zircaloy in the debris as alluded to by Rivard [7] and in the Quick Look report [2] is not consistent with this quantity of hydrogen.

The conclusion from this comparison is that the temperature escalation above the centre of the bundle during the flow reduction was well predicted in the calculation in comparison with experiment. Unlike in the experiment, at the lower elevations, there was little or no oxidation and rapid temperature escalation was not predicted in the calculation.

SENSITIVITY CALCULATION WITH INCREASED DRY-OUT

The degree of oxidation predicted by the reference calculation was generally less than experiment prior to the excursion. Not only is it difficult to predict the timescale of rampant oxidation exactly, eg only a part of the shroud was beginning to oxidise rapidly by the time of the final excursion, but there were portions of the rig not included in the analysis, which oxidised. This may account for why motion of fuel and structure material occurred [5] during the final minutes of the test, but none was predicted by the reference calculation. Any movement has a positive feed-back effect in that more heating of the relatively unoxidised Zircaloy in the lower bundle, as a consequence of material movement and flow blockage, could induce further clad melting and slumping etc. Such a chain of events probably occurred because it is thought that during the final minutes of the test there was essentially no water remaining in the test train [5].

A sensitivity calculation was performed to examine the effect of increased bundle dry-out during the temperature excursion. This was achieved by increasing the inlet enthalpy conditions during the last few minutes in order that by the time of quench only 12% of the lower bundle remained wetted (as opposed to about 25% in the reference calculation).

Figure 7 shows the predicted clad temperatures. Up to 200 mins the calculation is identical to the reference case described earlier. Also shown are the experimental results for 0.35 m. At the 0.29 m elevation the predicted clad temperature rose to about 1700K, into the threshold region for rapid oxidation to take place during the temperature excursion, 300K hotter than the reference calculation and in much better agreement with experiment. At the 0.5 m elevation the temperature rose to 2300 K, above the temperature for eutectic

formation, before the clad had completely oxidised, in contrast to the reference calculation.

A schematic of the eutectic distribution predicted in the calculation just prior to scram with these conditions of dry-out is shown in Figure 8. As found in the experiment the maximum accumulation was in the lower regions of the bundle and the breach and therefore maximum depletion occurred at 0.5 m. Some movement of fuel/clad upwards was observed in the experiment but there are no models in SCDAP to permit coolant drag on molten fuel or clad and consequently no fuel or eutectic can be transported upwards in the SCDAP calculation.

The predicted hydrogen release rates just prior to the scram were 3 times higher than in the reference calculation but still lower than estimated in the experiment. The cummulative hydrogen releases were also still less, presumably because oxidation of structure not modelled in SCDAP was still contributing a significant source to the total hydrogen.

SCDAP ASSESSMENT

Unlike previous versions of SCDAP incorporating TRAC-BD1 the boiling model was found to be energy conservative. Prediction near regions of dry-out are poor, partly because of the thermal equilibrium assumption and partly because of the coarse axial mesh description. Heat loss due to the numerical treatment of radiation [8] did not arise in the Scoping Test calculations, in any significant amount, because the large bypass heat loss kept the shroud temperature much lower than the coolant temperature. However in principle the problem remains.

Although the predictions of clad ballooning were reasonable here, in many other calculations erroneous results have arisen. These tended to be because of numerical problems in the model which in some cases produced unphysical ballooning at too low temperatures, at too large strain, and not at the axial elevation of peak temperature. Also the radiation model and some aspects of the fuel relocation models assume nominal geometry.

The qualitative predictions of the clad oxidation models seem reasonable within the steam rich conditions of the experiment. Recent experimental data from Battelle North West suggests that the Urbanic-Heidrick growth rate constants, invoked by SCDAP at clad temperatures exceeding 1850K may be rather low. However when these were increased appropriately in a sensitivity calculation, the main features in the predictions were unaffected. Concerning clad motion, the depletion of the centre region and accumulation of material at the bottom of the bundle were qualitatively predicted. The SCDAP model has the limitation that upward relocation of material as occurred in the experiment could not be predicted.

CONCLUSIONS

(1) Within their own limitations the SCDAP models performed adequately generally, though some shortcomings detailed earlier were identified, eg though clad ballooning was reasonably predicted here, in other

calculations with similar data unphysical results were obtained.

(2) The calculations indicate that a large proportion of the upper bundle region was probably well oxidised prior to the temperature excursion.

(3) The calculations confirm that such a flow reduction causes a major temperature excursion over most of the bundle. If significant dry-out is simulated eg as occurred in the experiment, then clad motion from the centre downwards results and overall good agreement with experiment is predicted.

(4) The catastropic oxidation of the bundle on such a short time-scale is consistent with deterioration of local heat transfer caused by thermal-hydraulic feed-back effects and the steam rich conditions of the experiment. A flame propagation downwards mechanism is not required to explain the events. Under flow and power conditions nearer those of the hypothetical severe accident the oxidation rate would be reduced by steam starvation and hydrogen blanketing effects.

Since the version of SCDAP used in this study was obtained there have been numerous modifications and corrections incorporated in subsequent versions by the code developers. The Scoping Test input data is also being currently reviewed [9]. The calculations presented here are believed to give a broad description of the essential features of the experiment although improved, detailed agreement may be possible using these later versions of the code with refined data.

ACKNOWLEDGEMENTS

Thanks are due to Dr A T D Butland*, and Dr D J Hill** for helpful discussions covering this work, and to Mr A J Lyons* for developing the graphical output for the SCDAP calculations.

REFERENCES

(1) BERNA, G. A. et al. SCDAP/MODØ: A Computer Code for the Analysis of LWR Fuel Bundle Behaviour During Severe Accident Transients. EG&G Report WR-NSMD-82-078, December 1982.

(2) MacDONALD, P. E. et al. Severe Fuel Damage Test Series - Severe Fuel Damage Scoping Test. Quick Look Report. EGG-2234, December 1982.

(3) SIEFKEN, L. J. Coolant Boiloff and Component-to-Component Radiation Models for SCDAP. EG&G Report IS-NSMD-83-023, June 1983.

---

* AEE Winfrith, Dorchester, Dorset, England
** Formerly AEE Winfrith, now Argonne National Laboratories, USA

(4) SIEFKEN, L. J. Private Communication, September 1983.

(5) CROWE, R. D. and ALBRECHT, R. W. Interpretation of Neutron Detector Signals During the PBF Severe Fuel Damage Scoping Test. EG&G Report FIN No A7305, October 1983.

(6) COOK, B. A., KALISH, P. A. and TOW, D. M. Posttest Examination of the Severe Fuel Damage Scoping Test Bundle Geometry. EG&G Report FIN No A605, January 1984.

(7) RIVARD, J. B. Review of the PBF Scoping Test. Private Letter, 1983.

(8) HILL, D. J., LILLINGTON, J. N. and LYONS, A. J. Internal Document.

(9) KNIPE, A. D. Private Communication, July 1984.

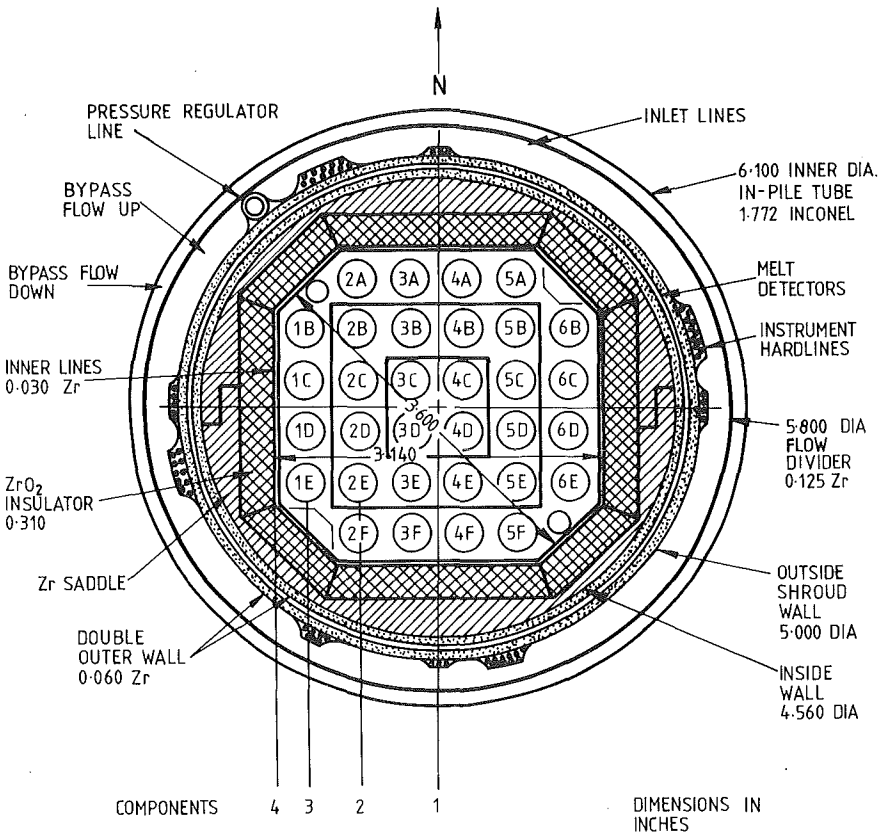

FIG 1 SECTION THROUGH THE PBF SFD TEST TRAIN AND COMPONENTS FOR SCDAP CALCULATION

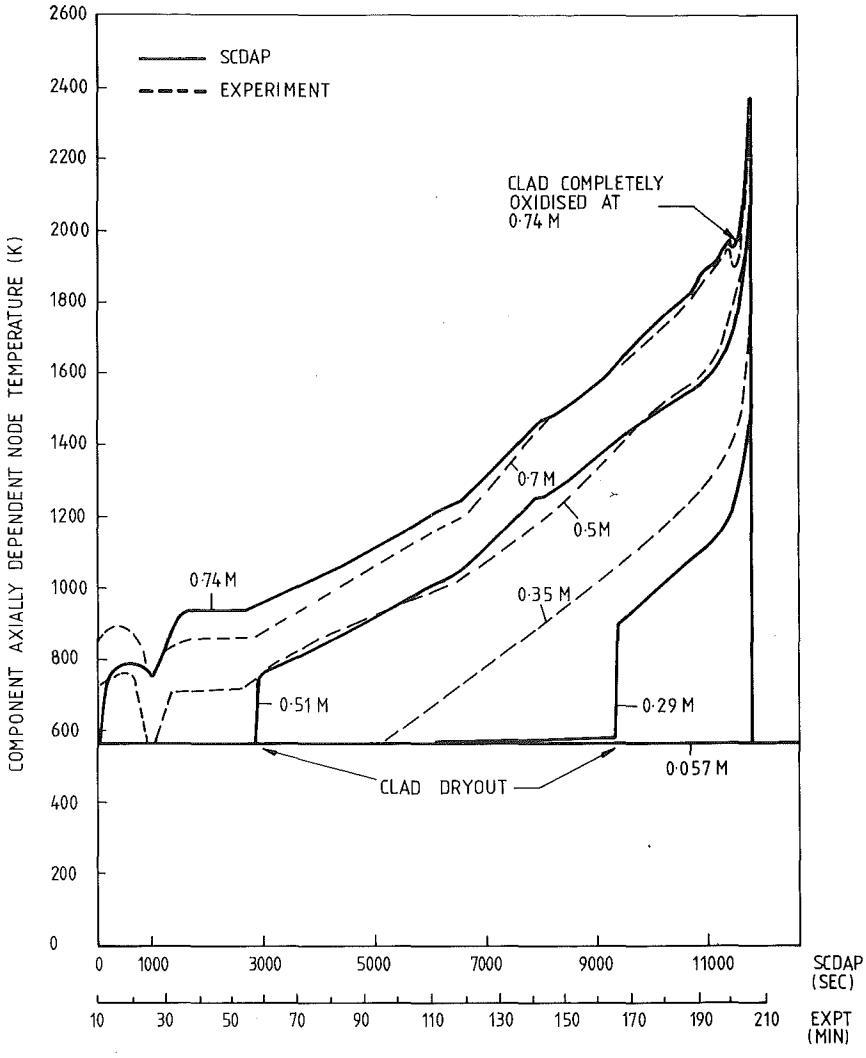

FIG 2 COMPARISON OF SCDAP PREDICTION OF COMPONENT 1 CLAD SURFACE TEMPERATURES WITH EXPERIMENTAL RESULTS

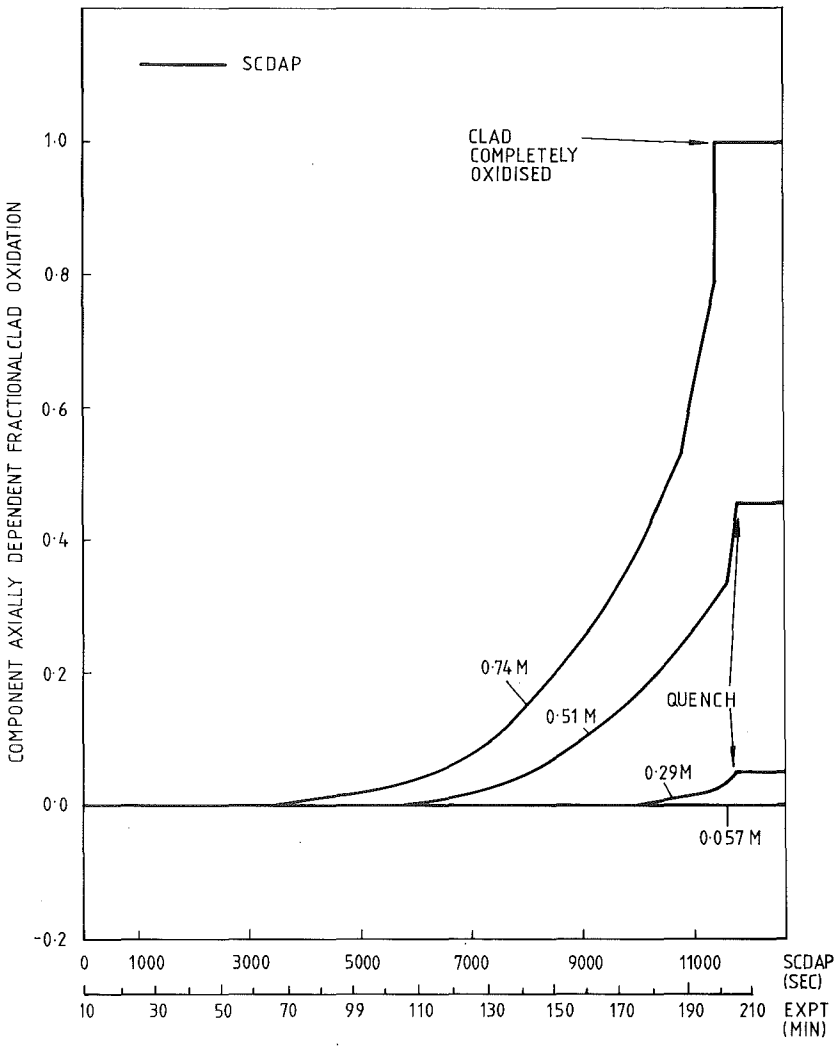

FIG 3 SCDAP PREDICTION OF COMPONENT 1 ROD FRACTIONAL CLAD OXIDATION

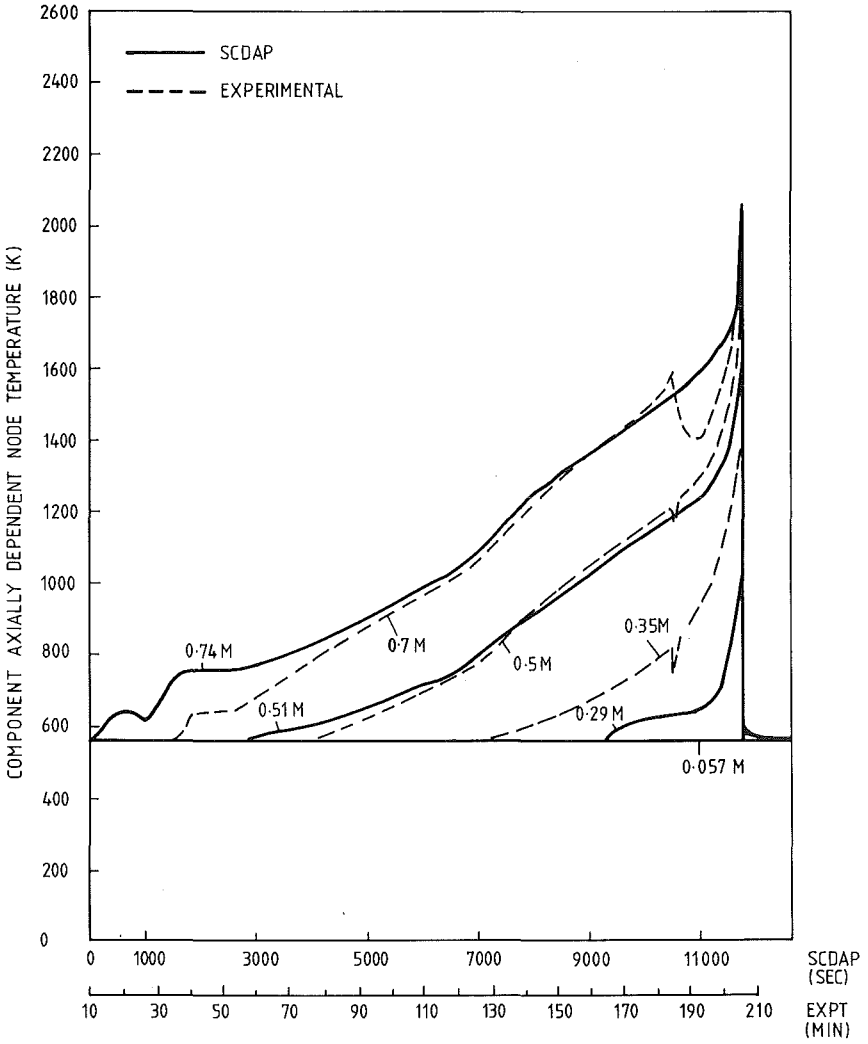

FIG 4 COMPARISON OF SCDAP PREDICTION OF INNER SHROUD SURFACE TEMPERATURES WITH EXPERIMENTAL RESULTS

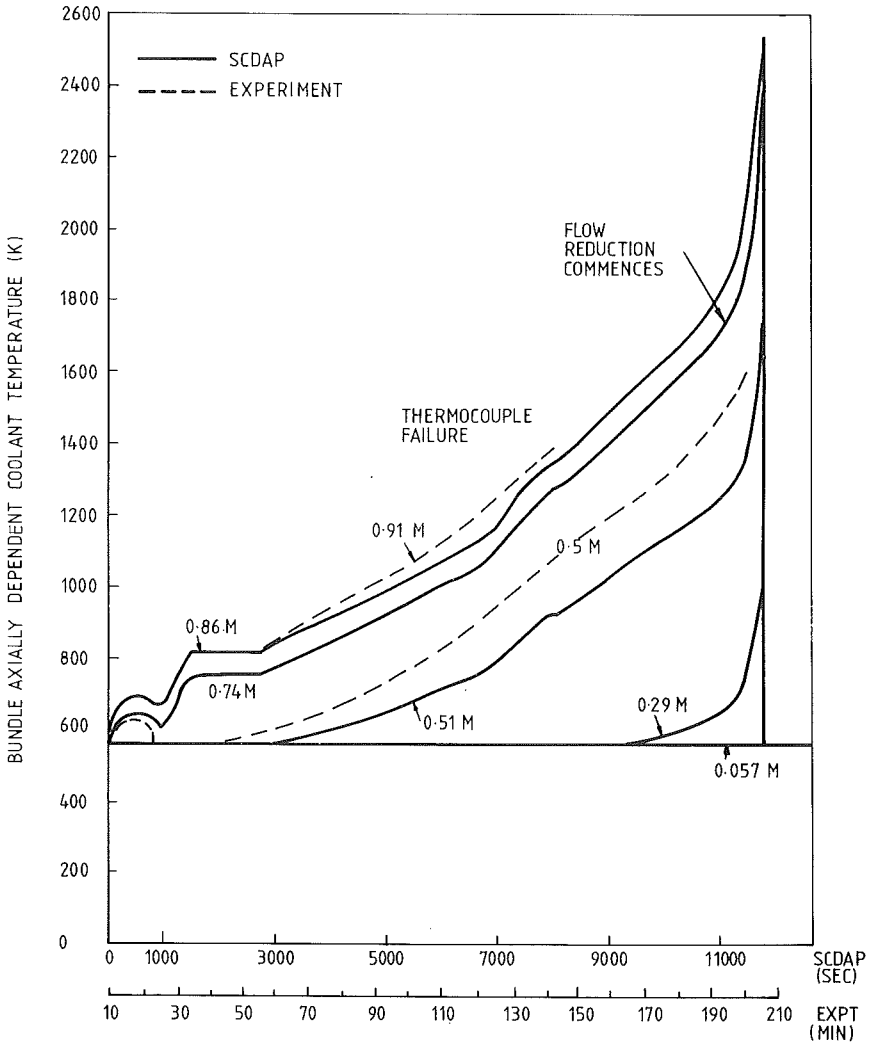

FIG 5 COMPARISON OF SCDAP PREDICTION OF COOLANT TEMPERATURES WITH EXPERIMENTAL RESULTS

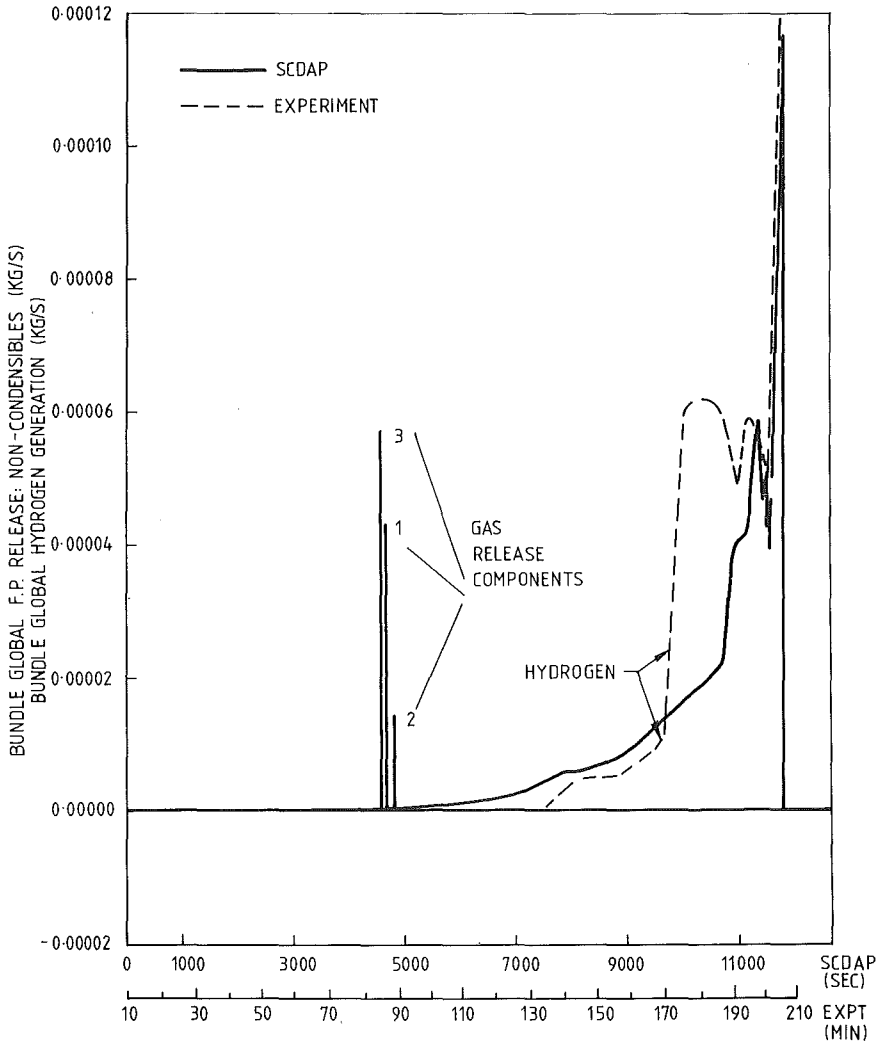

FIG 6 SCDAP PREDICTIONS OF FISSION GAS RELEASE AND HYDROGEN RELEASE IN COMPARISON WITH EXPERIMENT

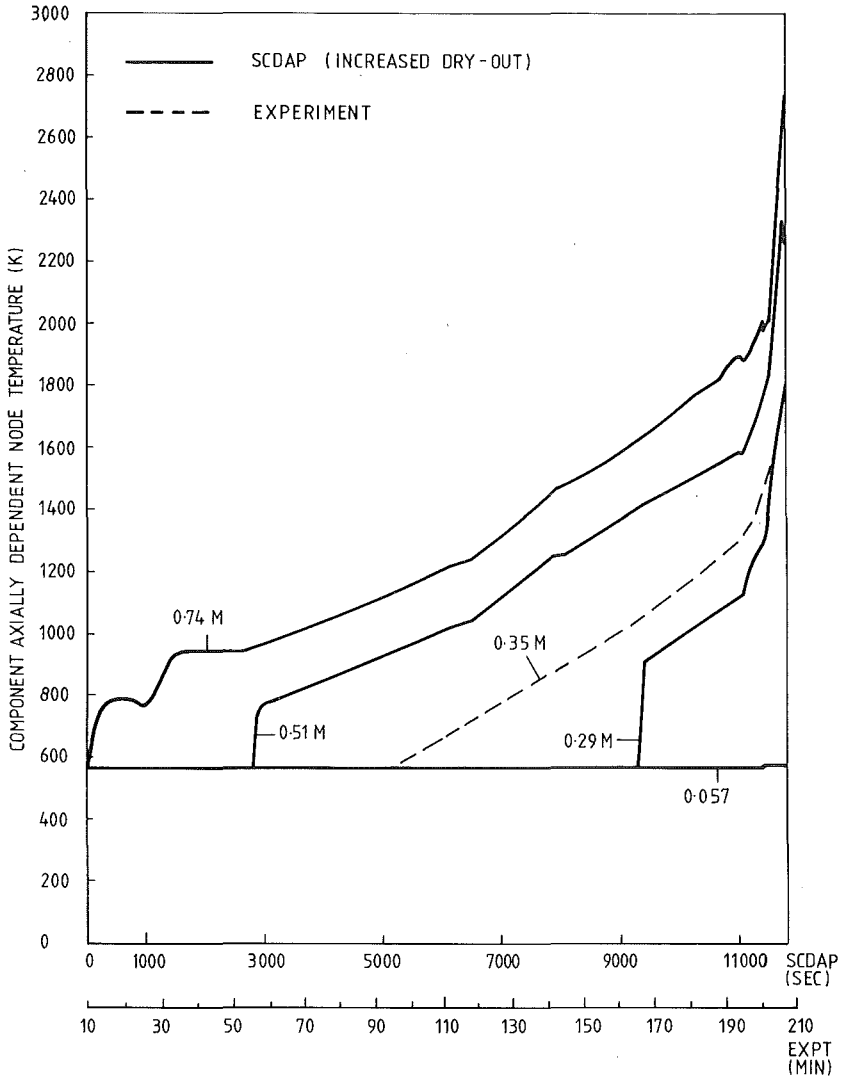

FIG 7 COMPARISON OF SCDAP PREDICTION OF COMPONENT 1 CLAD SURFACE TEMPERATURES, AFTER INCREASED DRY-OUT, WITH EXPERIMENTAL RESULTS

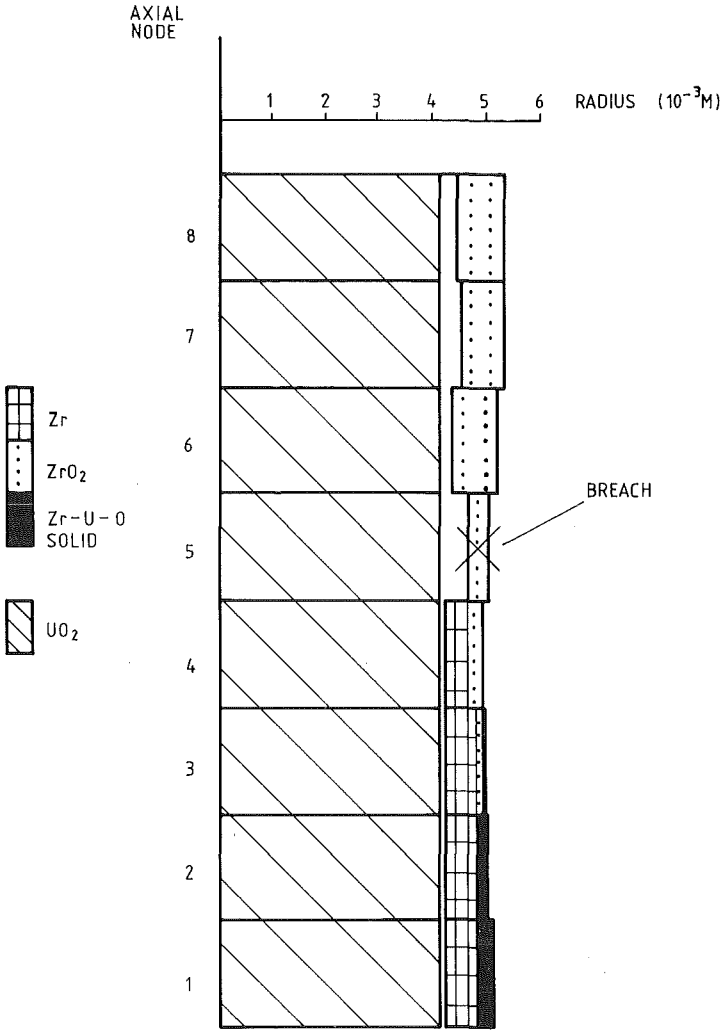

FIG 8 ZIRCONIUM MOTION IN COMPONENT 1 IMMEDIATELY PRIOR TO SCRAM AS PREDICTED IN THE SCDAP CALCULATION WITH INCREASED DRY-OUT

SEVERE FUEL DAMAGE TEST 1-1 RESULTS

P. E. MacDonald, C. L. Nalezny, and R. K. McCardell

EG&G Idaho, Inc.
Idaho Falls, ID 83415

ABSTRACT

A series of severe fuel damage tests is being performed in the Power Burst Facility to obtain data necessary to understand (a) fuel behavior and coolability; (b) fission product release, deposition, and transport; and (c) hydrogen release during degraded core cooling accidents. This report presents the preliminary results of the second experiment of the Severe Fuel Damage (SFD) series, Test SFD 1-1. The measurements indicate that the test conditions required to simulate the fuel damage and fission produce release in a 3000-MW(t) commercial pressurized water reactor core during a small break loss-of-coolant accident without emergency core coolant injection were successfully achieved. Such an accident is characterized by an initial slow heating rate to about 1600 K, followed by a very rapid heating rate driven by runaway metal-water reaction that is steam limited in the upper regions of the core. The fast heatup achieved during the SFD 1-1 test resulted in oxidation of about 30% of the cladding and shroud inner liner and melting of much of the cladding in the lower regions of the fuel bundle. Significant liquefaction of the UO_2 fuel occurred and molten cladding and liquefied fuel slumped to lower bundle elevations. The fission product release during this test was less than during the first experiment of the series (the Scoping Test, which was performed at relatively high steam flow rates), during which nearly all of the cladding was oxidized. Iodine and cesium followed the liquid pathway, and most of the tellurium remained within the test bundle.

INTRODUCTION

The light water reactor accident at the Three Mile Island Nuclear Station-Unit 2 (TMI-2) clearly demonstrated that large hydrogen and fission product releases to the containment can occur despite current engineered safety systems and procedures. Accordingly, the United States Nuclear Regulatory Commission (USNRC) has initiated an internationally sponsored[1] Severe Fuel Damage (SFD) research program to investigate fuel rod and core response, and the release and transport of fission products and hydrogen during degraded core cooling accidents. A major part of the USNRC's experimental program is being performed in the Power Burst Facility (PBF) at the Idaho National Engineering Laboratory.

The objective of the SFD test series is to obtain the data necessary to understand (a) fuel behavior under severely degraded conditions; (b) fission product release, deposition and transport; and (c) hydrogen generation. Four bundle experiments are presently planned for the SFD program. Parameters to be

varied during the four experiments are heatup rate (amount of cladding oxidation), inlet flow (hydrogen-to-oxygen ratio), cooldown rate (amount of fragmentation), test rod burnup, and presence of control material. Unirradiated test fuel rods were used in the first two experiments, and irradiated test fuel rods were used in the third test. Both previously irradiated fuel rods and control rods are to be included in the fourth test. The Series 1 SFD tests are summarized in Table I.

TABLE I. SFD SERIES 1 TESTS

Test	Heating Rate	Inlet Flow (g/s)	Test Bundle	Cooling
SFD-ST	0.15 K/s	16	Fresh rods	Quench
SFD 1-1	TMI-2[a]	0.6	Fresh rods	Slow
SFD 1-3	TMI-2[a]	0.6	Irradiated rods	Slow, no reflood
SFD 1-4	TMI-2[a]	0.6	Irradiated rods and control rod	Slow, no reflood

a. Characterized by slow heating rate up to 1600 K and rapid heating rate above 1600 K, driven by metal-water reaction.

Test SFD 1-1, the second test of Series 1, was completed on September 8, 1983. The SFD 1-1 experiment was designed to simulate the heatup and resulting fuel damage in the upper half of a 3000-MW(t) pressurized water reactor approximately 2 to 3 hours after initiation of a small break accident, when the core is approximately 75% uncovered. The steam flow, power, and primary system pressure within a large commercial plant would be 4 kg/s, 1.5% of full power, and 6.9 MPa, respectively. The appropriate scaled values for the approximately 1 meter PBF bundle were 0.6 g/s, 8 kW, and 6.9 MPa, with as much of the bundle uncovered as possible. These controlling parameters were successfully achieved. (Because of heat loss through the shroud, a variable bundle power, reaching a maximum of 35 kW, was required to produce a net bundle power of 8 kW.)

This paper presents a brief description of the SFD 1-1 test hardware and the fission product and hydrogen sampling and monitoring system; a discussion of the test scenario; descriptions of the thermal/mechanical behavior of the bundle and the fission product release; and conclusions.

FACILITY AND TEST TRAIN DESCRIPTION

The PBF reactor, shown in Figure 1, consists of a uranium oxide driver core and central flux trap contained in an open tank reactor vessel. An independent pressurized water coolant loop provides a wide range of coolant conditions within the flux trap test space.

The SFD 1-1 test train consisted of 32 zircaloy-clad UO_2 fuel rods arranged in a 6 x 6 array without the four corner rods. The active fuel length in the bundle was 0.914 m, and the fuel and cladding dimensions (except length) were similar to 17 x 17 type pressurized water reactor design fuel rods. The test bundle was contained in an insulating shroud consisting of low density zirconia insulation sandwiched between inner and outer zircaloy walls. A test

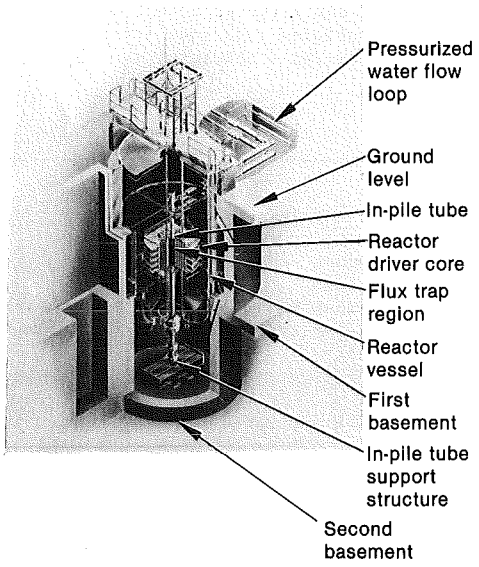

Figure 1. Power Burst Facility reactor cutaway view.

fuel rod enrichment of 6.2% was selected for all fuel rods. Figure 2 shows a cross-sectional view of the test train in the in-pile tube, and Figure 3 shows an axial view of the test train and in-pile tube. The test train was highly instrumented with 2 fuel rod centerline thermocouples, 18 inside cladding thermomocouples, 18 shroud thermocouples, 6 steam probes, 3 flowmeters, 10 pressure sensors, 8 fission chambers, 2 flux wires, 1 temperature profile detector, and a shroud penetration detector.

The test train coolant was routed via two flow paths: (a) the flow from the normal in-pile tube inlet was directed upward past the outside of the insulated shroud and outlet superheated steam line (this flow is called the bypass flow); and (b) the bundle coolant entered in the in-pile tube through a separate line and then passed through the bundle. If the bundle flow rate was high, the coolant left the bundle through a check valve and entered the bypass flow. The check valve was closed during the high temperature phase of

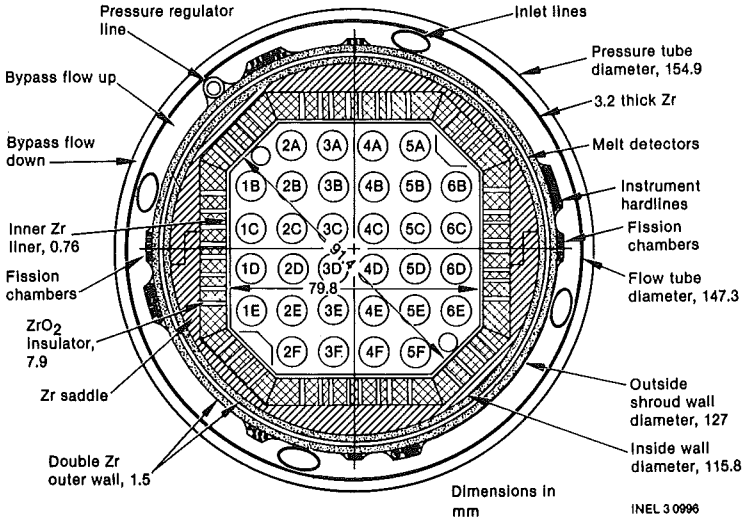

Figure 2. Cross-sectional view of the severe fuel damage test train.

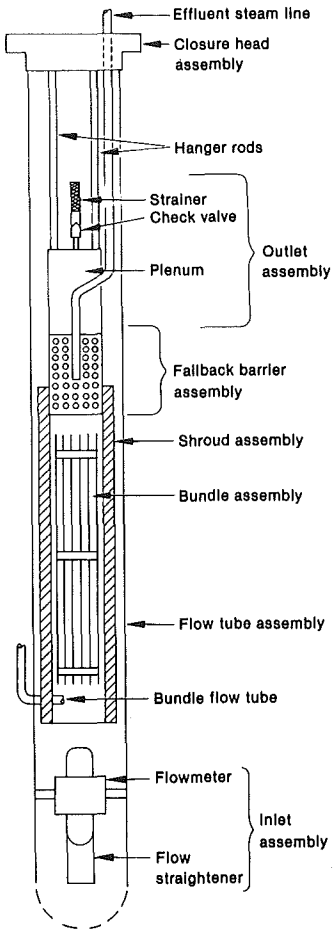

Figure 3. Axial view of the SFD 1-1 test train

the test when the bundle flow rate rate was low and coolant exiting the bundle was routed through a steam sample line which passed through the in-pile tube head closure. The entire bundle effluent--consisting of steam, fission products, and noncondensable gases--was routed though the sample line to a fission product and hydrogen sampling and monitoring system.

FISSION PRODUCT AND HYDROGEN SAMPLING AND MONITORING SYSTEM

The fission product and hydrogen sampling and monitoring system is shown schematically in Figure 4. The sampling and monitoring system consists of a steam sample line, condenser, gas-liquid separator, 6 steam sample bombs, 6 liquid sample bombs, particulate filter, a collection tank, and instrumentation. The instrumentation consists of a gamma spectrometer, ion chamber, sodium iodide spectrometer, and delayed neutron monitor located on the steam sample line; a gamma detector, sodium iodide detector, and hydrogen monitor located on the gas line between the separator and the collection tank; and a gamma spectrometer and sodium iodide detector on the liquid line between the separator and the collection tank.

A 30-g/s liquid flow was added to the system at the separator inlet to act as a carrier for the fission product activity through the liquid line, past the gamma spectrometer and liquid grab samples, and into the collection tank. A nitrogen purge gas was also added to the separator and was set at 68 g/min to keep hydrogen concentrations in the gas line below 70%. Finally, an argon sweep gas system was added to the facility to permit the introduction of gas into the bottom of the test bundle to move fission products through the sample system during periods when little or no steam and hydrogen would be released from the experiment. The argon system was designed to provide a flow of 30 cm^3/s at 560 K and 6.9 MPa.

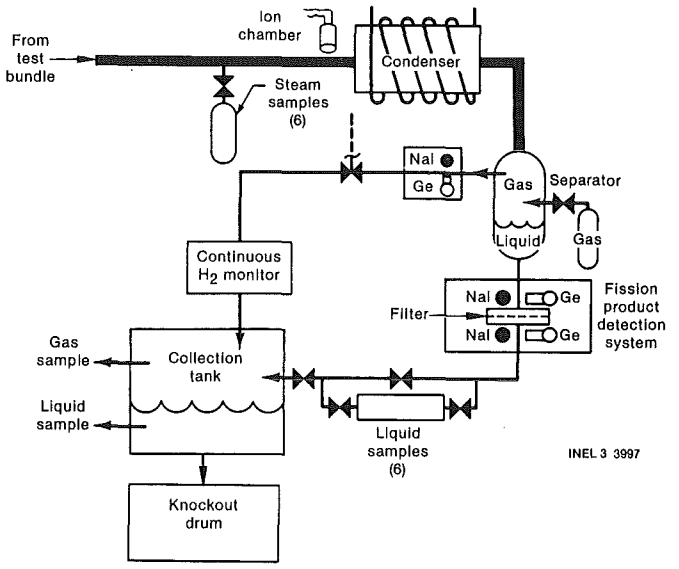

Figure 4. Test SFD 1-1 fission product and hydrogen sampling and monitoring system schematic.

TEST CONDUCT

The test consisted of bundle leakage measurements, a 3-day fuel conditioning and power calibration phase, a 10-day shutdown, bundle leakage measurements, a 4-h conditioning to build up short-lived fission products, and, finally, the high temperature transient.

Following the 4-h run, the bundle inlet coolant flow rate was established at 0.6 g/s with flow going to the fission product and hydrogen sampling and monitoring system and the bundle power was increased gradually to 6.6 kW to initiate boildown of the coolant in the bundle region to an equilibrium elevation of about 0.2 m from the bottom of the fuel stack (two-phase steam/single-phase steam interface level). The bundle outlet steam temperature was about 600 K (saturation temperature at 6.9 MPa was about 558 K). The bundle power was then increased slowly until it was about 8 kW at about 2 min into the transient (time zero is arbitrarily set at 13:30 on September 8), and was then held constant for 12 min while the peak cladding temperatures slowly rose to about 900 K and the liquid level dropped to about 0.08 m. The bundle power was then increased from 8 to about 14 kW at a rate of 0.6 kW/min, from 14 to 20 kW at a rate of 1.8 kW/min, from 20 to 28 kW at a rate of 1.2 kW/min, and from 28 to 35 kW at a rate of about 2.0 kW/m. The peak cladding temperatures were about 1130 K when the bundle power reached 14 kW at 25 min into the transient. The fission product detection system and the fuel rod internal pressure switches indicated that the fuel rods ruptured between 25 and 27 min into the transient. The cladding temperatures first reached values of about 2400 K at 31 min when the bundle power was about 24 kW. The shroud inner zircaloy liner failed at 32 min, shortly after the cladding temperatures spiked up to 2400 K. The measured cladding temperatures remained above the zircaloy melting point until about 38 or 39 min into the transient (7- or 8-min duration).

The maximum bundle power of 35 kW was reached at about 37 min into the transient. The bundle power was then held constant for about 3.7 min, during which time the measured cladding temperatures began to decrease, probably due to thermocouple junction relocation to relatively low elevations. The fuel centerline thermocouples indicated that some of the bundle remained at temperatures above the zircaloy melting point until well after the bundle power began to decrease. The bundle power was reduced from 35 to 25 kW at a rate of 7 kW/min and from 25 to 6.6 kW at a rate of 13 kW/min, following a coolant pressure increase of 0.26 MPa (rise time of 1.6 s) and an indication from the shroud melt-through detectors that the outer shroud wall was heating rapidly at about 41.4 min into the transient. The bundle power was then further decreased to approximately 4 kW over a 10-min interval.

The argon gas flush system was turned on at 53 min, rapidly cooling the bundle from about 950 to about 560 K. The bundle inlet coolant flow rate was increased to about 13 g/s to refill the bundle, and the reactor control rods were manually inserted to terminate the experiment at 60 min and at a bundle power of ∿2 kW. The general thermal response of the SFD 1-1 bundle is illustrated in Figure 5, which shows the inside cladding surface temperature on Rod C2 at the 0.5-m elevation and the bundle power.

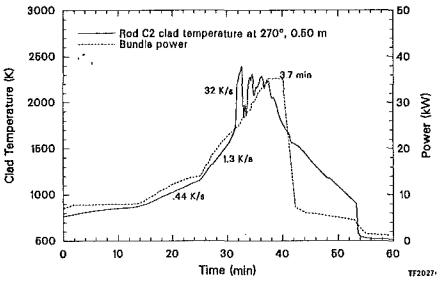

Figure 5. Comparison of Rod C2 cladding temperature at 0.5 m with bundle power.

FUEL ROD THERMAL/MECHANICAL BEHAVIOR DURING HEATUP AND COOLDOWN

Measured cladding temperatures of the fuel rods at the 0.35-m elevation are almost identical and indicate a very rapid increase in temperature to values above the zircaloy melting point at about 33 min. However, rapid temperature rises at the 0.7-m elevation on the centrally located rods began at about 31 min, well ahead of the rapid temperature rises at the 0.35-m elevation and also well ahead of the rapid temperature rise at the 0.7-m elevation on rods located near the bundle periphery. The rapid temperature increase at the 0.5-m elevation on one of the centrally located rods began at about 32 min. Therefore, it appears that the rapid temperature increase in the bundle began near the center at the 0.5- to 0.7-m elevation, and then spread radially outward and axially downward in a manner similar to a flame front propagation.

The total time at high temperature and the exact peak temperatures are unknown, but it is probable that portions of the bundle were at temperatures above 2400 K for more than 10 min.

Cladding ballooning began on all six instrumented fuel rods between 24.6 and 24.8 min at the 0.5- and 0.7-m elevations (indicated by the abrupt changes in the thermocouple traces). Cladding failure was indicated by the pressure switches on three fuel rods at 25.5, 26.2, and 27 min. The time between initiation of ballooning and rod failure (0.7 to 2.4 min) is consistent with expected ballooning times.

LIQUEFIED FUEL AND MOLTEN CLADDING RELOCATION AND HYDROGEN RELEASE

A neutron radiograph of the lower half of the SFD 1-1 test bundle is shown in Figure 6. As indicated in the figure, a large mass of previously molten zircaloy cladding and dissolved UO_2 fuel accumulated in and above the lower spacer grid. (A small amount of dissolved fuel also reached the tie plate at the -0.03-m elevation.) The previously molten material extends about 10 cm above the grid region. Evaluation of the fission chamber data indicates that this material moved to this location over a 3- to 4-min period starting at about 37 min into the transient. The material near the grid region is relatively uniform in composition, although fuel pellet fragments are present near the bundle periphery and at a few locations within the bundle and considerable closed porosity is present. This structure suggests that peak bundle temperatures may have reached values above the UO_2-zircaloy monotectic temperature of 2600 K.

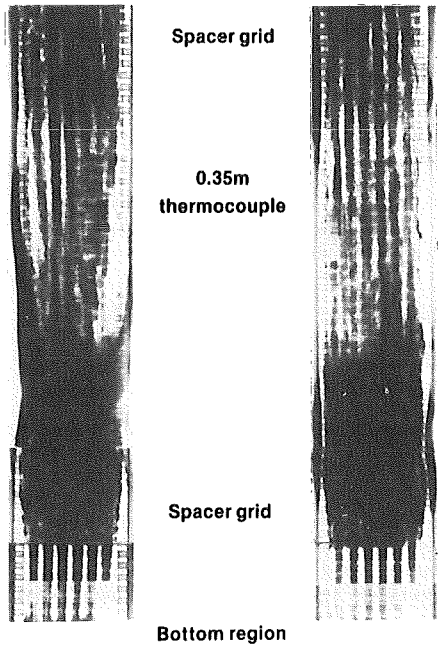

Figure 6. Neutron radiographs of the lower half of the SFD 1-1 bundle.

The fuel bundle elevations between about 0.16 and 0.35 m appear to have lost considerable fuel and cladding material, whereas the upper regions of the test bundle above 0.35 m generally retained their rod-like geometry, although in a highly oxidized state. The collapse of the shroud into the fuel bundle region at 0.12 m (shown in Figure 6) is believed to have been caused by flashing of water that leaked to the inside of the shroud and is not part of the experiment.

An overlay of the percent of light gases in the gaseous effluent from the separator, the integrated hydrogen release in grams, and the pressure in the coolant below the fuel bundle is shown in Figure 7. There is a delay time (about 6 min) between the measured release and the event that caused it. The first small peak and decline in the percent of light gases released was probably caused, not by hydrogen release, but by the helium from the interior of the fuel rods which was released when they failed. The second peak probably resulted from the rapid oxidation of the bundle which occurred between 31 and 39 min and was detected by the hydrogen monitor between 37.5 and 48 min. This peak was accentuated by the pressure spike which occurred at 41.4 min. The pressure spike was caused by liquefied material dropping into the pool of water below the test bundle.

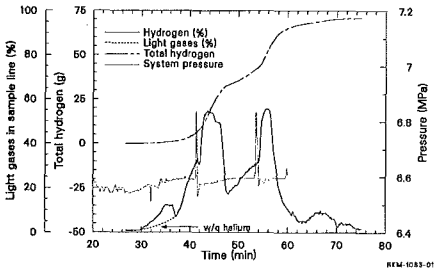

Figure 7. Overlay of percent hydrogen release, integrated hydrogen release, and system (bundle) pressure during Test SFD 1-1.

The decline in the second hydrogen peak was probably caused by a steam starved environment due either to flow blockage at the lower grid elevation or the first pressure spike removing liquid from the test train, or both. The third peak in the hydrogen release was then probably associated with the rein- troduction of steam into the bundle as the constant injection pump added more water to the system (at 0.6 g/s) and flow paths developed along or through the shroud. The third hydrogen spike was accentuated by the pressure spike caused by the introduction of the argon sweep gas. The final small peak and decline at approximately 67 min is believed to have been caused by the reflood of the bundle and resultant flushing out of hydrogen.

The total amount of hydrogen released during the test was found by integrating the mass release rate curve to obtain the total time-dependent hydrogen release shown in Figure 7. The total amount of hydrogen measured was 71 g, which represents oxidation of about one third of the zircaloy in the cladding and liner.

FISSION PRODUCT RELEASE

Figure 8 compares the steam line radiation measurement, which has been delay corrected to bundle time, with the fuel centerline and cladding temperatures on a centrally located fuel rod at the 0.5-m elevation. The initial fuel rod ruptures are indicated in the ion chamber reading by an increase in radiation level at about 24 to 25 min. The increased reading spans a period of approximately 4 min, indicating that the 32 test rods ruptured during this 4-min period.

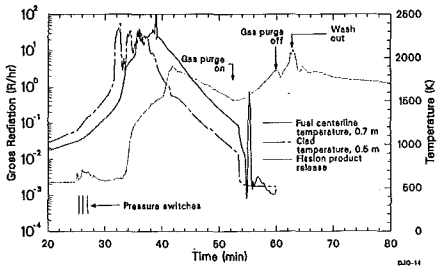

Figure 8. Comparison of delay-corrected radiation in the steam line, fuel centerline temperatures in Rod B4, and the cladding surface temperatures at 0.5 m on Rod C2.

Almost no fission product release was measured by the ion chamber between the time of rod rupture and the time that the fuel centerline temperatures reached approximately 1800 K. The fission product release then increased from 1700 to 2400 K, during the rapid heatup period. The fission product release continued to increase another order of magnitude during the 3.7-min hold at peak power. Much of this increase may be associated with the fuel liquefaction which occurred during the hold at peak power.

The fission product release was still increasing slightly as the bundle power was reduced. Approximately 0.8 min after the power reduction began, the pressure pulse and steam spike occurred at 41.4 min while temperatures in the bundle were probably still above the zircaloy melting temperature. The pressure pulse increased the flow rate in the sample line, reducing the delay time to the fission product monitors. As a result of the pressure pulse, the fission products in the sample line were pushed rapidly past the monitors, thus increasing the radiation reading eightfold in 75 s. Fission product concentrations then peaked about 1 min later.

The fission product release decreased in proportion to fuel temperature during the remainder of the cooldown period following the peak release at 42 min. An argon gas purge of 30 cm^3/s was activated at about 53 min to prevent flow reversal and provide a positive carrier for fission products out of the bundle and into the sample system. The fission product activity in the sample line, just prior to initiation of the argon flow, was rapidly pushed past the steam line detectors and into the separator vessel upon initiation of the argon flow. As a result, the liquid line concentrations increased tenfold, whereas the gas line concentrations increased only slightly.

When the argon purge was terminated at 60 min, the separator dilution flow was also terminated and bundle coolant flow was increased to approximately 13 g/s. The flow in the sample system momentarily stopped, with neither the argon gas nor steam flowing out of the bundle. Reflood liquid slowly filled the bundle and sample line, replacing the argon gas. The measured fission product concentrations again increased when the reflood liquid arrived at the detector locations. The magnitude of the increase in the gas line was moderate (approximately twice), but the fission product concentrations increased 12 times in the steam line, and 28 times at the liquid detector. The largest concentration of fission products measured in the liquid line during the SFD 1-1 test occurred during the reflood period.

Table II lists the isotopes identified in the steam, gas, and liquid lines. A few of the isotopic concentrations histories at the steam line detector station are plotted in Figure 9. Examination of this figure suggests a general conclusion about the observed fission product behavior; gaseous activity evolved predominantly during the high temperature transient phase of the test, whereas liquid activity evolved predominantly during the reflood phase. These results suggest that large fractions of nongaseous fission products are deposited on bundle and sample system surfaces during the high temperature transient and are later dissolved in the reflood liquid and washed through the sample system.

TABLE II. PRELIMINARY IDENTIFICATION OF ISOTOPES MEASURED IN THE SFD 1-1 TEST EFFLUENT

Steam Line
^{41}Ar
^{84}Br, ^{84m}Br
^{85m}Kr, ^{87}Kr, ^{88}Kr, ^{89}Kr, ^{90}Kr
^{88}Rb,[a] ^{89}Rb,[a] ^{90}Rb,[a] ^{90m}Rb[a]
^{91}Sr,[b] ^{92}Sr

TABLE II. (continued)

^{91m}Y,b ^{99}Mo,b ^{99m}Tcb

^{129}Te,b ^{131}Te, ^{131m}Te, ^{132}Te, ^{133}Te, ^{133m}Te, ^{134}Te

^{131}I, ^{132}I, ^{133}I, ^{134}I, ^{135}I

^{133}Xe, ^{135}Xe, ^{135m}Xe, ^{137}Xe, ^{138}Xe, ^{139}Xe

^{138}Cs,a ^{139}Csa

^{139}Ba, ^{140}Ba,b ^{141}Ba

^{140}Lab

Gas Line

^{41}Ar

^{85m}Kr, ^{87}Kr, ^{88}Kr, ^{89}Kr

^{88}Rb,a ^{89}Rba

^{131}I,c ^{132}I,c ^{135}Ic

^{133}Xe, ^{135m}Xe, ^{135}Xe, ^{135m}Xe, ^{137}Xe, ^{138}Xe

^{138}Cs,a ^{139}Csa

^{139}Ba

Liquid Line

^{83}Br, ^{84}Br,b ^{84m}Brb

^{85m}Kr, ^{85}Kr,b ^{87}Kr, ^{88}Kr, ^{89}Kr

^{88}Rb,a ^{89}Rb,a ^{90}Rb,a ^{90m}Rba

^{91}Sr,b ^{92}Srb

^{91m}Y,b ^{95m}Nb,b ^{97}Zr,b ^{99}Mo,b ^{99m}Tcb

^{129}Te,b ^{131}Te,b ^{132}Te, ^{133}Te, ^{134}Te

^{131}I, ^{132}I, ^{133}I, ^{134}I, ^{135}I

^{133}Xe, ^{135}Xe, ^{135m}Xe, ^{137}Xe, ^{138}Xe

^{138}Cs,a ^{139}Cs,a ^{140}Csa

^{139}Ba, ^{140}Ba,b ^{141}Ba

^{140}La

TABLE II. (continued)

a. Isotopes influenced by short-lived percent behavior.

b. Detected only after reactor shutdown.

c. Iodines were detected in the gas stream in isolated spectra taken from 84 to 105 min. Concentrations were nominally <0.1% of the steam line concentrations.

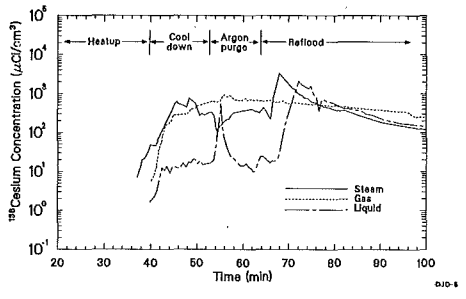

Figure 9. ^{135}Xe, ^{131}I, ^{138}Cs, and ^{132}Te concentrations at the steam line spectrometer during Test SFD 1-1.

The amount of tellurium measured in the sample system was relatively small. A comparison of these results with those of the SFD Scoping Test suggests that the tellurium release is influenced by the amount of zircaloy oxidation in the test bundle, i.e., greater zircaloy oxidization yields greater tellurium release. Additional fission product release information is presented in the paper by D. J. Osetek et al., "Behavior of Fission Products Released from Severely Damaged Fuel During the PBF Severe Fuel Damage Tests," presented at this meeting.

CONCLUSIONS

The SFD 1-1 experiment simulated the fuel heatup and damage and fission product release in the upper regions of a 3000-MW(t) commercial pressurized water reactor during a hypothesized small break loss-of-coolant accident without emergency core coolant injection which continued to peak cladding temperatures of about 2400 K. The heating rate for the SFD 1-1 test was specified to be relatively slow up to about 1600 K and rapid after 1600 K, driven by runaway metal-water reaction in a steam starved environment.

The runaway oxidation and rapid temperature increase began near the center of the bundle at the 0.5- to 0.7-m elevation and then spread radially outward and axially downward in a manner similar to a flame front propagation. It is probable that portions at the bundle were at temperatures of about 2400 to 2600 K for more than 10 min. The hydrogen release measurements indicate that the oxidation of the bundle was steam limited during the two separate peaks in measured release rate. A total of 71 g of hydrogen was measured, which corresponds to oxidation of about one third of the bundle fuel rod cladding and shroud inner liner.

A large mass of previously molten zircaloy cladding and dissolved UO_2 fuel accumulated in and above the lower spacer grid. This material appears to have come mainly from the 0.16- to 0.35-m elevations of the bundle. The upper regions of the test bundle appear to have retained their rod-like geometry.

Fission product release was first measured when the fuel rod cladding ruptured, but little fission product release was measured between the time of cladding rupture and the time that fuel temperatures reached about 1800 K. The fission product release was proportional to fuel temperature between 1800 and 2400 K, and was then influenced by fuel liquefaction during the constant power hold. The principal release of the gaseous fission product isotopes occurred during the high temperature transient, but the major release of fission products other than the noble gases occurred during the reflood and washout period. Evidently, large quantities of the volatile fission products were deposited on test train and sample system surfaces during the transient and were subsequently dissolved in the reflood liquid and transported through the sample system.

The information from this and subsequent severe fuel damage tests will be used to assess state-of-the-art computer models and analysis techniques, improve the understanding of fission product source terms from severe reactor accidents, and, ultimately, support improved risk assessments and emergency planning.

FOOTNOTE

1. Sponsors of the program include Belgium, Canada, Federal Republic of Germany, Italy, Japan, Netherlands, United Kingdom, and United States Nuclear Regulatory Commission.

NOTICE

Work supported by the U.S. Nuclear Regulatory Commission, Office of Nuclear Regulatory Research, under DOE Contract No. DE-AC07-76ID01570.

SCDAP CODE ANALYSIS OF THE POWER BURST FACILITY SEVERE FUEL DAMAGE TEST 1-1

L. J. Siefken

EG&G Idaho, Inc.
Idaho Falls, ID 83415, U.S.A

ABSTRACT

The SCDAP code models the processes taking place in a reactor fuel bundle during a severe reactor accident. This paper assesses the models in the code using the results of the PBF test SFD 1-1. Calculated and measured test bundle temperatures, hydrogen production, meltdown, and fission gas release are compared and found to be in good agreement. Calculations indicate that oxidation in the bundle proceeds at a rate proportional to the steam flow rate from coolant boil-off. The oxidation is confined to a moving axial region about 10 cm in height. Runaway oxidation is terminated by the flowing away of liquefied cladding. Most of the fission product release from the bundle fuel is calculated to be due to fuel dissolution.

INTRODUCTION

SCDAP (Severe Core Damage Analysis Package) [1] is a computer code designed to characterize and quantify the fuel damage processes in a reactor core during severe reactor accidents. The code calculates the reactor core temperature response, hydrogen production, meltdown and fission gas release. This paper presents the SCDAP code analysis of the response of the test fuel bundle in the Power Burst Facility (PBF) test Severe Fuel Damage (SFD) 1-1 [2]. This test measured the response of a fuel bundle subjected to conditions typical of that in a reactor core during a small break loss of coolant accident.

This paper is divided into four sections. In the first section, the PBF SFD Test 1-1 is described. The second section contains a description of the models in the version of SCDAP used to perform the calculations. In the third section calculations and experimental results are compared and analyzed. This section includes comparisons of calculated and measured bundle temperature, hydrogen production, extent of meltdown and fission gas release. The conclusions are given in the last section.

DESCRIPTION OF SFD TEST 1-1

The PBF SFD test 1-1 was designed to investigate fission product release, and fuel rod oxidation and damage that might occur in a pressurized water reactor (PWR) during a hypothesized small break loss-of-coolant accident without emergency core coolant injection. Specifically, the test conditions were designed to be typical of those in the top half of a fuel bundle during the Three Mile Island-2 reactor accident. The experiment subjected a bundle of thirty-two fuel rods to coolant boil-off in excess of bundle inlet flow, resulting in fuel rod uncovery, oxidation, and heatup to 2400 K. The test bundle consisted of a 6 x 6 array of fuel rods with the corner rods removed. Except for a length of 0.9144 m, the fuel rods were typical of fresh 17 x 17 PWR fuel rods. The test bundle was surrounded by an insulated shroud, with a wall thickness of 2 cm, made of ZrO_2 and Zr.

The fuel bundle was highly instrumented to measure temperature response, hydrogen production, and fission product release. The temperature response was measured by two fuel rod centerline thermocouples and eighteen subsurface cladding thermocouples. The thermocouple leads ran upward from the bottom of the fuel rods. The bundle hydrogen production and fission product release was measured using a system consisting of a steam sample line, condenser, gas-liquid separator, hydrogen monitor, six steam sample bombs, six liquid sample bombs, particulate filter, gamma spectrometers, and a collection tank.

The fuel bundle nuclear heat generation was controlled to compensate for heat loss through the flow shroud. The heat generation was 6.6 kW (0.225 kW/m per rod) during the coolant boil-off phase of the test. As the fuel bundle temperature increased, and heat loss through the shroud increased, the nuclear heat generation was pushed to a maximum value of 35 kW, and remained constant at 35 kW for 230 s. The nuclear heat generation was then rapidly decreased to initiate cooldown of the bundle.

The bundle coolant pressure and inlet flow rate remained constant during the test. The coolant pressure was 6.9 MPa and the inlet flow rate was 0.67 g/s. The inlet coolant was slightly subcooled.

DESCRIPTION OF THE SCDAP CODE

The SCDAP code is being developed at the Idaho National Engineering Laboratory under the sponsorship of the U.S. Nuclear Regulatory Commission, Office of Nuclear Regulatory Research. The code's mission is to calculate the thermal, mechanical, and chemical behavior of a light water reactor fuel bundle during a severe accident transient. The code has models for all of the relevant phenomena occurring in a fuel bundle during a severe accident. The outputs of the code include: bundle temperature distribution, hydrogen production, fuel and cladding movement, and fission gas release.

The analysis presented here was performed using a developmental version of SCDAP/MOD1/V0 [3]. A short description of the models in SCDAP/MOD1/V0 is given in Table I. The developmental version differed from SCDAP/MOD1/V0 in three respects. First, a factor of five multiplier was applied to the model calculating the amount of fuel dissolved by liquefied cladding. Second, the dissolution rate equation was eliminated and instant dissolution to the saturation state was assumed to occur. Third, the assumed temperature at which cladding oxide is immediately dissolved by liquefied zircaloy was changed from 2650 K to 2400 K. These changes to the code were made based upon the results of a study of severe fuel damage experiments by Allison, Hagrman, and Berna [7].

In the Allison, Hagrman and Berna study, the amount of fuel dissolution which occurred in severe fuel damage experiments was compared with the amount of dissolution calculated by the SCDAP model. The comparison showed that the SCDAP model may be underpredicting the amount of fuel dissolution by nearly an order of magnitude. This discrepancy between the SCDAP model and experimental results is considered to be due to the following two reasons. First, the SCDAP model is based upon measurements of the amount of fuel dissolved by cladding that is saturated with oxygen (29% atomic) prior to contact with fuel. In the rapid heatup occurring in severe fuel damage experiments, however, the cladding may liquefy without being saturated with oxygen. Second, the SCDAP model does not consider the possibility of unsaturated liquified cladding diffusing along grain boundaries and creating a nonequilibrium slurry mixture of fuel and cladding.

TABLE I. DESCRIPTION OF SCDAP MODELS

Phenomenon	Description of SCDAP Model of Phenomenon
Coolant boil-off	1-D quasi-steady drift flux model to calculate coolant swelling due to steam generation; quasi-steady heat transfer from fuel rods to coolant.
Heat and mass transport by coolant in uncovered region of core	1-D quasi-steady model which assumes coolant is a mixture of steam and hydrogen; heat transfer by convection and radiation between fuel rods and coolant mixture; axially varying geometry with consideration of cladding ballooning and fuel rod meltdown.
Fission product release from fuel	PARAGRASS model, which is empirical model derived from mechanistically based GRASS model. Noncondensible gases and volatile gases are treated separately [4].
Cladding oxidation	Cathcart-Pawel (temperature less than 1850 K) and Urbanic parabolic rate equations. Model takes into account oxidation limitation due to oxygen starvation and hydrogen blanketing.
Dissolution of UO_2 by liquefied zircaloy	Transient dissolution modeled by Turk's equation [5] and saturation dissolution is modeled by MATPRO [6].
Dissolution of ZrO_2 by liquefied zircaloy and uranium	If temperature is below 2650 K, no dissolution occurs. If temperature is greater than 2650 K, complete dissolution instantly occurs.
Breach in cladding ZrO2 shell containing liquefied Zr-U-O mixture	Calculation of stress in ZrO2 shell. If stress exceeds MATPRO rupture stress breach occurs.
Relocation of liquefied Zr-U-O mixture flowing through breach in ZrO2 shell and downward along outside of fuel rod	Motion of Zr-U-O mixture is calculated taking into account gravity and friction forces. Cooling and solidification of Zr-U-O mixture is calculated taking into account heat conduction from mixture into fuel rod.

TABLE I. (continued)

Phenomenon	Description of SCDAP Model of Phenomenon
Heat conduction in fuel rods and control rods	Stacked one-dimensional (radial) heat conduction is modeled using finite element method. Maximum of six nodes in fuel and cladding.
Heat transfer at surface of fuel rods and control rods	Heat transfer by convection and radiation between fuel rods and coolant mixture is modeled. In addition heat transfer by radiation between fuel rods and control rods is modeled.

COMPARISON OF CALCULATED AND MEASURED RESPONSE

The description of the fuel bundle response and the comparison of calculations and measurements is divided into the following four areas: temperature response, oxidation and hydrogen production, meltdown of fuel and cladding, and fission product release.

Temperature Response

The calculated and measured temperature response of a center fuel rod in the test bundle at an elevation of 0.35 m are compared in Figure 1. The elevation of 0.35 m is near the axial peak of the nuclear heat generation. The calculation and measurement are seen to be in good agreement. Both the calculation and measurement show a temperature increase of approximately 1 K/s until spontaneous runaway oxidation occurs at 1900 s. After spontaneous runaway oxidation occurs, both the calculation and measurement show a temperature increase of 10 K/s. This rate of temperature increase is similar to that observed by Hagen [8,9]. The calculation shows runaway oxidation beginning at a temperature of 1800 K, while the measurement indicates runaway oxidation beginning at a temperature of 1700 K. The calculated and measured maximum temperatures are 2420 and 2400 K, respectively. In the SCDAP calculation, runaway oxidation and rapid temperature increase are terminated by the flowing away of liquefied cladding. This result is consistent with behavior observed in the Hagen experiments.

The calculated and measured response at an elevation of 0.7 m are compared in Figure 2. The calculation and measurement are in reasonable agreement until 1800 s. Both show the cladding temperature increasing at a rate of 0.5 K/s. However, the measured cladding temperature abruptly increases at 1800s due to relocation of the thermocouple junction. The thermocouple leads are routed up the fuel rods from the bottom and pass through the hot region. Evidence of junction relocation is given by the similar response of this thermocouple, with thermocouples in the lower part of the bundle after 1800 s. The calculated temperature reaches a maximum value of 1870 K. Because of steam starvation, runaway oxidation was not calculated. The calculated temperature begins to decrease in response to the rapid decrease in nuclear heat generation at 2400 s.

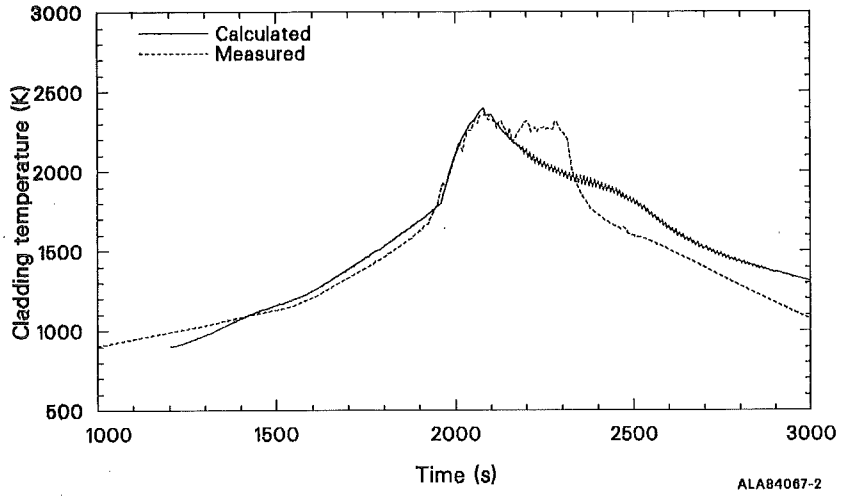

Figure 1. Comparison of calculated and measured temperatures at an elevation of 0.35 m.

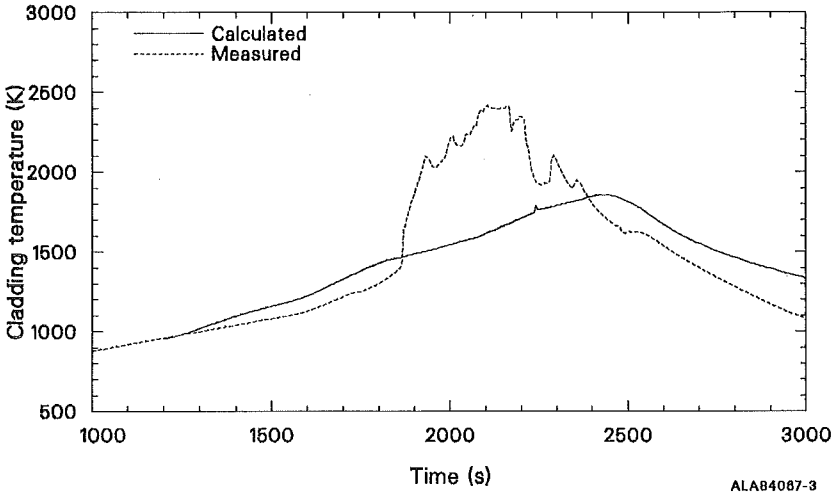

Figure 2. Comparison of calculated and measured temperatures at an elevation of 0.70 m.

Oxidation and Hydrogen Production

The calculated and measured cumulative bundle hydrogen production were in fair agreement, as seen in Figure 3. The measurement shown was time shifted by 6 min in an attempt to account for the inherent time delay in the hydrogen sensing system. The hydrogen production is calculated to be almost constant at

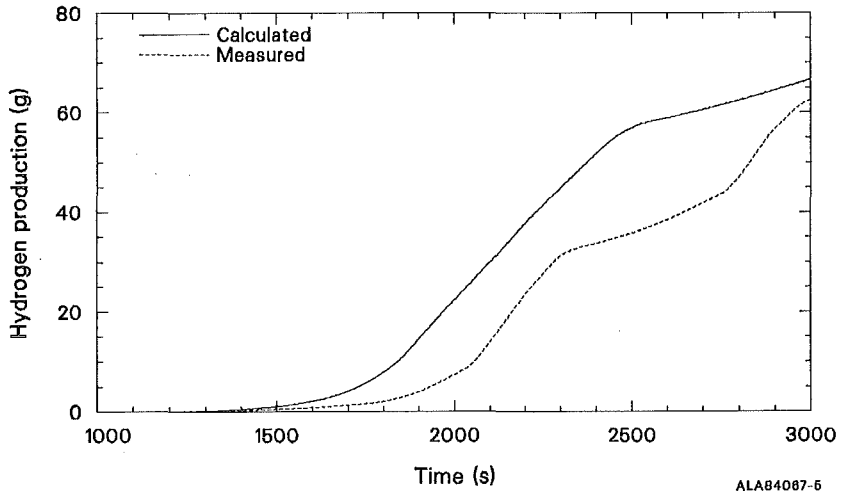

Figure 3. Comparison of calculated and measured bundle hydrogen production.

a rate of 0.074 g/s from 2100 to 2400 s. This constant rate of production is consistent with almost complete consumption of the steam entering the bundle at a rate of 0.67 g/s. After 2400 s, the calculated rate of hydrogen production rapidly decreases in response to bundle cooldown initiated by the rapid decrease in nuclear heat generation. The final calculated and measured hydrogen production were 66 g and 71 g, respectively. According to the calculation, 36% of the bundle cladding was oxidized. Oxidation of the Zr layer on the shroud inner surface accounted for 23% of the hydrogen produced.

The calculated and measured hydrogen production differ in two respects. First, the calculated hydrogen production precedes the measured hydrogen production by about 200 s. Second, the measurement shows two periods of rapid hydrogen production separated by a 450 s period of time with diminished hydrogen production. In the calculation, only one period of rapid hydrogen production occurs.

The discrepancy between calculated and measured hydrogen production is probably due to an experimental event not modeled by SCDAP. This experimental event was the rapid production of steam by liquefied fuel and cladding flowing downward into liquid water at the bottom of the bundle and quenching. The quenching of this liquefied material created enough steam flow to cool the bundle cladding below the temperature at which runaway oxidation occurs. As a result, the rate of hydrogen production was diminished for a period of time. SCDAP models the downward flow of liquefied fuel and cladding, but not the steam produced by quenching of this liquefied material. Some discrepancy between calculated and measured hydrogen production is also due to assuming a constant time delay of six minutes in sensing hydrogen. In reality, the time delay was calculated to vary from two to eight minutes, with the average value being six minutes.

During the period of intense oxidation in the calculation, the oxidation was confined to a region of about 10 cm in height. This region propagated downward, opposite to the direction of the steam flow. The propagation is illustrated in Figure 4, where the oxidation heat generation per unit length

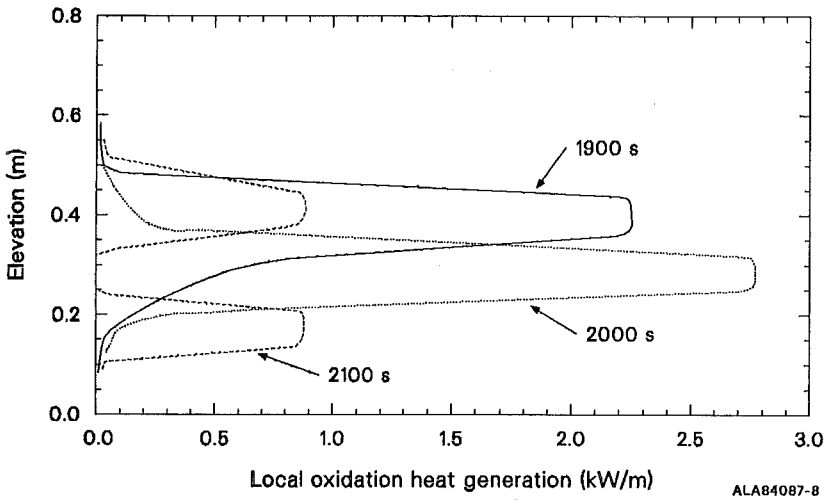

Figure 4. Calculated axial variation in fuel rod oxidation.

for a center bundle rod is plotted as a function of elevation at three different times. Initially, the oxidation was centered in the 0.35 to 0.45 m elevation span, where the nuclear heat generation was highest. As the region below the 0.35 m elevation continued to increase in temperature and rate of oxidation, the region above began to be starved of oxygen. This starvation suppressed the oxidation in the 0.35 to 0.45 m elevation span. At 2050 s, the cladding in the 0.25 to 0.35 m elevation span was calculated to flow away and oxidation resumed in the 0.35 to 0.45 m elevation span. After 2300 s, the oxidation in the 0.15 to 0.25 m elevation span was so intense that oxidation in the 0.35 to 0.45 m elevation span was again almost completely suppressed because of oxygen starvation.

Meltdown of Fuel and Cladding

The calculation indicates that in the hottest part of the bundle 40% of the fuel was dissolved and liquefied by liquefied cladding. A total of 6% of the bundle fuel was calculated to flow downward. Most of the flowing fuel and cladding solidified in the bottom 10 cm of the fuel bundle. These calculated results are in approximate agreement with the posttest gamma scan of the fuel bundle, which indicates that about 3% of the bundle fuel flowed downward and that most of the relocated fuel solidified at an elevation of 0.1 m [10].

Fission Product Release

The calculated and measured bundle noncondensible fission product releases (Xe and Kr) were 15 and 10-20%, respectively. The calculated release history is shown in Figure 5. The steps in the release history occur at the times that fuel was calculated to dissolve. If the factor of five multiplier had not been applied to the fuel dissolution model as discussed in the section on the SCDAP description, the calculated amount of fission product release would be considerably smaller.

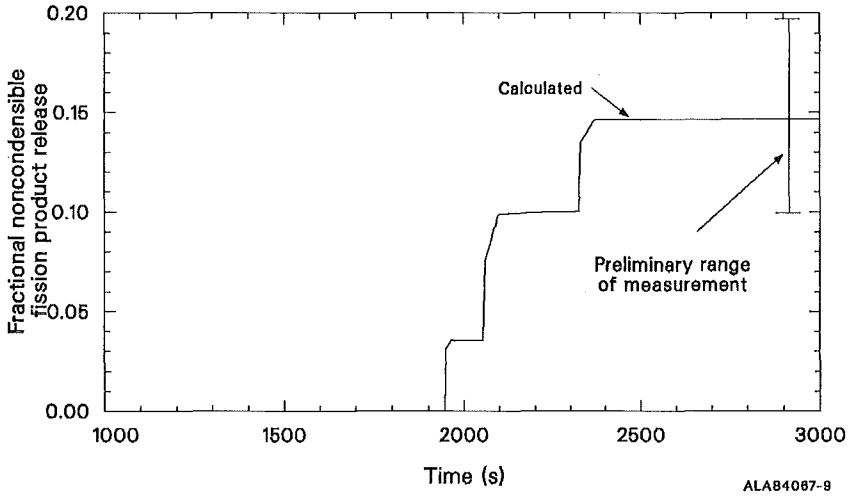

Figure 5. Calculated and measured release of bundle noncondensible fission products.

CONCLUSIONS

The comparison of the SCDAP/MOD1/V0 calculations with the results of the PBF SFD test 1-1 have shown that the code accurately calculates bundle heatup and oxidation. Both calculation and test result show that spontaneous runaway oxidation occurs after the bundle temperature exceeds 1800 K. During this period of intense oxidation, the oxidation proceeds at a rate proportional to the steam flow rate resulting from coolant boil-off. The oxidation is confined to a region about 10 cm in height and propagates in the axial direction. The runaway oxidation is terminated by the flowing away of liquefied cladding.

The comparison of calculations and experimental results also indicates that the SCDAP code is calculating the bundle meltdown and fission product release with reasonable accuracy. If a fuel bundle experiences temperatures in excess of 2400 K, the calculations and experimental results show that about 3 to 6% of the fuel in a bundle may liquefy and flow downward. For the SFD Test 1-1, the calculated and measured noncondensible fission product releases were both about 15%. The calculations show that most of the fission product release occurs due to fuel dissolution.

The comparison of calculations and experimental results suggests at least two improvements are needed in the SCDAP code. The first is the addition of a model to calculate the steam produced by liquefied material flowing into liquid water at the bottom of a bundle and quenching. The second is enhancement of the model that calculates the amount of fuel which is dissolved and liquefied by liquefied cladding. This model strongly affects both the amount of fuel which flows downward and the amount of fission product release. The model needs to be upgraded so that both of these variables are simultaneously brought into agreement with experimental results.

REFERENCES

1. C. M. Allison, E. R. Carlson, and R. H. Smith, "SCDAP: A Computer Code for Analyzing Light Water Reactor Severe Core Damage," Vol. 1, Proceedings of International Meeting on Light Water Reactor Severe Accident Evaluation, August 28 to September 7, 1983, Cambridge, Massachusetts.

2. P. E. MacDonald, C. L. Nalezny and R. K. McCardell, "Severe Fuel Damage Test 1-1 Results," Fifth International Meeting on Thermal Nuclear Reactor Safety, September 9-13, 1984, Karlsruhe, Federal Republic of Germany.

3. G. A Berna, C. M. Allison and L. J. Siefken, SCDAP/MOD1/VO: A Computer Code for the Analysis of LWR Vessel Behavior during Severe Accident Transients, 1S-SAAM-84-002, Rev. 1, FIN No. A6360, July 1982.

4. J. Rest et al, PARAGRASS: A Quick-Running Comprehensive Steady State and Transient Fission-Product Release and Swelling Model for Water-Reactor Fuel, ANL Draft Report, April 1982.

5. W. Turk, Design and Verification of Modular Computer Models for Interpreting Rod Melting Experiments, IKE-4-94, February 1980.

6. D. L. Hagrman et al, MATPRO-Version 11 (Revision 2): A Handbook of Materials Properties for Use in the Analysis of Light Water Reactor Fuel Rod Behavior, NUREG/CR-0497, TREE-1280, Rev. 2, August 1981.

7. C. M. Allison, D. L. Hagrman and G. A. Berna, "The Influence of Zircaloy Oxidation and Melting Behavior on Core Behavior During a Severe Accident," Fifth International Meeting on Thermal Nuclear Reactor Safety, September 9-13, 1984, Karlsruhe, Federal Republic of Germany.

8. S. Hagen et al, Temperature Escalation in PWR Fuel Rod Simulator Bundles due to the Zircaloy/Steam Reaction, Test ESBU-1 Test Results Report, KfK 3508, December 1983.

9. S. Hagen and S. O. Peck, Temperature Escalation of Zircaloy-Clad Fuel Rods and Bundles under Severe Fuel Damage Conditions, KfK 3656, August 1983.

10. Leo Sepold, personal communication, Idaho National Engineering Laboratory, August 30, 1984.

NOTICE

Work supported by the U.S. Nuclear Commission, Office of Nuclear Regulatory Research under DOE Contract No. DE-AC07-76ID01570.

THE INFLUENCE OF ZIRCALOY OXIDATION AND MELTING BEHAVIOR ON CORE BEHAVIOR DURING A SEVERE ACCIDENT

C. M. Allison, D. L. Hagrman, and G. A. Berna

EG&G Idaho
Idaho Falls, Idaho 83415, U.S.A.

ABSTRACT

The influence of zircaloy oxidation and melting on core temperatures, hydrogen generation, and fission product release is examined. The uncertainties in phenomena important to the modeling of zircaloy oxidation and melting processes including zircaloy oxidation kinetics, hydrogen blanketing, UO_2-zircaloy interactions, and ZrO_2 failure are estimated. These uncertainties are then applied to a sensitivity study of a boiloff-initiated severe accident similar to that which may have occurred in TMI-2. The results indicate that the major uncertainties are in the oxidation kinetics which can contribute a factor of ten to the uncertainties in fission product release and can affect the timing of that release.

INTRODUCTION

The influence of zircaloy oxidation and melting on core behavior during severe accidents was evident from the examination of the TMI-2 core subsequent to the accident in 1979. Core visual and ultrasonic examinations [1], core samples [2], and analyses [3-6] indicate that the core had regions of highly oxidized and fragmented debris and regions of prior molten zircaloy and dissolved UO_2. This damage was a direct consequence of the rapid heatup and embrittlement of core materials due to the exothermic oxidation of zircaloy and other structural material.

This paper investigates and quantifies the influence of the uncertainties in oxidation and melting phenomena (oxidation kinetics, hydrogen blanketing, UO_2 dissolution, and ZrO_2 failure) on the uncertainties in core behavior (core temperatures, hydrogen production, and fission product release). A review of representative experiments leads to a qualitative understanding of important phenomena. Uncertainties in these phenomena are then estimated and used in a sensitivity study to obtain uncertainties in core behavior for a boiloff-initiated severe accident much like that which may have occurred in TMI-2.

REVIEW OF REPRESENTATIVE EXPERIMENTS

A review of current experimental data from the Kernforschungszentrum Karlsruhe, West Germany and from the Idaho National Engineering Laboratory, USA, shows (much like the TMI-2 core) that zircaloy oxidation and melting can have a significant influence on fuel behavior during severe accidents. The ESSI series of tests [7], the ESBU-1[8] bundle test, and the Power Burst Facility Test, SFD-ST [9], were examined. A range of behavior was observed from no liquefaction of UO_2 and zircaloy, to significant zircaloy melting and relocation. The latter was accompanied by dissolution of UO_2, breach of the enclosing ZrO_2 shell, and subsequent flow of the molten mixture.

In all of these tests, the type of damage (the dissolution of the UO_2, the failure of the ZrO_2 shell, and the flow of liquefied Zr-U-O as summarized on Table I) was strongly dependent on the degree of zircaloy oxidation as shown in Figure 1.[1] For example, the zircaloy cladding in ESSI-4 and the 0.7 m elevation of SFD-ST were either completely oxidized by the time zircaloy melting temperatures were reached, or nearly so. This resulted in minimal relocation of liquefied Zr-U-O. At the other extreme, ESSI-1, ESSI-7, and the center rod for ESBU-1 were only slightly oxidized at the time zircaloy melting temperatures were reached, resulting in failure of the thin ZrO_2 shells and extensive relocation of liquefied Zr-U-O.

To further characterize the zircaloy oxidation and melting behavior that might be expected in an accident where initial heatup is controlled by core power and uncovery rate, it is necessary to understand the phenomena which control such behavior. Those phenomena include zircaloy oxidation kinetics, hydrogen blanketing and steam starvation, UO_2-Zr interactions, and ZrO_2 failure. These are discussed along with their uncertainties in the following section.

ZIRCALOY OXIDATION AND MELTING PHENOMENA

Zircaloy oxidation is highly exothermic in steam and there are extensive reviews and experiments which deal with the kinetics in steam [10-16]. The reviews conclude that the oxide layer is protective, i.e. remaining in place without spalling or cracking, over a limited range of oxide thickness at low temperatures ($\leq$ 1000 K) [13,14] and throughout oxidation of cladding at temperatures above 1250 K. The oxide remains protective at the higher temperatures because both zircaloy and the sub-stoichiometric oxide are ductile and can deform to accommodate volume changes during oxidation.

Oxidation of a material with a protective oxide is limited by oxygen diffusion across the oxide, or by the rate of steam supply to the outer oxide surface. When sufficient steam is available, the rate of oxygen up-take by an oxidizing semi-infinite surface is proportional to the reciprocal of the oxide layer thickness. A kinetics equation, shown below, can be derived from Fick's law assuming the oxygen concentration at the inner and outer oxide surface remains constant [17]:

$$\frac{dx}{dt} = \frac{1}{x} A \exp\left(-\frac{B}{T}\right) \quad , \tag{1}$$

where x is the oxide layer thickness (m) or weight gain per unit surface area of oxidizing metal (kg/m^2), T is the oxide layer temperature (K), t is time (s), and A and B are constants.

A number of authors have provided data or correlations for the constants A and B of Equation (1) [15,17-25]. Figure 2 shows the parabolic rate constant,

$$K_p = A \exp\left(-\frac{B}{T}\right) \quad , \tag{2}$$

as a function of reciprocal temperature from these sources. The agreement at temperatures less than 1850 K is quite good, except for the extrapolated Baker-Just data to low temperature. At temperatures above 1850 K (where a phase transition of pure zircaloy oxide changes the crystal structure from tetragonal to body centered cubic and alters the diffusion of oxygen through

TABLE I. CHARACTERIZATION OF THE DAMAGE FOR THE INTEGRAL TESTS

Test Designation	Damage		
	ZrO_2 Failure	UO_2 Dissolution	Zr-U-O Flow
ESSI-1	Entire surface was disrupted, portions swept away by melt.	~10% of pellet diameter dissolved over central elevations.	Molten material flowed down in nonwetting rivulets, flow inside and outside ZrO_2 shell.
ESSI-4	No failure, complete oxidation of cladding.	None	None
ESSI-5	Limited failure.	Limited amount.	Molten material contained in ZrO_2 shell, flowed internally.
ESSI-6	Upper portions swept away by melt.	Amount not quantified but significantly less than ESSI-7.	Molten material from upper elevations flowed down in nonwetting rivulets on ZrO_2 exterior. In lower elevations melt was contained by ZrO_2.
ESSI-7	Same as ESSI-1	> 34% of pellet diameter (complete dissolution of annular pellet surrounding heater element).	Combination of wetting and nonwetting rivulets inside and outside ZrO_2
ESBU-1	Same as ESSI-1	26-30% of pellet diameter dissolved over central for all nine rod elevations.	Nonwetting rivulets; extensive flow channel blockage in lower elevations.
SFD-ST	Lower elevations swept away by melt; upper elevations completely oxidized	Amount not quantified.	Nonwetting rivulets; extensive flow channel blockages in lower elevations.

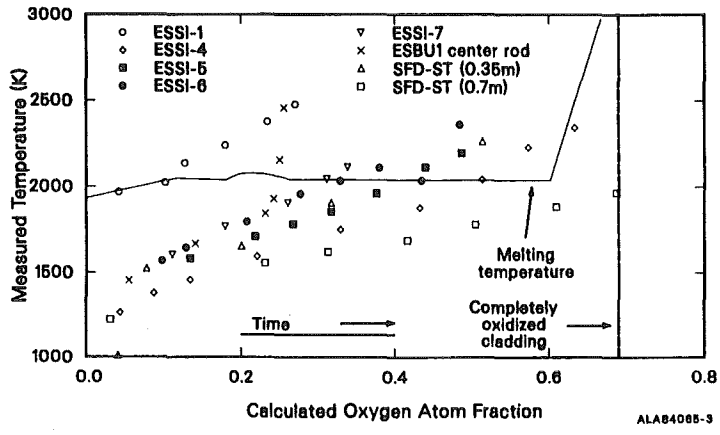

Figure 1. Calculated oxygen uptake versus measured temperature for representative integral experiments.

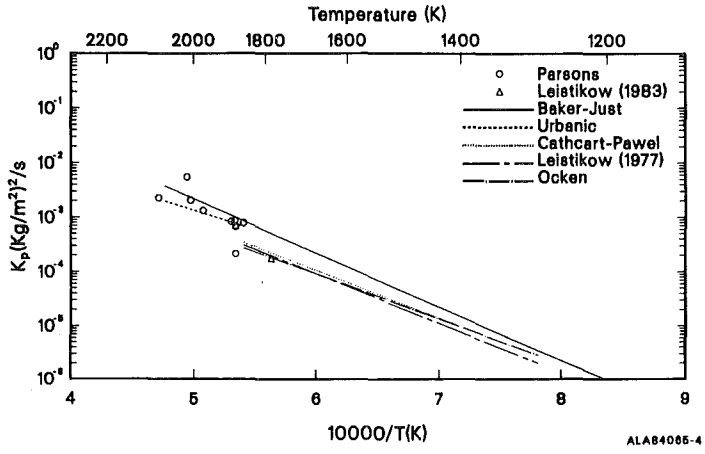

Figure 2. Parabolic rate constants for zircaloy oxygen weight gain versus inverse temperature.

the oxide to the metal) the data are also within a fairly narrow band. However, the band is shifted to the higher rates as one would expect for the relatively open body centered cubic oxide structure.

A fact that adds uncertainty is that Equation (1) is derived by assuming constant oxygen concentration on both oxide surfaces. Therefore, Equation (1) may not be appropriate for several conditions:

a. Cladding of finite thickness that is so heavily oxidized that a core of unoxidized metal no longer exists in the center. In this case, the oxygen concentration in metal near the inside oxide surface is no

longer constant. This may explain why there was no melting during ESSI-4; the actual oxidation would exceed the parabolic rate as the inner surface concentration increased.

b. Oxidation of liquid zircaloy. In this case, the oxygen concentration in metal near the inside surface is altered by rapid diffusion in liquid zircaloy. As discussed by Olander, [26] the ZrO_2 may actually thin as the zircaloy melts and the oxygen flux from the ZrO_2 inner surface increases rapidly.

c. Environments with high concentrations of gases other than steam. In this case, the oxygen concentration at the outside surface is no longer constant, and there may be an alteration of the outside surface by chemical reaction with other gases.

Inspection of Figure 2 and consideration of the additional uncertainties identified above, suggest an uncertainty estimate corresponding to a variation of nearly ±50 K in the 1400 to 1850 K range, and at least ±100 K for temperatures above 1850 K.

The effect of the steam environment often dominates during rapid heatup at high temperatures. In many severe accidents, including TMI-2, the steam generation rates are relatively low. This leads to hydrogen blanketing or steam starvation of the zircaloy surface and, in turn, limits the rate of oxidation. The data of Chung [27] suggest that the oxidation rates drop rapidly to the steam starvation limit as the partial pressure of hydrogen exceeds 0.5 of the total pressure. The uncertainty in the limit of 0.5 is considered relatively large, since the data were taken at low pressures and may vary from 0.5 to 1.0.

The effect of the interaction between UO_2 and zircaloy on melting and flow behavior was shown to be important by both the in-pile and out-of-pile tests discussed earlier. Separate effects experiments [28-34] were conducted as early as 1966 and are still being performed to reduce the uncertainty in UO_2 dissolution behavior. Analytical models [35,36] have also been developed to calculate this behavior. The uncertainties in UO_2-zircaloy interactions, however, are not yet clearly quantified for nonequilibrium conditions. For temperatures less than 2100 K, the uncertainties in the rate of layer growth in the UO_2 and zircaloy are expected to be less than those estimated for oxidation kinetics, since the temperature of the samples is more easily controlled. For temperatures greater than 2100 K, the uncertainties are much larger, due to the attack of UO_2 along grain boundaries and the resulting likelihood that strong influences of fuel morphology and cladding geometry may exist. Limited evaluation of the integral experiments described previously indicate that the amount of UO_2 interacting with molten zircaloy may be underpredicted by nearly an order of magnitude. For ESSI-1, ESSI-7, and the center rod for ESBU-1, where the amounts of UO_2 dissolved and ZrO_2 failure temperatures could be estimated, the mole fraction of UO_2 dissolved in the mixture of liquefied Zr-U-O was estimated to be 6 to 7 times that predicted from the pseudo-binary Zr(O)-UO_2 phase diagram [31]. Using a failure temperature of 2110 K and calculated mass of unoxidized zircaloy from the oxygen uptake analysis shown in Figure 1, the ratio of the estimated mole fraction to the pseudo-binary calculated mole fraction was found to be 6.02 for ESSI-7. For ESSI-1 and ESBU-1, the ratios were 6.09 and 6.86 for ZrO_2 failure temperatures of 2530 and 2480 K, respectively.

Another important phenomenon which affects zircaloy behavior during a severe accident is the failure of the ZrO_2. Available measurements of the failure stress of ZrO_2 show a rapid decrease from 80 to 10 MPa in the

temperature range 1500 to 1800 K. This loss of strength and the probable attack by any contained metallic zircaloy on the ZrO_2, limit the ability of an external oxide layer to contain liquid metallic zircaloy for long periods of time. Unfortunately, little detailed information is known about the relative importance of oxide stress failures and the formation of pin-holes through oxide layers due to chemical attack. The best evidence for the time of failure of oxide film comes from the observation as shown in Figure 1 that standing fuel rods do not appear to heat themselves above approximately 2530 K before the liquid zircaloy breaks free of the oxide and flows to cooler regions. A lower limit for oxide failure due to liquid metal is provided by the melting temperature of oxygen saturated zircaloy, approximately 2250 K. This leads to an uncertainty estimate of twelve percent.

INFLUENCE OF UNCERTAINTIES IN OXIDATION AND MELTING PHENOMENA

In order to quantify the relative importance of the uncertainties associated with the phenomena discussed above, the SCDAP [37] code (SCDAP/MOD1-Version 13) was used to perform a sensitivity analysis. The models which represent these phenomena were varied within the previously estimated uncertainty limits, and the effect of these uncertainties on predicted temperatures, fission product release, and hydrogen generation was noted. The base case was a simple boiloff scenario much like the TMI-2 accident. The core uncovery rate and decay power used are shown in the inset of Figure 3. The fuel rod used had the dimensions and fission product inventory of a centrally located rod in the TMI-2 core. The oxidation kinetics used were Urbanic [24] for temperatures greater than 1850 K and Cathcart-Pawel [18, 19] for temperatures less than or equal to 1850 K. A reduction in oxidation due to hydrogen blanketing based on the data of Chung [27] was modeled. The UO_2 dissolution was based on the kinetics equation of Turk [35] with equilibrium limits from the pseudo-binary $Zr(O)$-UO_2 phase diagram [31]. ZrO_2 failure is based on a stress failure limit for temperatures less than or equal to 2650 K. The ZrO_2 is assumed to be dissolved by molten zircaloy above 2650 K. Table II presents the sensitivity cases.

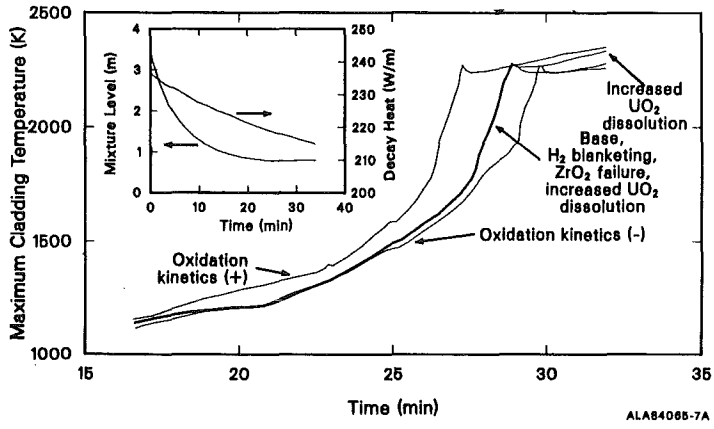

Figure 3. Maximum cladding temperature versus time for the TMI-2 base case and five sensitivity cases.

TABLE II. SENSITIVITY STUDY CASES

Case	Effect	Description of the Effect Varied
1,2	Oxidation kinetics (1: + limit) (2: - limit)	The temperature used in the parabolic rate equation is varied ±50 K for cladding temperatures (T) $\leq$ 1850 K and ± 100 K for T > 1850 K.
3	Hydrogen blanketing	Hydrogen blanketing effects are ignored; oxidation is limited only by steam starvation.
4	UO_2 dissolution	UO_2 dissolution is set to 6 times the UO_2 solubility limit from the pseudo-binary $Zr(O)$-UO_2 phase diagram. The rate of dissolution is assumed infinite.
5	Z_rO_2 failure	The Z_rO_2 is forced to fail at 2250 K.

The results are shown in Figures 3 and 4. Figure 3 shows the maximum cladding temperature for the base case and the five sensitivity studies. In all cases, the peak temperature is little altered because it is limited by a stress-induced failure of the ZrO_2 shell at a temperature $\sim$2250 K. The resulting variation in total hydrogen production and release of CsOH and CsI into the coolant channel are shown on Figure 4. The positive variation of the oxidation (Case 1), was consistently most influential for all computed parameters because of the significant increase in overall heatup rate. For this uncovery scenario the influences of hydrogen blanketing (Case 3), and ZrO_2 failure (Case 5), were negligible and therefore are not shown on the figure. Approximately twenty-two percent of the cladding was oxidized (compared to an estimated 40 to 50% for TMI-2), and less than 0.003% of the Cs and I was released to the coolant for the base case. Although not shown in the figures, all cases indicated extensive liquefaction of the fuel rod much like in ESSI-7. The largest amount of relocated Zr-U-O was for the case of enhanced UO_2 dissolution (Case 4) with five percent relocated. In that case two percent of the relocated Zr-U-O moved below the bottom of the rod, with the remaining three percent frozen on the rods. The ZrO_2 was breached over the upper 1/2 to 7/8 of the rod in all cases.

CONCLUSIONS

Zircaloy oxidation and melting can significantly influence the heatup and degradation of the core during a severe accident. The qualitative influence is being defined by a series of integral experiments and the examination of the damaged TMI-2 core. Those experiments show that the heatup rates, zircaloy oxidation, and zircaloy melting and relocation are intimately coupled. Slower initial heatup rates and heavier oxide buildups lead to embrittlement but maintenance of rod like geometries for temperatures greater than 2500 K. Rapid initial heatup rates result in rapid oxidation induced temperature excursions from 2100 to 2500 K, fuel rod liquefaction, and formation of masses of cohesive debris with low porosity.

The uncertainties in important zircaloy oxidation and melting phenomena can be estimated given the current state of integral and separate effects experiments. The uncertainties in the oxidation kinetics of solid zircaloy are

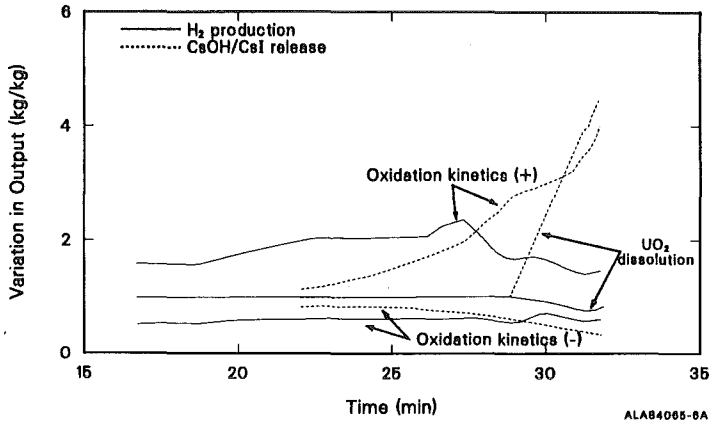

Figure 4. Variation in hydrogen production and CsI and CsOH release versus time for three sensitivity cases (oxidation kinetics plus and minus and UO_2 dissolution).

well characterized due to the large number of experiments which have been performed. The uncertainties in hydrogen blanketing are equally well characterized, even though the data base is extremely limited, because the influence of hydrogen blanketing is bounded by an unlimited steam supply on one hand and by complete steam starvation on the other. However, the uncertainties in UO_2-Zr interactions and ZrO_2 failure are poorly established and may change significantly as additional data are obtained.

The results of sensitivity studies are highly scenario dependent. However, for heatup rates of 1 to 2 K/s and a core uncovery of approximately 75%, the uncertainties in oxidation kinetics are the largest contributors to uncertainties in heatup rate, hydrogen production, fission product release, and loss of geometry. Lesser contributors, in order of importance are: UO_2 dissolution for fission product release and loss of geometry, hydrogen blanketing for hydrogen generation rates, and ZrO_2 failure for loss of geometry. The maximum temperature is not significantly altered from the base case scenario by these uncertainties.

FOOTNOTE

1. The scale representing the oxygen atom fraction describes the degree of zircaloy oxidation, with the zero denoting zero oxidation and 0.67 denoting complete conversion to ZrO_2. The curves were obtained from calculated oxygen atom fractions using the oxidation kinetics described in the next section and measured temperatures at the same elevation and time.

REFERENCES

1. L. S. Beller and H. L. Brown, Design and Operation of the Core Topography Data Acquisition System for TMI-2, GEND-INF-012, May 1984.

2. B. A. Cook and D. W. Akers, "TMI-2 Debris Analytical Methods and Results," ANS Topical Meeting on Fission Product Behavior and Source Term Research, Snowbird, Utah, (July 1984).

3. C. M. Allison et al., SCDAP/MOD1 Analysis of the Progression of Core Damage During the TMI-2 Accident, EG&G Report-SE-CMD-84-009, (June 1984).

4. Electric Power Research Institute, Analysis of the Three Mile Island Unit 2 Accident, NSAC-80-1, NSAC-1 Revised, (March 1980).

5. K. H. Ardron and D. G. Cain, TMI-2 Accident Heatup Analysis, NSAC-24, (January 1981).

6. E. C. Schwegler, P. J. Maudlin," Fuel Models and Results from the TRAC-PF1/MIMAS TMI-2 Accident Calculation," Proceedings, International Meeting on LWR Severe Accident Evaluation, Cambridge, Massachusetts, August 28 through September 1, 1983 pp 2.1-2 to 2.1-3.

7. S. Hagen, "Out-of-pile Experiments on the High Temperature Behavior of Zry-4 Clad Fuel Rods," 6th International Conference on Zirconium in the Nuclear Industry, Vancouver, British Columbia, June 28 through July 1, 1982.

8. S. Hagen et al., Temperature Escalation in PWR Fuel Rod Simulator Bundles due to the Zircaloy/Steam Reaction, Test ESBU-1 Test Results Report, Kernforschungszentrum Karlsruhe Report--KfK 3508, (December 1983).

9. P. E. MacDonald et al., "PBF Severe Fuel Damage Program: Results and Comparison to Analysis,", Proceedings, International Meeting on LWR Severe Accident Evaluation, Cambridge Massachusetts, August 28 through September 1, 1983, pp. 1.7-1 to 1.7-4.

10. L. Baker, Jr., An Assessment of Existing Data on Zirconium Oxidation under Hypothetical Accident Conditions in Light Water Reactors, ANL/LWR/SAF 83-2 (1983).

11. R. E. Pawel et al., "Diffusion of Oxygen in Beta-Zircaloy and the High Temperature Zircaloy-Steam Reaction," Zirconium in the Nuclear Industry, ASTM STP 633, pp. 119-133 (1977).

12. James M. Broughton et al., Experiment Requirements for In-pile Severe Fuel Damage Tests to Fuel Melting in the Power Burst Facility, EG&G Report (March 1984) to be released.

13. H. A. Porte et al., Oxidation of Zirconium and Zirconium Alloys, ANL-6046, (September 1959).

14. A. Van der Linde, Calculation of the Safe Life Time Expectancy of Zirconium Alloy Canning in the Fuel-Elements of the Nero Reactor, RC-41 (July 1965).

15. H. C.Brassfield et al., Recommended Property and Reaction Kinetics Data for Use in Evaluating a Light Water Cooled Reactor LOCA Incident Involving Zircaloy-4 or 304 SS Cladd UO_2, GEMP 482 (April 1968).

16. A. W. Lemmon, Studies Relating to the Reaction between Zirconium and Water at High Temperatures, BMI-1154 (1957).

17. N. L. Hampton and D. L. Hagrman, Cladding Oxidation (CORROS, COBILD, COXIDE, COXWTK, AND COXTHK), EGG-CDD-5647 (November 1981) with Errata.

18. J. V. Cathcart, Quarterly Progress Report on the Zirconium Metal-Water Oxidation Kinetics Program Sponsored by the NRC Division of Reactor Safety Research for April--June 1978, ORNL/NUREG/TM-41 (August 1976).

19. J. V. Cathcart, Quarterly Progress Report on the Zirconium Metal-Water Oxidation Kinetics Program Sponsored by the NRC Division of Reactor Safety Research for October--December 1976, ORNL/NUREG/TM-87 (February 1977).

20. Louis Baker, Jr. and Louis C. Just, Studies of Metal-Water Reactions at High Temperatures III. Experimental and Theoretical Studies of the Zirconium-Water Reaction, ANL-6548, (May 1962).

21. H. Ocken," An Improved Evaluation Model for Zircaloy Oxidation," Nuclear Technology 47, 343, (1980).

22. S. Leistikow et al., "Comparative Studies of Zircaloy 4/High Temperature Oxidation Under Isothermal and Temperature Transient Conditions," CSNI Specialists Meeting, Spatind, Norway, 1977.

23. S. Leistikow et al., "Comprehensive Presentation of Extended Zircaloy-4 Steam Oxidation Results, 600-1600°C," OECD-NEA-CSNI/IAEA Specialist Meeting on Water Reactor Fuel Safety and Fission Product Release in Off-Normal and Accident Conditions, Denmark, May 1983.

24. V. F. Urbanic and T. R. Heidrick, "High Temperature Oxidation of Zircaloy-2 and Zircaloy-4 in Steam," Journal of Nuclear Materials 75, pp. 251-261 (1978).

25. P. D. Parsons and W. N. Miller," The Oxidation Kinetics of Zirconium Alloys applicable to Loss-of-Coolant Accidents," ND-R-7(S), (1977).

26. D. R. Olander, "Oxidation of Liquid Zircaloy by Steam," Journal of Nuclear Materials 119, 1983, pp.p 245-250.

27. H. M. Chung and G. R. Thomas, "High-Temperature Oxidation of Zircaloy in Hydrogen-Steam Mixtures", 6th International Conference on Zirconium is the Nuclear Industry, Vancover, British Columbia, June 28 through July 1982.

28. General Electric Co., High Temperature Materials Programs. Part A Annual Report No. 6 January 31, 1966 through January 31, 1967., GEMP-475A (March 1967).

29. R. R. Hammer, Zircaloy-Y, Uranium Dioxide, and Materials Formed by Their Interaction. A Literature Review with Extrapolation of Physical Properties to High Temperatures, IN-1093 (September 1967).

30. C. Politis, Untersuchungen in Dreistoff system Umn-Zirkon-Saverstoff, KfK 2167 (1975). English Translation: SAND76-6027, Sandia Laboratories.

31. P. Hofmann and C. Politis, "The Kinetics of the Uranium Dioxide-Zircaloy Reactions at High Temperatures," Journal of Nuclear Materials 87, 1979, pp 375-397.

32. P. Hofmann and D. K. Kerwin-Peck, UO_2/Zircaloy-4 Chemical Interactions and Reaction Kinetics from 1000 to 1700°C under Isothermal Conditions (Final Report), KfK 3552, November 1983.

33. P. Hofmann et al., "Physical and Chemical Phenomena Associated with the Dissolution of Solid UO_2 by Molten Zircaloy-4," Proceedings, International Meeting on LWR Severe Accident Evaluation, Cambridge, Massachusetts, August 28 through September 1, 1983, pp 2.1.1 to 2.1-3.

34. P. Hofmann and H. J. Neitzel, "External and Internal Reaction of Zircaloy Tubing with Oxygen and UO_2 and its Modeling." Fifth International Meeting on Thermal Nuclear Reactor Safety, Karlsruhe, September 1984.

35. Walter Turk, Design and Verification of Modular Computer Models for Interpreting Rod Melting Experiments, Stuttgart, Germany: Institute for Nuclear Energetics and Numerical Analysis and the Department of Data Processing and Numerical Analysis, University of Stuttgart, IKE Report 4-94, February 1980, pp 50-52. (Translated by LANGUAGE SERVICES, Knoxville, Tennessee).

36. G. H. Beers, Liquid Cladding-Fuel Reaction Rate (PSUZ), EGG-CDD-5611 (November 1981).

37. C. M Allison et al., "SCDAP: A Computer Code for Analyzing Light Water Reactor Severe Core Damage," Proceedings, International Meeting on LWR Severe Accident Evaluation, Cambridge, Massachusetts, August 28 through September 1, 1983, pp 5.1-1 to 5.1-5.

NOTICE

Work supported by the U.S. Nuclear Regulatory Commission, Office of Nuclear Regulatory Research under DOE Contract No. DE-AC07-76ID01570.

ANALYSIS OF THE PBF SEVERE FUEL DAMAGE EXPERIMENTS WITH EXMEL-B

R. Bisanz and F. Schmidt

Institut für Kernenergetik und Energiesysteme (IKE)
University of Stuttgart, Pfaffenwaldring 31, 7000 Stuttgart 80, FRG

ABSTRACT

In order to provide informations on fuel and core response during severe accidents, severe fuel damage experiments are being performed in the Power Burst Facility (PBF) at the Idaho National Engineering Laboratory. The first of these experiments, the PBF Severe Fuel Damage Scoping Test (SFD-ST), was performed on October 29, 1982. The bundle and structural behavior during severe fuel damage accident were investigated by the modular program system EXMEL-B. EXMEL-B utilizes the RSYST software system as well as the experiences of the IKE in fuel rod and core modeling (SSYST, EXMEL and MELSIM). EXMEL-B is part of the Safety Analysis System (SASYST) of the IKE. Results of EXMEL-B application will be compared against the experimental data of the severe fuel damage experiments in the PBF. The paper will also suggest areas where further model development and code improvements are necessary.

INTRODUCTION

The accident in the Three Mile Island-2 (TMI-2) reactor has clearly demonstrated that severe accidents can be terminated successfully also far beyond the regulatory guidelines. It also has shown, that we have to be prepared to analyze them on a non-hypothetical basis.

As a result various experimental and theoretical programs have been initiated to analyze the fuel rod and core behavior during degraded core cooling conditions.
The objectives of the experimental program conducted in the Power Burst Facility (PBF) at the Idaho National Engineering Laboratory (INEL) are to investigate the

- fuel rod and bundle behavior during severe accident conditions,
- fission product release, deposition and transport and
- hydrogen generation.

MODEL AND CODE DEVELOPMENT AT IKE

In order to investigate the course of severe accidents new and complex computer and software techniques have to be used.

During the past years physical models and codes have been developed which allow the assessment of various accident scenarios. All the fuel rod and core behavior codes are part of Plant Simulation and Analysis System (SASYST) /1/, which is shown in Fig. 1. Within SASYST a module independent graphical system of the IKE /2/ can be applied to visualize the results obtained. Most of the figures of this paper were produced by this system.

With respect to the fuel rod behavior, Fig. 2 shows the contribution of the IKE to the code development in the Federal Republic of Germany: the modular program system SSYST (Safety System) /3/ describes the behavior of a light water reactor fuel rod during loss-of-coolant accidents. The SSYST code system has been developed within the frame of the Projekt Nukleare Sicherheit (PNS) in close cooperation between IKE and the Kernforschungszentrum Karlsruhe. The SSYST code system consists of a number of modules which treat heat conduction, changes in geometry, pressure in the gap between fuel and clad, thermal hydraulic in the coolant channel and metal water reaction.

The modules of the EXMEL /4/ program system allow a detailed analysis of the fuel rod behavior under melting conditions. Modules exist for the simulation of heat production, heat transfer, cladding oxidation, the definition of boundary conditions for the rod (including conduction, convection and radiation), the deformation of the rod by thermal strains, the melting of rod materials, the rupture of the cladding and the run-off of molten material.

The modular code system MELSIM3 /5/ has been developed in order to analyze the integral fuel rod, bundle and core behavior. The complex modeling of MELSIM3 includes the thermal behavior of the core or bundle surroundings.

MELSIM3 is also part of SASYST and represents the "best-estimate" modeling in the frame of KESS-2, which has been reported elsewhere /6/.

DESCRIPTION OF EXMEL-B

The modular program system EXMEL-B (see also Fig. 2) is also based on the RSYST software technology.

EXMEL-B combines the advantages of both, the single rod code EXMEL and the core wide code MELSIM3. The bundle code is designed to cover the range of accident scenarios which lead to severely damaged fuel rods up to the beginning of fuel rod desintegration. Thus, EXMEL-B may be placed between the code lines SSYST/EXMEL and MELSIM3. The bundle behavior is modeled in a two dimensional (r,z)-geometry. In each radial zone a representative fuel rod and an associated coolant channel is modeled. This approach has been proven to be sufficiently accurate for the bundle analysis.

Moreover, selected representative fuel rods may be analyzed in more detail by the single rod codes SSYST and EXMEL within the same computer run. The results may be fed into the EXMEL-B bundle calculation during a time step. In the same way, EXMEL-B results of the bundle calculation may be fed into the overall core analysis code MELSIM3, in order to allow a detailed

analysis of selected bundles within a core wide calculation.

The fuel rod bundle region is surrounded by heat structures which model the heat conduction in the solid material which may be separated by radiation gaps. Different material compositions and boundary conditions can be considered.

The fuel rod model considers:

- heat conduction in (r,z)-fuel rod geometry
- gap heat transfer
- deformation of the fuel rod
- metal-water reaction
- heat source and fission product release
- radiation to adjacent rods
- melting and slumping of fuel rod material
- strong modular coupling to fluid and structure material models.

The fluid model considers:

- axial enthalpy transport
  (subcooled, saturated or superheated water and hydrogen)
- swell level modeling
- channel blockage due to relocation of molten material
- hydrogen production
- steam starvation and hydrogen blanketing
- strong modular coupling to the fuel rod model.

The structure material model considers:

- heat conduction in (r,z)-geometry
- radiation between gap surfaces
- variable boundary conditions
- metal-water reaction in the solid materials
- strong coupling to bundle behavior.

With respect to the application to special experimental conditions some data, for example heat sources, pressure, mass flow, and mixture level history may also be handled as time dependent input data and have not to be provided necessarily by the modules in EXMEL-B.

SEVERE FUEL DAMAGE EXPERIMENT DESCRIPTION

The severe fuel damage scoping test (SFD-ST) has been conducted in October 1982. The test train (Fig. 3) /7/ consists of 32 fuel rods of 0.91 m length enclosed in an insulated shroud. The test train coolant was routed downward between the PBF in-pile tube and a flow divider to the bottom of the test train, and then upward passed the insulated shroud. The bundle coolant entered the in-pile tube through a separate line and passed through the bundle. The bundle was highly instrumented in order to measure water and steam flow, pressure, temperatures, etc.

At the beginning of the transient, the coolant flow and the pressure were maintained almost constant and the power increased. These conditions resulted in water boiloff and subsequently in a bundle heatup in the uncovered parts of the bundle. At the end of the experiment the power was dropped and the bundle reflooded.

EXMEL-B SIMULATION OF THE EXPERIMENT

The bundle region has been modeled by assuming three representative rods in radial direction and 40 axial meshes. Because of the different materials in the shroud, e.g. Zr, ZrO_2-insulator, Zr saddle and a double outer wall starting at the radial inner surface of the shroud (s. Fig. 3), it has been modeled as a two-dimensional heat conduction domain. The geometrical and material composition of the EXMEL-B simulation model is shown in Fig. 4. The shroud has been devided into 12 radial and 40 axial meshes. The nodalization of the bundle and the shroud in axial direction has been chosen equally in order to have a direct radiation coupling opportunity. The bundle coolant inlet flow rate, as well as power and pressure histories were provided as input data to the code EXMEL-B. This option, to specify selected time and/or space dependent input data, allows an easy adaption of the modular code system to specific requirements. The code interpolates the actual data from time and/or space dependent tables by using RSYST specific, standardized routines.

The time dependent input data were taken from measured data and are shown in Fig. 5.

VALIDATION OF EXMEL-B

The calculational results of the EXMEL-B application are based on the time dependent inlet mass flow rate and pressure history in the test section. However, the corresponding steam generation rate and the mixture level has been predicted with EXMEL-B.
Therefore, from a comparison of calculated and measured results, contributions to the validation of the following models of EXMEL-B can be expected:

- the fuel rod model,
- the coupling of fuel rods by radiation in the steam covered parts of the fuel rods,
- the fluid behavior in the steam and steam/hydrogen environment,
- the convective heat transfer modes,
- the coupling of the bundle region to the surroundings.

Fig. 6 compares the calculated cladding surface temperatue at the 0.7 m level against the experimental data. It is evident, that the agreement is reasonably good.

The cladding surface temperature in the upper third of the bundle includes all the effects of spatial and time dependent processes, e.g. radiation convection as well as mass flow, power and pressure histories. The slightly higher temperature gradient between 4000 s and 10 000 s in the calculated temperature history indicates that the heat transfer coefficient in the

experiment will be somewhat higher than predicted by the code.

The same effect also explains the differences between the calculated innermost shroud temperatures and the measured data (s. Fig. 7).

CONCLUSION

The results of the EXMEL-B code application are in good agreement with the experimental results of the PBF Scoping Test. To achieve such an agreement, experiences in the modeling of severe accident phenomena had to be considered /8, 9, 10/ as well as sensitivity studies for bundle heat up experiments /11/.

The calculational results demonstrate that the spatial, e.g. axial and radial, and the time dependent physical processes are modeled with the necessary accuracy and that the important phenomena have been taken into account. It also demonstrates that the EXMEL-B code is suitable to analyze severe accident phenomena in the models. Our analysis work has shown to us once more that the complex experiments have to be analyzed in order to understand the physical phenomena in any detail. This is especially true, if we try to analyze the debris formation and coolability in the cooldown phase.

REFERENCES

/1/ R. Rühle, R. Bisanz, W. Scheuermann, F. Schmidt, H. Unger: "SASYST - A New Approach in Total Plant Simulation During Severe Core Damage Accidents", Int. Meeting on Therm. Reactor Safety, Chicago, USA, 1982

/2/ R. Lang, B. Schlecht: "Farbgrafik in RSYST", IKE 4 R-9 (Mai 1983)

/3/ W. Gulden et al.: "SSYST-Mod 1 - Ein Programm zur Berechnung des Brennstabverhaltens bei einem Kühlmittelverlustunfall", IKE 4-51 (1975)

/4/ R. Bisanz, F. Schmidt, R. Rühle, H. Unger: "Fuel Rod Modeling Under Severe Core Damage Conditions", Applied Science Pub., England, 1983

/5/ R. Bisanz: "Modellierung und Analyse des Verhaltens von Leichtwasserreaktoren bei Störfällen mit schweren Kernschäden", submitted as dissertation May 1983

/6/ F. Schmidt, R. Bisanz: "KESS2 - Recent Development and Perspectives", Int. Meeting on Light Water Reactor Severe Accident Evaluation, Vol. II, Cambridge, Mass., USA, Aug./Sep. 1983

/7/ P. Cybulskis, R.O. Wooton: "MARCH2 Simulation of the Power Burst Facility Severe Fuel Damage Scoping Test", Proc. of the Int. Meet. on Light Water Reactor Severe Accident Evaluation, Aug./Sept. 1983 and private communication

/8/ R. Bisanz, F. Schmidt: "Analysis of the TMI Incident Using EXMEL and MELSIM3", Proc. of the Int. Meeting on Thermal Nuclear Reactor Safety, August 29 - September 2, 1982, pp. 1838 - 1843

/9/ R. Bisanz, U. Lang, W. Scheuermann, H. Unger: "Investigations on Steady-State and Transient Fuel Rod and Cluster Behavior During Severe Fuel Damage Conditions", Final Report, IKE 2-61, Jan. 1983

/10/ F. Schmidt, R. Bisanz: "Modeling of Light Water Reactor Core Melting and Slumping Phenomena", Final Report, EPRI-TSA 81-47Q and IKE 2TF-30, January 1983, in preparation

/11/ R. Bisanz, U. Lang, W. Scheuermann, H. Unger: "Analyse des Brennstabverhaltens in der Auslegungsphase der SUPER-SARA Experimente mit SSYST, EXMEL and MELSIM", Jahrestagung Kerntechnik, Berlin '83, Juni 1983

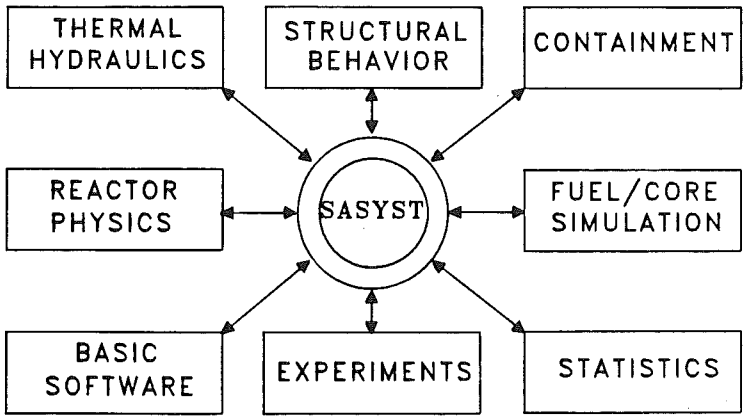

FIG. 1 : S A S Y S T

PLANT SIMULATION AND ANALYSIS SYSTEM OF IKE

CONTRIBUTION OF IKE TO THE CODE DEVELOPMENT

CODE	CONTRACT	APPLICATION	VALIDATION CODE-CODE	VALIDATION EXPERIMENT
SSYST	KFK	DESIGN BASIS ACCIDENTS SINGLE ROD (2D) THERMALHYDRAULIC (1D)	FRAP-S/T SUPER SARA	KFK, LOFT
EXMEL SSYST-4	BMFT KFK	SEVERE FUEL DAMAGE SINGLE ROD (2D) THERMALHYDRAULIC (1D)		KFK KFK (CORA)
EXMEL-B	IKE	SEVERE FUEL DAMAGE BUNDLE (2D), STRUCTURE THERMALHYDRAULIC (~2D)	SSYST-EXMEL	KFK PBF
MELSIM3	IKE	SEVERE CORE DAMAGE CORE WIDE ANALYSIS HYPO. CORE MELTDOWN	SSYST-EXMEL SUPER-SARA	PBF TMI-2
KESS-2	BMFT	CORE MELTDOWN ACCIDENTS RISK ASSESSMENT		SEPERATE EFFECT

FIG. 2 : MODULS FOR THE FUEL ROD MODELING IN THE IN THE FRAME OF *SASYST*

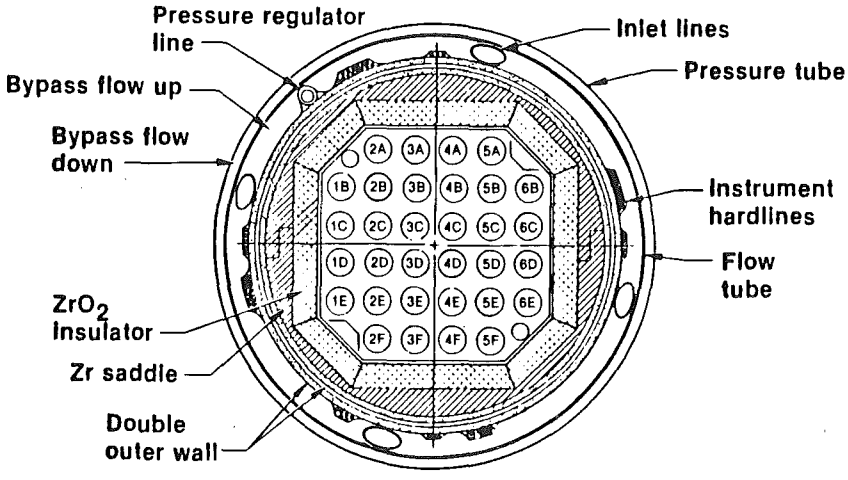

FIG. 3 : TEST TRAIN OF THE SFD-ST EXPERIMENT (BUNDLE REGION)

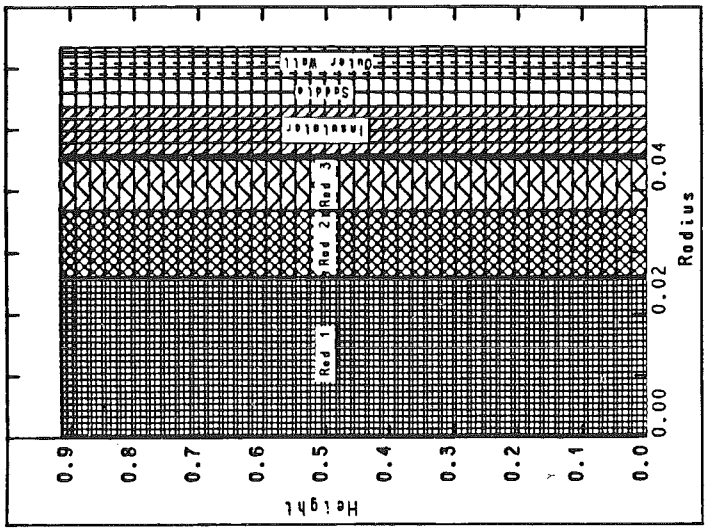

FIG. 4 : DISCRETIZATION OF THE TEST TRAIN FOR *EXMEL-B* CALCULATIONS

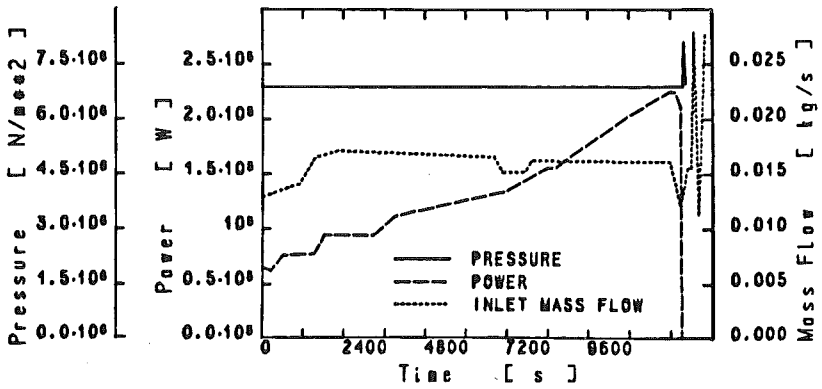

FIG. 5 : INITIAL CONDITIONS FOR CALCULATING THE SFD-ST EXPERIMENT

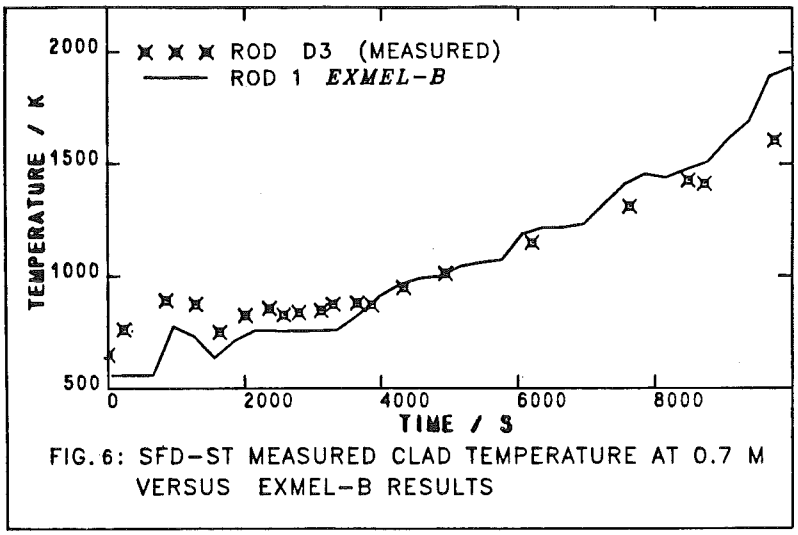

FIG. 6: SFD-ST MEASURED CLAD TEMPERATURE AT 0.7 M VERSUS EXMEL-B RESULTS

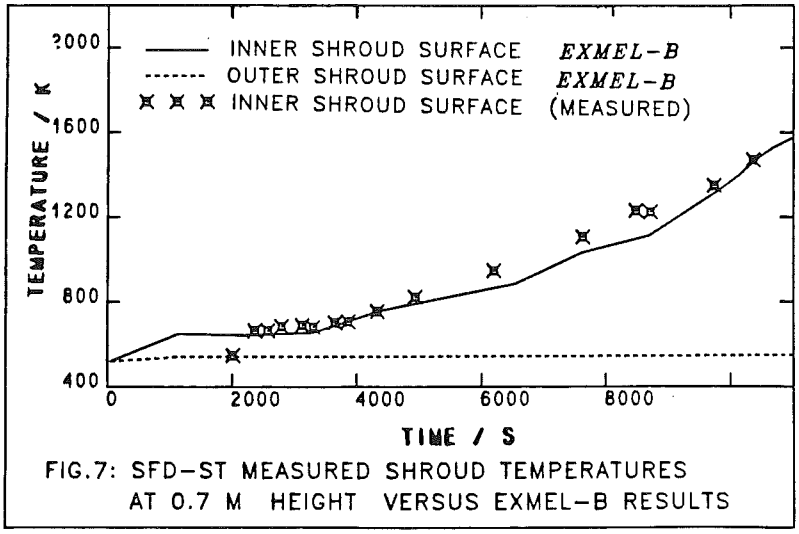

FIG. 7: SFD-ST MEASURED SHROUD TEMPERATURES AT 0.7 M HEIGHT VERSUS EXMEL-B RESULTS

DF-1: AN ACRR SEPARATE EFFECTS EXPERIMENT ON SEVERE FUEL DAMAGE*

A. C. Marshall, P. S. Pickard, K. O. Reil,
J. B. Rivard, and K. T. Stalker

Sandia National Laboratories, Albuquerque, NM 87185, USA

ABSTRACT

A series of in-pile experiments addressing LWR severe fuel damage phenomena is being conducted in the ACRR reactor at Sandia National Laboratories. The ACRR Damaged Fuel Relocation (DFR) experiments are separate effects tests which provide a data base for the development and verification of models for LWR severe core damage accidents. The first experiment in this series, DF-1, has been completed and the results and analysis to date are discussed in this paper. DF-1 examined the effect of low initial clad oxidation conditions on fuel damage and relocation processes. Visual observation showed early clad relocation and partial blockage formation at the grid spacer location with significant aerosol production. Oxidation-driven heating rates of 25 K/s and peak temperatures in excess of 2525 K were observed.

1. INTRODUCTION

The Debris Formation and Relocation (DFR) experiments being performed by Sandia National Laboratories consist of a series of in-pile separate-effects experiments that provide data for the development and verification of models of fuel and core damage phenomena. The DFR program is part of the integrated U. S. Nuclear Regulatory Commission's (NRC) Severe Fuel Damage Research Program [1]. The NRC Program focuses on the development of an improved database and analysis capability that may be utilized in assessing the consequences of possible severe core damage accidents in light water nuclear power plants.

The role of the DFR separate-effects experiments in the NRC Program is to supply data on the effects of important variables and conditions on fuel damage progression, and the severity of the end state attained following the damage process. The experiments examine a range of conditions relevant to severe accidents that are known to influence damage phenomena, including clad oxidation states, steam (and hydrogen) flow rates, and pressures. The emphasis of the DFR program is on the in-core processes that affect the mode and rate of damage and the environment for the release and transport of fission products.

*This work was supported by the U. S. Nuclear Regulatory Commission.

2. PROGRAM DESCRIPTION

In the DFR experiments, a short bundle (~0.5m) of LWR fuel rods is fission heated in flowing steam to high temperatures. From visual observations, from pressure, temperature, flow rate and hydrogen measurements, and from post-test examination and analysis of the experiment debris configuration, information on the effects of accident parameters and conditions on the damage progression, and on the end state is obtained. This information can be correlated with phenomenological models of the processes, yielding improved and/or verified models that can be used for accident analysis.

2.1 Experiment Description

The DFR experiments are performed in the Annular Core Research Reactor (ACRR), a pool-type reactor with a large central irradiation space, at Sandia National Laboratories. The experiment capsule (Fig. 2-1) is installed in the central irradiation space for each test. An external boiler-superheater system supplies steam to the 9-rod fuel bundle in the capsule. Hydrogen produced by oxidation of the fuel rod cladding is removed by CuO recombiner beds. The steam is condensed and collected in the condensate tank. Steam flow rates and axial power profiles are adjusted to simulate reactor conditions during an accident. A visual record of damage progression is obtained via cinematographic and video observation through an end-on view port, which also allows radiometric temperature measurements and hydrogen detection by a pulsed ultraviolet laser Raman spectrographic system. Hydrogen is also monitored by measurement of temperatures attained in the copper-oxide recombining beds employed in the experiments.

2.2 Test Matrix

The DFR experiment program is intended to provide data over a wide range of conditions studied in accident analysis. A key parameter in the DFR experiment matrix is the state of clad oxidation at the initiation of severe damage. The initial oxidation state, together with the steam flow rate, and the system/rod relative pressure are important in determining the ultimate core temperatures, hydrogen generation, and the fuel liquefaction and relocation modes that determine core damage severity and fission product release. The matrix parameters for the first four DF tests have been selected to provide broad investigation of fuel response; they are displayed in Table I.

3. TEST DF-1

As discussed in Section 2.2, the specific objectives of DF-1 were to determine the influence of low initial cladding oxidation conditions on fuel damage progression and end state, including

1. attained fuel temperatures,
2. extent of cladding oxidation,
3. mode and degree of cladding and fuel liquefaction and relocation,

Table I - DF Test Matrix

Test	Oxidation State	Steam Flow	Rod-System Rel.Press.	Purpose
1	Low[1]	Low/Med[2]	+[3]	Examine oxidation, liquefaction, relocation for low initial oxidation conditions
2	Mod	Low/Med	+	Compare fuel damage, relocation, blockage formation, for intermediate oxidation conditions
3	Mod	Med/High	-	Effect of low system pressure and clad ballooning on damage
4	High	Low/Med	+	Examine fuel behavior for high initial oxidation -- possible Cr materials test

[1]Low=10 percent oxidized, High=40 percent oxidized
[2]Low=0.02 g/s-rod, High=0.1 g/s-rod
[3]Range: +20 to -20 atmospheres

4. type and rate of blockage formation, and
5. bundle thermal-hydraulics.

The desired test conditions were obtained by limiting the preconditioning exposure time and cladding temperatures during which the fuel rods were heated up in a steam environment, so that less than about 10 percent of the cladding was oxidized in the upper half of the bundle prior to the main phase of the experiment.

A summary of the observations and some preliminary analysis of the experiment are reported below; it is expected that additional analysis of the data and post-test examinations which are now underway will yield greater understanding of the observations and processes.

3.1 Results

Chronology

Following the low-power preconditioning period during which the upper bundle cladding attained temperatures less than 1200 K, ACRR power was raised to 1.5 MW, and the upper-central region of the cladding quickly attained temperatures promoting vigorous oxidation. During this initial period of oxidation, temperatures increased at rates from about 5 to 8 K/s. Based on temperature indications and visual observation, the width of the oxidation zone was quite wide, extending from well below the fuel center nearly to the upper end of the fissile length. Figure 3-1 gives the rod nomenclature and shows the approximate visual field seen in the video record; Figure 3-2 gives a chronology of events keyed to the temperature indications of the tungsten-rhenium thermocouple located at the bundle midplane.

The visual record shows downward motion of apparently liquefied cladding material to the lower grid spacer as temperatures near 2300 K are attained. This is followed by apparent coalescence of rods 2 and 5, lateral motion and rod bowing. Within the next 30 seconds, large-scale motion of cooler material over hotter regions occurs and the field of view starts to become obscured by intense aerosol generation (see Section 3.2); maximum peak temperatures in excess of 2500 K were recorded during this period. (Correction of the raw thermocouple data for time and temperature response lags is now being performed and is expected to result in a somewhat higher peak temperature estimate.) As temperatures declined from these maximums, the obscuration of the visual field decreased and the highly distorted nature of the resulting fuel debris could be observed.

Hydrogen

Measurement of the hydrogen being produced by the oxidation during the experiment was obtained by a pulsed-ultraviolet-laser Raman spectrographic system. Due to the degree of obscuration of the visual field by aerosol clouds, the measured signal can be regarded as only a qualitative indication of the hydrogen densities during the unobscured portions of the experiment.

A better measurement of the time-history of the evolved hydrogen was obtained from temperature measurements in the copper-oxide recombiner beds; these signals represent the response of the beds to the exothermic chemical reduction of the oxide and hence are a measure of the rate of recombination of evolved hydrogen. This analysis indicated that hydrogen evolved rapidly during the initial oxidation phase at temperatures above 1600 K, was produced at maximum rates throughout the high temperature phase (about 5 minutes), and decreased rapidly as the temperature fell at the conclusion of this phase. Preliminary estimates place the total hydrogen evolved at 12 g.

Post-test Examination

Figure 3-3 is a post-test X-radiograph of DF-1. Visible in this photonegative are 1) general retention of pellet and rod geometry, but substantial lateral deformation (bowing) of the fuel rods in the upper half of the bundle, and evident erosion of some fuel pellets, and 2) a large globular volume of high-density material surrounding a low-density zone. The globular volume is located near the bottom of the fuel bundle and its dense portion is positioned at the axial location occupied originally by a PWR-type grid spacer made from Inconel 718.

Figure 3-4a,b shows cross-sections of the experiment taken a) near the top of the experiment and b) through the dense portion of the globular volume near the bottom of the bundle. The upper cross-section shows 8 fuel pellets with evidence of erosion and phase inhomogeneities surrounded by distended and broken oxidized cladding shells. Pieces of oxidized cladding not associated with pellets are also present. Substantial displacement of the rods from their original positions is clearly evident. The remainder of the cross-section is void and there is

no evidence of the ninth fuel rod. Some erosion of the low density Zirconia shroud is seen.

The lower cross-section (Figure 3-4b) shows a large mass of material which formed a partial blockage at the original location of the lower grid spacer. Liquefied material has flowed outward, substantially eroding the zirconia shroud, and occupying an area more than twice as large as the original flow passage. The nearly-original size, shape, and positioning of the 9 fuel rods are clearly discernible within the large mass in the original photograph. However, most of the cladding around the rods, and the grid spacer which originally positioned the fuel rods in this cross-section, are not seen. Visible are several small areas of metallic material, a few shards of oxidized cladding shells, and isolated pores (shown as the darkest tone at the center and left of center in Fig 3-4b).

3.2 Analysis

Temperature Comparisons

Thermal analyses of the DF-1 experiment using state-of-the-art computer models (SCDAP[2]/MELPROG[3])are being initiated. Limited analysis using simple fuel rod experiment analysis models has been performed to assess the comparisons with measured temperatures. Comparison using existing oxidation models yields reasonable agreement with upper bundle temperatures, but lower bundle calculated temperatures are below measured values.

Several refinements in the calculations are being considered to provide improved agreement. First, the axial distribution of fission power may have been greater than pre-test predictions near the lower end of the bundle due to condensation-caused moderation of the neutron spectrum.

Second, the indications of the high-temperature (W-Re) thermocouples deviate from actual temperatures because they were housed in Zirconia shrouds; corrected temperatures inferred from analysis of their behavior may agree better with modeling of the test. Initial estimates of the actual temperatures based on corrected thermocouple responses indicate actual peak temperatures at the bundle midplane exceed indicated values by 50--100 K, depending on the magnitude of radiative attenuation by aerosols.

Oxidation Behavior

As mentioned earlier, the apparent zone of oxidation was wide, extending from above the lower grid spacer nearly to the top of the bundle. These observations are partially confirmed by the presence of oxidized cladding shells in the metallographic cross-sections.

Because of the rapid rate of cladding temperature rise during the beginning of the main phase of the test (Figure 3-2), total steam flow limited the extent of oxidation of the upper portions of the bundle to about 10 percent prior to the attainment of temperatures exceeding the melting point of

Zircaloy-4 (2000K). Evidence of oxide thicknesses exceeding this value, although preliminary, must be ascribed to oxidation occurring at higher temperatures. This is consistent with the continued rise of central and upper bundle temperatures above 2000 K and the continued evolution of hydrogen during the high temperature period. Although considerable evidence of ZrO_2 (oxidized cladding shells) remains in the upper half of the bundle, only limited evidence of ZrO_2 phases in the lower part of the bundle is seen.

Fuel Liquefaction

Extensive liquefaction of fuel-clad species and erosion of fuel pellets occurred during DF-1; preliminary estimates based on cross-section photographs place the amount of fuel loss in the upper part of the bundle at 10-15 percent, and indicate local values greater than 40 percent in the lower blockage region.

Fuel and Cladding Relocation

Figures 3-3 and 3-4 illustrate the largely coherent rod structures which remained following the very severe conditions imposed during the experiment and despite the loss of cladding integrity throughout the bundle. Only the upper section of one rod has collapsed to lower regions. The pellet-to-pellet interfaces seen in Figure 3-3 are sharp, yet each intact rod has retained its structural identity. Further examination is underway to characterize the interfacial bonds between pellets and to understand whether this phenomenon is unique to fresh (unirradiated) fuel.

The initial cladding motions observed in the visual record consist of apparent flow of hot, glowing material onto the lower grid spacer when the peak temperature in the bundle attained about 2000 K. Later material motions consist of movements of larger-scale (apparently) cooler material over hotter material located in lower parts of the bundle. Because the cooler material remains stationary and retains its shape, it is inferred to be solid rather than liquid.

The blockage in the lower part of the bundle apparently was formed initially as downward-flowing liquefied material encountered the lower grid spacer and froze. Significant fuel liquefaction and pellet erosion (greater than 40 %) occurred later in this zone as zirconium interacted over an extended time with fuel above the grid spacer. This material moved downward and outward, forming the mass seen in Figure 3-4b, dissolving the grid spacer, and leaving behind a voided region. Pores in the blockage allowed continued flow of steam/hydrogen mixture into the upper parts of the bundle.

Aerosols

During the high temperature phase of the experiment, intense aerosol clouds were observed. The aerosol generation started when cladding began melting in the upper bundle regions and continued during the remainder of the high temperature phase. The source of this aerosol is believed to be volatilized tin

which is present as an alloying ingredient in Zircaloy-4. Tin has been identified during the post-test examination as present in the steel mesh filters located downstream of the test section.

Both the intensity and timing of aerosol production from non-radioactive sources may affect the character and transport of released fission products by either chemical reaction or enhanced agglomeration and settling processes. Although the magnitude of the effect of such aerosols in an accident situation requires careful analysis, it is clear that they may play a role in determining the fate of fission products in the in-vessel environment.

The estimated aerosol density required to produce the optical extinction observed in DF-1 is on the order of 1 g/m^3. The total amount of tin required is therefore only a fraction of that available in the Zircaloy cladding. The observed aerosol production is being compared to recently developed models, and the potential effects on the chemistry of fission products, particularly tellurium, are being examined. Because the density of the aerosol is sufficient to affect radiative heat transfer to boundaries and thermocouple locations, these effects are now being incorporated into the DF-1 analysis.

The next experiment in the series, DF-2, will provide information on intermediate oxidation conditions. It is scheduled later this year.

4. SUMMARY

The objective of DF-1 was to determine the influence of low initial cladding oxidation conditions on fuel damage progression and end state when LWR fuel is subjected to severe accident conditions. The results and analysis performed to date indicate that

1. Rapid oxidation with rates of temperature increase of more than 25 K/s were observed in early stages, with peak temperatures in excess of 2525 K occurring after significant liquefaction, relocation and formation of a partial blockage.

2. Low initial oxidation conditions yield early, large-scale relocation of cladding and formation of a partial blockage at the lower grid spacer location.

3. The blockage formed at the lower grid spacer was extensive but sufficiently porous to allow continued steam flow and subsequent oxidation and liquefaction. Substantial fuel liquefaction or pellet erosion (greater that 40%) is seen at one location in the blockage.

4. Generation of significant quantities of aerosols were observed during the high temperature stages, primarily due to volatilized tin from the cladding. The implications of this phenomenon are being investigated.

REFERENCES

1. M. Silberberg, et al,"The USNRC Severe Fuel Damage Research Program", Proceedings, International Meeting on Thermal Nuclear Reactor Safety, Chicago, IL, Aug 29-Sept 2, 1982, NUREG/CP-0027, V3, p1844-1853.

2. C. M. Allison, T. M. Howe, and G. P. Marino, "SCDAP: A Computer Code for Analyzing Light Water Reactor Severe Core Damage", Proceedings, International Meeting on Light Water Reactor Severe Accident Evaluation, August 28-September 1, 1983, Cambridge, MA, V2, p5.1-1 to 5.1-5.

3. M. F. Young and J. L. Tomkins, "MELPROG Code Development and Methods", Proceedings, International Meeting on Light Water Reactor Severe Accident Evaluation, August 28-September 1, 1983, Cambridge, MA, V1, p2.8-1 to 2.8-6.

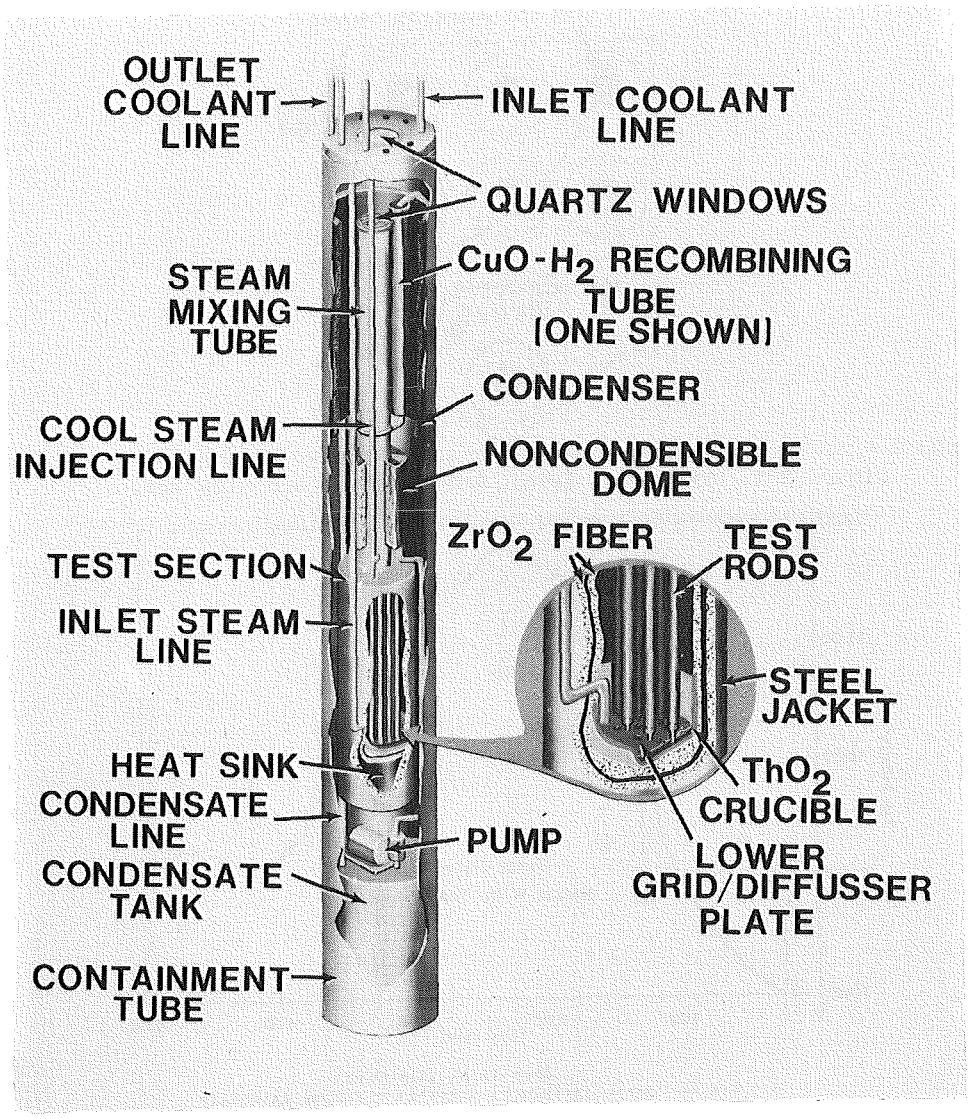

Figure 2-1 DFR Experiment Capsule Schematic

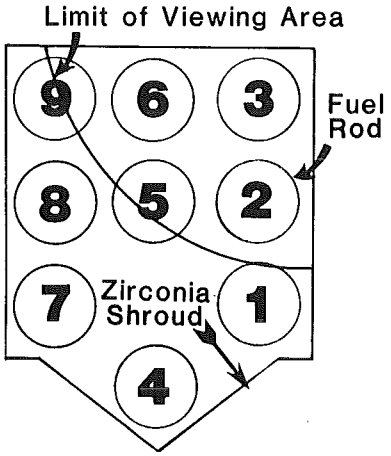

Figure 3-1 DF-1 9-Rod Bundle Nomenclature and View Area

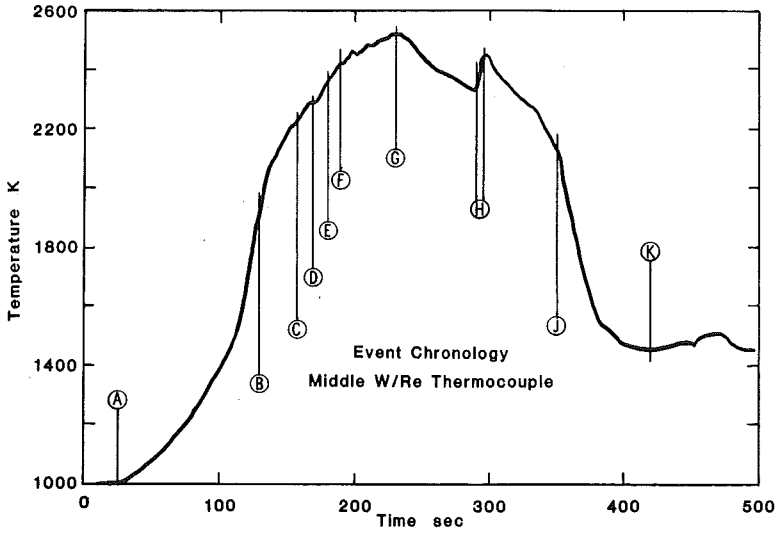

DF-1 EVENT CHRONOLOGY

A. Reactor power increased, vigorous cladding oxidation begins
B. Rod 2 bows towards rod 3
C. Cladding motion visible, aerosol cloud begins
D. Major motion of materials, rods 2 and 5 "fuse"
E. Severe bowing of rod 6 into rod 3
F. Major motion of materials beginning from rod 6, slumping obscures view of hottest region
G. Occurrence of maximum indicated temperature (2525 K); view obscured by aerosol cloud
H. 5 sec "window" in aerosol cloud; "spike" in temperature (2450 K)
J. Upper grid spacer melts; aerosol cloud dissipates
K. Reactor scrammed

Figure 3-2 DF-1 Event Chronology

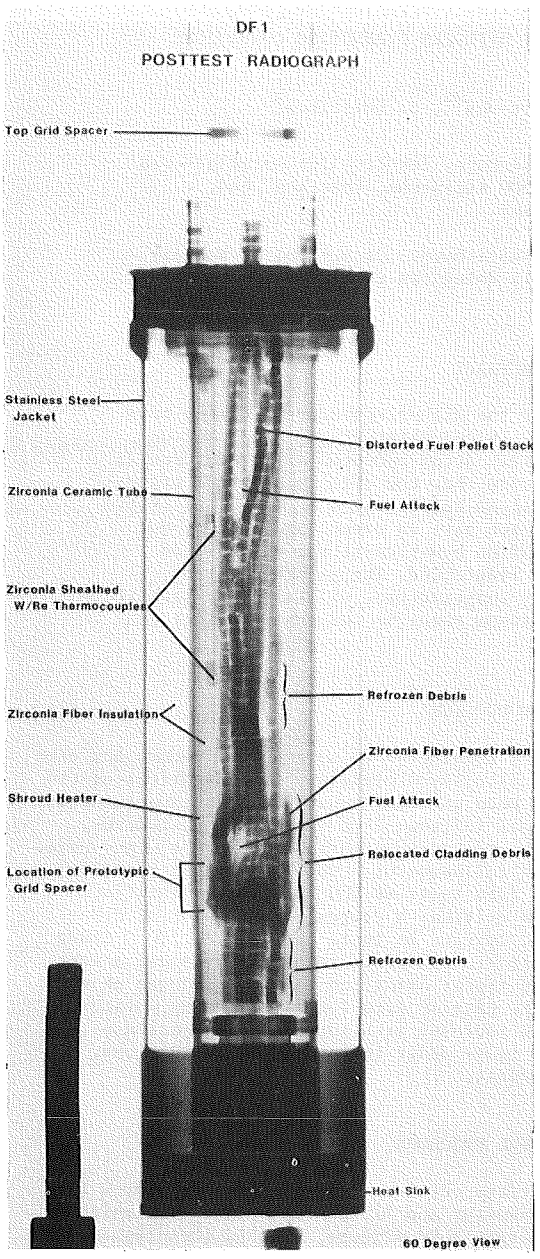

Figure 3-3 Posttest Radiograph of DF-1 Bundle

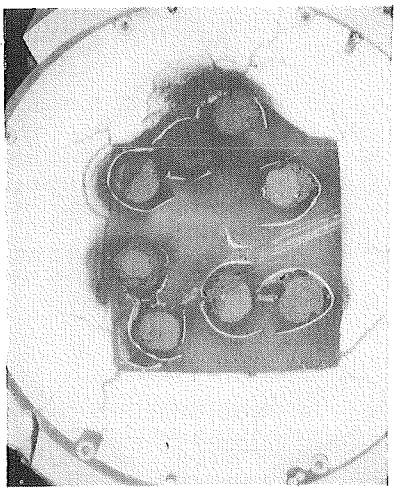

a.

b.

Figure 3-4

Cross Sections through Upper Bundle (a.-660mm elevation) and Lower Blockage (b.-271mm elevation)

INVESTIGATIONS OF ZIRCALOY-4 CLADDING OXIDATION UNDER STEAM STARVATION AND HYDROGEN BLANKETING CONDITIONS

G. Schanz[*], H. Uetsuka[**], S. Leistikow[*]

[*] Kernforschungszentrum Karlsruhe, Institut für Material- und Festkörperforschung, D-7500 Karlsruhe, Postfach 3640, Federal Republic of Germany

[**] JAERI, Tokai Research Establishment, Department of Nuclear Safety Research, presently delegated to KfK

ABSTRACT

As extension of investigations of the high-temperature and long-term oxidation behaviour of Zircaloy-4 in unlimited steam, the reaction under limited steam supply and under steam-hydrogen-argon mixtures is being investigated. The results show that the effects of steam starvation are restricted to very low steam supply rates of which the critical values were determined. Hydrogen acts as competing reactant but no moderating effect on the oxidation kinetics at the temperature level covered up to now has been identified. The parameter study, which will be continued at higher temperatures, will allow to backfit the modelling of the Zircaloy-4/steam reaction under severe accident conditions.

INTRODUCTION

One of the important factors to be considered in severe fuel damage accident analysis is the external oxidation of Zircaloy-4 cladding. Investigations of the oxidation kinetics in pure steam have been extended towards higher temperatures and longer durations [1,2]. Additional influences on the kinetics, however, can be expected from steam consumption and hydrogen enrichment in the atmosphere. Whereas Cathcart et al. [3] found no influence of 5 Vol.-% hydrogen in steam at 1100 and 1300°C, Furuta et al. [4] in tests at 950 to 1100°C identified fluctuations of the reaction rates for critical hydrogen/steam ratios of 0.2 to 0.4 and hydrogen uptake above these levels. In tests at 1200 to 1700°C Chung and Thomas [5,6] registered lower parabolic oxidation rates and hydrogen uptake in hydrogen-containing atmospheres and linear oxidation rates due to gas phase or surface transport limitations in the case of even lower steam supply rates. The influence of hydrogen was found to increase with increasing temperature. Our own investigations are parametric tests under better defined conditions, realized by stationary flowing atmospheres.

EXPERIMENTAL PROCEDURE

The specimens are 30 mm long sections cut from PWR-specific Zircaloy-4 tube material (Tab. I) of 10.75 mm outer diameter and 725 µm wall thickness, which are degreased, pickled in a fluoric-nitric acid mixture, and finally cleaned in boiling distilled water. This specimen length is considered to be short enough to allow measurements of averaging character and to avoid major changes of the atmosphere due to depletion/enrichment of the reactants.

	/¯Wt.-%_7		/¯ppm_7
Sn	1.58	O	1100
Fe	0.22	N	<100
Cr	0.10	H	6

Tab. I: Chemical Analysis of Zircaloy-4 Tube Material

The test equipment consists of a furnace-heated tubular test section, an evaporator and a condenser within a closed atmospheric pressure steam loop. One test type is performed under steam of reduced flow velocities, realized by power control of a small evaporator and calibrated through the total evaporation during several hours of steady-state operation. Another test type is performed under mixtures of steam with argon or hydrogen and argon (Fig. 1). Hydrogen and argon are dosed by flowmeters, mixed and bubbled through the evaporator or fed into an inlet line above the water level. By these two options and variation of the evaporator temperature, steam is transported in constant proportions to the gas supply. The inert carrier gas argon allows the dosage of very low steam supply rates without the risk of stagnant conditions, improves mixing of the atmospheres and permits tests with high hydrogen-to-steam ratios without burning or explosion hazards. The reduced steam supply rates are calibrated by measuring the amount of condensate or the dew point of the atmosphere, the humidity extracted with phosphorus pentoxide or finally the condensation at about 150 K after cooling the atmosphere by liquid nitrogen.

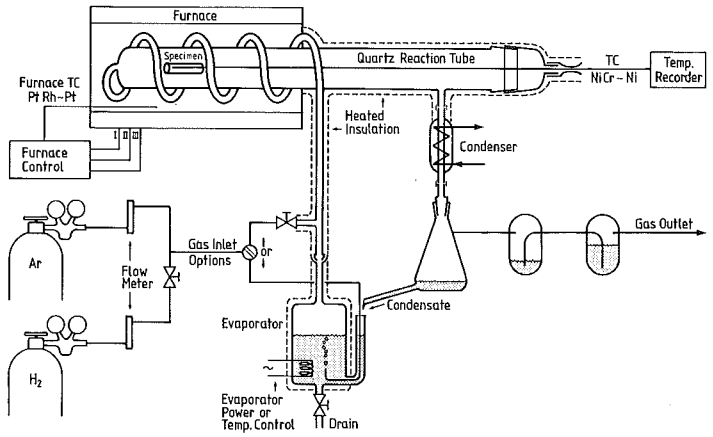

Fig. 1: Apparatus for Reaction Experiments under Mixed Atmopheres of Steam with other Gases

The specimen is inserted into the tubular quartz test section within the laboratory furnace. If necessary, temperature overshooting is avoided by shifting the specimen from a slightly cooler position to the constant temperature zone of the furnace after dissipation of the heat produced at the start of the reaction. In addition to measurement of mass increase and metallographic evaluation, selected specimens are analysed for dimensional changes, oxygen and hydrogen content.

RESULTS AND DISCUSSION

Tests in steam under reduced flow rates have been performed at 1000 and 1300°C. Fig. 2 shows the weight gain of Zircaloy-4 specimens as function of steam supply rate for 15 min at 1000°C. The steam supply rate is defined as the mass of steam passing the unit cross sectional area (ca. 3 cm^2) of the reaction tube in one minute, i.e. mg/cm^2 min. For comparison purposes the dotted line is included, which represents the weight gain expected for unlimited steam as calculated according to the following empirical expression developped by Leistikow et al. (1) :

$$W^2/2\ [(g/cm^2)^2] = 0.262\ t \exp(-174\ 300/RT) \quad R[J/mol\ K] \qquad (1)$$

Above the critical value of steam supply rate of some 13 mg/cm^2min (corresponding to 41 mg/min or 51 ml (STP)/min of total steam inlet rate, 1.3 cm/s of steam flow velocity at 1000°C or 2.1 mg/cm^2min steam supply rate per unit specimen surface area) the weight gain settles on a constant level, roughly in agreement with the calculated value. Below the critical steam supply rate a sharp decrease of weight gain with decreasing steam supply is observed. This can be taken for the effect of steam starvation.

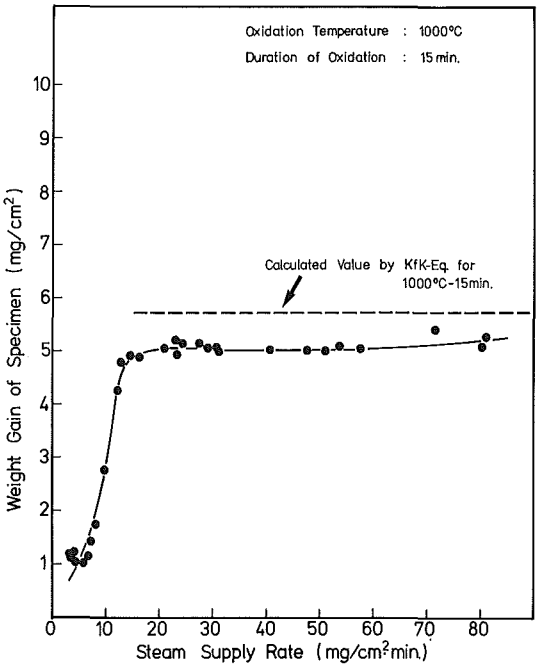

Fig. 2: Mass Increase as Function of Steam Supply Rate to the Cross-Sectional Area of the Reaction Tube (15 min, 1000°C)

Fig. 3 shows the correlation between weight gain and duration of oxidation at 1000°C for three different steam supplies and in comparison to unlimited steam. For the lowest steam supply the initially very small weight gain increases sharply with increasing reaction duration. In the case of the intermediate steam supply rate the weight gain kinetics can be expressed as parabolic function up to 15 min followed by a linear one, whereas parabolic behaviour persists for 60 min in case of the higher steam supply. Breakaway of the oxide film was observed on all the specimens oxidized for 60 min and under steam supply rates of 3.2, 12.7 and 40.7 mg/cm²min. As corresponding hydrogen contents 2300, 1400 and 400 ppm were analyzed.

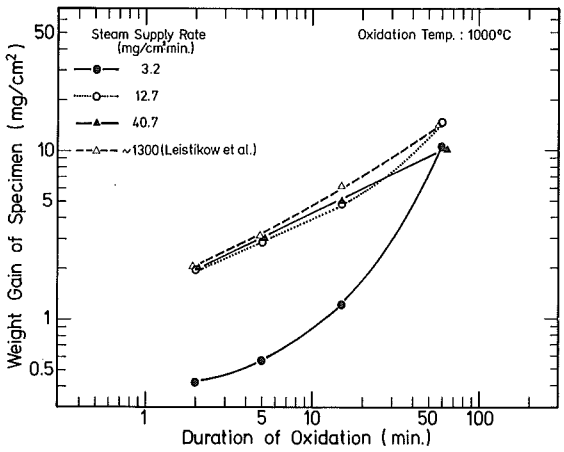

Fig. 3: Mass Increase as Function of Duration of Oxidation in Steam at different Supply Rates (2-60 min, 1000°C)

Fig. 4 shows the steam supply dependence of the weight gain for 15 min at 1300°C. Below the critical steam supply rate of some 20 mg/cm²min a sharp decrease of weight gain is observed. Between 20 and 60 mg/cm²min a peak is obvious, with its maximum about 15 % above the level expected for unlimited steam. Relatively high contents of hydrogen between 340 and 1300 ppm were analyzed for the specimens oxidized in this range. But the acceleration of oxidation could also be correlated with relatively high volume ratios of released hydrogen in these atmospheres. At higher steam supply rates the weight gain decreases gradually to a nearly constant level.

Tests under mixed atmospheres and comparison tests in steam have been performed at 800°C and are being continued at higher temperatures. The following results refer to 800°C tests. Fig. 5 shows the time dependence of mass increase for reactions of Zircaloy-4 specimens in steam under high and reduced supply rates and in argon-steam and argon-hydrogen-steam mixtures. The close comparison of the results as represented by a single curve demonstrates, that argon and hydrogen additions are without influence if only sufficient amounts of steam are provided. In contrast Fig. 6 shows for the example of 15 min and further reduced steam supply rates that hydrogen begins to act as a competing reactant. Especially in case of the atmospheres with higher hydrogen content the hydrogen uptake of the specimens increases with decreasing steam supply as expressed by the weight gain results. At the ordinate intersections of the para-

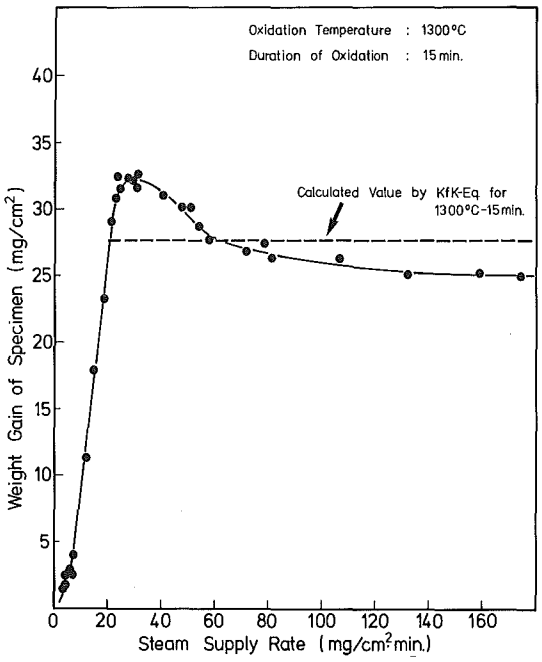

Fig. 4: Mass Increase as Function of Steam Supply Rate (15 min, 1300°C)

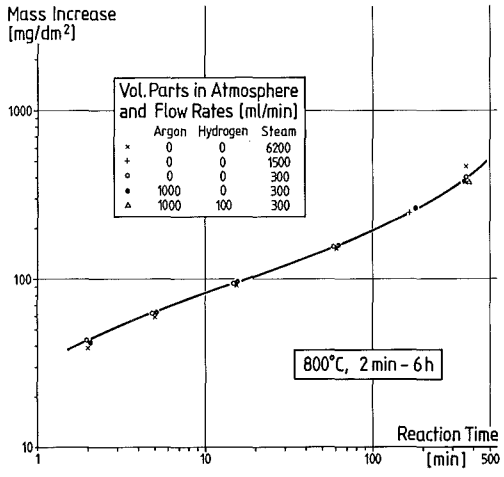

Fig. 5: Mass Increase as Function of Time of Exposure to Steam and Gas Mixtures, Independent of Argon and Hydrogen Additions (2 min-6 h, 800°C)

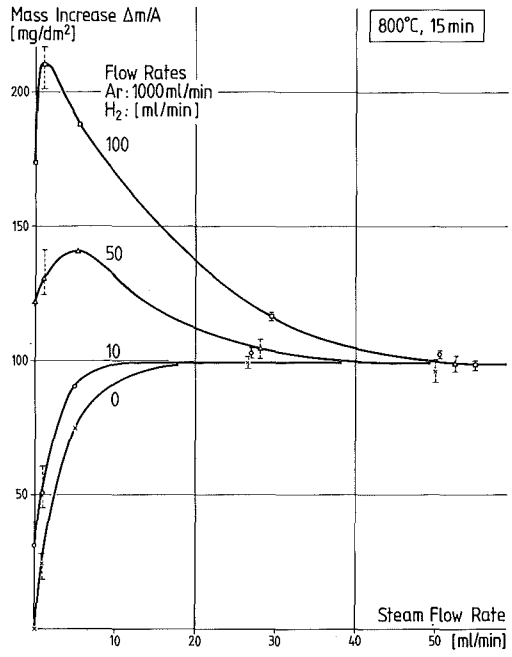

Fig. 6: Mass Increase as Function of Steam Flow Rate in Argon-Steam and Argon-Hydrogen-Steam Mixtures (15 min, 800°C)

metric curves the amounts of hydriding by argon-hydrogen atmospheres can be read. The maxima for the atmospheres containing roughly 10 and 5 % hydrogen in combination with high hydrogen to steam ratios are explained by already appreciable oxidation which however has not yet suppressed hydriding. In addition hydrogen uptake was identified by specimen swelling (up to 3 % of linear dimensional increase), exothermal heat of hydrogen solution (up to 30 K overshooting of reaction temperature), heat of hydride formation during specimen cooling (reduced cooling rate around 500°C), microstructural changes (transformation tendency towards β-Zr phase due to the β-stabilizing hydrogen, hydride precipitation), and hot extraction analysis (up to 9000 ppm, equivalent to the composition of ZrH).

Surprisingly no influence of hydrogen on the oxidation kinetics was identified. However, a slight "hydrogen blanketing", i.e. a moderating effect on the oxidation, if existent at all at 800°C, could have been overcompensated by hydrogen uptake. The steam starvation limit for 15 min at 800°C could be given as roughly 10 ml (STP)/min, which corresponds to 8 mg/min total steam inlet rate, 0.8 mg/cm²min of flow rate reduced to unity of test flow channel cross section (10 cm²), 3.9 cm/min of steam flow velocity (of atmospheric pressure at 800°C) or 0.4 mg/cm²min steam supply rate per unit specimen area.

A comprehensive test series in steam-argon mixtures between 2 min and 6 h showed (Fig. 7), that only substantial reduction of steam supply results in reduced oxidation and shifts the parabolic kinetics towards linear. The long-term behaviour is characterized and complicated by earlier breakaway oxidation at

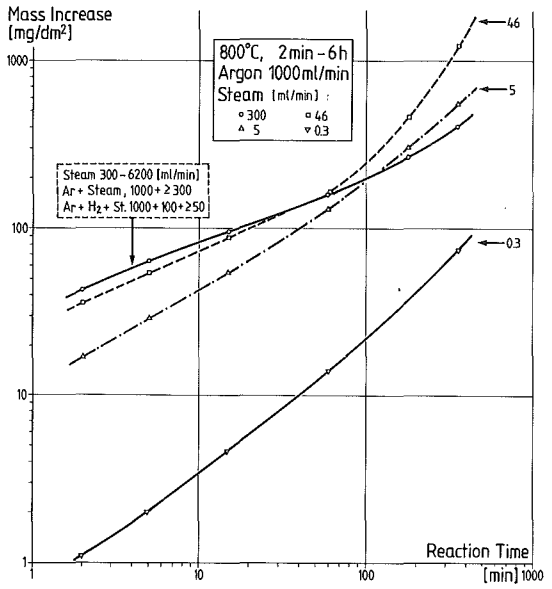

Fig. 7: Mass Increase as Function of Time of Exposure to Argon-Steam Mixtures (2 min-6 h, 800°C)

intermediate steam supply rates, as confirmed by metallographic observation of the defective scales and the increased hydrogen uptake analyzed.

A similar test series in steam-hydrogen-argon mixtures under comparable conditions of reduced steam supply rates showed that the reduction of the oxidation is accompanied by substantial hydrogen reaction. This complicates the interpretation of the kinetic curves (Fig. 8). Compared to the dotted line for the reaction with hydrogen, which first shows linear kinetics and later the constant level of hydrogen saturation, the curves for intermediate steam supply show, that the reduced hydrogen uptake visible for the shorter times is overcompensated for the longer times by the increase in oxidation. The curve representing 50 ml/min of steam is identical with the curve of Fig. 5, so that this small steam supply rate is already sufficient to suppress hydrogen influences. Fig. 9, a comparison of scales and microstructures shows the trend towards β-phase due to uptake of the β-stabilizing hydrogen when the steam supply is reduced below the starvation limit.

The presently available results for 900 and 1000°C of this type of tests in mixed atmospheres have shown that the behaviour of Zircaloy-4 is changing gradually. Fig. 10 gives the hydrogen uptake of the material from hydrogen-argon mixtures in time dependence for the three temperatures. Because the hydrogen saturation level is decreasing with increase of temperature, the oxidation increase with temperature is expected to dominate at the higher temperatures. Breakaway-related effects ought to disappear above 1000°C, according to the present knowledge. So the future parametric tests at higher temperatures promise a good chance to study in detail the "hydrogen blanketing", the moderating effect of hydrogen on the oxidation as described in the literature, with less interference from the competing effects described above.

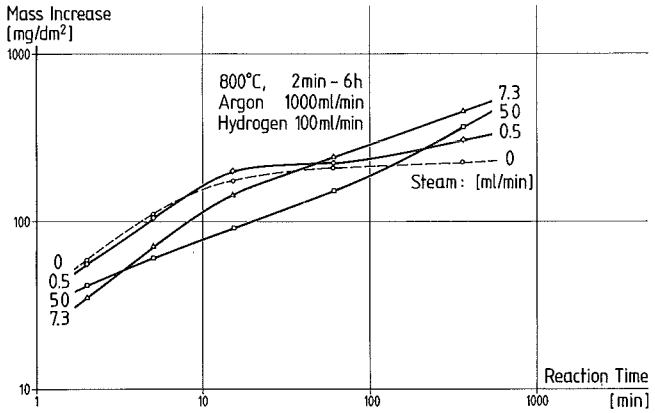

Fig. 8: Mass Increase as Function of Time of Exposure to Argon-Hydrogen-Steam Mixtures (2 min - 6 h, 800°C)

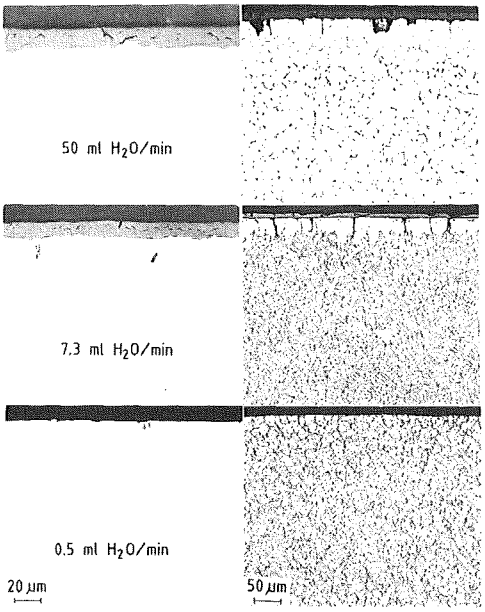

Fig. 9: Influence of Steam Supply Rate on ZrO_2-Scale Growth and Microstructure during Tests in Argon-Hydrogen-Steam Mixtures (6 h, 800°C)

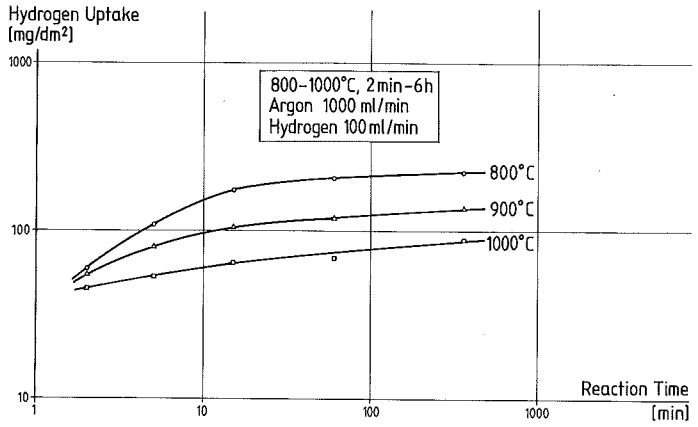

Fig. 10: Hydrogen Uptake as Function of Time of Exposure to Hydrogen-Argon Atmospheres (2 min-6 h, 800-1000°C)

CONCLUSIONS

The test results show that effects of steam starvation are restricted to very low levels of steam supply rate, for which the critical values are determined. Hydrogen is identified as additional reactant and proves to be of important influence only in case of limited steam supply and substantial hydrogen content in the atmosphere. Hydrogen has to be considered as additional heat source and embrittling agent. Oxide scale deterioration in combination with enhanced hydrogen uptake have been identified below critical steam supplies and in atmospheres enriched with hydrogen. In contrast to published results no "blanketing" effect of hydrogen is identified at the lower temperature level of the presently available results. The development of an improved Zircaloy reaction kinetics code, for which the basis is being provided, should treat the limited oxidation below the quantified steam starvation level and should regard the consequences of the reaction with hydrogen. The experimental investigations will be continued at higher temperatures.

REFERENCES

[1] S. Leistikow, G. Schanz, H. v. Berg, A.E. Aly
"Comprehensive Presentation of Extended Zircaloy-4 Steam Oxidation Results (600 - 1600°C)
OECD-NEA-CSNI/IAEA Meeting, Risø National Laboratory (Denmark), 16-20 May, 1983, IAEA-Summary Report IWGFPT/16 (1983) 188-199

[2] V.F. Urbanic, R.T. Heidrick
"High Temperature Oxidation of Zircaloy-2 and Zircaloy-4 in Steam"
J. Nucl. Mater. 75 (1978) 251-261

[3] J.V. Cathcart et al.
"Zirconium Metal-Water Oxidation Kinetics IV. Reaction Rate Studies"
ORNL/NUREG-17 (1977)

/4/ T. Furuta, S. Kawasaki
"Reaction Behaviour of Zircaloy-4 in Steam-Hydrogen Mixtures at High Temperature"
J. Nucl. Mater. 105 (1982) 119-131

/5/ H.M. Chung, G.R. Thomas
"High Temperature Oxidation of Zircaloy in Hydrogen-Steam Mixtures"
Proc. 6th Internat. Conf. on Zirconium in the Nuclear Industry, Vancouver, Canada, June 28 - July 1, 1982

/6/ H.M. Chung, G.R. Thomas
"The Retarding Effect of Hydrogen on Zircaloy Oxidation"
NSAC-29, 1981

SEVERE FUEL DAMAGE IN STEAM AND HELIUM ENVIRONMENTS OBSERVED IN IN-REACTOR EXPERIMENTS

S. Saito and S. Shiozawa

Japan Atomic Energy Research Institute
Tokai-mura, Ibaraki-ken 319-11, Japan

ABSTRACT

The behavior of severe fuel damages has been studied in gaseous environments simulating core uncovery accidents in the in-reactor experiments utilizing the NSRR. Two types of cladding relocation modes, azimuthal flow and melt-down, were revealed through the parametric experiments. The azimuthal flow was evident in an oxidizing environment in case of no oxide film break. The melt-down can be categorized into flow-down and move-down, according to the velocity of the melt-down. Cinematographies showed that the flow-down was very fast as water flows down while the move-down appeared to be much slower. The flow-down was possible in an unoxidizing environment, whereas the move-down of molten cladding occurred through a crack induced in an oxide film in an oxidizing environment. The criterion of the relocation modes was developed as a function of peak cladding temperature and oxidation condition. It was also found that neither immediate quench nor fuel fracture occurred upon flooding when cladding temperature was about 1800 °C at water injection. The external mechanical force is needed for fuel fracture.

INTRODUCTION

The severe fuel damage research is one of the essential items in the field of severe accident research. Several programs are progressing in U.S.A. and FRG by utilizing PBF, ACRR or ex-reactor test facilities to investigate fuel behavior under simulated core uncovery accident conditions.

The behavior of severe fuel damages has been studied simulating postulated core uncovery accidents also in the NSRR (Nuclear Safety Research Reactor) Program at Japan Atomic Energy Research Institute (JAERI). The specific objectives of the present work are to determine fuel rod relocation modes through the extensive in-reactor experiments and to study the transient behavior of the fuel rod damages by a specially-developed optical system [1].

A total of 15 tests including 4 tests for cinematographies was conducted so far under various test conditions changing peak fuel temperature, oxidation condition and so on.

EXPERIMENTAL FACILITIES AND PROCEDURE

The NSRR facility and its capability have been reported previously [2]. Briefly, the NSRR is a modified TRIGA-ACPR (Annular Core Pulse Reactor) whose salient feature is the large pulsing power capability which enables to energize test fuel by nuclear fission over the melting temperature of UO_2. The size of the reactor core is 62 cm in equivalent diameter and 38 cm in height. The diameter of the dry experimental cavity located in the center of the core is about 20 cm.

Each test fuel rod was individually contained within a small inner capsule or surrounded by a quartz tube which was also contained in an outer capsule filled with water at ambient temperature and atmospheric pressure, as shown in Fig. 1. The outer capsule was placed in the central experimental cavity and the test fuel rod was subjected to rapid energy deposition by pulsing operation of the NSRR. The test fuel rods used in the experiments were identical with 14 × 14 PWR type fuel rods with exceptions of fuel length and enrichment. The design details of the test fuel rod are provided in Table I.

Table I Test Fuel Rod Design Summary

UO_2 Pellet		Cladding		Element	
Diameter	9.29 mm	Material	Zircaloy-4	Active fuel length	135 mm
Length	10 mm	Wall thickness	0.62 mm	Pellet-cladding gap	0.095 mm
Density	95% TD	Outer diameter	10.72 mm	Filled gas	He
Enrichment	10 %				

A test fuel rod was previously pressurized in two specific tests, and cladding was previously oxidized on the outer surface in several cases. Each fuel rod was generally instrumented with 0.2 mm O.D. Pt/Pt-13% Rh intrinsic junction thermocouples to measure cladding surface temperatures, and some had W/W-Re sheathed thermocouples to measure fuel centerline temperature.

Atmospheric pressure of air was used instead of steam for most of the oxidizing environment surrounding a test fuel rod, due to easiness of setup of test condition. However, the amount of oxygen in an air environment might not be enough for sufficient cladding oxidation in the cinematography tests because of limited space. A helium gas at atmospheric pressure was employed for the unoxidizing environment to simulate an extreme steam starvation condition.

EXPERIMENTAL RESULTS AND DISCUSSION

A total of 15 tests was performed in an oxidizing or unoxidizing environment changing energy deposition in fuel. The typical temperature histories of fuel centerline and cladding outer surface measured are presented in Fig. 2. As found in the figure, the heating rate of the cladding is an order of 1,000 °C/s. The transient tests were generally terminated by natural cooling with a cooling rate of 35∿50 °C/s. This thermal response is different from that in LOCA's. However, fundamental behavior of fuel rod damage under a severe accident condition has been obtained in the present study.

The test conditions and major results are summarized in Table II. The following subsections detail the experimental results and discuss the behavior of fuel rod damages.

Table II Summary of Test Conditions and Major Results

Test No.	Energy Deposition (cal/g·UO_2)	Test Fuel Rod		Environmental Gas	Peak Cladding Temperature (°C)	Mode of Fuel Rod Relocation
		Pre-oxide thickness (μm)	Pre-Pressurized (MPa)			
1	180	none	0.1	Steam	1600 ∿ 1800	No Relocation
2				He		
3	210	none	0.1	Steam	1850 ∿ 1950	Azimuthal Flow
4		12		He		
5		30		He		
6	250	∿100	0.1	He+ Air	> 2000	
7	210	none	7	Air	1850 ∿ 1950	Melt-down
8		none	0.1	He		
9 [1]	220	none	0.1	Air [2]	∿ 2000	
10 [1]	250	none	2	Air	> 2000	
11 [1]		none	0.1	He+ Air		
12		10	0.1			
13		none	0.1	He		
14		30	0.1			
15 [1),3)]	220	none	0.1	Air [2]	∿ 2000	Melt-down, No fracturing

Note :

1) Tests for cinematographies
2) The amount of air was not enough for sufficient oxidation.
3) Water was injected after heatup.

(1) Modes of Fuel Rod Relocation

Neither significant deformation nor melting was observed in the post-test fuel rod which was subjected to an energy deposition of 180 cal/g·UO_2, regardless of environmental gas. The peak cladding temperature was found to be lower than the melting temperature of β-Zircaloy. Above 210 cal/g·UO_2 which resulted in cladding temperature higher than the melting temperature of β-Zircaloy, two types of fuel rod relocation modes were revealed: cladding azimuthal flow and cladding melt-down, as indicated in Table II.

(i) Azimuthal Flow of Cladding

In an oxidizing environment of steam, the cladding was oxidized and azimuthal flow of cladding was evident when the test fuel rod was subjected to an energy deposition of 210 cal/g·UO_2 as seen in Test No. 3. No significant axial flow of the cladding was observable. The post-test fuel rod appearance is shown in Fig. 3. Peak cladding temperature was estimated from metallographies to be between the melting temperature of β-Zircaloy and that of oxygen-stabilized α-Zircaloy, i.e. 1850 °C and 1950 °C, respectively. The method of the temperature estimation has been reported elsewhere /3/. The cross-sections of the rod and the cladding microstructures are presented in Fig. 4. The azimuthal flow was apparently caused by β-Zircaloy melting. The solid combined oxidation layers of α-Zircaloy and Zircaloy oxide at the outer surface are thought to have been about 100 μm thick upon β-Zircaloy melting, and seem to have worked as a crucible for the melt.

Then, test fuel rods with cladding slightly pre-oxidized at the outer surface were examined in a helium environment in Test Nos. 4 and 5 in order to confirm the solid layer's role, as well as to study the fuel rod behavior under a steam starvation condition. The test results indicated that the azimuthal flow occurred even in the cladding with only 15 μm of initial oxide thickness if the cladding temperature was between the melting temperatures of β-Zircaloy and α-Zircaloy. The original oxygen in the oxide phase diffuses into metallic part of the cladding to produce oxygen-stabilized α-phase during the heatup, therefore, the melt of β-Zircaloy can be covered with solid α-Zircaloy layer at the outer surface. The α-Zircaloy was as thick as approximately 100 μm and no oxide film was observable in the post-test fuel rod. In this case the solid α-Zircaloy layer is presumed to have worked as a crucible.

In the next, a fuel rod with cladding previously-oxidized to almost 100 μm was subjected to an energy deposition of 250 cal/g·UO_2 in a helium environment in Test No. 6. The azimuthal flow occurred above the melting temperature of α-Zircaloy. In the post-test fuel rod, the oxide layer thickness at the outer surface was approximately 100 μm. A small amount of air seemed to have been included in the environmental gas of helium, therefore, the diffusion of oxygen in the oxide phase is thought to have been compensated by the additional oxidation, resulting in the same oxide layer thickness as the original one. Then, the oxide film of about 100 μm worked as a crucible in this case, since α-Zircaloy was completely molten.

(ii) Melt-down of Cladding

Two types of melt-down of cladding were observed according to the velocity of the melt-down, namely, flow-down and move-down. A typical cladding flow-down was observed in Test Nos. 8 and 11 in which the test fuel rods were irradiated in a helium environment at energy depositions of 210 cal/g·UO_2 and 250 cal/g·UO_2, respectively. As seen in Fig. 3, the molten cladding flowed down along the rod surface and refroze in the non-heated region. Only a thin layer of once-molten cladding remained in the heated region in contact with UO_2 pellets.

The cinematography showed that the melt flowed down very fast as water does, suggesting very low viscosity of the melt. All of the fuel pellets remained in place during the transient, glued together by the thin layer of the melt. The peak cladding temperature was metallurgically estimated to be between 1850 °C and 1950 °C in Test No. 8, although the temperature higher than 1950 °C was obvious in the very thin layer of the cladding in contact with the UO_2. In this case, no oxidation layer was observed at the outer surface, thus the melt of β-Zircaloy flowed down. The cross-sections of the post-test fuel rod and cladding microstructure in Test No. 8 are shown in Fig. 5.

In Test No. 11, the peak cladding temperature was above 1950 °C, and the cladding was oxidized at the outer surface, since a small amount of air seemed to have been mixed in helium. However, the thickness of the oxide layer was estimated to be negligibly small to keep the melt within the oxide, when the flow-down was initiated just after the melting of α-Zircaloy. As can be expected from the above results, the cladding flow-down was evident when fuel rods with the cladding previously oxidized to form oxide film of 10∿30 μm were examined in a helium environment at an energy deposition of 250 cal/g·UO_2 in Test Nos. 12 and 14. In this case, oxygen in the original oxide diffused into the metallic region to form α-Zircaloy and the cladding temperature exceeded the melting temperature of α-Zircaloy.

Another type of cladding melt-down was observed in Test No. 10 when the fuel rod previously pressurized to 2 MPa was examined in an air to visually observe the process of the fuel damage. Some amounts of molten cladding were pushed out through a burst opening and moved down slowly along the outer surface and froze in the non-heated region, following cladding burst. Figure 6 shows the representative pictures of flow-down process as well as move-down process printed from the slow motion films. The post-test fuel rod in Test No. 10 is shown in Fig. 3. The similar molten cladding move-down is thought to have occurred in Test No. 7, since the fuel rod was previously pressurized to 7 MPa. As mentioned previously, the azimuthal flow was observed in a steam, namely, oxidizing environment. However, the cladding melt-down is also possible in an oxidizing environment if a burst opening exists. For the same reason, if the oxide layer breaks during the transient, the melt would come out through the broken part of the cladding and move down along the outer surface.

The velocity of the cladding melt-down and the volume of the molten-down cladding appear to become greater with increase in temperature and decrease in the extent of oxidation, judging from the cinematography and the post-test examination.

(iii) Criterion for Fuel Rod Relocation

It is important to study the modes of fuel rod relocation for a postulated LOCA-initiated severe accident, since the mode of fuel rod relocation may determine the subsequent progression of the accident. The extensive experimental efforts have been made in the NSRR to determine the mode of fuel rod relocation as described in the preceeding subsections.

The test results clearly showed that the mode of fuel rod relocation was affected strongly by

(1) energy deposition, namely, maximum cladding temperature,
(2) environment gas or pre-oxidation, namely, the extent of cladding oxidation, and
(3) internal fuel rod pressure, namely, whether a burst opening exists or not.

The results can be summarized roughly as shown in Fig. 7. No significant relocation was possible below the melting temperature of Zircaloy. The cladding melting is said to be initiated at about 1300 °C by the UO_2-Zircaloy reaction [47]. However, the solid layer is generally left outside the melt and protects unnegligible relocation of the cladding. Therefore, the threshold temperature

of the fuel rod relocation is thought to be the melting temperature of β-Zircaloy, independent of heating rate and environment gas. Above the melting temperature of β-Zircaloy, the azimuthal cladding flow takes place if the melt is completely covered with solid layers of approximately 100 μm or more, since the solid layers work as a crucible. The solid layers are Zircaloy oxide for the temperature over 1950 °C, oxygen-stabilized α-Zircaloy and their combined layers for temperature range of 1850∿1950 °C. Without significant amount of solid layers, the cladding melt-down was observed in the experiments above the melting temperature of Zircaloy. Minimum thickness of the solid layers to prevent the melt-down is not obtained yet. The melt-down is possible also in an oxidizing environment if the cladding bursts or the oxide layer is broken, when the cladding still keeps high temperature over the melting point of metallic Zircaloy.

In comparison with the results of the ex-reactor severe fuel damage experiments performed at KfK, the fuel rod seems to be damaged more severely and the melt-down of the cladding is likely to occur in the ex-reactor experiments. In other words, the oxide film at the outer surface of the cladding appears to be stronger to keep the melt within the oxide in the NSRR experiments. The difference may be associated with the difference in the heating rate.

No significant amount of UO_2 fuel relocation was observed in any of the experiments. All of the fuel pellets were found by the cinematography to remain in place during any of the transients, and almost all of the pellets were in original shape in the post-test observation with an exception of fracturing. Metallurgically, the cladding melt, of course, included (U-rich, Zr) metal and (U-rich, Zr) oxide in the matrix, depending on temperature, and the UO_2 fuel contained apparent uranium metal and zirconium composition in some extent. However, the amount of the UO_2 dissolution observed is obviously too small to cause a significant amount of fuel pellet relocation. The peak cladding temperatures attained in the present study ranged from 1600 °C to 2200 °C. Then, a different type of the fuel rod relocation may be possible above 2400 °C, since the pseudo-binary phase diagram between α-Zircaloy and UO_2 developed in KfK /5/ suggests large amount of UO_2 dissolution insuccessively above 2400 °C. Figure 8 shows the UO_2-Zircaloy reaction at the UO_2 / Zircaloy interface in the meta-sample of Test No. 9. As indicated in the figure, small precipitates of (U-rich, Zr) oxide are present in oxygen-stabilized α-Zircaloy. The concentration of the precipitates changes abruptly at the dotted line superimposed in the figure. The peak temperature was estimated metallurgically to be about 2400 °C at the interface and below 2400 °C outside the dotted line. As can be expected from the figure, a large amount of UO_2 can be dissolved in the molten cladding above 2400 °C, which might result in fuel pellet relocation.

(2) Fuel Rod Damage upon Flooding

In a specific test of Test No. 15, water was injected just after the fuel rod attained its maximum temperature, simulating a reflood phase to be obtained by the delayed functioning of ECCS. The cinematography clearly showed that no immediate quench occurred when the cladding temperature was approximately 1800 °C upon flooding. It was also found that the fuel rod was not fractured during the transient although the molten cladding flowed down before the water injection. The post-test fuel rod was severely embrittled, then the rod was completely broken into several pieces during the process of decapsuling and the broken pieces were fragmented in further smaller particles with an average diameter of about 1 mm in the process of fuel rod handling, as shown in Fig. 9. These results imply that external mechanical force like hydraulic vibration other than thermal shock or its stress is needed for fuel fracture when a fuel rod was fixed at one side. On the other hand, fuel debris with a particle size of about 1 mm is likely to be formed by rather small mechanical force, if a

fuel rod is once heated up to the significantly elevated temperature and then cooled down.

CONCLUSIONS

The major conclusions are as follows;

(1) Cladding azimuthal flow is evident in an oxidizing environment, unless oxide film at the outer surface breaks or cladding bursts. On the other hand, cladding melt-down occurs in an unoxidizing or incomplete oxidizing environment. The oxide film break or cladding burst results in the cladding melt-down even in an oxidizing environment.
(2) The threshold temperature for these relocation is the melting temperature of metallic Zircaloy.
(3) A certain extent of oxidation layers at outer surface of a fuel rod prevents the melt-down since the oxidation layers work as a crucible.
(4) The flow-down of molten cladding is very fast as water flows down, while the move-down of molten cladding appears to be much slower.
(5) Immediate quench or fuel fracture does not occur upon flooding when cladding temperature is about 1800 °C. External mechanical force is needed for fuel fracture or fragmentation.

ACKNOWLEDGEMENTS

Thanks are due Messrs. T. Tsuruta and T. Nakamura and NSRR staff for their assistance in performing the experiments.

REFERENCES

/1/ S. Saito, et al.; "Development of In-reactor Fuel Behavior Observation Facility", J. Nucl. Sci. Tech., 18, No. 6, (1981).
/2/ S. Saito, et al.; "Measurement and Evaluation on Pulsing Characteristics and Experimental Capability of NSRR", ibid., 14, No. 3, (1977).
/3/ S. Shiozawa, S. Saito, et al.; "Zircaloy-UO_2 and -Water Reactions and Cladding Temperature Estimation for Rapidly Heated Fuel Rods under an RIA Condition", ibid. 19, No. 5 (1982).
/4/ P. Hofmann, et al; "The Kinetics of the Uranium Dioxide-Zircaloy Reactions at High Temperatures", J. Nucl. Mater. 87 (1979).
/5/ P. Hofmann, et al; "Konstitution und Reaktionsverhalten von LWR-Materialien beim Coreschmelzen" PNS Halbjahresbericht 1974-2, KfK-2130 (1974).

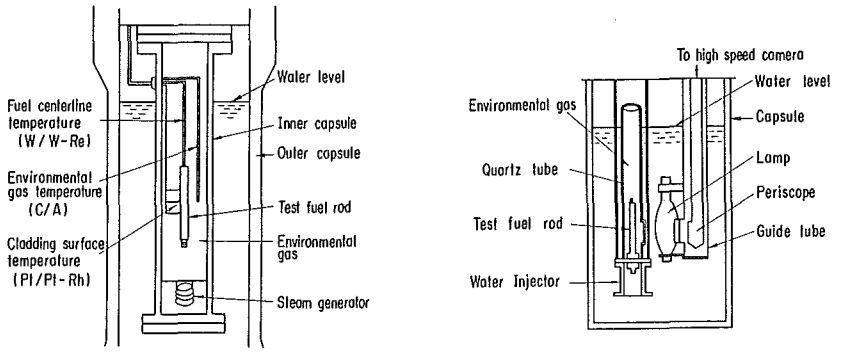

(a) For Standard Test (b) For Cinematography Test

Fig. 1 Schematic Arrangement of Test Section.

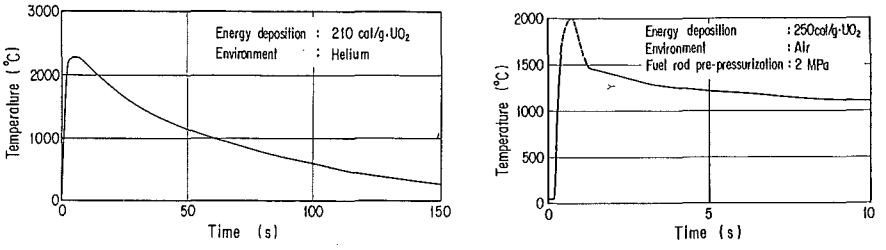

(a) Fuel Centerline (b) Cladding Outer Surface

Fig. 2 Typical Measured Temperature Histories of (a) Fuel Centerline and (b) Cladding Outer Surface.

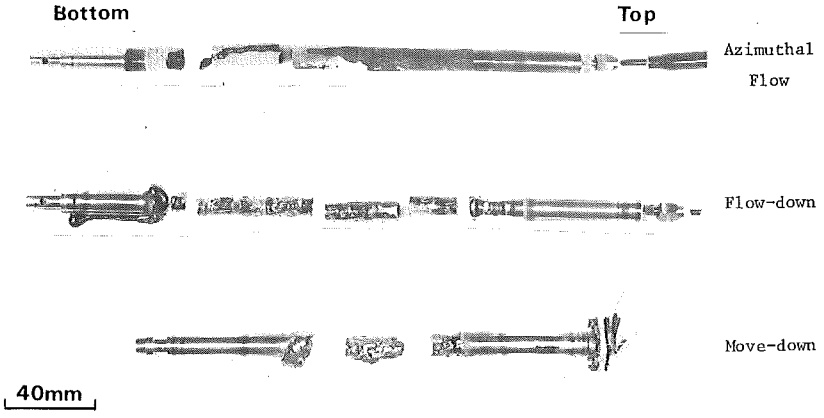

Fig. 3 Post-test Fuel Rod Appearances Showing Fuel Rod Relocation.

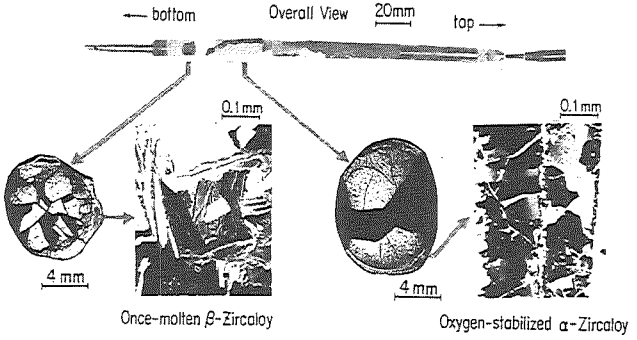

Fig. 4 Cross-sectional Views and Cladding Microstructures in the Fuel Rod of Which Cladding Flowed Azimuthally. (Test No. 3, 210 cal/g·UO_2, in Steam)

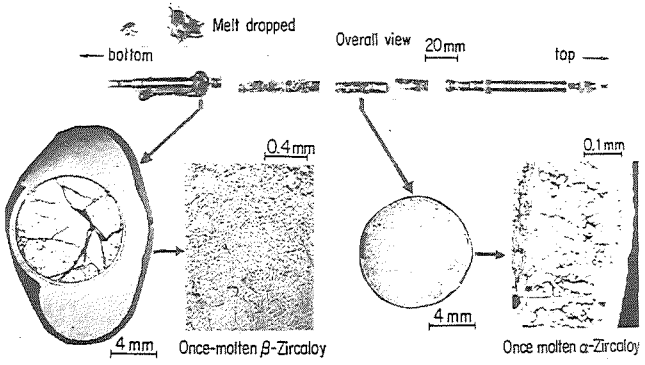

Fig. 5 Cross-sectional Views and Cladding Microstructures in the Fuel Rod of Which Cladding Flowed Down. (Test No. 8, 210 cal/g·UO_2, in Helium)

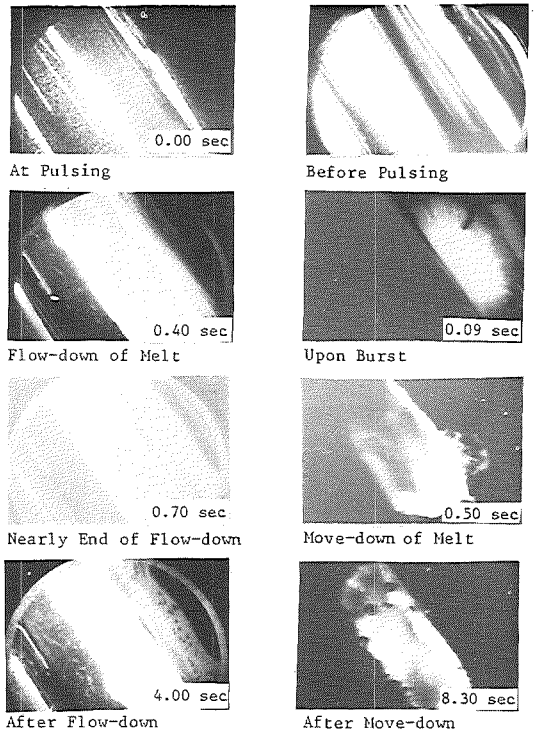

Fig. 6 Representative Pictures Printed from Slow Motion Films, Showing a) Flow-down and b) Move-down. (Time indicates the time after pulsing.)

Peak Cladding Temperature (°C)	Status of Cladding at Melting			
	Cladding Burst or Oxide Break	No Cladding Burst and No Oxide Break		
		No. Oxidation	Limited Oxidation	Heavy Oxidation
			Only α-Zr (O) 100μm	ZrO_2 100 μm
<1850		○ 2	No Relocation	○ 1
1850 ∫ 1950	○ 7	○ 8	?	○ 4 ○ 5 Azimuthal Flow ○ 3
1950 ∫ 2200	○ 10	○ 13	○ 11	○ 9,12 14,15 ? ○ 6

(Open circles and associated figures indicate data points and Test Nos, respectively.)

Fig. 7 Simplified Criterion for Cladding Relocation.

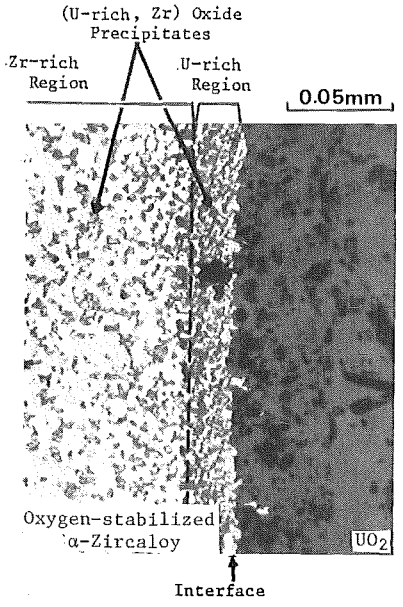

Fig. 8 UO_2-Zircaloy Reaction at UO_2/Zircaloy Interface, Showing Abrupt Change in Amount of UO_2 Dissolution. (Test No. 9, 220 cal/g·UO_2, in Air)

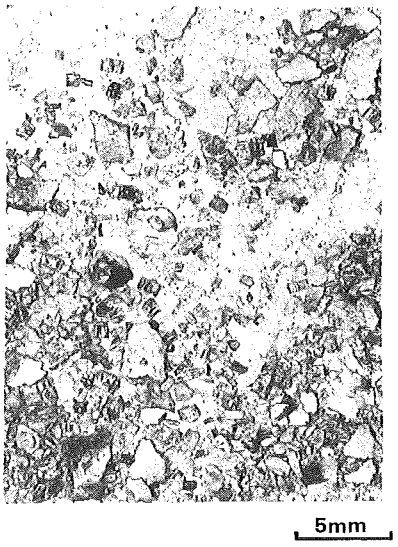

Fig. 9 Fuel Rod Fragments after Flooding Test. (Test No. 15, 220 cal/g·UO_2, in Air, Water Injected)

ANALYSIS OF THE FUEL HEATUP AND MELTING EXPERIMENTS NIELS-CORA WITH THE CODE SYSTEM SSYST-4*

U. Lang, F. Schmidt, R. Bisanz

Institut für Kernenergetik und Energiesysteme (IKE),
University of Stuttgart, Pfaffenwaldring 31, 7000 Stuttgart 80, FRG

H. Borgwaldt

Institut für Neutronenphysik und Reaktortechnik
Kernforschungszentrum Karlsruhe GmbH, 7500 Karlsruhe 1, FRG

ABSTRACT

The ESSI-1 fuel rod heatup and melting experiment was analysed by the SSYST-EXMEL Code System. The analysis revealed good agreement between calculations and experimental results up to the heavy burning of the Zr-H_2O reaction. During this analysis several areas were identified, where improvements of SSYST-3 were necessary to allow satisfactory interpretations of the NIELS-CORA melting experiments. These improvements will enable the SSYST system to model fuel rod behavior under severe accident conditions, that is up to about 2 500 K. The improved system SSYST-4 is under validation by recalculating several of the ESSI-experiments with special emphasis on ESA-1.X and ESSI-4. The present paper discusses the main improvements of SSYST and demonstrates the importance of the new modeling by comparisons of calculated and measured data.

INTRODUCTION

The code system SSYST was originally developed in a common effort by the University of Stuttgart (IKE) and the PNS of the Karlsruhe Nuclear Research Center. The original purpose of the system was the detailed analysis of fuel rods under LBLOCA conditions (maximum temperatures less than 1500 K) /1/. An improved version of the system (SSYST-2) was made available by PNS for the NEA data bank /2/.

Recent development of SSYST resulted in a package to perform statistic analysis and a more detailed modeling of the zirconium oxidation process. This version of the system is known as SSYST-3 and concludes the modeling of LBLOCA behavior in SSYST /3/.

---

*Work performed under contract of Projekt Nukleare Sicherheit (PNS)

The behavior of fuel rods in higher temperature ranges (severe fuel damage) was originally investigated experimentally by Hagen /4/ and modeled in the EXMEL system /5/. The increased interest in understanding of severe fuel damage resulted in the planning of series of fuel rod melting experiments in the NIELS and CORA setups of Hagen. The new experiments can partly be analysed by a combination of SSYST and EXMEL modules. This was demonstrated by an analysis of the ESSI-1 experiment. However, the analysis also revealed the necessity of further improvements and adaptions of the module system and the data acquisition. As all the previous versions, the new system SSYST-4, uses the RSYST-1 software technique /6/. The envisaged purpose of SSYST-4 is to analyse single rods under LOCA- and SFD-conditions.

SSYST-4 MODULE SEQUENCE FOR SFD SIMULATION

During SFD-accidents temperatures up to 2500 K are reached. Therefore under SFD conditions physical effects become relevant, which had not to be modeled in the frame of earlier SSYST versions. To simulate the behavior of fuel rods during the heatup and melting phase presently new models which treat these effects are added to SSYST-3 to build SSYST-4.

Besides the refinements in physical modeling adaptions of modules to better fit geometries of the experimental setups became necessary. This will allow a better understanding of the new experiments and also help to analyze more precisely the qualitative experimental results.

Earlier versions of most of the new SSYST-4 modules have been available as part of the EXMEL system and are now included into the SSYST-3 environment. The resulting module sequence, which used for calculation of the ESA-1.X experiment, is shown in Fig. 1. Only a short description of the modules will be given.

MODULE EWQUEL

The module serves to determine the spatial density of heat sources in electrical heaters and fuel rod simulators. Measured electrical tension or current can be used as input. Due to the modular concept of RSYST additional heat sources may be added through other modules.

MODULE DEHN

The module considers radial thermal expansion effects in fuel rods and in multi-layer rod simulators. The outermost gap is treated separately. The deformation computed with DEHN may be combined with other contributions to deformation.

MODULE WALTRA2D

WALTRA2D solves the transient heat transport equation for a 2-dimensional (r,z) grid and, thus, is a generalized version of ZET-2D. The generalization, necessary for modeling SFD experiments, concerns the consideration of radiative heat transport in axial gaps, anisotropic heat conduction, and more complex interfacing with the rest of physical models.

MODULE OXI

In a similar sense, this module is a generalized version of ZIRKOX. Main changes are the consideration of steam starvation and of oxidation on all free surfaces. In the case of 2-sided oxidation, which occurs in experiments, this means simulation of 2 oxidation fronts, which may meet somewhere. Another distinguishing feature of OXI is the extension of modeling to an arbitratry number of oxidable materials distributed over the free surfaces.

MODULE BOFF

This new module serves to model heat and mass transfer between oxidizing cladding and steam in a coolant channel under boil-off conditions. It is a single-channel model, and - as typical for SFD conditions - steam velocity is assumed to be low.

The purpose of BOFF is to model the concentration of steam and generated hydrogen in the channel near the cladding surface. Of special interest are the phenomena of steam starvation and hydrogen blanketing, which influence decisively oxidation kinetics under SFD conditions.

The model considers convective heat transfer between channel and surface and radiative heat transport between opposite surfaces. Zircaloy oxidation contributes to both, the heat balance in the gas volume near a surface and to a change of the local steam/hydrodgen concentrations. Special versions of the module exist which allow the simulation of other coolant gases like Ar, He or oxigen.

MODULE SABAN

SABAN is a first attempt to model the formation of liquified phases, e.g. dissolving a surface layer of UO_2 by molten zircaloy. Also modeled is the accompanying so-called candling, i.e. downflow of liquified rod areas and freezing out in lower, colder zones.

Essentially, SABAN treats the liquified phase of molten Zircaloy and dissolved fuel as being contained by a shroud of ZrO_2. Dissolving of the fuel is handled, quite conveniently, as a diffusion process with appropriate diffusion coefficients depending on temperature /5/.

DESCRIPTION OF ESSI-1 EXPERIMENT

The ESSI-1 experiment is part of an out-of-pile program using electrically heated fuel rod simulators. The temperature escalation was caused by the exothermal zircaloy/steam reaction, whose reaction rate increases exponentially with the temperature.

Different oxide layers as a major parameter to influence the temperature escalation were obtained by varying the heatup rates and steam exposure times /7/. Fig. 2 shows the side cross section of the fuel rod simulators with shroud and insulation. The fuel rod simulator corresponds to German PWR dimensions. The length of the simulator was 0.25 m. To simulate the exothermal reaction energy of neighbouring rods a zircaloy shroud was instaled around the fuel rod simulators.

To inhibit radial heat losses the simulator and shroud were surrounded by fiber ceramic insulation consisting of ZrO_2 and Al_2O_3/SiO_2.

Preheated steam was led to the shroud through a double tube system at the lower end of the annular channel surrounding the fuel rod simulator. Temperatures on the surfaces of the rod and shroud were measured by two color pyrometers 140 mm above the lower end of the rod.

Test ESSI-1 was intended to have a minimum initial oxide thickness and thus the rod was heated in argon, until the surface temperature reached about 2000 K. Only then steam was introduced. The rod temperature increase due to the zircaloy/steam reaction increased the rod resistance, which caused a decreased current and input power. After the reaction stopped, steam cooling significantly lowered the rod temperature, decreasing the resistivity and thus increasing the input current and power.

The ESSI-1 experiment was chosen to define both further modeling and data aquisition needs.

COMPARISON OF EXPERIMENTAL AND CALCULATIONAL RESULT

The heatup phase was recalculated with different mass flows in the circumferential flow channels to simulate the influence of natural convection around the insulation. Higher mass flows led to an axial asymmetric temperature distribution in the fuel rod simulator. The temperature of the rod before the escalation occured was also lowered significantly by this measure /8/.

It could be also seen from the calculations that the axial temperature asymmetry is strongly influenced by the boundary conditions at the upper and lower bound of the fuel rod simulator.

During the oxidation phase the distribution of vapor inflow was varied between the two circumferential channels. Vapor input only to the channel between rod and Zr-shroud lead to the temperature history shown in Fig. 3, which agreed best with the measured temperatures. With 10 % of the vapor mass flow in the second channel between Zr-shroud and insulation a strong temperature increase could be noted. The reason is the doubling of the released oxidation energy by allowing a two-sided oxidation of the Zr-shroud to take place. As the rod and shroud were not preoxidized, a strong metal-

water reaction used all the oxigen in the lower third of the channel between shroud and insulation. Locally the temperature in the shroud raised above the clad temperature and resulted in an increase of clad temperature by radiation coupling.

CONCLUSIONS FROM THE ESSI-1 CALCULATIONS

The following conclusions were drawn from the ESSI-1 calculations:

- As in earlier comparisons /5/, good overall agreement could be reached between measured and calculated temperatures during the heating phase. However, the local temperature history is strongly influenced by initial conditions, e.g. initial temperatures, boundary conditions, e.g. mass flow of gas or heat flux at the upper and lower ends of both, rod and shroud, and material properties, e.g. heat conductivity in the insulation.

- The temperature escalation during the oxidation phase appeared to be limited during both, experiments and calculations.

- Modeling in the past did not allow a detailed explanation of the limiting effects. Several concurrent effects were identified, which have to be investigated simultaneously. To distinguish between different effects, both, local temperatures and local oxigen supply have to be modeled quite accurately. Therefore, a more detailed description of the oxidation process seems to be desirable only, if a refined description of the local steam and H_2 supply from both, a thermalhydraulic and a diffusion point of view is available.

As a consequence from these conclusions, a new series of experiments was designed. It is called ESA-1.X. The main goal of the new experiments is to have experiments with well understood and documented initial and boundary conditions and to provide a variety of measured data to further improve the calculational models.

DESCRIPTION OF ESA-1.1 EXPERIMENTS

The ESA-1.X experiment series was designed to take into account the results and conclusions, that were drawn after recalculating the ESSI-1 experiment. The different experiments of this series are performed with varied atmospheres. ESA-1.1 used argon during the whole experiment, whereas vapor and oxigen atmospheres are planned for further experiments.

The geometrical design differs from that of the ESSI-1 experiment. The second flow channel was removed to supress the influence of additional heat sources by oxidation, or the influence of natural convection flow in that channel. The Zr-shroud is in the same position as in the ESSI-1 experiment. The insulation is in direct contact with the outer surface of the shroud.

At constant flow rate, argon flows at the bottom end into the channel

during the whole experiment. The flow rate as well as the temperature of the heated argon was measured to have a defined flow situation. Top, bottom and outer boundary conditions defined the temperatures of tungsten heater, clad, shroud and insulation, which were measured during the whole experiment. Additional temperatures were measured at different axial positions on the shroud and clad surface as well as in the flow channel and in the insulation. The measurements were performed using thermocouples and color pyrometers.

The ESA-1.1 experiment was carried out in 3 major phases. The first phase of 6000 s with nearly no electrical power input was done to have appropriate initial conditions. During the second phase with a duration of approximatelly 2700 s a temperature equilibrium with clad surface temperatures of 740 K was reached. In the third phase (2400 s) the electrical power input was raised continuously from 100 to 2700 W. Selected measured temperatures are shown in Fig. 4.

COMPARISON OF EXPERIMENTAL AND CALCULATIONAL RESULTS

The recalculation of the ESA-1.1 experiment was started after the first 6000 s of experiment time. Initial and boundary conditions were estimated from measured temperatures at the boundary and in the different axial and radial positions of the experimental facility. The energy source distribution was calculated from the measured electrical current and the actual temperature dependent resistance of the tungsten heater. In comparison with the ESSI-1 modeling the number of modules could be reduced, because the module BOFF for the second channel as well as one heat conduction module WALTRA2D for the separated insulation could be removed.

The consideration of the copper electrodes, which was necessary in the ESSI-1 recalculation could also be removed by considering the measured temperatures at the upper and lower end of the rod simulator as boundary conditions. These simplifications lead to a strong reduction of computational costs compared to the ESSI recalculations. (Problem time to computer time was approximately 50 to 1 on a CRAY-1 M).

The comparison of the calculated and measured clad and shroud temperatures showed an excellent agreement as can be seen in Fig. 5. The measurement points are located at an axial height of 150 mm. The small differences during the first 1500 s of the recalculation result from presumed axial and radial temperature distributions on rod, shroud and insulation. These temperatures might have slightly differed from the real initial conditions.

At other axial levels with measured temperatures the same good agreement of clad and shroud surface temperatures was noted. A variation of material properties of the ZrO_2 fiber insulation revealed a strong influence on the temperature history. A similar effect was much weaker on the ESSI-1 recalculation, because of the decoupling of the second flow channel. Calculations with different values for the radiation emissivity were performed to simulate the influence of varied oxidation of clad and shroud. The result were notable changes of the surface temperatures even at the low temperatures of the second phase of the experiment. The best agreement between measu-

sured and calculated temperatures was obtained asuming an emissivity of nonoxidized Zr at lower temperatures changing to ZrO_2 property at higher temperatures.

As the first experiment of the ESA-1.X series was done in argon atmosphere no energy production by metal/water reaction occured.

As the calculations used measured temperatures as boundary conditions, the computations could only be done as long as the thermocouples delivered values.

The temperature distributions in the fuel rod simulator, as well as in the Zr-shroud and insulation at the end of the calculation time are shown in Fig. 6 and 7.

CONCLUSIONS FROM THE ESA-1.1 CALCULATIONS

- Temperature distributions during the experiment can be reproduced almost as accurate as the measured results. However, this requires a good understanding of the experiment and a fairy good knowledge about initial and boundary conditions.

- The well defined boundary and initial conditions in the ESA-1.1 experiment were also necessary to separate effects of the various parameters influencing the temperature distribution. Thus, the ESA-1.1 experiment and recalculations will be the basis to analyze ESA-1.X experiments under oxidizing atmospheres.

- Several effects are still not yet understood completely. They cause differences of measured and calculated temperatures in the order of 50 K. This will be investigated further.

- An extension of the analyses to higher temperature ranges (after melting of the thermocouples at the boundaries) is in preparation.

These conclusions are also supported by calculations, which were done for the ESSI-4 experiment.

REFERENCES

/1/ W. Gulden et a.: "Dokumentation SSYST-1", KfK 2496 and IKE 2-32 (1977)

/2/ SSYST-2, Modular System for Transient Fuel Rod Behavior under Accident Conditions, Nuclear Data Base Abstract NEA 0648 (1983)

/3/ H. Borgwaldt, W. Gulden: "SSYST, A Code System for Analysing Transient LWR Fuel Rod Behavior under Off-normal Conditions" in : Water Reactor Fuel Element Performance Computer Modeling, ed. by J. Gittus, Applied Science Pub., 1983
R. Meyder: "SSYST 3 Eingabebeschreibung und Handhabung",KfK 3654 (1983)

/4/ S. Hagen: "Out-of Pile Experiments on the High Temperature Behavior of Zry-4 Clad Fuel Rods", KFK 3567 (1983)

/5/ R. Bisanz, F. Schmidt, R. Rühle, H. Unger: "Fuel Rod Modeling Under Severe Core Damage Conditions" in: Water Reactor Fuel Element Performance Computer Modeling ed. by J. Gittus, Applied Science Pub., 1983

/6/ R. Rühle: "RSYST, ein integriertes Modulsystem mit Datenbasis zur automatisierten Berechnung von Kernraktoren", IKE-Bericht Nr. 4-12, 1973

/7/ S. Hagen, H. Malauschek, K.P. Wallenfels, S.O. Peck: "Temperature Escalation in PWR Fuel Rod Simulators due to the Zircaloy/Steam Reaction: Tests ESSI-1, 2, 3", KfK 3507 (1983)

/8/ U. Lang, F. Schmidt, R. Bisanz, W. Scheuermann, W. Gulden: "SSYST-EXMEL Rechnungen zur Interpretation des ESSI-1 Experiments", unpublished report 1983

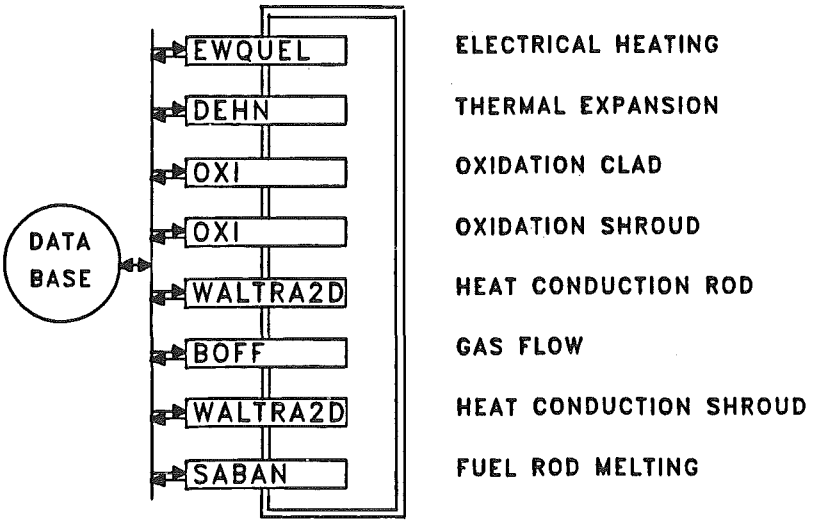

FIG. 1 SSYST-4 SEQUENCE FOR SFD SIMULATION

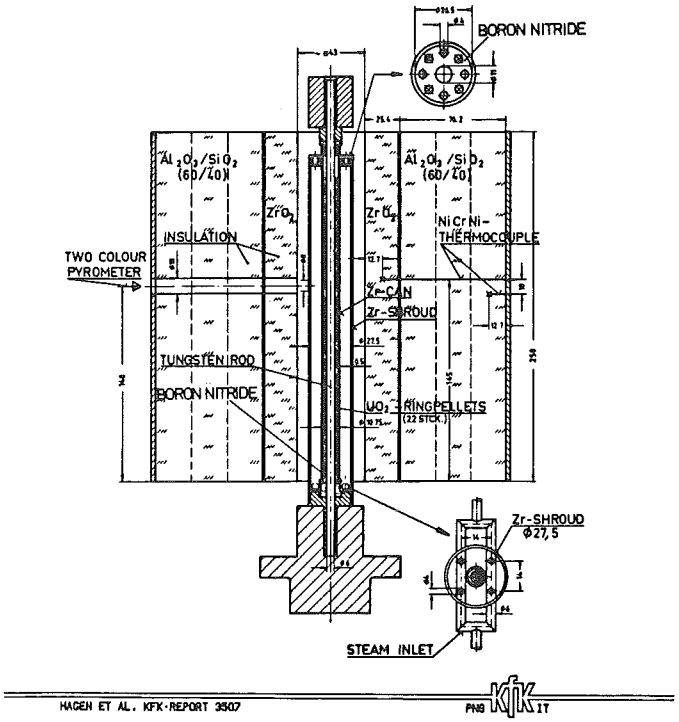

FIG. 2 SIDE CROSS SECTION OF ESSI-1 EXPERIMENT

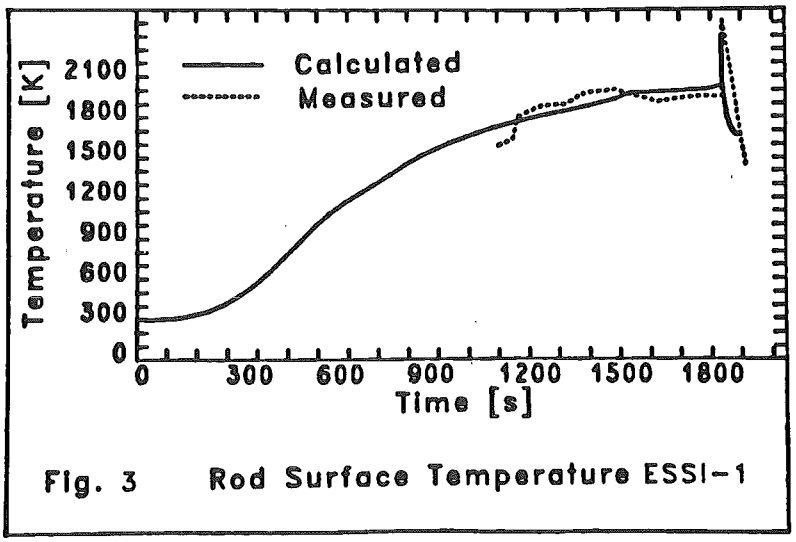

Fig. 3 Rod Surface Temperature ESSI-1

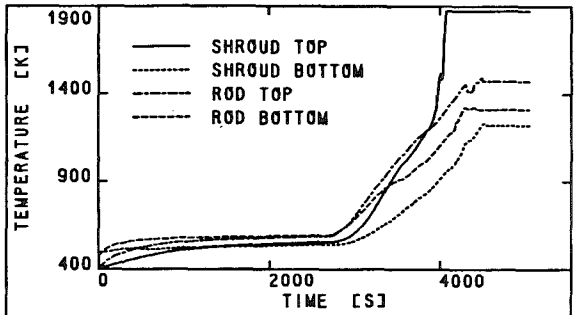

FIG. 4 MEASURED TEMPERATURES ESA-1.1

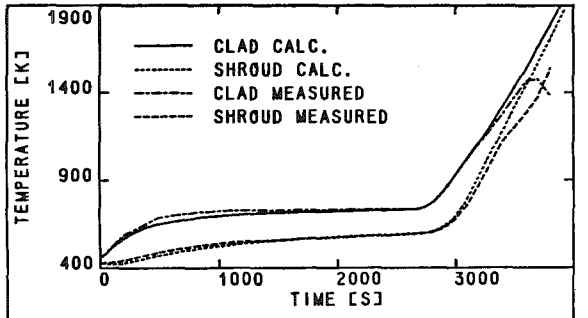

FIG. 5 SURFACE TEMPERATURES ESA-1.1

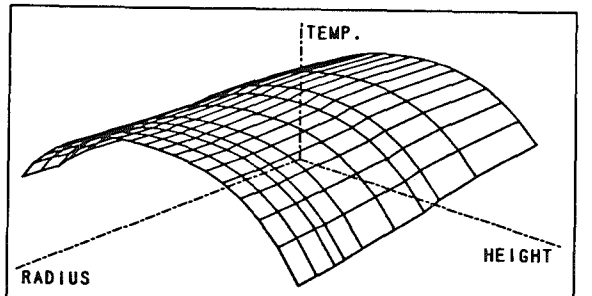

FIG. 6 ROD TEMPERATURE ESA-1.1

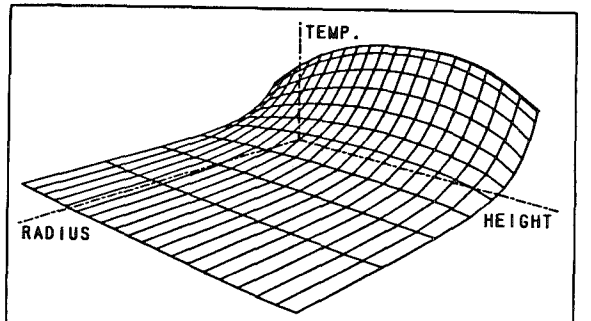

FIG. 7 SHROUD TEMPERATURE ESA-1.1

AN ANALYSIS OF CORE MELTDOWN ACCIDENTS FOR BWRS*

S. H. Kim

R. P. Taleyarkhan

M. Z. Podowski

R. T. Lahey, Jr.

Department of Nuclear Engineering
Rensselaer Polytechnic Institute
Troy, New York 12180-3590 USA

ABSTRACT

A new computer code for the analysis of BWR degraded core phenomena, MELRPI, has been developed at Rensselaer Polytechnic Institute under sponsorship by Oak Ridge National Laboratory. The MELRPI code uses a mechanistic approach to modeling such phenomena as heat transfer, coolant thermal-hydraulics for a partially or fully uncovered core, metal oxidation, and the melting/relocation of individual core materials. The purpose of this paper is to highlight differences between MELRPI and the MARCH code, including both the modeling concepts and results. The TQUV BWR accident scenario was used for the numerical comparison. It has been shown that these two codes yield considerably different results.

INTRODUCTION

Because of substantial differences in systems design, the course of a core meltdown accident in a Boiling Water Reactor (BWR) may be considerably different from that in a Pressurized Water Reactor (PWR). Consequently, the analysis of such accidents requires computer codes specifically designed for each reactor type.

The most common analytical tool used in the United States for the overall analysis of degraded core accidents in Light Water Reactors (LWRs) has been the MARCH code. Although MARCH was originally developed for PWRs, it has also been applied, after some modifications, to BWRs. In particular, a BWR version of MARCH[1] was developed at Oak Ridge National Laboratory (ORNL). Since the original modeling concept has not been substantially changed, the BWR version of MARCH still uses a number of simplistic, nonmechanistic models.

---

*Work sponsored by the Severe Accident Sequence Analysis (SASA) Program at Oak Ridge National Laboratory (ORNL) under the Containment Systems Research Branch at the Division of Accident Evaluation, Office of Nuclear Regulatory Research.

In order to overcome some of the deficiencies implicit in MARCH, the MELRPI code has been developed at Rensselaer Polytechnic Institute. MELRPI can be used for the analysis of the in-core phenomena during a severe BWR accident, including core heatup, degradation and meltdown, and the release of molten debris into the lower plenum. The various mathematical models used in MELRPI[2-4] are mechanistically-based. They account for such BWR core components as channel boxes and cruciform control rods. Also, a new thermal-hydraulic model for the coolant has been developed specifically for BWR geometry.

The purpose of this paper is to highlight the differences between MARCH and MELRPI, including both the modeling concepts and the results obtained from these two codes. It has been widely hypothesized that MARCH gives conservative results. This, however, has not been substantiated by comparisons with other analytical tools. In this paper, we show various differences between the MELRPI and MARCH results, in such core parameters as temperature and molten mass of various materials, hydrogen production, etc.

DESCRIPTION OF MELRPI

The MELRPI computer code addresses a wide range of problems specific to the BWR design and important for a realistic assessment of the consequences of severe accidents. A brief description of the basic modeling principles used in the development of MELRPI is given below.

Core Nodalization Scheme

The BWR core geometry is modeled by using a two-dimensional, multi-material core nodalization scheme. In the axial direction the core is divided into a user specified number of sections. Each radial zone represents an annulus (except for the cylindrical central zone) containing canisters, fuel rod bundles, and control rods. The number of canisters in each zone can also be set up by the user. Each individual radial zone is represented by an average fuel rod surrounded by two sections of channel walls and a control rod between the adjacent zones. The two sections of channel wall in each node are used to distinguish between the different wall temperatures at the inner and outer boundary of each radial zone.

Core Heat Transfer

The above mentioned nodalization scheme constitutes the basis for a two-dimensional (nodal) model for core heat transfer. Specifically, the following modes of heat transfer are taken into account:

- Transverse Direction. Heat conduction between the fuel and cladding, heat convection and radiation between the fuel rods/channel boxes/control blades and the coolant, and thermal radiation between the fuel rods, channel boxes, and control blades;
- Axial Direction. Node-to-node heat conduction in the fuel, cladding, channel boxes, and control rods.

Concerning the heat transfer outside the core it is assumed that the outer sections of the channel wall in the last radial zone radiate heat to the

core shroud, while the top and bottom nodes radiate heat to the upper and lower vessel structures, respectively. At present, no out-of-core elements of the reactor pressure vessel are modelled in MELRPI, thus the temperatures of the above-mentioned structures are evaluated as follows. The core shroud and the upper structure temperatures are taken as the minimum of the local coolant temperature and the melting temperature of stainless steel. The coolant temperature, in turn, is calculated as either the average steam/hydrogen temperature in the outermost radial zone (for the core shroud), or the steam/hydrogen mixture temperature (for the upper structures). The lower structure is assumed equal to the saturation temperature, since it is assumed that there is always some water left at the bottom of the lower plenum.

The overall multi-node, multi-material model for core heat transfer is given by a system of first order differential equations for such state variables as the: temperatures, amount of oxidized materials, and amount of molten materials.

Coolant Thermal-Hydraulics

Because MELRPI has been developed mainly for the analysis of long-term, slow transients, the model of coolant thermal-hydraulics is limited to the phenomena occuring in the reactor core after the core starts uncovering. In general, two axial core regions are considered: the single-phase/two-phase pool, and the dry steam/hydrogen mixture region. In order to account for the fact that individual fuel bundles are separated from one another by the channel walls, the coolant flow and heat transfer parameters inside the canisters, such as, the evaporation rate, void fraction, and the height of swollen pool level, are evaluated separately for each radial zone. On the other hand, since all radial sections of the interstitial region are interconnected, and the amount of heat transferred into the coolant in this region is relatively small, only one, single-phase level, is evaluated for the entire bypass region. In order to make MELRPI compatible with the MARCH code, another option has also been developed, in which one time-dependent pool level for the entire core can be used as an input parameter.

In the submerged portion of the core, the following modes for heat transfer are considered: single-phase natural convection, nucleate boiling, CHF, transition boiling, and stable film boiling.

In the uncovered core region, a one dimensional model is used in modeling the steam/hydrogen mixture flow. For a given flow rate of saturated steam at the top of the pool, the model evaluates the superheat of the steam flowing to the upper nodes, as well as the rates of steam consumption and hydrogen production due to metal/water reaction. The oxidation rate for both the cladding and canister walls is calculated in MELRPI by the ZRWATR subroutine of MARCH. In addition, a separate model is used for stainless steel oxidation.

Fuel Rod Failure Criteria

Three different fuel failure modes are considered in MELRPI. Two of them deal with clad breach, the third one is related to fuel rod slumping and rubble bed formation. It is assumed that clad rupture occurs when the calculated stress reaches some limiting value. A specific clad failure mechanism depends on whether the difference between the fission gas pressure

inside the clad tube and that of the coolant is either positive or negative. In the case of the former a hoop stress criterion for balooning and rupture is used, while a buckling criterion is applied for the latter. The fuel rod slumping criterion applies when, due to zirc melting and oxidation, the cladding wall section in any particular node is unable to support the weight of the materials in the nodes above. As a result, the node may collapse, forming a localized rubble bed. In MELRPI, the onset of rod slumping is evaluated by using a beam buckling criterion.

Molten Material Relocation Model

In order to account for the relocation of molten zirc and stainless steel, flowing over the walls of fuel rods, canisters, and control rods, a liquid slug model is employed in MELRPI. This model evaluates such parameters of the falling liquified material as: velocity, temperature, and freezing rate. If the core is completely uncovered, the portion of molten material that did not freeze reaches the lower core support plate, and may be dropped into the lower plenum. If the core is only partially uncovered, the molten material is assumed to freeze instantaneously when reaching the pool level. In either case, the thickness of the frozen crust is used to calculate the reduction in the area for coolant flow.

Rubble Bed Model

If the conditions for rubble bed formation are met in an arbitrary node, the intact geometry model for this node is replaced by a rubble bed model. MELRPI uses two basic criteria for rubble bed formation.

- the fuel slumping criterion,
- the quenching criterion, which can be met when hot fuel rod surfaces are suddenly rewetted due to a rising pool level.

The model for a rubblized node is characterized by such parameters as, the node porosity, average temperature, and mass of component materials. It is assumed that molten materials, such as zircaloy and stainless steel, are instantaneously released from the rubblized node. The node height is a function of the node porosity and the mass of solid components, and it can vary with time (specifically, decrease due to melting). When the only component in a node is UO_2, and it starts melting too, it is assumed that the molten fuel fills up the pores in a solid debris. The melting process can propagate both upwards and downwards, with the bottom of the molten fuel region being located at the bottom of the lowest node to reach the melting temperature of UO_2. When molten fuel appears in the bottom nodes of the core, it starts leaking to the lower plenum.

RESULTS OF NUMERICAL CALCULATIONS

The MELRPI computer code was extensively tested for various accident scenarios. The results reported in this paper have been obtained for a TQUV*

*From the Reactor Safety Study, WASH-1400, T = transient, Q = failure of normal feedwater system to provide core make-up water, U = failure of the HPCI to provide core make-up water, V = failure of low pressure ECCS to provide core make-up water.

sequence, with stuck-open relief valve. Such a transient has been selected for the analysis in order to compare the MELRPI calculations with those of the MARCH code. The results obtained from an improved BWR version of MARCH were provided by the Oak Ridge National Laboratory (ORNL). In order to make the two codes compatible, the input parameters to MELRPI, such as the time-dependent system pressure, core steam inflow, and two-phase swollen level history, were taken directly from MARCH and are plotted in Figure 1. Both codes used the ANS curve to evaluate the decay heat power of the reactor. They also used the same oxidation models, based on the Baker-Just and Cathcart correlations.

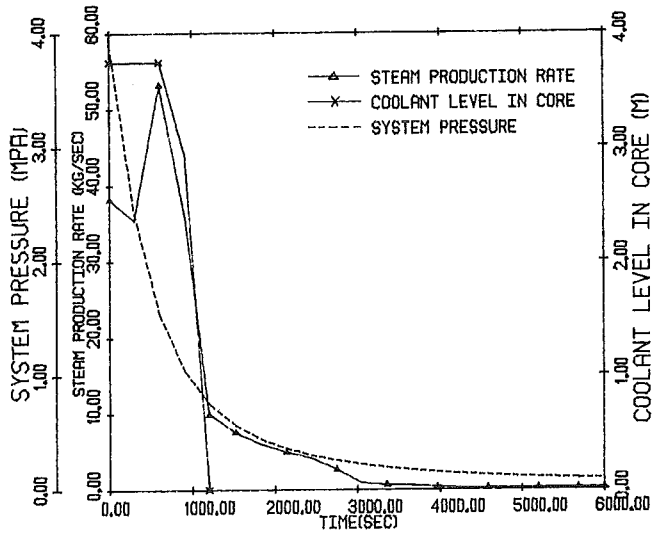

Figure 1. MARCH results used as input to MELRPI.

Two specific runs were made with MELRPI. In the first run, the core nodaliation scheme was identical as in MARCH (i.e., 20 axial nodes and 5 radial nodes) and so was the power distribution. In particular, a bottom-peaked axial power distribution was assumed with the axial peaking factor of 1.19, and a dromedary shape was imposed in the radial direction with the radial peaking factor of 1.10. Calculations were made over the time period from 0 to 7000s. The calculations were stopped after fuel temperature in the hottest node reached the melting point of UO_2 (assumed as 3033K). It should be also mentioned here that the MARCH calculations were stopped after about 5500s (i.e., when 75% of the core materials were completely melted).

The second run utilized a simplified core nodalization scheme, 5 axial and 3 radial nodes. Using the same input parameters as in the previous case, calculations were performed until 20,000s after the accident began. The purpose of this run was to study the sensitivity of calculated parameters to the nodalization scheme used, and also, to obtain long-term results without excessive computer expense.

The results of computer calculations for both runs, as compared with those obtained from MARCH, are shown in Figures 2 through 6. The variations of the fuel temperature for three different locations along the central radial zone: bottom (axial node 1), middle (axial node 10), and top (axial node 20), as calculated by MELRPI (20 x 5 model), are shown in Figure 2. It is interesting to note that the maximum axial fuel temperature is initially reached in the top-most node, which gets uncovered first. This axial temperature distribution eventually changes, so that the melting temperature of UO_2 is reached first in the central node, due to its higher decay heat generation rate. The bottom node temperature remains below those of the central and upper nodes because of two main reasons. One of them is the nodal decay heat generation rate (nodal pecking factor = 0.46). The other reason has to do with radiation heat transfer to the cold (i.e., saturation temperature) lower structures. Next, the midplane temperature in the same radial zone is plotted in Figure 3 for two MELRPI nodalization schemes, node (10,1) for the (20 x 5) model and node (3,1) for the (5 x 3) model, and compared with the MARCH result. As it is seen, both models used in the MELRPI calculations yield similar results for this particular core region. Such a conclusion is not always true, however, as will be shown later. For both nodalization schemes, the fuel temperature obtained from MELRPI rises faster then that from MARCH, especially after the threshold temperature for oxidation (~1250K) is reached. Since these two codes use the same models for oxidation heat generation, it appears that the above mentioned difference is caused by differences in the thermal-hydraulic modeling used in both codes. For instance, in MELRPI, the coolant temperature in the dry region (filled with a superheated steam/hydrogen mixture) is evaluated using mechanistic time-dependent energy and continuity equations, while in MARCH it is calculated in a very simplistic manner. Also, it should be noted that the MARCH calculated fuel temperature is limited to 2673K (4352F), which is the user-supplied melting temperature for a mixture (UO_2, Zr, and ZrO_2) of fuel rod materials, and is significantly lower than the melting point of UO_2. This limitation has been used in MARCH because the fuel and cladding are treated there as a lumped mass and are assumed to remain in place with unaltered geometry until a given (user-specified) fraction of the entire core has become molten.

A typical comparison between the coolant temperatures in the middle of the central radial zone, obtained from MELRPI versus MARCH, is shown in Figure 4. The increase in the temperature calculated by MELRPI closely follows the fuel temperature, including the steepening of the gradient due to the onset of metal/water reaction. As can be seen, the coolant temperature history obtained from MARCH is considerably different from that calculated by MELRPI. In particular, the calculated temporary temperature decrease beginning at about time 3600s in the MARCH results has no known physical basis. The large decrease at time 4500s occurs because the fuel-cladding mixture is predicted to be molten at this time; since a molten node would not actually remain in place, a user-input switch has been positioned to cut off heat transfer from each node whenever it becomes molten. This approach was necessary in MARCH because there is no provision in the code for consideration of the effects of rubble bed formation or fuel relocation within the core.

The amount of hydrogen produced in the reactor core, is shown in Figure 5. Again, a significant difference exists between the MELRPI and MARCH calculations. The model used in MELRPI assumes that, upon melting, the metallic zircaloy gradually drops to the bottom of the core and then is being

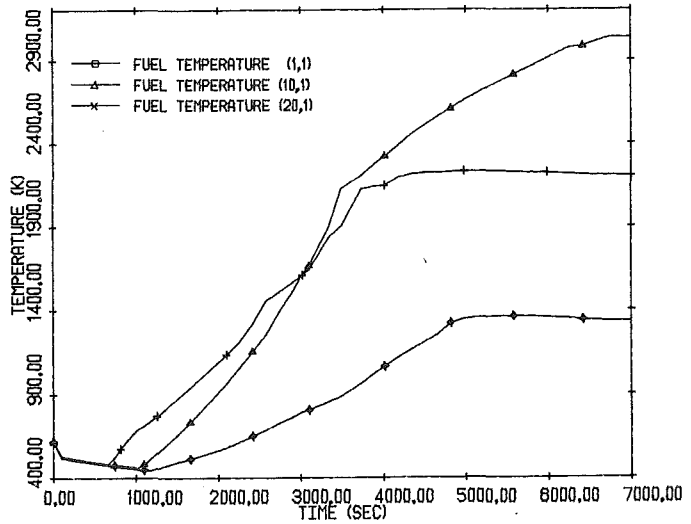

Figure 2. Fuel temperature at various axial locations in the central radial zone of the core, obtained from MELRPI.

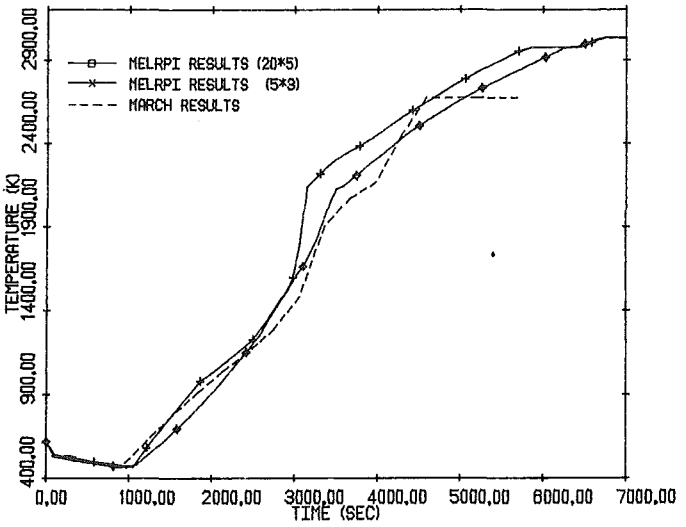

Figure 3. Fuel temperature at the core center; comparison between MELRPI and MARCH calculations.

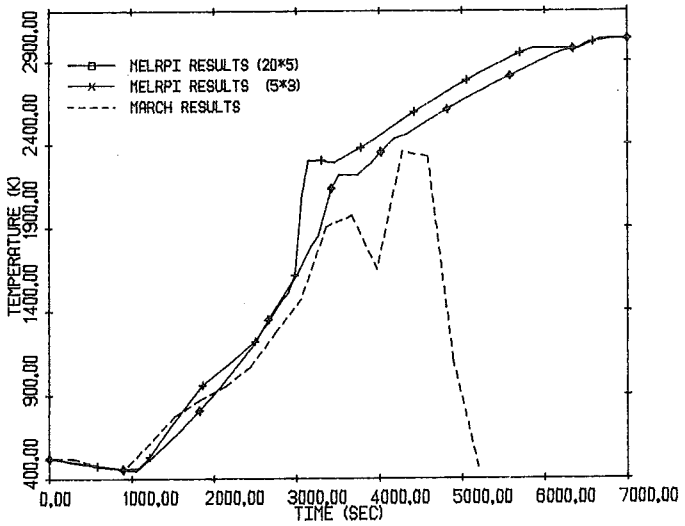

Figure 4. Coolant temperature at the core center; comparison between MELRPI and MARCH calculations.

released to the lower plenum. Hence, its oxidation is limited, and so is the hydrogen production rate. For MARCH results, the metal/water reaction begins earlier because of the lumped mass approach for the fuel and cladding, which produces higher cladding temperatures during the period when the only energy source is decay heat. Once the metal/water reaction begins, however, the lumped mass approach artificially restricts the cladding temperature increase, subsequently reducing the hydrogen generation rate. This is seen in Figure 5 for the period from about 2400s to about 3300s. The rate of increase of the total amount of hydrogen established at that time remains almost constant thereafter. The main reason for that is the assumption made in MARCH that all the melting nodes remain in place, so that the oxidation process of both solid and molten zirc continues in each node until this node becomes completely molten. Although the existing version of MELRPI does not calculate a certain additional amount of hydrogen that can be produced from the molten/freezing zirc oxidation occuring at the bottom of the core and in the lower plenum, it should not drastically change the present MELRPI results. Hence, the mass of hydrogen, as calculated by MARCH, seems to be too conservative.

Another comparison between MELRPI and MARCH is shown in Table-1. Given there is the accident history, described in terms of the time sequence of some characteristic stages of core degradation and meltdown. As can be seen, the MARCH calculations yield considerably different results from those obtained from MELRPI. Also, substantial differences are observed betwen the two nodalization schemes used in MELRPI. The former differences are mainly caused by the fact that lumping a few non-uniformly heated nodes into a single node dramatically changes the temperature distribution of the peripheral nodes.

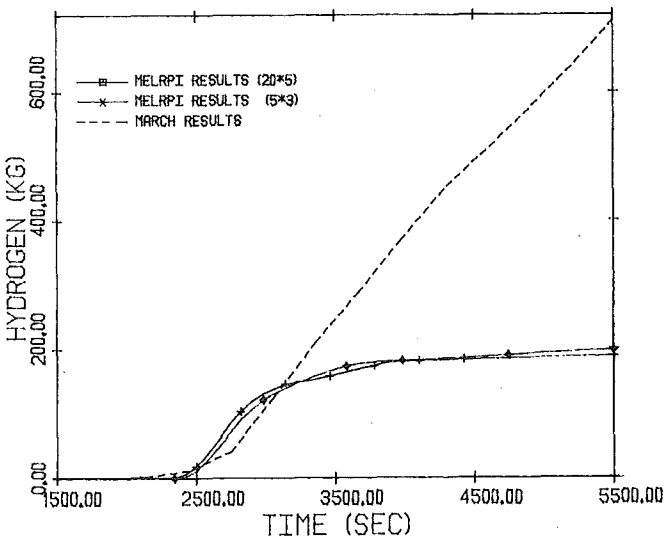

Figure 5. Hydrogen production; comparison between MELRPI and MARCH results.

TABLE 1

Event	Time (s)		
	MELRPI (20X5)	MELRPI (5X3)	MARCH
Cladding Failure	1020	1940	--
Start of Zircaloy Oxidation	2420	2420	2748
Start of Stainless Steel Melting	2980	2980	3360
Start of Zircaloy Melting	3340	3060	3360
50% of Stainless Steel Melted	3180	3080	3666
50% of Zircaloy Melted	3580	3220	4277
Start of ZrO_2 Melting	6020	5860	--
Start of Fuel Melting	6740	6660	3666
10% of Fuel Melted	--	14,580	--
16% of Fuel Melted	--	20,000	--
75% of Core Materials Melted	--	--	5687

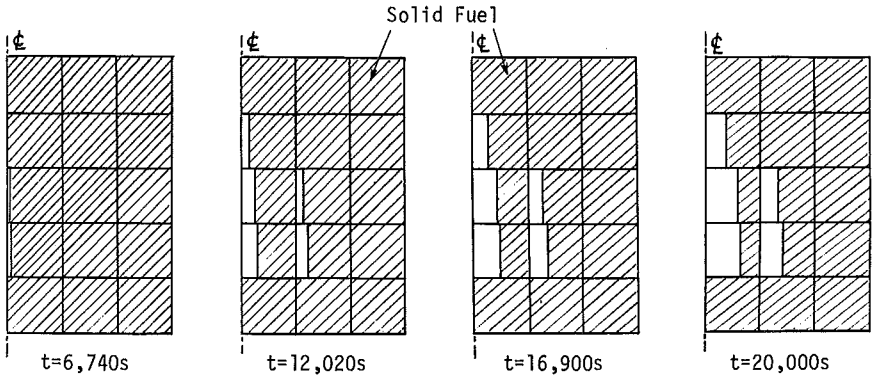

Figure 6. Fuel melting progression as calculated by MELRPI, (5X3) nodalization scheme; - reactor core center line.

As a supplement to Table 1, Figure 6 presents a schematic of the progression of fuel melting until 20,000s, obtained from the (5 x 3) nodalization scheme in MELRPI.

CONCLUSIONS

A comparison between the MARCH and MELRPI computer codes has been performed. The results obtained show substantial differences in the predicted course of the TQUV accident of a boiling water nuclear reactor. The MARCH results seem to be particularly conservative in two aspects of the calculations, the progression of core meltdown and the production of hydrogen. Both of these aspects are very important for the analysis of the overall consequences of severe reactor accidents.

ACKNOWLEDGMENTS

The authors wish to acknowledge the financial support by, and stimulating technical discussions with, Dr. S. Hodge, SASA Project Manager, ORNL.

REFERENCES

1. R.O. Wooten and H.I. Avci, "MARCH Code Description and User's Manual", NUREG/CR-1711, 1980.
2. M.Z. Podowski, R.P. Taleyarkhan, and R.T. Lahey, Jr., "The Modeling of Heat Transfer in a Degraded Core", AIChE Symposium Series, 79, 1983.
3. M.Z. Podowski, R.P. Taleyarkhan, and R.T. Lahey, Jr., "An Analysis of Molten Material Relocation and Rubble Bed Formation in a Degraded BWR Core", ASME preprint, 83-WA/HT-15, 1983.
4. M.Z. Podowski, R.P. Taleyarkhan, and R.T. Lahey, Jr., "Mechanistic Core-Wide Meltdown and Relocation Modeling for BWR Applications", NUREG/CR-3325; ORNL/Sub/81-9089/1, 1983.

IN-VESSEL HYDROGEN GENERATION ANALYSES WITH MARCH 2

Peter Cybulskis

Battelle's Columbus Laboratories
Columbus, Ohio 43201 USA

ABSTRACT

The results of MARCH 2 calculations on the dependence of hydrogen generation during the in-vessel phase of severe reactor accidents on various modeling assumptions are presented. The specific factors examined include: the effective core liquifaction temperature, assumptions regarding channel blockage on melting, meltdown model and core slumping variations, core debris particle size and configuration. The overall extent of reaction is generally found to be limited by the availability of steam for the reaction. Thus, modeling assumptions that lead to increased steam production during the core overheating process lead to the prediction of enhanced extent of reaction; model assumptions that limit steam production or the access of steam to unoxidized cladding tend to reduce the extent of reaction.

INTRODUCTION

Probabilistic Risk Assessments (PRA's) of various reactor designs have indicated that the accumulation and combustion of the hydrogen generated during severe reactor accidents can result in significant threats to containment integrity. The hydrogen burn that occurred during the Three Mile Island, Unit 2 (TMI-2) accident [1], while not a threat in itself, served to call attention to the possible implications of hydrogen burning during reactor accidents. As a result of these concerns, the United States Nuclear Regulatory Commission has imposed requirements [2] that certain types of containment designs include hydrogen control systems capable of accommodating the hydrogen that may be generated during severe reactor accidents. The magnitude of the challenges to the containment as well as the potential effectiveness of hydrogen control systems, such as deliberate ignition, can be dependent on the timing, rate, and magnitude of the hydrogen release to the containment. There is considerable controversy regarding the extent of hydrogen generation that would be associated with accidents leading to core melting and the ability to confidently predict such phenomena. Some recent studies [3,4] have indicated that hydrogen mitigation measures, such as deliberate ignition, may not be completely effective in the event of complete core melting. This paper presents the results of a series of MARCH 2 [5] calculations on the dependence of hydrogen generation during the in-vessel phase of severe reactor accidents to various assumptions regarding the behavior of the overheated reactor core.

BACKGROUND

The principal factors that affect the prediction of in-vessel hydrogen generation include the chemical reaction constants, the availability of steam, the surface area available for reaction, and the buildup of the reaction products zirconium oxide and hydrogen. The generation of significant amounts of hydrogen implies that portions of the core are heated to temperatures approaching melting, which in turn implies uncovery of significant fractions of the core for prolonged periods of time. With the initial core geometry intact, the surface area available for reaction is well defined and the amount of steam available to react with the overheated portions of the core would be determined by boiloff from the covered portions of the core, radiation from the uncovered and overheated portions, and in some cases, flashing due to continued depressurization of the primary system. As long as the initial core geometry can be assumed to be substantially maintained, the core thermal hydraulics (including steam generation) are believed to be reasonably predictable. The prediction of hydrogen generation up to this point can be done with reasonable confidence. [6] When the initial core geometry is distorted and lost, substantial uncertainties arise as to the rates of steam generation as well as the surface area available for reaction. Fuel movement within the core can lead to increased steam generation as the debris contacts water as well as leading to flow blockages; the former would tend to enhance cladding oxidation while the latter would tend to limit it. Such effects are highly uncertain and difficult to predict. After some progression of core melting, materials may begin to fall onto the lower core support structures and into the vessel head. The manner in which the overheated core materials relocate out of the core region and into the bottom head is very uncertain. The generation of steam from the interaction of the debris with water in the bottom head can lead to the rapid oxidation of overheated but steam-starved regions of the core that have not slumped at that time. Also, the unreacted Zircaloy in the debris may undergo oxidation in the vessel bottom head. This paper explores the effects of a variety of modeling assumptions during the above phases of the accident progression on the predicted extent of in-vessel hydrogen generation.

MARCH 2 MODELING ASSUMPTIONS

The MARCH 2 modeling of Zircaloy-steam reactions has been previously described. [7] Based on this work, it was concluded that prediction of the overall extent of reaction is not sensitive to the particular rate constants utilized, with those of Urbanic-Heidrick [8] being recommended and utilized in the present analyses. The buildup of high local concentrations of hydrogen, while leading to appreciable local effects, was found to have a small influence on the prediction of core-wide extent of reaction. The availability of steam for the reaction together with geometry/surface area considerations are believed to be the most sensitive factors affecting the prediction of in-vessel hydrogen generations and are the main topics explored in this paper.

The MARCH code does not attempt to mechanistically describe the deformation and movement of overheated and/or liquified fuel materials. Instead it provides several simulations of possible core damage progression scenarios together with a number of user-selected options regarding the effects of core deformation on steam flow and metal-water reactions. The particular factors considered in this study include:

1) Effective core melting (liquidus) temperature, 2090-3150 K.

2) Complete as well as no blockage of flow channels upon node liquifaction.
3) Meltdown model and core slumping variations, including gradual (regionwise), coherent, and node-by-node fuel slumping.
4) Debris particle sizes for interactions in the bottom head of 12.7 and 1.27 mm.
5) Homogeneous mixing of metal and oxide phases of the debris in vessel head, as well as segregation of metallic Zircaloy.

ACCIDENT SCENARIO CONSIDERED

The calculations described here were performed for a pressurized water reactor (PWR) transient accident sequence in which coolant makeup to both the primary and secondary systems is lost and core overheating and melting take place at high system pressure. The timing of the events for the reference case is given in Table I. The timing of the events through core uncovery was invariant for all the cases considered; the onset of core melting and the subsequent core slump, head dryout, and bottom head failure were found to vary somewhat with changes of assumptions from case to case, as indicated in Table II.

TABLE I. REFERENCE EVENT TIMES

Event	Time, minutes
Steam Generator Dry	67.5
Core Uncover	95.5
Start Melt	118.3
Core Slump	146.3
Start Head Heatup	147.8
Vessel Dryout	152.8
Head Fail	157.3

RESULTS

The results of the analyses conducted are summarized in Table III. The extent of cladding reaction and the fraction core melted for Case 1, the reference case, are illustrated in Figure 1. This case assumed a core liquifaction temperature of 2550 K, continued metal-water reactions after melting (incomplete or no blockage), debris particle size in the bottom head of 12.7 mm , homogeneous distribution of metal and oxide phases within the debris in the vessel head, and utilized meltdown Model A with regionwise fuel slumping. It may be noted that these assumptions are similar to those in the BMI-2104 analysis. [3] From Figure 1 it can be seen that the extent of reaction increases quite rapidly after core uncovery while steam flow through the core is relatively high; as most of the core becomes uncovered, the steam flow decreases and the extent of reaction levels off at about 19 percent. An abrupt increase in the extent of reaction takes place when the melt front within the core intercepts the water level; the energy from the increased metal-water reaction accelerates core melting, with

TABLE II. PREDICTED VARIATIONS IN EVENT TIMING

	Time in Minutes			
Case	Start Melt	Start Slump	Collapse	Vessel Dry
1	118.3	146.3	147.8	152.8
2	118.3	152.5	153.0	158.5
3	118.3	152.5	153.0	158.8
4	118.3	146.3	147.5	153.0
5	118.3	152.5	153.3	162.5
6	117.0	140.0	141.0	147.0
7	117.0	140.0	140.5	147.0
8	118.3	152.8	153.3	159.8
9	121.5	176.3	176.8	181.8
10	118.3	157.3	157.8	162.0
11	121.5	156.8	157.5	163.5
12	118.3	123.8	---	149.8

the criteria for initial fuel slumping being met at 146.3 minutes. At that time, 33 percent of the cladding is predicted to have oxidized. The steam generation from the interaction of the debris with water in the vessel head leads to further oxidation and heating of the core, with collapse of the entire core into the vessel head predicted at 147.8 minutes. The above progression of events is generally representative of the other cases considered. The total extent of cladding oxidation calculated for the reference case (Case 1) is 57 percent; of this about 2 percent is predicted to take place within the debris in the bottom head.

Case 2 is similar to Case 1, above, except that the cladding oxidation in melted nodes is not permitted; this is equivalent to assuming complete blockage of the core region upon node melting and no new surface for cladding oxidation. The results for Case 2, illustrated in Figure 2, show somewhat lower reaction than the preceding case, but the reduced reaction in the melted nodes delays the onset of core slumping and collapse and provides more time for reaction in the still solid nodes. Thus, the assumption of channel blockage upon melting does not lead to as significant reduction in total oxidation as may be expected. In this, as in the previous case, 2 percent of the total reaction is predicted to take place in the vessel bottom head.

Cases 3 and 4 assume that the metal and oxide phases are separate in the bottom head, thus making the unreacted Zircaloy more accessible for oxidation. The results are illustrated in Figures 3 and 4. In comparing Figures 2 and 3 and Figures 1 and 4, the substantial increase in the total cladding oxidation is associated with the predicted reaction of 21 percent in the vessel head in both cases.

Comparison of the results for Cases 2 and 5 illustrates the effect of particle size for homogeneous debris particles on the extent of reaction. Figure 5 illustrates the extent of reaction for the small particle case; the differences between Figures 2 and 5 are noticeable but not dramatic.

Comparison of Cases 6 and 7 illustrates the effect of homogeneous versus separated phases in the debris for a low assumed liquidus temperature. Case 6 is noteworthy as being the one with the lowest extent of reaction of those considered. This low predicted reaction is largely due to the combined effects

TABLE III. RESULTS FOR IN-VESSEL HYDROGEN GENERATION

Conditions*	Fraction Clad Reacted			
	Before Slump	During Slump	In Vessel Head	Total
1) A, D, F, H, J	0.33	0.22	0.02	0.57
2) A, E, F, H, J	0.40	0.02	0.02	0.44
3) A, E, F, I, J	0.40	0.01	0.21	0.62
4) A, D, F, I, J	0.33	0.21	0.21	0.75
5) A, E, G, H, J	0.40	0.01	0.09	0.50
6) B, E, F, H, J	0.24	0.00	0.02	0.26
7) B, E, F, I, J	0.24	0.00	0.17	0.40
8) A, E, F, H, K	0.41	0.00	0.02	0.43
9) C, E, F, H, K	0.65	0.00	0.02	0.67
10) A, D, F, H, K	0.63	0.01	0.01	0.65
11) C, D, F, H, J	0.44	0.15	0.01	0.60
12) A, E, F, H, L	0.13	0.30	0.01	0.44

* Key to Conditions:

A - Core melting temperature of 2550 K.

B - Core melting temperature of 2090 K.

C - Core melting temperature of 3150 K.

D - Zirconium-steam reaction allowed to continue in molten nodes.

E - No zirconium-steam reaction in molten nodes.

F - Particle size in vessel head of 12.7 mm.

G - Particle size in vessel head of 1.27 mm.

H - Homogeneous distribution of metal and oxide phases within particles in vessel head.

I - Metallic zirconium on the outside of particles in vessel bottom head.

J - Meltdown Model A with regionwise slumping.

K - Meltdown Model A with coherent slumping.

L - Meltdown Model C.

of a low melting temperature and the assumption of complete channel blockage on melting, with the other variables being less important.

Contrast of the results for Cases 2 and 8 illustrates the effect on the predictions of changing from the gradual to the coherent core slumping model, with no reaction in the molten nodes for both cases. The difference is minimal under these assumptions. Contrast of the results for Cases 1 and 10 illustrates that the difference between the gradual and coherent slumping model can be appreciable if oxidation is allowed to continue in the molten nodes.

Comparison of the results for Cases 2 and 6 illustrates the effect of the effective fuel liquification temperature in combination with the gradual slumping assumption; Cases 8 and 9 give another illustration of the effect of melting

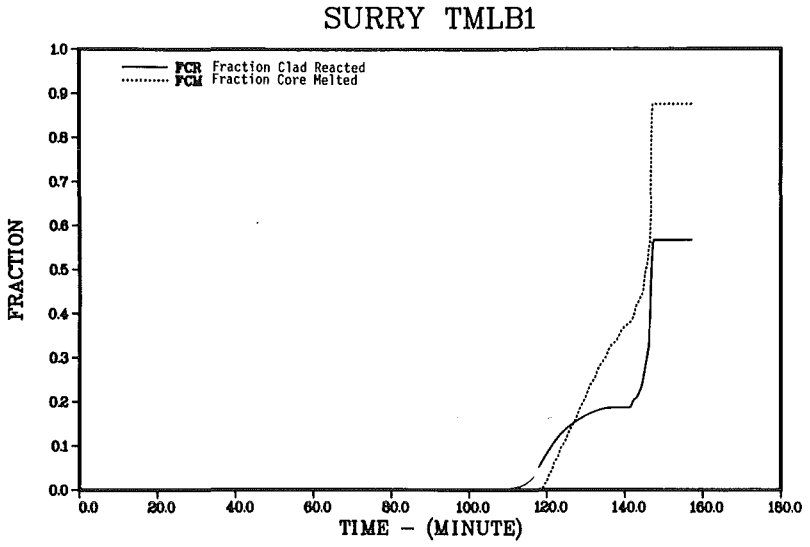

FIGURE 1. EXTENT OF CLADDING OXIDATION AND CORE MELTING FOR CASE 1

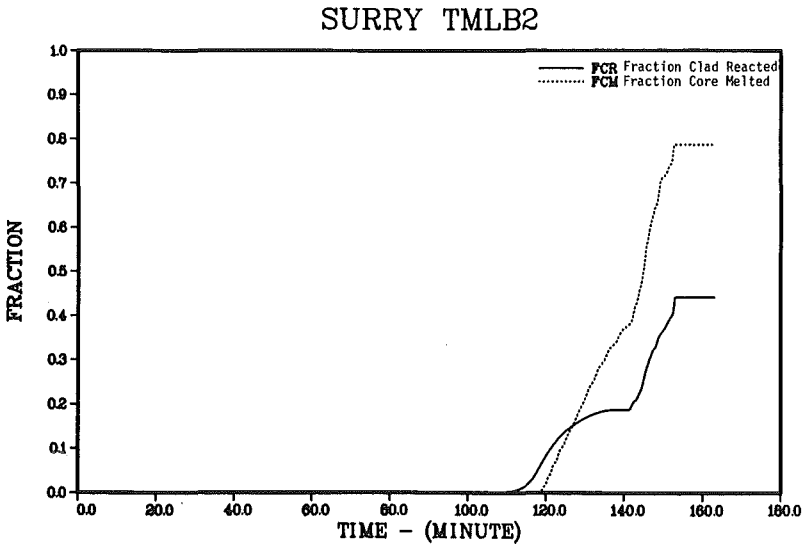

FIGURE 2. EXTENT OF CLADDING OXIDATION AND CORE MELTING FOR CASE 2

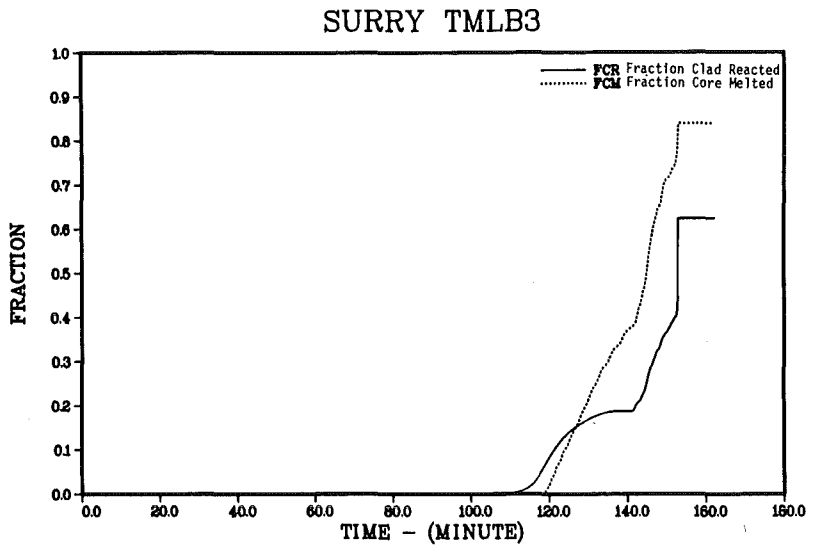

FIGURE 3. EXTENT OF CLADDING OXIDATION AND CORE MELTING FOR CASE 3

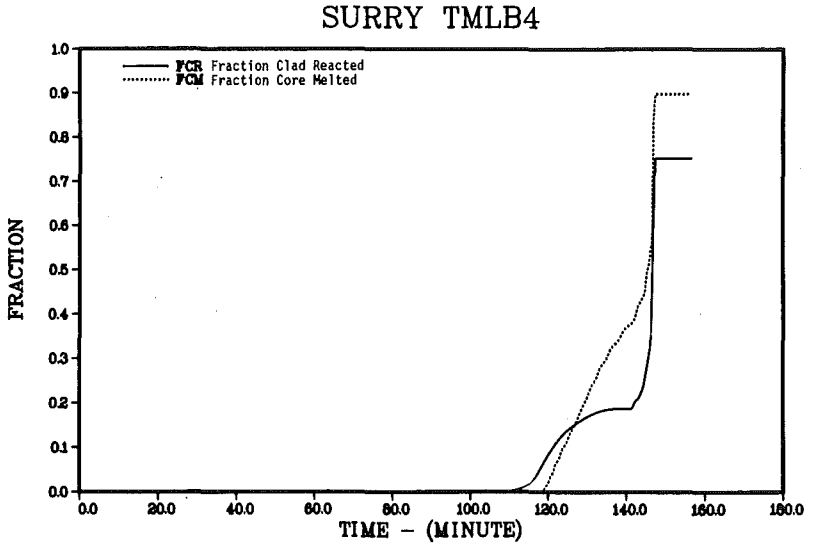

FIGURE 4. EXTENT OF CLADDING OXIDATION AND CORE MELTING FOR CASE 4

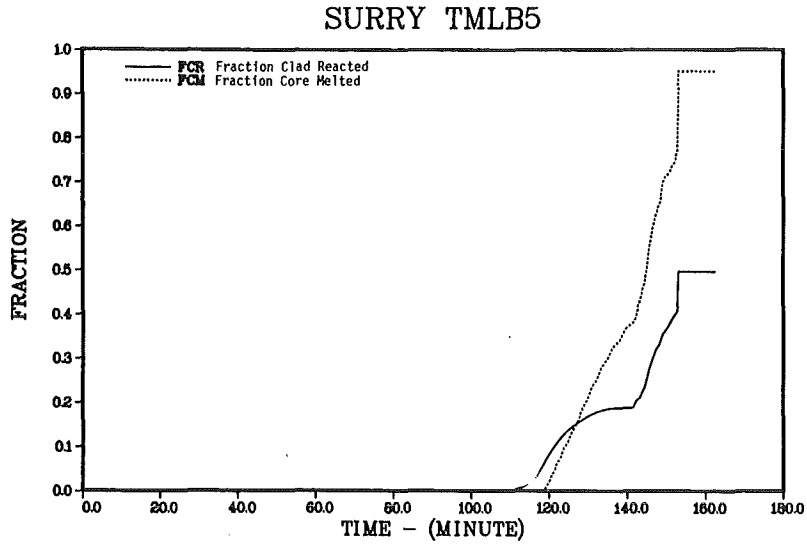

FIGURE 5. EXTENT OF CLADDING OXIDATION AND CORE MELTING FOR CASE 5

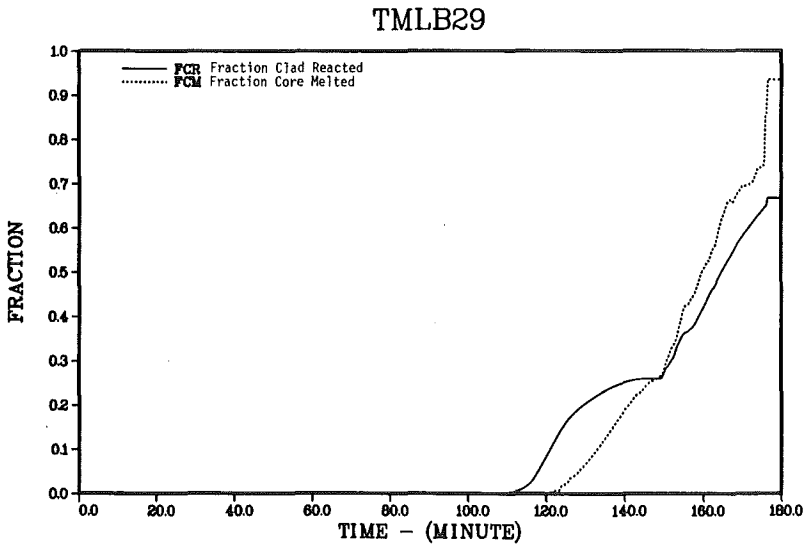

FIGURE 6. EXTENT OF CLADDING OXIDATION AND CORE MELTING FOR CASE 9

temperature in combination with the coherent slumping model. The differences in both cases are appreciable. Comparison of the results for Cases 1 and 11 which incorporate the gradual slumping model and allow cladding oxidation in melted nodes, on the other hand, indicates that the results are not very sensitive to the assumed melting point. The assumption of continued reaction in the melted nodes dominates the results in these cases.

Figure 6 illustrates the extent of reaction for Case 9; where the assumptions of a high melting point, shutoff of the metal-water reaction due to channel blockage on melting, and coherent slumping lead to relatively long times to core collapse, thus permitting significant extent of reaction even for low steam flow rates. Radiation from the core to the water in the bottom head provides steam for the reaction in this case.

The results for Cases 2 and 12 contrast the gradual slumping assumptions in MARCH meltdown Model A with the nodewise slumping inherent in meltdown Model C. While the overall extent of reaction is essentially identical for the two cases, it is interesting to note that for Model A most of the reaction takes place prior to slumping, while for Model C most of the reaction is predicted to occur during the slumping process. In both cases, the extent of reaction in the bottom head was found to be minimal, consistent with the results for a number of other cases.

The highest extent of cladding oxidation was found for Case 4, where a significant portion of the reaction was predicted to take place in the vessel bottom head. It may be noted that comparable levels of oxidation have been seen in specific accident analyses even without appreciable oxidation in the bottom head. [3] Very extensive cladding oxidation is typically found for scenarios that involve repeated core overheating and quenching, such as may take place if the accumulators discharge onto a partially melted core.

CONCLUSIONS

The extent of predicted in-vessel hydrogen generation has been found to be relatively insensitive to a wide variety of modeling assumptions regarding the behavior of the fuel following the onset of deformation and movement. While the results do vary with modeling assumptions, in essentially all cases considered the predicted extent of cladding reaction was higher than 40 percent, with a maximum of 75 percent. The lowest extent of reaction (26 percent) occurred for the combination of the lowest effective core melting temperature together with the assumption of complete steam flow blockage throughout a region upon node melting.

The use of the gradual slumping model typically leads to the prediction of enhanced cladding reaction due to the steam generated by the quenching of the initial slumped portions of the core; this steam is predicted to react vigorously in flowing past the yet uncollapsed regions of the core.

The assumption of complete flow blockage in a core region upon node melting leads to the prediction of lower overall reaction, but, with the exception noted above, not dramatically different from assuming that oxidation continues in the melted nodes. The shutoff of the reaction in the melted nodes slows the melt progression and allows more time for oxidation in the unmelted nodes.

The extent of oxidation during debris interactions in the bottom head was generally found to be quite limited (1 or 2 percent), with large reactions requiring extremely small particle sizes and/or separation of the unreacted Zircaloy from the oxides in the debris.

REFERENCES

1) Rogovin, M., and Frampton, G. T., Jr., "Three Mile Island: A Report to the Commissioners and to the Public", Nuclear Regulatory Commission, Special Inquiry Group (1980).

2) Nuclear Regulatory Commission, 10 CFR Part 50, Interim Requirements Related to Hydrogen Control, Federal Register, Vol. 46, No. 246, p 62281, Wednesday, December 23, 1981.

3) Gieseke, J. A., et al, "Radionuclide Releases Under Specific LWR Accident Conditions", Volumes II-VI, BMI-2104 (July, 1984).

4) Haskin, F. E., Behr, V. L., and Camp, A. L., "HECTR Results for Ice-Condenser Containment Standard Problem", Proceedings of Second Workshop on Containment Integrity (June, 1984).

5) Wooton, R. O., Cybulskis, P., and Quayle, S. F., "MARCH 2 (Meltdown Accident Response Characteristics) Code Description and User's Manual", NUREG/CR-3988, BMI-2115 (August, 1984).

6) Cybulskis, P., and Wooton, R. O., "MARCH 2 Simulation of the Power Burst Facility Severe Fuel Damage Scoping Test", paper presented at International Meeting on LWR Severe Accident Evaluation, Cambridge, MA, August 28-September 1, 1983.

7) Manahan, M. P., "An Improved Zircaloy-Steam Reaction Model for Use with the MARCH 2 Code", paper presented at the International Meeting on LWR Severe Accident Evaluation, Cambridge, MA, August 28-September 1, 1983.

8) Urbanic, V. F., and Heidrick, T. R., "High-Temperature Oxidation of Zircaloy-2 and Zircaloy-4 in Steam", J. Nucl. Matls., 75, pp 251-261 (1978).

POST ACCIDENT HYDROGEN PRODUCTION AND CONTROL IN ONTARIO HYDRO CANDU REACTORS

C. Blahnik, W.J. Dick and D.W. McKean

Ontario Hydro, Toronto, Canada

ABSTRACT

The derivation of hydrogen source terms is described for severely degraded cooling conditions in CANDU reactors. Parameters which influence these source terms are examined and their effects quantified. The implications for the design of hydrogen mitigation systems in the multi-unit containment envelope are discussed. The maximum pressures in containment are evaluated for the distributed ignition system aided by forced mixing.

INTRODUCTION

The multi-unit CANDU stations owned and operated by Ontario Hydro have several unique design features which influence the approach taken to post-accident hydrogen control, viz:

- a "negative pressure containment" (NPC) system [1] consisting of four reactor vaults connected to the vacuum building via a common fuelling/pressure relief duct;
- a large containment volume;
- a relatively low containment design pressure;
- a long-term controlled and treated venting of the containment atmosphere following a loss of coolant accident.

The large dilution volume (on the order of $10^5 m^3$) and the provision for containment venting are highly effective for long-term hydrogen management. Consequently, any source of hydrogen which requires a considerable time to reach flammable concentrations (such as hydrolysis or general corrosion) need not be considered in detail. On the other hand, any rapid sources of hydrogen which could locally and temporarily accumulate to flammable concentrations are important, bearing in mind the relatively low pressure loads that can be tolerated by the containment structures (in excess of 300 kPa(a)). Thus, the need for hydrogen mitigation depends largely on the rate and quantity of hydrogen produced by the Zircaloy/steam reaction during the high-temperature stage of a postulated accident (called the "hydrogen source term" in this paper). Parameters which influence this source term are examined, and their implications on the design of hydrogen mitigation systems in Ontario Hydro CANDU reactors are discussed.

HYDROGEN PRODUCTION

In Canadian licensing environment, plant-specific hydrogen source terms are derived using conservative analysis. The production of hydrogen is greatest under those severely degraded cooling conditions which present small steam flows to the fuel, sufficient to maintain the exothermic metal/water reaction but insufficient to cool the fuel. In CANDU reactors, such conditions are associated with postulated loss-of-coolant accidents (LOCA) coincident with a failure of the Emergency Coolant Injection System (ECIS). The parallel, horizontal fuel channels become completely voided in these accidents on a timescale ranging from seconds to hours. Subsequently, the fuel is cooled by only a small flow of steam and hydrogen supplied from the common headers and by heat transfer to heavy-water moderator (Figure 1). The fuel temperature will rise in order to accommodate

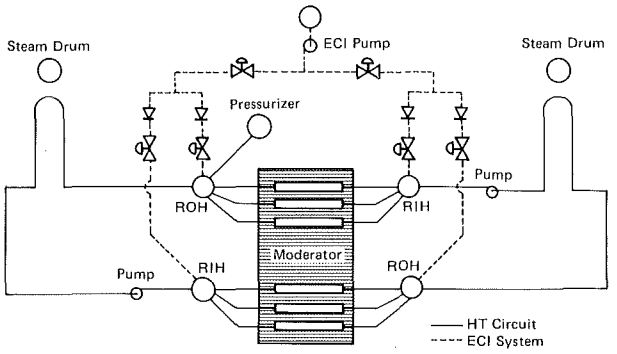

FIGURE 1
Simplified Diagram of Heat Transport Loop

rejection of decay and chemical reaction heat to these two principal heat sinks. Because of the distributed heat sink provided by the moderator, the peak fuel temperatures remain well below the UO_2 melting temperature, and the integrity of fuel channels is maintained for all postulated LOCA's [2]. Generally, much of the fuel in the core will remain at "moderate" temperatures throughout the accident and only some fuel bundles in high-power channels will achieve highly elevated temperatures for long periods of time illustrated in Figure 2.

Realistic estimates of hydrogen production are particularly difficult for a CANDU core arrangement since the fuel in each channel experiences a unique temperature excursion, governed by its decay power level, steam flow rate and extent of mechanical deformation. Steam flowrates may differ widely throughout the core due to different hydraulic resistances and elevations of parallel fuel channels. The composition of the steam/hydrogen mixture at the channel inlet may also vary depending on the flowrate and the location of post-accident water supply. There is no large reservoir of water in the core, and without an external supply, the production of hydrogen would be severely limited by the lack of oxidizing reagent. Furthermore, a range of thermal/mechanical deformations of fuel and pressure tube comes into play at the highly elevated temperatures of degraded cooling

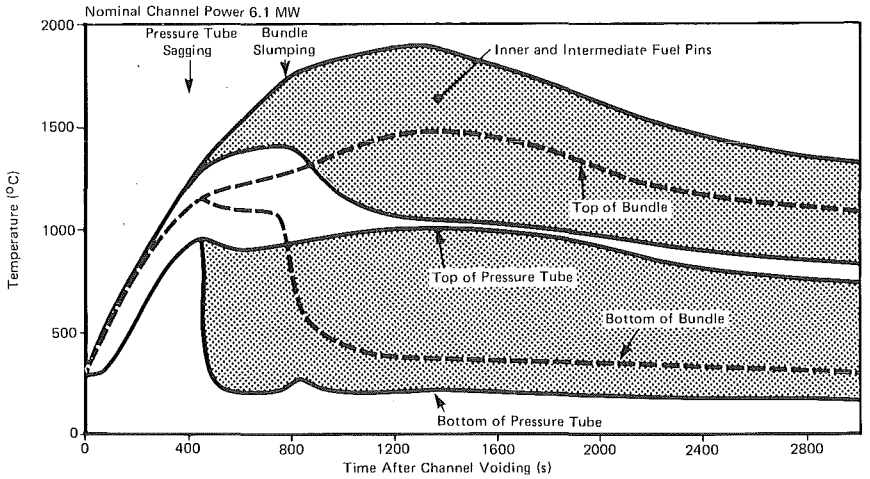

FIGURE 2
Temperature Transient at Hottest Bundle Position
Channel Voiding Time 40 s, Constant Steam Flow @ 10 g/s Thereafter

accidents as illustrated in Figure 3. These deformations tend not only to increase the rate of heat removal to the moderator, but also to alter the rate of metal/water reactions by reducing the supply of steam to the interior subchannels of fuel bundles. Detailed modelling of each individual fuel channel's thermo-mechanical response is therefore essential.

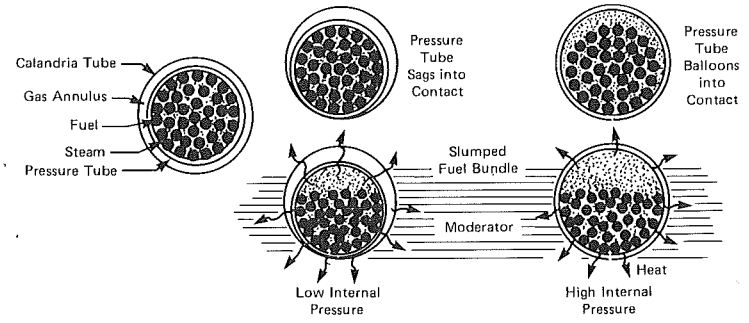

FIGURE 3
Geometry Distortions in a Fuel Channel

A computer code CHAN-II [3] was developed to analyze the various feedback effects on fuel temperatures in a CANDU fuel channel. It calculates the temperature transients of the fuel, pressure tube and calandria tube at each bundle position along the fuel channel, as a function of channel power and steam flow rate. The latter is user-specified or it is derived from an iterative solution by equating the input header-to-header pressure drop to the frictional losses across the fuel channel and feeders, taking due account of the loss characteristics of the subchannel flow paths, and the temperature dependent thermo-physical properties affecting the frictional losses. The code employs a concentric ring model which accounts

for internal heat generation, convection, conduction and radiation, and heat generated by the cladding oxidation. Various types of deformations can be modelled in the code, including pressure tube ballooning, sagging, fuel sheath ballooning, and fuel bundle slumping. The changes in the steam flow pattern through a deformed location is evaluated using the parallel-pipe approach.

A core basis hydrogen source term is readily derived from individual channel response simulations for any given accident scenario. To avoid an unmanageable number of accident scenario simulations, a conservative source term can be derived for the purposes of licensing analysis, by arbitrarily choosing channel conditions which maximize the extent as well as the rate of metal/water reaction. Such conditions involve minimum possible fuel and pressure tube distortions combined with small flowrates of fresh steam on the order of 10 g/s per channel (or 0.3 to 0.5 g/s per fuel pin). If it is assumed that these conditions prevail indefinitely in all fuel channels of the core, hydrogen production becomes strictly a function of channel decay power during the degraded cooling period, which is determined by the time of core voiding after reactor trip.

Figure 4 illustrates the effect of the core voiding time on these conservative hydrogen production estimates in a large CANDU core (480 fuel channels, 2800 MWth). If the coolant voids from the channels within a few seconds after the break, little of the fuel's stored energy is removed during the blowdown. The whole core undergoes rapid heatup at elevated system pressures which results in considerable fuel and pressure tube distortions (illustrated at the right side of Figure 3), establishing a relatively efficient heat rejection path from the fuel to the moderator. At later voiding times the fuel heatup is slower, commencing from a lower stored energy level at lower system pressures. In the absence of internal pressure, the pressure tubes may only achieve bottom contact with their calandria tubes (left side of Figure 3) resulting in a lower heat removal to the moderator. Also, the fuel elements can experience only relatively minor distortions by sagging between the spacer supports, because considerable oxidation strengthening of the sheaths can occur due to the slow heatup [4]. Although the production rates are more gradual for these "delayed heatup" scenarios, the amount of hydrogen generated can be larger than in the "early heatup" scenarios. With further delays in core voiding, the heat removal to the moderator does not change appreciably, but the fuel

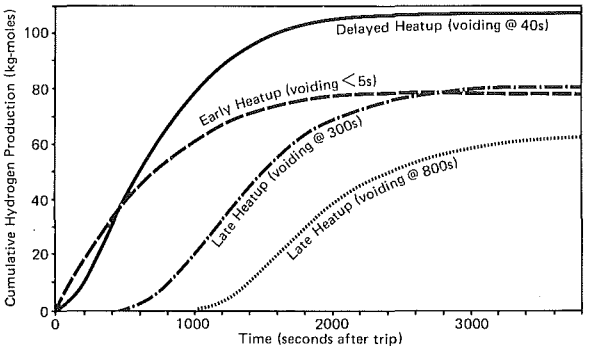

FIGURE 4
Hydrogen Production Transients for Degraded Cooling Accidents

decay power continues to decrease. Fewer fuel bundles in the core reach highly elevated temperatures and the residence times at temperature become shorter. Consequently, the maximum amount of hydrogen produced in an accident decreases with increasing time to core voiding.

The large and rapid source terms associated with short core voiding times can be reduced substantially by taking into account more realistic deformation and steam flow patterns in the core. As an example, Figure 5 compares several hydrogen generation transients for a large break with the core voiding time of 40 seconds. The highest curve corresponds to the licensing estimate of 110 kg moles shown previously. It implies that about 30 percent of the fuel cladding and end plates in the core has been oxidized, with the largest contribution coming from the high-power fuel channels. Recall that this estimate considers only the minimum pressure tube and fuel deformation (by sagging), in conjunction with an indefinite supply of optimum steam flow. Following a rapid blowdown depressurization, the core can experience slightly elevated system pressures for a period of time (caused, for example, by post-accident operation of D_2O feed pumps). The sagging of pressure tubes would then be complemented by gradual radial expansion into a full circumferential contact with the calandria tubes. This "ballooning" phenomenon alone reduces the amount of hydrogen produced to about 75 kg moles. If, in addition, it is recognized that the steam will not be distributed uniformly in the complex network of parallel fuel channels, further reductions of the source term are obtained. For example, for an accident scenario in which the steam is driven through the core by a low header-to-header pressure differential of 5 kPa (producing about the same total throughput as the above case), the amount of hydrogen produced drops to 40 kg moles. If slumping of thin-walled, horizontal fuel bundles is considered, with its attendant conductive heat transfer to the moderator and the reduction of steam access to the interior subchannels, the hydrogen source term reduces to about 30 kg moles.

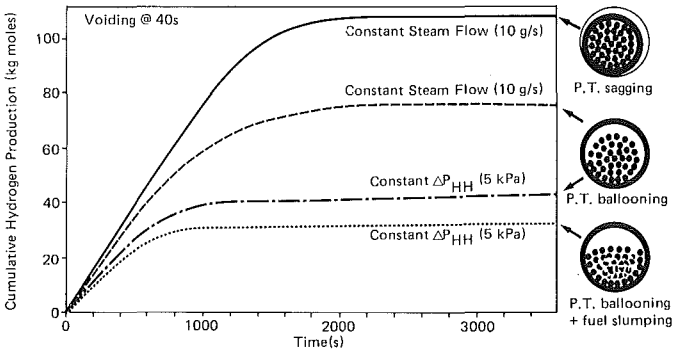

FIGURE 5
Effect of Mitigating Phenomena on Hydrogen Source Terms

For the full range of degraded cooling scenarios, the emerging trend is toward considerably lower core source term estimates as illustrated in Figure 6. The largest releases tend to shift towards longer core voiding times (smaller breaks) for which limited deformations may be realistic. However, since the requirement is for conservative analysis, the application

of this trend in licensing and design is still some time away. A number of experimental programs are jointly being pursued by AECL and Ontario Hydro to verify and improve our understanding of the full and channel thermal-mechanical-chemical behaviour at very high temperatures and thus the source term methodology. The fuel programs range from separate effect experiments with fuel simulators in steam (reaching temperatures well in excess of 2000°C) to steam tests with full-scale fuel bundles (reaching temperatures of about 2000°C). Some of the results are being reported in separate papers at this conference [4][5]. The fuel channel programs have explored the full range of deformation modes over the past several years [6][7] and a detailed analysis of the results is now in progress.

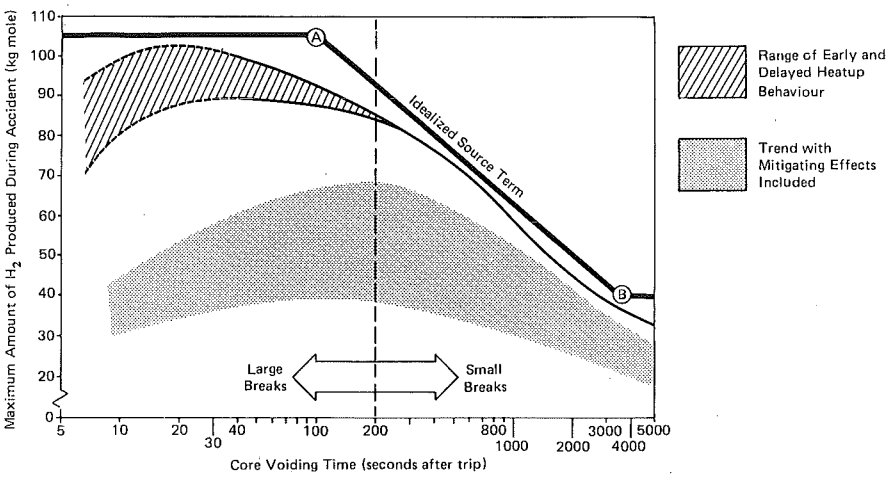

FIGURE 6
Hydrogen Source Term as a Function of Core Voiding Time

HYDROGEN MITIGATION

In the large containment envelope of CANDU multi-unit stations, even the highest of the preceding source terms would yield a hydrogen concentration below the flammability limit if a homogeneous mixing could be assured throughout the containment volume. Within the individual vaults, effective mixing is provided by large vault coolers with a volume turnaround time of a few minutes. However, for rapid hydrogen release transients, the source term dilution into the adjacent vaults may not be effective. During a post-LOCA blowdown, the steam/air mixture is vented from the accident reactor vault into the vacuum building to relieve the containment pressure. After the end of blowdown, when the hydrogen can be generated in the voided core, steam in the accident vault condenses resulting in a return flow of air back into the accident vault. This flow tends to impede the dispersion of hydrogen into the adjacent reactor vaults. It may persist for about an hour, coinciding with the duration of the large hydrogen source terms described previously. Thus, high hydrogen concentrations in air could temporarily be present in the accident reactor vault at the end of steam condensation period.

To avoid an inadvertent ignition at these unfavourable mixture compositions, Ontario Hydro has opted for a distributed ignition system in each vault (Tayco glow plugs) to provide short-term mitigation. The basic principle is to initiate the burn as soon as the hydrogen-steam-air mixture is ignitable, thus minimizing its consequences. The ignitors are activated early, before the flammable mixtures could develop in the vault. Any mixtures with high hydrogen content will thus be burned while there is still a significant steam content. Lean mixtures will be removed in a number of discrete burns as the hydrogen is produced.

Over the full range of degraded cooling accidents, a wide spectrum of mixture compositions may develop in the accident vault, depending on the actual timing and rate of hydrogen production relative to the timing and rate of dispersion. The number of compositions that have to be analysed can be reduced to manageable proportions by defining an "assured ignition criterion" shown in Figure 7. This criterion identifies hydrogen-air-steam proportions by which the ignition will have had occurred, regardless of the previous transient composition. It was derived from tests in small and medium-scale vessels [8,9] which show that three conditions must be met for the assured ignition: the hydrogen concentration must exceed 8 percent, the steam concentration must be below 40 percent and the air concentration must exceed 30 percent. Superimposed is the flammability limit for hydrogen-air-steam mixtures. Should ignition occur at the flammability limit instead of the assured ignition criterion, the burn consequences would be much milder.

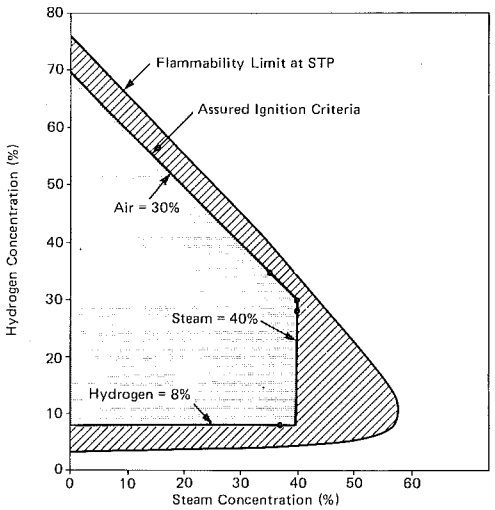

FIGURE 7
Assured Ignition Criterion for Hydrogen-Air-Steam Mixtures

The maximum challenge to containment structures can be quantified from the parametric analysis of burns along the "assured ignition" lines. The computer code VENT [10] is used, which calculates the pressure and temperature transients in spherical or cylindrical volumes. The code assumes a spherically-shaped flame front and employs empirically-based correlations for flame velocity as a function of mixture composition and

turbulence. Pressure relief by venting of burnt or unburnt gases into adjacent volumes is considered. Heat transfer to structures or the dissociation of burnt gases are neglected for conservatism.

Estimates of the peak pressure within a reactor vault obtained by such parametric analysis are shown in Figure 8 as a function of hydrogen concentration at the instant of ignition. If the ignition is governed by the availability of hydrogen, (i.e., previous transient conditions are such that the ignition occurs as soon as the hydrogen concentration reaches 8%), the peak combustion pressures range from 90 to 140 kPa(a). The variability of the peak pressure at the constant hydrogen concentration is due to changes in adiabatic flame temperature and flame velocity over the range of possible mixture compositions. If the ignition is governed by steam condensation (i.e., ignition occurs as soon as steam concentration drops to 40%), relatively high hydrogen concentrations must be present. The peak pressure rises rapidly to about 260 kPa(a) with the increasing hydrogen content, reaching a broad plateau around the stochiometric composition. Should the ignition become governed by the availability of air (implying a hydrogen-rich atmosphere which ignites when the air concentration reaches 30 percent), the peak pressure could start rising again with the increasing hydrogen concentration. However, the amounts of hydrogen needed to yield such rich mixtures are well in excess of even the most pessimistic source term described previously.

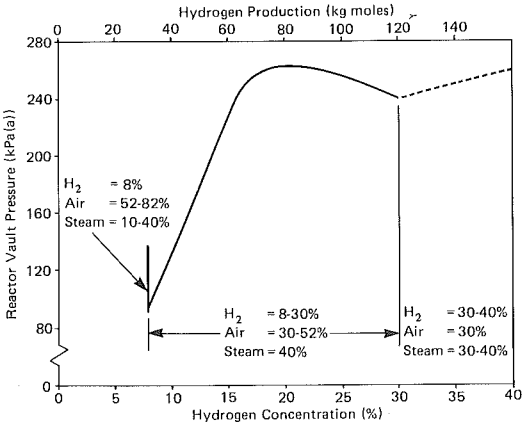

FIGURE 8
Peak Pressures in Reactor Vault

On the basis of preceding results, the largest challenge to the CANDU containment structures comes from early and fast hydrogen production transients which allow accumulation of relatively high hydrogen concentrations in steam-rich mixtures within a single reactor vault. This challenge is estimated at 260 kPa(a) using conservative models, and it is acceptable from the standpoint of containment integrity. An experimental program of verification of the pressure transients associated with combustion of such mixtures has been mounted in order to provide more realistic estimates of the challenge. Results to date indicate that the "assured ignition criterion" in Figure 7 is conservative (i.e., ignition is

closer to the flammability limits) and that the current modelling of deflagration overestimates the pressure challenge. In parallel, an alternate mitigation system is being investigated which has the potential of further reducing the pressure challenges at a comparable cost. As illustrated in Figure 9, the basic concept involves the removal of hydrogen from the accident reactor vault atmosphere by circulating it through a cooler/combuster unit. The cooler condenses the steam and the hydrogen is then burned off in a standing flame within the combuster exhaust. The hydrogen is thus continuously removed as it is produced, unimpaired by steam content, resulting in minimal pressure excursions.

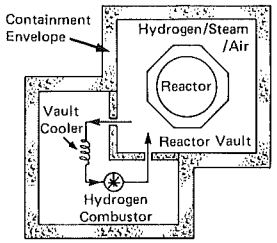

FIGURE 9
Hydrogen Combustor Concept

CONCLUSIONS

- For a large CANDU core typical of Ontario Hydro's reactors, the hydrogen source term is less than 110 kg moles for the most severely degraded cooling accident. The duration of hydrogen release is about one hour from the time of core voiding.

- A number of phenomena come into play in degraded cooling accidents, ranging from limited or excessive supply of steam into the core, through non-uniform distribution of steam among parallel fuel channels, to geometry distortions within the channels. These phenomena acting alone or in combination can substantially reduce the source term.

- In the multi-unit Negative-Pressure-Containment systems, the timing of hydrogen release is a major consideration in the design of mitigating systems.

- A distributed ignition system aided by forced mixing limits the peak pressure loads to less than 260 kPa(a). This provides adequate protection for containment integrity.

REFERENCES

[1] C. Blahnik, D.W. McKean, D.A. Meneley, J. Skears, N. Yousef; "PRINCIPLES OF OPERATION OF CANDU MULTI-UNIT CONTAINMENT SYSTEMS"; paper presented at the International Conference on Containment Design; Toronto, Canada; June 1984.

[2] R.A. Brown, C. Blahnik, A.P. Muzumdar; "DEGRADED COOLING IN A CANDU"; paper presented at the Second International Topical Meeting on Nuclear Reactor Thermal-Hydraulics, Santa Barbara, California, USA; January 1983 (to be published in Nuclear Science and Engineering).

[3] J.H.K. Lau et al; "FEEDBACK EFFECTS OF DEFORMATIONS ON FUEL TEMPERATURES DURING DEGRADED COOLING ACCIDENTS IN CANDUS"; paper presented at the IAEA Specialist Meeting on Water Reactor Fuel Element Performance Computer Modelling, Bownes on Windermere, UK; April 1984.

[4] G.I. Hadaller et al; "EXPERIMENTS INVESTIGATING THE THERMAL-MECHANICAL BEHAVIOUR OF CANDU FUEL UNDER SEVERELY DEGRADED COOLING"; paper No. 195.

[5] H.E. Rosinger et al; "UO_2 DISSOLUTION BY MOLTEN ZIRCALOY", paper No. 158.

[6] R.S.W. Shewfelt, P.D. Godin; "BALLOONING OF THIN-WALLED TUBES WITH CIRCUMFERENTIAL TEMPERATURE VARIATIONS", AECL-3817, to be published.

[7] G.E. Gillespie, R.G. Moyer, G.I. Hadaller; "AN EXPERIMENTAL INVESTIGATION OF THE CREEP SAG OF PRESSURE TUBES UNDER LOCA CONDITIONS"; paper presented at the Canadian Nuclear Society meeting, Saskatoon, Canada; June 1984.

[8] H. Tamm, R.K. Kumar, W.C. Harrison; "A REVIEW OF RECENT EXPERIMENTS AT WNRE ON HYDROGEN COMBUSTION", Proceedings of the Second International Workshop on The Impact of Hydrogen on Water Reactor Safety. Albuquerque, New Mexico, October 1982.

[9] W.E. Lowry, B.R. Bowman, B.W. Davis; "FINAL RESULTS OF THE HYDROGEN IGNITER EXPERIMENTAL PROGRAM", Lawrence Livermore National Laboratory, NUREG/CR-2486, UCRL-53036, February 1982.

[10] S.R. Malpuru, G.B. Wilkins; "A MODEL FOR VENTED DEFLAGRATION OF HYDROGEN IN A VOLUME", AECL-6826, February 1982.

EXPERIMENTS INVESTIGATING THE THERMAL-MECHANICAL BEHAVIOUR OF CANDU FUEL UNDER SEVERELY DEGRADED COOLING

G.I. Hadaller, R.Sawala

Westinghouse Canada Inc. - Nuclear Products Dept.
P.O. Box 510
Hamilton, Ontario L8N 3K2, Canada

E. Kohn

Atomic Energy of Canada Ltd. - CANDU Operations
Sheridan Park Research Community
Mississauga, Ontario L5K 1B2, Canada

G.H. Archinoff, S.L. Wadsworth

Ontario Hydro - Nuclear Studies and Safety Dept.
700 University Avenue
Toronto, Ontario M5G 1X6, Canada

ABSTRACT

Two experiments are described in which unirradiated production CANDU fuel bundles were heated in steam to temperatures exceeding 2000°C. The purpose of the experiments was to improve the understanding of CANDU fuel thermal-mechanical behaviour during accidents with severely degraded cooling, in which gross slumping of horizontal fuel is anticipated. The experimental apparatus and procedure is described, including unique aspects such as the use of an oxy-hydrogen torch to provide highly superheated steam, and on-line video recording of the fuel as it experiences severe temperature excursions and distortion, as well as details of the post-test fuel examination.

INTRODUCTION

Accident analysis for CANDU reactors addresses the complete range of pipe break size and location in the primary heat transport piping system. In this analysis, coincident failure of the Emergency Coolant Injection System to operate on demand is also postulated, leading to severely degraded core cooling conditions for an indefinite period of time. Under these circumstances decay heat is rejected through the pressure tubes and calandria tubes to the cool moderator. This paper describes experiments carried out to improve the understanding of the thermal-mechanical behaviour of CANDU fuel bundles subjected to severely degraded cooling conditions.

The CANDU reactor core consists of about 400 fuel channels which contain the high pressure coolant and the fuel. The fuel consists of 0.5 m long bundles lying end-to-end within each 10 cm diameter pressure tube. The bundles are made up of 37 UO_2/Zircaloy clad fuel elements which are spaced from each other and the pressure tube by end plates, spacers and bearing pads.

The individual fuel channel design allows geometrically representative, integrated experiments to be performed with a simple and compact apparatus employing a single fuel bundle.

TEST DESCRIPTION

A single unirradiated production CANDU fuel bundle was placed inside a test section pressure tube and heated by highly superheated steam from a torch fed with a stoichiometric ratio of hydrogen and oxygen . The torch provided up to 9 g/s of steam while producing 120 kW of power. The torch steam is mixed with cooler plant steam (100°C) to allow control of total steam flow and temperature. Instrumentation in the tests includes steam flow measurement, on-line hydrogen monitors, an emmissivity-insensitive optical pyrometer and platinum-rhodium thermocouples for measuring fuel cladding temperatures, and video cameras which record bundle deformation during each test.

The external heating method in these tests might be expected to cause the sheaths to be hotter than the fuel. This is not true for the reactor case with decay power heating when the sheath is at a lower temperature (less than 1500°C). However, at higher temperatures (greater than 1600°C) external sheath heating would occur in reactor when the Zircaloy oxidiation reaction becomes the dominant heat source.

Two experiments were conducted, each with test conditions representing an extreme in the spectrum of degraded cooling accident scenarios. In the first experiment, designated HTBS-001, the bundle was contained in a tight-fitting, insulated shroud, to minimize distortion and radial heat loss. This geometry is an approximation of that within a pressure tube which does not deform significantly during the accident. A schematic of the apparatus is shown in Figure 1. The conditions in HTBS-002 were representative of accident scenarios (1,2) in which the fuel and pressure tube heat up while the system pressure, although rapidly decreasing, is still high enough to cause the hot pressure

tube to strain into full circumferential contact with its calandria tube. This establishes an effective heat transfer path to the moderator, which maintains the pressure tube/calandria tube at low temperatures (about 200°C) and allows steam to bypass the bundle. In HTBS-002, the bundle was contained in a section of Zr-2.5% Nb pressure tube, which had been strained radially 18 percent such that it would fully contact the calandria tube. This provided greater clearance for the bundle to deform under its own weight. Minor apparatus modifications were made prior to the second test, to enable the upstream end plate to be directly viewed by the optical pyrometer and video camera. The outside of the pressure tube was cooled with plant steam, however, its temperature was kept relatively high, between 600°C and 1200°C, to ensure high fuel temperatures would be achieved. For this test the bundle temperature was stabilized between 800°C - 1200°C before being subjected to 9 g/s of steam from the torch at 1800°C - 2000°C. A schematic of the apparatus used for HTBS-002 is shown in Figure 2.

OBSERVATIONS

Figures 3 and 4 show the post-test appearance of the bundle used in HTBS-001 after it had been carefully removed from the test section. Figures 5 and 6 compare views of the upstream end of the bundle before and after the test. Cross-sections of the bundle near the upstream end and at the mid-plane are shown in Figures 7 and 8. Typical temperature and hydrogen evolution transients are plotted in Figure 9. The maximum recorded temperature in HTBS-001 was 1700°C. However, there is indirect evidence which indicates that the upstream portions of the bundle, where there was no temperature instrumentation, reached at least 2000°C.

The major observations from HTBS-001 are as follows:

(a) A clear flow path remained through the bundle. Many of the triangular flow subchannels, particularly those surrounding the centre fuel pin, became blocked;

(b) Oxidation caused the bundle to become very brittle and fragile (the outer two rings of fuel sheaths were oxidized over their full original thickness, while the inner element sheaths had partially reacted with UO_2 during heatup and therefore the remaining oxide layer was thinner);

(c) Most of the upstream end plate and some of the upstream end caps became detached, exposing bare UO_2 pellets;

(d) Molten U/Zr eutectic formed in regions where the Zircaloy had not fully oxidized during heatup but did not relocate during the test;

(e) Yellow and black deposits were observed on the oxidized cladding, with the yellowish deposits appearing to emanate from the exposed UO_2 pellets (analysis showed that U and Zr were the major constituents of the deposits, with Zircaloy alloying materials comprising the minor constituents);

(f) Additional deposits, primarily UO_2 and Zr, were found downstream of the test bundle and on the condenser filter;

(g) The O/U ratio increased from the initial value of 2.0 to a maximum of 2.2 in the upstream exposed pellets.

It was evident from the observed temperature transients and the post-test appearance of the bundle that peak fuel temperatures significantly exceeded the steam inlet temperature, due to heat generation from the Zircaloy-steam reaction.

Temperatures and hydrogen evolution for HTBS-002 are shown in Figure 10. The maximum recorded temperature was 2010°C. The pre-test and post-test appearance of the upstream end of the bundle as well as bundle cross sections is shown in Figures 11 to 14.

The observations from HTBS-002 are similar to those from HTBS-001, except that only the inner rings of fuel elements of the upstream third of the bundle reached temperatures above 1500°C, probably due to steam bypassing and heat losses through the pressure tube. Even so, there was slumping in the hotter regions, with the outer elements sagging downward and outward to contact the pressure tube.

CONCLUSIONS

The conclusions drawn from the two high temperature bundle sag experiments conducted to date are:

(a) The experimental technique captures the major phenomena expected in severely degraded cooling accidents, particularly the rapid temperature excursions produced by the Zircaloy-steam reaction.

(b) Under degraded cooling conditions in CANDU bundles, significant coolant flow area will remain in the channel, either in the large square subchannels or in the area above the bundle provided by expansion of the pressure tube and/or slumping of the bundle. However, some subchannel blockage, particularly of triangular subchannels, will occur if fuel sheath temperatures approach 2000°C.

(c) In accidents with temperature ramp rates and peak temperatures similar to those of these experiments, there will be little formation of molten material, and virtually no relocation of this molten material.

(d) Severe temperature excursions in steam result in a loss of fuel sheath integrity, and partial loss of end cap and end plate integrity due to oxidation, allowing the bundle to settle either during or after the temperature excursion if it is not externally restrained.

(e) Uranium and zirconium particulates will be carried and deposited downstream during degraded cooling conditions. In HTBS-001 approximately 0.5% of the bundle mass was carried downstream to the condenser.

These conclusions, particularly those relating to geometry, are important to accident analysis of CANDU's (3,4) because they indicate the nature of the steam flow patterns and heat transfer to be expected during degraded cooling.

The results of these and future experiments will be fed back into the analysis, to ensure it conservatively accounts for the phenomena observed during these simulated degraded cooling tests.

ACKNOWLEDGEMENT

We acknowledge the contributions of F. Stern and C. Blahnik for their inputs in directing the program. We also acknowledge the contributions of the staff at the Systems Test Laboratory where the tests were carried out, especially F.B. Russell who wrote the data acquisition program and W. Bernhardt who sectioned and photographed the bundles.

REFERENCES

1. Brown, R.A., et al, "Degraded Cooling in a CANDU", presented at Second Int'l Topical Meeting on Nuclear Reactor Thermal-Hydraulics, Santa Barbara, California, January 11-14, 1983.

2. Muzumdar, A.P., et al, "Fuel Temperature Excursions During Accidents With Degraded Core Cooling in CANDU Reactors", presented at Second Int'l Topical Meeting on Nuclear Reactor Thermal-Hydraulics, Santa Barbara, California, January 11-14, 1983.

3. Thompson, P.D., and Kohn, E., "Fuel and Fuel Channel Behaviour in Loss of Coolant Accident Without the Availability of the Emergency Coolant Injection System", IAEA Specialists' Meeting on "Water Reactor Fuel Safety and Fission Product Release in Off-Normal and Accident Conditions", RISO, Denmark, May 16-20, 1983.

4. Muzumdar, A.P., et al, "Fuel Channel Behaviour During Accidents With Degraded Cooling in CANDU Reactors", IAEA Specialists' Meeting on "Water Reactor Fuel Safety and Fission Product Release in Off-Normal and Accident Conditions", RISO, Denmark, May 16-20, 1983.

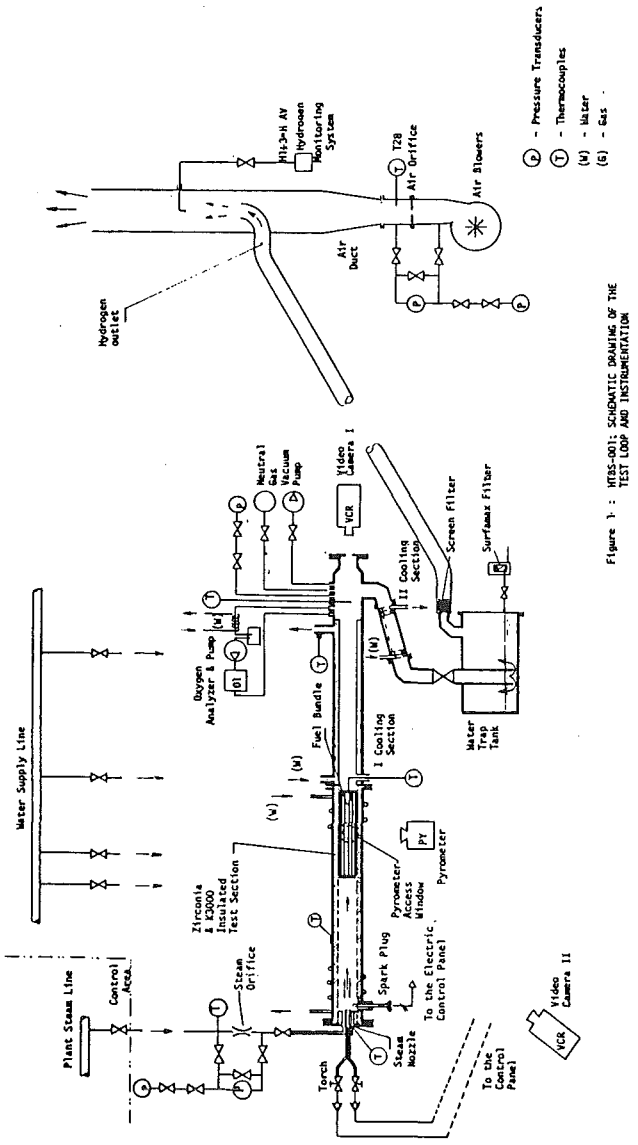

Figure 1 : HT3S-001: SCHEMATIC DRAWING OF THE TEST LOOP AND INSTRUMENTATION

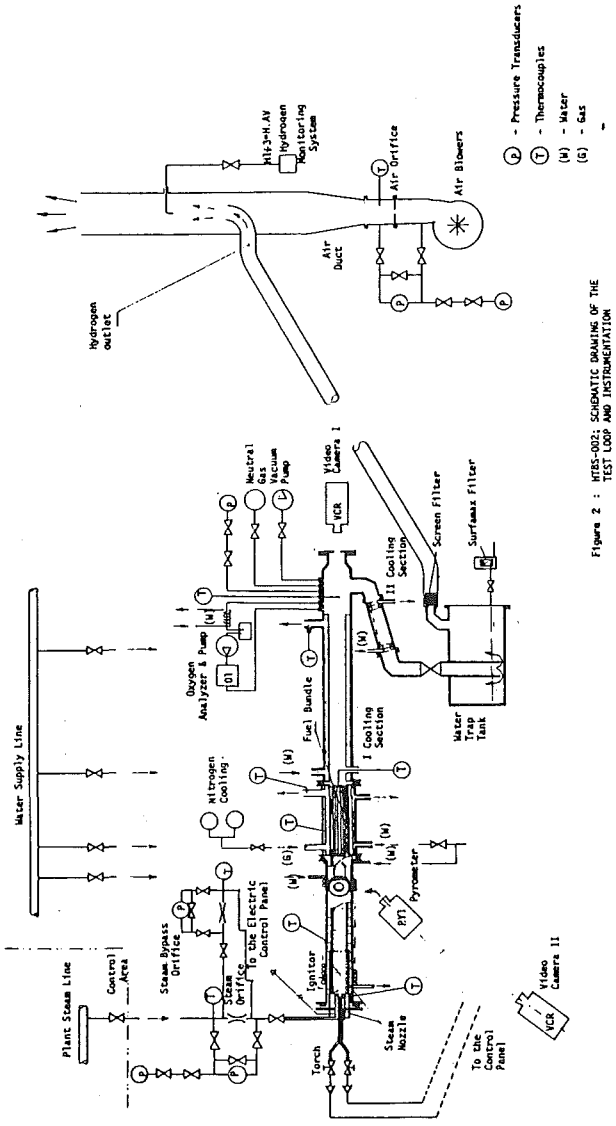

Figure 2 : HTBS-002; SCHEMATIC DRAWING OF THE TEST LOOP AND INSTRUMENTATION

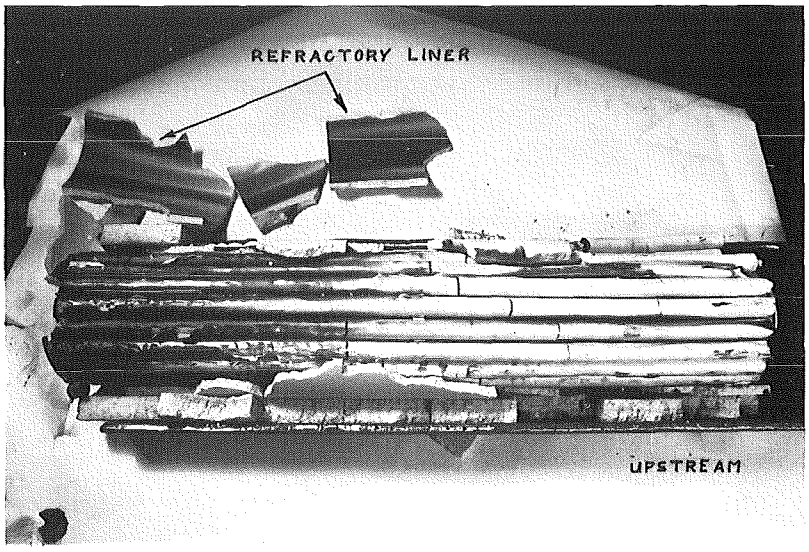

FIGURE 3: HTBS-001 POST-TEST APPEARANCE, PLAN VIEW

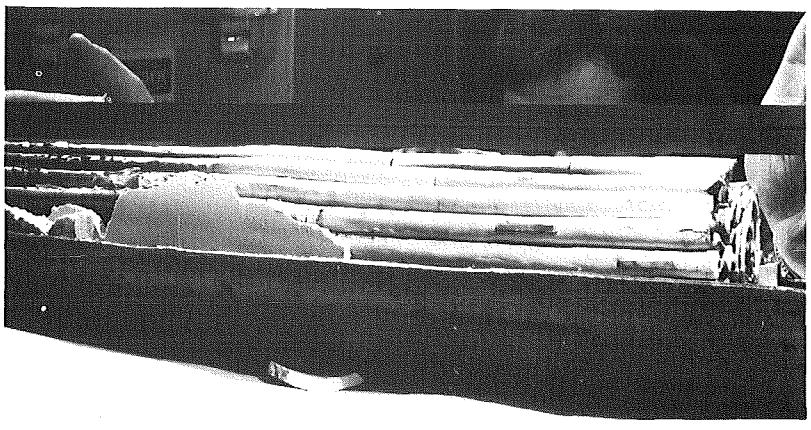

FIGURE 4: HTBS-001 POST-TEST APPEARANCE, SIDE VIEW

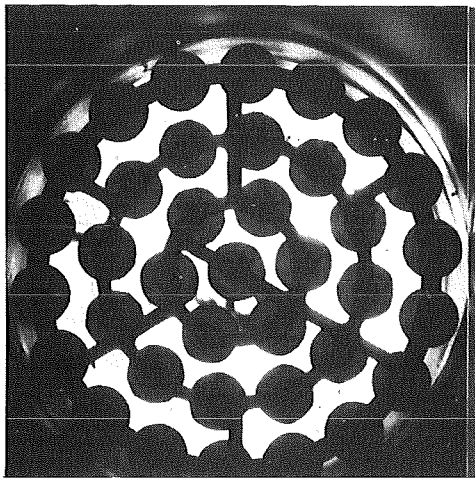

FIGURE 5: PRE-TEST UPSTREAM VIEW

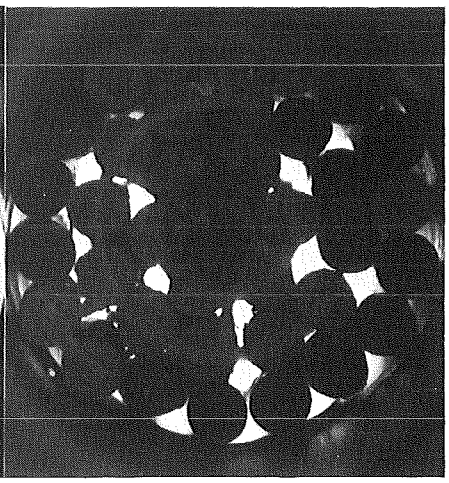

FIGURE 6: POST-TEST UPSTREAM VIEW

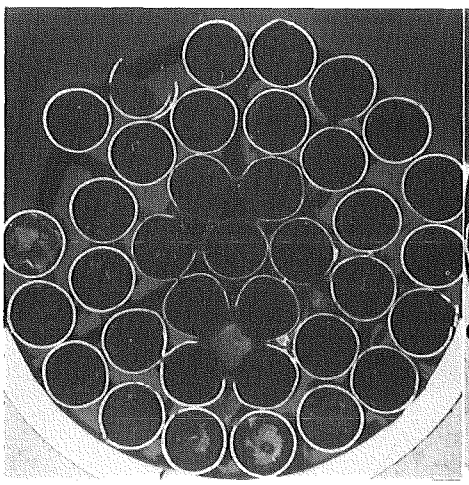

FIGURE 7: POST-TEST UPSTREAM SECTION (47 mm)

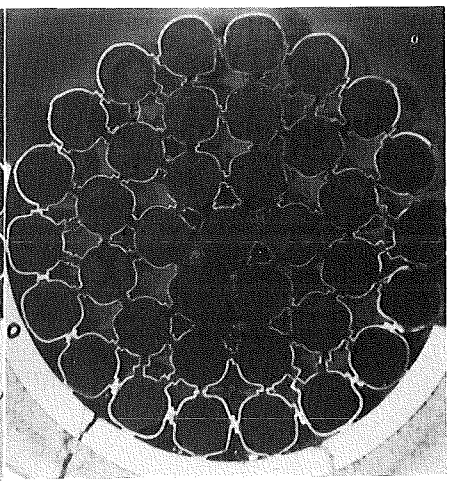

FIGURE 8: POST-TEST MID-PLANE SECTION (250 mm)

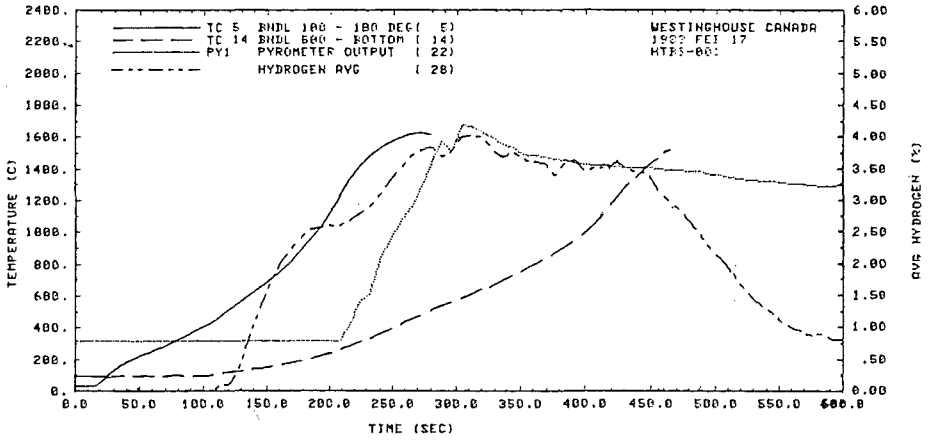

FIG.9 TEMPERATURE AND HYDROGEN PRODUCTION HISTORIES (HTBS-001).

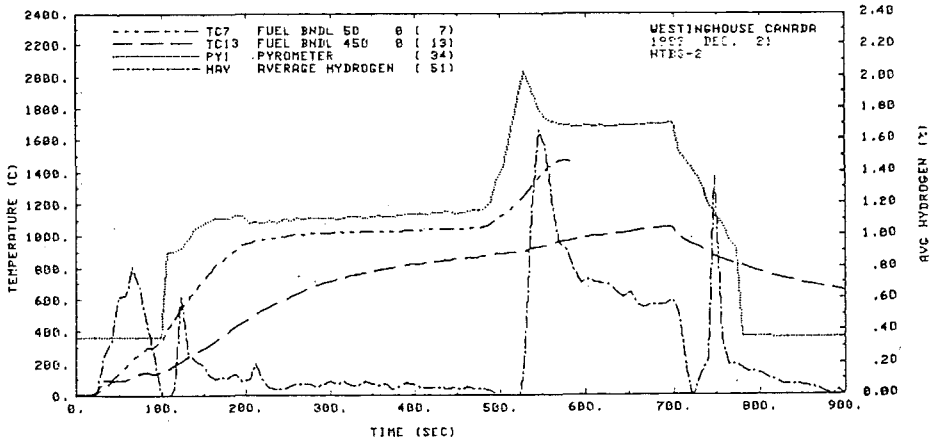

FIG.10 TEMPERATURE AND HYDROGEN PRODUCTION HISTORIES (HTBS-002).

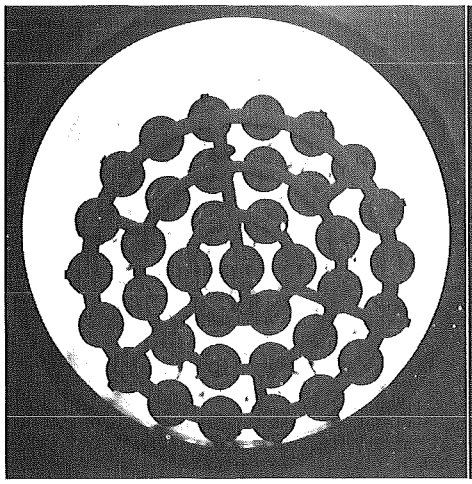

FIGURE 11: PRE-TEST UPSTREAM VIEW

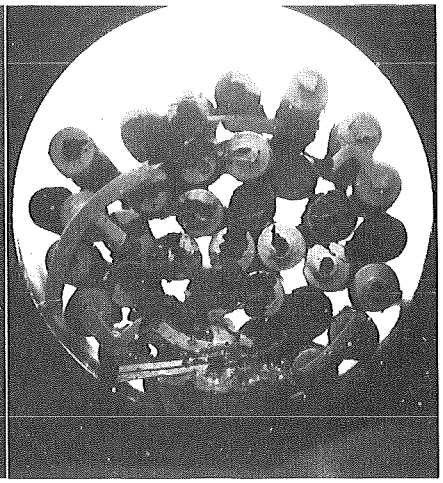

FIGURE 12: POST-TEST UPSTREAM VIEW

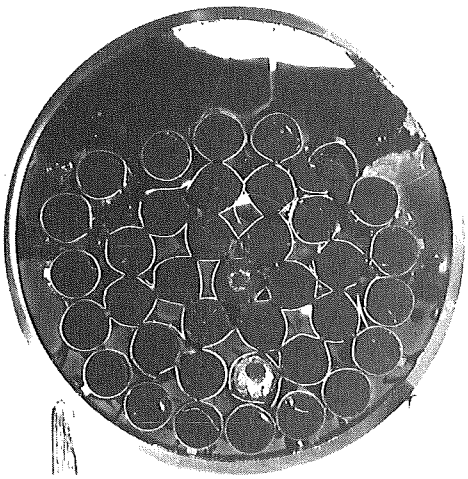

FIGURE 13: POST-TEST SECTION UPSTREAM END (47 mm)

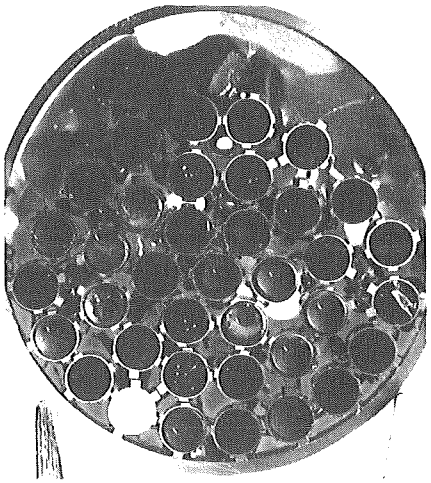

FIGURE 14: POST-TEST SECTION MID-PLANE (250 mm)

POST-ACCIDENT HEAT REMOVAL ANALYSIS: AN ASSESSMENT OF THE COMPOSITION OF CORE DEBRIS BEDS

Mohamed S. El-Genk, Sung-Ho Kim, and Dale Erickson

Department of Chemical and Nuclear Engineering
University of New Mexico
Albuquerque, New Mexico 87131, U.S.A.

ABSTRACT

An analytical model was developed to study suspension settling of mixtures having two particle species of unequal densities and of different sizes. The model predictions of the settling mode were in good agreement with the results of settling experiments. The model predictions of the composition of nuclear debris beds of UO_2 and zircaloy particles showed that these beds may have a single layer of mixed particles or may have two layers: a mixed layer at the bottom and top layer composed of either zircaloy particles or UO_2 particles.

INTRODUCTION

Determining the composition of debris beds that may form during a severe core damage accident in a nuclear reactor is important for post-accident heat removal. If a severe core damage accident in a Light Water Reactor (LWR) were to occur, the fuel rods may disintegrate and the UO_2 fuel and zircaloy cladding fragments could settle through a column of water coolant and form debris beds on available horizontal surfaces in the core. These beds could be several meters thick and would consist of a spectrum of particle sizes (a few microns to several millimeters) and shapes. Debris beds could also form in a Liquid Metal Fast Breeder Reactor (LMFBR) core following a hypothetical core meltdown accident. The molten fuel and steel cladding could fragment upon mixing with sodium coolant and form debris beds. The decay heat removal from such beds is important because inadequate cooling could cause a section of the bed to reach a temperature high enough to melt the particles and to thermally attack the supporting structures of low melting point stainless steel. In general, the coolability of core debris beds strongly depends on the morphology and size of particles, as well as on the composition of the beds [1-4].

The objectives of this work were to: (a) develop an analytical settling model for suspension settling of mixtures of two particle species of unequal densities and of different sizes; and (b) apply the model to the settling of mixtures of UO_2 and zircaloy particles through water. The composition of the UO_2-Zr particle beds was predicted as a function of the initial particle concentration, and as a function of the volume ratio and the size ratio of zircaloy to UO_2 particles in the water before settling.

SETTLING MODEL

Recently, Lockett and Bassoon [5] have shown that the slip velocity for a particle species, i, in a polydisperse system of N particle species can be given as

$$V_i = Vo_i \left(1 - \sum_{i=1}^{N} \alpha_i\right)^{n_i - 2} , \tag{1}$$

where $Vo_i = vo_i(\rho_i - \rho_c)/(\rho_i - \rho_f)$, (2)

and $$\rho_c = \left(1 - \sum_{i=1}^{N} \alpha_i\right)\rho_f + \sum_{i=1}^{N} (\alpha_i \rho_i) . \tag{3}$$

Equation (1) is based on Richardson and Zaki's correlation for the effective settling velocity of spherical particles [6] from a homogeneous suspension. The second term on the right-hand side of equation (1) accounts for the effect on the settling of particles of the increased drag due to the proximity of other particles in the suspension. The value of the index, n, was given as [7]:

$$n = 4.65 + 19.5(D_p/D_t) , \qquad Re < 0.2$$

$$n = 4.36 + 17.6(D_p/D_t)\, Re^{-0.03} , \qquad 0.2 < Re < 1$$

$$n = 4.45\, Re^{-0.1} , \qquad 1 \leq Re < 500$$

$$n = 2.39 , \qquad 500 \leq Re < 7000 . \tag{4}$$

Equation (1) is also applicable to nonspherical particles although the index, n, has a greater value [6,8]. For fine particles (4 to 7 μm in diameter), the index, n, is equal to 10.5 [7] and for millimeter-sized particles and creeping flow (Re < 0.1), the index, n, varies in value from 5.4 for cubics to 5.8 for angular particles [8].

In experimenting with the sedimentation of a binary mixture of spheres of different materials but of the same free-falling velocity, Richardson and Meikle [7] observed that the composition of the sediment strongly depends on the initial concentration of the particles in the suspension. (See Figure 1a.) When the concentration of the particles was less than 8 percent by volume, the sediment had two distinct layers: (1) a bottom layer of mixed particles and (2) an upper layer of light particles only (mode 1). As the concentration of particles increased above 8 percent, three distinct layers were identified in the sediment: (1) only dense particles at the bottom, (2) a mixture of both particles in the middle, and (3) light particles alone at the top (mode 2). At concentrations above 15 percent, complete segregation between the two particle species was achieved (mode 3). These settling modes were confirmed later by Smith and Phillips [9] who experimented with suspensions of two species of particles of different sizes and unequal densities.

Lockett and Bassoon have recently studied the settling of two particle species of different sizes and the same density in a diluted suspension (mode 1). This paper extends Lockett and Bassoon's [5] work to the settling of two particle species of different sizes and unequal densities. Unlike Lockett and Bassoon's model [5] which is limited only to mode 1, the present model can predict any of the three settling modes (that is, mode 1, mode 2, and mode 3).

Model Development

Consider a homogeneous suspension of N distinct particle species where settling of particles and displacement of host fluid occur only in the vertical direction. In the settling column, just after settling commences, the number of the settling zones depends on the settling mode of the sediment: N zones for mode 1 and N+1 zones for both mode 2 and mode 3. (See Figures 1 and 2.) The composition in the Nth zone in all settling modes is the same as the initial suspension. However, the composition of the zone N+1 of mode 2 differs from that of mode 3. In the zone immediately below the clear zone, (N=1) only light (slower) particles will be present. The interface between any two subsequent zones moves with the velocity of the dense (or the fastest) particle species in the zone immediately below the interface.

The slip velocity of a particle species, i, in zone k (where zones are numbered from zone k = 1 immediately below the clear zone and i = 1 is the light (or slowest) particle species) can be given as [5]

$$V_{ik} = Vo_i \left(1 - \sum_{i=1}^{k} \alpha_{ik}\right)^{n_i - 2} , \tag{5}$$

and in terms of the particle and fluid fluxes in zone k as

$$V_{ik} = \frac{\phi_{ik}}{\alpha_{ik}} - \frac{\phi_{fk}}{1 - \sum_{i=1}^{k} \alpha_{ik}} , \tag{6}$$

$$\text{where } Vo_i = \left(\frac{\rho_i - \rho_c}{\rho_i - \rho_f}\right) vo_i \tag{7}$$

$$\text{and} \quad \rho_c = \left(1 - \sum_{i=1}^{N} \alpha_i \rho_f\right) + \sum_{i=1}^{N} (\alpha_i \rho_i) . \tag{8}$$

For a settling column that is closed at its base, the conservation of mass in zone k gives

$$\sum_{i=1}^{k} \phi_{ik} + \phi_{fk} = 0 \tag{9}$$

Substituting equations (6) and (9) into equation (5) and summing the results over all particle species in zone k gives:

$$f_{ik} \sum_{\substack{i=1 \\ i \neq i}}^{k} \phi_{ik} + \phi_{ik} \left(1 - \sum_{\substack{i=1 \\ i \neq i}}^{k} \alpha_{ik}\right) = f_{ik} \gamma_{ik} , \tag{10}$$

where $f_{ik} = \dfrac{\alpha_{ik}}{\sum_{i=1}^{k} \alpha_{ik}}$, (11)

and $Y_{ik} = Vo_i\left(\sum_{i=1}^{k} \alpha_{ik}\right)\left(1 - \sum_{i=1}^{k} \alpha_{ik}\right)^{n_i-1}$ (12)

Equation (10) can be used to obtain the fluxes of the particle species in each of the settling zones; there are k equations for zone k where $k < N$. In mode 1, the number of zones equals the number of particle species in the system. However, in modes 2 and 3, there is an additional zone (N+1) immediately above the sediment. In this zone there are N and N - 1 equations for particle fluxes in mode 2 and in mode 3, respectively. (See Figure 2.)

Since $\phi_{ik} = V_{ik}\alpha_{ik}$, equation (10) can be rewritten in terms of the settling velocity of the particle species i in zone k as

$$f_{ik} \sum_{i=1}^{k} \alpha_{ik} \sum_{\substack{i=1 \\ i\neq j}}^{k} V_{ik}\alpha_{ik} + V_{ik}\alpha_{ik}\left(1 - \sum_{\substack{i=1 \\ i\neq j}}^{k} \alpha_{i}k\right) = f_{ik}\, Y_{ik} \quad (13)$$

The continuity equation of species i across the boundary between zones k and k - 1 gives

$$\alpha_{i,k-1} = \frac{(V_{ik} - V_{kk})\alpha_{ik}}{(V_{i,k-1} - V_{kk})} , \quad (14)$$

where V_{kk} is the velocity of the interface. For example, V_{11} and V_{22} are the velocities of the boundary between the clear zone and the first zone and between the first and second zones, respectively.

For the settling of two particle species of unequal sizes and densities, equations (5) through (14) were used to obtain expressions for the particle fluxes and for the velocities of the boundaries between settling zones. For simplicity, it was assumed that the volume concentration of each particle species in a given settling zone is uniform throughout the zone. However, in reality, particle concentrations can vary with height. The settling column consists of two zones for settling mode 1, and of three zones in modes 2 and 3. (See Figure 2.)

Zone 1 (k = 1) in All Three Settling Modes--Because there is only particle 1 in zone 1, equation (7) was reduced to:

$$Vo_1 = vo_1 (1 - \alpha_{11}) , \quad (15)$$

equation (5) to $$V_{11} = vo_1 (1 - \alpha_{11})^{n_1} , \quad (16)$$

and equation (14) in zone 1 to $V_{11} = \dfrac{(V_{12} - V_{22})\alpha_{12}}{\alpha_{11}} + V_{22}$. (17)

Eliminating V_{11} between equation (16) and (17) yields

$$\frac{V_{12} - V_{22}}{\alpha_{11}} \alpha_{12} + V_{22} - vo_1(1 - \alpha_{11})^{n_1} = 0 \ . \tag{18}$$

Equation (18) was used to determine the volume fraction, α_{11}, in zone 1. Then V_{11} was found by substituting the volume fraction, α_{11}, in either equation (16) or (17). Expressions for the velocities V_{12} and V_{22} of particle 1 and particle 2 in zone 2, respectively, are derived in the following section. The flux of species 1 in zone 1 can be given from equation (10) as:

$$\phi_{11} = Y_{11} \ . \tag{19}$$

Zone 2 (k = 2) in All Three Settling Modes--In this zone the two particle species are both present and the volume fluxes for the light (particle 1) and dense (particle 2) species are given, respectively, as:

$$\phi_{12} = \frac{f_{12}}{1 - \alpha_2} [Y_{12} (1 - f_{12}\alpha_2) - Y_{22}f_{22}\alpha_2] \ , \tag{20}$$

and $$\phi_{22} = \frac{f_{22}}{1 - \alpha_2} [Y_{22}(1 - f_{22}\alpha_2) - Y_{12}f_{12}\alpha_2] \ . \tag{21}$$

The velocities of particles 1 and of particle 2 in zone 2 are

$$V_{12} = (\phi_{12}/\alpha_{12}) \ , \tag{22}$$

and $$V_{22} = (\phi_{22}/\alpha_{22}) \ . \tag{23}$$

The volume concentrations α_{12} and α_{22} are the same as in the initial suspension.

Zone 3 (k = 3) in Settling Mode 3--In this zone only dense particles are present because they settle much faster than light particles. The volume flux of particle species 2 (dense particles) was given as:

$$\phi_{23} = Y_{23} \ , \tag{24}$$

and the settling velocity

$$V_{23} = \frac{\phi_{23}}{\alpha_{23}} \ . \tag{25}$$

To solve for V_{23} and α_{23} in equation (26), an equation similar to equation (18) was obtained:

$$\frac{V_{22} - V_{12}}{\alpha_{23}} \alpha_{22} + V_{12} - vo_2(1 - \alpha_{23})^{n_2} = 0 \tag{26}$$

Zone 3 (k = 3) in Settling Mode 2--In mode 2, the dense particles settle faster than light particles. However, the velocity differential is smaller than in mode 3. Thus, complete separation of the two particle species does not occur in zone 3 immediately above the sediment. In this zone the light particles are displaced by the dense particles so that the net fluid flow is zero [9].

$$\phi_{13} + \phi_{23} = 0 \ . \tag{27}$$

To solve for ϕ_{13} and ϕ_{23}, an additional equation for ϕ_{13} was developed below. The settling velocities of light and dense particles, V_{13} and V_{23} in zone 3, mode 2 can be written as:

$$V_{13} = \frac{\phi_{13}}{\alpha_{13}} = Vo_3(1 - \alpha_3)^{n_1-2+0.4} + b + c \tag{28}$$

$$V_{23} = \frac{\phi_{23}}{\alpha_{23}} = Vo_3(1 - \alpha_3)^{n_2-2+0.4} + b - c \tag{29}$$

where $\alpha_3 = (\alpha_{13} + \alpha_{23})$. The quantity 0.4 was added to the exponent (n_i-2) in equation (5) at the suggestion of Mirza and Richardson [10]. They found that using the exponent 1.6 instead of 2 produced good agreement with experimental results at high particle concentration. Also, the coefficients b and c were introduced to account for the excess drag on the settling of particles due to the high particle concentration in this zone. A limiting case in zone 3, mode 2 is that the volume flux of light particles becomes equal to zero when the density of the mixture becomes equal to the density of the light particles (that is, $\alpha_{13} \gg \alpha_{23}$):

$$\phi_{13} = 0 \ , \text{ when } \rho_c = \rho_1 \ . \tag{30}$$

In this case, concentration of particle 1 in this zone 3 is

$$\bar{\alpha}_{13} = \frac{\rho_1 - \varepsilon\rho_f - (1 - \varepsilon)\rho_2}{\rho_1 - \rho_2} \ . \tag{31}$$

Substituting equatons (30) and (31) into equations (28) and (29) gives:

$$b = -c, \text{ and } 2b = -\bar{\alpha}_{13}Vo_2(1 - \alpha_3)^{n_2-1.6} \ . \tag{32}$$

Substituting in equation (28) gives the following expression for ϕ_{13}:

$$\phi_{13} = \frac{Vo_1(1 - \alpha_3)^{n_1-1.6} - Vo_2(1 - \alpha_3)^{n_2-1.6} + \bar{\alpha}_{13}Vo_2(1 - \alpha_3)^{n_2-1.6}}{\frac{1}{\alpha_{23}} + \frac{1}{\alpha_{13}}} \tag{33}$$

The velocity of V_{2+3} of the boundary between zone 2 and zone 3 in mode 2 can be given as:

$$V_{2+3} = \frac{\phi_{12} - \phi_{13}}{\alpha_{12} - \alpha_{13}} \quad . \tag{34}$$

The rising velocities of the different layers in that sediment can be given as follows:

(a) Mixed particle sediment in settling modes 1 and 2

$$up_{1+2} = \frac{\phi_2}{\alpha_2 - \varepsilon_{1+2}} \quad , \tag{35}$$

where $\alpha_2 = (\alpha_{12} + \alpha_{22})$ and $\phi_2 = (\phi_{12} + \phi_{22})$.

(b) Light particle sediment in settling modes 1 and 2

$$up_1 = \frac{\phi_{11}}{\alpha_{11} - \varepsilon_1} \quad . \tag{36}$$

(c) Light particle sediment in settling mode 3

$$up_1 = \frac{\phi_{13}}{\alpha_{13}} \quad . \tag{37}$$

(d) Dense particle sediment in all three settling modes

$$up_2 = \frac{\phi_{23}}{\alpha_{23} - \alpha_2} \quad . \tag{38}$$

COMPARISON OF MODEL WITH EXPERIMENTS

The governing equations (15), (17), (18-27), (31), and (33) were solved simultaneously to calculate the volume fraction and the fluxes of the two particle species in the different settling zones. The rising velocity of the sediment and the settling velocities of the particle species were calculated through use of equations (35-38). These velocities were then used to calculate the heights of the settling zones as well as the thicknesses of the particle layers in the sediment as functions of time. Ultimately, the composition of the sediment and the mode of settling were determined. The settling mode was determined as follows:

(a) If the settling velocity of light particles (particles 1) in zone 2 (V_{12}) was negative, but greater in magnitude than the rising velocity of the dense particles (Up_2), then mode 3 will result. In this case, the light particles will be moving upward faster than the sediment of dense particles is rising; so no light particles can be trapped in the sediment until all the dense particles have settled.

(b) If the rising velocity of the sediment of dense particles in mode 2 was approximately zero, and the rising velocity of the mixed zone (Up_{1+2}) was not zero, then mode 1 will occur.

(c) If both Up_2 and Up_{1+2} (in mode 2) are not zero, then the settling mode 2 will occur.

The rising velocity of each particle layer in the sediment was taken to be constant throughout the sedimentation process. For simplicity, the porosity of the different particle layers in the sediment was assumed uniform and equal to 0.4. Practically, the porosity will vary with the size and the morphology of the particles [2], as well as with the composition of the particle layer. However, when the porosity was taken as 0.3 instead of 0.4, there was no change in the predicted settling mode or the relative height of the particle layers in the sediment, but rather in the total height of the sediment.

In tables I through IV, the model predictions of the settling mode were compared with the experimental results of Smith and Philips [9]. As shown in table I, when the particle size ratio was 0.98, there was excellent agreement between the model predictions and the experiments in all cases. In table II, where the particle size ratio was 1.08, the correct settling mode was predicted in 19 out of 22 experiments. However, when the particle size ratio was 2.60 and 4.31, the agreement between the model and the experiments occurred only in 12 out of 20 experiments (table III), and two out of four experiments (table IV), respectively. Smith and Philips did not report the total height and thicknesses of different layers of the sediment. The values listed in tables I through IV were calculated using two methods. In the first method, the height of sediment was determined by adding up the thicknesses of particle layers calculated by the model; and in the second method, the height was determined by assuming a uniform porosity 0.40 in the sediment.

In summary, the settling model predictions of the sediment composition were in excellent agreement with experimental results when the particle size ratio was < 1.08. When the size ratio of the two particle species was 2.41 and 4.31, the agrement between the model and the experimental results occurred only in about 50 percent of the cases. Such disagreement could have been caused by an error in identifying the settling mode experimentally. Additionally, increasing the size ratio of the particle species in the suspension could have resulted in a mixed flow condition in the settling column, a creep flow from small particles, and a transition or turbulent flow from large particles. These mixed flow conditions could be partially responsible for the disagreement between the present settling model, developed mainly for creep flow, and some of the experiments that used particle species with a large size ratio.

APPLICATION TO POST-ACCIDENT HEAT REMOVAL

The settling model was applied to the settling from a suspension of UO_2 and zircaloy particles. The height of the settling water column was taken as 2.5 meters, and sizes of UO_2 and zircaloy particles varied from 10 to 10^4 μm. The following assumptions were made: (1) UO_2 and zircaloy particles were in a homogeneous suspension in water initially at 300°C before settling; (2) creep flow prevailed during particle settling, (3) porosity of sediment was uniform and equal to 0.40; (4) the support structure on which the particle bed formed was impermeable; and (5) lateral mixing of the particle species was negligible.

Figures 3 through 5 present the predicted composition of core debris bed as a function of the size ratio and of the volume ratio of zircaloy to UO_2 particles. As shown in Figure 3, the sediment of the core debris generally had two distinct layers: a layer of mixed UO_2 and zircaloy particles at the bottom; and a top layer of either zircaloy or UO_2 particles, except when the particle size ratio (D_{Zr}/D_{UO_2}) was equal to a critical value. (See Figure 6.) As shown in Figure 6, the critical particle size ratio increased as the total volumetric concentration of the particles and/or the volume ratio of zircaloy to UO_2 particles in the suspension (V_{Zr}/V_{UO_2}) increased. At the critical particle size ratio, the effective settling velocity of the zircaloy particle was equal to that of UO_2 particles. This produced a sediment that only had a single layer of mixed UO_2 and zircaloy particles. When the particle size ratio was smaller than the critical value (for example, $D_{Zr} \ll D_{UO_2}$), UO_2 particles settled faster than zircaloy particles. This dissimilarity in particle sizes produced a top layer of zircaloy alone. (See Figure 4.) The thickness of this layer, which was smaller than the total height of the debris bed, decreased as (D_{Zr}/D_{UO_2}) increased or as (V_{Zr}/D_{UO_2}) decreased. On the other hand, when the particle size ratio was higher than the critical ratio (for example, $D_{UO_2} \ll D_{Zr}$), UO_2 particles settled more slowly than zircaloy particles, thus producing a top layer of only UO_2 particles. (See Figure 5.) Unlike the top layer of zircaloy particles, the top UO_2 particle layer increased in thickness as (D_{Zr}/D_{UO_2}) increased or as (V_{Zr}/V_{UO_2}) decreased.

SUMMARY AND CONCLUSIONS

This research developed a model for the settling from suspension of two particle species of different sizes and unequal densities, including sediment buildup. The thickness and the composition of various layers of sediment (that is, the settling mode) can be predicted. The model predictions of the modes of settling (modes 1, 2, or 3) were in excellent agreement with experimental results when the particle size ratio was < 1.08; when the size ratio was 2.60 and 4.31, the agreement occurred in only about 50 percent of the cases.

The settling model was used to predict the composition of nuclear debris beds of UO_2 and zircaloy particles, settling through water. Calculations showed that the sediment may have either a single layer of mixed particles or may have two layers: a mixed layer at the bottom and a top layer of zircaloy particles or UO_2 particles. The exact composition and the relative thickness of these layers in the debris beds depend on the initial concentration of UO_2 and zircaloy particles in the suspension as well as on the volume ratio and the size ratio of zircaloy to UO_2 particles. These results may be applied to actual nuclear reactor accident conditions where lateral mixing of particle species is limited and the height of the settling water column is quite deep. The present model can also be used to predict the composition of debris beds (mainly UO_2 and stainless steel particles) forming in a liquid metal fast breeder reactor following a hypothetical core meltdown accident. Future research should include a study of the effects on the dryout power limits of various compositions of debris beds. Such limits could differ appreciably from limits previously detected in beds of single type particles. Additionally, investigate the effects on the bed composition of lateral mixing of particle species during settling.

NOMENCLATURE

f = parameter [equation (10)]
Re = Reynolds number ($\rho_f v_o D_p / \mu_f$)
Up = rising velocity of sediment (cm/sec)
V = effective settling velocity of the boundary between zones or particle species (cm/sec)
v_o = terminal velocity of a spherical particle (cm/sec)
V_o = modified terminal velocity [equation (6)]
Y = parameter [equation (7)]

Greek letters

α = volume fraction of a particle species in suspension
$\bar{\alpha}$ = effective particle volume fraction [equation (30)]
ε = volume fraction of the particles in the sediment
μ = dynamic viscosity (poise)
ϕ = volumetric particle flux (cm/sec)
ρ = density (g/cm^3)
ρ_c = density of suspension (g/cm^3) [equation (9)]

Subscripts

f = liquid in settling column
i = ith particle species
k = settling zone or number of particle species
ik = particle species i in settling zone k
s = solid sphere
1 = slower or light particle species
2 = faster or dense particle species
1+2 = mixed particles

REFERENCES

1. El-Genk, M. S. and Bergeron, E. D. "Dryout Heat Flux in Particulate Bed of Steel Grit," Trans. Am. Nucl. Soc., 44, 377-378 (1983).

2. El-Genk, M. S. et al. "Dependence of Porosities and Capillary Pressure in Particle Beds on the Morphology and the Size of the Particles," AiChE, Symposium Series 225, 70, 256-267 (1983).

3. Dhir, V. K. and Catton, I. "The Dryout Heat Flux in Debris Beds Containing Non-heated Constituents and Particles of Different Sizes," Trans. Am. Nucl. Soc., 28, 455 (1977).

4. El-Genk, M. S. and Kim, Sung-Ho. "Experimental Studies of Lateral Distribution and Composition of Sediments of Single and Binary Particle Mixtures," AIChE Symposium Series, 22nd ASME/AIChE National Heat Transfer Conference, Niagara Falls, NY, (August 6-8, 1984).

5. Lockett, M. J. and Bassoon, K. S. "Sedimentation of Binary Particle Mixtures," Powder Technology, 24, 1-7 (1979).

6. Richardson, J. F. and Zaki, W. N. "Sedimentation and Fluidization: Part I," Trans. Inst. Chem. Engrs, 32, 35-51 (1984).

7. Richardson, J. F. and Meikle, R. A. "Sedimentation and Fluidization, Part III: The Sedimentation of Uniform Fine Particles and of Two-component Mixtures of Solids," Trans. Inst. Chem. Engrs, 44, 348-356 (1961).

8. Chong, Y. S. et al. "Effects of Particle Shape on Hindered Settling in Creeping Flow," Powder Technology, 23, 55-56 (1979).

9. Smith, T. N. and Philips, C. R. "Modes of Settling and Relative Settling Velocities in Two-Species Suspensions," Ind. Eng. Chem. Fundam., 10, 581-587 (1971).

10. Mirza, J. and Richardson, J. F. "Sedimentation of Suspensions of Particles of Two or More Sizes," Chem. Engr. Sci., 34, 447-454 (1979).

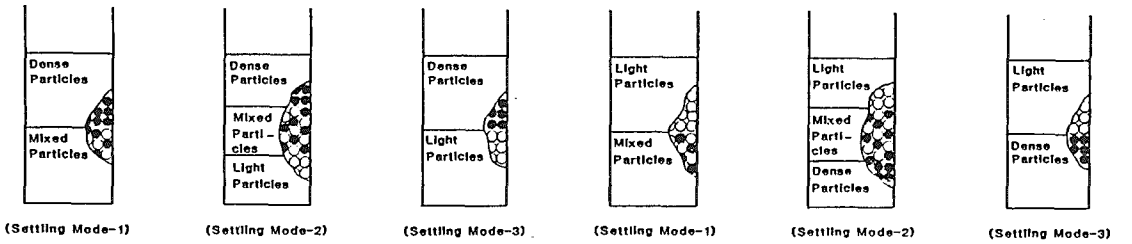

(b) Free falling velocity of dense particles is much smaller than that for light particles.

(a) Free falling velocity of dense particles is larger than that for light particles.

Figure 1. Sediment compositions in binary particle system.

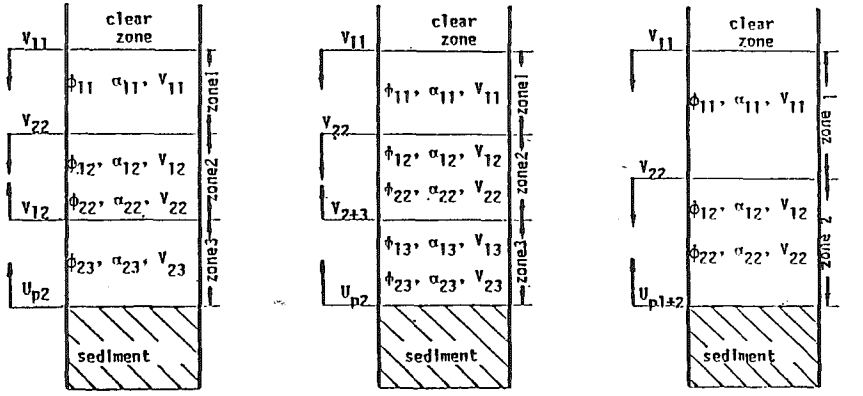

(a) Settling Mode 3 (b) Settling Mode 2 (c) Settling Mode 1

Figure 2. Various zones in the settling column of binary particle mixtures.

Table I

Comparison of the Settling Model with Suspension Settling Experiments (particle size ratio = 0.98)

Settling column: fluid = glycerol; height = 76 cm; inner diameter = 6.97 cm

ρ_f = 1.1405 g/cm³ ρ_{p_2} = 1.4093 g/cm³ D_{p_1} = 0.0577 cm $(V_o^P/V_o^L)^*$ = 5.95

ρ_{p_1} = 1.1877 g/cm³ μ_f = 0.0875 poise D_{p_2} = 0.059 cm Size ratio = 0.98

Total Concentration of Particles	Volume Fraction of Particles 1 to 2	Calculated Height of Layers (cm)			Calculated Height of Sediment (cm)		Settling Mode	
		Dense Particles	Mixed Particles	Light Particles	Method 1*	Method 2†	Predicted††	Observed
0.10	0.250	0	10.06	2.71	12.77	12.77	1	1
	0.500	0	7.37	5.40	12.77		1	1
	0.750	0	4.70	8.07	12.77		1	1
0.20	0.250	0	20.11	5.44	25.55	25.55	1	1
	0.500	0	14.72	10.82	25.54		1	1
	0.750	0	9.33	16.22	25.55		1	1
0.30	0.250	0	30.46	7.86	38.32	38.32	1	1
	0.500	0	22.42	15.90	38.32		1	1
	0.750	0	14.27	24.05	38.32		1	1
0.40	0.250	0	41.85	9.24	51.09	51.09	1	1
	0.500	0	31.46	19.63	51.09		1	1
	0.750	0	20.49	30.60	51.09		1	1

*The ratio of free falling velocity of dense particle to that of light particle.
†Predicted by the model.
††Assuming a homogeneous porosity of 0.405 in the sediment.

Table II

Comparison of the Settling Model with Suspension Settling Experiments (particle size ratio = 1.08)

Settling column: fluid = glycerol; height = 76 cm; inner diameter = 6.97 cm

ρ_f = 1.255 g/cm³ ρ_{p_2} = 2.96 g/cm³ D_{p_1} = 0.059 cm $(V_o^D/V_o^L)^*$ = 9.50

ρ_{p_1} = 1.4093 g/cm³ μ_f = 8.0 poise D_{p_2} = 0.0617 cm Size ratio = 1.08

Total Concentration of Particles	Volume Fraction of particles 1 to 2	Calculated Height of Layers (cm)			Calculated Height of Sediment (cm)		Settling Mode	
		Dense Particles	Mixed Particles	Light Particles	Method 1††	Method 2††	Predicted	Observed
0.10	0.500	0.37	6.55	5.85	12.77	12.77	2	2
0.15	0.333	0.49	12.71	5.96	19.16	19.16	2	2
	0.667	0.37	7.09	11.70	19.16		2	2
0.20	0.25	0.59	10.93	6.03	25.55	25.55	2	2
	0.50	0.53	13.12	11.09	25.54		2	2
	0.75	0.37	7.65	17.52	25.54		2	2
0.25	0.200	0.70	25.12	6.01	31.93	31.93	2	2
	0.400	0.67	19.28	11.98	31.93		2	2
	0.800	0.38	8.25	23.30	31.93		2	2
0.30	0.167	0.80	31.64	5.87	38.31	38.31	2	2
	0.333	0.82	25.61	11.89	38.31		2	2
	0.833	0.38	8.94*	28.99	38.31		2	2
0.35	0.167	0.90	37.29	6.51	44.71	44.71	2	3
	0.429	0.92	26.25	17.53	44.70		2	2
	0.833	0.45	10.64	33.62	44.71		2	2
0.40	0.250	1.00	39.48	10.61	51.09	51.09	2	2
	0.500	1.03	27.35	22.71	51.09		2	2
	0.750	0.73	16.13	34.23	51.09		2	2
0.45	0.222	1.01	47.39	9.09	57.48	57.48	2	3
	0.556	1.09	29.26	27.12	57.47		2	2
0.50	0.200	0.89	56.21	6.77	63.87	63.87	2	3
	0.800	0.61	21.79	41.47	63.87		2	2

*The ratio of free-falling velocity of dense particle to that of light particle.
†Predicted by model.
††Assuming a homogeneous porosity of 0.405 in the sediment.

Table III

Comparison of the Settling Model with Suspension Settling Experiments (particle size ratio = 2.60)

Settling Column: fluid = glycerol; height = 76 cm; inner diameter = 6.97 cm

ρ_f = 1.255 g/cm³ ρ_{p_2} = 2.96 g/cm³ D_{p_1} = 0.059 cm $(V_0^D/V_0^L)^*$ = 1.64

ρ_{p_1} = 1.4093 g/cm³ μ_f = 8.0 poise D_{p_2} = 0.0227 cm Size ratio = 2.60

Total Concentration of Particles	Volume Fraction of Particles 1 to 2	Calculated Height of Layers (cm)			Calculated Height of Sediment (cm)		Settling Mode	
		Dense Particles	Mixed Particles	Light Particles	Method 1[1]	Method 2[2]	Predicted	Observed
0.10	0.500	6.24	1.24	3.29	12.77	12.77	2	2
0.15	0.333	12.78	0	6.38	19.16	19.16	3	2
	0.667	7.56	2.25	9.35	19.16		2	2
0.20	0.250	19.16	0	6.38	25.54	25.55	3	2
	0.750	6.73	4.40	14.41	25.54		2	2
0.25	0.200	25.55	0	6.38	31.93	31.93	3	3
	0.400	19.16	0	12.77	31.93		3	2
	0.800	6.48	5.75	19.70	31.93		2	2
0.30	0.167	31.93	0	6.39	38.32	38.32	3	3
	0.333	25.55	0	12.77	38.32		3	2
	0.833	6.64	6.51	25.17	38.32		2	2
0.35	0.143	38.31	0	6.40	44.71	44.71	3	3
	0.429	25.54	0	19.16	44.70		3	2
	0.857	7.14	6.76	30.80	44.70		2	2
0.40	0.250	38.32	0	12.77	51.09	51.09	3	3
	0.500	25.55	0	25.54	51.09		3	2
	0.750	12.77	0	38.32	51.09		3	2
0.45	0.111	51.10	0	6.38	57.48	57.48	3	3
	0.222	44.72	0	12.76	57.48		3	3
0.50	0.000	12.77	0	51.09	63.86	63.07	3	2

*The ratio of free-falling velocity of dense particle to that of light particle.

[1]Predicted by the model.

[2]Assuming a homogeneous porosity of 0.405 in the sediment.

Table IV

Comparison of the Settling Model with Suspension Settling Experiments (particle size ratio = 4.31)

Settling column: fluid = glycerol; height = 76 cm; inner diameter = 6.97 cm

ρ_f = 1.154 g/cm³ ρ_{p_2} = 2.96 g/cm³ D_{p_1} = 0.0415 cm $(V_0^D/V_0^L)^*$ = 0.38

ρ_{p_1} = 1.4093 g/cm³ μ_f = 0.11 poise D_{p_2} = 0.0096 cm Size ratio = 4.31

Total Concentration of Particles	Volume Fraction of Particles 1 to 2	Calculated Height of Layers (cm)			Calculated Height of Sediment (cm)		Settling Mode	
		Dense Particles	Mixed Particles	Light Particles	Method 1	Method 2	Predicted	Observed
0.20	0.500	20.74	1.24	3.57	25.55	25.55	2	2
0.30	0.167	31.93	0	6.39	38.32	38.32	3	2
0.35	0.286	31.93	0	12.78	44.71	44.71	3	2
	0.714	21.76	11.18	11.77	44.71		2	2

*The ratio of free-falling velocity of dense particle to that of light particle.

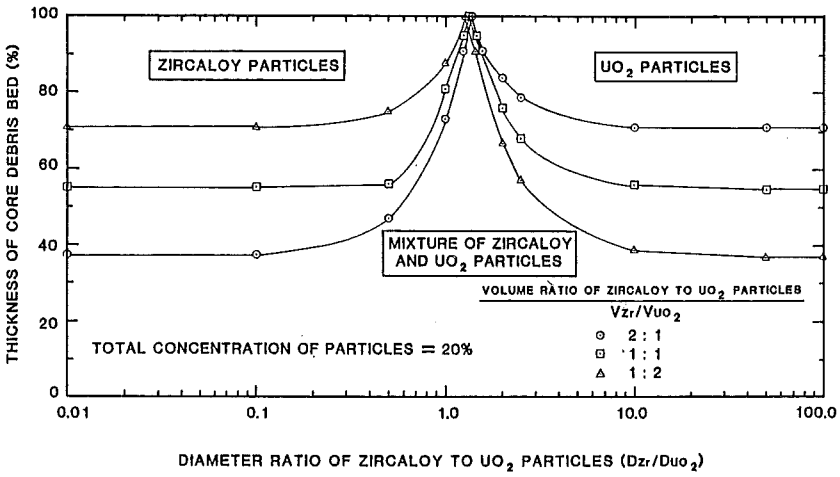

Figure 3. The composition of debris beds as a function of size ratio and volume ratio of zircaloy to UO_2 particles.

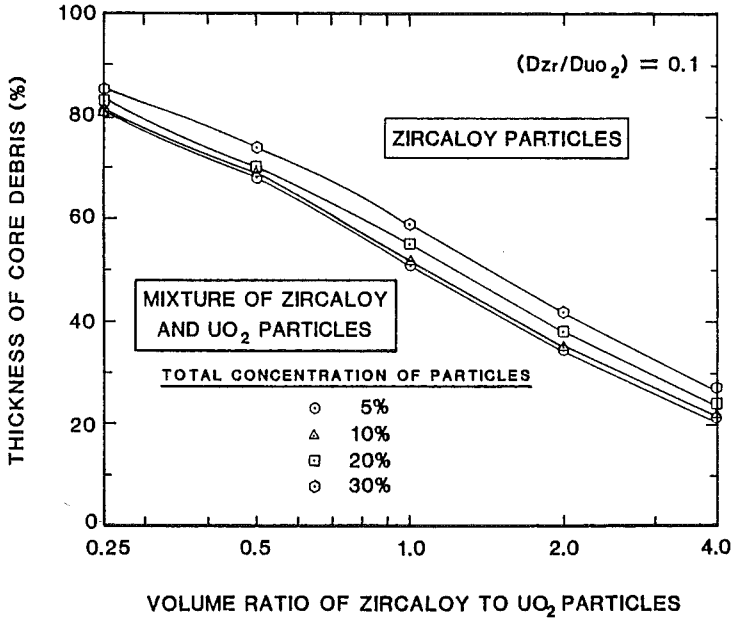

Figure 4. The thickness of debris beds as a function of the total particle concentration at a volume ratio of zircaloy to UO_2 particles for $(D_{Zr}/D/_{UO_2})$ less than the critical particle size ratio.

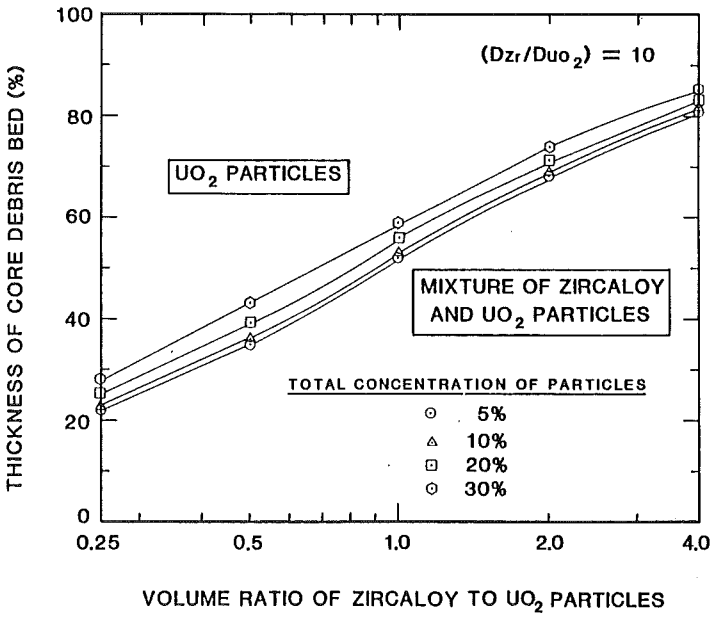

Figure 5. The debris bed thickness as a function of the total particle concentration at a volume ratio of zircaloy particle to UO_2 particles for (D_{Zr}/D_{UO_2}) greater than the critical size ratio.

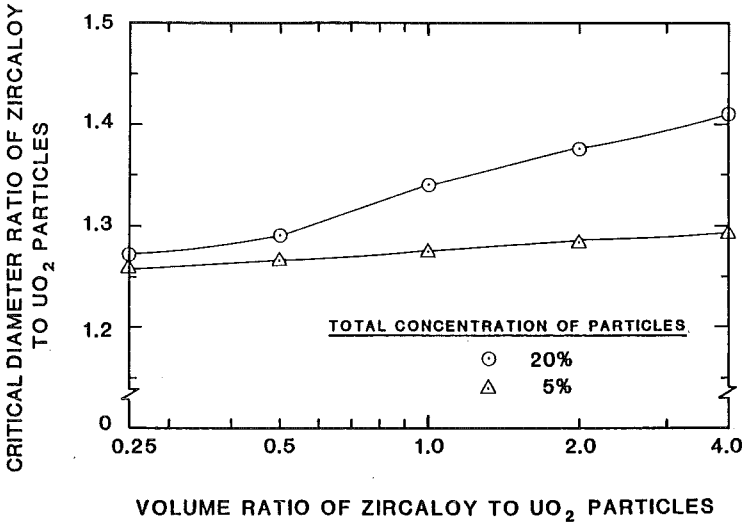

Figure 6. Critical size ratio of zircaloy to UO_2 particles as a function of volume ratio of zircaloy to UO_2 particles and particle concentration.

EXTERNAL AND INTERNAL REACTION OF ZIRCALOY TUBING WITH OXYGEN AND UO_2 AND ITS MODELING

P. Hofmann[1], H.J. Neitzel[2]

Kernforschungszentrum Karlsruhe
[1]Institut für Material- und Festkörperforschung
[2]Institut für Reaktorbauelemente
Postfach 3640
D-7500 Karlsruhe
Federal Republic of Germany

ABSTRACT

Under severe fuel damage conditions a combined external and internal oxidation of the fuel rod cladding occurs due to a reaction with steam on the outside surface and the UO_2 fuel on the inside surface. These reactions result in the formation of oxygen-stabilized α-Zr(O) phases, ZrO_2 and a (U,Zr) alloy. The reaction kinetics have been studied with both isothermal and transient temperature experiments above 800°C. The tests were performed using short LWR fuel rod sections in an (Ar + 25 Vol.% O_2) environment. The numerical model PECLOX has been developed which solves the Fick and Stefan equations. It predicts the formation, growth, and disappearance of the various interaction layers and the corresponding oxygen profiles as functions of temperature and time.

INTRODUCTION

In hypothetical light water reactor (LRW) accidents, nuclear fuel rods may be subjected to very high temperatures for periods sufficient to cause severe fuel damage (SFD). A wide variety of scenarios can be postulated in which SFD may occur at an essentially unchanged high coolant pressure or at low pressure conditions.

Since Zircaloy-4 (Zry) is thermodynamically unstable with respect to H_2O and UO_2 the cladding can react chemically with the oxygen of the steam and the fuel. A quantitative description of the combined H_2O/Zry and UO_2/Zry chemical interaction as a function of temperature and time is needed to predict LWR fuel rod behavior in SFD accidents. For this reason extensive out-of-pile UO_2/Zry reaction experiments have been performed. The results under inert gas conditions are published in /1,2/, and the results with an oxidizing environment are described in this paper.

The present work describes the results of out-of-pile annealing experiments with LWR fuel rod sections conducted from 800 to 1700°C in an oxidizing atmosphere (Ar + 25 Vol.% O_2) under isothermal and transient temperature conditions, with an external overpressure of about 40 bar and annealing times of 1 to 150 min. In addition, a numerical computer model has been developed which is able to predict the extent of the chemical interactions.

The modeling of the combined internal and external cladding interactions resulted in the numerical model PECLOX (pellet cladding oxidation). PECLOX solves the Fick and Stefan equations. It predicts the formation, growth, and disappearance of the various interaction layers and the corresponding oxygen profiles as a function of temperature and time. The external oxidation of Zry cladding due to the interaction with the steam has been extensively studied and described in models. However, the UO_2/Zry interaction has not yet been satisfactorily described in models, especially for transient temperature conditions and also not for combined internal and external cladding oxidation.

The first attempt to model the complex UO_2/Zry chemical interaction was made by Cronenberg and El-Genk /3/.They derived an oxygen diffusion model which solves a two-media problem with a moving boundary in Zry due to the alpha-beta phase change. In this analysis substantial simplifications were made since not all experimentally observed interaction layers were considered. Olander /4/ developed a sophisticated model that accounts for the formation and growth of all three interaction layers between the UO_2 and the Zry. The kinetics of the process are governed by diffusion of oxygen, uranium and zirconium. However, the application of the theoretical model is limited since the necessary kinetic and thermodynamic data are not all available. Denis and Garcia /5/ developed an analytical model which solves the oxygen diffusion problem in all the phases which form due to UO_2/Zry interaction, without taking into account uranium and zirconium diffusion. The main goal of this model was to determine the temperature-dependent oxygen diffusion coefficients in the various UO_2/Zry interaction layers and the oxygen concentrations at the interfaces; these data are used in the PECLOX calculations. All the models /3,4,5/ attempt only to simulate the kinetics of the system during the first stages of the process when all the interface movements obey parabolic rate laws (infinite systems). The model PECLOX has been developed to calculate the external and internal cladding oxidation for constant and transient temperature conditions up to complete Zry oxidation.

EXPERIMENT DESIGN AND CONDUCT

The out-of-pile UO_2/Zry reaction experiments were performed in an (Ar + 25 Vol.% O_2) gas mixture with short cladding tube specimens filled with stoichiometric high-density UO_2 pellets in the high temperature/high pressure autoclave apparatus MONA /1,2/. The specimens were 100 mm long with an outside diameter of 10.75 mm and a wall thickness of 0.72 mm. The chemical composition of the fuel and cladding are given in /1,2/. The specimen is contained in a high pressure vessel and inductively heated, with the cladding as the susceptor. The experiment conduct is described in detail in /1,2/.

EXPERIMENT RESULTS

Due to oxygen uptake by the Zry cladding from reaction with gaseous oxygen on the outside and from reaction with UO_2 on the inside, oxygen-stabilized α-Zr(O) phases, ZrO2 and a (U,Zr) alloy formed. The sequence of the various phases at all temperatures is from the inside:

$$[UO_2+U]\rightarrow[\alpha\text{-}Zr(O)_a+(U,Zr)^*]\rightarrow[U,Zr]\text{alloy}\rightarrow\alpha\text{-}Zr(O)_b\rightarrow\beta\text{-Zry}\rightarrow\alpha\text{-}Zr(O)\rightarrow ZrO_2.$$

---

* the (U,Zr) alloy within the α-$Zr(O)_a$ layer is mainly concentrated at the grain boundaries

Figure 1 shows the sequence of the external and internal interaction layers. The α-Zr(O) layers which form at the inside and the α-Zr(O) layer which form at the outside grow into the cladding at roughly the same rates. Moreover, due to the elevated oxygen potential (oxygen partial pressure) of the gas mixture or steam compared to stoichiometric UO_2, a ZrO_2 layer also forms on the external cladding surface. Results obtained at 1020 and 1300°C are presented in figure 2, with the thickness of the reaction zones plotted versus $\sqrt{t}$. With increasing time the β-phase of the cladding disappears due to oxygen uptake and transformation into α-Zr(O). The growth of the various layers as functions of temperature and time and the increase in fuel rod diameter due to the formation of ZrO_2 are evident. The time required to completely convert the β-Zry region in the center of the cladding to α-Zr(O) is strongly temperature dependent. After the disappearance of the β-phase, the oxidized cladding tube is completely embrittled, and no longer mechanically stable. Minor forces acting during cooldown or subsequent handling cause the fuel rod sections to break apart. Since embrittlement of the cladding occurs as a result of the formation of α-Zr(O) the internal oxidation contributes to approximately the same extent as the external oxidation. For this reason embrittlement of the cladding occurs about four times faster than by one-sided oxidation alone.

The UO_2/Zry interaction can only continue until oxygen saturation is reached in all the α-Zr(O) phases. The UO_2/Zry interaction can not proceed beyond oxygen saturation of the α-Zr(O) due to insufficient oxygen potential of the stoichiometric fuel, therefore, ZrO_2 will not form on the cladding inside surface. However, the high oxygen potential of the outside environment (oxygen, steam) results in the formation of a ZrO_2 layer on the cladding outside surface. When oxygen saturation in the combined α-Zr(O) layer is reached, the initially formed metallic (U,Zr) layer is converted to a $(U,Zr)O_2$ mixed oxide solid solution. The final stable reaction products of the combined cladding interactions are ZrO_2 and $(U,Zr)O_2$.

A comparison of the total reaction zone growth rate equation for the UO_2/Zry, O_2/Zry, and H_2O/Zry reaction are shown in figure 3. Note that the total UO_2/Zry growth rate curve overlaps the steam/Zry region (results of six investigations) above about 1100°C. That is, the UO_2/Zry reaction occurs as rapidly as the steam/Zry reaction above about 1100°C. The total growth rate curve for the O_2/Zry gas mixture lies partly within the steam/Zry region. For this reason, the (Ar + 25 Vol.% O_2) gas mixture can be used to simulate a steam environment.

MODELING RESULTS

The numerical model PECLOX is based on the fact that the chemical processes for the internal and external oxidation of the cladding are controlled by the oxygen diffusion in the pellet and in the cladding. Therefore the primary objective of the model is to calculate the temperature- and time-dependent oxygen concentration profiles in the various reaction layers as well as the movement of the interfaces between the individual reaction layers.

PECLOX solves Fick's two laws for the diffusion process in the different layers and the Stefan equation for the interface movement (figure 4). Because the diffusion process of the internal oxidation is effective up to the center of the pellet a cylindrical coordinate system was chosen. The model also takes into account the swelling/shrinking effects of the fuel rod due to density changes at the interfaces. Furthermore, PECLOX has an option for a limited oxygen flux on the outer cladding boundary, for example due to steam starvation in the coolant channel. The temperature transient and radial tempera-

ture profile has to be given as input from an experiment or another computer model. Because the temperature is not constant with time and space in a SFD accident and because of the finite geometry of the fuel rod, the differential equations must be solved numerically. Because of its simplicity, the explicit integration method was chosen. A stability criterion for the integration time step must therefore be fullfilled. To decrease the computer time a mesh size profile for each phase is applied, i.e. small radial steps close to the interfaces and larger radial steps in the middle of the phase.

As pointed out in reference /4/, in the case of the internal interaction the growth of the (U,Zr) phase cannot be calculated by oxygen diffusion. In agreement with experimental results /1,2/, in the PECLOX model it is assumed that the inner boundary of the (U,Zr) phase stays at the same location and that its thickness is about 15% of the $[\alpha\text{-Zr(O)}_a + \text{(U,Zr)}]$-phase thickness. This causes oxygen flux differences at the boundaries of the (U,Zr) phase to be determined by the assumed interface movement. At all other interfaces their movement is a result of the Fick and Stefan equations. Since the (U,Zr) phase is very thin compared to the other phases, it is of minor importance that the metal diffusion (U and Zr; similar to /4/) required for the growth of the (U,Zr) phase is not considered in the PECLOX model. For the $[\alpha\text{-Zr(O)}_a + \text{(U,Zr)}]$ phase with channels of the (U,Zr) alloy at the $\alpha\text{-Zr(O)}_a$ grain boundaries an effective oxygen diffusion coefficient was taken from reference /5/.

First calculations were performed by the PECLOX model to calculate the one sided pellet/cladding interaction and the combined inner and outer chemical attacks of the cladding. Figure 5 is a three dimensional plot of the radial oxygen concentration profile versus time for the one sided chemical pellet/cladding interaction at 1500°C under inert gas condition. Each curve is an oxygen concentration profile for a given time; the time step from curve to curve is 2.5 minutes. One can see the evolution of the different reaction phases e.g. the disappearance of the (β-Zry) phase and the flux of oxygen from the pellet into the cladding region generating the α-Zr(O) phases.

Figure 6 shows a comparison of calculated interface movements with experimental data. Due to the density change, especially at the interface between the (U,Zr) alloy and $\alpha\text{-Zr(O)}_b$ phase, the rod diameter shrinks with time.

Figures 7a, 7b and 8 show the calculated oxygen concentration profiles and interface movements for the combined inner and outer cladding tube interaction at 1100°C under oxidizing conditions. Figure 7 shows, beside the oxygen concentration profiles, the radial location of the interfaces and the phase thicknesses at different reaction times. Figure 8 is a graph of the phase boundaries movement versus time in a square root scale. The comparison with experimental data shows good agreement with the model only at small reaction times. An explanation could be that a radial and time dependent temperature profile existed in the fuel rod during the experiment, and that the measured temperature refers to the outer cladding surface. In the experiment the rod was heated by inductive coupling with the metal region of the cladding, and no thermal insulation of the rod existed. Therefore a large temperature difference is developed with time over the growing ZrO_2-phase with a lower temperature at the outer ZrO_2 surface. However, when a time-dependent temperature difference in the ZrO_2 layer is assumed (0 K at 0 seconds linearly increasing up to 100 K at 4000 seconds, and then held constant at 100 K thereafter), the resulting agreement between experiment and model calculations is better except for the thickness of the $[\alpha\text{-Zr(O)}_a + \text{(U,Zr)}]$ layer.

Figure 9 is a fictitious example of a calculated combined inner and outer cladding oxidation with increasing temperature up to very high temperatures. For this calculation the unavoidable temperature escalation, which takes place

due to the exothermic steam/Zry reaction after a temperature of about 1500°C has been exceeded, was not considered. One can see the final total oxidation of the cladding to ZrO_2 and the strong non parabolic interface movements.

Future work will be directed toward a systematic model verification using various experimental data sets, the model implementation into the LWR code system SSYST and the application to SFD conditions. Furthermore a model improvement is planned with respect to steam starvation and hydrogen blanketing conditions on the external cladding tube surface.

SUMMARY AND CONCLUSIONS

- The external steam/Zircaloy or oxygen/Zircaloy and internal UO_2/Zircaloy chemical interactions in LWR fuel rods under SFD conditions result in the formation of following reaction layers at all temperatures examined.

$$[UO_2+U]\rightarrow[\alpha\text{-}Zr(O)_a + (U,Zr)]\rightarrow(U,Zr)\text{alloy}\rightarrow\beta\text{-Zry}\rightarrow\alpha\text{-}Zr(O)\rightarrow ZrO_2$$

- The growth of the reaction layers initially obeys a parabolic rate law. The diffusion of oxygen into the cladding is the rate-determining step. After some time, the growth rate of the various phases increases due to the finite cladding wall thickness.

- The UO_2/Zircaloy reaction occurs as rapidly as the steam/Zircaloy and (Ar + 25 Vol.% O_2)/Zircaloy reaction. The (Ar + 25 Vol.% O_2) gas mixture can be used to simulate the steam environment.

- Oxygen uptake by the Zircaloy causes the cladding to become embrittled. Due to the combined external and internal cladding oxidation the embrittlement of Zircaloy tubing occurs about four times faster than oxidation from either surface alone.

- Since the oxygen potential (partial pressure) of the steam or the (Ar + 25 Vol.% O_2) gas mixture is higher than that of the UO_2 the final stable reaction product is ZrO_2. The initially metallic (U,Zr) alloy will be converted into a $(U,Zr)O_2$ mixed oxide phase.

- On the basis of oxygen diffusion with moving interfaces, the numerical computer model PECLOX can calculate the chemical processes of the external steam (oxygen)/Zircaloy and internal UO_2/Zircaloy interaction.

- PECLOX is able to calculate the concentration profiles in the various interaction layers as well as the movement of the interfaces as function of temperature and time up to the total oxidation of the cladding. Time-dependent temperature profiles can be taken into account for the model calculations.

- First calculations show a reasonable agreement with experimental data with respect to reaction layer thicknesses and cladding diameter changes.

- Further improvements on the material properties (oxygen diffusion coefficients in the various interaction layers oxygen concentrations at the interfaces and densities of the interaction layers) are needed to get a better agreement between calculation and experiment.

ACKNOWLEDGEMENT

We would like to thank Prof. Dr. W. Dienst, Dr. D.L. Hagrman, and Dr. R.R. Hobbins for their critical and thorough review of the manuscript. We also gratefully acknowledge the helpful discussions with Dr. E.A. Garcia, Mr. S. Malang, Dr. R. Meyder, and Dr. M. Reimann in developing the PECLOX model, and the assistance of Mr. G. Gausmann in performing and evaluating the experiments, and of Mr. H. Metzger in performing the metallographic investigations. The work was sponsored by the "Projekt Nukleare Sicherheit" at the Kernforschungszentrum Karlsruhe (KfK) and was performed within the cooperation agreement between the Comisión Nacional de Energía Atómico (CNEA) and the KfK in the field of "Peaceful Uses of Nuclear Energy".

LITERATURE

/1/ P. Hofmann, D.K. Kerwin-Peck; UO_2/Zry Chemical Interactions and Reaction Kinetics from 1000 to 1700°C under Isothermal Conditions. KfK 3552 (1983)

/2/ P. Hofmann, D.K. Kerwin-Peck; UO_2/Zry Chemical Interactions under Isothermal and Transient Temperature Conditions. J. of Nucl. Mat. 124 (1984) 80-119

/3/ A.W. Cronenberg, M.S. El-Genk; An Assessment of Oxygen Diffusion during UO_2-Zircaloy Interaction. J. of Nucl. Mat. 78 (1978) 390-407

/4/ D.R. Olander; The UO_2/Zry-Chemical Interactions. J. of Nucl. Mat. 115 (1983) 271-285

/5/ A. Denis, E.A. Garcia; A Model to Describe the Interaction between UO_2 and Zry in the Temperature Range 1000 to 1700°C. J. of Nucl. Mat. 116 (1983) 44-54

FIGURES

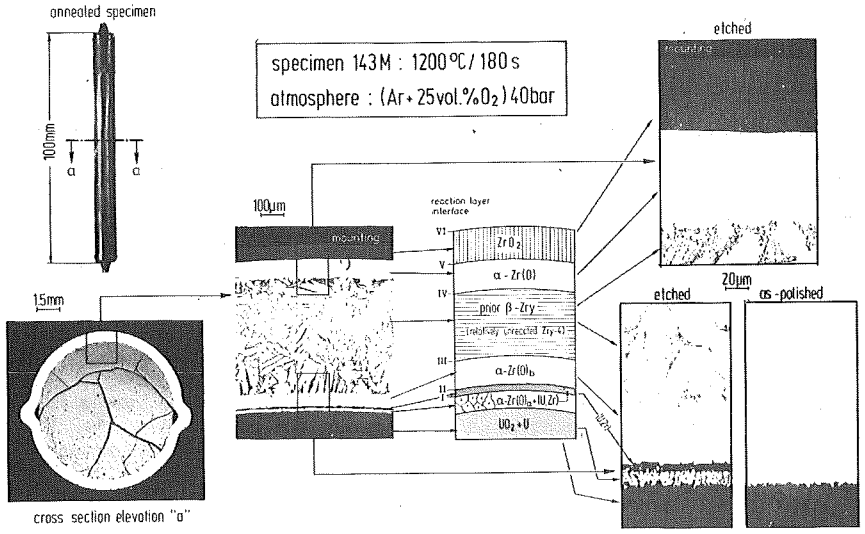

Figure 1: Sequence of the external oxygen/Zircaloy-4 and internal UO_2/Zircaloy-4 interaction layers of an oxidized LWR fuel rod segment.

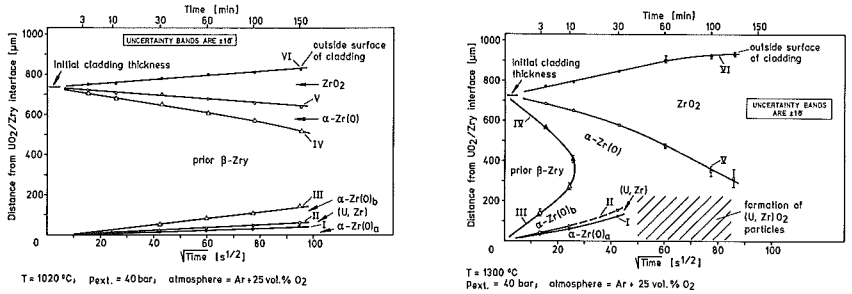

Figure 2: Oxygen/Zircaloy-4 and UO_2/Zircaloy-4 reaction zone thicknesses versus time at 1020°C (left figure) and 1300°C.

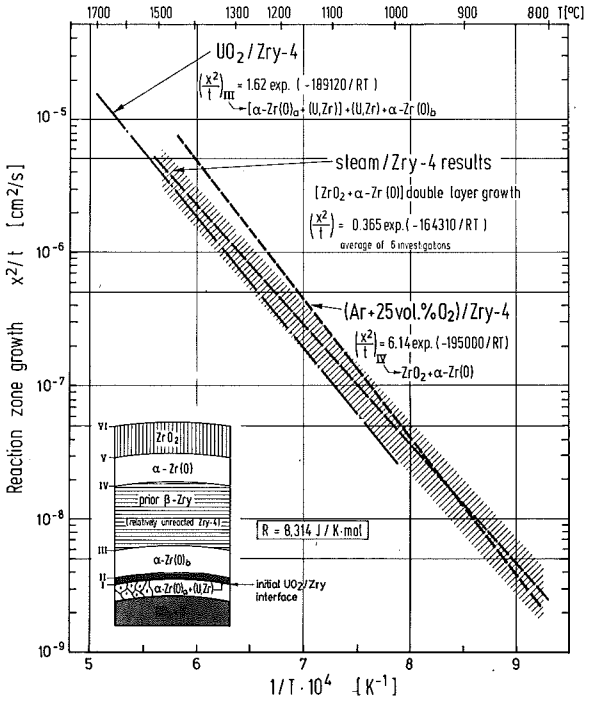

Figure 3: Comparison of the growth rate equations for the steam/Zircaloy-4, UO_2/Zircaloy-4, and oxygen/Zircaloy-4 reactions.

OXYGEN DIFFUSION WITH INTERFACE MOVEMENT

A.) THE TWO F I C K'S LAWS FOR A CYLINDRICAL SYSTEM

1.) FLUX : $F = -2 \cdot \pi \cdot R \cdot D \cdot \frac{\partial C}{\partial R}$

2.) TIME GRADIENT OF THE CONCENTRATION :

$$\frac{\partial C}{\partial \tau} = \frac{1}{R} \cdot \frac{\partial}{\partial R} \left(R \cdot D \cdot \frac{\partial C}{\partial R} \right)$$

B.) S T E F A N - EQUATIONS FOR THE INTERFACE MOVEMENT WITH SWELLING/SHRINKING EFFECT

$$\frac{\partial S}{\partial \tau} = \frac{F_L - F_R}{2 \pi S (C_L - C_R \rho_L / \rho_R)}$$

$$\frac{\partial V}{\partial \tau} = 2\pi \cdot S \cdot (1 - \rho_L / \rho_R) \cdot \frac{\partial S}{\partial \tau}$$

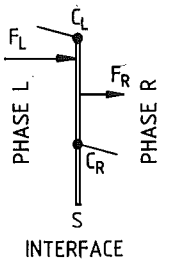

R = RADIAL COORDINATE

τ = TIME

C = CONCENTRATION

D = DIFFUSION COEFFICIENT

V = VOLUME OF THE INDIVIDUAL PHASE PER AXIAL LENGTH UNIT

S = INTERFACE POSITION

F = FLUX

ρ = DENSITY OF METALLIC PORTION OF THE INDIVIDUAL PHASE

INDICES: L = LEFT , R = RIGHT

Figure 4: Theoretical basis of PECLOX model: Fick and Stefan equations.

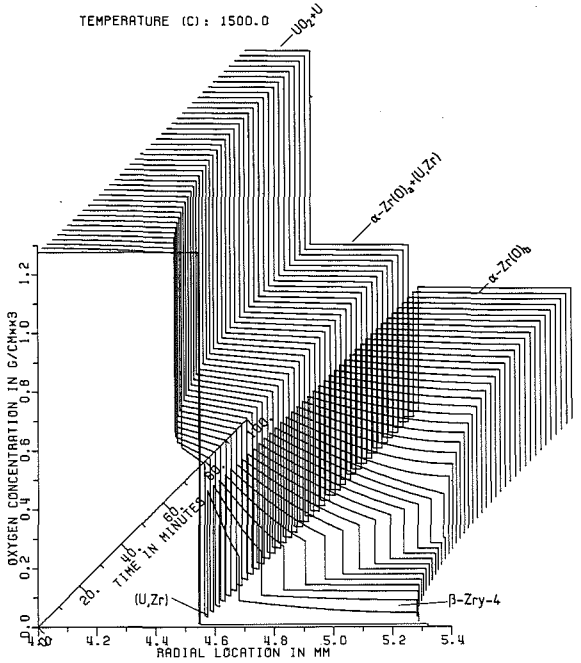

Figure 5: Oxygen concentration profile of a UO_2/Zircaloy-4 diffusion couple versus radial location and time at 1500°C under inert gas conditions.

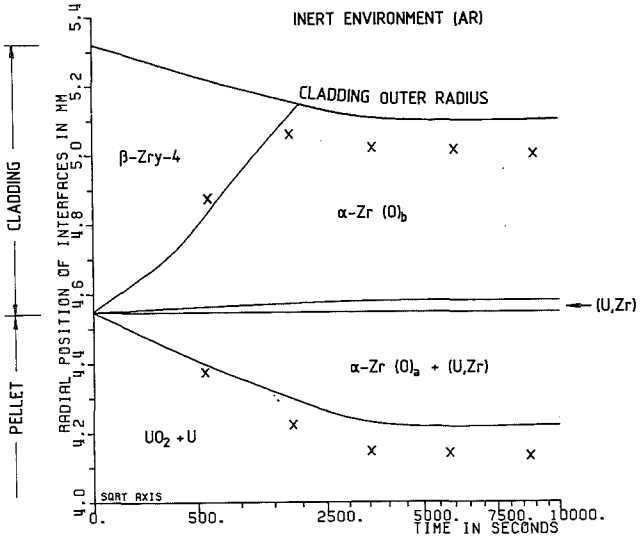

Figure 6: Thickness of the reaction zones versus time (interface movements) of a UO_2/Zircaloy-4 diffusion couple at 1500°C under inert gas conditions.

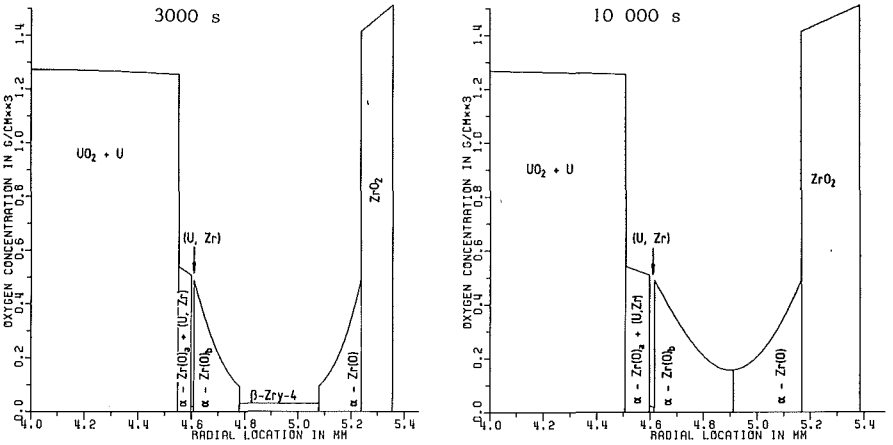

Figure 7: Oxygen concentration profile versus radial location of a UO_2/Zircaloy-4 diffusion couple at 1100°C under oxidizing conditions (Ar + 25 Vol.% oxygen) after 3000 seconds (left figure) and 10 000 seconds.

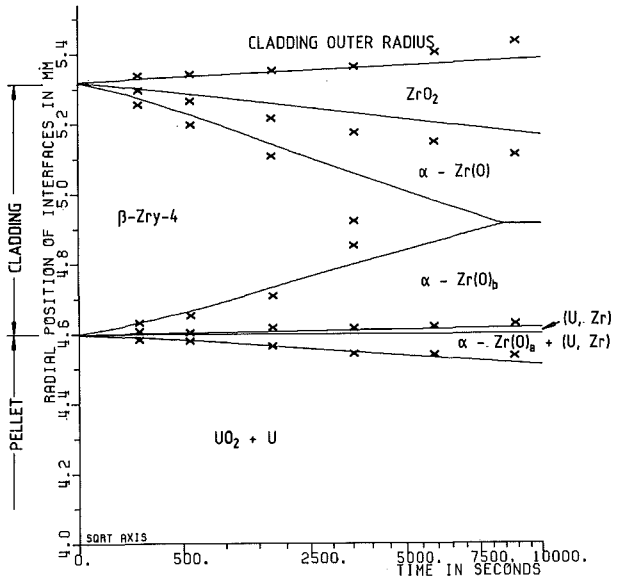

Figure 8: Thickness of the reaction zones versus time (interface movements) of a UO_2/Zircaloy-4 diffusion couple at 1100°C under oxidizing conditions (Ar + 25 Vol.% oxygen).

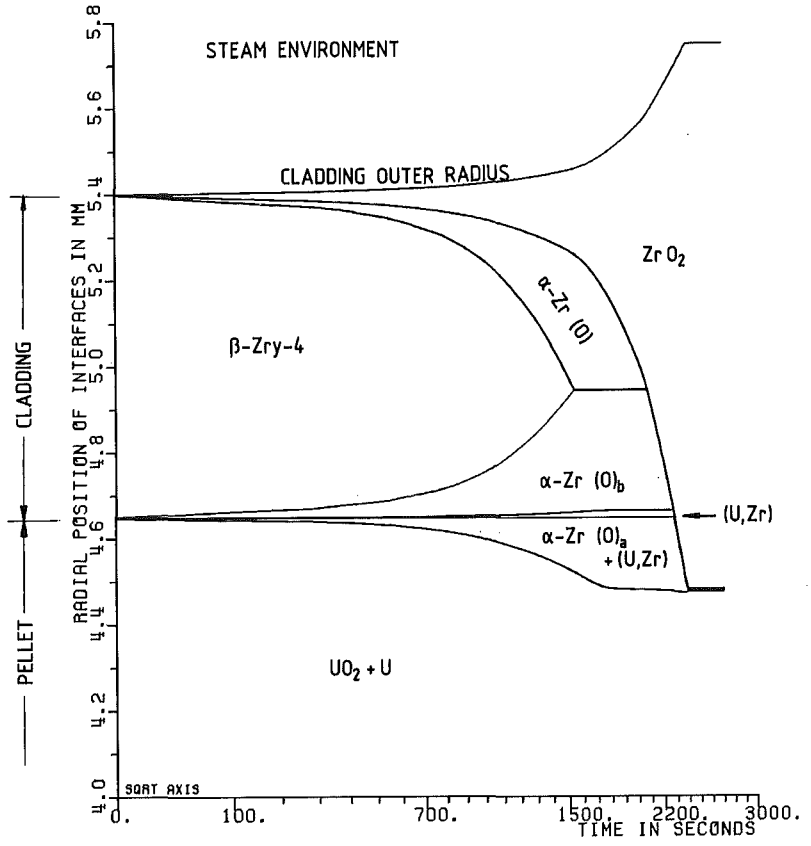

Figure 9: Thickness of the reaction zones versus time (interface movements) of a UO_2/Zircaloy-4 diffusion couple under fictitious transient temperature conditions (0.4 K/s) in an oxidizing atmosphere (in reality an uncontrolled temperature escalation will take place at about 1500°C).

SIMULATION OF THE INTERACTION BETWEEN URANIUM DIOXIDE AND ZIRCALOY

A. Denis and E.A. García

Centro Atómico Constituyentes, Comisión Nacional de Energía Atómica
Avda. del Libertador 8250, 1429 Buenos Aires, Argentina

ABSTRACT

The code solves the oxygen diffusion equations of the five phases formed during the UO_2/Zircaloy interaction, using an implicit finite difference method with parabolic interpolation at the interfaces. Uranium and Zirconium mass conservation are considered. The code gives a good simulation of the experimental results for isothermal conditions.

BACKGROUND

The calculation code is based on a previously developed model (1). The hypothesis are:

- oxygen diffusion controls the rate of phase growth
- infinite system
- interface movements obey parabolic rate laws
- density changes are not considered
- Uranium and Zirconium balance at the interfaces are not considered

THE INFINITE SYSTEM ANALYTICAL SOLUTION

The model results (fig. 1) in the determination of:

- oxygen diffusion coefficients in the five phases
- oxygen concentration at phase boundaries
- oxygen concentration profile

THE INFINITE SYSTEM, NUMERICAL SOLUTION, HITO CODE

The code simulates the UO_2/Zircaloy interaction as a high temperature oxidation (HITO) of Zircaloy in contact with solid UO_2. The code results in the determination of:

- oxygen concentration in the five phases as a function of time
- disappearance of certain phases.

INSTABILITY OF THE INTERFACE (U,Zr)/α-Zr(O)

The model (1) solution corresponds to metastable equilibrium of ξ_3

The numerical solution becomes instable: ξ_3 accelerates forward or backwards and phase α-$Zr(O)_a$ or (U,Zr) respectively, disappears.

It may be shown by virtual displacements that the instability has physical nature, fig. 2.

The interface accelerates in the same sense as the virtual displacement.

The instability problem is solved by adding a conservative equation for the uranium mass:

$$\frac{d}{dt} \int_{-\infty}^{+\infty} C_U \, (x,t) \, dx = 0$$

to keep the system consistent with the oxygen mass balance at ξ_3, the concentration C_6 is allowed to change with time. With these assumptions the code gives a good simulation of the experimental results (2) for isothermal conditions, fig. 3. The errors introduced by the code are relatively small (lower than 0.9%), fig. 4.

FINITE SYSTEM, ANALYTICAL SOLUTION

Experiments performed in an inert environment (2) show that the cladding radius decreases as the reaction progresses. Zirconium mass conservation must be considered:

$$\frac{d}{dt} \int_{-\infty}^{+\infty} C_{Zr} \, (x,t) \, dx = 0$$

and a convective term must be consequently included in the diffusion equation. A new analytical solution is found.

FINITE SYSTEM, NUMERICAL SOLUTION

The numerical solution for the finite system is achieved by employing the HITO code together with the analytical solution just described. This numerical solution is similar in every respects to that in fig. 1 with the only differences that: Zirconium rigid displacement and a new moving interface (Zry/Argon), with zero oxygen flux through it, are considered. Interface positions as functions of time are shown in figs. 5-10 for two coordinate systems:

a) fixed to the initial position of ξ_2, and
b) distances measured from ξ_1; this enables the comparison of numerical with experimental results reported in (2).

The oxygen concentration profiles at 1300°C for different times are shown in figs. 11-12.

CONCLUSIONS

The simplified model (1) and the HITO code seem to give a good description of the experimental results. However, the results for 1500°C are less satisfactory than for 1300°C or 1100°C. The reason is that the input data have certain error due to a large dispersion of the experimental data (2). For example at 1500°C the phase (U,Zr) tend to disappear in the experimental Arrhenius plot, but this is not true in the kinetic plots for this temperature.

Future work

- the HITO code will be extended to seven phases in order to consider external oxidation.
- the HITO code will be tested during temperature transients.

REFERENCES

/1/ A. Denis and E.A. Garcia; J. Nucl. Mater. 116 (1983) 44
/2/ P. Hofmann, D.K. Kerwin-Peck; KfK 3552 (Nov. 1983)

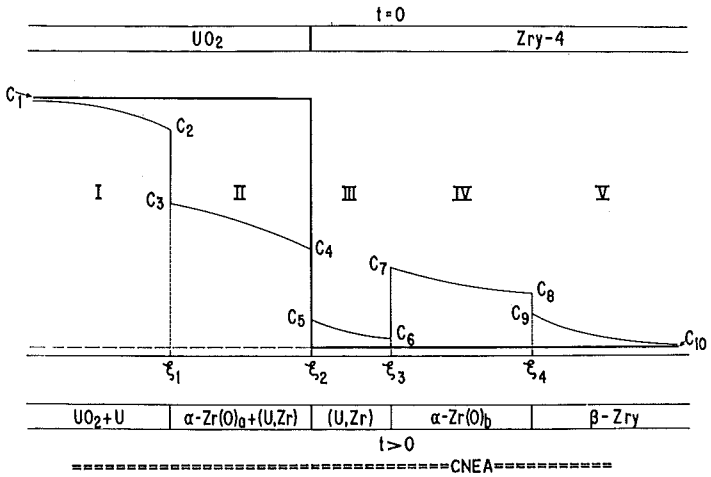

CNEA

FIG. 1 INFINITE SYSTEM . ANALYTICAL SOLUTION . CONCENTRATION PROFILE

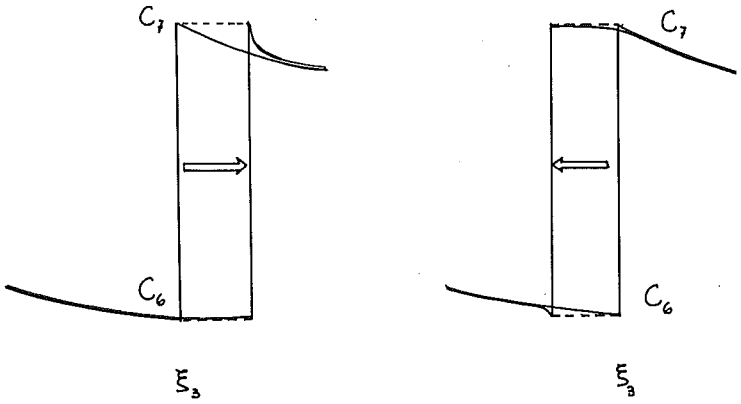

CNEA

FIG. 2 SCHEME OF THE VIRTUAL DISPLACEMENT

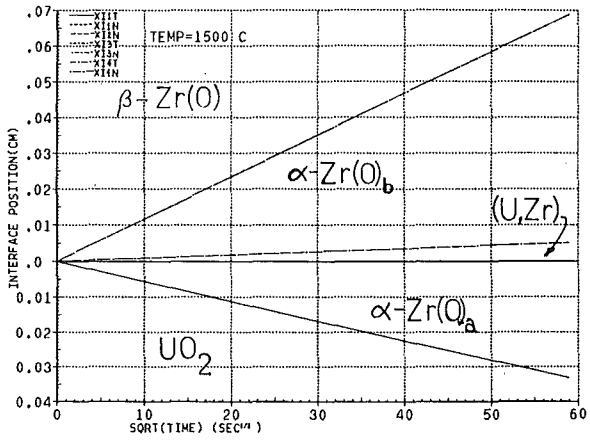

CNEA

FIG. 3 INFINITE SYSTEM.
COMPARISON OF NUMERICAL AND EXPERIMENTAL RESULTS.

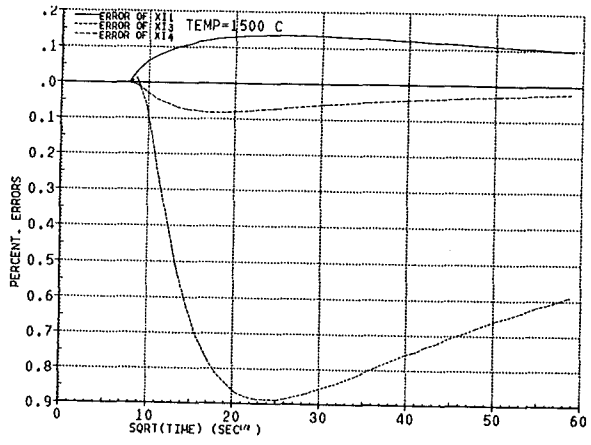

CNEA

FIG. 4 INFINITE SYSTEM.
RELATIVE ERROR OF THE NUMERICAL RESULTS

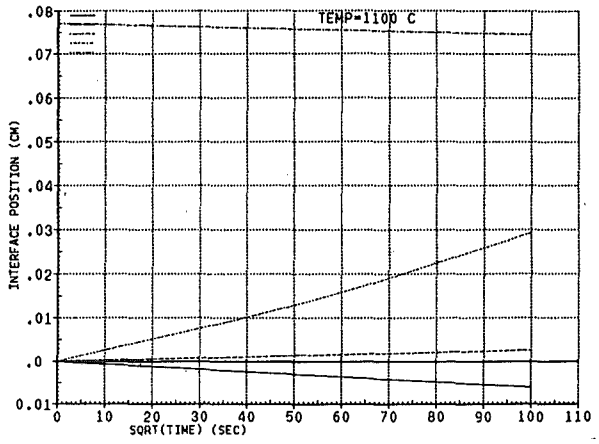

==========CNEA==========

FIG. 5 HITO CODE . FINITE SYSTEM.
INTERFACE POSITIONS . ORDINATES ORIGIN Ξ_2

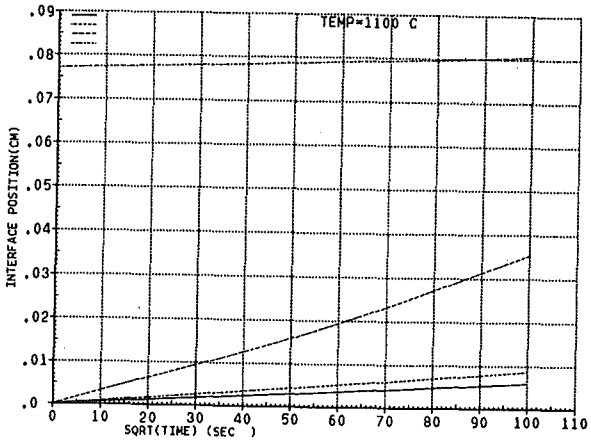

==========CNEA==========

FIG. 6 HITO CODE . FINITE SYSTEM.
INTERFACE POSITIONS . ORDINATES ORIGIN Ξ_1

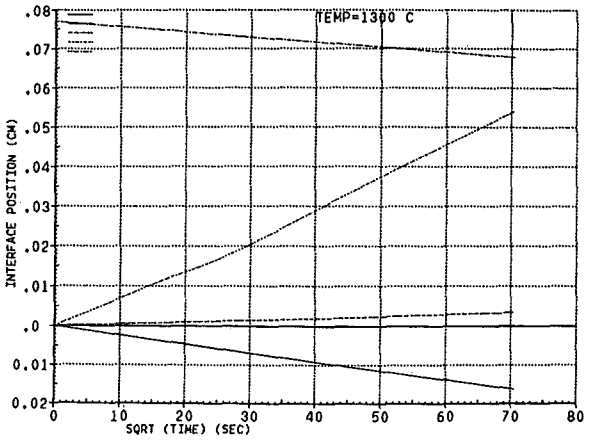

==========CNEA==========

FIG. 7 HITO CODE . FINITE SYSTEM.
INTERFACE POSITIONS . ORDINATES ORIGIN ξ_2

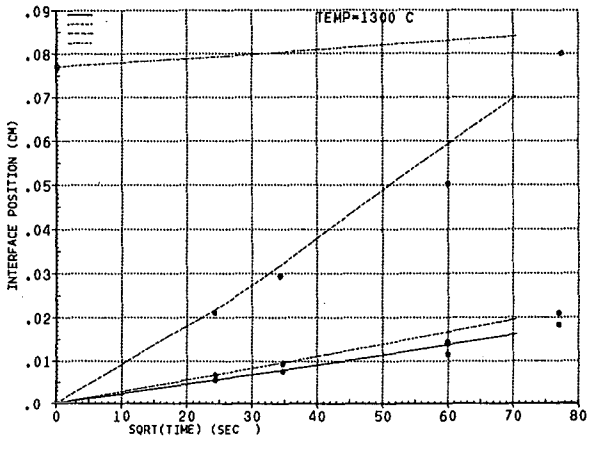

==========CNEA==========

FIG. 8 HITO CODE . FINITE SYSTEM.
INTERFACE POSITIONS . ORDINATES ORIGIN ξ_1

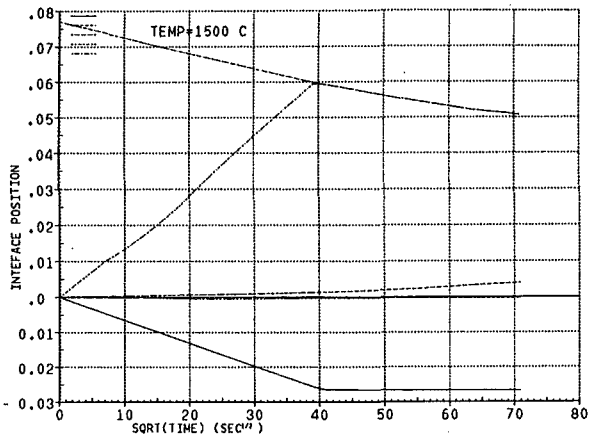

CNEA

FIG. 9 HITO CODE . FINITE SYSTEM.
INTERFACE POSITIONS . ORDINATES ORIGIN ξ_2

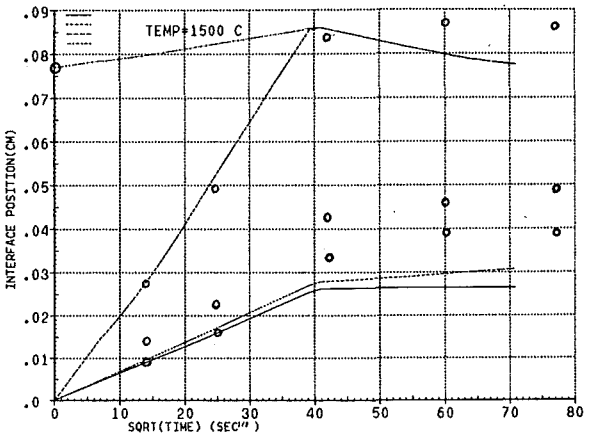

CNEA

FIG. 10 HITO CODE . FINITE SYSTEM.
INTERFACE POSITIONS . ORDINATES ORIGIN ξ_1

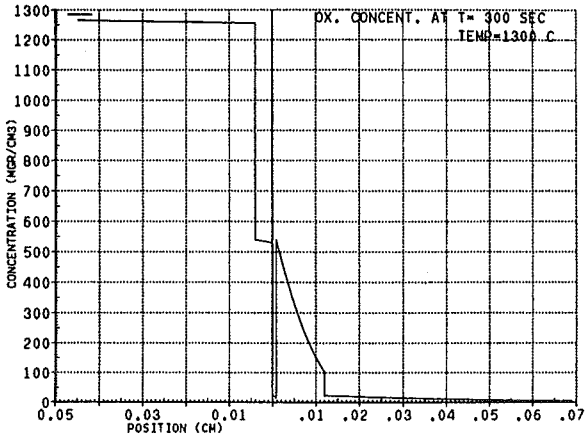

==========CNEA==========

FIG. 11 HITO CODE . FINITE SYSTEM.
OXYGEN CONCENTRATION PROFILE.

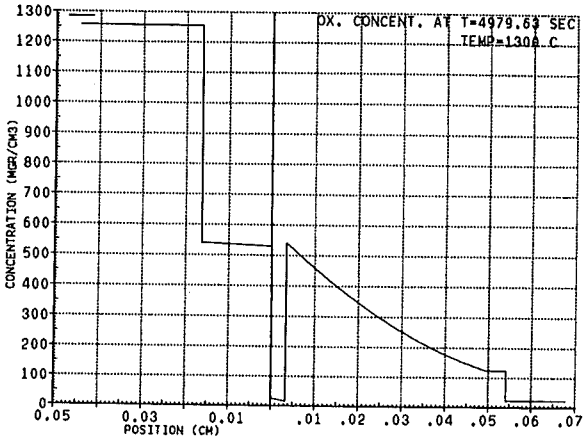

==========CNEA==========

FIG. 12 HITO CODE . FINITE SYSTEM.
OXYGEN CONCENTRATION PROFILE.

High Temperature Phase Relations in the U-Zr-O System

A. Skokan
Kernforschungszentrum Karlsruhe
Institut für Material- und Festkörperforschung I
Karlsruhe

Introduction

The first investigations of the phase stability relations in the ternary U-Zr-O system were performed by Saller and coworkers /1/, who proposed three tentative isothermal sections at temperatures up to ∿1100°C. Further investigations were performed by Politis /2/ to determine the melt and phase equilibria at higher temperatures. The results obtained relate to the isothermal sections at 1000, 1500 and 2000°C and the quasibinary section between UO_2 and oxygen-saturated α-Zr, which was designated Zr(O). As shown by these experiments, the most important features of the ternary system up to 1500°C are the existence of a large central three-phase-region (UO_2+α-Zr(O)+γ-U/β-Zr or melt) and a quasibinary join between UO_2 and α-Zr(O). With regard to the UO_2-Zr interaction these results explain the observed ternary corrosion reaction by which uranium oxide is reduced partially to metallic uranium as long as zirconium is not saturated with oxygen. However, the occurrence of a sandwiched (U,Zr) alloy between two α-Zr(O) layers which had been observed in the UO_2/Zircaloy interaction tests /3/ could not be explained in terms of the ternary system without assuming complicated diffusion paths. The necessity to resume the investigations in this ternary system resulted from the current investigations being performed in the area of severe fuel damage (SFD). In particular, to interpret the results of UO_2/Zry chemical interaction tests, it was necessary to extend the equilibria examinations between 1500 and 2000°C. The purpose of the renewed tests is, first, to clarify the contradictions between the ternary isothermal sections and the temperature-concentration diagram of the quasibinary join α-Zr(O)-UO_2 in the earlier work /2/, as well as the determination of

the liquidus curves in isothermal steps between 1500 and 2000°C. If possible, investigations concerning the occurrence of the (U,Zr) alloy layer between two α-Zr(O) layers should also be performed in order to examine whether this configuration can be thermodynamically explained, for example by the existence of a miscibility gap in the ternary α-Zr(O) region, as it has been supposed /4/.

Experimental methods

The specimens were fabricated from homogeneous powder mixtures of $UO_{2.0}$, $ZrO_{2.0}$ and Zr. Tungsten, thoria and zirconia were used as crucible materials. Isothermal annealing experiments, high temperature differential thermal analyses (DTA) and optical measurements of the melting temperatures were performed in argon atmosphere. The agreement between the results from the DTA and pyrometer measurements of the melting temperatures lies within the measurement uncertainty. Identification and characterization of the phases were performed by metallography and X-ray diffraction.

Results

The quasibinary join Zr(O)-UO_2

Oxygen-stabilized α-Zr exhibits a wide homogeneous region with a temperature-dependent oxygen saturation concentration (at the eutectic temperature, the maximum oxygen solubility is ∿34 at %, at 1500°C: ∿31 at % /5,6/). Therefore, on the Zr-rich side of the Zr(O)-UO_2 diagram, the oxygen concentration should be chosen low enough to get a quasibinary system. For the revised diagram (Fig. 1), the oxygen-concentration in α-Zr(O) was fixed at 30 at % (in /2/: 34 at %). In the earlier work /2/ there was a noticeable inconsistency between the diagram of this subsystem and the ternary isothermal sections, concerning the liquidus curve of the two-phase region $(U,Zr)O_{2-x}$+L at the Zr-rich side. In the ternary isothermal section at 2000°C this curve cuts the join UO_2-Zr(O) at ∿26 at % $U_{0.33}O_{0.67}$ (≙ 14 mol % UO_2), whereas in the quasibinary join the liquidus

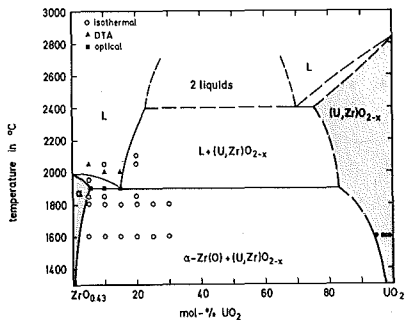

Fig. 1: Revised temperature-concentration diagram of the quasibinary system α-Zr(O)-UO_2 in mol %

at 2000°C lies at ∿8 mol % UO_2 (≙ 15 at % $U_{0.33}O_{0.67}$). From the results of this work, the temperature of the eutectic (1840°C in /2/) is about 60°C higher than the earlier result. It has been measured by differential thermal analysis of a specimen containing 15 mol % UO_2 (Fig. 2), as well as by optical observation with a pyrometer. The new eutectic temperature of ∿1900°C agrees with the α-Zr(O)-ZrO_2 eutectic temperature of the binary system Zr-O, measured by Domagala /7/ and Gebhardt /5/, whereas

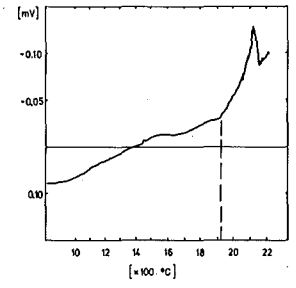

Fig. 2: Differential thermal analysis of a specimen containing (in mol %) 85 Zr(O)-15UO_2, showing the eutectic temperature by an endothermic peak at ∿1900°C

Ackermann /6/ measured a significantly higher value for the Zr-O eutectic temperature. The eutectic point in the quasibinary system Zr(O)-UO_2 does

not lie at 5 mol % UO_2 as determined earlier /2/, but at ∿15 mol % UO_2. This was determined from microstructural examinations of the melt specimens containing 10, 15 and 20 mol % UO_2 (Fig. 3).

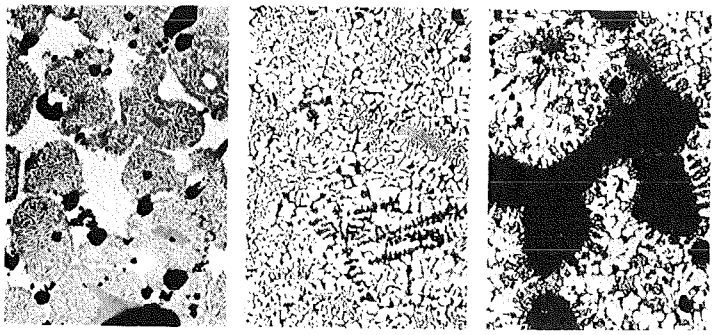

a) b) c)

Fig. 3: Microstuctures of melt specimens containing (in mol %)
a) 90 Zr(O)-10 UO_2, b) 85 Zr(O)-15 UO_2, c) 80 Zr(O)-20 UO_2.
From >1900°C quenched. Unetched, magnification 100 x:
a) α-Zr(O)+eutectic, b) eutectic, c) UO_2+eutectic

Due to these changes, the liquidus line of the two-phase field $(U,Zr)O_{2-x}$+L on the Zr-rich side is shifted to higher UO_2 contents. The results show that the maximum amount of UO_2 which can be dissolved at 2000°C is ∿16 mol %. This value agrees with the phase field distribution in the isothermal section U-Zr-O at 2000°C significantly better than the earlier value of ∿8 mol %. The shape of the liquidus curve with increasing UO_2 content was not determined. It was assumed that at 2400°C, the liquidus line again joins the curve determined in the earlier work. The two-phase liquid region and the corresponding monotectic temperature (2400°C) were also not checked.

On the UO_2-rich side, the results of this work indicated a higher solubility of Zr(O) in UO_2. Thus, the $(U,Zr)O_{2-x}$ one-phase field was extended towards lower UO_2 contents.

For a comparison with the ternary U-Zr-O sections which are given in

at %, the concentrations of the quasibinary diagram had to be converted from mol % to at %. For a more convenient direct comparison, the quasibinary system is represented in at % $Zr_{o.7}O_{o.3}$-$U_{o.33}O_{o.67}$ in Fig. 4.

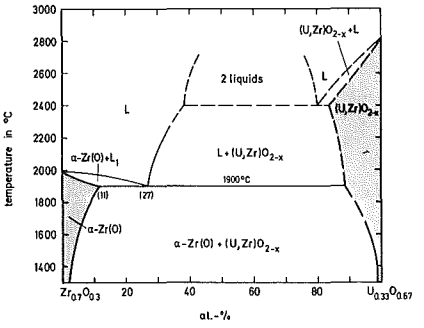

Fig. 4: Temperature-concentration diagram of the quasibinary Zr(0)-UO_2 system in at %, for direct comparison with the ternary sections

Ternary isothermal U-Zr-O sections

The results of the experimental investigations of the ternary isothermal sections at 1600 and 1800°C are given in Fig. 5 and 6. There is not much difference between these two sections and that at 1500°C. With increasing

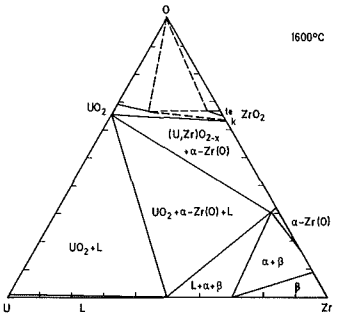

Fig. 5: Isothermal section of the ternary U-Zr-O system at 1600°C

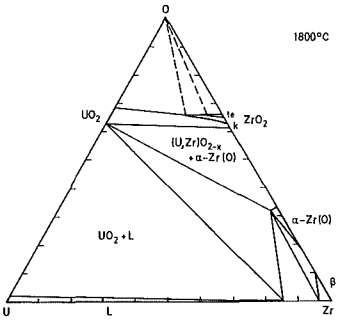

Fig. 6: Isothermal section of the ternary U-Zr-O system at 1800°C

temperature, the field of the U-Zr melt extends towards Zr and thus the concentration of the liquid phase in the central three-phase field changes likewise. Since at temperatures >1525°C cubic ZrO_{2-x} is coexisting with α-Zr(O) /8/, a complete range of miscibility between UO_{2-x} and ZrO_{2-x} has been assumed resulting in a large two-phase field $(U,Zr)O_{2-x}$+ α-Zr(O) instead of a three-phase field at 1500°C. The ternary region near the α-Zr(O) field has been checked for the existence of a supposed miscibility gap, but no evidence for this supposition was found.

On the basis of literature data and some own experiments, the isothermal sections at 1905 and 1950°C are represented as tentative diagrams (Figs.7 and 8). The binary eutectic between α-Zr(O) and ZrO_2 is assumed to occur at 1900°C, according to /5,7/ (though a higher value (2065°C) has been reported by /6/), and to extend into the ternary region, where the eutectic temperature of the join α-Zr(O)-UO_2 has been measured at 1900°C in the present work. With the higher value of the binary eutectic temperature, the own results could have been explained only by the assumption of a ternary eutectic.

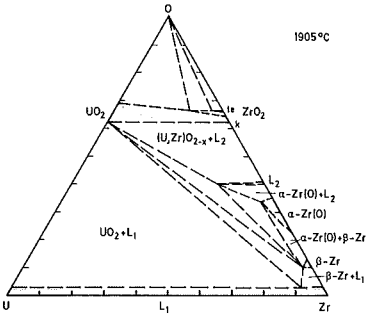

Fig.7: Tentative isothermal section of the ternary U-Zr-O system at 1905°C

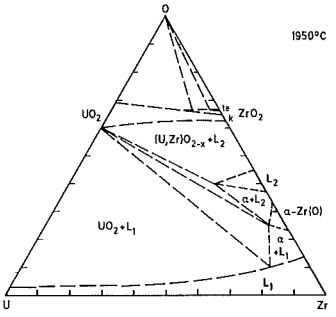

Fig.8: Tentative isothermal section of the ternary U-Zr-O system at 1950°C

These sections between 1900 and 2000°C are characterized by two liquid fields, one metallic (L_1), and the second one with considerable amounts of oxygen (L_2). With increasing temperature, the two melt fields extend on the Zr-side and combine above the melting temperatures of the solid

phases in between, β-Zr and α-Zr(O). Differing values have been reported also for these temperatures (/5,7/ and /6/). For the construction of the tentative ternary sections in this work, preference has been given to the lower values of /5,7/ because they fit better with own results.

Ternary temperature-concentration diagrams

Considering the phase relations of the corrosion couple UO_2-Zr, it is perhaps advantageous to show not only the diagram of the quasibinary system α-Zr(O)-UO_2, but also additional temperature-concentration diagrams representing the phase relations at different oxygen potentials. Therefore, on the basis of the results obtained so far, the diagrams of the ternary joins Zr-UO_2 and $Zr_{0.5}O_{0.5}$-UO_2 are shown in the Figs. 9 and 10. For a direct comparison with the isothermal ternary section, the concentrations are specified in at %. Since the phase equilibria above the eutectic temperatures are not sufficiently cleared, the upper temperature limits are 1900 and 2000°C, respectively.

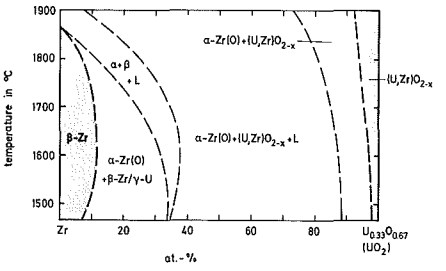

Fig. 9: Tentative temperature-concentration diagram of the ternary join Zr-UO_2 in at %

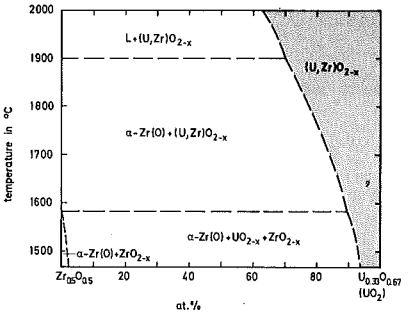

Fig. 10: Tentative temperature-concentration diagram of the ternary join $Zr_{0.5}O_{0.5}$-UO_2 in at %

Conclusions

The inconsistencies of the earlier results regarding the quasibinary α-Zr(O)-UO_2 diagram and the U-Zr-O isothermal section at 2000°C were eliminated. New results were obtained in the temperature range between 1500 and 2000°C. Regarding the layer configuration of the UO_2/Zr interaction couple, no evidence was found for a thermodynamical explanation in terms of the ternary U-Zr-O phase diagram.

Literature

/1/ Saller, A. et al., BMI 1023 (1955)
/2/ Politis, C., KfK 2167 (1975)
/3/ Hofmann, P. and Politis, C., J.Nucl.Mater., 87 (1979) 375
/4/ Picklesimer, M.L., private communication
/5/ Gebhardt, E. et al., J.Nucl.Mater., 4 (1961) 255
/6/ Ackermann, R.J. et al., J.Am.Ceram.Soc., 60 (1977) 341
/7/ Domagala, R.F. and McPherson, D.J., Trans.AIME, 200 (1954) 238
/8/ Ackermann, R.J. et al., J.Am.Ceram.Soc., 61 (1978) 275

THE DISSOLUTION OF UO_2 BY MOLTEN ZIRCALOY-4 CLADDING

H.E. Rosinger, K. Demoline and R.K. Rondeau

Atomic Energy of Canada Limited
Whiteshell Nuclear Research Establishment
Pinawa, Manitoba ROE 1LO Canada

ABSTRACT

The dissolution of UO_2 by molten Zircaloy-4 cladding, and structural changes to the UO_2 matrix, have been investigated using internally heated fuel rod simulators. The simulators were heated in an inert atmosphere at a fixed temperature ramp rate, and held at cladding surface temperatures (1800°C to 2200°C) above the melting point of the cladding (1760°C) for one second to ten minutes.

The experiments show that a complex microstructure is formed between the UO_2 pellets and the molten Zircaloy-4 cladding. The molten cladding contains varying proportions of uranium and oxygen that come from the dissolution of the UO_2 pellets by the molten Zircaloy-4. There is no penetration of Zircaloy-4 into the solid UO_2, even along grain boundaries.

Measurements of dissolved uranium in the cladding, by scanning Auger microscopy and chemical analysis, show that only small amounts of UO_2 (less than 3.5 vol.%) are dissolved by the molten cladding.

INTRODUCTION

In postulated reactor accidents, involving a loss of coolant, reactor shutown and impaired cooling, the initial temperature rise in the fuel is due to decay heat. As the temperature rises, and given the availability of steam, additional heat is generated on the Zircaloy-4 cladding surface by the exothermic Zircaloy-4/steam reaction. The nuclear fuel rods may reach temperatures high enough to promote reactions between the cladding and the uranium dioxide (UO_2) fuel pellets. At temperatures above the melting point of the Zircaloy-4 cladding, it has been observed that solid UO_2 can be partially dissolved by the molten cladding, and that structural changes occur in the fuel pellets. Any dissolution of the UO_2 by molten Zircaloy-4, or any structural changes occurring in the pellet, may result in an increased fission-product release from the UO_2 pellet. In addition, the uptake of oxygen from the UO_2 causes the cladding to become embrittled.

The single-effect experiments to be described were done to ob a tain comprehensive understanding of UO_2 dissolution by molten Zircaloy-4 cladding under well-defined boundary conditions of temperature, time and atmosphere. The experimental program was undertaken

- to study the extent of the interaction between solid UO_2 and molten Zircaloy-4,
- to determine the amount of UO_2 dissolved by molten Zircaloy-4,
- to determine the resultant reaction products, and
- to study, indirectly, the wettability of solid UO_2 by molten Zircaloy-4.

EXPERIMENTAL PROCEDURE

The experiments were done using the test apparatus shown in Figure 1. The fuel rod simulator consisted of an internal tungsten heater surrounded by annular high-density (10.55 to 10.65 Mg/m^3) stoichiometric UO_2 pellets in a standard CANDU-PHWR* Zircaloy-4 fuel cladding. The dimensions of the simulator were as follows: tungsten heater, $6.00^{+0.0}_{-0.02}$ mm; UO_2 pellet, 6.10 ± 0.03 mm ID, 14.27 ± 0.01 mm OD; and fuel cladding, 14.40 mm nominal ID, 15.24 mm nominal OD. The simulator was positioned horizontally in a quartz containment tube so that the melting behaviour could be viewed and recorded.

During a typical test, power was fed from a 100 kV.A power/temperature controller to the tungsten heater (melting point 3410°C) via water-cooled copper electrodes. Temperatures were measured at one location on the top central portion of the simulator by three or four emissivity-insensitive dual-wavelength pyrometers, which operate in the range 750°C to 3500°C. Since we wanted to simulate, at least in part, the behaviour of a failed fuel rod, no pressure differential was applied across the cladding wall. The differential expansion of UO_2 and Zircaloy-4 on heating to high temperature was used to generate the contact pressure.

In these "MELT" tests, the 250-mm long, horizontal simulator was heated, in a purified inert gas atmosphere, at 10 to 20°C/s to 1600°C, and then at 1°C/s to the required test temperature. The simulators were held at constant temperatures in excess of the melting point (1760 ± 10°C [1]) of the as-received cladding for times between one second and ten minutes. The majority of the "MELT" tests were carried out on simulators having as-received cladding and no CANLUB [2] coating. Three tests were carried out on simulators having a CANLUB coating between the cladding and the UO_2 pellets. To complete the isothermal hold, the power to the simulator was turned off and it was allowed to cool. Several tests were carried out at other heating rates, 10°C/s and 35°C/s, above 1600°C.

After each experiment, the simulators were encapsulated in epoxy, sectioned, polished and examined metallographically, and by Scanning Electron Microscopy (SEM) and Scanning Auger Microscopy (SAM), to identify the reaction products.

The cladding was chemically analyzed for uranium content.

---

* CANada Deuterium Uranium - Pressurized Heavy Water Reactor

RESULTS

For the tests carried out at a heating rate of 1°C/s above 1600°C, the molten cladding wetted the UO_2 pellets around their complete circumference. In no case did the molten cladding flow off and drip to the catch tray located below the test assembly. Figure 2 shows a typical cross-section of a fuel rod simulator after being heated at a surface temperature of 2200°C for ten minutes. A large amount of UO_2 (melting point 2865°C) has melted around the heater. The remaining UO_2 near the cladding has not melted, but considerable interaction has occurred between the UO_2 and the molten cladding. This interaction resulted in an increase in volume of the cladding.

When the cladding melted between 1760°C and 1970°C (depending on heating rate and oxygen content), a vapour was given off that deposited on the cooler quartz tube. Spectrographic analysis of the deposit showed that it consisted of tin, chromium and iron, all alloying elements of Zircaloy-4.

For simulators heated in an inert atmosphere at faster rates, e.g. 35°C/s above 1600°C, it was found that the molten cladding no longer completely wetted the UO_2 pellets. At this heating rate, the top of the UO_2 pellet was not covered with molten cladding, i.e. some cladding flowed to the bottom of the horizontal simulators. In this case, less oxygen was dissolved in the molten cladding, and hence there was less wetting of the UO_2 [3].

Complex microstructures were formed between the solid UO_2 and the cladding. Even though no pressure differential was applied to the cladding wall, the thermal expansion of the two components was sufficient to cause good contact at temperatures in excess of 1600°C. When the temperature on the surface of a section of the simulator did not exceed the melting point of the cladding, the microstructure shown in Figure 3 was obtained. This microstructure consists of UO_2, an oxygen-saturated α-$Zr(O)_a$ phase next to the UO_2/Zircaloy-4 interface, a (U,Zr)-alloy phase, and then an oxygen-saturated α-$Zr(O)_b$ phase. Depending on the uranium content of the (U,Zr)-alloy, the melting temperature of this phase could be as low as 1132°C. This (U,Zr)-alloy was also distributed along the grain boundaries of the α-$Zr(O)_a$ phase. Thus, the structure of the cladding just below its melting point consisted of a low-temperature (U,Zr)-alloy situated between two α-Zr(O) layers.

If the melting temperature of the as-received cladding is exceeded, it is possible that only a portion of the cladding melts. Shown in Figure 4 is a typical microstructure. Since Zircaloy-4 picks up oxygen from the UO_2, the melting point near the UO_2/Zircaloy-4 interface can be raised to as high as 1970°C. The outer section of the cladding, which has not picked up oxygen from the UO_2, melts at temperatures above 1760°C.

Raising the temperature to 2000°C melted all of the cladding and a homogenized dendritic structure, shown in Figure 5, was obtained. The scalloped structure of the UO_2 indicates that it was dissolved by the molten cladding. The microstructure thus consisted of the original Zircaloy-4 plus varying amounts of uranium and oxygen arising from the dissolution of the UO_2 by the molten cladding. An important point to note is that the solid UO_2 does not contain any zirconium.

The amount of uranium dissolved in the cladding was determined by SAM and chemical analysis. The results (see Table I) show that less than 42 wt.% uranium dissolved in the molten cladding. The presence of the CANLUB coating between the cladding and the UO_2 had no measurable effect.

DISCUSSION

For the experiments conducted with no differential pressure on the cladding wall, partial UO_2/cladding contact occurred only due to their differential expansion. The fuel/cladding gap closed at about 1600°C and thus some UO_2/Zircaloy-4 interaction (see Figures 3 and 4) occurred even without an external pressure. Consequently, the cladding melted over a range of temperature, 1760°C to 1970°C.

When there is good contact between the UO_2 and solid cladding, previous work [4-6] has shown that the sequence, at room temperature, of the individual layers from UO_2 to Zircaloy-4 can be represented as:

$$\{UO_2 + U\} \rightarrow \left\{ \begin{matrix} \alpha\text{-Zr(O)}_a \\ +\text{(U,Zr)-alloy} \end{matrix} \right\} \rightarrow \{\text{(U,Zr)-alloy}\} \rightarrow \{\alpha\text{-(Zr(O)}_b\} \rightarrow \{\text{Zr-4}\}$$

In the solid-state reaction, the (U,Zr)-alloy phase, found between the two oxygen-saturated α-Zr(O) layers, has a very low solubility for oxygen [7] and has a relatively low melting point, i.e. 1500 - 1132°C, for alloys ≥ 50 wt.% uranium, which decreases with increasing uranium content. This alloy will thus be liquid before the Zircaloy-4 melts. On cooling, the (U,Zr)-alloy consists of regions, as shown in Figure 3, of high zirconium with low uranium, and low zirconium with high uranium.

With increasing temperature, a solid α-Zr(O) layer and a (U,Zr)-alloy phase form at the UO_2/Zircaloy-4 interface, as seen in Figure 4. The melting point of the oxygen-saturated α-Zr(O) is about 1970°C. With, however, a slight increase in temperature, the solid α-Zr(O) layer melts, and a homogeneous (Zr,U,O)-phase is formed, as shown in Figure 5. The transformation of the (Zr,U,O)-phase during cool-down appears to be oxygen-dependent [8]. With a lower oxygen content in solution, two metallic phases exist in the refrozen melts, i.e. a (U,Zr)-alloy phase of high but varying uranium content, and oxygen stabilized α-Zr(O). With high oxygen content in solution, the molten phase forms two metallic and one ceramic phase: (a) an oxygen-stabilized α-Zr(O)phase containing varying amounts of uranium, (b) a metallic uranium-rich (U,Zr)-alloy, and (c) a ceramic $(U,Zr)O_2$ phase with low but varying zirconium content. According to the equilibrium phase diagram, one metallic phase, α-Zr(O), is in equilibrium with two ceramic phases, UO_2 and ZrO_2, and no (U,Zr)-alloy should be present. For the non-equilibrium conditions existing in this work, a single $(U,Zr)O_2$ phase of varying uranium and zirconium concentration, rather than the separate UO_2 and ZrO_2 constituents, is present at ambient temperature.

The interaction between UO_2 and molten cladding also effects the overall UO_2 microstructure. The molten homogeneous (Zr,U,O)-phase interacts with solid UO_2 to pick up more uranium and oxygen. The UO_2 is consequently reduced to UO_{2-x}, i.e. depleted of oxygen. When the oxygen content of the

UO_{2-x} is further depleted of oxygen, the UO_{2-x}/U solvus boundary of the U-O phase diagram is reached. At this point, liquid uranium forms in the UO_{2-x}. On cooling to room temperature, the UO_{2-x} plus liquid uranium form stoichiometric UO_2 and α-U. Figure 6 is a typical post-test micrograph, showing the stoichiometric UO_2 with the α-U preferentially formed along the UO_2 grain boundaries, and in the UO_2grains.

The major focus of this work was to determine the volume percent of UO_2 that could be dissolved by the molten cladding. Of particular concern was the data of Hofmann et. al [1, 5] which suggested that 9.2 vol.% UO_2 could react with the cladding.

In determining the vol.% UO_2 dissolved by the molten cladding, it is important to note that the amount of uranium (or UO_2) dissolved by the cladding is a function of cladding volume relative to the UO_2 volume. Larger cladding volumes will dissolve more UO_2. Shown in Figure 7 is a plot of the UO_2 pellet volume decrease as a function of the UO_2 content in the cladding, for three typical cladding and UO_2 dimensions. It can be seen that fuel rods having less cladding volume, such as those in the Pickering and Bruce CANDU reactors, can dissolve less UO_2 than fuel rods having larger cladding volumes.

Using the data from Table I and a plot of UO_2 pellet volume decrease as a function of the uranium content in the cladding, the vol.% UO_2 dissolved during the MELT tests was calculated. The results are shown in Table II. It can be seen that, for CANDU fuel, less than about 3.5 vol.% UO_2 is dissolved by the molten cladding. For other fuel rod dimensions, however, the vol.% UO_2 dissolved by the molten cladding would be different.

CONCLUSIONS

In this work, UO_2 dissolution by molten Zircaloy-4 cladding, and structural changes in the UO_2 matrix, have been studied by holding fuel rod simulators for one second to ten minutes in an inert atmosphere at temperatures above the melting point of the cladding.

A complex microstructure is formed between the UO_2 pellets and the cladding. Depending on the temperature, a reaction is possible between the UO_2 and solid cladding, resulting in the formation of an oxygen-stabilized α-Zr(O)-phase with a melting temperature of about 1970°C, or a homogeneous (Zr,U,O)-alloy phase. There is no penetration of Zircaloy into the solid UO_2, even along grain boundaries.

Only small amounts of UO_2 (less than 3.5 vol.%) are dissolved by the molten cladding.

ACKNOWLEDGEMENT

The authors gratefully acknowledge the contribution of the WNRE support staff, especially W. Hutchings (metallography), K. Ross (SEM), D. Brown (SAM) and A. Gerwing (chemical analysis).

This project was partially funded under the AECL/Ontario Hydro CANDEV program.

REFERENCES

1. P. Hofmann, "Out-of-Pile UO_2/Zircaloy-4 Experiments Under Severe Fuel Damage Conditions," OECD-NEA-CSNI/IAEA Specialists' Meeting on Water Reactor Fuel Safety and Fission Product Release In Off-Normal and Accident Conditions, RISO National Laboratory, Denmark, 1983 May 16 - 20.

2. R.D. Page, "Canadian Power Reactor Fuel," Atomic Energy of Canada Limited Report, AECL-5609 (1976).

3. P. Nikolopoulos, P. Hofmann and D. Kerwin-Peck, "Determination of the Interfacial Energy and Work of Adhesion in the UO_2/Zircaloy-4 Diffusion Couple," J. Nucl. Mater., 124 (1984) 106.

4. P. Hofmann and C. Politis, "The Kinetics of the Uranium Dioxide-Zircaloy Reactions at High Temperatures," J. Nucl. Mater., 87 (1979) 375.

5. P. Hofmann and D. Kerwin-Peck, "UO_2/Zircaloy-4 Chemical Interactions from 1000 to 1700°C under Isothermal and Transient Temperature Conditions," J. Nucl. Mater., 124 (1984) 80.

6. H. Rosinger, "A Study of the Pellet/Clad (Uranium Dioxide/Zircaloy-4) Interaction at 1373 K and 1473 K", Atomic Energy of Canada Limited Report, AECL-7785 (1983).

7. P. Hofmann and D.K. Kerwin, "Preliminary Results of UO_2/Zircaloy-4 Experiments under Severe Fuel Damage Conditions," IAEA Specialists' Meeting on Water Reactor Fuel Element Performance Computer Modeling, Preston, England, 1982 March 14 - 19.

8. P. Hofmann and D.K. Kerwin-Peck, "Chemical Interactions of Solid and Liquid Zircaloy-4 with UO_2 Under Transient Non-Oxidizing Conditions," Inter. Meeting on Light Water Reactor Severe Accident Evaluation, Cambridge, Mass. U.S.A., 1983 Aug. 28 - Sept. 1.

TABLE I
WEIGHT PERCENT URANIUM DISSOLVED IN MOLTEN CLAD

MELT no.	By Scanning Auger Microscopy	By Chemical Analysis
8	18.5 ± 11.9	16.7 ± 0.7
9	19.1 ± 3.4	14.4 ± 0.6
10	11.8 ± 7.6	12.4 ± 0.5
11	9.4 ± 0.6	1.7 ± 0.1
12	11.3 ± 11.3	27.2 ± 1.1
13	15.1 ± 8.0	11.0 ± 2.0
14	33.3 ± 7.9	24.0 ± 1.0
15	19.8 ± 2.2	19.0 ± 3.0
16*	8.5 ± 2.3	15 ± 3.0
17*	10.8 ± 4.2	7.5 ± 0.4
18*	11.9 ± 0.4	10.0 ± 1.0

*CANLUB coated

TABLE II
VOLUME PERCENT OF UO_2 DISSOLVED BY MOLTEN CLAD

MELT No.	By Scanning Auger Microscopy	By Chemical Analysis
8	0.9 ± 0.7	0.95 ± 0.2
9	0.9 ± 0.2	0.85 ± 0.2
10	0.6 ± 0.4	0.7 ± 0.1
11	0.4 ± 0.1	0.5 ± 0.1
12	0.8 ± 0.5	1.8
13	0.8 ± 0.5	0.6 ± 0.15
14	2.0 ± 1.0	1.5
15	1.0 ± 0.2	1.2 ± 0.2
16*	0.4 ± 0.1	0.9 ± 0.2
17*	0.6 ± 0.3	0.4 ± 0.1
18*	0.5 ± 0.1	0.55 ± 0.1

*CANLUB-coated

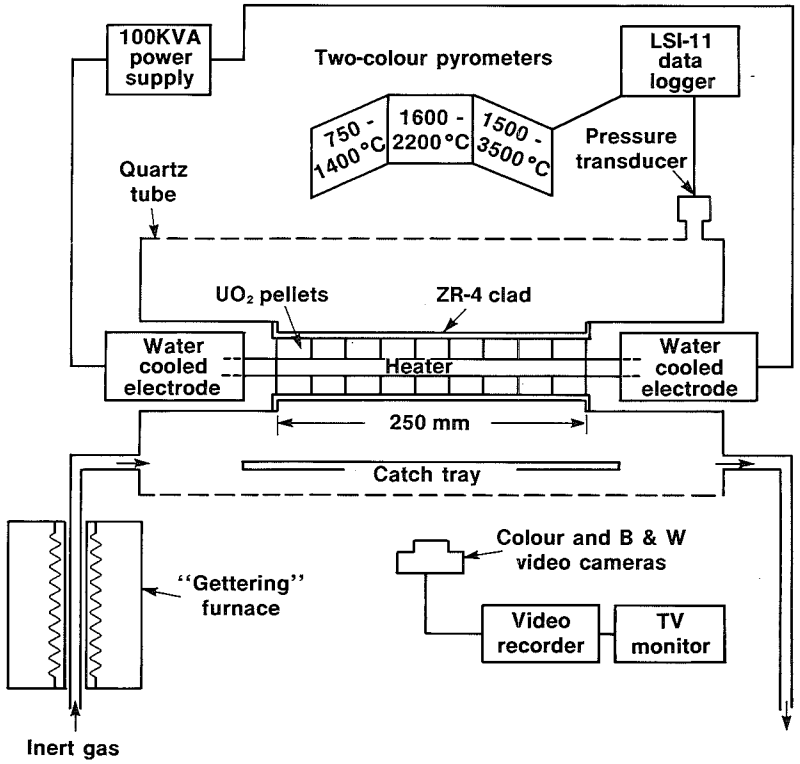

Figure 1: Schematic of the Test Assembly Used to Study UO_2 Dissolution by Molten Zircaloy-4

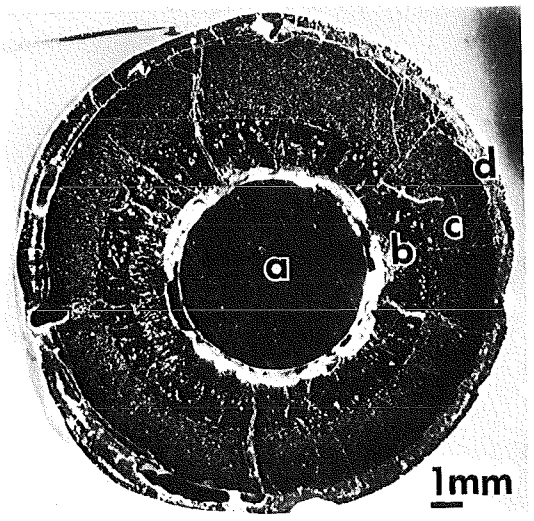

Figure 2: Transverse Cross-Section of Fuel Rod Simulator from Test MELT-11 (Surface Heated at 2000°C for 10 min.). Shown are (a) Tungsten Heater, (b) Molten UO_2, (c) UO_2, and (d) Molten Zircaloy-4 Cladding

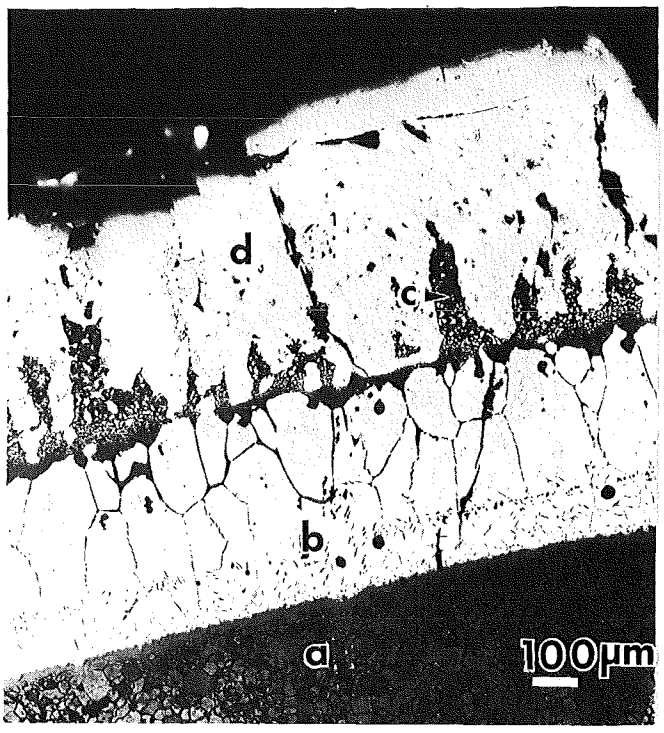

Figure 3. Typical Microstructures Obtained When The Simulator Did Not Exceed The Melting Point Of The As-Received Cladding. Shown are (a) UO_2 + α-U, (b) {α-Zr(O)$_a$ + (U,Zr)-alloy}, (c) (U,Zr)-alloy, and (d) α-Zr(O)$_b$.

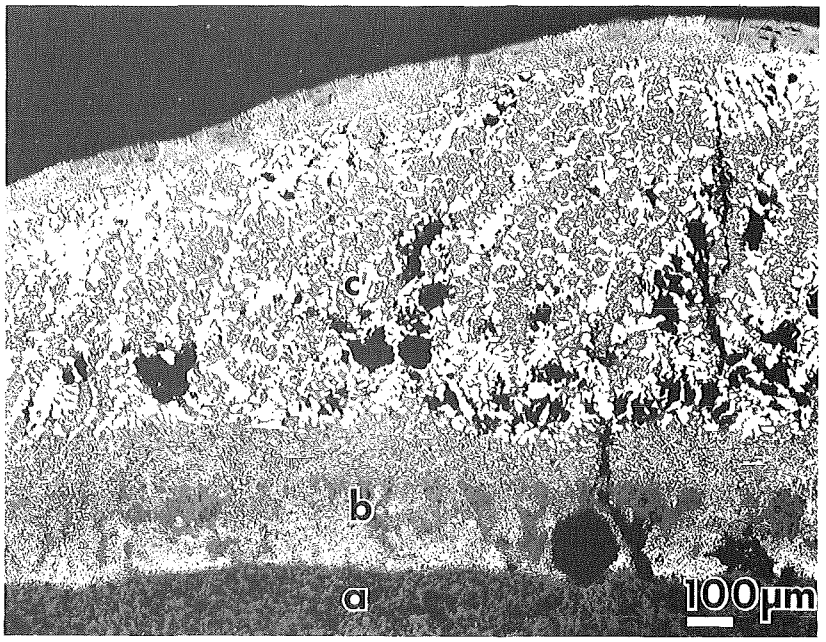

Figure 4. Typical Microstructures Obtained When The Cladding Reacted With The UO_2. Shown are (a) UO_2 + α-U, (b) {α-Zr(O) + (U,Zr)-alloy}, and (c) (Zr,U,O)-alloy phase.

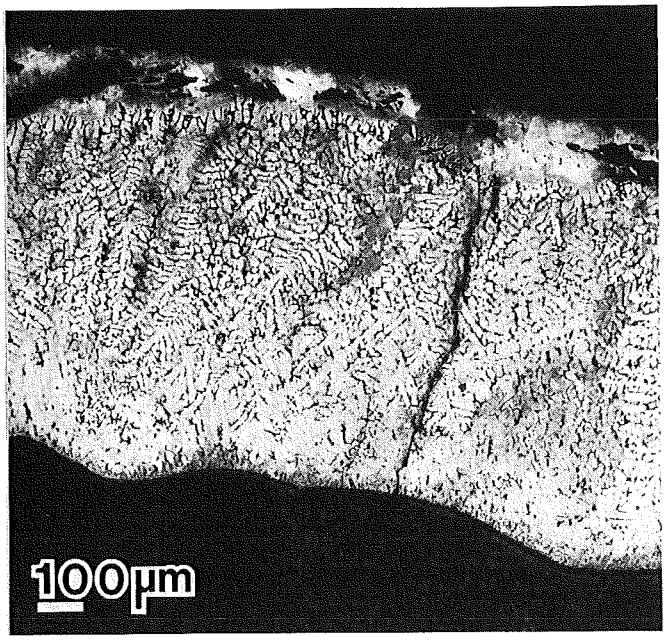

Figure 5. Dendritic Microstructure Obtained When All The Cladding Melted And Reacted With The UO_2 To Form A (Zr,U,O)-Alloy Phase.

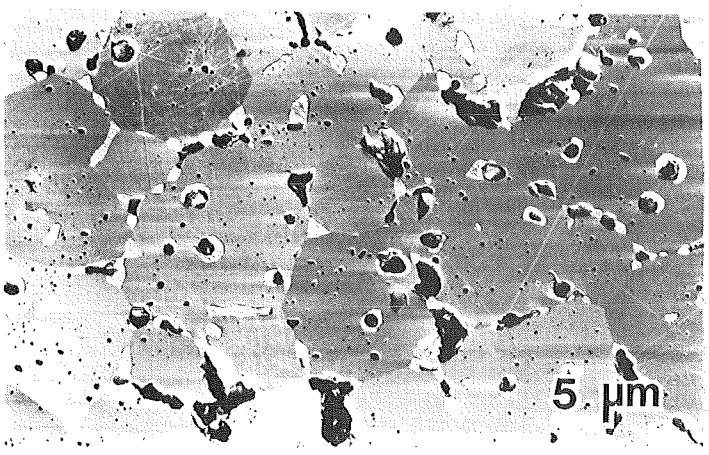

Figure 6. Typical Micrograph of UO_2 With α-U Along Grain Boundaries, And In The UO_2 Grains.

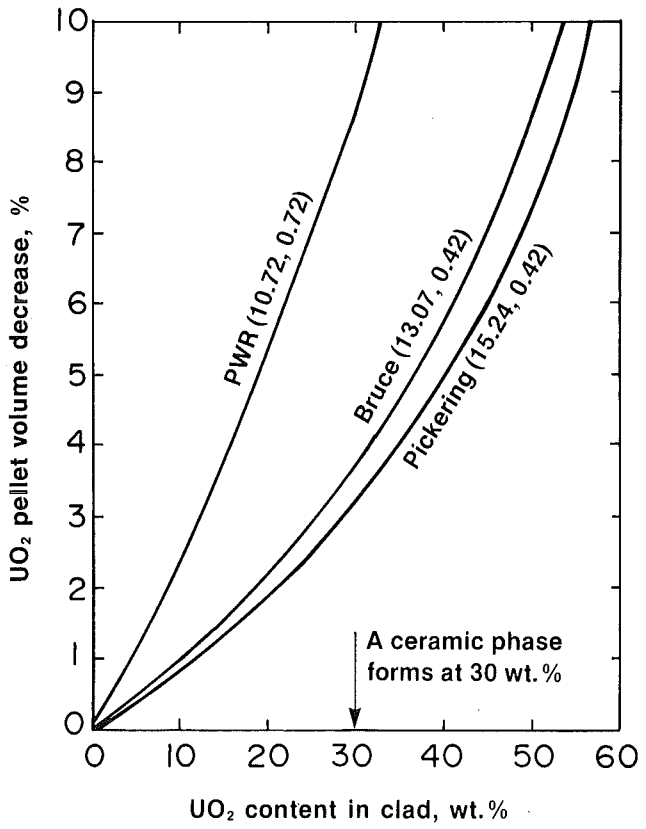

Figure 7. UO_2 Pellet Volume Decrease As A Function of the UO_2 Content In The Cladding. The Cladding Outside Dimensions and Thicknesses, in mm, Are Given.

THERMAL HYDRAULIC SEVERE ACCIDENT PHENOMENA IN SMALL FUEL ROD BUNDLES DURING SIMULATION EXPERIMENTS

W. Eifler

CEC Joint Research Center
Ispra (Varese), Italy

ABSTRACT

Inpile or out-of-pile experiments for simulating severe accidents are performed with test bundles consisting of a small number of rods. Three-dimensional perturbations of the flow and temperature field in such small rod bundles may complicate the analysis of such experiments. A computer simulation of a typical inpile experiment, the PBF scoping test, has been performed with the computer programme VELASCO. The good agreement between computational and experimental results leads to the conclusion that VELASCO may provide a useful contribution for the analysis of such experiments.

INTRODUCTION

Severe accidents similar to that which happened in the Three-Mile-Island Nuclear Station 2 are characterized, when in an advanced stage of development, by the following events.

The coolant inlet flow to the core may be very low or may even have stopped. The power is at decay heat level. The pressure is still relatively high. The coolant boils slowly down and core uncovery occurs. The steam flow through the uncovered core region has not the capacity for transporting the generated heat out of the core. The uncovered core region heats up eventually to extremely high temperatures. Additional heat is generated by the chemical reaction between the zircaloy cladding and the steam, the heat up is accelerated. The heat up spreads out radially to cooler core regions. However, radial temperature gradients are relatively small.

For the experimental simulation of such severe accident scenarios, only a small part of the core can be considered. Fig. 1 shows the cross-section of a typical inpile test train containing a 32 fuel rod bundle. For protecting the reactor environment against the extremely high temperatures the fuel rod bundle is contained in a highly insulating shroud. However, no material has perfect insulating characteristics, so that, still, a significant amount of heat is transferred to the shroud and conducted to a bypass cooling system. This results in three-dimensional perturbations of the flow and temperature field. An additional source of such perturbations may be the radial variation of the fission power which is dependent on the characteristics of the reactor hosting the experiment.

In the frame of the CEC project SUPER SARA (cancelled in 1983), VELASCO, an existing steady-state computer programme [1], has been further developed into a tool for the analysis of three-dimensional transient steam flows in fuel rod bundles. In this paper first the main features of VELASCO are described. The following section deals with the treatment of heat transfer by thermal radiation and convection, which are - together with the heat generation by the zircaloy-steam reaction - the key phenomena during the heat up phase of severe accidents. Finally the results of a VELASCO simulation of the PBF scoping test are presented.

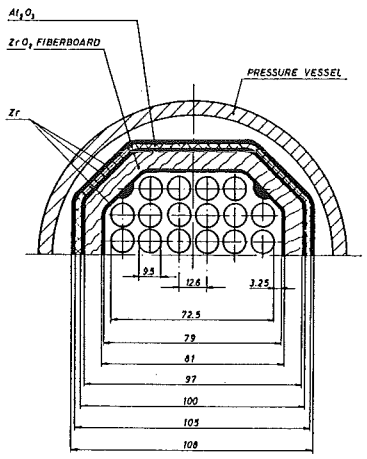

Fig. 1: CROSS SECTION OF A TYPICAL IN PILE TEST TRAIN FOR SEVERE FUEL DAMAGE EXPERIMENTS (SUPER SARA, PBF)

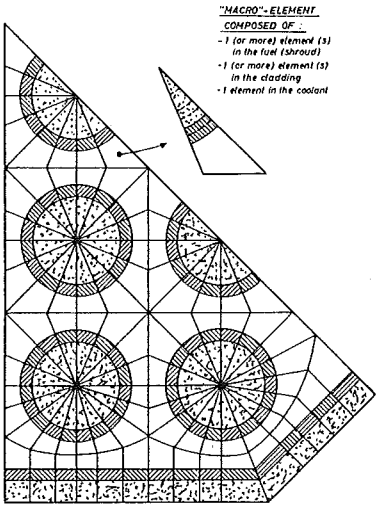

Fig. 2: VELASCO DISCRETISATION SCHEME APPLIED TO A 1/8-SYMMETRY SECTION OF A 32 ROD BUNDLE.

THE COMPUTER PROGRAMME VELASCO

The actual 3DV version of VELASCO computes three-dimensional transient steam flow in fuel rod bundles. The application of a single phase programme to severe accident boildown situations is justified by the fact, that for typical thermal hydraulic conditions the steam velocities near the water level are quite low (in the order of 10 cm/sec) and that droplet entrainment may be neglected. The computations start downstream of the two-phase boundary, assuming at the latter a uniform flow of dry vapour at saturation temperature. The actual position of this boundary may either be determined by a steady-state heat balance, or be specified as input, resulting either from separate computations with available two-phase computer programmes [2,3], or, in the case of an experiment simulation, from the measurements.

The main features of VELASCO are the following.

Modelling of the geometry

An example of the discretisation of a fuel rod bundle cross-section is shown in Fig. 2. The bundle length is subdivided into a number of axial steps the height of which may vary from step to step.

Mathematical features

For the three volume elements of a macro-element formed by the cross-sectional area elements and by the axial step heigth, 7 fully implicit balance equations are set up: three momentum balances, a mass balance and a heat balance for the coolant region, and heat balances for the cladding and fuel region respectively. The number of equations per macro-element may increase due to further subdivisions of the cladding and fuel region. An iterative solution procedure is applied, starting with an explicit estimate of the solution which converges towards the implicit final results via a "trial and error" technique controlled by the balance error. The computer time per iteration step and macro-element is independent of the total number of elements. On an AMDAHL 470/V8 this time amounts to 1.7 msec for a "7 equation" macro-element. The number of iterations per time step and the size of the time steps depend on the characteristics of the specific case.

Thermal hydraulic characteristics

Special attention has been given to the modelling of the thermal radiation. More details are given in the next section. The momentum and heat transport between surface elements and the coolant is described by using suitable relationships for the friction factor and the heat transfer coefficient (for more details concerning the latter see next section). In the case of a turbulent flow regime, momentum and heat transfer between adjacent coolant elements include the contribution of turbulent diffusion. The heat transfer through the cladding-fuel gap is treated in a simplified way using a constant gap heat transfer coefficient. The heat generated by the chemical reaction between steam and both the zircaloy fuel rod cladding and the zircaloy inner liner of the shroud is computed using oxidation-rate-temperature correlations. The thermal conductivity of the oxidising materials is continuously updated depending on the oxide layer thickness. This is especially important for the correct description of the peripheral conduction in the fuel rod claddings. The heat transfer conditions at the outer radial boundary have to be specified as input.

THE TREATMENT OF SPECIAL HEAT TRANSFER PROBLEMS

Radiation heat transfer

Figure 3 shows a result of a separate study on the influence of the rod surface discretisation on the radial temperature distribution inside the rod bundle. It is seen that it is very important to use a rather detailed discretisation scheme. In order to limit the resulting computer time to acceptable values, surface-to-surface radiation and surface-to-steam radiation are dealt with separately. The surface-to-surface radiation is computed ignoring the presence of a radiation absorbing and emitting medium. The surface-to-steam radiation is described by an apparent heat transfer coefficient. Details concerning this method may be found in ref. [4]. Fig. 4 shows the apparent heat transfer coefficient as a function of the wall temperature. It is observed that especially for high pressures the radiation heat transfer to the steam may be quite important.

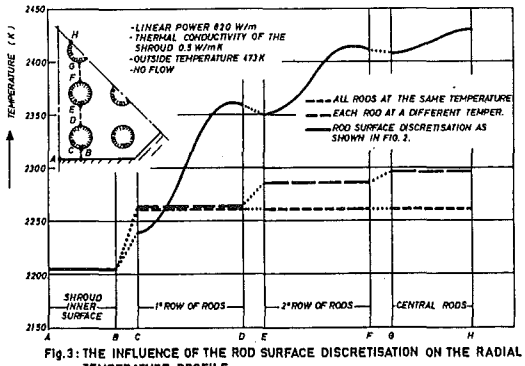

Fig.3: THE INFLUENCE OF THE ROD SURFACE DISCRETISATION ON THE RADIAL TEMPERATURE PROFILE.

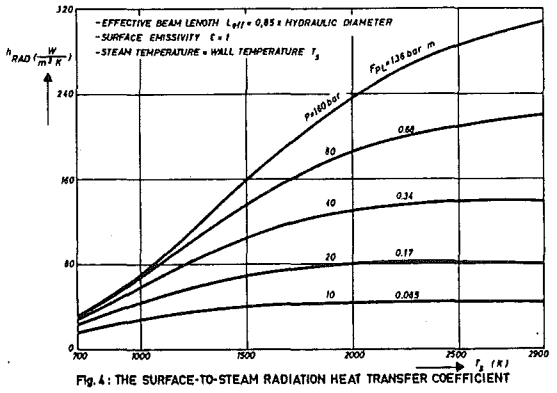

Fig. 4: THE SURFACE-TO-STEAM RADIATION HEAT TRANSFER COEFFICIENT

Heat Transfer by mixed free and forced convection laminar flow

During the advanced stages of severe accidents laminar flow is the prevailing flow regime. Heat transfer by low velocity laminar flow is very much influenced by free convection [5]. Figs 5 and 6 show some typical results of ref. [5] obtained for an annulus equivalent to a rod bundle with a pitch-to-diameter ratio 1.33. CN and CN_o depend on the geometry and on local thermal hydraulic conditions. They are related to the local Grashof number by the equation

$$GR_x = PR \cdot RE \cdot CN / \{ NU \cdot [1 + CN_o \cdot x / (y_o \cdot RE)]^3 \}$$

where x and y_o are respectively the axial coordinate and the radial profile length, and where PR, RE and NU are respectively the local Prandtl-, Reynolds- and Nusselt number. For typical severe accident conditions CN and CN_o may be of the order 10^5 and 10 respectively. Under those conditions the Nusselt number may be considerably higher than that for fully developed flow.

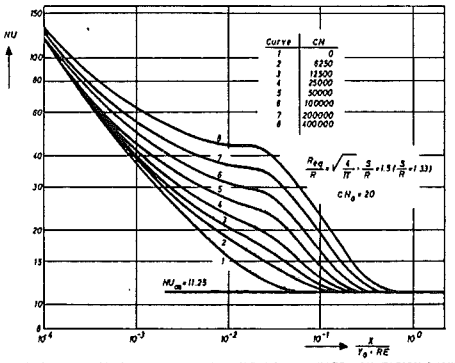

Fig.5: THE INFLUENCE OF BUOYANCY FORCES ON FORCED CONVECTION LAMINAR HEAT TRANSFER (PARAMETER CN)

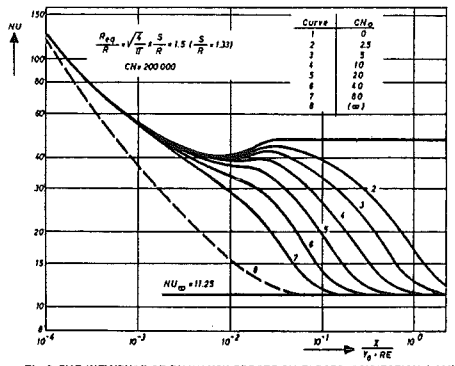

Fig.6: THE INFLUENCE OF BUOYANCY FORCES ON FORCED CONVECTION LAMINAR HEAT TRANSFER (PARAMETER CN_o)

SIMULATION OF THE PBF SCOPING TEST WITH VELASCO

Boundary conditions and modelling assumptions

Information on the test train design is obtained from ref. [6]. This report contains also information on pretest laboratory measurements of the shroud conductivity. In view of the complex structure of the shroud a constant value of 96 W/m^2K has been assumed for the overall heat transfer coefficient between the inner liner of the shroud and the bypass coolant. In ref. [7] the axial and radial fission power profiles are specified, which have been used for precalculations of the PBF scoping tests; these data are used also for the VELASCO computations. From this paper results also an indication on the bypass and test train inlet water temperature (518 K). No other information being available, this value is used as input. The bundle pressure during the experiment is given in ref. [10] and amounts to 7,2 MPa. The time histories of the fission power, of the inlet mass flow rate and of the water level are taken from Fig. 3 of ref. [8]. The curves represented in this figure have been smoothed, as shown in Fig. 7, retaining as important events the variations of the power-time gradient and the rapid decrease of the inlet mass flow rate after 196 minutes, accompanied by an accelerated falling of the water level. The VELASCO computations start at 54 min. During the experiment the initial period of 54 min was used for reaching suitable steady-state conditions.

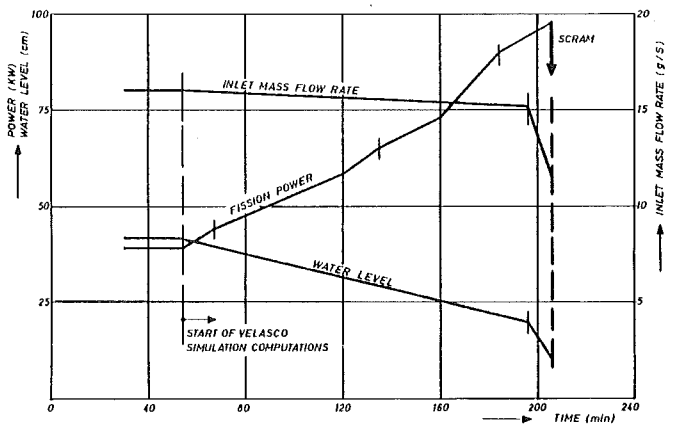

Fig.7: BUNDLE FISSION POWER, INLET MASS FLOW RATE, AND WATER LEVEL HISTORIES USED AS INPUT FOR THE VELASCO SIMULATION COMPUTATIONS OF THE PBF SCOPING TEST.

The zircaloy-steam reaction is described with two different correlations, depending on the temperature. For the lower temperature range (< 1853 K) the Cathcarth-Pawel [11] relation is used, for higher temperatures the Baker-Just [12] relation is used. As inlet condition to the steam region radially uniform mass flow at saturation conditions is assumed. The axially developing heat transfer is computed with a correlation obtained by a separate study [5], which has been illustrated in the previous section.

Results

Figures 8 to 11 show a comparison of computational and experimental results. The computed axial temperature profiles in Fig. 8 represent quite well the measured values. The discrepancy between the analytical and the experimental steam temperature at the 0,5 m elevation cannot be explained and is probably due to a measuring error. Fig. 9 shows the steam temperatures at the outlet of the fuel rod bundle. The calculated temperature history follows well the line representing the measurements. This allows the conclusion that the overall heat balance is respected during the computer simulation. Agreement between the computed and the experimental time history of the cladding and shroud temperatures (Figs 10 and 11) is quite excellent, with the exception of some systematic deviations. These deviations are explained as follows.

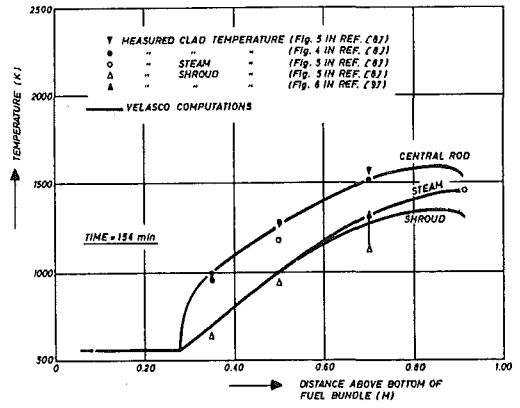

Fig. 8 : AXIAL TEMPERATURE DISTRIBUTIONS AT 154 MINUTES.

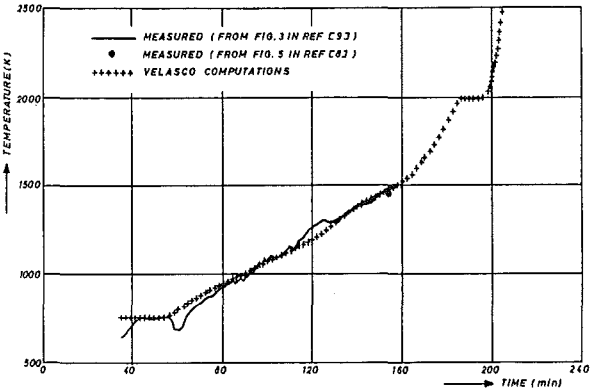

Fig. 9 : AVERAGE STEAM TEMPERATURE AT THE 0.91 m ELEVATION

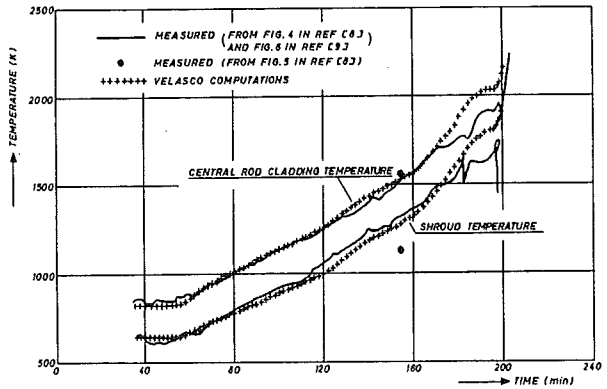

Fig. 10: CLADDING AND SHROUD TEMPERATURE AT THE 0.7m ELEVATION

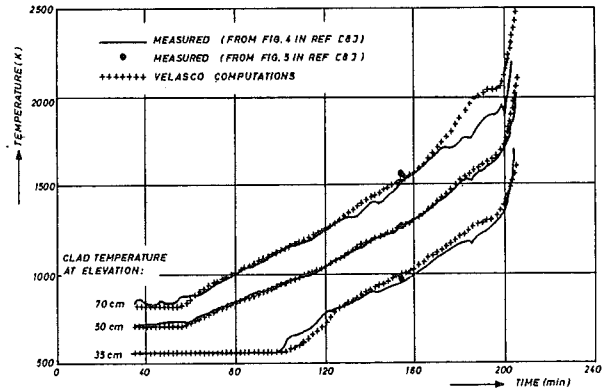

Fig. 11: CENTRAL ROD CLADDING TEMPERATURES AT THREE ELEVATIONS

The confrontation of the central rod cladding temperature and the shroud inner liner temperature shows that - except for an initial time period - the difference between them is systematically too high by about 20%. Probably a too high value of the shroud conductivity has been assumed.

At times beyond 170 minutes the temperatures computed for the 0,7 m elevation deviate more and more from the experimental temperatures. This may be explained by a sudden increase of the shroud conductivity in the upper part of the test train during the experiment. Such an increase could be due to a loss of the inner liner integrity allowing the infiltration of steam into the fiberboard insulator.

The computed temperature gradients during the mass flow decrease in the final phase of the transient are much lower than the experimental temperature gradients. This is probably due to the fact that the simulated mass flow decrease is less sharp than the real one.

FINAL REMARKS

The analysis of experiments simulating thermal hydraulic severe accident phenomena is quite complex because of the three-dimensional perturbations of the flow- and temperature fields due to the reduced bundle size. The computer programme VELASCO 3DV is a tool which may be used for the computation of such three-dimensional effects. Its application for the simulation of the PBF scoping test shows that the results obtained with VELASCO are quite realistic.

Acknowledgement

The assistance of Messrs G. DE VRIES and H. RUCHTI in performing the computer calculations is gratefully acknowledged.

REFERENCES

[1] W. EIFLER and R. NIJSING
A new approach for the prediction of steady-state flow and temperature fields in subassemblies without and with failure.
Proc. Int. Meeting Fast Reactor Safety Technology, Seattle, Washington, August 19-23, 1979

[2] R. NIJSING
Boildown modelling by a 1-D combined thermal analysis of coolant and fuel rod
CSNI Specialists Meeting on Water Reactor Fuel Safety and Fission Product Release in Off - Normal and Accident Conditions,
Risø Nat. Lab. (Denmark), 16-20 May, 1983

[3] I.M. SHEPHERD
BUTRAN - A multirod code for studying core uncovery transients
Technical Report EUR 9262EN, 1984

[4] W. EIFLER and I.M. SHEPHERD
The use of a heat transfer coefficient for describing the radiative exchange between water vapour and the bounding walls
Technical Report EUR 8344EN, 1982

[5] W. EIFLER
Buoyancy effected laminar steam flow and temperature fields in the entrance region of annular flow sections
Publication in preparation

[6] O. SIMONI and R. ZEYEN
Mission Report on a visit to Battelle of Richland (USA)
SUPER SARA Doc. No. SP.A1.MR.104.006, March 1982

[7] B.J. BUESCHER, G.E. GRUEN and P.E. MacDONALD
Fuel performance during severe accidents
Proc. Int. Meeting on Thermal Reactor Safety
August 29 - September 2, 1982, Chicago, Illinois

[8] P.E. MacDONALD, B.J. BUESCHER, R.R. HOBBINS, R.K. McCARDELL and G.E. GRUEN
PBF severe fuel damage program: results and comparison to analysis
Proc. Int. Meeting on Light-Water Reactor Severe Accident Evaluation, Cambridge, MA, August 28 - September 1, 1983

[9] P. CYBULSKIS and R.O. WOOTON
MARCH 2 simulation of the PBF severe fuel damage scoping test
Proc. Int. Meeting on Light-Water Reactor Severe Accident Evaluation, Cambridge, MA, August 28 - September 1, 1983

[10] D.J. OSETEK, K. VINJAMURI, D.E. KUDERA and R.R. HOBBINS
Jodine and Cesium behaviour during the first PBF severe fuel damage test
Proc. Int. Meeting on Light-Water Reactor Severe Accident Evaluation, Cambridge, MA, August 8 - September 1, 1983

[11] R.E. PAWEL, J.V. CATHCARTH and R.A. McKEE
The kinetics of oxidation of zircaloy-4 in steam at high temperatures
Electrochemical Science and Technology, 126(7), July 1979

[12] L. BAKER and L.C. JUST
Studies of metal water reactions at high temperatures
III Experimental and theoretical studies of the zirconium-water reaction
ANL-6548, 1982

POST-IRRADIATION EXAMINATION OF FUEL SUBJECTED TO PRESSURISED HIGH TEMPERATURE TRANSIENTS IN WAGR

A W P Newbigging, A I Russell and E Turner

UKAEA, Windscale

ABSTRACT

The prototype WINDSCALE ADVANCED GAS-COOLED REACTOR (WAGR) closed down in 1981. In the 82 days following the formal shutdown a collaborative series of safety related 'concluding experiments' were performed which were jointly funded by the UKAEA, CEGB and SSEB. This series included four pressurised high temperature transients, in a loop of the reactor, which were intended to take the fuel pin cladding close to melting.

Post-irradiation examination of the fuel after these four transients has confirmed the success of the experiments and has demonstrated that the present fuel design for COMMERCIAL AGRs (CAGR) should be able to endure such transients and continue safe operation thereafter.

INTRODUCTION

The loop chosen for these experiments provided a facility whereby the fuel could be irradiated within the core but in a self-contained coolant circuit with its own coolant control plant. Two sets of Burst Cartridge Detection Gear (BCDG) and a continuous on-line gamma spectrometer, monitoring for Kr^{89} and Mn^{56}, sampled the loop coolant so that failures in fuel pins could be detected immediately. The coolant pressure in the loop was 26 bars compared to 20 and 40 bars in the cores of WAGR and CAGR respectively. The coolant composition was CO_2 with 1% CO.

The aim of the experiments was to examine the behaviour of CAGR type fuel under the high temperature transient conditions postulated to occur in some limiting pressurised faults in a CAGR. Four experiments were conducted, the first two with new specially instrumented fuel and the last two with instrumented stringers previously irradiated in the core of WAGR (Table I).

TABLE I
Experiment summary

Experiment number	Type of fuel	Transient control	Calculated peak clad temperature (°C)	Time of transient (mins)
1	NEW	FLOW	1280	18
2	NEW	POWER	1330	18
3	5 GWd/t(1)	FLOW	1270	12
4	15 GWd/t	FLOW	1280	20

(1) The irradiation values quoted are stringer means. Peak temperature element value = (mean x 1.2).

The engineering design, heat transfer and experimental control aspects have been published previously [1][2], this paper summarises the results obtained by post-irradiation examination of all four experiments.

EXPERIMENTAL DETAILS

The fuel consisted of annular pellets of enriched uranium dioxide inside 0.38 mm thick 20% Cr, 25% Ni, Nb stabilised stainless steel cladding initially filled with helium at 1 bar. Each fuel pin 1 m long and 1.52 cm diameter contained 69 fuel pellets and every fifth pellet carried a V-shaped groove, into which the cladding was pressurised, to inhibit pellet stacking and the development of interpellet gaps. Nine such fuel pins arranged in a single ring (7.2 cm PCD) comprised one fuel element and four elements made up one fuel stringer. The fuel pins were fixed at the bottom end into a machined grid and were supported laterally at mid-span and top end by braces fabricated from spot welded 18/8/Ti strip. The support system was carried by a graphite centre tube and locked inside two half length inner and one full length outer graphite sleeve. The fuel pin and support structure designs were similar to those used in CAGR.

The original intention was to take the cladding as close as possible to the melting point (1370°C). Temperature control during the transients was achieved by thermocouples buried in the wall of special fuel pins with thick walls (1.8 mm). Allowances had to be made for local heat transfer aberrations caused by carbon deposits on the pre-irradiated fuel pins, thermal radiation shielding at brace positions and for the possibility that fuel pins might bow to touch and then overheat at the point of contact. In the event fuel pin bowing did not occur and consequently the hottest position, expected then to be below the upper brace of element 3, was somewhat below the melting point.

The irradiation conditions at the peak of the transient and the variation in temperature during the transient is illustrated in Fig 1 for the first experiment.

POST-IRRADIATION EXAMINATION

The primary aim of the post-irradiation examination was to determine whether a 'coolable geometry' had been maintained. Interest therefore centred on the integrity of the graphite sleeves and grid/brace support structures, the bowing of fuel pins to touch each other or graphite components, and the physical integrity of the fuel pins which might have been jeopardised by certain possible failure modes.

Immediate preliminary examinations were made of the first two experiments with new fuel which established that 'coolable geometry' had been maintained, and on the basis of this a decision was taken to proceed with the final two experiments using pre-irradiated fuel. The results of examining all four experiments can be summarised as follows:-

Graphite components. No physical defects were observed in graphite sleeves or centre tubes that could be attributed to the transient irradiation. Dismantling procedures are such that these components were subjected to considerable stress. These procedures revealed no evidence of weakness or friability of the graphite in any of the four experiments. The graphite centre tubes in the top elements were expected to experience temperatures approaching 1000°C. By comparing the first transient test

centre tubes with similar specimens oxidised thermally in the laboratory, it was confirmed that under-irradiation the surface corrosion was not worse than thermally oxidising the graphite at 1000°C for 20 mins.

Support structures. The inferior corrosion resistance of the 18/8/Ti stabilised stainless steel used for grids and braces gave some cause for concern; particularly the spot-welded braces in which the crevices between adjoining strips represent ideal sites for oxide jacking. Thorough visual inspection of all these components indicated no cause for concern. Metallographic examination of the hottest brace from experiment No. 4 revealed no oxide jacking; good condition spot welds; some oxidation and carburisation and the continued existence of a dense carbon deposit laid down during the 15 GWd/t irradiation in the core. Some evidence was obtained for rubbing between fuel pins and braces at the pin support contact positions but no doming of the braces had resulted indicating that the interactions were of a minor nature.

Thermocouples. The new stringers built for the first two experiments had Nicrosil/Nisil thermocouples at the peak temperature positions but the pre-irradiated experiments 3 and 4 had to rely on the existing Chromel/Alumel thermocouples. The durability of the latter gave cause for concern but they performed satisfactorily and metallography showed that even after 15 GWd/t they were in excellent condition at the hot junction.

Pellet/clad interactions. The 'weak cladding' concept employed in AGRs means that the clad and fuel interact physically during power and temperature cycles. These interactions which influence fuel pin dimensional changes and bowing have been modelled [3][4] and so the relative contributions from irradiation in the core and loop can be assessed. Fuel pin bowing measurements were made which can be summarised as shown in Table II.

TABLE II
Summary of fuel pin bowing

Experiment	Maximum pin bow (mm)			
	Element 1	Element 2	Element 3	Element 4
1	2.0	2.0	2.0	2.5
2	-	-	1.5	NO FUEL
3	2.0	3.8	3.8	7.6
4	2.5	3.0	3.0	10.2

The straightness tolerance of a fuel pin as-manufactured is 1.5 mm and the pin/pin and pin/graphite clearances were 9.75 and 7.25 mm respectively. The bowing of fuel pins in the peak temperature element 3 did not therefore cause concern (Fig 2). The larger bows in the element 4 position of the two pre-irradiated experiments 3 and 4 were due to collapse of the cladding into interpellet gaps which developed by ratchetting. The computer model [3] and measurements on other similar core stringers indicated that interpellet gap development and clad collapse would have taken place during the core irradiation for the higher burn-up stringer (experiment 4) whereas collapse was considered unlikely for the lower irradiation (experiment 3). It is possible that the majority of cladding collapse and bowing observed in the latter stringer occurred during the transient. This is an important deduction because it is suspected that a barely detectable failure occurred in this stringer, during the transient, due to this mechanism.

Interpellet gap development, end-cap inward doming, length changes, local axial strain variations and associated clad wall thickness changes were measured and found to be consistent with the principles embodied in the computer models [3]. For the pre-irradiated fuel it is concluded that the bulk of the changes observed occurred during the core-irradiation and not during the transients.

Fuel behaviour. By extracting and analysing the gas content of the fuel pins in the pre-irradiated stringers it has been calculated that the fraction of the stable Xenon generated which had been released into the voidage of the standard fuel pins was as shown in Table III.

TABLE III
Fission gas release summary

Experiment	Mean stringer burn-up (GWd/t)	Maximum release of stable Xe (%)			
		Element 1	Element 2	Element 3	Element 4
3	5	0.03	0.10	0.36	0.14
4	15	0.02	0.09	0.12	0.03

The levels of release in the peak elements (2 and 3) are only slightly greater than expected from athermal processes and this is consistent with the observation that fission gas bubbles were only present in the fuel, around the bore of the pellets, at the peak rated ends of these elements. The model used to predict fission gas release in AGR fuel [5] correctly predicted the levels of release and indicated that no further significant release took place during the transients; this is in agreement with the observations. Cracking of the ceramic fuel pellets due to thermal gradient induced stresses was normal. The transient had not caused any further cracks and the annular fuel pellets remained mechanically stable.

Cladding behaviour. Grain growth by secondary recrystallisation was observed in the cladding of all four experiments. By studying the distribution it was concluded that the hottest point was at the top brace position of element 3 as expected and that obvious cross-pin temperature gradients existed during the transients. Grain growth in the pre-irradiated cladding was inhibited presumably by the presence of helium bubbles and precipitates formed during the in-core irradiation (Fig 3). Where grain growth did take place in the pre-irradiated cladding it was restricted, by a critical strain annealing mechanism, to areas of cladding which had been strained in tension by the ratchetting process. Regions over pellet ends subjected to axial compressive creep were less susceptible to grain growth. The levels of axial strain observed in the higher irradiation (experiment 4) were the highest recorded on WAGR fuel with thinning strains of up to 20% over pellet centres; well above the levels required for a critical strain anneal mechanism to operate.

The depth of oxidation of the cladding at the peak temperature position was as shown in Table IV.

TABLE IV
Clad oxidation at hotspot position

Experiment	Fuel type	Temperature peak (°C)	Oxide depth (um) at hotspot	
			Uniform	Local
1	NEW	1280	4	10
2	NEW	1330	30	15
3	5 GWd/t	1270	4	10
4	15 GWd/t	1280	5	20

The levels of oxidation of the new cladding in experiments 1 and 2 are as expected by comparison with laboratory simulations. The oxidation of the pre-irradiated cladding is no worse than predicted from the in-core irradiation. The existence of a healing layer of Cr rich oxide has inhibited further oxidation in these transients. Evidence for spalling of oxide after the transient was obtained which confirms that this was the probable cause of the rise in Mn^{56} signal at the on-line spectrometer. The maximum local pitting oxidation in experiment 4 occurred during the transient at a site from which the uniform oxide layer had spalled.

There was no evidence for thinning strains over radial fuel cracks indicating that pellet/clad interaction (PCI) had not occurred during the transient rise in temperature.

The possibility that the pre-irradiated cladding might be carburised, due to either the CO_2/CO coolant or the carbon deposits on the surface, gave cause for concern since this would lower the melting point. There was no sign of incipient melting and nuclear microprobe analyses of samples of cladding from the hottest elements of experiment 4 (15 GWd/t) proved that the cladding had not carburised.

CONCLUSIONS

It has been demonstrated that irradiated fuel of the CAGR design can undergo short term pressurised transients to can temperatures between 1270°C and 1330°C without:-

(a) losing coolable geometry;

(b) showing physical or chemical degradation of the graphite components;

(c) physical distortion of grid and brace support structures due either to interaction with bowed pins or by oxide jacking;

(d) significant fission gas release, fuel relocation or structural changes;

(e) clad melting or serious loss of section by oxidation.

The present design of fuel pin for Commercial AGRs has more anti-stacking grooves than those used for these loop transient experiments in WAGR. The model [3] predicts that in such pins, operating at a coolant pressure of 40 bar, the axial gaps between fuel pellets will not exceed the critical size for cladding collapse. It can be concluded that such CAGR fuel could endure similar transients and continue to operate safely thereafter.

ACKNOWLEDGEMENTS

The help of many colleagues at the Windscale Laboratories of the UKAEA is gratefully acknowledged; in particular the guidance received from Mr M Kendal the Project Engineer.

REFERENCES

[1] BRIDGE M J and KENDAL M. "High temperature loop experiments - WAGR concluding experiments". BNES, BRISTOL, SEPT 1982, Paper 125, Pages 81-89.

[2] GALLIE R R and KENDAL M. "Concluding experiments in the Windscale AGR". NUCLEAR POWER EXPERIENCE, VOLUME 3, 1983, IAEA-CN-42/123.

[3] BRADSHAW K A. "Fuel pin dimensional changes in CAGRs". BNES, BRISTOL, SEPT 1982, Paper 66, Pages 37-42.

[4] CROSSLAND I G. "Fuel pin bowing in CAGR". BNES, BRISTOL, SEPT 1982, Paper 67, Pages 43-48.

[5] BEATHAM N, HARGREAVES R, WALKER R D and KIRKBRIDE R. "A comparison of measured fission gas releases for Windscale AGR fuel above 18 GWd/t with those predicted using the computer code MINIPAT D" - from "Water Reactor fuel element performance computer modelling" - Edited by J Gittus. Published by APPLIED SCIENCE PUBLISHERS LTD, 1983.

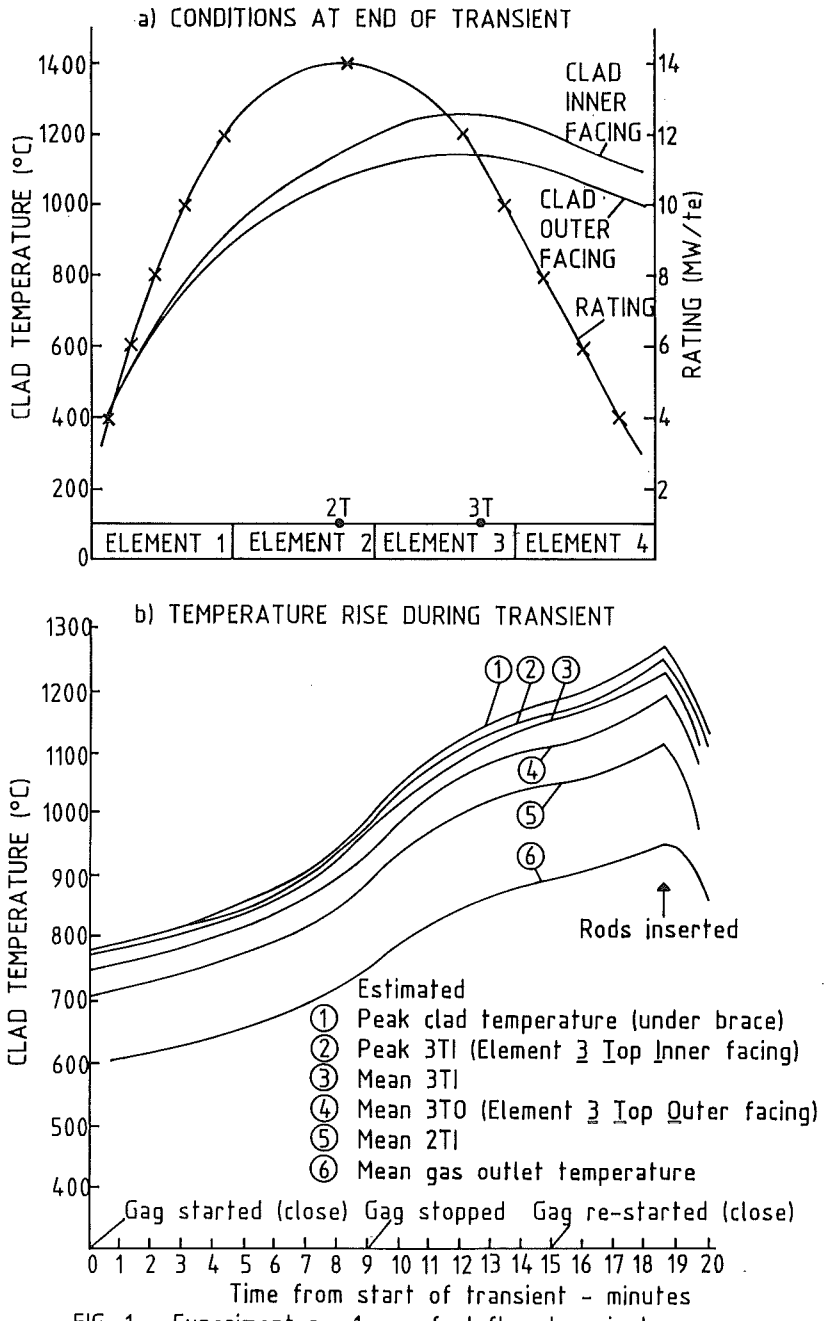

FIG. 1 Experiment no. 1 new fuel flow transient.

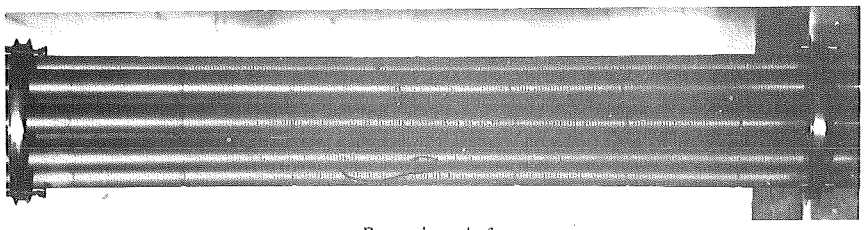

Experiment 1

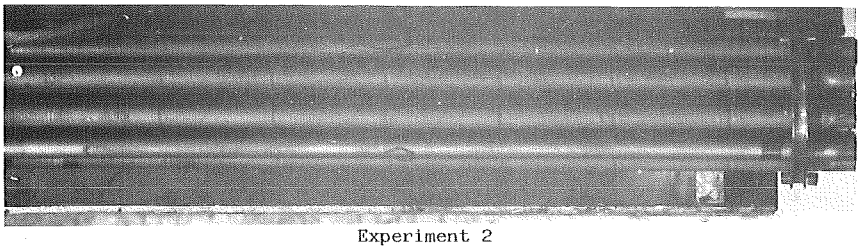

Experiment 2

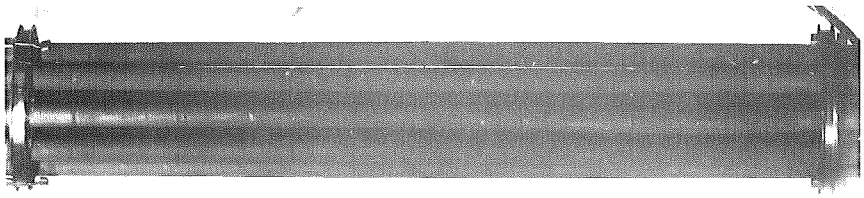

Experiment 3

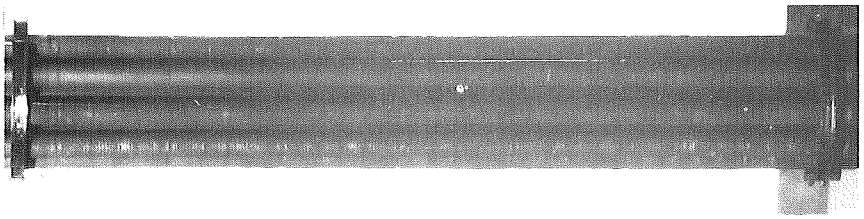

Experiment 4

Coolant flow ⟶

FIG 2. Fuel pins in upper half of peak temperature Element 3 after transient

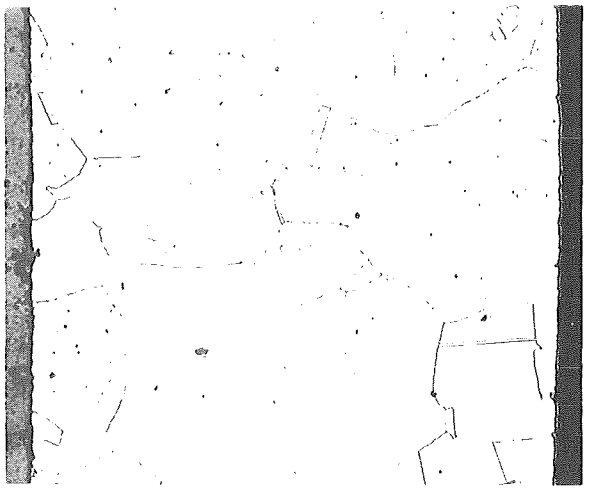

(a) Experiment 1 - New fuel

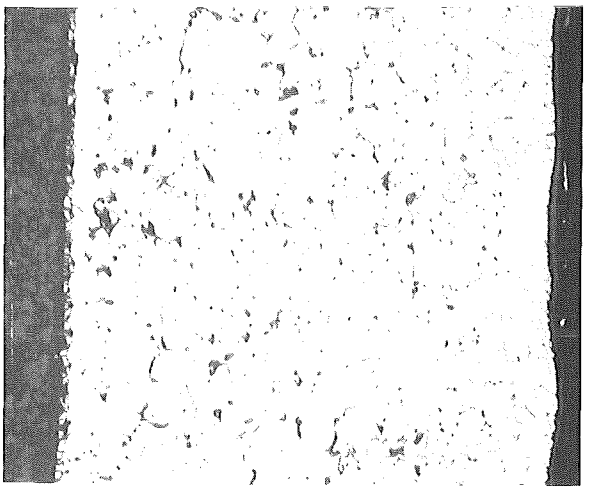

(b) Experiment 4 - 15 GWd/t

FIG 3. Clad structures at peak temperature position showing inhibition of grain growth by pre-irradiation

Chapter 7
Core Debris Behavior and Core Concrete Interaction

RESULTS AND ANALYSIS OF REACTOR-MATERIAL EXPERIMENTS ON EX-VESSEL CORIUM QUENCH AND DISPERSAL

B. W. Spencer, L. M. McUmber, and J. J. Sienicki

Argonne National Laboratory
Argonne, Illinois 60439

D. Squarer

Electric Power Research Institute
Palo Alto, California 94303

ABSTRACT

The results of reactor-material experiments and related analysis are described in which molten corium is injected into a mock-up of the reactor cavity region of a PWR. The experiments address ex-vessel interactions such as steam generation (for those cases in which water is present), water and corium dispersal from the cavity, hydrogen generation, direct atmosphere heating by dispersed corium, and debris characterization. Test results indicate efficiencies of steam generation by corium quench ranging up to 65%. Corium sweepout of up to 62% of the injected material was found for those conditions in which steam generation flowrate was augmented by vessel blowdown. The dispersed corium caused very little direct heating of the atmosphere for the configuration employing a trap at the exit of the cavity-to-containment pathway. Corium sweepout phenomena were modeled for high-pressure blowdown conditions, and the results applied to the full-size reactor system predict essentially complete sweepout of corium from the reactor cavity.

INTRODUCTION

A program of reactor-material experiments and related analysis is under way at Argonne National Laboratory, under sponsorship of the Electric Power Research Institute (EPRI), examining the thermal and hydrodynamic interactions involving molten core materials (corium) and water in the reactor cavity region of the reactor containment building (RCB). The experiments and analysis are performed to aid understanding of events taking place ex-vessel for those postulated accident sequences which include core meltdown, failure of the reactor pressure vessel (RPV) lower head, and drainage (or ejection) of the corium into the reactor cavity.

The purpose of the present paper is to describe results of experiments and related analysis following the initial scoping tests [1]. These tests have examined corium entry into water under conditions simulating both low initial RPV pressure (large break) and high RPV pressure (small break, loss of

heat sink). The former cases are characterized by relatively slow corium drainage through the vessel breach by gravity head and the retention of most of the debris in the form of a bed in the cavity. The latter cases are characterized by corium being largely levitated and swept out from the cavity by the high pressure and high velocity flow of the blowdown gas, augmented in some cases by steam generated from corium-water thermal interaction. The case of corium entering a dry cavity followed by water injection atop the corium melt layer has been described previously and is not considered here [1]. Details of the experiment apparatus, technique, and instrumentation are presented in Ref. 1. The test apparatus is illustrated in Fig. 1.

HIGH RPV PRESSURE CASES

The conditions for the high-pressure dispersal tests are listed in Table I. Tests 1, 4, and 5 were all performed with a sufficient mass of water initially present in the cavity mock-up to completely quench the injected corium. In test #6, the cavity was dry, and the only water present in the system was in the bottom of the expansion vessel (EV). The tests performed with water in the cavity consistently showed that as the corium began to enter the water, the water underwent a vigorous levitation process, driven by the abrupt steam generation. Displaced water filled the pipeway and was first ejected as a slug and continued to be ejected in a dispersed droplet flow regime. Corium was also swept out of the cavity by the high velocity gas and steam efflux through the pipeway. The mass of corium swept out of the cavity ranged from 20 to 62% of the mass of corium injected into the cavity. Actually, the mass swept out was even greater since the corium masses which were observed in the motion pictures to fall back into the pipeway from the trap were not readily measurable and were not included as swept-out material. (In CWTI-4, for example, it was estimated that 34% rather than 20% was actually swept out including that which fell back into the pipeway.) Of the corium which was swept out, most consisted of crust-like accumulation within and immediately surrounding the trap. Debris in particulate form was recovered from the bottom of the EV and from atop the baffle plate. The particulate ranged in median size from 100 μm (airborne material dispersed far from the pipeway) to ~ 1000 μm (particulate near the pipeway). In tests 1 and 4, the debris remaining in the cavity consisted of a single, slab-like mass solidified on the base. The corium contained both large-scale voids plus distributed small-scale porosity in the oxide phase. The top surface was glazed over, seemingly imporous, and very irregular in contour. The cross section revealed that the metallic constituent had segregated into a pancake-shaped ingot totally imbedded within the oxide. At the bottom, immediately atop the lavite base, was a thin, dense oxide crust; above this was the imporous metal ingot, and atop this was the thick, porous oxide layer.

In tests 5 and 6, the X-ray motion pictures showed that the corium channeled through the levitated water (test #5), impinging directly upon the base, whereupon the corium splashed upward off the base and was itself levitated (dispersed droplet flow regime) by the high-velocity gas and steam velocity in the cavity. The levitated corium left thick crusts frozen on all the inside surface area of the cavity vessel. In test #5, there was less than 10% of the injected corium remaining on the cavity base; 21% remained on the base in test #6.

Figure 2 shows pressure traces from the cavity region for tests 5 and 6. In test #5 with water present in the cavity, a nonequilibrium pressure buildup is evident during the time of water and corium expulsion from the cav-

ity. Table II summarizes selected results from the tests. The time to reach peak pressure is short in these high-pressure dispersal tests, ranging from 0.5 to 3.8 s at 90% of peak. The efficiency of steam production, the actual measured steam pressure (corrected for hydrogen and inert gas partial pressures) as a percent of that calculated based upon all corium enthalpy going into steam generation, ranged from 10% (dry cavity case) to 65%. The remainder of the energy went primarily into heatup of the structure, and a small fraction went into heatup of the atmosphere. Although luminescent corium particulate was dispersed into the containment atmosphere in all tests, as observed in the motion pictures, the direct energy transfer to the containment atmosphere was very small. In tests 1 and 5, the containment atmosphere actually cooled during the interaction due to the vigorous dispersal of water from the cavity. In test #6, in which the cavity was dry, the containment heatup attributable to the 1.2 kg of dispersed corium amounted to a temperature rise of 53 C, only ~ 6% of the 842 C heatup calculated for temperature equilibration between the dispersed corium and the containment atmosphere.

LOW RPV PRESSURE CASES

Conditions for the four low pressure tests performed to date are listed in Table I. Tests CWTI-7 and -8 utilized the scaled apparatus to investigate the entry of corium into the cavity mock-up by gravity drainage only. In test CWTI-7, the injector throat diameter was 5.08 cm (2") which scales to ~ 4.5 ft dia opening size in the Zion RPV lower heat (14.4 ft I.D.). In test CWTI-8, the injector throat diameter was 1.27 cm (0.5") which scales to ~ 1.1 ft dia opening size in the RPV lower head. This latter size is representative of the breach for failure of a welded instrument guide tube penetration when the ablation-induced enlargement is included.

In test 7 the first corium fell as discrete particles or droplets followed by a brief stage of filament-type flow. Subsequently, the corium drainage was very dense and occupied essentially the full nozzle diameter. The X-ray motion picture showed that the water appeared to levitate uniformly upward starting upon initial corium entry. The entire water pool was levitated by 500 ms and showed net motion toward the exit pipeway between 500 and 675 ms, driven by the rapid steam efflux. There was no more water visible in the cavity by 770 ms. Hence, a large fraction of the injected corium entered the cavity while there was either very little water present or while it was in a highly fluidized state. In general, the molten corium appeared to collect upon the base with little indication of splashing in this test. There was little indication of crust formation on the walls compared to the previous high-pressure tests.

The pressure data showed an abrupt pressure rise of 0.027 MPa (3.9 psi) in the IV with a risetime of 30 ms at the start of corium injection. Steam generation from the initial corium-water contact created a pressure imbalance between the IV and EV which peaked at 0.033 MPa (4.9 psi) at 480 ms. This nonequilibrium pressure difference was caused by the presence of water and corium masses in the pipeway. The pressure imbalance vanished at ~ 525 ms, and thereafter the IV and EV pressures tracked one another. Overall, the system pressure increased from 0.100 to 0.145 MPa during the time scale of the corium injection, and thereafter increased at a more gradual rate as the debris bed was cooled until peaking at 0.203 MPa at 15 s. The appearance of a pressure maximum at 15 s was attributable to complete dryout occurring in the cavity at about that time rather than the corium layer being fully quenched.

Of the total mass of debris retrieved following the test, 195 g (6.6%) had undergone sweepout into the EV. The median particle size of the dispersed particulate was ~ 1200 μm which is considerably larger than the debris collected in high-pressure tests. The debris remaining in the IV was in the form of a large ingot of oxide and metallic constituents of corium. This material had not been quenched into solid particulate during the fall to the base, but apparently had collected on the base in the molten state and had gradually solidified and cooled as a porous slab. The layer ranged from 0.75 to 1.9 cm in thickness, with an average thickness of 1.27 cm. The average density was 5.1 g/cm^3. There were numerous globular metallic inclusions which varied in size from 10's μm to the order of 1 cm. The large metal globules had a density of 6.2 g/cm^3.

Gas samples were extracted from the EV at ~ 2-3 min after the test and were analyzed for H_2 content. The results indicated that 5.2 ± 1.1 g of H_2 was produced during the test. This amounts to 23% of the maximum calculated hydrogen generation based upon oxidation of all the Fe present in the injected corium to Fe_2O_3. The hydrogen partial pressure was 0.006 MPa. Additional test results based upon analysis of data are summarized in Table II.

Test CWTI-8 with the reduced nozzle diameter was very similar to test 7. The leading edge of the corium column caused a crater and splash wave to form in the water followed by levitation and dispersal of water from the pool. Most of the corium remained unquenched during its fall to the base. It was eventually quenched as a thick, crust-like layer on the base. There was negligible sweepout of corium debris by the steam for this prolonged corium entry condition. The material on the base was a large, porous ingot with an exceedingly irregular upper surface similar to CWTI-7. There was a marked separation of the metal and oxide phases. There was an irregular-shaped oval ring of metallic material whose density measured 8.0 g/cm^3. The porous oxide material averaged ~ 1 cm in thickness and had a density of 3.97 g/cm^3. The gas samples extracted from the EV indicated that 5.6 ± 1.5 g of hydrogen were produced during this test. This amounts to 76% of the maximum calculated hydrogen generation based upon oxidation of all Fe present in the injected corium to Fe_2O_3. Other test results are summarized in Table II.

Tests CWTI-9 and -10 were performed to examine modeling concepts of corium breakup, mixing, and quench in water. In order to achieve substantial quench during the fall through water, the pool depth was increased to ~ 35 cm which is ~ 12 jet diameters. (The Corradini mixing model [2] predicts complete breakup and mixing in ~ 4 diameters depth of water.) The two tests parameterized on the temperature of the water. In test CWTI-9, the water was initially heated to close to saturation temperature. A total of 2.18 kg of molten corium drained into the pool over a time span of ~ 0.9 s. Test data indicated that the steam generated by corium-water thermal interaction as the corium first entered the water caused an abrupt pressurization in the cavity (Fig. 3) which was followed by a prolonged dispersal of water and some corium from the IV into the EV. The X-ray motion picture showed an abrupt boilup of the water pool into a fluidized state at that time. The corium sweepout, attributable to the high steam efflux velocity, amounted to 318 g, 13.3% of the injected corium. The debris remaining at the bottom of the IV could not be characterized as a particle bed; instead, it was a highly porous ingot suggesting that the major portion of the corium was not quenched to below its solidus while falling to the base, in contrast to model predictions.

Test CWTI-10 was similar to the previous test except that the water was highly subcooled at 25C. The outcome of this test was vastly different in the sense that no net steam generation was measured due to rapid condensation by the subcooled water and structure (Fig. 3), there was no appreciable water

levitation, there was no sweepout of corium, and the debris bed had the characteristics of a loose aggregate rather than a solidified ingot. Although results of the deep pool tests have not yet been fully analyzed, selected results are summarized in Table II.

MODELING AND ANALYSIS

To provide an interpretation of sweepout in the pressure-driven experiments and to bridge the gap between the small-scale tests and the reactor system, development of an integrated computer model [3] to calculate the time dependent sweepout of corium from the cavity/tunnel region and related phenomena has been undertaken. The model considers the pressure-driven flow of corium, water, steam, and gas in terms of a constant slip (i.e., velocity) ratio between the steam/gas phase and each of the corium and water phases, freezing out of corium as crusts upon structural surfaces, and levitation of corium and water by the impinged and deflected vessel blowdown gas jet. The model was applied to the CWTI experiments using the TV, IV, and EV pressures actually recorded during the tests to drive the calculation of corium and water sweepout. Model predictions are compared with the experiment results in Table III.

In CWTI-5 and CWTI-6, the corium injections were carried out at high initial TV pressures. The model predicts that as a result of interaction with the high velocity follow-on gas jet, the corium and water are broken down into liquid droplets which are levitated by the impinged and deflected gas stream to form a dispersed droplet flow regime. The calculation predicts that the corium retention reflects the freezing of levitated corium droplets as crust until all remaining droplets have been swept out of the IV. For CWTI-6 (dry cavity), the predicted sweepout fraction (29%) is in excellent agreement with the observed extent of sweepout (30% based upon the retrieved masses). The calculated sweepout fraction for CWTI-5 (wet cavity) of 44% is somewhat less than the experimental sweepout of 57%. The lower observed retention may principally reflect the quenching effects of water within the IV which were not modeled in the calculation. Specifically, corium droplets which have begun to freeze as a result of heat transfer to levitated water droplets would not be expected to adhere as well to solid surfaces thereby limiting subsequent crust growth.

In CWTI-1 and CWTI-4, the injections were performed at low initial TV pressure. The velocity of the injected gas flow is predicted to be insufficient to sustain the levitation of corium as droplets within the IV. Accordingly, the corium forms a layer resting upon the IV base and the lower portion of the horizontal pipeway such that freezing induced retention takes place on these surfaces. The calculation predicts that most of the retained mass is due to the decay of the IV driving pressure before the greater portion of the molten corium can be dispersed from the IV and pipeway.

The sweepout model was applied to the prediction of corium sweepout by the blowdown steam jet from a full-size reactor cavity of Zion dimensions [3]. Initial conditions at meltthrough were taken representative of the TMLB' sequence: primary system pressure = 17 MPa, cavity/containment pressure = 0.4 MPa (0.3 MPa steam plus 0.1 MPa air), water absent from cavity, corium mass ejected from vessel = 86500 kg. When molten corium contacts concrete, gas evolution and concrete melting are expected to commence immediately such that the melted concrete and corium crust would be expected to be swept away. However, to indicate the effects of scale upon crust growth induced retention, the present calculations model freezing upon the cavity and tunnel concrete walls as well as the RPV lower head. Table IV shows the effects of

varying the breach flow area upon the percentage of ejected corium swept out of the cavity and tunnel. Because the sweepout time is significantly shorter than the vessel blowdown time, the corium predicted to be retained within the cavity and tunnel is that which can be frozen as crust before all remaining molten corium droplets have been swept out (as in the CWTI-5 and CWTI-6 tests). If crust formation were not modeled, the calculated dispersals would be 100% of the corium entering the cavity. However, even with freezing upon structure, a high sweepout of 90% or greater is predicted. The calculations show that the relatively low sweepout fractions obtained in the CWTI experiments are principally the result of the greater surface-to-volume ratio of the small-scale tests favoring solidification upon structure as well as the use of a steel rather than concrete-lined cavity mock-up.

For those experiments in which corium was gravity dropped into pools of water within the IV and pipeway (CWTI-7 and CWTI-8), analysis has focused upon steam and hydrogen generation. Most of the corium was found in the form of a coherent solidified layer on the IV base and the lower portion of the pipeway suggesting that with the exception of the small fraction of corium which was swept out, the injected corium mostly fell through the water pool and accumulated as a molten layer upon the IV base. Calculations were carried out modeling the steam and hydrogen production resulting from the quenching of a planar corium layer by film boiling heat transfer to an overlying water pool and thermal conduction into the underlying stainless steel base using the layer quenching computer code developed for analysis of the CWTI-2 experiment [4]. The calculation assumes that a corium mass corresponding to that retrieved from the lower portion of the IV and pipeway is suddenly formed upon the IV base beneath a water mass of 1.0 kg, representative of that portion of the initial water inventory not swept out of the IV. Based upon the analysis of CWTI-2, the corium upper surface was assumed to possess surface irregularities which effectively enhance the interfacial area for film boiling heat transfer by a factor of 3.5.

For CWTI-7 and CWTI-8, Figs. 4 and 5 compare the predicted total system pressure with the measured pressure over the inferred cavity dryout time. Good agreement is obtained between the calculated and observed total pressures at dryout. For CWTI-8, the system pressurization rate throughout the dryout interval also agrees with the measurement suggesting that the effects of additional steam generation associated with corium-water intermixing as the corium penetrates the water and forms a layer are minimal in this experiment. In contrast, for CWTI-7, the pressurization rate during the first 2 s of time following the inception of steam formation is underpredicted by a factor of greater than two. The disagreement here may indicate that either corium-water intermixing effects are a significant source of early steam formation in the test, or the effective enhancement in interfacial area due to surface irregularities is greater than that characteristic of CWTI-8 or CWTI-2. The predicted total hydrogen production of 3.6 and 2.0 g for CWTI-7 and CWTI-8, respectively, is somewhat less than the measured H_2 generation (5.2 ± 1.1 and 5.6 ± 1.5 g). Both the calculated and experimental H_2 masses are significantly less than those corresponding to complete oxidation of the iron and chromium present within the corium (42 and 26 g for CWTI-7 and CWTI-8, respectively).

CONCLUSIONS

The results of the high pressure tests have demonstrated the importance of modeling dispersed flow for both the water and corium under high-pressure

blowdown conditions. The magnitude of corium dispersal into other parts of the system has been found to be significant, and related analysis has shown that the percentage of sweepout may be considerably greater at full-scale [3]. The test results suggest that the dispersed corium causes relatively little direct heating of the containment atmosphere for the configuration employing a trap at the exit of the pipeway. With water present in the cavity, the containment atmosphere heatup effect was essentially nonexistant. The results of the gravity drain tests suggest that the coherent corium jet can effectively channel its way through water without extensive breakup and mixing over greater depths than suggested by current modeling. The steam generation rates can be effective in terms of levitating and dispersing water from the cavity, but without augmentation by vessel blowdown, most of the corium remains as a bed at the bottom of the cavity.

Based upon modeling of hydrodynamic dispersal and freezing phenomena, the relatively small corium sweepout attained in the high-pressure dispersal tests (20-62%) is principally the result of the greater surface-to-volume ratio of the small-scale experiments favoring solidification of stable crusts upon the steel surfaces of the interaction vessel; sweepout in the reactor system is predicted to exceed 90% of the corium mass entering the cavity during the blowdown.

ACKNOWLEDGEMENT

This work was sponsored by the Electric Power Research Institute under Contract No. 1931-2. R. Sehgal (EPRI) and L. W. Deitrich (ANL) provided invaluable support in this work. D. Gregorash, R. Aeschlimann, and B. Banez assisted in various aspects of the experiments. The manuscript was prepared by V. Eustace.

REFERENCES

1. B. W. Spencer, et al., "Results of Scoping Tests on Corium-Water Thermal Interactions in Ex-vessel Geometry," Proc. AIChE Symp. Series, Heat Transfer, No. 225, Vol. 79, Seattle, WA, July 24-27, 1983.

2. M. R. Corradini, "Proposed Model for Fuel-Coolant Mixing During a Core-Melt Accident," Proc. Intl. Mtg. Thermal Nuclear Reactor Safety, Chicago, IL, August 29-September 2, 1982.

3. J. J. Sienicki, B. W. Spencer, and D. Squarer, "Debris Dispersal in Reactor Material Experiments on Corium Water Thermal Interactions in Ex-Vessel Geometry," Heat Transfer-Niagara Falls 1984, ed. N. M. Farukhi, AIChE Symposium Series, No. 236, Vol. 80, p. 402, American Institute of Chemical Engineers, New York (1984).

4. J. J. Sienicki and B. W. Spencer, "Analysis of Reactor Material Experiments on Corium-Water Thermal Interactions in Ex-Vessel Geometry, "Proceedings International Meeting on Light Water Reactor Severe Accident Evaluation," Cambridge, MA, August 28-September 1, 1983, Vol. 2, p. 12.1-1, American Nuclear Society, LaGrange Park (1983).

TABLE I. INITIAL CONDITIONS FOR CORIUM/WATER INTERACTION TESTS

		CWTI-1	CWTI-4	CWTI-5	CWTI-6	CWTI-7	CWTI-8	CWTI-9	CWTI-10
I.	Test Apparatus								
	A. Water depth, cm (h/D_t[1])	5.4(0.5)	10.8(1.0)	10.8(1.0)	0.0	4.42(0.41)	3.5(0.37)	31.0	35.6
	B. Water temperature, C	99	95	93	-	95	92	94	25
	C. Expansion vessel gas	N_2[2]	Ar	Ar	Ar	Ar	Ar	Ar	Ar
	D. Gas temperature, C	120	126	146	135	147	130	141	25
	E. Gas pressure, MPa	0.10	0.14	0.10	0.10	0.10	0.10	0.10	0.10
II.	Corium Injector								
	A. Injector throat dia, cm	5.08	1.27	1.27	1.27	5.08	1.27	2.54	2.54
	B. Mass of reactants loaded, kg	4.03	4.07	4.17	4.13	4.06	4.16	4.07	4.11
	C. Mass of corium injected, kg	1.94	4.06	3.94	3.75	2.95	1.75	2.18	1.31
	D. Injection pressure, MPa	0.49	0.36	5.0	4.7	0.10	0.10	0.10	0.18
	E. Corium injection time, s	0.070	0.50	0.30	0.15	0.7	1.5	0.9	~ 0.8
	F. Injector blowdown time, s	0.35	1.5	1.2	0.7	-	-	-	-

[1]Ratio of initial water depth and pipeway diameter.

TABLE II. SUMMARY OF RESULTS FOR HIGH-PRESSURE CORIUM INJECTION TESTS

		CWTI-1	CWTI-4	CWTI-5	CWTI-6	CWTI-7	CWTI-8	CWTI-9	CWTI-10
A.	Mass of corium injected, kg	1.94	4.06	3.94	3.75	2.95	1.75	2.18	1.31
B.	Corium sweepout, %	35	20	62	32	6.6	0.9	13.3	0
C.	IV peak pressure rise, MPa	0.25	0.13	0.81	0.18	0.103	0.100	0.150	0.002
D.	EV peak pressure rise, MPa	0.12	0.13	0.38	0.13	0.103	0.100	0.150	0.002
E.	Time to reach 90% of EV peak pressure, s	1.0	3.8	0.9	0.5	6.7	28.5	35	1
F.	Efficiency of steam production, %	65	14	44	10	42	67	55	0.0
G.	Max. steam/gas velocity through pipeway, m/s	380	84	580	225	02	49	151	3.3
H.	Max. measured temp. rise in EV, C	~10	15	~2	53	-	-	-	-
I.	Efficiency of containment atmosphere heatup, %	0.0	3.6	0	6.2	-	-	-	-

TABLE III. COMPARISON OF PREDICTED AND OBSERVED SWEEPOUT IN GAS PRESSURE-DRIVEN CWTI EXPERIMENTS

Test	Initial Injection Pressure, MPa	Initial Water Depth, h_o/D_{pipe}[1]	Injected Corium Mass, kg	Observed Completion of Sweepout, s	Predicted Completion of Sweepout, s	Observed Corium Sweepout[2] %	Predicted Corium Sweepout, %
CWTI-1	0.49	0.5	1.94	0.32	0.32	32	30
CWTI-4	0.36	1.0	4.06	~ 1.8	1.8	35	34
CWTI-5	5.0	1.0	3.94	0.7	0.53	57	44
CWTI-6	4.7	0.0	3.75	0.6	0.71	30	29

[1]Ratio of initial water depth and pipeway diameter.
[2]Based upon retrieved masses.

TABLE IV. PREDICTED CORIUM SWEEPOUT FROM REACTOR SYSTEM CAVITY

Breach Area, m^2	Corium Sweepout Time, s	Vessel Blowdown Time, s	Corium Sweepout, %
0.021	6.0	167	90.4
0.085	3.3	41	92.9
0.34	2.1	10	94.3
0.85	1.7	4	94.9

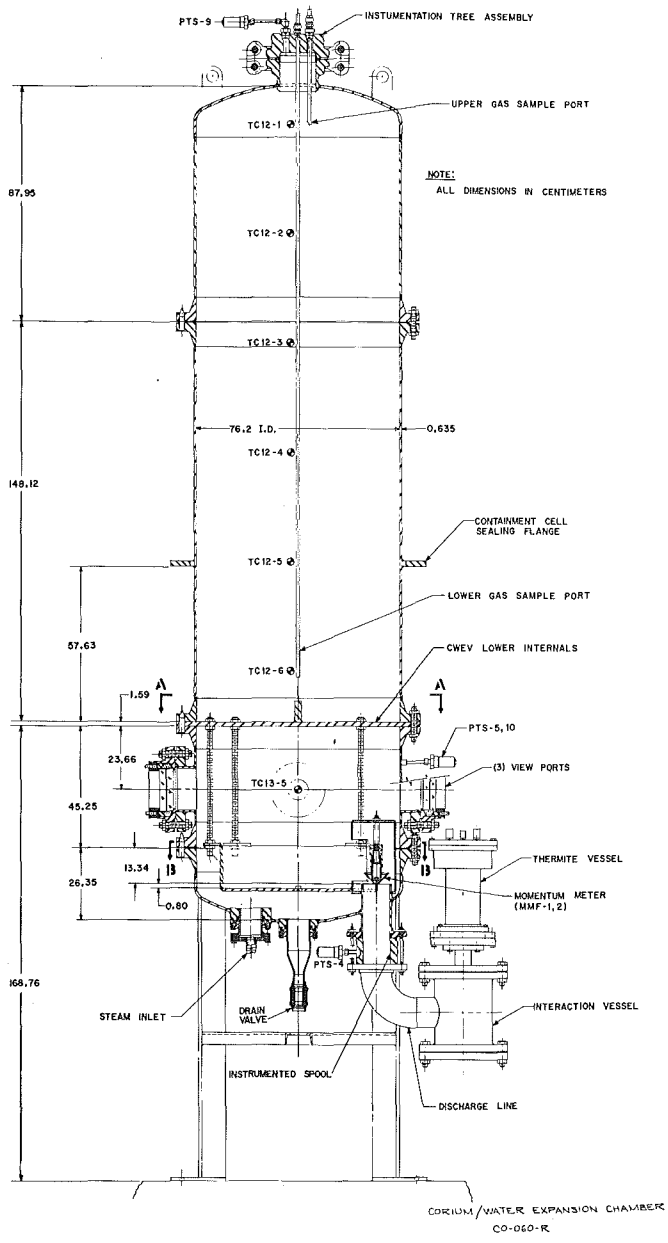

Figure 1. Experiment Apparatus used for Corium/Water Thermal Interaction (CWTI) Tests.

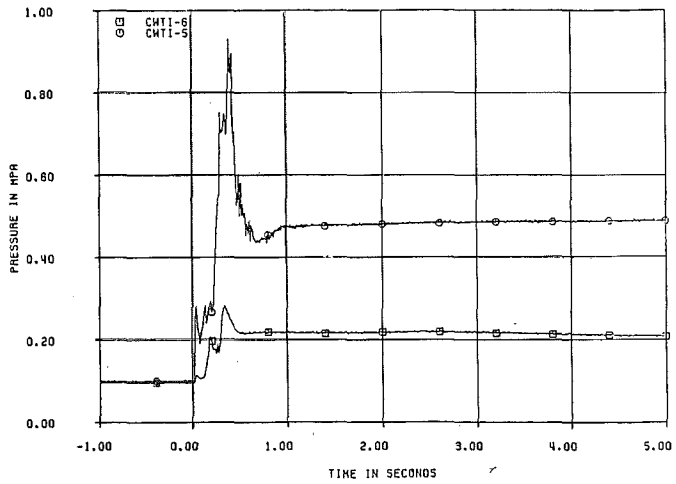

Figure 2. Interaction Vessel (IV) Pressure Data from CWTI-5 and 6.

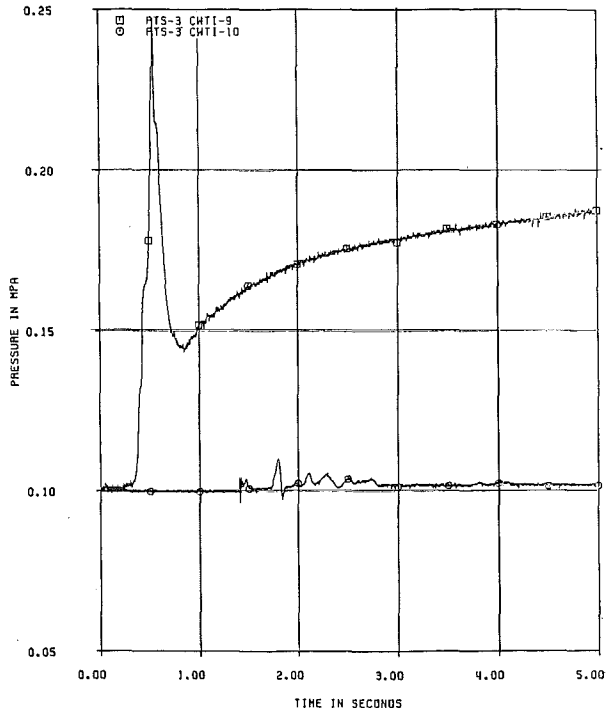

Figure 3. Pressure Data from Interaction Vessel for Deep Pool Gravity Drain Tests CWTI-9 & 10.

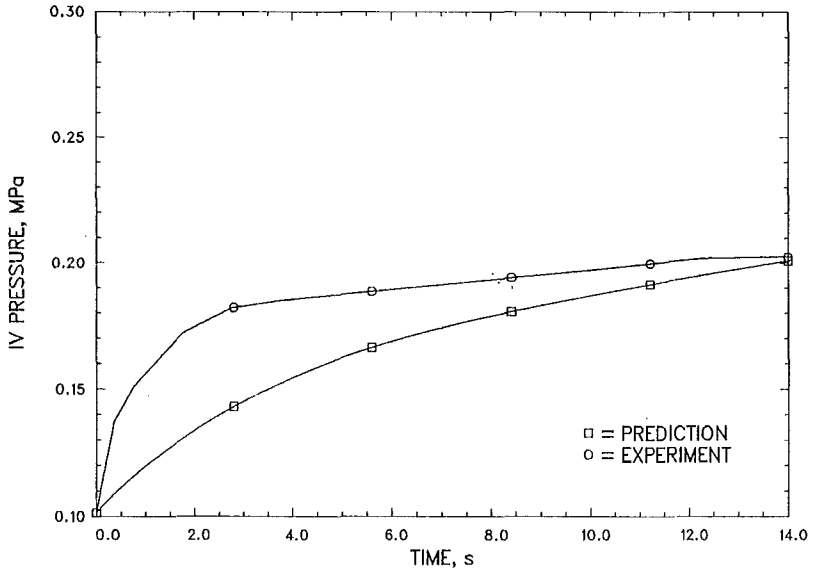

Figure 4. Simulation of CWTI-7: Comparison of Predicted and Measured System Pressure versus Time.

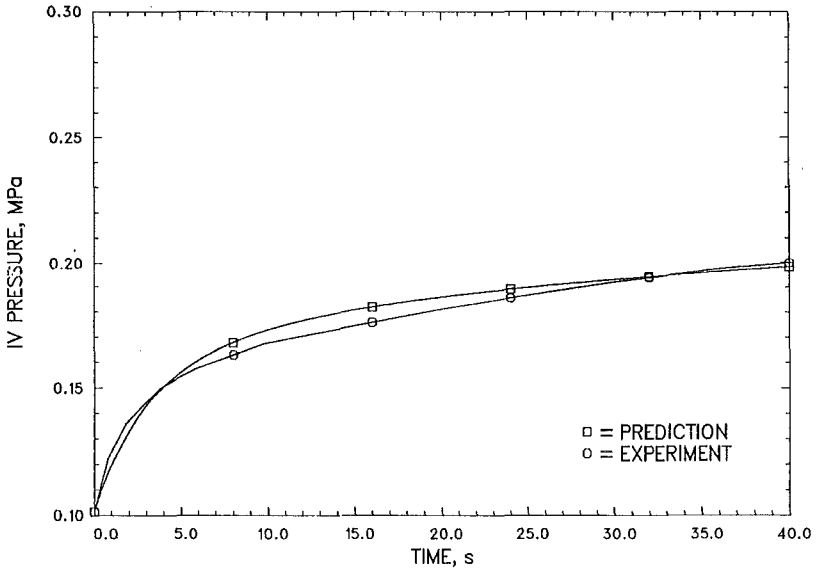

Figure 5. Simulation of CWTI-8: Comparison of Predicted and Measured System Pressure versus Time.

A REFINED MODEL FOR THE COOLABILITY OF CORE DEBRIS WITH FLOW ENTRY FROM THE BOTTOM

T. Schulenberg*, U. Müller

Kernforschungszentrum Karlsruhe
Institut für Reaktorbauelemente
Postfach 3640, 7500 Karlsruhe 1
Federal Republic of Germany

ABSTRACT

A refined model for two-phase flow in particle beds is presented. Compared to earlier models the improved model takes into account the effect of interfacial drag forces between liquid and vapor, which are important in coarse debris beds. The model is based on the momentum equations for separated flow, which are closed by empirical relations for the wall shear stress and the interfacial drag. When the new model is applied to LWR severe accident scenarios an increased dryout heat flux is pedicted for debris beds with flow entry from the bottom driven by a moderate downcomer head.

INTRODUCTION

In the context of a hypothetical severe accident in a light water reactor also debris beds of a coarse particle size are discussed. If the bed is located on a permeable support structure, coolant can enter from the bottom of the bed. Then a convective flow circulating through a surrounding downcomer can enhance the coolability, which was first demonstrated by Hofmann /1/ and Stevens and Trenberth /2/. It can also be derived from pressure drop measurements of Naik and Dhir /3/ and Tung et al. /4/. In order to predict the limit of coolability of such debris, a two-phase flow model has been applied which neglects pressure differences between both phases as well as channeling effects /1/. However, since interfacial drag forces between liquid and vapor may enhance the coolability, this effect has been taken into account in the model of the present work.

The important role of interfacial drag forces was pointed out earlier by Tutu et al. /5/. As a first step for a new model they extended the separated flow model of Lipinski /6/ by including an interfacial drag term, which they derived from bubbly or churn turbulent flow in pipes. However, large discrepancies with respect to their experimental results limited the usefulness of this model. The present work is aimed at refining this model with respect to the particular properties of debris beds.

* Present adress: Dornier System GmbH, Postfach 1360, 7990 Friedrichshafen, FRG

FUNDAMENTAL EQUATIONS

Following Tutu et al. /5/ the balance of momentum for the liquid (index f) and the gas phase (index g), respectively, in a coarse debris bed is given by

$$\frac{\partial p_f}{\partial z} + \rho_f g + \frac{\mu_f}{K K_f} v_f + \frac{\rho_f}{\eta \eta_f} v_f |v_f| - \frac{F_{fg}}{s} = 0, \qquad (1)$$

$$\frac{\partial p_g}{\partial z} + \rho_g g + \frac{\mu_g}{K K_g} v_g + \frac{\rho_g}{\eta \eta_g} v_g |v_g| + \frac{F_{fg}}{1-s} = 0, \qquad (2)$$

where v_f and v_g denote the superficial velocities of the liquid and the gas respectively. As a good approximation for coarse debris beds the pressure p_f in the liquid phase may be assumed to be equal to the pressure p_g in the gas phase. K and η are the permeability and the passability, respectively, for single-phase flow of either component in a saturated porous medium. For uniform spherical particles they are related to the particle diameter d and the porosity ϵ according to Ergun /7/ as

$$K = \frac{d^2}{150} \frac{\epsilon^3}{(1-\epsilon)^2}, \qquad (3)$$

$$\eta = \frac{d}{1.75} \frac{\epsilon^3}{1-\epsilon}. \qquad (4)$$

The relative permeabilities K_f and K_g are functions of the effective saturation s and the shape of the particles. These have been measured in a different context by Brooks and Corey /8/ for various sands. For beds consisting of uniform spherical particles their result can be approximated by

$$K_f = s^3, \qquad (5)$$

$$K_g = (1-s)^3, \qquad (6)$$

Relations for the relative passabilities η_f and η_g have been proposed by Lipinski /6/ and have recently been corrected by Lipinski /9/ on the basis of a theoretical work of Reed /10/. In our investigation the functional dependence of the relative passabilities on the saturation has been determined by measurements.

To model the interfacial drag force F_{fg} the following considerations are made: The force F_{fg} can only be a function of the following four relevant quantities:

- the buoyancy force $(\rho_f - \rho_g) g$,
- the viscous forces in the liquid phase with respect to the relative velocity of the phases $\frac{\mu_f}{K} \left(\frac{v_g}{1-s} - \frac{v_f}{s}\right)$,
- the inertia in the liquid phase with respect to the relative velocity $\frac{\rho_f}{\eta} \left(\frac{v_g}{1-s} - \frac{v_f}{s}\right)^2$,

- the capillary force σ/K.

Viscous forces and inertia of the gas phase are small compared to the forces discussed above and they are therefore neglected. Since indications for an interfacial drag have only been observed in beds of coarse particles /3/ inertia forces, which are dominant in beds of coarse particles, are assumed to be responsible for the momentum transfer between both phases. Capillary forces will separate the flow and thus reduce the momentum transfer. The viscosity of the liquid may increase the momentum transfer in the case of bubbly flow, which is expected to occur at high saturations. At lower saturations viscous forces may stabilize a separated flow and thus reduce the momentum transfer. It is expected that at moderately high saturations both effects due to viscosity compensate. If only the dominant parameters are taken into account, the interfacial drag force F_{fg}, scaled with the buoyancy force, can be modeled such that it depends only on the ratio of inertia to capillary forces, and on the effective saturation. The latter effect is expressed by a function W(s) which has to be determined. We obtain

$$\frac{F_{fg}}{(\rho_f-\rho_g)g} = W(s)\,\frac{\rho_f K}{\eta\,\sigma}\,\left(\frac{v_g}{1-s}-\frac{v_f}{s}\right)^2 . \qquad (7)$$

In agreement with Tutu et al. /5/, F_{fg} is proportional to the square of the relative velocity, but the dependence on capillary forces is stronger in the model proposed by us.

EMPIRICAL CLOSURE EQUATIONS

In order to determine the empirical functions $\eta_f(s)$, $\eta_g(s)$ and W(s), the pressure drop was measured of a vertical two-phase flow of air and water or air and an aqueous solution of 48 % ethanol through a bed of nearly spherical glass beads. The test section is sketched in figure 1. The saturation was determined by the amount of liquid displaced. Liquid and gas mass flow rates were measured separately before the two fluids were supplied through a porous plate at the bottom of the bed. The properties of the beds are listed in table 1. The permeability and the passability were measured with a single-phase flow using liquid only. The effective particle diameter mentioned corresponds to the measured permeability or passability, if it is inserted in equations (3) and (4).

	1st experiment	2nd experiment
mean particle diameter	3 mm	7 mm
porosity	0.378	0.412
permeability	$5.8\ 10^{-9}$ m^2	$4.38\ 10^{-7}$ m^2
passability	$1.24\ 10^{-4}$ m	$3.87\ 10^{-3}$ m
effective particle diameter	2.5 mm	5.7 mm
bed height	1000 mm	1000 mm
bed diameter	110 mm	110 mm
system pressure	1 bar	1 bar
system temperature	20 °C	20°C
residual saturation in water	0.085	0.024
residual saturation in 48 % ethanol	0.068	-

Table 1: Properties of debris beds of the test section

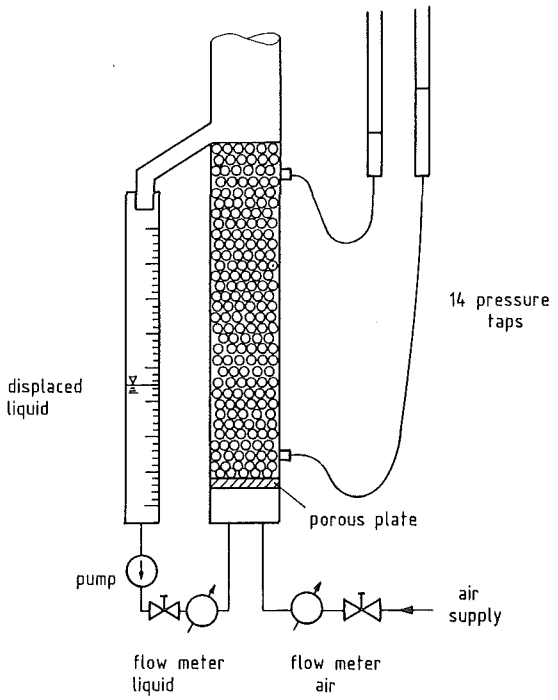

Fig. 1 Sketch of the test section.

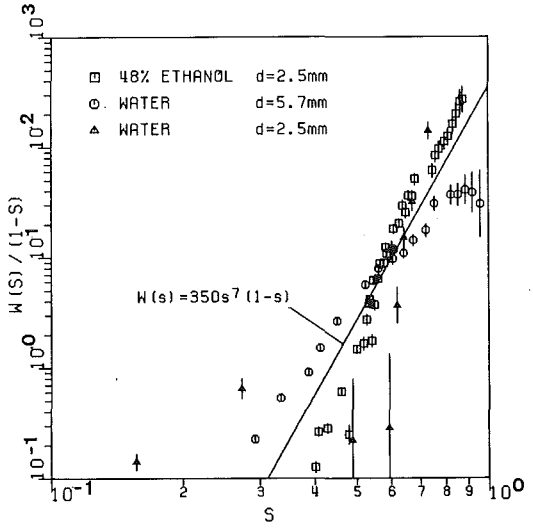

Fig. 2 Dependence of the interfacial drag on the effective saturation.

The empirical function W(s) was determined by evaluating the experiments at a zero liquid flow rate with eqs. (1) and (7). Results are shown in figure 2. Vertical bars denote the experimental error bounds. For moderately large effective saturations of about 0.6 the same function W could be reproduced for different liquids and particle sizes. These facts support the assumptions made in eq. (7). For higher saturations the increased viscosity of 48 % ethanol results in higher values for W, whereas at values below 0.5 an opposite behavior can be noticed. This result is in accordance with the considerations above concerning the influence of viscosity. For all liquids and particle sizes W(s) can be fitted as

$$W(s) = W_o \, s^m (1-s), \qquad (8)$$

where $W_o = 350$ and $m = 7$ can be taken as mean values.

If the relative permeabilities are described by equations (5) and (6), and if the function W is fitted as in equation (8), the relative passabilities η_g and η_f can be determined from equations (1) and (2). Results are shown in figures 3 and 4, respectively. The experimental data can be approximated as

$$\eta_f = s^5,$$
$$\eta_g = (1-s)^6, \quad \text{if } s < 0.68$$
$$\eta_g = 0.1\,(1-s)^4, \quad \text{if } s > 0.68.$$

These relative passabilities are smaller than those which were first assumed by Lipinski /6/, but they agree better with his improved model /9/.

APPLICATION TO LIGHT WATER REACTOR SCENARIOS

If the debris bed, generated during a hypothetical core melt-down accident, has a permeable base the amount of fluid penetration through the bottom into the bed and the maximum heat flux through the top, the so-called dryout heat flux, are functions of the driving downcomer head surrounding the bed. If this downcomer level is similar to the bed height the dryout heat flux will be significantly increased compared to the dryout heat flux of a debris bed on an impermeable, adiabatic plate. In figure 5 this increase of the dryout heat flux is calculated as a function of the downcomer height H_d, which has been scaled with the bed height H_b. Applying our new model the increase is predicted to be higher than that calculated by Lipinski /6/, even if his new model /9/ is applied. This difference is due to the lack of interfacial drag forces in the models of Lipinski. Our new model is supported by an experiment of Hofmann /1/, also plotted in figure 5. This experimental result even exceeds our predicted results.

SUMMARY

The separated flow model proposed by Lipinski /6/ has been extended. By measuring the pressure drop and the saturation in an unheated particle bed empirical correlations for the relative passabilities were obtained. Their values are generally smaller than those predicted by the correlation of Lipinski /6/, but they agree better with his recent assumptions /9/. In addition a simple relation for the interfacial drag has been developed. The relation expresses the dominant influence due to liquid inertia and capillary forces. If the model is applied to light water reactor severe accident scenarios, an increased dryout heat flux is predicted for the case of flow entry from the bottom driven by a moderate downcomer head.

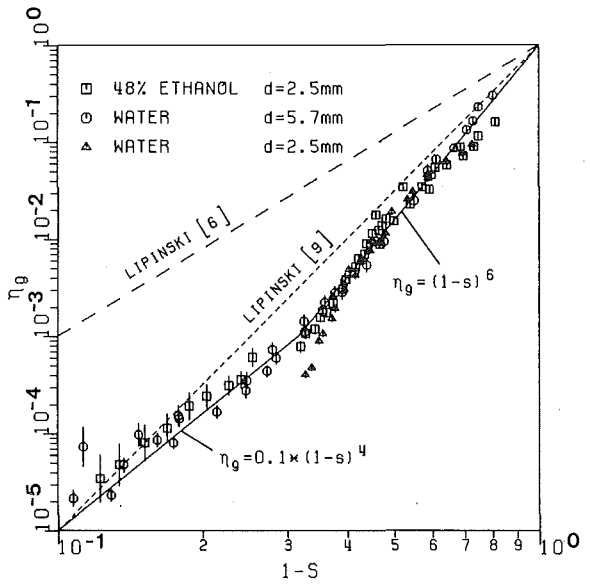

Fig. 3 Relative passability η_g of the gas phase.

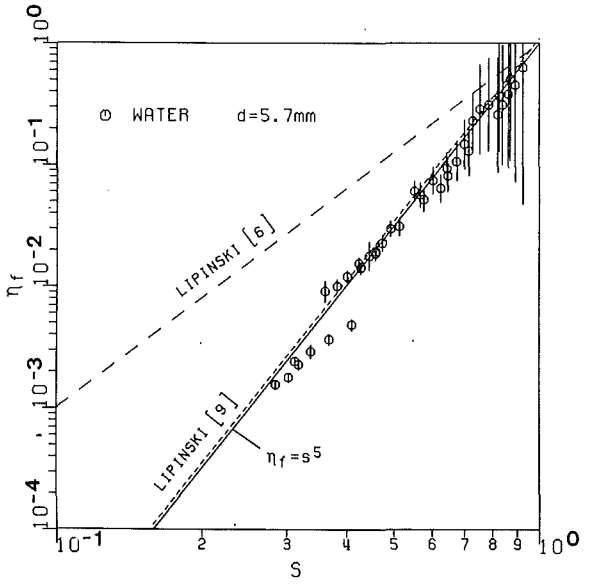

Fig. 4 Relative passability η_f of the liquid phase.

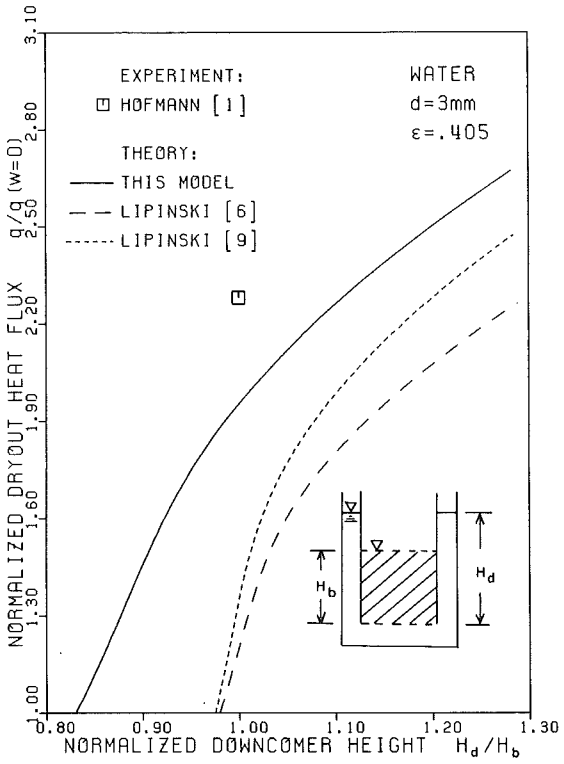

Fig. 5 Increase of the dryout heat flux if liquid is refilled through the bottom of the debris bed.

NOMENCLATURE

d	particle diameter
F_{fg}	interfacial drag
g	acceleration due to gravity
H_d	downcomer height
H_b	bed height
K	permeability
K_f, K_g	relative permeabilities of the liquid and gas, respectively
m	constant
p	pressure
q	dryout heat flux

s	effective saturation
v	superficial velocity
w	mass flux through the bottom of the bed
W	saturation dependent factor of the interfacial drag
W_o	constant
z	vertical coordinate
ε	bed porosity
η	passability
η_f, η_g	relative passabilities of liquid and gas, respectively
ρ	density
μ	viscosity
σ	surface tension

REFERENCES

/1/ G. Hofmann: On the Location and Mechanisms of Dryout in Top-Fed and Bottom-Fed Particulate Beds, Nuclear Technology 65, 36-45 (1984).

/2/ G.F. Stevens, R. Trenberth: Experimental Study of Boiling Heat Transfer and Dryout in Heat Generating Particulate Beds in Water at 1 Bar, Proc. of the Fifth Post Accident Heat Removal Information Exchange Meeting, U. Müller, Cl. Günther (ed.), pp. 108-113, G. Braun, Karlsruhe 1982.

/3/ A.S. Naik, V.K. Dhir: Forced Flow Evaporation Cooling of a Volumetrically Heated Porous Layer, Int. J. Heat Mass Transfer, 25, 541-552 (1982).

/4/ V.X. Tung, V.K. Dhir, D. Squarer: Forced Flow Cooling Studies of Volumetrically Heated Porous Layers, Therm. Hydr. of Nucl. Reactors, Santa Barbara, 876-883 (1983).

/5/ N.K. Tutu, T. Ginsberg, J.C. Chen: Interfacial Drag for Two-phase Flow through High Permeability Porous Beds, 21st National Heat Transfer Conference, Seattle, Washington, July 24-28, 1983.

/6/ R.J. Lipinski: A Model for Boiling and Dryout in Particle Beds, NUREG/CR-2646, SAND 82-0765 (1982).

/7/ A.E. Scheidegger: The Physics of Flow through Porous Media, University of Toronto Press, Toronto (1974).

/8/ R.H. Brooks, A.T. Corey: Properties of Porous Media Affecting Fluid Flow, J. of Irrig. and Drainage Division, Proc. of ASCE, IR2, 61-89 (1966).

/9/ R.J. Lipinski, A Coolability Model for Post-Accident Nuclear Reactor Debris, Nuclear Technology 65, 53-66, 1984.

/10/ A.W. Reed, The Effect of Channeling on the Dryout of Heated Particulate Beds Immersed in a Liquid Pool, Ph.D. Thesis, MIT, Cambridge, Mass., 1982.

RECENT FILM BOILING CALCULATIONS: IMPLICATION ON FUEL-COOLANT INTERACTIONS

B.J. Kim and M.L. Corradini

University of Wisconsin-Madison
Madison, WI 53706, USA

ABSTRACT

A transient film boiling model was developed to study the film boiling dynamics that would occur when a molten spherical fuel droplet is immersed in a coolant. The focus of this study was to investigate the effects of noncondensible gas, coolant temperature, and ambient pressure on film boiling during the initial growth phase. These parameters were found to have the greatest influence on the triggering of the small scale fuel-coolant interactions. The results indicate that the film generally stabilizes with more noncondensible gas present and higher coolant temperatures. Our calculations indicate that small ambient pressurizations cause violent fluctutaion of the film pressure while higher ambient pressures suppress these oscillations. These results are in good agreement with Nelson's experimental data for a single fuel droplet in water.

INTRODUCTION

For an energetic FCI to occur, film boiling between the fuel and coolant is a prerequisite for a coarse fuel-coolant mixture to develop. Only when there is an insulating vapor film is there enough time to mix the hot and cold components without premature rapid heat transfer taking place. Only a few analytical studies have been done to simulate transient vapor film boiling around a hot sphere [1,2]. However, calculations were done up to only 1 ms, which was too short to describe even the initial growth behavior of film; usually it takes longer for the vapor film to grow and enter a quasi-steady state. The purpose of this study is to develop a dynamic model of film growth which can give the initial conditions for the film collapse phase which triggers the FCI; this is usually initiated by an external pressure pulse in the small scale single droplet experiments [3,4].

FORMULATION OF THE MODEL

Our model is of a spherical fuel droplet immersed in a large volume of coolant, Figure 1, which is the characteristic of small scale single droplet experiments. Our basic assumptions are:

1. The fuel-coolant system is spherically symmetric; it implies that the variation of the film thickness is small compared to droplet radius and is observed in the small scale FCI experiments [3,4].
2. All the vapor produced is retained in the film; no vapor generated was detached from the film during the initial film boiling in the experiments.
3. The pressure in the film is spatially uniform; the film around the droplet is very thin and the time elapsing as a pressure disturbance is transmitted across the film is much less than the time involved in

appreciable change in the average film pressure.

4. The vapor and other gases, if any, in the film are considered to be perfect gases; the critical point of the coolant is avoided during the film growth.
5. A small gaseous film initially exists at the surface of the sphere; the initial gaseous film is comprised of both the gas generated at the surface of the drop due to chemical reaction and the gas swept into the coolant as the droplet falls freely through the surrounding gas. In the model, only the gas swept into the coolant is considered.
6. Coolant and fuel liquid are considered to be incompressible; the velocity of the film-coolant interface is far less than the speed of sound.
7. The thermophysical properties are considered to be constant except the latent heat of the coolant and density of air; since the film undergoes severe oscillations during growth, the latent heat of coolant is given as a function of the saturation temperature of the coolant.

Mathematical Formulations

The dynamic film boiling process was modelled by writing a momentum equation for film dynamics and an energy equation for each region of the system (fuel, coolant vapor, and liquid) and linking each region by the appropriate boundary conditions. The integral approach was used in each region for the energy equations where the differential equation was integrated over the region and a temperature profile was assumed.

The momentum equation for film growth is modelled by a general Rayleigh equation [5], where the effect of viscosity and surface tension are included.

$$\frac{dU}{dt} = \frac{1}{R_\delta}\left[\frac{P_f - P_\infty - \frac{2\theta_c}{R_\delta} - \frac{4\mu_c}{R_\delta}U}{\rho_c} - \frac{3}{2}U^2\right] \tag{1}$$

The evaporation or condensation rate is obtained from a simple kinetic theory of gas model under a non-equilibrium condition at the vapor-liquid interface [6].

$$\frac{dM_v}{dt} = 4\pi R_\delta^2 \beta \sqrt{\frac{M}{2\pi G}}\left(\frac{P_{co}}{\sqrt{T_{co}}} - \frac{P_v}{\sqrt{T_{vs}}}\right) \tag{2}$$

where accommodation coefficient was assumed to be 0.04 in this application; separate studies indicate that the effects of accommodation coefficient are negligible.

The velocity of the vapor-liquid interface is then given by

$$\frac{dR_\delta}{dt} = U + \frac{dM_v/dt}{4\pi R_\delta^2 \rho_c} \tag{3}$$

The heat transfer in the fuel droplet is governed by Fourier's conduction equation.

$$\frac{\alpha_h}{r^2}\frac{\partial}{\partial r}\left[r^2 \frac{\partial}{\partial r} T_h(r,t)\right] = \frac{\partial}{\partial t} T_h(r,t) \tag{4}$$

Since the temperature wave may not have penetrated to the center of droplet during the time of interest, the droplet is treated as a semi-infinite mass and integrated from $r=R-\lambda_h$ to $r=R$.

$$\alpha_h \int_{R-\lambda_h(t)}^{R} d\left[r^2 \frac{\partial}{\partial r} T_h(r,t)\right] = \int_{R-\lambda_h(t)}^{R} \frac{\partial}{\partial t} T_h(r,t)\, dr \tag{5}$$

A quadratic temperature profile satisfying the boundary conditions within the thermally active region is assumed as

$$T_h(r,t) = T_{hi} + (T_{ho} - T_{hi})\left(1 - \frac{R-r}{\lambda_h}\right)^2 \tag{6}$$

where boundary conditions satisfied are

$$T_h(R-\lambda_h,t) = T_{hi}(t) \tag{7.1}$$

$$T_h(R,t) = T_{ho}(t) \tag{7.2}$$

$$\left.\frac{\partial T_h(r,t)}{\partial r}\right|_{r = R-\lambda_h(t)} = 0 \tag{7.3}$$

When this temperature profile is substituted into Equation (5), the result is

$$\left[\frac{1}{6} - \frac{1}{6}\left(\frac{\lambda_h}{R}\right) + \frac{1}{20}\left(\frac{\lambda_h}{R}\right)^2\right] \frac{d\lambda_h}{dt} = \frac{\alpha_h}{\lambda_h} + \frac{\lambda_h}{2(T_{hi}-T_{ho})}\left[\frac{1}{3} - \frac{1}{6}\left(\frac{\lambda_h}{R}\right) + \frac{1}{30}\left(\frac{\lambda_h}{R}\right)^2\right] \frac{dT_{ho}}{dt} \tag{8}$$

The energy equation for the coolant is similar to Equation (4) except that a radial convective term is included to account for the movement of the vapor film and the subsequent movement of the liquid.

$$\frac{\partial T_c}{\partial t} + \frac{\partial r}{\partial t} \cdot \frac{\partial T_c}{\partial r} = \frac{\alpha_c}{r^2}\left[\frac{\partial}{\partial r}\left(r^2 \frac{\partial T_c}{\partial r}\right)\right] + K \cdot Q_r'' \tag{9}$$

where the last term in the right hand side is the fraction of radiation energy deposited in the thermally active region of coolant. The radiation energy from the fuel was considered as volumetric energy generation within and without the thermal boundary layer. Constant K is given as a function of the surface temperature of droplet and the thickness of thermal boundary layer in the coolant. Again a parabolic temperature profile is assumed in the liquid thermal boundary layer. Boundary conditions are

$$T_c(R_\delta,t) = T_{co}(t) \tag{10.1}$$

$$T_c(R_\delta + \lambda_c,t) = T_{ci}(t) \tag{10.2}$$

$$\left.\frac{\partial T_c(r,t)}{\partial r}\right|_{r = R_\delta + \lambda_c(t)} = 0 \tag{10.3}$$

Temperature profile in the thermally active region of coolant becomes

$$T_c(r,t) = T_{ci} + (T_{co} - T_{ci})\left(1 - \frac{r - R_\delta}{\lambda_c}\right)^2 \tag{11}$$

By substituting this temperture profile into Equation (9) and integrating over the thermal boundary layer, it becomes

$$\left[\frac{1}{6} + \frac{1}{6}\left(\frac{\lambda_c}{R_\delta}\right) + \frac{1}{20}\left(\frac{\lambda_c}{R_\delta}\right)^2\right]\frac{d\lambda_c}{dt} = \frac{\alpha_c}{\lambda_c} + \frac{1}{2}U + \frac{K R^2 \varepsilon \sigma T_{ho}^4}{2R_\delta^2 \rho_c c_{pc}(T_{co} - T_{ci})}$$

$$- \frac{\lambda_c}{2(T_{co} - T_{ci})}\left[\frac{1}{3} + \frac{1}{6}\left(\frac{\lambda_c}{R_\delta}\right) + \frac{1}{30}\left(\frac{\lambda_c}{R_\delta}\right)^2\right]\frac{dT_{co}}{dt}$$

$$- \left[\frac{1}{2} + \frac{1}{3}\left(\frac{\lambda_c}{R_\delta}\right) + \frac{1}{12}\left(\frac{\lambda_c}{R_\delta}\right)^2\right]\frac{dR_\delta}{dt} \tag{12}$$

Using a lumped parameter energy equation for the vapor film, the energy conservation equation is given as

$$\frac{d}{dt}\left[M_v u_v + M_g u_g\right] = Q_v - P_f \frac{dV}{dt}$$

$$+ 4\pi R_\delta^2 \beta \sqrt{\frac{M}{2\pi G}}\left[\frac{P_{co}}{\sqrt{T_{co}}} h_v(T_{co}, P_{co}) - \frac{P_v}{\sqrt{T_{vs}}} h_v(T_{vs}, P_v)\right] \tag{13}$$

where

$$Q_v = 4\pi R^2 \frac{2k_v}{\delta}(T_{ho} - T_v) - 4\pi R_\delta^2 \frac{2k_v}{\delta}(T_v - T_{co}) \tag{14}$$

$$h_v(T_v, P_v) = C_{pv}(T_v - T_{co}) + h_{fg} + C_{pc}(T_{co} - T_{ci}) \tag{15}$$

u_v and h_v are the specific internal energy and specific enthalpy of vapor. As long as lumped energy equation is used, temperature profile assumed for the vapor film does not affect the general film behavior very much.

Another relation between the rate of change of T_{ho} and λ_h is obtained from the boundary condition at the droplet-vapor interface given as

$$\left[\frac{2k_h}{\lambda_h} + \frac{2k_v}{\delta} + 4\varepsilon\sigma T_{ho}^3\right]\frac{dT_{ho}}{dt} = -\frac{2k_h}{\lambda_h^2}(T_{hi} - T_{ho})\frac{d\lambda_h}{dt}$$

$$+ \frac{2k_v}{\delta^2}(T_{ho} - T_v)\frac{dR_\delta}{dt} + \frac{2k_v}{\delta}\frac{dT_v}{dt} \tag{16}$$

The heat transfer rate in the coolant was determined by choosing the higher transfer rate between conduction and convection. Forced convective heat transfer coefficient is calculated from the correlation for the flow past a

solid sphere [7] and is given by,

$$Nu = 2.0 + 0.6\ Re^{1/2}\ Pr^{1/3} \tag{17}$$

The final equation is obtained from the vapor film-liquid coolant boundary condition given as

$$\left(\frac{2k_v}{\delta} + \frac{2k_c}{\lambda_c}\right)\frac{dT_{co}}{dt} = \frac{2k_v}{\delta}\frac{dT_v}{dt} - \frac{d}{dt}\left[h_{fg}\ \beta\ \sqrt{\frac{M}{2\pi G}}\left(\frac{P_{co}}{\sqrt{T_{co}}} - \frac{P_v}{\sqrt{T_{vs}}}\right)\right]$$

$$+ \frac{2k_v}{\delta^2}(T_v - T_{co})\frac{dR_\delta}{dt} + \frac{2k_c}{\lambda_c^2}(T_{co} - T_{ci})\frac{d\lambda_c}{dt} \tag{18}$$

For a forced convection-dominating heat transfer, the rate of change of λ_c is neglected and the conduction heat transfer coefficient in the coolant is replaced by the forced convection heat transfer coefficient.

The pressure in the vapor film is determined from Dalton's law of partial pressure;

$$P_f = P_v + P_g \tag{19}$$

where vapor is treated as an ideal gas and noncondensible gas is assumed to behave isentropically. The initial noncondensible gas film thickness is considered to be some fraction of the boundary layer thickness of the flow over sphere before it enters the coolant pool and given as

$$\delta_g = C \cdot D \cdot (Re_D)^{-1/2} \tag{20}$$

where the constant C is parametrized and varied from 0.01 to 0.1 in this model.

Equations 1, 2, 3, 8, 12, 13, 16, and 18 constitute a set of non-linear first order differential equations in the eight time-dependent variables R_δ, U, T_v, T_{co}, T_{ho}, λ_h, λ_c, and M_v. A simultaneous solution has been obtained by using one step Runge-Kutta-Merson technique which is a modification of 4th order Runge-Kutta integration [8].

Applications of the Model: Results and Discussions

The model developed has been applied to the growth of a vapor film around a molten iron oxide droplet in water; this fuel-coolant pair was used by Nelson [3,4] in his single droplet FCI experiments. The basic initial conditions are given in Table I. Initially the rapid vaporization results in a pressure rise in the film which accelerates the film-coolant interface outward. However, the outward motion of the interface continues beyond the equilibrium position. Thus the film pressure falls below the ambient pressure leading to deceleration of the interface. The movement of the film-coolant interface is reversed and the film starts to collapse. This cycle of growth and partial collapse repeats with an increase in the film thickness and the amplitude of the film pressure oscillations until it reaches its maximum values. Then the film oscillation decreases, which appears to enter a stable state. Under certain sets of initial conditions (i.e. fuel and coolant temperature, ambient pressure, noncondensible gas film thickness) we observed that the film oscillations do not die away but continue over long time at large amplitude. We have verified that these prolonged oscillations are not numerically based. Therefore, we believe they represent the case where the film is not inherently stable and surface instabilities (e.g. Taylor instabilities) would cause fuel-coolant

liquid contact, film collapse, and triggering of the FCI. This set of conditions is of importance to us because they probably represent the conditions where Nelson found the single fuel droplet tests to be easily triggered. Therefore, we have parametrically investigated the set of initial conditions which Nelson found to be important in affecting the triggering of the FCI in the single droplet tests (i.e. gas entrained, coolant temperature, and ambient pressure). We feel one can explain the change in triggerability due to the film growth dynamics when these initial conditions are varied.

Effect of Intial Noncondensible Gas Film Thickness

The influence of the initial noncondensible gas on the film growth is significant (Figure 2). The oscillations of film were diminished enormously with an increase of the initial noncondensible gas film thickness due to the retardation of initial heat transfer across the film and its damping effect on pressure fluctuation. This result suggests that the occurrence of spontaneous triggering of the single droplet FCI at a lower drop fall height can be explained by a smaller amount of noncondensible gas; i.e. the lower drop fall height reduces the entry Reynolds number and therefore amount of noncondensible gas entrained in the film causing large film and pressure oscillations, film collapse, and FCI triggering.

Effect of Coolant Temperature

Figure 3 shows that the decreasing water subcooling stabilizes film boiling, which is consistent with experimental data [9]. Damped oscillations at lower subcooling is due to the continuous and higher evaporation rate which tends to prevent the pressure in the film falling below the ambient pressure. Thus lower water subcooling makes film collapse more difficult due to these effects on forming a more stable and thicker film around the drop.

At constant water subcooling, the oscillations of the pressure in the film have a smaller amplitude and damps more quickly with higher ambient pressure (Figure 4). Higher ambient pressure suppresses the oscillation of the film and higher water temperature induces easier vaporization leading to the more stable film.

Effect of Ambient Pressure

The duration of film pressure fluctuation becomes shorter as ambient pressure increases as illustrated in Figure 5. Also the time required to reach its maximum film pressure during the film growth also decreases with ambient pressure. The maximum film pressure increases sharply as the ambient pressure increases from 0.1 MPa to 0.2 MPa and then remains almost unchanged as P_∞ increases up to 0.4 MPa. For the further increases in ambient pressure, the peak film pressure generated decreases relatively slowly. In some aspects these film behavior explains why small ambient pressurizations lead to the easier initiation of FCI and shorter interaction time. These effects of ambient pressure are related to the suppression of oscillation and easier vaporization due to lower latent heat of water at higher ambient pressure against the higher subcooling of water.

CONCLUSIONS AND RECOMMENDATIONS

Our conclusion on this study is that a simple model of film boiling dynamics can qualitatiely predict the characteristics of small scale single droplet FCI in terms of film growth and its thickness, film pressure oscillation and its amplitude, and time scale, which are strong functions of evaporation rate throughout the boiling process. The initial noncondensible

gas film thickness and coolant temperature have consistent and predictable effects on film growth by diminishing the oscillation of film pressure. Ambient pressure affects film behavior depending upon the magnitude of pressurization, and results in the most violent pressure oscillation at a certain intermediate ambient pressure. However, the influence of any one parameter on the film boiling can be suppressed or enhanced by varying another parameter; they are closely interrelated to each other.

Once the initial conditions for the collapse phase are obtained, film collapse behavior due to external pressure pulse can be examined. During this phase, film pressure is considered to increase rapidly and closer liquid-liquid contact due to the surface instabilities is very likely. Therefore we are continuing to study film collapse behavior in connection with surface instabilities.

REFERENCES

1. M.S. Kazimi, "Theoretical Studies of Some Aspects of Molten Fuel-Coolant Interactions," PhD Thesis, MIT, Cambridge, May 1973.
2. M.L. Corradini, "Phenomenological Modelling of the Triggering Phase of Small-Scale Steam Explosion Experiments," Nucl. Sci. Eng., 78, 1981, pp 151-170.
3. L.S. Nelson, P.M. Duda, "Steam Explosion Experiments with Single Drops of Iron Oxide Melted with CO_2 Laser," Sandia Laboratories, SAND81-1346, NUREG/CR-2295, September 1981.
4. L.S. Nelson, P.S. Duda, "Steam Explosion Experiments with Single Drops of Iron Oxide Melted with a CO_2 Laser; Part 2. Parametric Studies," Sandia Laboratories, SAND82-1105, NUREG/CR-2718, 1982.
5. Lord Rayleigh, "On the Pressure Developed in a Liquid During the Collapse of a Spherical Cavity," Phil. Mag., 94, 1917.
6. R.W. Schrage, A Theoretical Study of Interphase Mass Transfer, Columbia Univ. Press, NY, 1953.
7. W.H. McAdams, Heat Transmission, 3rd Ed., McGraw-Hill, NY, 1954.
8. G.N. Lance, Numerical Methods for High Speed Computer, Iliffe & Sons, 1960, pp 54-57.
9. S.J. Board, "An Experimental Study of Energy Transfer Process Relevant to Thermal Explosion," Int. J. Heat Mass Transfer, 14, 1971, pp 1631-1641.

NOMENCLATURE

C_p: Specific heat
h: Heat transfer coefficient
k: Thermal conductivity
P: Pressure
R_δ: Film radius
T: Temperature
U: Velocity
α: Thermal diffusivity
γ: Gas Index
ε: Emissivity
λ: Boundary layer thickness
ρ: Density
G: Gas constant
h_{fg}: Latent heat of vaporization
M: Molecular weight
R: Droplet radius
r: Radius
t: Time
V: Volume
β: Accommodation coefficient
δ: Film thickness
θ: Surface tension
μ: Viscosity
σ: Boltzman constant

Subscript

c: Coolant
ci: Coolant bulk
co: Coolant surface
f: Film
g: Gas
h: Molten droplet

hi: Droplet center
v: Vapor

ho: Droplet surface
vs: Vapor surface at film-coolant interface

TABLE I

Parameter Values Used in Application

Droplet radius	1.4 mm
Initial droplet temperature	2233 K
Coolant bulk temperature	300 K
Ambient pressure	0.1 MPa

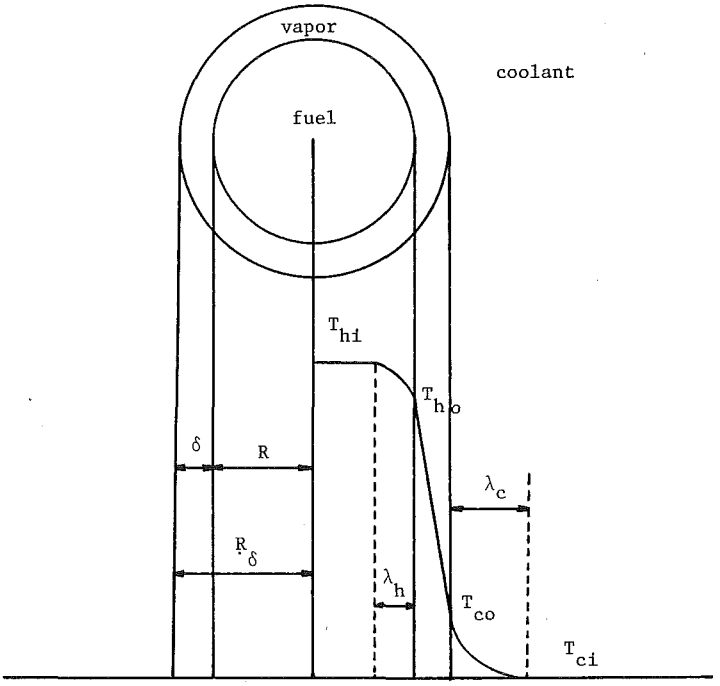

Figure 1. Schematic Diagram of Dynamic Film Growth and Collapse Model

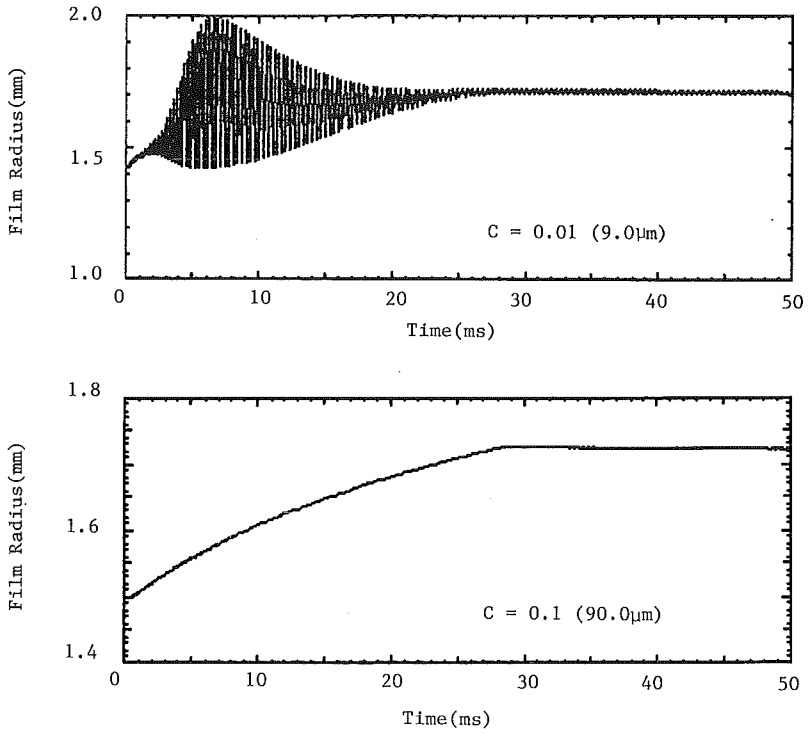

Figure 2. Effect of Initial Gas Film Thickness on Vapor Film Radius-Time History during Film Growth

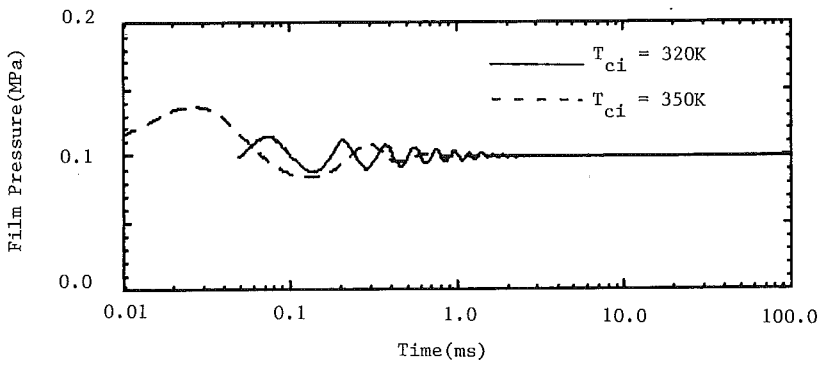

Figure 3. Effect of Water Temperature on Vapor Film Pressure-Time History during Film Growth (Constant Ambient Pressure)

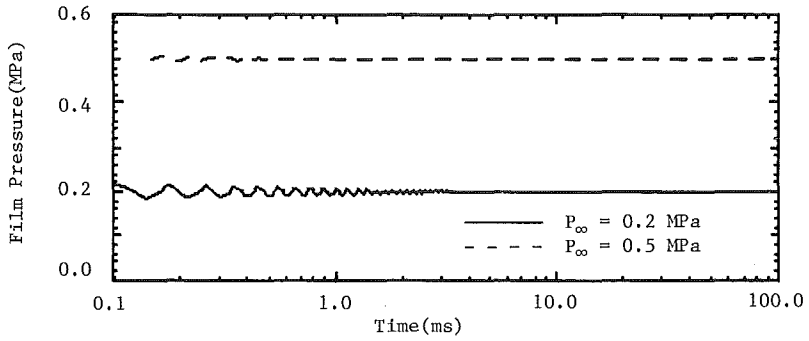

Figure 4. Effect of Water Temperature on Vapor Film Pressure-Time History during Film Growth (Constant Water Subcooling)

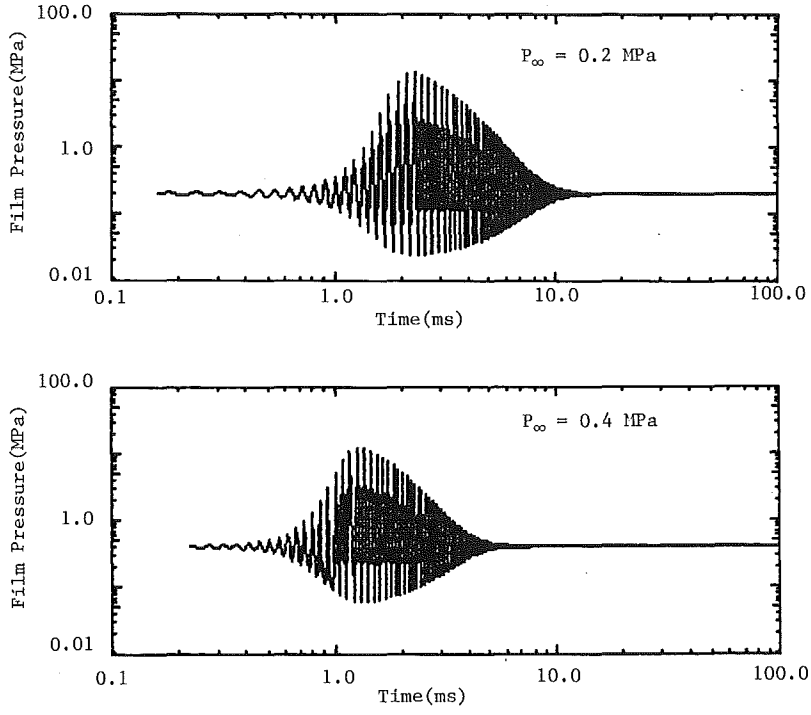

Figure 5. Effect of Ambient Pressure on Vapor Film Pressure-Time History during Film Growth

QUENCH COOLING OF SUPERHEATED DEBRIS BEDS IN CONTAINMENT DURING LWR CORE MELTDOWN ACCIDENTS

T. Ginsberg

Brookhaven National Laboratory
Department of Nuclear Energy
Upton, New York 11973

J. C. Chen

Lehigh University
Department of Chemical Engineering
Bethlehem, Pennsylvania 18015

ABSTRACT

Light water reactor core meltdown accident sequence studies suggest that superheated debris beds may settle on the concrete floor beneath the reactor vessel. A model for the heat transfer processes during quench of superheated debris beds cooled by an overlying pool of water has been presented in a prior paper. This paper discusses the coolability of decay-heated debris beds from the standpoint of their transient quench characteristics. It is shown that even though a debris bed configuration may be coolable from the point of view of steady-state decay heat removal, the quench behavior from an initially elevated temperature may lead to bed melting prior to quench of the debris.

INTRODUCTION

Core meltdown accident sequence studies in light-water reactors suggest that reactor vessel failure would occur as molten core material (corium) thermally attacks the lower vessel dome. In many important sequences water would be available in the region beneath the vessel. As indicated schematically in Fig. 1, melt would be ejected from the reactor vessel upon failure and some degree of corium-water mixing would occur, accompanied by rapid steam generation, and possibly steam explosions. The melt would be partially quenched by the water and would eventually settle to the concrete floor beneath the reactor vessel ("quench" implies reduction of debris temperature to water saturation temperature). Much uncertainty exists as to the state and configuration of the melt at this point. The corium may be in the form of a partially quenched solid debris bed or in the form of a molten pool, which is both attacking the concrete and transferring heat to the overlying coolant layer. The lack of convincing evidence from large scale tests regarding the nature of the debris following arrival to the concrete floor necessitates consideration of the impact of two scenarios on the accident progression: (i) the quench of solid debris beds by overlying pools of water and their coolability, and (ii) the cooling behavior of molten pools which attack the concrete and are cooled by overlying pools of water. This paper considers the quench cooling of superheated debris beds in containment during core melt accidents.

Debris bed quench heat transfer has in the past been computed using a single lumped-parameter energy equation for the debris bed, together with steady-state debris bed heat removal formulations [1]. As a consequence of this assumption, the debris temperature would be predicted to decrease monotonically with time if the bed were coolable based upon steady-state debris coolability considerations [2]. Experimental results suggest that steady

state heat removal concepts can, indeed, be used to predict the debris bed heat removal rate under transient quench conditions [3,4]. The data, however, indicate that the bed quench is a complex, multi-dimensional process that cannot be treated using a single-volume energy equation method of analysis. Models have been developed [5,6] to characterize the transient debris bed quench process. Early results [5] suggested that remelting of the debris is possible under some circumstances, dependent on bed parameters and initial conditions. The objective of this paper is to discuss the coolability of superheated debris beds under conditions of transient quench cooling. Coolability limits are discussed for decay-heated debris beds.

BED QUENCH MODEL AND ITS BASIS

Figure 2 presents a conceptualized view of a superheated debris bed under transient quench conditions. Experimental data [3-5] suggest that packed beds of superheated particles (with no internal heating), which were cooled by water supplied from overlying pools of water, were quenched in a two-stage cooling process. Water initially penetrated the beds during the initial downward frontal progression. This process was irregular and left channels or pockets of dry particles. It was estimated [3] that approximately 30-40% of the initial stored energy was transferred to the water during this time period. During the initial frontal progression, the bed is conceptualized consisting of three regions. The uppermost partially quenched region (as represented in Fig. 2) consists of wetted channels of particles which are quenched to the saturation temperature and channels of unquenched particles close to their initial temperature. A two-phase region follows below. The particles in the wetted channels in this region are not yet quenched to the saturation temperature and the surrounding fluid is composed of steam and water. The bottom-most region is completely dry. No liquid has yet penetrated to the particles in this region. The speed of the downward-progressing cooling front is v_d. A final upward-progressing front, moving at speed v_u, began its traverse subsequent to completion of the downward process. During this final upward frontal progression, the remaining stored energy was removed from the particles and the bed was completely quenched and filled with water. The experimental measurements further show that the steam flow rate was nearly constant for the entire duration of the quench process, inclusive of both frontal progression periods [7]. This is taken to imply that the rate of heat transfer from the bed to the water was limited by processes common to both frontal periods. The steam flow rate data indicate that the bed-to-water heat transfer rate is well-approximated using the Lipinski [2] model for steady-state heat removal from debris beds. The evidence suggests, therefore, that the rate of quenching of a superheated debris bed is limited by the hydrodynamics of countercurrent two-phase flow within the bed.

The above observations were applied to development of a model characterizing the quench of a superheated debris bed of uniform-size particles and uniform porosity with decay heat generation Q'''. The analytical model, presented in an earlier paper [5], considers that a decay-heated, superheated debris bed is cooled in the two-stage quench front propagation process represented schematically in Fig. 2. Coolant is assumed to initially penetrate the bed, leaving dry regions of particles which continue to heat under decay heating. Upon arrival of the downward front to the base of the bed, a final upward-directed front propagates up the bed, removing the remaining stored energy. The bed cooling rate is modeled using the Lipinski formulation [2], modified to account for transient liquid storage within the bed which takes place during the quench process. The quench fronts are assumed to propagate at a rate limited by the rate of liquid supply to the front. Particles in the unquenched region of the

bed are assumed to increase in temperature due to the internal heat source. Steam cooling of the debris and steam superheating are neglected.

The complete formulation of the model includes: (i) a coolant mass conservation equation, (ii) a pair of momentum equations, one for liquid and the other for vapor, (iii) a quench front propagation equation and (iv) an energy equation for the unquenched particles. The reader is referred to the Appendix for details of the model.

CALCULATIONAL RESULTS

Calculations were performed for the range of conditions shown in Table 1. Figures 3 and 4, which are representative results, present the downward- and upward-frontal positions as a function of time for uniform beds of 6-mm particles, of depth 0.5 and 1.0 m, respectively. It was assumed in these calculations that 40% of the bed cross-sectional area is quenched during the downward propagation period. The remaining energy is removed during the upward frontal propagation time. The effect of initial bed temperature is shown on each figure. The temperature rise of the unquenched debris is shown in Fig. 5 for each initial temperature condition. It is noted that since the effect of steam superheating is not considered, the temperature rise rate is simply proportional to the decay-heating rate.

Table 1. Debris Bed Characteristics

Debris Density	8000 kg/m^3
Debris Specific Heat	600 J/kg K
Bed Porosity	0.4
System Pressure	0.5 MPa
Debris Particle Diameter	1-, 3-, 6-, 12-mm
Initial Bed Temperature	1000 K-3000 K
Bed Height	to 1.0 m
Decay Heat Generation (per volume bed)	1.5 MW/m^3
Coolant	Water
f_d	0.4

Referring to Figs. 3 and 4, the quench process begins with the progression of the downward front from the top of the bed, and is represented as the lines with the negative slope. This front reaches the bottom of the bed, at which time the upward-directed front begins its progression, refilling the bed during the process. The quench process is complete when the front reaches the top of the bed. During the entire quench process, the dry unquenched channels are assumed to continue to heat, as represented by the heating curves of Fig. 5. If the quench process is complete before the bed melting temperature is reached, then the bed is considered coolable. In comparing Figs. 3 and 5, for example, one observes that beds of 6-mm particles with 0.5 m height are coolable at initial temperatures up to nearly 3000 K. On the other hand, a comparison of Figs. 4 and 5 suggests that beds of 1-m height are quench coolable only if their initial temperature is relatively low, i.e., in the range of 1000 K.

Figure 6 presents the steady-state debris bed heat flux, based on the Lipinski [2] model as a function of particle size, along with the maximum coolable bed height computed on the basis of the heat flux. These results indicate, based upon steady-state heat removal from uniform debris beds, that beds of

6-mm particles up to 1.5 m in height are coolable from the standpoint of decay heat removal. It is thus clear, based upon the model assumptions characterized above, that debris beds which are coolable based upon steady state, decay heat removal calculations are not necessarily coolable from the standpoint of transient quench heat removal. Bed melting may occur prior to transition to the decay heat removal mode of bed cooling.

Calculations similar to those described above were used to construct debris bed quench coolability maps for the conditions and particle diameters represented in Table 1. As discussed above, a bed was judged to be coolable if the quench process was completed prior to fuel remelting in the unquenched vapor channels. The results of these calculations are shown in Figs. 7-10. The range of bed initial conditions leading to a coolable final state are presented for each of the particle diameters considered.

The results presented in Figs. 7-10 clearly demonstrate that debris quenching imposes an additional constraint on establishment of conditions for bed coolability.

SUMMARY AND CONCLUSIONS

A model for the heat transfer processes during quench of superheated debris beds cooled by an overlying pool of water is used to discuss the coolability of decay-heated beds from the standpoint of their transient quench characteristics. The analytical model is based on observations made during experimental simulations of the quench process using beds of spherical particles of uniform diameter.

Debris bed quench coolability maps were constructed for beds of spherical particles of 1- to 12-mm diameter, up to 1 m in height. Initial bed temperatures in the range 1000 K-3000 K were considered. A bed was considered coolable if the quench process was completed prior to fuel remelting in the unquenched vapor channels. The coolability maps so constructed were compared with coolability considerations based on steady state, decay-heated particle bed analysis. The Lipinski two-phase countercurrent hydrodynamics treatment for the bed heat flux was used in the transient quench formulation (modified to account for the transient liquid bed refill mechanism) and also in the steady-state coolability calculations.

The results demonstrate that debris bed quenching imposes an additional constraint on establishment of conditions for bed coolability. Even though a debris bed configuration may be coolable from the point of view of steady-state decay heat removal, the quench behavior from an initially elevated temperature may lead to bed melting prior to quench of the debris. The question of steady-state, decay heat removal debris coolability is moot unless one can first demonstrate that conditions are favorable for debris quench to the coolant saturation temperature. These results point to the need for more detailed examination of debris bed initial conditions and of the physical mechanisms which lead to bed formation.

The analysis presented here may be overly conservative in that it was postulated that particles in the dry, unquenched regions of the superheated particle bed continue to increase in temperature despite the presence of flowing steam in these regions. The questions of heat transfer from the particles to the steam and superheating of the steam will be addressed in future work.

NOMENCLATURE

c_p	Specific heat of debris
f_d	Fraction of bed quenched during downward front period
h_{fg}	Latent heat of vaporization of water
H	Bed height
Q	Volumetric heat generation rate (per unit bed volume)
t	Time
T_o	Initial bed temperature
T_p	Particle temperature
T_{SAT}	Water saturation temperature
u_{go}	Velocity of steam exiting bed
$u_{\ell o}$	Velocity of liquid entering bed
u_ℓ^*	Velocity of liquid at quench front
v_d	Speed of downward front
v_u	Speed of upward front
z	Axial position in debris bed
z_d^*	Position of downward front
z_u^*	Position of upward front
ε	Bed porosity
ρ_g	Steam density
ρ_ℓ	Liquid density
ρ_p	Particle density

ACKNOWLEDGEMENTS

The authors gratefully acknowledge the help of Ms. Laura Zaharatos in preparation of this manuscript for publication.

This work was performed under the auspices of the U.S. Nuclear Regulatory Commission, Office of Nuclear Regulatory Research.

REFERENCES

[1] Wooton, R. O. and Avci, H. I., "MARCH (Meltdown Accident Response Characteristics) Code Description and User's Manual," Battelle Columbus Laboratories, NUREG/CR-1711 (October 1980).

[2] Lipinski, R. J., "A Review of Debris Coolability Models," Proceedings of International Meeting on Light Water Reactor Severe Accident Evaluation," Cambridge, MA, TS-18.2 (August 1983).

[3] Ginsberg, T. et al., "Transient Core Debris Heat Removal Experiments and Analysis," Proceedings of International Meeting on Thermal Nuclear Reactor Safety, Chicago, IL, NUREG/CR-0027, Vol. 3, p. 996 (August 1982).

[4] Cho, D. H. et al., "Debris Bed Quenching Experiments," Proceedings of International Meeting on Thermal Nuclear Reactor Safety, Chicago, IL, NUREG/CR-0027, Vol. 2, p. 987 (August 1982).

[5] Ginsberg, T. and Chen, J. C., "A Model for Superheated Debris Bed Quench for Severe Accident Containment Calculations," First Proceedings of Nuclear Thermal Hydraulics, 1983 Winter Meeting of the American Nuclear Society, San Francisco, CA (October 1983).

[6] Gorham-Bergeron, E., "An Analytical Model for Predicting Dryout and Quench Behavior in a Volumetrically Heated Particle Bed," Proceedings of International Meeting on Light Water Reactor Severe Accident Evaluation, Cambridge, MA, TS-15.4 (August 1983).

[7] Ginsberg, T. et al., "Measurements and Analysis of Steam Generation Rate from Quenching of Superheated Debris Beds," Trans. Am. Nucl. Soc., 44, 375 (June 1983).

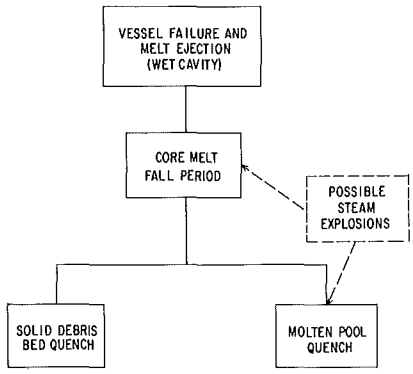

Fig. 1 Accident Progression Following Vessel Faliure

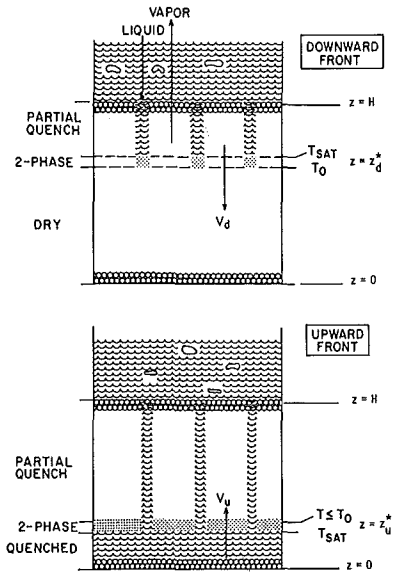

Fig. 2 Schematic of Superheated Debris Bed Quench Front Propagation

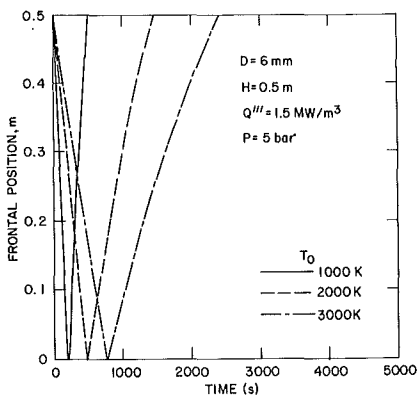

Fig. 3 Quench Front Propagation for 0.5 m Height Bed

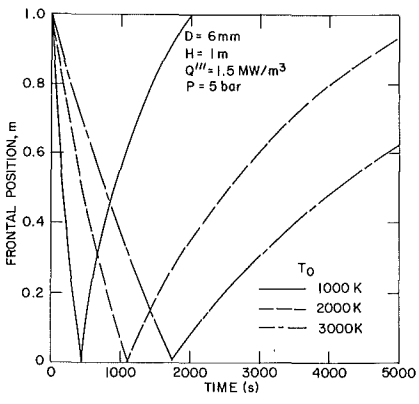

Fig. 4 Quench Front Propagation for 1.0 m Height Bed

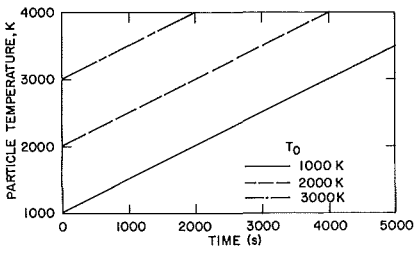

Fig. 5 Particle Temperature Results as Function of Initial Temperature

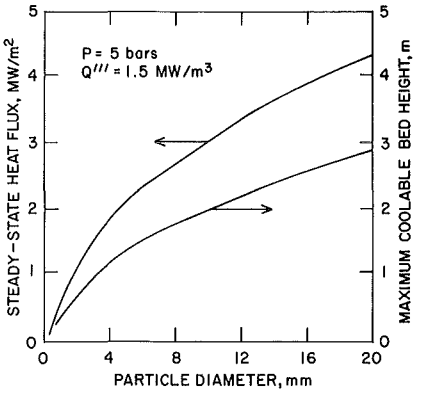

Fig. 6 Steady-State Coolability Map for Beds of Spherical Particles

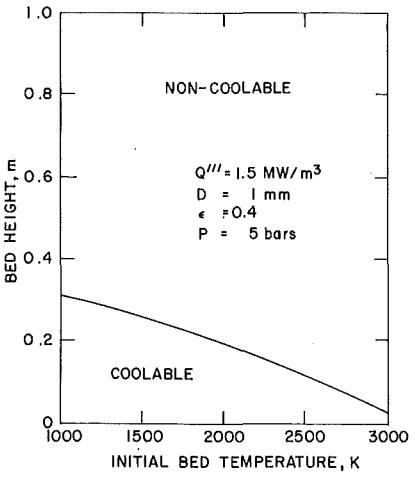

Fig. 7 Quench Coolability Map: D = 1 mm

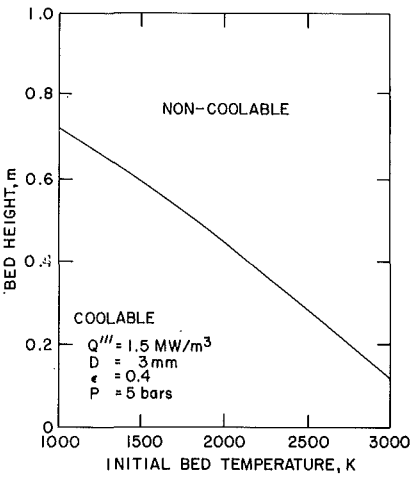

Fig. 8 Quench Coolability Map: D = 3 mm

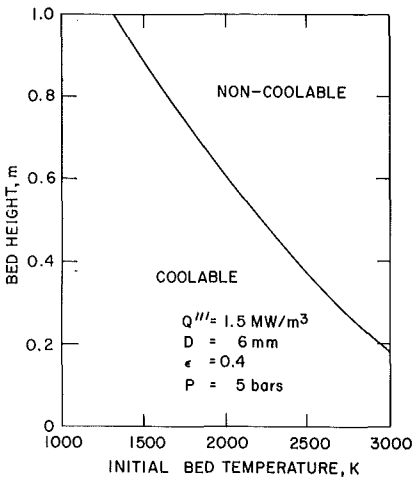

Fig. 9 Quench Coolability Map: D = 6 mm

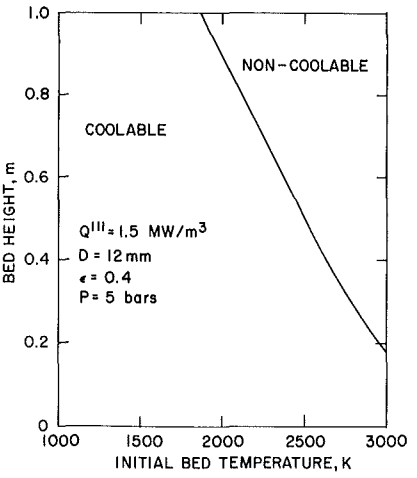

Fig. 10 Quench Coolability Map: D = 12 mm

APPENDIX: FORMULATION OF BASIC EQUATIONS

The analysis presented below focuses on the calculation of the frontal propagation speeds and on the particle temperatures.

It is assumed that the quench front is propagated at a speed limited by the rate of liquid flow to the quench front, and that the thickness of the two-phase front is negligible. The front is assumed located at $z=z^*(t)$, as shown in Fig. 2. During the downward front propagation period

liquid available for vaporization	=	liquid flow to front	-	liquid flow to fill voids in quenched region

An energy balance across the quench front then yields

$$(1-\varepsilon)f_d\rho_p c_p(T_p-T_{SAT})\frac{dz_d^*}{dt} = [\varepsilon f_d u_\ell^*\rho_\ell - \varepsilon f_d v_d \rho_\ell]\, h_{fg} \,. \qquad (1)$$

A mass balance on the liquid phase yields

$$f_d\rho_\ell\varepsilon\frac{du_\ell}{dz} = -\frac{Q''' f_d}{h_{fg}} \,, \qquad (2)$$

which when integrated from z^* to H yields

$$u_\ell^* = u_{\ell o} - \frac{Q'''(H-z_d^*)}{\rho_\ell h_{fg}\varepsilon} \,. \qquad (3)$$

Combining Eqs. (1) and (3), with $v_d = dz_d/dt$ gives

$$\frac{dz_d^*}{dt} = \frac{(1-\varepsilon)\rho_\ell h_{fg}}{(1-\varepsilon)\rho_p c_p \Delta T + \varepsilon\rho_\ell h_{fg}} \times \left[u_{\ell o} - \frac{Q'''(H-z_d^*)}{h_{fg}\rho_\ell\varepsilon}\right] \,, \qquad (4)$$

where $\Delta T = T_p - T_{SAT}$.

A similar set of equations can be written for the time period of the upward-progressing front. During this time period, liquid supplied from the pool is used to remove decay heat from the debris which is already quenched, including those for which $z < z_u^*$. The resulting frontal propagation equation is

$$\frac{dz_u^*}{dt} = \frac{\varepsilon f_d \rho_\ell u_\ell^* h_{fg} - Q''' z_u^*}{(1-\varepsilon)(1-f_d)\rho_p c_p \Delta T + \varepsilon(1-f_d)\rho_\ell h_{fg}} \,. \qquad (5)$$

The energy equation for the unquenched particles is

$$\rho_p c_p (1-\varepsilon) \frac{dT_p}{dt} = Q''' \quad . \tag{6}$$

while for the quenched particles $T_p = T_{SAT}$. The effect of steam cooling has been neglected.

The overall coolant conservation equations are

$$\begin{aligned} u_{\ell o} f_d \rho_\ell + u_{go}(1-f_d)\rho_g &= f_d v_d(\rho_\ell - \rho_g) \qquad \text{down-front} \\ &= (1-f_d)v_u(\rho_\ell - \rho_g) \qquad \text{up-front} \end{aligned} \tag{7}$$

where $u_{\ell o}$ and u_{go} are the liquid and vapor velocities at the top of the bed.

The above set of equations can be solved once u_{go} and $u_{\ell o}$ are related. This is accomplished by assuming, as discussed above, that the heat transfer from the debris bed to water is limited by countercurrent two-phase flow conditions near the top of the bed. The Lipinski model supplies the additional required relationship between $u_{\ell o}$ and u_{go}.

Equations (4)-(7), together with the formulations for the bed heat removal, were solved simultaneously using Gear's method of integration.

IMPROVEMENTS TO CORE-CONCRETE INTERACTION MODELS

B.D.Turland and N.J.Brealey

UKAEA,Culham Laboratory
Abingdon,Oxon OX14 3DB,England

ABSTRACT

Current computer codes for the interaction of core debris with concrete concentrate on the high temperature phase of the interaction and are not designed for prediction of the long-term behaviour when conduction into the concrete becomes important. This paper describes models of various levels of complexity for thermal penetration into concrete. A simple model of thermal penetration is included in substantially improved version of the INTER code; this is compared with an alternative version which uses isotherm migration routines for conduction. A code, CONIMM, that uses fully two-dimensional isotherm migration routines and includes a simple model for water release is also described. If coupled with a 'pool' model, CONIMM would have the capability of calculating the long-term thermal penetration.

1.INTRODUCTION

The most widely available code for modelling the interaction of core debris with concrete is the INTER code originally written by Murfin of Sandia Laboratories [1] and subsequently incorporated into the MARCH code [2]. The INTER code was written prior to much of the experimental work on core-concrete interactions and so, as Murfin noted "The model presented is to some extent based on conjecture... Because of the number of assumptions and estimates, it should not be supposed that the model can "predict" such critical variables as the time of containment melt-through. The model can best be utilized to determine the general effect of changing parameters..." [1]. The Sandia assessment of the use of INTER in MARCH [3] supported this interpretation of the code.

Rather than develop INTER in the light of more recent experimental information, effort has generally gone into the development of new codes such as WECHSL[4] and CORCON [5]; both these latter codes allow more flexibility in the pool shape than is available in INTER, contain more detailed chemistry, and use more physically based models for heat transfer in liquid layers. The published versions of these newer codes concentrate on detailed modelling of the high temperature phase of the interaction during which the debris itself and the concrete decomposition products are molten. The use of such models is limited because (i) core debris need not be molten at the start of the

interaction, and (ii) solidification of constituents of the debris may occur early in the interaction. Furthermore neither the published versions of WECHSL or CORCON contain models for heat loss by conduction into the concrete (i.e. heat loss in excess of that required to supply the sensible heat of ablated concrete); whilst this is probably not significant during the high temperature phase of the interaction it would determine (a) the initial gas release if the concrete is heated by a dried-out debris bed and (b) the long-term growth of the interaction region, as it provides a significant heat sink over periods of days and months. The modelling of concrete ablation is discussed in detail in section 2.

As noted above the model formulations in INTER are generally less mechanistic than those of the later codes; however the original code does allow for solidified layers of debris, and for thermal penetration into the concrete. In section 2.2 a revised expression for the thermal penetration distance is given. This, and other changes, have been incorporated into a revised version of INTER, which includes the bulk of the original coding, to give an improved fast-running code that is capable of modelling all phases of the core-concrete interaction. This new version INTER is described in section 3.

The more detailed treatment of ablation and conduction into concrete described in section 2.4 has not, as yet, been incorporated into any of the current codes, but has been programmed as a separate code CONIMM, which is described in section 4.

2.MODELLING OF CONCRETE ABLATION

2.1.Basic equations.

Experiments [6] indicate that the attack of debris on concrete is primarily a thermal process: heat from the debris raises the concrete to a temperature at which it becomes generally molten. Although concrete actually melts over a range of temperatures, this process may be approximated by the relationship:

$$\rho L \underset{\sim}{u} = \Phi + k(\partial T/\partial \zeta)\Big|_{\zeta = 0+\varepsilon;\ \varepsilon \to 0} \qquad (1)$$

where $\underset{\sim}{u}$ is the normal velocity of the ablation front, and ζ is a local normal co-ordinate into the concrete from its interface with the debris region, Φ is the (position dependent) heat flux on the debris side of the interface; ρ, L and k are the concrete density, latent heat of fusion and conductivity at the melting point (T_m) respectively.

Within the concrete heat is transferred by (i) conduction, (ii) the movements of steam and other gases produced by the decomposition of the concrete, and (iii) the movement of free water under the influence of the pressures set up by the gas flow. The Sandia code USINT[7] models these processes in one-dimension, but does not include an ablation front. Simple scaling arguments indicate that when a steady rate of ablation is assumed, the ratio of heat transferred by the steam and gas flow is only a fraction of that carried by conduction; the expulsion of water depends strongly on the boundary conditions and is expected to lead to only small effects for a large concrete block. Thus for simplicity only conduction in the concrete is considered below (the coefficient of conduction may be modified to take into account other processes), i.e.

$$\rho c(\partial T/\partial t) = \underset{\sim}{\nabla}.(k\underset{\sim}{\nabla}T) \qquad (2)$$

where c (the specific heat) and k may depend on temperature.

2.2.Simple approximations.

Consider a locally 1-D approximation to the melt-front; equation (1)

applies with $T = T_m$ at $\zeta = 0$. On transforming to the frame moving with the front, equation (2) becomes

$$\rho c\left(\frac{\partial T}{\partial t} - u\frac{\partial T}{\partial \zeta}\right) = \frac{\partial}{\partial \zeta}\left(k\frac{\partial T}{\partial \zeta}\right), \qquad (3)$$

at large values of ζ, $T \to T_a$ (the ambient concrete temperature). An approximate solution for the temperature profile is

$$T^* = T_a + (T_m - T_a)\exp(-\zeta/\delta), \qquad (4)$$

where δ (the thermal penetration distance) is a function of time. The residual of equation (3) with the approximation (4) is constructed:

$$R(\zeta) = \rho c\left(\partial T^*/\partial t - u\partial T^*/\partial \zeta\right) - \partial\left(k\left(\partial T^*/\partial \zeta\right)\right)/\partial \zeta. \qquad (5)$$

The weighted residual method[e.g.8] may now be used to find an approximate equation for δ; i.e.

$$\int_0^\infty R(\zeta).\, w(\zeta)\delta\zeta = 0 \qquad (6)$$

where $w(\zeta)$ is the weighting function. There are two obvious choices for $w(\zeta)$ - uniform weighting, and, for Galerkin's method: $\exp(-\zeta/\delta)$. A general form covering these two cases is

$$w_n(\zeta) = \exp(-n\zeta/\delta). \qquad (7)$$

For constant thermophysical properties, equations (4)-(7) imply

$$\frac{d\delta}{dt} = (n+1)\left[\frac{k}{\rho c\delta} - u\right] \qquad (8)$$

and substituting (4) into (1), assuming $T = T^*$ implies

$$\rho L u = \Phi - k(T_m - T_a)/\delta. \qquad (9)$$

Thus equations (8) and (9) give a simple approximation that allows for thermal penetration variation during concrete ablation. Note that (i) the approximation is dependent on the user's choice of n, and (ii) it gives exact answers in the case of ablation that occurs at a uniform rate.

2.3. Introduction to the isotherm migration method (IMM)-1D applications.

Once ablation has started the problem is characterized by a relatively thin front over which the concrete temperature falls from its melting point to close to ambient temperature; this front may move several metres as the interaction proceeds, and eventually broaden. A suitable numerical method for such problems is the isotherm migration method (IMM) in which the position of isotherms are treated as the dependent variables [9] - this ensures that there is always adequate meshing in the region of the front.

For one-dimensional problems it can be shown that equation (2) transforms to

$$\rho c\frac{\partial}{\partial t}\left(\frac{r^N}{N}\right) = -\frac{\partial}{\partial T}\left(\frac{kr^{N-1}}{\partial r/\partial T}\right) \qquad (10)$$

where r(T,t) is the 'radius' of the isotherm of temperature T at time t; N=1 for cartesian co-ordinates, 2 for cylindrical co-ordinates, and 3 for spherical polar co-ordinates. The equation

$$\rho L\left(\frac{\partial r}{\partial t}\right)_{T=T_m} = \Phi + \left.\frac{k}{\partial r/\partial T}\right|_{T=T_m} \qquad (11)$$

applies at the melting front. Turland [10] has shown that equations (10) and (11) when discretized in conservation form give very good results for test problems involving thermal fronts; note that (10) and (11) are valid when c and k are functions of temperature.

2.4. The 2-D application of the IMM.

In the previous section the radial co-ordinate r was treated as a function of temperature and time; to perform calculations for axisymmetric melt-pools it is necessary to introduce a new spatial variable. It is convenient to take an origin of co-ordinates and construct a set of radial lines (determined by the angle variable θ) - the equations are now expressed in the form of measuring the radial position of the intercepts of the lines and the isotherms (i.e. we have $r \equiv r(\theta,T,t)$). If θ = 0 on the axis of symmetry then equation (2) transforms to [10]

$$\frac{\sin\theta}{3}.\rho c\,\frac{\partial}{\partial t}\left(r^3\right) = -\frac{\partial}{\partial T}\left(\frac{kr^2\sin\theta}{r_T}\left(1+\frac{r_\theta^2}{r^2}\right)\right) + \frac{\partial}{\partial\theta}\left(k\sin\theta.r_\theta\right) \qquad (12)$$

where r_x denotes the partial derivative of r with respect to X. The condition on the ablation front (equation (1)) becomes

$$L\left(\frac{\partial r}{\partial t}\right)_{T=T_m} = \Phi\left(1+\frac{r_\theta^2}{r^2}\right)^{1/2} + \frac{k}{r_T}\left(1+\frac{r_\theta^2}{r^2}\right)\Big|_{T=T_m} \qquad (13)$$

Equations (12) and (13) may be discretized in a conservative form in the space of the independent variables (θ and T) (see section 4). The performance of the method on a number of test problems is discussed in [11].

3.A REVISED VERSION OF INTER

3.1.Principal modifications.

The principal modifications that have been made to the INTER code, as incorporated into MARCH1.0, are as follows:

(i) A detailed check of the heat and mass balances for each layer, and between the upper layer and overlying water (if present) revealed a number of coding errors. The most significant of these affected only those parts of the sequence where metal overlay oxide, and led to conservative predictions. The code has been corrected.

(ii) The original code preferentially reacted CO_2 with Fe, and Zr with H_2O. For the first 1000 seconds it also reacted FeO with Zr, leading, in effect, to preferential oxidation of Zr. The new code allows the FeO reaction with Zr to proceed at all times thus ensuring that the effect of the modelling is the preferential oxidation of Zr.

(iii) If debris has not been quenched earlier in the accident the new code assumes that heat transfer to any overlying water is by film boiling - the new model also allows for crust formation at the top of the debris.

(iv) The original code made undocumented changes to the user's input values of heat transfer coefficient from debris layers to the concrete - the new code only uses the input values.

(v) The original code had uniform thermal boundary layers thicknesses in the upward, downward and lateral directions for each layer - the new code allows the user to specify enhanced upward and/or lateral heat transfer when debris is molten.

(vi) Substantial improvements have been made to the models of concrete ablation, thermal penetration and water release (see section 3.2).

(vii) The decomposition temperature of the concrete has been raised to the concrete melting point from the decomposition temperature of calcium hydroxide.

Modifications (iv) and (v) were made to improve the use of INTER as a code for scoping studies - the user must make external judgements on these important heat transfer quantities.

3.2. Thermal penetration model and water release.

The shape of the debris (including ablated concrete) region in INTER is characterized by two dimensions - R_b the radius of curvature of a bottom section, which is a section of a sphere, and r_c the radius of an overlying cylindrical section (see Fig.1). The downwards progression (z) and the

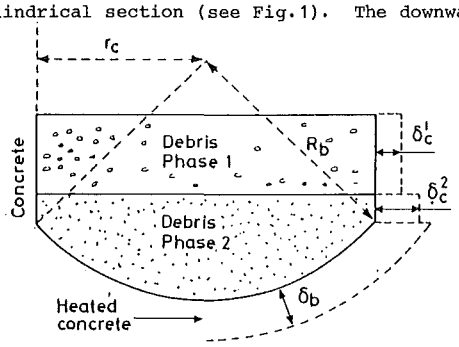

FIG 1: Pool geometry assumed in INTER - the different penetration distances are also shown.

increase in r_c are calculated separately. The original code effectively used the following relations:

$$\dot{\delta} = \frac{0.72k}{\rho c \delta} - \bar{u} \qquad (14)$$

$$\rho L \dot{z} = \Phi_b - k(T_m - T_a)/\delta \qquad (15)$$

$$\rho L \dot{r}_c = \Phi_c - k(T_m - T_a)/\delta \qquad (16)$$

and $$\bar{u} = (\dot{z}A_b + \dot{r}_c A_c)/(A_b + A_c) \qquad (17)$$

where a dot denotes differentiation with respect to time. A denotes surface area, and suffices b and c refer to the base and cylindrical sections respectively.

For a uniform rate of ablation these relationships do not conserve heat, and also exhibit an undesirable coupling between the heat transfer downwards and that sidewards through the use of the common penetration distance δ.

The new code uses separate penetration distances δ_b, δ_c^o and δ_c^m for the different directions (superscripts o and m denote the concrete in contact with oxide and metal respectively). These penetration distances are updated using equation(8)where $u = \dot{z}$, $\dot{r}_c^o$ and $\dot{r}_c^m$ (for pool geometry these latter quantities

are still averaged). To maintain linear stability in the case of a uniform rate of ablation it is found that the timestep must satisfy

$$\Delta t < \frac{2\delta}{(n+1)u} \cdot \frac{L}{L+c(T_m-T_a)} \qquad (18)$$

This criterion is used where δ and u are current values.

The exponential temperature profile assumed here (equation 4) may be used to calculate water release from the concrete. The current version of the code assumes that free water is liberated at its boiling point T_w; thus the rate of progression of the dry region $\dot{s}$ in the concrete is given by

$$\dot{s} = u + \dot{\delta} \ln[(T_m - T_a)/(T_w - T_a)] \qquad (19)$$

If the concrete is not ablating, T_m is replaced by the current concrete interface temperature. Other decomposition processes could be represented by similar expressions.

A version of INTER has also been constructed that uses 1-D isotherm migration routines (see section 2.3) to evaluate separately the three thermal penetration distances. Whilst all penetration distances are less than 0•02m the approximation (8) is still used; on switching to the IMM an exponential temperature profile is discretized. Six isotherms are used in all cases.

3.3.Example calculations.

Because of the unverified nature of some of the conjectures in the INTER model, and the use of arbitrary values for some of the user supplied parameters, the calculations reported in this section should not be regarded as predictions, rather they are part of a wider range of parametric studies. The calculations reported here illustrate the concrete ablation model.

The debris is assumed to consist of 45 tonnes of UO_2 with 11 tonnes of Zr (of which 50% is oxidized at the start of the interaction) and 10 tonnes of steel. The concrete is assumed to consist of a basaltic aggregate with composition by weight: 3% $CaCO_3$, 10% $Ca(OH)_2$, 4% water, 55% silica and 28% other oxides (treated as Al_2O_3). It is assumed to decompose at 1600K. For conservation of heat it is necessary to choose the concrete specific heat to be consistent with values given in the INTER subroutine ENTH - for the above data a value of 1390 J $Kg^{-1}K^{-1}$ is appropriate. The initial radius of the debris pool is 3•5m, and it is assumed to have an almost flat bottom. The interaction is assumed to start 3 hours after the beginning of an (unspecified) accident sequence when the decay heat produced in the debris is 15MW (30% in the metallic phase). The heat transfer coefficient at the interface between the debris and concrete is set to 500$Wm^{-2}K^{-1}$, and both lateral and upward heat transfer in a molten layer are enhanced by a factor of three compared with the original code. There is no overlying water.

Results have been calculated using the simple approximations for thermal penetration with n = 0 and n = 1 (see equations (7) and (8)), and using the version of INTER that incorporates the IMM routines (n = 0 initially). Runs were terminated at 40 hours, used about 4000 timesteps and took a few minutes CPU on a medium-sized computer (PRIME-9950). A comparison of the three runs is given in Table I; it is seen that there are no major differences. The IMM run gives support for use of the simpler thermal penetration model.

PROPERTY		20 mins		1 hour	
		n=0	n=1	n=0	n=1
Metal temperature	K	1801	1801	1742	1748
Oxide temperature	K	2128	2162	1853	1857
Depth eroded	M	0.121	0.113	0.386	0.380
Width eroded	M	0.263	0.256	0.482	0.481
Mass concrete eroded	te	16.2	15.1	52.2	51.5
Water released	te	1.1	1.2	3.4	3.5

PROPERTY		5 hours			40 hours		
		n=0	n=1	IMM	n=0	n=1	IMM
Metal temperature	K	1619	1620	1618	1613	1613	1613
Oxide temperature	K	1735	1738	1735	1706	1708	1703
Depth eroded	m	0.548	0.561	0.546	1.050	1.093	1.038
Width eroded	m	0.739	0.750	0.751	1.443	1.479	1.480
Mass conc. eroded	te	83.1	85.3	83.4	204	219	209
Water released	te	6.0	6.4	5.9	16.2	18.7	16.0
δ_w^m	m	0.034	0.036	0.034	0.137	0.142	0.138
δ_w^o	m	0.031	0.032	0.032	0.109	0.112	0.114
δ_b	m	0.045	0.047	0.045	0.137	0.142	0.139

TABLE I: Dependence of major parameters in INTER runs on thermal penetration models; n refers to exponent in equation 7 and IMM indicates isotherm migration routines were used. For times less than 1 hr the penetration distance is so small that the IMM routines were not used by the code (see text). Note - the number of significant figures in this table are given solely to allow an adequate comparison of the numerical methods - they do not represent the accuracy of prediction with the code.

In the calculations the oxide melts after 2•5 minutes, and becomes the lighter phase after 14 minutes; the zircaloy is totally oxidized after 54 minutes, but the iron is not completely oxidized at the end of the run. After 40 hours a total of 1•17 TJ of decay heat has been generated in the pool (compared with 0•04 TJ from chemical reactions); 0•56 TJ has been transferred to the concrete and 0•84 TJ radiated from the upper surface. Fig.2 shows the pool growth as a function of time, whilst fig.3 shows the thermal penetration distances.

4.THE 'CONIMM' CODE FOR CONCRETE ABLATION

4.1 Calculation of pool growth and thermal penetration.

The CONIMM code uses the 2-D version of the isotherm migration method described in section 2•4. A uniform mesh in (T,θ) (i.e.temperature, angle) space is used for the discretization; this divides the (T,θ) plane into cells with a mesh point at the centre of each cell. There are additional mesh points located at the melt-front ($T=T_m$). A zero flux condition is used at the ambient isotherm. An explicit numerical scheme has previously been used

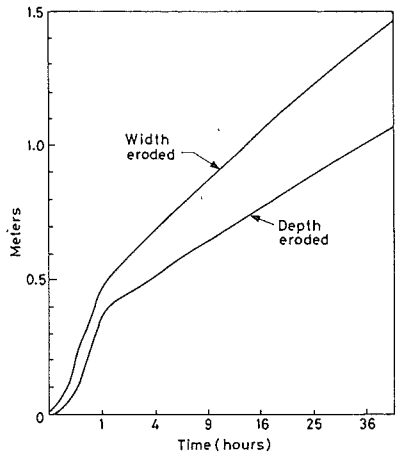

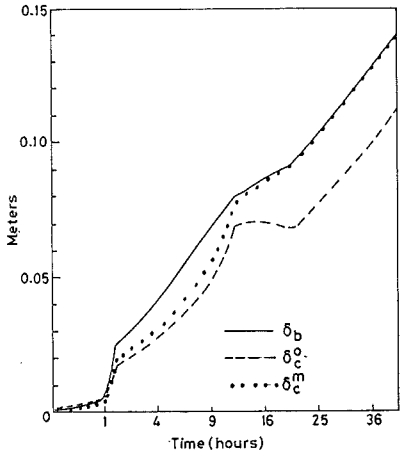

FIGS 2 and 3: Results of example calculations: Fig 2 - pool growth, Fig 3 - thermal penetration distances.

successfully [11]. The explicit scheme is fully conservative for the quantity $\int\int \rho c r^3 . \sin\theta . dT . d\theta$, which is related to the heat content of the thermal front; however there are constraints on the timestep which become severe when the isotherms are closely spaced:

$$\Delta t < \rho c (\Delta r)^2 / 2k \quad \text{and} \quad \Delta t < \rho c (r\Delta\theta)^2 / 2k \qquad (20)$$

in all cells where Δr is the radial distance between mesh points.

Implicit methods need not be subject to these constraints. Even for constant thermal properties the transformed equations (12 and 13) are non-linear, so to construct an implicit scheme it is necessary to linearize. This is achieved in CONIMM by using predicted values in the evaluation of the coefficients of the highest derivatives, which enables the use of the alternating direction implicit method [12]. Rather than iterate at each timestep (which would be possible), the timestep is chosen to ensure that the actual movement of the isotherms and the predicted movement do not differ by significant amounts. This method destroys exact conservation, and so CONIMM has been tested against the original explicit coding. Using a coarse mesh of 6 isotherms and 6 angles (which is known to give reasonable accuracy in the explicit calculations), calculations were performed for the growth of a melt-pool in a basaltic concrete. Heat input was typical of the decay heat from the whole core of a 1•3GW(e) reactor, and the horizontal heat flux was assumed to be twice that downwards (for other angles an interpolation function was used). The calculations were started when the major radius of the pool was 2•48m (minor radius ≡ depth 1•24m) at time 4000s, and were continued up to 2×10^7s (231 days). It was found that the predictions of the movement of the melt-front and all the isotherms by the CONIMM implicit coding agreed with the explicit coding to better than 1% (at 2×10^7s the predicted pool radius is 10•5m, and the thermal front is typically 3m thick). Although CONIMM took less than one-third the number of timesteps required for the explicit scheme, it was only 20% faster because of the increased computation at each timestep; savings would be more significant on a finer mesh. (The CONIMM run used 5104 timesteps and took 327s cpu on a PRIME750 computer).

4.2. Calculation of total water release.

When concrete is heated, water is released at temperatures well below the concrete's melting point. The release of water is a complex process; experimental data show that it occurs over a broad temperature range rather than at a set of well-defined temperatures [13]. Release processes may be modified by the transport of steam through the concrete matrix.

For CONIMM it is assumed that at any given temperature there is an equilibrium saturation of free and bound water in the concrete. Assuming that this equilibrium saturation is reached on a short time-scale, the calculation of water release is essentially one of integration.

The calculation of water release from an interior cell (in (T,θ) space) is straightforward; the volume of the cell is calculated and it is all assumed at the temperature of the central mesh-point. The same assumption cannot be made for the exterior mesh cells as they have infinite volume; it is necessary to consider a temperature profile in this region. The choice of profile is arbitrary, but it should be consistent with the total heat content (above ambient) in the cell. The CONIMM model uses this constraint, and fits the profile to the location of the $T = T_a + \Delta T$ isotherm, the position of which is estimated by quadratic interpolation through nodes with temperature $T_a + (2m + 1)\,\Delta T/2$; $m = 0$, 1 and 2. A quadratic dependence of water release on temperature is assumed within the exterior region; there is no release at ambient temperature. The water loss associated with the linear term in this dependency does not depend on the choice of temperature profile because the integral involved is the same form as the integral for heat content. For CONIMM the temperature profile is assumed to be a decaying exponential in the radial direction (it has been found that a profile with an additional inverse dependence on radius gives very similar results).

For test calculations the steady-state water release curve for basaltic concrete of Kent [13] has been used. The test problem is identical to that in section 4.1, except that for the water release calculations the number of isotherms have ben varied (6, 7 and 10). For the interior regions spot values of water release at the nodal temperatures are used, whilst for the exterior region the (assumed) quadratic dependence of water release on temperture was obtained by fitting the data of [13] at $T = T_a$, $T_a + \Delta T/2$ and $T_a + \Delta T$. Results are given in Table II, which indicate that reasonable accuracy can be

Time (s)	6 isotherms	7 isotherms	10 isotherms
4000	2.46	2.47	2.47
10^5	27.3	27.5	27.6
10^6	87.4	89.2	89.5
2×10^7	878	911	930

TABLE II: Calculation of water release (in tonnes) from concrete for the test problem described in the text. The calculations were performed to investigate the numerical accuracy of the approach rather than to make predictions for a particular accident sequence.

achieved. The additional coding for the water loss model adds a negligible amount to the cost of running CONIMM; more sophisticated water loss models would require significantly more computation.

5. DISCUSSION AND CONCLUSIONS.

Models for thermal penetration into the concrete have been developed. A simple model using the weighted-residual method has been derived and incorporated into the INTER code (the model in the original code was found to have poor heat conservation properties). Other substantial changes to INTER have also been made to provide an improved fast-running parametric-type code that is capable of modelling all phases of the core-concrete interaction. A further version of INTER has been produced in which the thermal penetration model has been replaced by finite difference calculations using one-dimensional versions of the isotherm migration method (IMM). At times up to a few days calculations with this version give support to the simpler model.

A code (CONIMM) for long-term thermal penetration which uses a 2-D version of the IMM has been written and checked; this code incorporates a simple model for water release from the concrete employing experimental data. CONIMM uses a radial mesh, as does the CORCON code [5], which has a much more detailed treatment of the debris pool; it may be feasible to couple these codes to give a mechanistic model for the long-term interaction of core debris with concrete.

REFERENCES

[1] W.B.Murfin. A preliminary model for core-concrete interactions. Sandia Laboratories report SAND77-0370 (1977).

[2] R.O.Wooton and H.I.Avci. MARCH (Meltdown Accident Response Characteristics) Code: Description and User's Manual. Battelle Columbus report BMI-2064 [NUREG/CR-1711](1980).

[3] J.B.Rivard (ed). Interim technical assessment of the MARCH code. Sandia Laboratories report SAND81-1672 [NUREG/CR-2285] (1981).

[4] M.Reimann and W.B.Murfin. The WECHSL code: A computer program for the interaction of a core melt with concrete. Karlsruhe report KfK-2890 (1981).

[5] J.F.Muir, R.K.Cole Jr, M.L.Corradini and M.A.Ellis. CORCON-MOD1: An improved model for molten core/concrete interactions. Sandia Laboratories report SAND80-2415[NUREG/CR-2142](1981).

[6] D.A.Powers and F.E.Arellano. Large-scale transient tests of the interaction of molten steel with concrete. Sandia Laboratories report SAND81-1753 [NUREG/CR-2282] (1982).

[7] J.V.Beck. Sensitivity analysis for USINT - A program for calculating heat and mass transfer in concrete subjected to high heat flux. Sandia Laboratories report SAND81-0026[NUREG/CR-2180] (1981).

[8] e.g.S.Nakamura. Computational methods in engineering and science, Chapter 6. J.Wiley (1977).

[9] R.C.Dix and J.Cizek. The isotherm migration method for transient heat conduction analysis, in 'Heat Transfer 1970' (V.Grigull and E.Mahne, eds.). Elsevier (1970).

[10] B.D.Turland. A general formulation of the isotherm migration method for reactor accident analysis. Paper B3/5, 5th international conference on Structural Mechanics in Reactor Technology, Berlin (1979).

[11] B.D.Turland. Finite difference front-tracking algorithms for Stefan problems arising in reactor safety studies. In "Free boundary problems: theory and applications vol.1 (A Fasamo & M.Primicerio, eds), 293-305. Pitman (1983). (Also CLM-P662 (1982)).

[12] D.W.Peaceman and H.H.Rachford Jr. J.soc.ind.appl.Math., 3, 23 (1955).

[13] L.A.Kent, Water release from heated concretes. Sandia Laboratories report SAND-81-1732 [NUREG/CR-2279](1982).

CONTRIBUTIONS TO CONTAINMENT THREAT FROM HIGH-TEMPERATURE CORE-DEBRIS CAVITY INTERACTIONS

S. Bradley Burson, Ph.D., D.Sc.

United States Nuclear Regulatory Commission
Office of Nuclear Regulatory Research
Washington, D. C. 20555, U.S.A.

ABSTRACT

In the event of primary vessel failure during a severe accident, many of the potential threats to containment building integrity are traceable to the interactions between high-temperature core debris and the concrete reactor cavity. The nature and current status of understanding of the phenomena associated with core-concrete interactions are reviewed. The atypical thermal and physical loads that are imposed upon the containment structure by such phenomena are delineated. Current analytical capability for predicting the parameters that contribute to containment loading is reviewed. Representative calculations made with the CORCON MOD2 and CONTAIN 1.0 codes are presented.

1.0 INTRODUCTION

The principle societal risk identified with nuclear power generation is the potential release of radioactive fission products to the environment. There are two intrinsic characteristics of nuclear power reactors that dominate the hazard that is identified with them. The first is the inventory of radioactive fission products that accumulates in the fuel. Typically, after a few months of operation, a large plant will contain approximately one ton of fission products in its core. Human exposure to the intense radiation emanating from this material is indisputably deleterious; most public concern focuses on this characteristic. Public safety is thus identified with the ability to confine the reactor core. Secondly, after a reactor is shut down, the fission-product inventory continues to constitute an uncontrollable heat source which can not be interrupted or modified. The heat must be dissipated as the radioactive decay dies out; the thermal energy can not be confined nor compressed. The ultimate safety of nuclear reactors thus requires a system which prevents the escape of core material and, at the same time, provides a pathway by which the thermal energy can be dissipated in some benign fashion.

The nature and magnitude of the radiological risk is perceived in vastly different ways, depending upon the point of perspective of the individual. Vendors of power generating equipment and utility companies are influenced by the profit motive as well as their intrinsic obligation to provide reliable electric service to the public. Their concept of safety relies heavily on adherence to established engineering-design safety margins. Excessive overdesign is prohibitively costly. On the other hand, regulators such as the Nuclear Regulatory Commission (NRC) take a more skeptical view and ask the

question "...But if something does go wrong, what are the consequences to the public?...". This pragmatic attitude stimulates the identification of potential risks previously overlooked and aids in the establishment of research priorites. Until the core-damage accident at Three-Mile Island in March 1979, little attention was paid to accidents beyond the design basis. Since that event, the NRC Office of Research has developed an extensive program, the Severe Accident Research Program (SARP), to address accidents involving core-damage and failure of the primary vessel. In the discussion that follows, core melt-down and vessel failure are assumed to have occurred.

For convenience in delineating the problem of severe accidents, one may consider three well-defined physical barriers between the fission products and the external environment: (1) the fuel cladding, (2) the primary vessel and its associated components, and (3) the reactor containment system. In this review, it is assumed that the first two barriers have failed and that the core has found its way into the reactor cavity below the primary vessel. In particular, we wish to examine the phenomena which characterize the interactions between high-temperature core debris and the structural concrete of the reactor cavity. These phenomena will be discussed in terms of their relevance to the development of abnormal thermal and physical loading of the reactor containment system.

The primary force that drives the interaction between core debris and concrete is the decay power of the fission-product inventory. The principle phenomena of interest are, therefore, primarily governed by the thermal balance between the decay-heat source and the heat sinks available during the course of the accident. To provide a framework in which to discuss the interactions of interest, we assume an arbitrary containment design and a set of initial conditions which will ensure occurrence of the phenomena we wish to explore. At approximately 3 hours after shutdown, the entire core, which has become molten, falls through the bottom vessel head onto the concrete floor of the reactor cavity; it is accompanied by a comparable mass of steel from the core-support structures and the lower vessel head. It is also assumed that only refractory fission products remain in the debris, approximately one third of the initial inventory having left as gaseous or volatile species during the meltdown. The initial decay-power level will be approximately 25 MWt. We will consider some of the early transient phenomena, but focus primarily on properties of long-term quasi-steady-state concrete attack.

2.0 HYPOTHETICAL ACCIDENT CONDITIONS

After vessel failure, thermal ablation of the concrete begins instantly and within a few minutes reaches a quasi-steady-state condition and proceeds at a rate primarily determined by the decay-heat power level. The assumptions on which the hypothetical example of a molten-core accident is based are given in Table I.

2.1 Accident Initiation

The term "severe accident" implies total or partial core melt-down followed by penetration of the lower vessel head. In the determination of ultimate containment loading, the accident-related events prior to vessel failure will leave a trail of conditions that must be accounted for in the analysis, e.g., ruptured pipes, disabled safety features, failed-open relief valves, etc. In this discussion, no effort is made to delineate or focus on this aspect of the problem; only the circumstances following release of molten core materials into the reactor cavity are considered.

Table I Assumptions Used in Hypothetical Accident Example

- Composition of Core Debris (entire core of 3400 MWt PWR)

100	MT Uranium Oxide		
10	MT Zircalloy Oxide	10	MT Zircalloy Metal
4.5	MT Stainless-Steel Oxide	85.5	MT Stainless-Steel Metal

- Cavity Description

Geometry - cylindrical, radius = 3.0 m
Concrete Composition
(a) U.S. common-sand limestone
(b) KfK BETA crucible

- Initial Conditions

Molten-core deposited in cavity 3 hours after shutdown
Debris temperature = 2500 K
Initial fission product decay power = 22 MWt
(excludes volatile fission product species lost at melt-down)
Initial cavity atmosphere pressure = 1.5 bar
Coolant
(a) dry cavity
(b) overlying water layer present

2.2 Influence of Containment Design

The consequences of a core melt-down accident depend heavily upon the nature of vessel failure and the geometric configuration of the structure below the reactor. Containment systems vary markedly in their architectural features, not only with respect to reactor types (PWR or BWR) but also from plant to plant. The shapes, as well as the free volumes of the three BWR containment systems currently used, are quite different. Likewise, PWRs are housed in a variety of large dry containments as well as smaller structures supported by ice-condenser steam suppression.

The three generic types of BWR containments have a number of features in common. The reactor primary vessel is housed in an enclosure (called the "drywell") having a relatively small free volume. The drywell is connected by a number of vent pipes or "downcomers" to an auxiliary volume partially filled with water (the suppression pool). The vents exit below the pool surface so that, in the event of primary system failure, the escaping steam is forced to bubble through the pool where it is condensed. These suppression-pool systems permit the use of smaller primary containment structures having lower design pressures. In all cases, the BWR primary containment (drywell plus suppression pool) is enclosed in a much larger secondary reactor containment building; it, however, is not intended to provide significant protection against external radiological release. Some of the characteristics of typical Mark I - III containments are shown in Table II.

A number of PWRs are housed in what is referred to as "large dry containment" systems. As the name implies, there is no engineered system to condense steam in the event of a loss-of-coolant accident (LOCA). Rather, the containment structure has a sufficiently large free volume and design pressure high enough to sustain the insult of a severe LOCA. The "ice-condenser" plants are

analogous to BWR containment systems in that escaping steam is forced to pass through a chamber filled with baskets of ice where it is condensed. The ice condenser functions like a BWR suppression pool which permits the use of a smaller containment building. Some relevant specifications of typical PWR containments are also shown in Table II.

Table II Typical Containment Design Specifications

(a) BWR Systems

Mark	Drywell Vol,m^3	P (bars)	T($^{\circ}$C)	Wetwell Free Vol	P	T
I	4500	3.9	138	3370	3.9	138
II	7050	3.8	171	3625	3.8	104
III	7645	2.1	166	39,643	2.1	85

(b) PWR Systems

Type	Vol.	P
Large Dry (Zion)	80,200	3.2
Subatmosphere (Surry)	55,500	3.06
Ice-Condenser (Sequoyah)	37,000	0.75

Because of this diversity in building design, no effort is made to interpret the impacts of core-concrete interactions upon any particular containment system. Rather, a hypothetical sample case is presented which can be approximately identified with the reactor cavity configurations found in some of the existing containment systems. In particular, the Mark III BWR containment design has a closed cavity in the reactor pedestal directly below the primary vessel. Upon bottom vessel-head failure, the molten corium would fall into this cavity where concrete ablation would begin immediately. For most containment systems, other than the BWR Mark III, the example used in this discussion would be considered conservative.

3.0 CORE-DEBRIS CAVITY INTERACTIONS

The phase of the hypothetical accident assumed in this treatment begins with penetration of the lower vessel head by molten core debris. The spectrum of ensuing phenomena can be considered as either transient or quasi-steady-state. Even before this separation can be made, a branch point is encountered, i.e., whether or not the reactor vessel is at high pressure at the time of failure. It has been demonstrated experimentally that the velocity with which the melt is ejected has a significant impact on aerosol production, debris dispersal, and containment heating. A second branch point is encountered simultaneously, i.e., whether or not the reactor cavity is flooded with water at the time of debris deposition. Clearly, within the four accident scenarios suggested by these branch points, a continuum of potential situations exists. Since it is not possible to consider more than a few representative examples, most of the phenomena will be described briefly while a few will be considered in greater detail. The corium-cavity phenomena expected to be of significance, to the loading of containment are shown in Table III.

3.1 Transient Phenomena Accompanying Reactor Vessel Failure

3.1.1 Dispersal of Core Debris: Molten corium is known to be quite fluid so that it can be expected to flow readily throughout the cavity. If the vessel is at high pressure, one can expect the debris to be more widely distributed. One possible effect of high-pressure dispersal is to render the debris more coolable at later times. On the other hand, the increased contact between the debris and concrete surface augments the initial gas release rates thus making an early contribution to containment pressurization. Correspondingly, extensive prompt dispersal of core debris increases the direct structural attack from thermal radiation.

Table III Core-Debris Cavity Phenomena

Debris Expulsion From Reactor Vessel

- High-pressure debris dispersal
- Mechanical damage to structural components and ESFs
- Direct atmosphere heating (sensible plus chemical-reaction heat)
- Steam explosions

Quasi-Steady-State Phenomena

- Concrete ablation and disposition of heat
- Basemat penetration
- Generation of combustible and noncondensable gases
- Generation of aerosols and release of fission products
- Crust formation and freezing

3.1.2 Potential for Mechanical Damage: Significant inertial effects can be expected to accompany the sudden release of many tons of dense liquid driven by high vessel pressure. The kinetic energy of the molten mass has the capability of doing direct physical damage to structural components below the reactor and in particular to components of engineered safety features which might otherwise be sufficiently remote as not to be threatened.

3.1.3 Direct Heating of the Containment: It has been shown in small experiments that corium ejected under high pressure fragments into fine particulates and aerosols. This has two effects: sensible heat is rapidly transferred to the atmosphere, and in addition, elemental metals (zircalloy and steel) present in the melt can rapidly oxidize while airborne. These reactions are highly exothermic and rapidly elevate the temperature of the atmosphere. The threat of failure by overpressurization is augmented since there is insufficient time to transfer the heat to the available heat sinks.

3.1.4 Potential for Steam Explosions: If the reactor cavity is flooded when the corium enters it, there is the possibility of rapid steam generation from explosive thermal interactions with the water. The probability for and possible magnitude of such interactions is still not adequately quantified and continues to be the subject of intense research. These issues will not be discussed here. It is only pointed out, that although an ex-vessel steam explosion might not of itself constitute a significant threat to containment overpressurization, in conjunction with other factors, it might become significant. Conversely, such explosions could prove beneficial in that the core debris might become more widely dispersed and fragmented, thus rendering it more coolable.

3.2 Core-Concrete Interactions: Quasi-Steady-State Phenomena

After the transient conditions that accompany vessel failure have subsided, it is assumed that a relatively stable pool of core debris is formed in the cavity. The modelling and capability for analyzing these longer-term processes is relatively advanced. The CORCON MOD2 computer code[11] developed at Sandia National Laborities under NRC sponsorship treats the thermal and chemical interactions that accompany the attack on concrete by high-temperature core debris. The representative data used to illustrate the phenomena described below have been derived by CORCON MOD2 analysis of the hypothetical conditions described in Table I.

3.2.1 Concrete Ablation and Disposition of Heat: Once a temperature profile is established in the concrete, and the ablation temperature reached at the surface, as much as one third of the heat absorbed by the concrete is permanently dissipated by endothermic dissociation reactions. In terms of decay-heat removal, concrete ablation is desirable because a significant portion of the absorbed energy is permanently dissipated, thus reducing the total heat available for other threatening thermal processes. Conversely, the hot ablation products, gases, aerosols, etc., tend to augment the containment threat.

3.2.2 Slag Dilution of the Debris Pool: Although a considerable fraction of the concrete is decomposed into gaseous reaction products, large amounts are refractory and mix, or dissolve into the core debris. The oxidic components are miscible with the UO_2 fuel and as ablation continues, the specific power density of the debris is reduced. This process thus slows down concrete penetration and, at the same time, lowers the bulk temperature and renders the debris more coolable.

3.2.3 Penetration of the Basemat: Basemat penetration is the most readily identifiable consequence of attack on the cavity floor. Although release of radioactivity to the ground water through this avenue is highly improbable in most cases, for certain reactor designs and some plausible accident scenarios, the possibility can not be definitely precluded. Axial basemat penetration in the hypothetical case assumed for illustration, has been computed for a 24-hour period with the CORCON MOD2 code. These results are shown in Table IV.

Table IV Corium Penetration of Concrete

Time (h)	Limestone-sand (cm)		BETA Crucible (cm)	
	Dry	Wet	Dry	Wet
0.5	27.0	24.6	21.9	19.4
1.0	40.0	34.6	45.6	42.2
2.0	57.4	45.7	72.6	71.9
4.0	71.0	52.0	98.0	98.6
8.0	81.2	62.0	112.7	113.0
16.0	94.5	78.7	135.8	139.6
24.0	105.0	91.4	153.1	162.2

The calculation was made for each of two types of concrete, typical limestone-sand (commonly used throughout the U.S.) and for the material used in the KfK BETA test facility. For each type of concrete, the calculation was carried out under two additional assumptions - - with and without an overlying pool of water.

3.2.4 Release of Water Vapor: All concretes contain a large amount of water (approximately 60-80 Kg/t); some is chemically bound in the concrete, while some is entrained as free water in the interstices. At various temperatures during thermal ablation, both types of water are liberated so that a large amount of water vapor accompanies the decomposition. The water vapor contributes to the formation of a gas layer at the debris-concrete interface and thus influences the ablation rate. As the water vapor and other decomposition gases leave the surface of the concrete, they bubble upward through the molten pool which tends to mix and agitate the pool. This process has a significant influence on the heat-transfer characteristics of the system. If there are metallic components in the molten debris, some of the water vapor will reactor chemically with them to form H_2 and oxides of the metals. For the sample problem, integrated water-vapor released from the debris-pool surface is shown in Table V.

Table V Water Vapor and Gas Released from Concrete (CORCON MOD2 Calculation)

Time	Limestone-Sand (kg-mol)				BETA (kg-mol)			
(h)	CO	CO_2	H_2	H_2O	CO	CO_2	H_2	H_2O
Dry Cavity								
0.5	162	34	87	19	8	3	90	14
1.0	216	65	116	36	9	10	157	50
2.0	228	101	155	56	47	16	233	80
4.0	341	161	182	90	62	24	305	116
8.0	379	249	199	142	70	34	347	164
16.0	430	332	221	192	84	44	411	214
24.0	468	371	237	218	92	49	446	246
Flooded Cavity								
0.5	148	21	80	953	2	1	71	389
1.0	188	39	102	2067	2	2	134	1265
2.0	232	62	125	4017	44	3	218	2794
4.0	256	88	138	7406	60	6	294	6073
8.0	293	144	158	8405	68	13	332	8391
16.0	357	269	190	8476	83	36	405	8503
24.0	390	338	204	8517	94	56	454	8610

3.2.5 Hydrogen Production (Metal-Water Reactions): At the high temperatures existing in the debris pool, the water vapor released from the concrete can react with the metallic components (zircalloy and steel) to produce hydrogen and metal oxides. The H_2 gas is released from the pool surface while the oxides will mix with the other oxidic components in the pool. These metal-water reactions are exothermic and contribute to the heat source in the pool. The H_2 gas can contribute to containment loading in either of two ways. Hydrogen is noncondensable and can contribute to overpressurization of inerted systems such as the BWR Mark I and Mark II. In systems that are not inerted, combustion of the H_2 can cause overpressurization as well as thermal and/or mechanical damage resulting from combustion. The integrated H_2 generation associated with the sample problem is shown in Table V.

3.2.6 Release of CO_2 From Concrete Ablation: When subjected to high temperature, the $CaCO_3$ limestone aggregate dissociates into CaO and CO_2. The refractory CaO dissolves into the oxidic component of the debris pool while the CO_2 gas bubbles upward. The gas which is not further reacted in the pool escapes from the surface of the pool. Since the CO_2 is noncondensable it contributes to containment overpressurization.

3.2.7 Generation of CO: Some of the CO_2 released from the concrete can further react in the pool to form CO, depending upon the availability of elemental metals. Again, the metal oxides remain behind while the gas escapes from the pool surface. In addition to being noncondensable, the CO is also combustible and carries with it the same hazards that are associated with H_2.

3.2.8 Aerosol Generation: As gases from the concrete pass through the molten debris pool and bubbles break at the surface, aerosols are produced as the result of film rupture and the condensation of vapors contained within the bubbles. These aerosols carry high-temperature particulate debris (some of which contain radioactive fission products) into the cavity atmosphere.

3.2.9 Crust Formation and Freezing: As the debris cools, freezing begins; crusts may form either at the top or bottom, or within the pool depending upon its composition and circumstances. Crusts at the pool surface are more likely to form if overlying water is present. The thickness of such crusts are "self-adjusting" since increased thickness also increases thermal resistance with consequent rise in pool temperature. Although models are included in the CORCON MOD2 code which treat crust formation and freezing, there is little experimental data available as yet for the validation of these models.

4.0 THREATS TO CONTAINMENT INTEGRITY RELATED TO MOLTEN-CORE CAVITY INTERACTIONS

The importance of accident imposed loads depends on the particular containment system involved. It is the purpose of this review to identify the principal sources of such abnormal loads and not to quantify their effects. Most of the discussion in Section 3 is focussed on the phenomena occurring below or at the top surface of the debris pool. Except for potential basemat penetration, most of the containment threats have their source identified with the pool surface. These are briefly summarized.

4.1 Upper Cavity Phenomena

Heat leaves the surface of the pool in two modes: thermal radiation and convection to the atmosphere. During early stages of the accident, the upward thermal attack is dominated by radiation. Clearly, this is influenced by the presence of overlying water, and also by the opacity of the atmosphere. Under some conditions, it can be expected that dense aerosol clouds will be present. The upward heat flux will rapidly elevate the temperature of the exposed structural surfaces above the pool. Concrete spallation, thermal weakening, and ablation may occur. This upward concrete attack can release additional water vapor and other gases into the atmosphere. In some systems, direct attack on the reactor pedestal itself may be possible.

4.2 Overpressurization by Noncondensable Gases

The data in Table V provide an illustration of the significance of noncondensable gas production from concrete attack. It is assumed here that the hydrogen has not been burned; this may be the case if the containment is inerted, or if the steam concentration is high enough to inhibit combustion. The most extreme case is used, i.e., limestone aggregate concrete in a dry cavity. At the point 24 hours after vessel failure, a total of 1076 kmoles of gas (H_2, CO, and CO_2) are produced. This corresponds to approximately 24,000 m^3 of gas at STP. If this gas were introduced into a Mark I BWR primary containment, it would contribute a partial pressure in excess of 3 bars. When corrected for the expected higher temperature, this contribution alone would

exceed the design pressure of the structure. Clearly, for the large dry PWR systems, threat of overpressurization from this source becomes minimal.

4.3 Burning of Combustible Gases - H_2 and CO

As noted in Section 3.2, metal-water reactions produce H_2; and CO; both gases are combustible. Gas burning in the atmosphere elevates the pressure and can threaten engineered safety features.

4.4 Degradation of Engineered Safety Features

Direct lateral concrete attack by the pool could, depending on the containment design, damage specific safety feature components, i.e. pumps, etc. Aerosols in the atmosphere could clog fan coolers or cause thermal damage by deposition of radioactive fission products.

4.5 Influence of Aerosols on Containment Loading

During the discharge of molten core materials from the reactor vessel, and later, during debris-concrete interactions, copeous amounts of aerosols are generated and become airborne. Those which carry fission products contribute heat to the atmosphere as the active species decay. This bulk heat source adds to that already present in the form of volatile and gaseous species that were released during the meltdown. Calculations with the CONTAIN 1.0 code have demonstrated that accurate predictions of containment loading must include the interactions of these aerosols with the thermal-hydraulic behavior of the atmosphere. Aerosols leaving the pool surface can have a strong influence on the intensity of the ultimate radiological source term as it evolves during the accident.

5.0 CURRENT ANALYTICAL CAPABILITY

5.1 Core-Concrete Interaction Analysis

The CORCON MOD2 code is a highly-mechanistic computer program that models a stratified pool of molten, or partially molten, core debris in a concrete reactor cavity. It calculates the rate of concrete attack, the change of cavity shape as ablation proceeds, and the evolution of gases and radiant heat from the pool surface. CORCON-MOD2 includes the behavior of slurries and crusts within the pool as well as the influence of overlying water. A corresponding code, WECHSL, is under development at KfK in Karlsruhe, FRG. Both codes suffer some lack of credibility resulting from a dearth of experimental data against which they can be validated. This latter deficiency is actively being remedied by experimental programs, both in the U.S. and in West Germany. CORCON has been used to compute the examples presented in this report.

5.2 Analysis of Containment Loading

The CONTAIN 1.0 code[2] is a generic systems code which models an arbitrary (independent of reactor type or structural design) reactor containment system. Source terms (resulting from primary system failure) are provided by other codes such as CORCON, WECHSL, VANESSA, MELPROG, etc. The thermal-hydraulic behavior of a coupled network of compartments is treated as an interactive integrated system. Structural response depends upon the specific containment system being modelled and is not incorporated into the CONTAIN code. Although specific CONTAIN 1.0 calculations have not been

presented since quantification of loading is outside the scope of this report, many of the conclusions concerning response to debris-cavity phenomena are based on CONTAIN 1.0 results.

6.0 SUMMARY

From this brief overview of high-temperature molten-core cavity phenomena a number of conclusions can be drawn. Further research is needed before accurate mechanistic models can be developed for many of the phenomena. Further experimentation is necessary to provide the data base needed for the validation of such models. The mathematical treatment of such complex physical and chemical processes demands an interactive integrated analysis. The consequences of such severe accidents are dependent, not only on the initiating events, but upon the specific design details of each plant. Whenever and wherever appropriate, the influence of possible operator action must be factored into the analysis.

ACKNOWLEDGEMENT

The author wishes to express his appreciation to Drs. K. D. Bergeron, D. Bradley, R. K. Cole, Jr., K. K. Murata and, D. A. Powers of Sandia National Laboratories and Dr. G. A. Greene of Brookhaven National Laboratory for carrying out the CORCON MOD2 and CONTAIN 1.0 calculations on which the tables are based, and for their consultation and advice in the preparation of this report. In particular, the cooperation and assistance of Mr. R. Celestin of the U.S. Nuclear Regulatory Commission in preparing the manuscript for publication are deeply appreciated.

REFERENCES

1. Cole, R. K., Jr., D. P. Kelly, and M. A. Ellis. 1984. "CORCON-MOD2: A Computer Program for Analysis of Molten-Core Concrete Interactions." U.S. Nuclear Regulatory Commission, NUREG/CR-3920.

2. Bergeron, K. D., et al. 1984. "User's Manual for CONTAIN 1.0, A Computer Code for Severe Nuclear Reactor Accident Containment Analysis," U.S. Nuclear Regulatory Commission, NUREG/CR-2224.

TRANSIENT MOISTURE MIGRATION IN CONCRETE DURING SEVERE REACTOR ACCIDENTS

P. G. Kroeger
Y. Shiina[1]

Brookhaven National Laboratory
Upton, New York 11973
U. S. A.

ABSTRACT

In the most severe hypothetical core heatup accidents in High Temperature Gas Cooled Reactors, the heatup of the concrete reactor vessel can result in gas release from degrading concrete which can ultimately lead to containment building failure. This gas release is largely affected by the moisture migration during concrete heatup. Moisture migration in concrete is also of interest in Light Water Reactor core meltdown accidents. Therefore, the general problem of moisture migration in a heated concrete slab, has been analyzed including the effect of water evaporating close to the heated surface and recondensing in cooler regions. Results for early phases of core heatup transients are being given. Their implication on the accident progression is being discussed.

INTRODUCTION

During hypothetical Unrestricted Core Heatup Accidents (UCHA) in High Temperature Gas Cooled Reactors (HTGR) the Liner Cooling System (LCS) assumes a crucial role. This system of water cooled pipes is designed to protect the liner and the prestressed concrete reactor vessel (PCRV). If the LCS fails during UCHA scenarios and is not restored to service within about 2 days, the PCRV concrete will heatup, and thermal barrier and liner failures will result at about 40-70 hr [1,2]. The concrete decomposition gases (predominantly H_2O and CO_2), can ultimately cause containment building failure due to overpressurization. The amount and timing of this gas release strongly depend on the migration of the physically and chemically bound water in the concrete during the gradual but severe heatup.

Vapor migration in concrete slabs heated on one side is also of interest in severe accidents for Light Water Reactors (LWR). While this paper concentrates on vapor migration in HTGR accident scenarios, the analysis and the code VAPMIG are equally applicable to LWR accidents.

As the porous concrete is heated at its exposed surface, some of the water is vaporized, causing a pressure increase and a flow of gas and liquid phases into cooler regions, where recondensation can occur. When concrete temperatures exceed the local vapor saturation temperature, a "dry region" is

---

[1]Permanent address: JAERI, Japan.

formed in which water exists in the vapor phase only. This dry region expands with an "evaporation front" moving into the concrete. Beyond the front, in the "wet region" water exists as liquid and as vapor, in equilibrium. A further important aspect is the presence of a non-condensible gas (generally air). The problem is essentially one of a phase change front motion with a thermally driven flow field, with significant feed back from the flow field to the temperature field.

Moisture migration in porous media has been of interest in many applications, as for instance in drying processes[3], or in building structures exposed to fires[4]. This work extends a previous idealized model of the current authors[5]. A more comprehensive listing of recent literature can be found there. Of importance for the nuclear industry are primarily the analytical work of Dayan and Gluekler[6,7] as well as the permeability measurements of McCormack et al.[8]. Dayan[7] solved the vapor migration problem without presence of a non-condensable gas and for a permeable outer surface using similarity solutions. Our work[5] extended that work by including the effects of a non-condensable gas, and considering the case of an impermeable outer surface. The disadvantages of these idealized solutions is that they cannot represent the actual process with time varying boundary conditions and temperature dependent material properties. However, with their simplicity they do provide valuable insight into the basic phenomena and permit rapid parametric evaluations. Dayan and Gluekler[6] solved the vapor migration in concrete subject to severe surface heating in a more general numerical analysis without explicit tracking of a phase change front. While such solutions are simpler to obtain, it has been generally recognized[9] that solutions explicitly tracking the phase change front are harder to develop, but are ultimately more accurate and more reliable.

The current work, therefore, represents a finite difference solution of the full partial differential equations of mass and energy conservation with Darcy's momentum equation, considering two separate regions, a "dry" region and a "wet" region, separated by a moving phase change front. As pointed out before[5,8] the motion of gas and liquid in concrete heated beyond 100°C is predominantly due to pressure gradients, and the vapor motion by molecular diffusion is therefore being neglected.

THE MODEL

A semi-infinite (or finite) slab of concrete is being considered with no-flux boundary conditions at the far end. The domain is divided into a dry region, containing concrete and superheated vapor, and a wet region containing concrete, water in liquid as well as in saturated vapor form, and air. The absence of air from the dry region is a result of the gas flow from the evaporation front [5]. Local thermodynamic equilibrium is assumed.The thermal boundary condition at the outer surface (z=0) is that of a prescribed time varying source temperature, and outside heat transfer coefficient.

The resulting conservation equations for the dry region are

vapor mass

$$\frac{\partial}{\partial t} m_v = - \frac{\partial}{\partial z} \rho_v u_g \tag{1}$$

mixture energy

$$\frac{\partial}{\partial t} E + \frac{\partial}{\partial z} \rho_v h_v u_g = \frac{\partial}{\partial z} k_D \frac{\partial \theta}{\partial z} \tag{2}$$

where the dry region mixture internal energy is

$$E = (1-\varepsilon) (\rho c)_S (\theta - \theta_{ref}) + m_v e_v \tag{3}$$

The vapor flow follows from Darcy's law as

$$u_g = - \left(\frac{K}{\mu}\right)_g \frac{\partial p_T}{\partial z} \tag{4}$$

The current model uses spline functions of high accuracy for the water properties. In the dry region these are generally solved as $p_v = p_T = p\ (\rho_v, \theta)$ where $\rho_v = m_v/\varepsilon$, but solutions for $\rho = \rho\ (p,\theta)$ are also provided.

The conservation equations for the wet region are

water mass

$$\frac{\partial}{\partial t}\ m_w = - \frac{\partial}{\partial z} (\rho_v u_g + \rho_\ell u_\ell) \tag{5}$$

air mass

$$\frac{\partial}{\partial t}\ m_a = - \frac{\partial}{\partial z} \rho_a u_g \tag{6}$$

energy

$$\frac{\partial}{\partial t} E + \frac{\partial}{\partial z} \left[(\rho_v h_v + \rho_a h_a)\ u_g + \rho_\ell h_\ell u_\ell\right] = \frac{\partial}{\partial z} k_W \frac{\partial \theta}{\partial z} \tag{7}$$

where the mixture internal energy is

$$E = (1-\varepsilon)\ (\rho c)_S (\theta - \theta_{ref}) + m_v e_v + m_\ell e_\ell + m_a e_a \tag{8}$$

and of course

$$m_w = m_v + m_\ell. \tag{9}$$

The wet region Darcy flow relationships are

$$u_g = - a_g \left(\frac{K}{\mu}\right)_g \frac{\partial p_T}{\partial z}\ ;\ u_\ell = - \left(\frac{K}{\mu}\right)_\ell \frac{\partial p_T}{\partial z} \tag{10}$$

Equation (10) allows for the use of separate liquid and vapor permeabilities, to simulate the effect of reduced liquid flow which has been suggested by some authors[4,6]. Furthermore, in particular for large liquid volume fractions an impairment of the gas flow has been suggested. To simulate that effect the factor a_g was added in the gas flow equation. Optionally this factor can be set to 1.0 (no gas flow reduction) or to $a_g = S_g = \alpha_g/\varepsilon$.

The wet region state relationships for water are obtained from spline fits to the 1967 IFC formulation, except for the liquid density which was assumed as constant (1000 kg/m^3). Air was treated as an ideal gas. All phases were assumed to be locally in thermodynamic equilibrium. The total pressure is then the sum of the partial pressures $p_T = p_v + p_a$.

At the vaporization front, mass and energy must be conserved. Mass conservation of water for a vaporization front moving with velocity U_{fr} requires

$$(m_{v1} - m_{w2})\ U_{fr} = [\rho_v u_g]_1 - [\rho_v u_g + \rho_\ell u_\ell]_2 \tag{11}$$

where subscripts 1 and 2 refer to front properties on the dry side and on the wet side respectively.

Energy conservation at the front requires

$$(E_1 - E_2)\ U_{fr} = - \left[k \frac{\partial \theta}{\partial z}\right]_1 + \left[k \frac{\partial \theta}{\partial z}\right]_2 + (\rho_v h_v u_g)_1 - [\rho_v h_v u_g + \rho_\ell h_\ell u_\ell]_2 \tag{12}$$

where E_1 and E_2 follow from Equations 3 and 8 respectively. Note that the u_i in Equations 11 and 12 are superficial velocities while the front velocity U_{fr} is an actual velocity.

The equations were solved in a completely conservative finite difference formulation using a space coordinate system moving with the front. Details regarding this formulation and the experience obtained with it are being documented in a future report[12].

RESULTS

For the application to PCRV heatup transients, two flow boundary conditions at the heated surface are of interest. Up to the time of liner failure, the heated surface is impermeable to flow, and the boundary condition is

$$u = \frac{\partial p}{\partial z} = 0; \quad z = 0 \tag{13}$$

Subsequent to liner failure, vapor can flow into the core cavity and the core inside pressure will provide the pressure boundary condition

$$p = p_{core}; \quad z = 0 \tag{14}$$

At first, a general application of the model was considered, to facilitate comparison with previous work [5]. Considering impermeable wall boundary conditions, a step change in temperature to 250°C was imposed at the outer surface of a semi-infinite slab, using the input data of Reference 5. Some results are shown in Figure 1, indicating that the previous approximation, assuming a constant front temperature for the case of a step change in wall temperature, was well justified. Also the approximate front progression of $z_{fr} \propto \sqrt{t}$ was confirmed to be accurate within 1% over the time range from 60 s to 4 hr. Frame b shows typical temperature, pressure and liquid fraction distributions. The temperatures and pressures are slightly lower here, which is apparently due to the improved latent heat relationships. Altogether, the close agreement with the previous results confirms the validity of the simplified model, and establishes confidence in this new and more general model.

The model was next applied to the early phases of PCRV heatup under UCHA conditions using as source typical thermal barrier core side temperatures for the 2240 MW th design, ranging from 300°C to 1000°C over the period of 0 to 80 hr [1,2]. The thermal barrier consisted of 67 mm of kaowool insulation. Other data are given in Table I. (The code does provide for temperature dependent properties, and constant values were applied here only for simplicity). The concrete thermal properties are representative of PCRV concrete [10] while the permeabilities are based on the data of Reference 8.

Results for the PCRV heatup prior to liner failure are shown in Figure 2. The core side thermal barrier temperature (source) is included in Frame a. Two cases are are being considered: The best estimate permeabilities of Table 1 were used in the first case (BE PERM). In the other case, following a frequently suggested assumption that the liquid phase is immobile or moves at a much reduced rate [4,6], the liquid permeability was reduced by two orders (LL PERM). In this second case the evaporation front will be slowed down as all liquid must essentially be evaporated first to then move as vapor into colder regions of the concrete, while in the first case a significant part of the mass transfer into cooler regions is due to liquid flow.

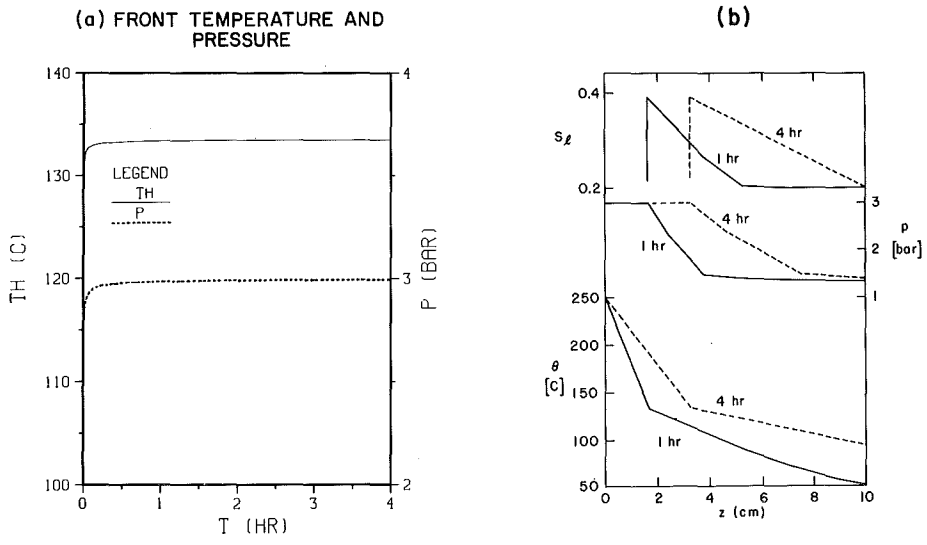

Figure 1. Temperature, pressure, and liquid fraction during transient heatup with step change in surface temperature.

Table I

Properties and Input Data for Case of Simulated PCRV Heatup

Thermal Conductivities

kaowool	0.54 W/mK
concrete dry	2.8 W/mK
concrete wet	3.2 W/mK

Permeability

gas $\left(\frac{K}{\mu}\right)_g = 1\times10^{-5} \quad \frac{m^2}{\text{bar s}}$

liquid $\left(\frac{K}{\mu}\right)_\ell = \left(\frac{\mu_G}{\mu_\ell}\right)_{200°C} \times \left(\frac{K}{\mu}\right)_g = .05 \times \left(\frac{K}{\mu}\right)_g$

$(\rho c)_S = 1.92 \times 10^6 \ \frac{J}{m^3 K}$ (w/o voids)

$p_\infty = 1$ bar; $\theta_\infty = 20°C$; $\varepsilon = 0.35$; $S_{\ell\infty} = 0.4$

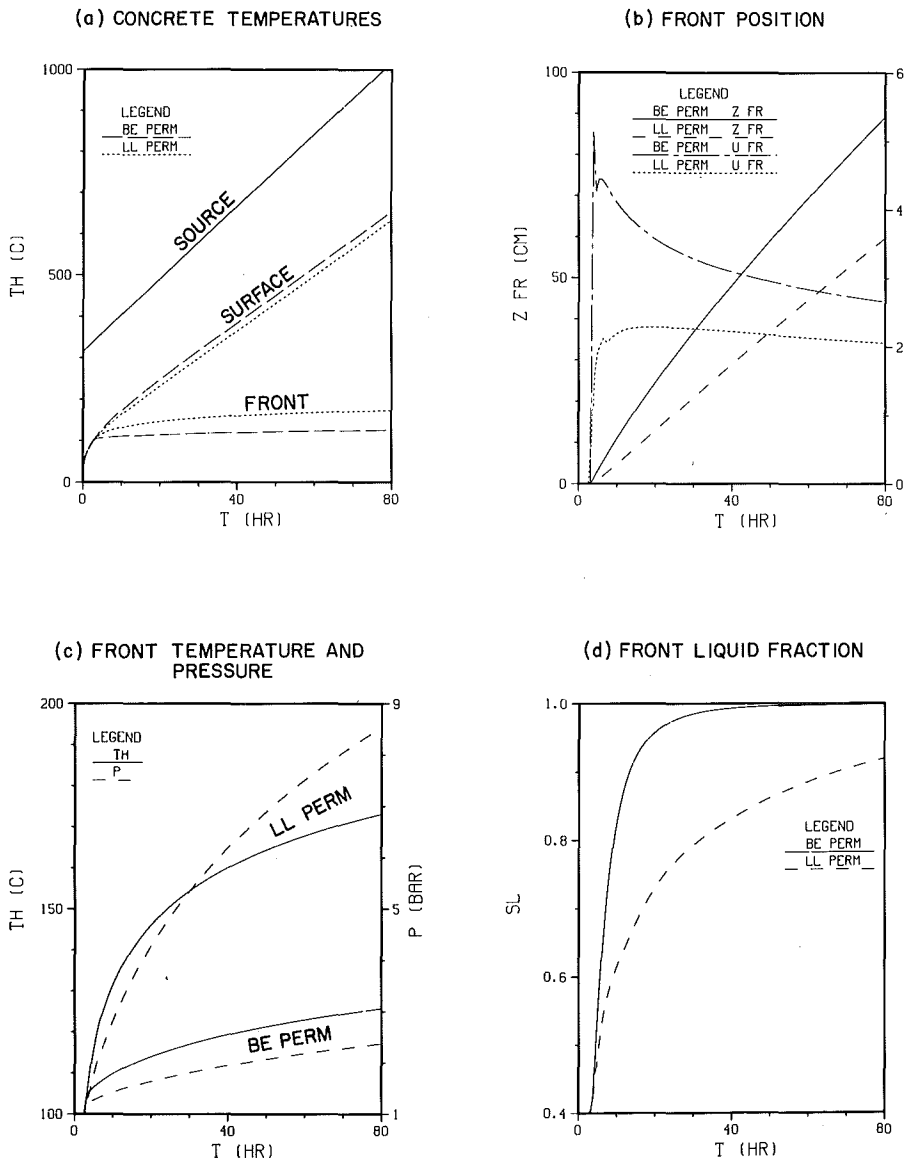

Figure 2. Simulated PCRV heatup prior to liner failure for cases of best-estimate concrete permeabilities (BE PERM) and for case of reduced liquid mobility (LL PERM).

Frame b shows the front progression, indicating that the dry region forms at about 3 hrs, and is of substantial width in either case at the time of anticipated liner failure of 60 to 80 hr. At that time the dry region temperatures extend up to about 600°C which could result in further release of some of the chemically bound water with further pressure increases and flow towards the wet region. While this effect is modeled in the VAPMIG code, the current sample application, considered the physically bound water only.

For typical concrete permeabilities (BE PERM) the dry region pressures only rise to about 2 bars with a front temperature of about 120°C (Frame c). (With an impermeable outer surface the pressure is virtually constant across the dry region). In the wet region adjacent to the front the pores are almost completely filled with liquid (Frame d).

In the extreme case of reduced liquid mobility (LL PERM) the dry region pressures become quite significant and exceed 8 bars at 80 hr. The liner anchoring to the PCRV is generally designed for fluid pressures on the PCRV side of about 6 bars, at LCS temperature levels of 30 to 50°C. Whether the liner and its anchors can accommodate above back pressures at 300 to 600°C is questionable. Therefore, earlier thermal barrier failure due to excessive back pressures could be possible, if this case is representative for PCRV concretes. Further more detailed data on PCRV concrete permeabilities, and a sensitivity study on the input data of this analysis would be required to confirm or reject this potential earlier failure mechanism.

Of crucial effect on the accident progression is the water ingress from the PCRV into the core cavity subsequent to liner failure. The simulations of Figure 2 were therefore extended, assuming liner failure and a corresponding flow boundary condition at $z = 0$. Results are shown in Figure 3. There was virtually no change in the evaporation front velocity at failure time and the front progression into cooler regions continued. In the case of best estimate permeabilities (BE PERM) front temperatures and pressures did not change visibly and continued there slight upward trend. For the case of reduced liquid mobility (LL PERM) the liner failure essentially terminated the upward trend of front temperature and pressure. The resulting mass flows of vapor into the core cavity are shown in Frame b. For the best estimate case the actual ingress was about 0.035 kg/m^2hr while for the case of reduced liquid mobility it remains an order higher at about 0.5 kg/m^2 hr. The PCRV heatup rates used here are the most severe ones, occurring at the center of the core side barrel only. Either of the above mass flows is significantly lower than the previously assumed value[2,11] of about constant ingress of 1 kg/m^2hr averaged over the total core cavity surface. Such reduced water ingress could significantly extend the CB failure time beyond the current estimate of 10 days.

For the case of reduced liquid mobility with its significant dry region pressure an earlier liner failure at 40 hr was considered. The resulting water ingress is included in Frame b of Figure 3. It is about equal to that observed at later liner failure, except that this ingress now arises earlier.

In summary, the formation of a dry region and removal of most of the moisture beyond the evaporation front protects the core cavity from most of the original water in the concrete. As this front is driven by the heatup of the concrete, a reversal would only be possible with concrete cooldown, which cannot occur in this accident scenario. We assumed two different cases of concrete permeability and obtained significantly different results. The case of reduced liquid permeability can be considered as an upper limit for potential water ingress. Whether actual PCRV behavior could be close to this limit would have to be determined by experimental efforts, since currently available permeability

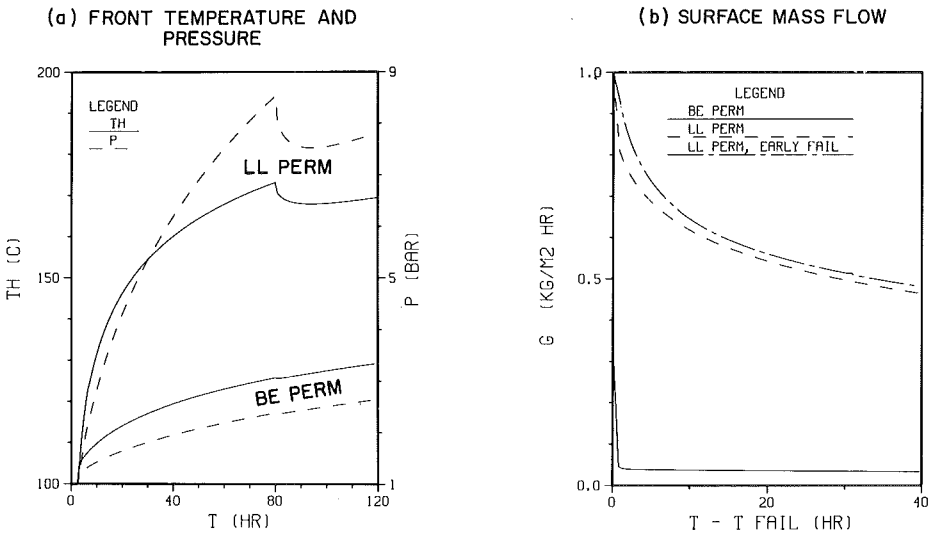

Figure 3. Simulated PCRV heatup subsequent to liner failure for cases of best-estimate concrete permeabilities (BE PERM) and for case of reduced liquid mobility (LL PERM).

data are not sufficiently detailed. Special efforts are made to obtain high conductivities in PCRV concretes[10] requiring dense structures. Therefore, it is possible that PCRV concrete behavior might tend towards the case of reduced liquid mobility.

The exponential increase of concrete permeability with temperature [8], will be included in future simulations. However, the strong increase of permeability with temperature is only expected to effect the outer parts of the dry region which contain very little vapor. Thus, it is not expected that these simulations will affect our current conclusions significantly.

CONCLUSION

A generalized model of vapor migration in porous concrete being heated at one side has been presented. The model agrees well with previous results, thus confirming some of the assumptions made in the previous work and establishing confidence in the new model.

Applying the model to PCRV heatup conditions it is found that considerable pressures may be generated in a large dry region close to the liner, potentially leading to earlier liner and thermal barrier failure. However, due to the significant width of the dry region of 40 to 80 cm, the previous estimates of water ingress into the core appear to have been excessive. With considerably reduced water ingress the time of containment building failure could increase significantly beyond the current estimate of 10 days.

Further work is suggested, to obtain improved PCRV concrete permeability data and to consider such effects as the observed significant increase in concrete permeability with temperature as well as the increase in containment building pressure with time.

NOTATION

c	specific heat
E_i	internal energy of species i per unit volume of porous medium
e_i	internal energy of species i per unit mass of species i
h	enthalpy
k	thermal conductivity (D=dry region; W=wet region)
K	permeability
m_i	mass of species i per unit volume of porous medium
p	pressure
S_i	fraction of pore volume occupied by phase i (i=gas, or liquid) ($S_i=\alpha_i/\varepsilon$)
t	time
u_i	volumetric flow per unit area of species i (superficial velocity)
U_{fr}	evaporation front velocity
z	axial coordinate
z_{fr}	evaporation front position
α_i	volume fraction (for i = solid, liquid, gas)
ε	concrete porosity
θ	temperature
θ_{ref}	reference temperature for zero internal energy (0°C used here).
κ	thermal diffusivity
ρ_i	density of species i

Subscripts

a	air	T	total
D	dry	v	vapor
fr	at evaporation front	W	wet
g	gas	w	water
ℓ	liquid	∞	initial uniform value
S	solid		

ACKNOWLEDGEMENT

This work was performed under the auspices of the United States Nuclear Regulatory Commission.

REFERENCES

1. P. G. Kroeger, J. Colman, and K. Araj, "Thermohydraulics in a High Temperature Gas Cooled Reactor Prestressed Concrete Reactor Vessel During Unrestricted Core Heatup Accidents," First Proceedings of Nuclear Thermal Hydraulics, ANS, p. 123, 1983.

2. H. J. Reilly, et al, "Preliminary Evaluation of HTGR Severe Accident Source Terms," Appendix F, EGG-REP-6565, EG&G Idaho, April 1984.

3. H. Saito and N. Seki, Mass Transfer and Pressure Rise in Moist Porous Material Subjected to Sudden Heating, J. Heat Transfer, 99C, pp. 105 (1977).

4. K. Min and H. W. Emmons, "The Drying of Porous Media," Proc. of 1972 Heat Transfer and Fluid Mechanics Institute, Stamford University, 1972.

5. Y. Shiina and P. G. Kroeger, "Transient Moisture Migration and Phase Change Front Propagation in Porous Media," ASME AICHE National Heat Transfer Conference, ASME Paper No. 84-HT-7, Buffalo, N.Y., August 1984.

6. A. Dayan and E. L. Gluekler, Heat and Mass Transfer Within an Intensely Heated Concrete Slab, Int. J. Heat Mass Transfer, 25, pp. 1461 (1982).

7. A. Dayan, "Self-Similar Temperature Pressure and Moisture Distributions within an Intensely Heated Porous Half Space," Int. J. of Heat Mass Transfer, 25, pp. 1469, 1982.

8. J. D. McCormack, A. K. Postma, J. A. Schur, "Water Evolution from Heated Concrete," Hanford Engineering Development Laboratory, HEDL-TME-78-87, February 1979.

9. W. D. Murray and F. Landis, "Numerical and Machine Solutions of Transient Heat Conduction Problems Involving Melting or Freezing," Journal of Heat Transfer, Trans ASME, 82C, pp. 106, 1959.

10. Final Safety Analysis Report, Fort St. Vrain HTGR, Appendix E.

11. "HTGR Accident Initiation and Progression Analysis Status Report - Phase II Risk Assessment," GA-A15000, General Atomic Company, April 1978.

12. P. G. Kroeger and Y. Shiina, "Transient Moisture Migration of Physically and Chemically Bound Water in PCRV Concrete During Severe HTGR Accidents," BNL-NUREG-51813 or NUREG/CR-3946, Brookhaven National Laboratory, 1984.

INTERACTIONS AND FEEDBACK EFFECTS IN SEVERE ACCIDENT ANALYSIS

R. S. Denning

Battelle's Columbus Laboratories
Columbus, Ohio 43201, U.S.A.

ABSTRACT

In the Source Term Reassessment Study, the suite of computer codes was operated in a serial fashion such that many feedback mechanisms were approximated or ignored. The purpose of this paper is to identify the most important feedback mechanisms and to discuss their potential impacts on source term predictions.

INTRODUCTION

In order to predict the behavior of severe accident scenarios in light water reactors it is necessary to model complex and interacting phenomena. In state-of-the-art computer codes, such as those used in the Source Term Reassessment Study for the analysis of severe accidents, approximations are sometimes employed in which feedback effects are either ignored or treated simplistically.

In the United States severe accident analyses are being performed by the Nuclear Regulatory Commission to develop a better understanding of the risk to the public from severe accidents in existing nuclear plants, to determine the adequacy of proposed future standard plant designs to protect against severe accidents and to evaluate improved methods for predicting the release of radioactivity to the environment (source terms) in severe accidents. The results of these analyses will be used by the NRC to make decisions that could lead to changes in regulations or regulatory requirements. It is therefore necessary to develop a quantitative understanding of the level of uncertainty associated with unmodeled or poorly modeled feedback effects or to develop improved models in which the feedback effects are included in the analysis. The purpose of this paper is to identify some of the important interactions and feedback effects which are either ignored or treated simplistically in state-of-the-art methods of analysis.

BACKGROUND

Subsequent to the accident at the Three Mile Island Unit 2 Plant, the NRC undertook the Severe Accident Research Program (SARP) /1/ to develop a better understanding of severe accidents in light water reactors and the level of risk posed by these accidents to the public. At the conclusion of Phase I of SARP, consideration will be given to the adequacy of existing plant designs to protect against severe accidents and to possible changes in regulations and regulatory requirements to account for an improved understanding of accident source terms. Two major studies integrate the results of Phase I research:

(1) Source Term Reassessment Study (NUREG-0956) /2/--the basis for Source Term Rulemaking which integrates the results of source term analyses (BMI-2104) /3/, the QUEST Study /4/ of source term uncertainties, and two special study groups on containment loads and containment performance.

(2) Severe Accident Risk Rebaselining/Risk Reduction Program (SARRP) /1/--the basis for severe accident decision-making which employs a methodology consistent with the BMI-2104 analyses to evaluate the public risk and the cost/benefit tradeoffs of modifications to the design and operation of six reference plants.

The computer codes used in the BMI-2104 analyses are identified in Figure 1. In the BMI-2104 Study these codes were applied in the serial fashion indicated in the figure. Thus some potentially important feedback effects between the fundamental processes were ignored or treated in an approximate manner.

Whereas Phase I of SARP involved a broadly-based research program aimed at developing a comprehensive understanding of severe accidents, Phase II of SARP will be more closely focused on the resolution of specific issues. Many of the most important issues that have been identified involve interactions and feedback effects that are the subject of this paper. In addition, Phase II of SARP will be directed at the completion and validation of a set of mechanistic codes for severe accident analysis. It is anticipated that the mechanistic codes will be grouped into code packages in which transfers are made between codes as a function of time permitting feedback effects in the analysis. Figure 2 illustrates the relationships among the principal mechanistic codes under development.

POTENTIAL INTERACTIONS AND FEEDBACK EFFECTS

In performing severe accident safety studies, such as those in the Source Term Reassessment Study and the Severe Accident Risk Rebaselining/Risk Reduction Program, it is necessary to analyze a number of fundamental processes that are part of severe accident behavior. For the purpose of this paper we consider the following fundamental processes:

Thermal behavior
Mass transport--aerosols and fission products
Mass transport--coolant and gases
Mass transport--corium
Fission product decay
Chemistry
Reactor kinetics
Structural response
Operator response

Interactive phenomena are those in which coupling occurs between different processes. Table I identifies and shows a number of important interactive phenomena that were treated superficially or ignored in the BMI-2104 analyses. Each of these interactive phenomena will be briefly described and its potential importance to accident consequences discussed.

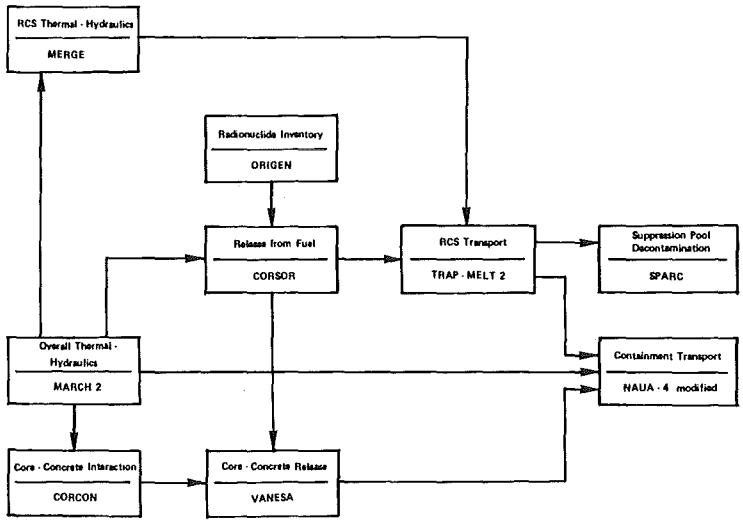

FIGURE 1. BMI-2104 COMPUTER CODES

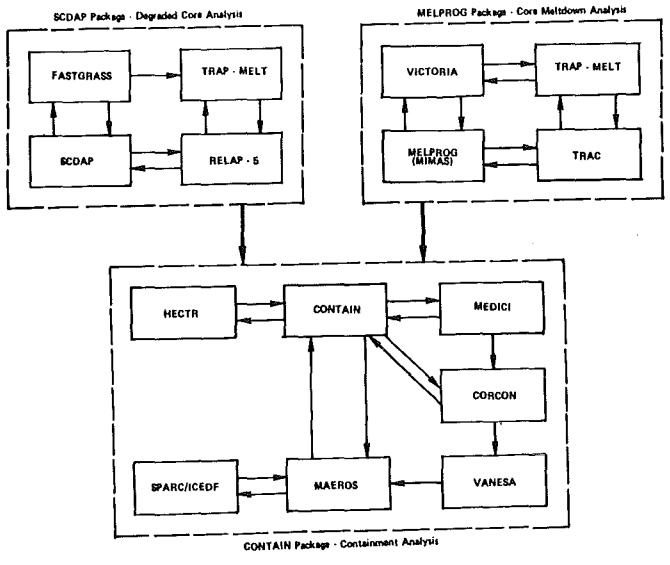

FIGURE 2. MECHANISTIC CODES UNDER DEVELOPMENT

TABLE I. INTERACTIVE PHENOMENA IN SEVERE ACCIDENT ANALYSIS

Interactive Phenomena / Fundamental Process Analyzed	Thermal	Mass Transport-Aerosols and Fission Products	Mass Transport-Coolant and Gases	Mass Transport-Corium	Fission Product Decay	Chemistry	Reactor Kinetics	Structural Response	Operator Response
Decay heat distribution	X	X	X	X	X			X	
Natural convection flow	X	X	X		X			X	
Radiation heat transfer-aerosol interaction	X	X							
Mass transport limitations to fission product and aerosol release	X	X	X			X			
Changes in chemical form of fission products	X	X	X		X	X			
Fuel slumping-hydraulic interactions	X	X	X	X		X		X	
Reevolution of deposited fission products	X	X	X		X	X			
Aerosol resuspension		X	X					X	
Coupling between containment thermal-hydraulics and aerosol processes	X	X	X			X			
Containment performance under containment loads	X		X	X				X	
Operator actions to control the accident			X				X		X

Decay Heat Distribution

In the MARCH 2 code the loss of decay heat from the fuel associated with fission product release, and the transport of this heat source is modeled but not in a manner that is completely consistent with the fission product release and transport analyses performed by CORSOR, TRAP-MELT, and NAUA. The prediction of the partitioning of the heat source to the containment atmosphere, to ice beds, to suppression pools, and to sumps can affect the loads on containment, the timing of containment failure and the thermal-hydraulic conditions in the containment atmosphere.

One of the key outstanding issues in source term analysis is the decay heating of RCS surfaces by deposited radionuclides potentially resulting in the reevolution of fission products. Table II indicates the fractional decay heat associated with each of the fission product groups at one hour after shutdown. Since the BMI-2104 analyses indicate that large fractions of these radionuclides would be deposited within the RCS for most core meltdown sequences, it is evident that a great deal of heat (e.g., on the order of 10 MW) could be released to RCS surfaces.

TABLE II. FRACTION OF DECAY HEAT ASSOCIATED WITH RADIONUCLIDE GROUPS (1 HOUR AFTER SHUTDOWN)

Group	Xe	I	Cs	Te	Sr	Ru	La
Fraction of Decay Heat	0.039	0.193	0.063	0.091	0.056	0.078	0.481

Natural Convection Flow

The MARCH 2 code models the flow through the RCS as one dimensional with the flow rate driven by the leakage from the system during depressurization, boiloff of water from the core and condensation of steam in the steam generator. Recently, analyses have been performed that indicate recirculation patterns may be established within the vessel /5/, particularly between the hot core and colder upper plenum structures of a PWR. The effects of recirculating flow could have a major impact on the timing and phenomenology of severe accidents such as: increased time to meltdown, increased hydrogen production from Zircaloy and steel oxidation, melting of steel structures, increased release of fission products from the fuel, decreased retention of fission products within the RCS, and even alternate modes of failure of the RCS due to overheating. The magnitude of convective flow patterns in the RCS is a major outstanding issue. Analyses are being performed with the TRAC code, a new two-dimensional version of the MIMAS code, and the COBRA code to determine the magnitude of the effect. It appears likely that, in the future, severe accident analysis codes will need to account for recirculation flow in-vessel.

Natural convection in the containment may also be an important phenomenon. Within a compartment, natural convection is typically accounted for as a mechanism that enhances heat transfer between the surfaces and atmosphere. Natural convection may also be a component of the driving force for flow between compartments in a multi-compartment analysis, however. A minor effort

was undertaken in BMI-2104 to examine the effects of compartmentalization on source term analyses. Comparisons with more mechanistic models such as COBRA-NC are required to determine the adequacy of lumped parameter containment models to characterize natural convection driven flow.

Radiation Heat Transfer-Aerosol Interaction

The effect of aerosols on radiation heat transfer is not accounted for in the MARCH 2 code. Within the RCS, aerosols could act to inhibit heat transport by radiation between regions of the core and between the core and neighboring structures.

During concrete attack, significant heat loss is predicted to occur from the upper surface of the melt to structural surfaces in the reactor cavity. The presence of aerosols in the gas above the corium would result in reducing the heat loss to the cavity walls and increasing the gas temperature in the cavity.

Mass Transport Limitations to Fission Product and Aerosol Release

The CORSOR code uses empirically-based release coefficients for fission products and inert sources of aerosol material (e.g., control rods). These coefficients cannot account for potentially limiting mechanisms within the fuel, at the surface of the fuel, and in the gas. As discussed by Taig /6/, the large masses of inert aerosol-forming material predicted to be vaporized by the CORSOR code may be inconsistent with the equations of state of these materials. A mechanistic fission product release model, VICTORIA, is being written for the MELPROG code which can be used to evaluate the limits of applicability of a simple empirical model like CORSOR. Since significant credit is currently given to RCS retention of fission products in many sequences analyzed in BMI-2104, a reduction in the aerosol source term (with less sedimentation in the RCS) or a holdup of fission products in the fuel until after vessel failure can have a significant impact on the predicted release to the environment.

Changes in Chemical Form of Fission Products

In the BMI-2104 analyses chemical forms of the fission products are assumed which do not change during transport through the plant. A number of processes are being studied in NRC-supported research that could change the chemical forms of fission products and their subsequent transport behavior. Emphasis has largely focused on the chemical forms of iodine. Some processes under consideration are reactions of fission product species with borates from control materials, oxidation in standing or propagating flames, reaction with silver, radiation induced change, oxidation in high-temperature regions of the containment such as a reactor cavity or BWR drywell, evolution from water pools and reactions at containment surfaces to form organic iodides. As source terms are reduced by taking greater credit for the capture of the primary species released from the fuel and from the RCS, greater attention must be given to the secondary species produced later in the accident such as elemental iodine and organic iodides.

Fuel Slumping--Hydraulic Interactions

The selection of fuel slumping models in MARCH 2 has been shown to have a major effect on the amount of hydrogen produced in-vessel, the flow-rate through the RCS and the temperatures of RCS structures. Slumping of hot fuel debris into the reactor lower plenum can produce steam that feeds steam-starved regions of hot Zircaloy, enhancing oxidation. Slumping can, however, also lead to flow blockage and the isolation of regions of hot fuel. Similarly runoff of hot cladding can either enhance oxidation as fresh surface is exposed to steam or reduce oxidation by cooling the Zircaloy cladding material. Although the early stages of fuel degradation are being studied experimentally, the latter stages involving major slumping and hydraulic interactions would involve a scope of experiments beyond those currently planned. It will be necessary to rely on advanced modeling efforts, such as MELPROG, to provide a basis for determining the range of conditions that is possible.

Reevolution of Deposited Fission Products

The BMI-2104 analyses have focused on the initial removal of the fission product primary species released from the core and from the RCS. However, once these primary species have been removed from the gas region of the RCS or containment, consideration must be given to processes that could lead to reevolution of fission products and make them again potentially available for release. Within the RCS the principal issue involves the potential for the release of volatile fission products as the result of decay heating of structures. Consider a deposit of 80 percent of the volatile fission products equally distributed on 45 MT (100,000 lbm) of steel in a PWR upper plenum. At one hour after shutdown the adiabatic heatup rate for this mass of material would be 1710 K/hr (3,070 F/hr). Assuming gas phase equilibrium the maximum quantities of CsI and CsOH that could be in vapor form in the upper plenum of a PWR as a function of temperature are illustrated in Table III. Thus if the upper plenum temperatures reach the vicinity of 1089 K (1500 F) significant revaporization of CsI and CsOH from surfaces could occur. Whether or not these temperatures will be reached or not will depend on the heat loss from the RCS and the extent of natural circulation. The delayed release of volatiles from RCS surfaces could be particularly effective in increasing the environmental source term, since the release could result in small aerosols with slower removal rates in the containment, perhaps being released near to or following containment failure.

TABLE III. HYPOTHETICAL MAXIMUM QUANTITIES OF SPECIES AIRBORNE IN RCS UPPER PLENUM AS A FUNCTION OF TEMPERATURE

Temperature		CsI		CsOH	
		Mass Airborne	Percent Core Inventory	Mass Airborne	Percent Core Inventory
F	K	kg	%	kg	%
1000	811	4.8×10^{-3}	1.9×10^{-2}	5.3×10^{-2}	4.0×10^{-2}
1500	1089	1.24	4.9	5.07	3.8
2000	1366	25.9	102	71.5	54

As discussed earlier, the release of fission products to the containment atmosphere from water pools and surfaces can be a particularly important consideration in accident sequences in which the primary source of fission product species is very effectively attenuated. In the BMI-2104 study a generic analysis of the long-term release of more volatile forms of iodine was made that indicated a potential source of 10^{-4} to 10^{-3} release fraction for the more volatile iodine forms.

Aerosol Resuspension

Aerosol resuspension is analogous to vapor reevolution. Within the RCS, resuspension could occur in high pressure sequences at the time of core slumping into the lower head of the vessel. The potential for resuspension of aerosols is being studied experimentally at ORNL.

Within the containment, aerosols could be resuspended as the result of blowdown forces at the time of containment failure or as the result of the flashing of water pools in the containment following massive containment failure. Analyses performed in the QUEST study indicated that containment hole sizes would have to exceed the order of 10 m^2 for either mechanism to become significant. Recent studies by the Containment Performance Working Group /7/ of the NRC indicate that this type of massive failure of a containment is unlikely.

Coupling Between Containment Thermal-Hydraulics and Aerosol Processes

In the BMI-2104 analyses, thermal-hydraulic conditions in the containment obtained from the MARCH 2 code were provided to the NAUA code to calculate such effects as aerosol growth by condensation and diffusiophoretic deposition resulting from steam condensation on surfaces. In actuality, the processes are closely coupled and the magnitudes of these effects as analyzed in the BMI-2104 studies must be considered representative rather than best-estimate. Further analyses with the CONTAIN code and the results of DEMONA tests planned in the FRG should help to resolve uncertainties in this area.

A major outstanding issue is the potential for the production of aerosolized core material in high pressure meltdown accidents at the time of vessel failure and the potential for direct heating of the containment atmosphere by this dispersed core debris. This issue has been addressed by the Containment Loads Working Group of the NRC /8/. Sensitivity studies performed by group members indicated that heating of the containment atmosphere by heat transfer alone from aerosolized core debris would probably not threaten the integrity of a large dry PWR containment. Significant chemical reaction of unoxidized zirconium, steel and uranium dioxide in the aerosol could however result in pressures well in excess of the expected containment failure pressure. Resolution of the issue will be obtained through an experimental and model development effort at Sandia.

Containment Performance Under Containment Loads

In parallel with the BMI-2104 analyses, the NRC has been investigating the likelihood and expected modes of containment failure in severe accidents. The Containment Loads Working Group has been assessing the character and magnitudes

of imposed loads and the Containment Performance Working Group has been investigating likely modes of containment failure leading to increased leakage. The results of the BMI-2104 analyses and the two working groups are to be integrated in the report NUREG-0956. Preliminary analyses have been performed with the BMI-2104 codes in order to evaluate the effects on source terms of enhanced leakage as opposed to massive failure of the containment. The results of these analyses indicate that the source term is sensitive to the hole size, the timing of increased leakage versus the release of fission products to the containment, and the rate of gas generation in the containment. In order to influence the thermal-hydraulic character of the accident or result in significant environmental release the leakage must be orders of magnitude higher than design leakage (e.g., 50 percent per day). Enhanced leakage with increased pressure, rather than massive failure at a threshold pressure, does not necessarily lead to reduced environmental source terms of radionuclides for all accident sequences. In those important sequences in which containment failure could follow closely after core meltdown, however, enhanced leakage rather than massive failure would provide additional time for deposition in the containment and prevent the very large source terms calculated for these sequences in WASH-1400.

Operator Actions to Control the Accident

With the BMI-2104 code suite it is possible to make a priori assumptions about how the operator will respond to an accident sequence and to adjust the appropriate boundary conditions of the problem accordingly. Primarily operators can by their actions directly affect reactor kinetics and reactor hydraulics. Modeling the response of operators to their perception of plant parameters is beyond our level of understanding of human behavior, however.

The behavior of the operator is a major source of uncertainty in the analysis of severe accidents. The operator has the potential to turn minor events into major accidents, as in the TMI-2 accident, or to take innovative actions to minimize the consequences of an accident. Improving operator performance is probably the most cost-effective means of risk reduction. Operator performance is being investigated in the Severe Accident Sequence Analysis program and in accident management studies in the United States.

CONCLUSIONS

Although the methodology demonstrated in the BMI-2104 analyses represents a major improvement in the modeling of accident phenomena relative to WASH-1400, a number of feedback effects are either treated approximately or neglected in the analyses. Some of the feedback effects have the potential to lead to major changes in predicted source terms. Of these the most important appear to be: reevolution of radionuclides from RCS surfaces, recirculating flow patterns in the reactor coolant system, changes in fission product chemical form, direct heating of the containment atmosphere by dispersed aerosols, containment performance under containment loads, and operator actions. Phase II of the NRC's Severe Accident Research Program is focusing on the resolution of these key outstanding issues. Resolution of the issues will be obtained in the form of improved computer models, reasonably validated against experimental data, which are operated in parallel as necessary to allow for feedback between phenomena.

REFERENCES

1. "Nuclear Plant Severe Accident Research Plan", NUREG-0900, January, 1983.

2. "Source Term Reassessment Study", NUREG-0956, to be published.

3. J. A. Gieseke, et al, "Radionuclide Release Under Specific LWR Accident Conditions", draft Volumes I to VI, 1984.

4. R. J. Lipinski, et al, "Uncertainty in Radionuclide Release Under Specific LWR Accident Conditions", SAND84-, to be published, 1984.

5. V. E. Denny and B. R. Sehgal, "Analytical Prediction of Core Heatup/Liquefaction/Slumping", International Meeting on Light Water Reactor Severe Accident Evaluation, P 5.4-1, August, 1983.

6. A. R. Taig, "Release and Retention Phenomena in Degraded Cores", ANS Topical Meeting on Fission Product Behavior and Source Term Research, July, 1984.

7. C. H. Hofmayer, et al, "Containment Leakage During Severe Accident Conditions", Second Workshop on Containment Integrity, June, 1984.

8. Memorandum from Melvin Silberberg to Distribution "Containment Loads Working Group Meeting at EPRI, Palo Alto, February 1-3, 1984", March 30, 1984.

THE EFFECTS OF GAS EXPLOSIONS IN FREE AND PARTIALLY CONFINED CLOUDS ON NUCLEAR POWER PLANTS

H. Pförtner, H. Schneider

Fraunhofer-Institut für Treib- und Explosivstoffe
7507 Pfinztal, Germany

W. Drenkhahn, C. Koch

Kraftwerk-Union AG, 8520 Erlangen, Germany

ABSTRACT

For the design of a nuclear power plant it is very important to know realistic values of the overpressure build-up in a chemical explosion. To obtain a further insight into the complex pattern of events in this field experimental investigations were carried out in free and partially confined homogenous clouds with hydrogen as a fuel. The results of the experiments in an unconfined hemispherical configuration show a distinct dependence of the flame velocity on the cloud size which does not exceed, however, an upper limiting value. To increase the turbulence effects in the experiments under partially confined conditions a fan was used. Depending on the fan speed the flame velocity was strongly influenced. In the case of the maximum fan capacity a transition from deflagration to detonation was observed.

INTRODUCTION

Extensive studies and the accidents which occur despite intensified primary explosion protection have shown that chemical explosions cannot be entirely excluded. Accordingly, additional protective measures must be taken, irrespective of the probability of occurence of such an event. To estimate these measures further information about the generation of chemical explosions and their effects on buildings and plants must be compiled. Especially for the design of a nuclear power plant it is of substantial interest to know realistic values of the overpressure build-up produced by chemical explosions.

Despite the fact that a lot of experiments carried out in this field and most of the accidents have shown that in a more or less free cloud a deflagration with rather low overpressures is by far the most probable mode of combustion in an accidental situation, a detonation with considerably higher overpressures is discussed, too.

Therefore, the most important question in this connection is under which conditions the transition from a deflagration to a detonation will occur in a free or partially confined gas cloud near the plant.

EXPLOSIVE EVENTS IN A FUEL AIR MIXTURE

If an explosible fuel/air mixture is ignited, there will always be, initially, a combustion wave whose rate of propagation is given by the laminar burning velocity and the ratio of the densities ahead of and behind the flame front. Now, as a result of turbulence effects this velocity could increase as the distance covered by the flame increases, which means that the velocity would have to be expanded by a turbulence factor to get the actual flame velocity.

The information of a shock wave as a precondition to the change from a deflagration to a detonation is therefore determined by the nature of the process of flame acceleration which is closely linked with the rate of energy release. Flame propagation at normal flame velocities, well below the sound velocity of the unburned gas mixture, will certainly not result in a detonation. On the other hand, there must be a detonation if the energy density, as a function of time, is high enough to initiate a shock of sufficient intensity. This high power density necessary to initiate a detonation is normally only available from high explosives.

RESULTS OF FORMER EXPERIMENTAL INVESTIGATIONS

This statement is confirmed by many experiments which have been carried out in our institute within the last ten years. Quantities as low as 8 g, 30 g and 80 g of high explosive, respectively, were sufficient to initiate gas detonations in stoichiometric ethylene/air, propylene/air and propane/air mixtures; it was not possible to initiate a detonation in methane/air mixtures even with 2.500 g of high explosive.

In a real cloud of propylene/air with its concentration gradients 300 g of high explosive did not suffice to initiate a detonation compared with 30 g in a stoichiometric mixture.

When igniting with flames, exploding wires or pyrotechnical fuses no events resembling a detonation were observed, in the case of methane even in volumes up to 12,000 m^3 with fan and obstacle induced turbulence. The overpressures measured in the interior of the reacting mixtures were less than 0,1 bar. Similar results were obtained in plastic tube experiments up to a length of 28 m which, when ignited deflagratively, no significant flame acceleration could be found even with turbulence generating obstacles.

In double balloon experiments, where two balloons were connected with an opening of about 30 cm in diameter, the possibility was simulated that a detonation starts in a building or facility and is then transmitted to a free spherical cloud.

In the second balloon which had not been ignited initially this merely triggered a fast deflagration whose velocity decreased with increasing distance of the flame. When the detonation was transmitted into a plastic tube filled with stoichiometrically premixed ethylene/air mixture, it was propagated, however, over the whole length; i.e. the propagation of a detonation obviously depends on the geometry of the cloud, too.

In other experiments the effect of an isochoric explosion transmitted into a gas mixture in an outer space after failure of a wall was investigated with failure pressures between 0.17 and 3.6 bars. Independent on the size of the outer cloud there was no essential acceleration of the flame. The overpressures generated by the flame were much lower than the values due to the failure pressure up to a distance of 25 m. In summary it can be said, indeed, that free gas clouds can be made to detonate only by sufficiently strong detonative initiation, if at all.

Nevertheless, as already mentioned, there still exists the idea that especially in large clouds the acceleration of the flame due to turbulence effects could become high enough to cause a detonation.

RESULTS OF RECENT EXPERIMENTAL INVESTIGATIONS

To get a further insight into the flame acceleration mechanisms within the PNP safety research program experimental investigations were carried out in free and partially confined clouds the aim of which was to measure the flame velocity and the overpressure depending on the cloud size and the partial confinement. The experiments under partially confined conditions were extended to fan induced turbulences to increase the turbulence effects. Because of the high laminar burning velocity and the importance in the PNP-project hydrogen was used as a fuel. These experiments were performed with Interatom as a contractor.

The free gas clouds were simulated by hemispherical balloons consisting of thin polyethylene foil. The balloons were filled with nearly stoichiometric hydrogen/air mixtures with volumes between 7.5 and 2100 m^3 corresponding to balloon diameters between 3.0 and 20.0 m. The gas mixtures were ignited by exploding wires in the center of the balloon. In this way a good spherical symmetry of the pressure field and the flame propagation without any reflections of the pressure wave was obtained. The overpressures were measured by piezoresistive gages installed on the floor. The flame propagation was filmed by high speed cameras. The maximum overpressures measured were between 22 mbar and 63 mbar corresponding to flame velocities between 39 and 84 m/s (Table I). These results show that there is a evident dependence of these values on the cloud size due to flame induces turbulence increasing with the volume of the fuel/air mixture. The recalculated turbulence factors, i.e. the ratio of turbulent and laminar burning velocity, indicate that there exists a limiting value which is reached asymptocally so that the flame front velocity cannot increase arbitrarily with increasing flame path.

This result which is in agreement with statements of Strehlow and Wagner [1,2] is logical insofar as the velocity fluctuations u' cannot exceed the flow velocity

$$u = (E - 1) \cdot S_t \qquad (1)$$

were S_t is the turbulent burning velocity and E the expansion ratio, i.e. the ratio of the densities ahead of and behind the flame front, respectively. So, several turbulent flame models lead to a maximum turbulence factor between (E-1) and E.

Karlovitz [3] correlates the flame induced turbulent velocity component with the difference in the kinetic energies of the expansion and the normal velocity component. In connection with this consideration the experimental results lead to the relation

$$f_t = 1 + (E-1) \cdot \left[1 - \left(\frac{21.22 \cdot S_o}{21.22 \cdot S_o + r_o} \right)^2 \right]^{1/2} \qquad (2)$$

Abdel-Gayed et al. [4] show that the eddy diffusivity is proportional to $[1 - \exp(-t/t_L)]$, where t is the elapsed time for cloud growth and T_L a scaling parameter. The time t is linked with the cloud radius r_o and the burning velocity S_o. As the turbulence factor is proportional to the square root of the diffusivity, it can be described by the relation

$$f_t = 1 + (E-1) \cdot \left[1 - \exp\left(- \frac{0{,}55\ r_o}{(E-1) \cdot S_o} \right) \right]^{1/2} \qquad (3)$$

This very important result means that in a stoichiometric hydrogen/air mixture at room temperature with $E \sim 7$ the maximum flame front velocity of about 125 m/s will not be exceeded even in very large clouds corresponding to a maximum overpressure of about 130 mbar.

The checkup of these equations for other fuels but hydrogen like methane and propane shows that there exists a general validity if

$$f_t = 1 + (E-1) \cdot \left[1 - (1 + 0{,}02\ r_o)^{-2} \right]^{1/2} \qquad (2a)$$

or

$$f_t = 1 + (E-1) \cdot \left[1 - \exp(-0{,}038\ r_o) \right]^{1/2} \qquad (3a)$$

In Figure 1 Eq. (2a) and Eq. (3a) are compared with the experimental values for a stoichiometric hydrogen/air mixture with E = 6.93.

Very similar results were obtained under partially confined conditions. The partial confinement consisted of two parallel walls, 3 m high and 10 m long in a distance of 3 m closed at one end. The ignition took place in the center of the closed side.

The results of these experiments which were carried out with rich hydogen/air mixtures show that in absence of an additional turbulence the flame velocity is not influenced by the confinement and it is determined by the initial hemispherical propagation of the flame front (Table II).

Only when the flame leaving the confinement a stronger acceleration due to the jet-like expansion of the gas mixture ahead of the flame front was observed. By this jet additional turbulence effects were induced so that the flame front velocity reached values in the unconfined space up to 200 m/s corresponding to overpressures of more than 200 mbar.

In order to increase the turbulence effects accelerating the flame in a more defined way a fan was located near the ignition source at the closed end of the lane. The fan had a diameter of 1.25 m and a maximum capacity of 24.000 m^3/h. It produced a turbulent flow field in the lane which was maintained during the combustion process.

Different experiments with 50, 75, 90 and 100 % of the full fan capacity were carried out. While in all cases the flame front velocity between the ignition source and the fan was about the same as in the experiments without additional turbulence it increased strongly after the flame had passed the fan (Table III). So, with lower fan capacities the flame velocities reached values between 170 and 190 m/s which, in a certain distance from the fan dropped to a velocity of about 110 m/s. With the full capacity, however, a flame front velocity of 222 m/s was measured. After a flame path of about 3,5 m from the ignition point the flame was still accelerated and the transition from deflagration to detonation occured near the wall. As the flame velocity is well below the sound velocity of the unburned mixture it is assumed that the high flow velocity induced by the high flame velocity interacted with the boundary layer near the wall producing still higher turbulences which initiated the detonation. This was the first time that such a transition was observed in a more or less free cloud only confined by two parallel walls.

Figure 2 shows the flame contours and the path/time dependence of the flame front which results in a detonation velocity of about 2080 m/s. The overpressure measured was as high as 25 bars.

CONCLUSIONS

The flame front velocity in an unconfined premixed cloud depends distinctly on the cloud size due to flame induced turbulences. An upper limiting value is not exceeded, however.

In partially confined regions like a lane without additional turbulences the flame velocity is determined by the initially formed hemispherical flame front. Only at the end of the lane a flame acceleration occurs because of the jet-like expansion. With additional turbulences within the lane produced by a fan with a sufficiently high fan capacity the transition from a deflagration to a detonation occurs at least with hydrogen as a fuel.

This transition, however, is likely restricted to hydrogen, because turbulence factors greater than 30 require very high turbulent velocity fluctuations which can only be produced under extreme conditions. In contrast to hydrogen most of the hydrocarbons have much lower laminar burning velocities so that the flame velocity necessary for the transition will not be obtained.

REFERENCES

[1]	Strehlow, R.A.	13th Loss Prevention Symp. (1980)
[2]	Wagner, H.Gg.	PTB-Mitteilungen 91 (1981)
[3]	Karlovitz, B.	Selected Comb. Problems (1954)
[4]	Abdel-Gayed, R.G. Bradley, D. Lwakabamba, S.B.	First Specialist Meeting (Int.) of the Comb. Inst. (1981)

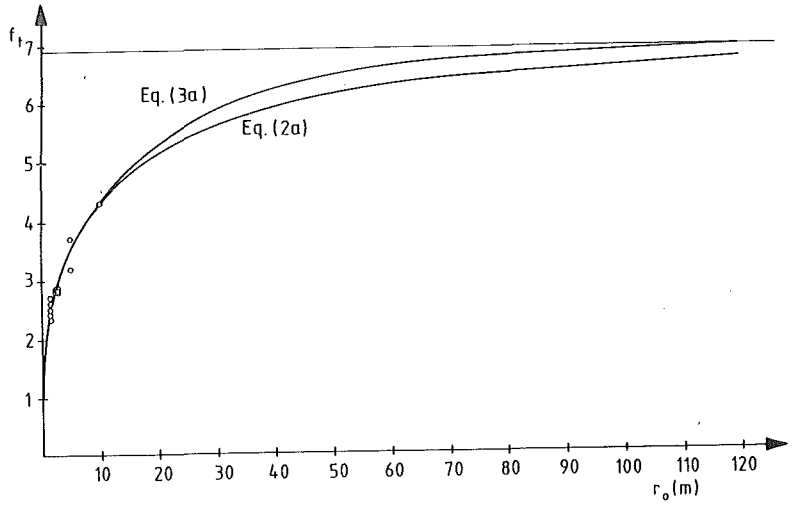

Figure 1 Turbulence factor f_t as a function of the cloud radius r_o for a stoichiometric hydrogen/air mixture (E^o= 6,93)

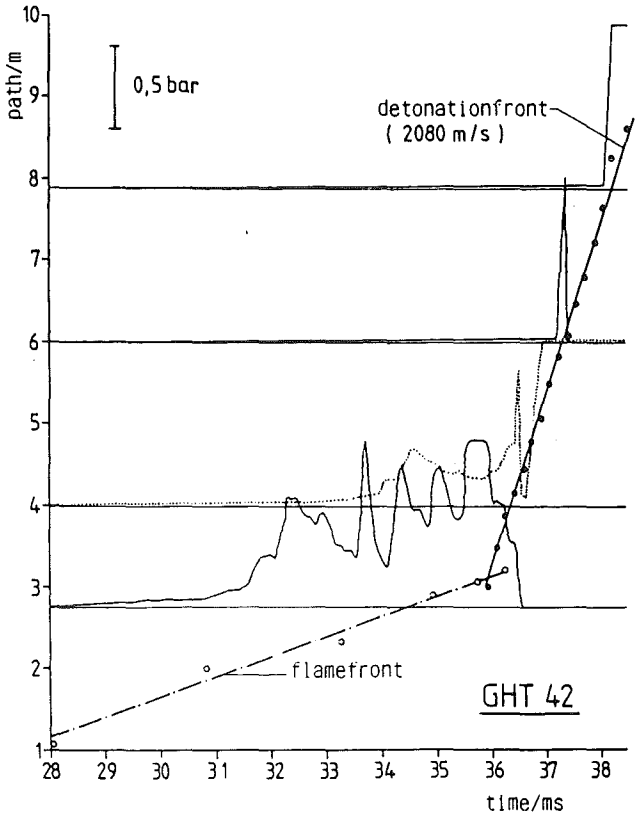

Figure 2 Top: Flame path/time diagram and typical pressure/time curves at 3, 4, 6 and 8 m distance from the ignition point

Bottom: Flame propagation with time;
dashed lines: deflagration
full lines: detonation

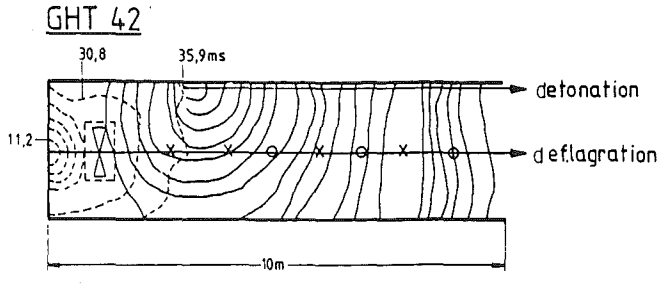

TABLE I: Results of the Balloon Tests

r_o (m)	c (Vol%)	M_o (g/mol)	M_F (g/mol)	T_o (K)	T_F (K)	S_o^{293} (m/s)	$S_o^{T_o}$ (m/s)	E (-)	S_F (m/s)	f_t (-)	$\bar{f}_t$ (-)
1,53	30,1	20.8	24,1	283	2378	2,59	2,44	7,25	-	-	
1,53	28,6	21,2	24,5	279	2341	2,41	2,22	7,26	46	2,85	
1,53	29,2	21,0	24,4	282	2374	2,48	2,32	7,25	46	2,73	
1,53	29,1	21,0	24,4	282	2369	2,47	2,31	7,23	42	2,51	2,58
1,53	29,1	21,0	24,4	282	2369	2,47	2,31	7,23	41	2,45	
1,53	29,5	20,9	24,3	281	2378	2,52	2,35	7,28	45	2,63	
1,53	29,2	21,0	24,4	281	2373	2,48	2,32	7,29	39	2,31	
2,88	27,2	21,5	24,8	286	2273	2,23	2,14	6,89	43	2,92	
2,88	29,4	20,9	24,3	279	2374	2,51	2,31	7,32	50,5	2,99	2,96
2,88	29,5	20,9	24,3	279	2376	2,52	2,32	7,32	54 korr.	(3,18) 2,96	
5,00	31,0	20,5	23,9	281	2368	2,68	2,50	7,23	59	3,26	3,46
5,00	25,9	21,9	25,1	283	2195	2,06	1,94	6,77	48	3,65	
10,00	29,7	20,9	24,2	283	2378	2,54	2,39	7,26	83,6 korr.	(4,82) 4,48	4,48

TABLE II: RESULTS OF THE LANE TESTS WITHOUT ADDITIONAL TURBULENCE

r_0 (m)	c (Vol%)	M_0 (g/mol)	M_F (g/mol)	T_0 (K)	T_F (K)	S_0^{293} (m/s)	$S_0^{T_0}$ (m/s)	E (-)	S_F (m/s)	f_t (-)	$\bar{f}_t$ (-)
1,50	35	19,5	22,5	281	2318	3,11	2,90	7,15	49	2,36	
1,50	39,1	18,4	21,0	272	2209	3,40	3,00	7,11	54	2,53	2,39
1,50	39,0	18,4	21,0	276	2213	3,40	3,07	7,02	49	2,27	

TABLE III: RESULTS OF THE LANE TESTS WITH FAN INDUCED TURBULENCE

r_0 (m)	c (Vol%)	M_0 (g/mol)	M_F (g/mol)	T_0 (K)	T_F (K)	S_0^{293} (m/s)	$S_0^{T_0}$ (m/s)	E (-)	Q (m^3/h)	S_F (m/s)	f_t^*
1,50	41	17,9	20,3	291	2178	3,46	3,42	6,60	12 000	172	7,62
1,50	38	18,7	21,4	293	2260	3,35	3,35	6,74	18 000	176	7,79
1,50	41	17,9	20,3	292	2179	3,46	3,44	6,58	18 000	179	7,91
1,50	41	17,9	20,3	288	2175	3,46	3,36	6,66	21 600	190	8,49
1,50	37	18,9	21,8	298	2290	3,28	3,38	6,66	21 600	186	8,26
1,50	36	19,2	22,1	285	23,02	3,20	3,05	7,02	24 000	222	10,37

DESCRIPTION OF VAPOR EXPLOSIONS BY THERMAL DETONATION AND HYDRODYNAMIC FRAGMENTATION MODELING

M. Bürger, C. Carachalios, D.S. Kim and H. Unger

Institut für Kernenergetik und Energiesysteme (IKE),
University of Stuttgart, Pfaffenwaldring 31, 7000 Stuttgart 80, FRG

H. Hohmann and H. Schins

Commission of the European Communities,
Joint Research Center, Ispra Establishment, 21020 Ispra (Varese), Italy

ABSTRACT

A hydrodynamic fragmentation model has been developed which is based on the stripping of the crests of waves produced by shear flow instabilities at the surface of the melt drop. The comparison with experimental investigations supports this model at least for Weber numbers > 1000 with respect to the general features, the fragmentation times and the drift and deformation behavior of the drops of melt. Incorporating this model in a steady state thermal detonation code, detonation cases for certain corium-H_2O premixtures are determined, which deliver input values for analysing the load to structures in structural dynamics codes. The fragmentation model is also used in a transient thermal detonation code for determining the escalation behavior under given triggering conditions.

INTRODUCTION

Vapor explosions caused by the contact of molten core material with coolant are an important issue within reactor safety analysis, because they could produce an early threat to the containment within a core melt accident. Many analyses have therefore been performed already in order to evaluate the possible load to structures due to vapor explosions as well as the conditions of initiation of large scale explosions. However, the load calculations are usually based on experimentally obtained conversion ratios of thermal to mechanical energy or on parametric models for the determination of the rapid heat transfer and pressure buildup. In recent models, see for instance /1/, the heat transfer from the fragments to the coolant is determined by means of an unsteady-state heat conduction model. Such approaches however cannot always assure absolutely conservative estimates. In particular, the conduction model of heat release for instance does not account for the turbulent flow effects inside a detonation wave. Although the choice of a rather small fragment size as compared to experimental values of large scale experiments may compensate for this, this procedure restricts the capability for extrapolations.

More insight into the processes and a more reliable means for extrapolations and use for reactor conditions can only be gained from a detailed modeling according to the essential physical mechanism of large scale vapor explosions, the thermal detonation mechanism /2/, /3/. A crucial point in this modeling is the description of the fragmentation process, which determines the heat transfer. While after initiation of the interaction in a

coarse premixture of melt and coolant thermally induced fragmentation must dominate, hydrodynamic fragmentation processes should dominate after some escalation of the pressure pulse. The latter processes are produced by the relative velocity of melt drops and coolant inside the detonation wave. The velocity equilibration taking place inside the wave, promoted by the fragmentation itself, gives however a strong restriction to the fragmentation and thus to the rapid heat release to the coolant. A restriction of similar efficacy is not evident from realistic considerations on the heat transfer from the fragments, at present.

Thus, in order to obtain the restrictions to the violence of explosions inherent in the interaction of the physical processes and in order to allow an extrapolative use of the model, e.g. to reactor conditions, the above processes have to be described within the thermal detonation modeling. The best estimate as well as conservative character of the model has then to be proved experimentally. First comparisons have already been performed /4/, globally with thermal detonation experiments and - for analysing the main part of the model - with hydrodynamic fragmentation experiments. A more detailed analysis of the latter will be shown here. At first, a short description of the hydrodynamic fragmentation model will be given. Finally, the model will be applied within a steady state and a transient thermal detonation model to corium-water sample cases.

MODELING OF DYNAMICS AND FRAGMENTATION

Part of the modeling, which has been done in addition to earlier thermal detonation models /2/, /3/ and which is described already in /4/, conceives improvements of the dynamic description, which determines the velocity equilibration between the flow components (coolant, melt). Instead of using empirical values for a mean drag coefficient of the drops of melt (which have been derived from single drop experiments and can therefore not be extrapolated to dispersions), a correlation is used which is related to the actual states of the drops in the dispersion. It includes the dispersion effects as well as the effect of drop deformation. For this, the deformation process had to be modeled, which was done by assuming deformation to ellipsoidal shapes. Thus, the description of the processes inside the detonation wave includes the movement of the drops of melt, their deformation and their mass loss due to fragmentation.

Detailed models on hydrodynamic fragmentation, caused by the relative flow of melt and coolant inside a detonation wave, have also been described in /4/. From these models, the wave stripping model seems to be the most appropriate from a first comparison with the experiment. It delivers also the strongest fragmentation. Therefore, only this model is considered here. The model is based on the stripping of capillary waves produced on the drop surface by the shear flow of the coolant. Traveling and growing waves are considered on the ellipsoidal drops of actual state. Stripping of fragments due to the relative flow derives from stripping criteria. These define a minimum wave (basic) amplitude for the occurence of stripping of the crests of the waves as well as - by an energy consideration - the stripped mass and the fragment size. Since the basic amplitude is reestablished by stripping, repeated stripping events at subsequent locations occur on the drop. These are accumulated in the region of the drop equator. Summing up the stripping rates at the different locations gives finally the actual stripping rate on the whole drop within a quasi-steady state approach.

Some modifications and extensions of the modeling described in /4/ have been performed in the meantime. While in /4/ a fixed deformation state of the drop has been assumed, argueing that the pronounced stripping at the

equator of the drop counteracts the deformation process, it has now been tried to model this effect. Within a rough approach, a cylindrical model of the drop - used already in /4/ for the Taylor instability model of breakup - is used complementarily to the ellipsoidal model. The stripped mass calculated from the ellipsoidal model is - within the cylindrical model - assumed to be only stripped at the cylindrical surface. The radius of the cylinder is then reduced correspondingly. Since this radius has been chosen equal to the semi-axis of the ellipsoid perpendicular to the flow, the reduction is directly transformed to the ellipsoidal model. This effect is added to the deformation of the drop due to the surrounding flow.

In addition, some small modifications have been performed. E.g., stripping is assumed to stop shortly behind the equator of the drop, whereas in the earlier model /4/ stripping was also considered on the lee side of the drop, using the irrotational flow solution without taking account of the flow separation. This means a reduction of the fragmentation rate as compared to /4/. An initial phase can be defined with respect to the motion of the drops and the fragmentation process. During an initial phase of potential flow the drops are not accelerated. On the other hand, deformation occurs due to the pressure distribution of the potential flow solution. A characteristic scale for the duration of this initial phase is given by the time the flow needs to pass the drop diameter. An initial phase of fragmentation may be needed to establish at first a pattern of waves with sufficiently high amplitudes on the drop. In a first approach a delay time corresponding to the drift delay may be assumed.

TRANSIENT THERMAL DETONATION MODEL

The transient thermal detonation model, described already in /5/, has been improved along the same lines as the steady state model. However, a simplified method has been chosen for the description of the fragmentation process. Instead of the fragmentation model a correlation for the actual rate of stripped mass has been developed and fitted to the model by comparing results obtained from the steady-state model with the respective formulations. The calculations give a very good agreement of the correlation with the model over a wide range of conditions (mass ratios of melt to coolant, initial mixture configurations, shock front pressures, Weber numbers, etc.). The constant of proportionality must however be determined separately for every material combination, but shows only small differences for the materials considered here. It must be mentioned, that - in contrast to other transient thermal detonation models (see /5/) - the present model includes the description of the relative motion of the drops of melt and the coolant (also taking into account the drop deformation) and, based on this, the coupling of hydrodynamic fragmentation to the actual flow situation. This is also valid for the correlation derived here.

In addition to this description of hydrodynamic fragmentation a thermal fragmentation model according to Corradini /6/ was incorporated in the transient model. With the inclusion of this thermal fragmentation model a detailed analysis of the escalation process can in principle be performed, starting with local vapor film collapse in some region of the coarse mixture, e.g. near a solid wall. While in the beginning only thermal fragmentation exists, the increase of the pressure pulse leads to an increase of hydrodynamic fragmentation, which should finally dominate. Within the present modeling the two fragmentation mechanisms can act separately or in a combined way. Thus, their relative importance on the escalation and propagation behavior of a thermal detonation wave and the development of a spontaneous interaction to a full steady-state detonation wave with possibly changing

fragmentation behavior can be examined.

Other improvements of the transient thermal detonation model concern the formulation of the triggering and boundary conditions. While in the earlier modeling an inflow plane behind the wave was defined by a somewhat artificial coupling of outside and inside conditions, a more physical description has now been performed, prescribing the physical conditions either at a solid wall, at a source point for spherical propagation or at an open end. In addition, the effect of arbitrary triggers can be superposed. Since saturation of the coolant often occurs at a wall side due to the induced flow, causing a pressure release, vaporisation had also to be considered within the model in order to analyse the further development of the detonation wave. This has been done by assuming equilibrium conditions between the coolant phases. Improvements have also been done with respect to the numerical formulation, especially of the shock fitting procedure. These improvements of the transient model allow more reliable analyses of the escalation process as well as of the transition to a steady-state detonation wave. By inclusion of the deterministic fragmentation description a deterministic prediction of the energy release and the pressure buildup during a thermal detonation is achieved.

RESULTS

Firstly, calculations have been performed for hydrodynamic fragmentation experiments with single drops of gallium in water streams in order to examine the hydrodynamic fragmentation model as well as the dynamic description of the drift and deformation processes of the drops. Based on this validation of the key parts in the thermal detonation model, sample cases which are relevant for reactor conditions have been analysed by use of the steady-state as well as the transient detonation model.

Experimental Examination of the Hydrodynamic Fragmentation, Deformation and Drift Models

A first comparison of the hydrodynamic fragmentation modeling with the experimental results gained at the IKE has already been presented in /4/. At least for Weber numbers greater than 1000 the experiments support the wave stripping model by phenomenology as well as by the results for the fragmentation times and the fragment sizes. Because of the modifications and extensions of the model mentioned above and also of a more detailed analysis of the experimental results /7/, the comparison is repeated now.

1. Fragmentation Times

A reexamination of the experimental results of /4/ has already been done in /7/, introducing modified as well as additional criteria for the fragmentation time. These various criteria have been chosen because of the uncertainties in determining the experimental fragmentation times due to the inherent difficulties to distinguish between the drop and the fragments. On one hand, the different criteria allow to determine fragmentation times for different, roughly defined stages of the fragmentation process and, on the other hand, to get a confirmation with respect to the trend of the data. As an important result it can be seen from Fig. 1, that no obvious tendency with the Weber number can be detected for the dimensionless fragmentation times (defined as usually, e.g. /4/) from any of the different criteria (for $We \gtrsim 400$). This result is adequate to a stripping model of fragmentation. Increases for $We \lesssim 400$ may indicate a different region of fragmentation, defined by strip-

ping of coherent skins with subsequent breakup instead of fully developed wave stripping with direct stripping of fragments from the wave crests (see also /4/, /7/).

In addition to the Criteria 1-3, which are the same as in /7/ (because of a printing error in /7/ it must however be remarked that Criterion 2 corresponds to doubling of the projected area of the "drop"), a new Criterion 4 has been introduced, replacing that of /7/ which overestimates the fragmentation time. This criterion assumes complete fragmentation after the lateral expansion of the shadow of the drop together with its stripped fragments has stopped. It is based on the consideration that after a phase of dominance of the deformation processes of the drop the stretching of the cloud of fragments in the direction of the flow should finally dominate. As can be seen in Fig. 1, the results from this criterion lie between the results of Criteria 2 and 3. Since the Criteria 2 to 4 are related to more final stages of the fragmentation process, a constant dimensionless fragmentation time of complete fragmentation in the range of 2.5 to 3.5 may be derived from the experiments, at least for Weber numbers We $\geq$ 400.

The results for different fragmentation grades (ratio of fragmented to initial drop mass) with the modified wave stripping model are also included in Fig. 1. Above certain limits of fragmentation, which occur especially for higher fragmentation grades because of the velocity equilibration, also practically constant dimensionless fragmentation times for certain fragmentation grades are obtained. The limits of fragmentation are stronger than in /4/, and the dimensionless fragmentation times for certain fragmentation grades are nearly doubled. This must already result approximately from stopping the fragmentation just behind the equator of the drop. Since the fragmentation process may be assumed to be essentially completed for fragmentation grades between 0.75 and 0.9, a dimensionless time of 1.5 to 2 for complete fragmentation may be derived as compared to the experimental values between 2.5 and 3.5. Thus, the theory gives the experimental order of magnitude. The lower theoretical results can be explained by the severe idealizations of the modeling. They assure the conservativity of the detonation description with respect to reactor safety.

2. Fragment Sizes

Mean values of the fragment diameter are derived from an evaluation of photographs of the experimentally obtained fragment distribution. For the gallium-water experiments DS-12, DS-15 and DS-18 (see /7/) the following values result respectively: 250 µm, 90 µm, 40 µm. The respective theoretical values, determined by mass averaging, are: 106 µm, 98 µm, 50 µm. Although the agreement for DS-15 and DS-18 appears rather good, smaller theoretical values were expected because of the idealizations of the modeling. However, further breakup of the stripped toruslike crest of a wave ring is not considered here, which would lead to significantly smaller theoretical fragment sizes. The much larger fragment size obtained experimentally for DS-12 can be explained by the lower Weber number of 630, for which the wave stripping may not yet be fully developed.

3. Deformation and Drift Processes

Fig. 2 shows results of the deformation behavior of the gallium drops from some of the experiments together with the theoretical results. In the model the pressure coefficient characterizing the pressure distribution around the drop was set to 1 during the initial delay phase. A theoretical value of 2.25 corresponds to the initial potential flow around a spherical drop. During the development of boundary layer separation this value must however

decrease to 0.7 in the region of developed flow. The value of 1 can therefore be understood as some average between the limiting values for potential and developed flow. Until now only data for spherical shapes have been taken due to a lack of data.

In the dimensionless representation by Fig. 2, the deformation behavior of the different experimental cases with Weber numbers varying from 630 to 3520 is rather close. This is also valid for the theoretical results which agree rather well with the experimental results until theoretically a maximum is reached. Experimentally the lateral extension continues to grow until a maximum is reached much later (see fragmentation Criterion 4, Fig. 1). However, while the theoretical results only concern the drop remnant, the cloud of fragments enlarges the apparent "drop" in experiment. This lateral enlargement can be explained by the effects of lateral flow of the fragments as well as by deformation effects of the cloud of fragments. It is however counteracted and finally stopped by the stretching of the cloud of fragments in the flow direction, caused by the subsequent stripping of fragments and the increase in fragment sizes.

The experimental results on the drift of the gallium drops can be seen in Fig. 3. Again the experiments DS-12, -15, -18 in the regime of higher Weber numbers (630 - 3520) are considered. They deliver nearly the same drift behavior in the dimensionless representation. This effect is reproduced by the theory. However, the theoretical drift develops more rapidly, which may be explained by the neglection of virtual mass effects, which are due to the momentum transfer to the coolant and the fragments. The mass loss history of the drop of DS-15 (fragmentation grade) is also included in Fig. 3 for illustration.

Due to the coupled description of the fragmentation, deformation and drift processes the present modeling allows detailed examinations of the experiments and thus enables to identify the dominant processes as well as to limit the regions of uncertain physical values, such as the pressure coefficient, for instance. Because these uncertain quantities are related to specific processes, they can in principle also be determined easily for relevant ranges by separate, specific experiments. Thus, the detailed modeling allows extrapolations with the detonation model. In contrast to this, the global correlations and parameters used in the earlier detonation models /2/, /3/, which were derived from single drop experiments, do not allow reliable extrapolations.

From the above comparisons it can be concluded that the present model is consistent with the experimental results on the fragmentation, deformation and drift behavior of single drops. Also the theoretical fragment sizes lie in the experimental range. Conservativity with respect to the use in safety considerations is assured by the comparison on the fragmentation times, which indicates, that the times - although lying in the experimental range - are smaller than the experimental ones. Further analyses and comparisons should however be performed with other single drop experiments as well as with respect to dispersion cases in order to learn more about the capabilities of the models.

Thermal Detonation Calculations for Corium-Water Systems

After validation of key parts of the thermal detonation model, the application of the model to reactor related conditions may be justified, although some work has still to be done. Firstly, the stability considerations for the steady state model are restricted until now to the occurence of saturation at the Chapman-Jouguet plane. Secondly, nonhomogeneous heating of the coolant is not considered. Both restrictions make the conservativity of the results unsure and need therefore to be investigated in future. For this

paper, calculations have been performed with the steady state as well as with the transient detonation model, the latter without taking into account an initial delay phase. In both cases the same data of the coarse premixture have been chosen, which are given in Fig. 5.

1. Results from the Steady-State Model

The main result of the calculation shown in Fig. 4 is the strong restriction of the fragmentation grade and thus of the transfered heat, which occurs due to the counteraction of velocity equilibration. The results can be used for determining the possible load to structures. The main effects result from the expansion processes of the high pressurized region which is left behind by the detonation wave at the end state of the wave. In order to calculate the possible loads from such expansion processes, hydrodynamics codes such as PISCES (see /1/) can be used, taking the results of the detonation model as input values. Only some evaluations on the basis of the energy release calculated from the detonation model could be made here, using results from load calculations given in the literature.

For calculations with PISCES the heat flux into the water pool is needed. If a spherical propagation of the detonation wave is considered and the result of the plane wave calculation of Fig. 4 is used approximately, a coarse mixed region of volume 18.3 m^3 is affected in 4 ms. With a fragmentation grade of 13 %, a heat transfer of $7.5 \cdot 10^9$ J into 8.9 t water during this first rapid phase of vapor explosion results. On the other hand, a sample calculation with PISCES and ANSYS given in /1/ shows that 10^{10} J of heat, released in 4 ms into 10 t water, do not lead to a break of the reactor pressure vessel (RPV) of a nuclear reactor of Biblis type. Thus, the detonation case calculated here should not mean a threat to the RPV. This result must however be considered as preliminary, since it is only calculated for one coarse mixture configuration. Also the effects mentioned which question the conservativity of the model must be investigated further.

2. Results from the Transient Model

Calculations have been performed for an interaction starting at a solid wall. Instead by a thermal fragmentation model the initial energy release in a certain region near the wall is here parametrized. After a certain time only hydrodynamic fragmentation according to the wave stripping model is considered further. However, at the present state of the develoment of the transient model numerical problems still occured with the fragmentation rates determined from the wave stripping model. Therefore, these fragmentation rates have been halved for the present calculations. Thus, these results cannot be taken directly for safety considerations, but give in any case some insight in the escalation behavior and in the relation to the steady state case. In order to analyse this relation, the steady state case has been determined correspondingly with halved fragmentation rates.

The results show an escalation to a steady-state propagation, which can be seen in Fig. 5. A saturation plane follows a reaction zone and propagates with the same velocity as the shock front. Behind, a region with coolant vapor with nearly constant pressure is established, approximately equal to the end pressure at the saturation plane. In the saturation plane also velocity equilibration occurs. Thus, the wave is compatible with the calculation from the steady-state model. Also the characteristic quantities are practically the same. The shock front pressure of both models is about 25 MPa and the end pressure 9 MPa. In both cases the fragmentation grades are approximately 12 % and the lengths of the wave are 9 cm. Fig. 6 shows the time

development of the phase velocities and the fragmentation grade at a place after the arrival of the shock front for both the transient and the steady state model. Again the very good agreement can be demonstrated.

These results prove the consistency of the transient with the steady-state detonation model. Furthermore the escalation process can be considered. In the present case a length of approximately 5 times the wave length is required. An escalation threshold results, depending on the initial energy input. Only with an energy release of more than 500 J per cm^2 cross-section into a region of the length of 5 cm within a time of 100 µs an escalation occurs, whereas with a smaller input the wave finally decays (Fig. 7). Further analyses are necessary for interpretation of these results.

CONCLUSIONS

Detailed descriptions of the dynamics and of the fragmentation of the drops of melt have been incorporated in a steady-state and a transient thermal detonation model. These descriptions have been validated by means of experiments with single gallium drops. Applications of the detonation models for corium-water sample cases showed - besides an excellent consistency of the models - strong restrictions to the heat release. However, the transient model could only be used with a reduced fragmentation rate due to numerical problems. Based on the result of the steady-state model with the full rate, an evaluation on the threat to the RPV of a nuclear reactor was performed, using results from literature on load calculations. The result indicates that the RPV should withstand the explosion in this sample case. Further calculations with other cases and an extended modeling are however necessary to assure this conclusion. After solving the numerical problems with the transient model, this will give another important tool for risk analyses, delivering information on the escalation requirements and the effects of inhomogeneities in the coarse premixture as well as allowing examinations of the steady-state model with respect to stability considerations.

ACKNOWLEDGMENTS

This work was sponsored by JRC Ispra, Italy and the German Government (BMFT) through GRS.

REFERENCES

1. K. Wagler et al., "Druck und Beanspruchungsverläufe im RDB während einer postulierten Dampfexplosion im Verlauf eines hypothetischen Kernschmelzunfalls", Abschlußbericht BMFT 1500 493/9, KWU, Erlangen, Okt. 1983

2. A. Sharon and S.G. Bankoff, "On the Existence of Steady Supercritical Plane Thermal Detonations", Int. J. Heat Mass Transfer, Vol. 24, No. 10, 1981, pp. 1561-1572

3. W. Schwalbe, M. Bürger and H. Unger, "Investigations on Shock Waves in Large Scale Vapor Explosions", Proc. of Winter Annual Mtg. of ASME, Washington, D.C., Nov. 1981

4. M. Bürger et al., "Two Phase Description of Hydrodynamic Fragmentation Processes within Thermal Detonation Waves", 21st National Heat Transfer Conf., Seattle, July 1983

5. C. Carachalios, M. Bürger and H. Unger, "A Transient Two-Phase Model to Describe Thermal Detonations Based on Hydrodynamic Fragmentation", Int. Mtg. on LWR Sev. Acc. Eval., Cambridge, Mass., Aug. 1983

6. M.L. Corradini, "Analysis and Modeling of Steam Explosion Experiments", SAND 80-2131, Sandia National Lab., Albuquerque, N.M., April 1981

7. D.S. Kim et al., "Experimental Investigation of Hydrodynamic Fragmentation of Gallium Drops in Water Flows", Int. Mtg. on LWR Sev. Acc. Eval., Cambridge, Mass., August 1983

FIGURES

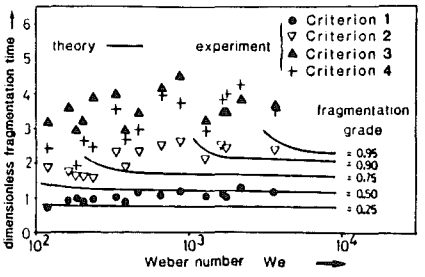

Fig. 1: Experimental and theoretical times for hydrodynamic fragmentation of single gallium drops in water streams

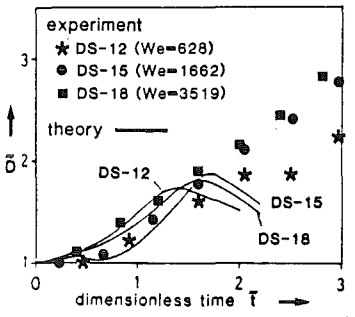

Fig. 2: Experimental and theoretical deformation behavior ($\tilde{D}$ = ratio of actual to initial drop diameter perpendicular to the flow)

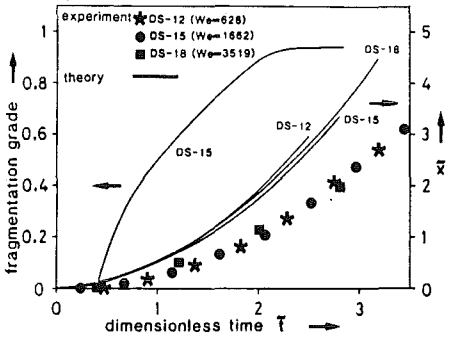

Fig. 3: Experimental and theoretical drift ($\tilde{x}$ = displacement of forward stagnation point, related to initial drop diameter)

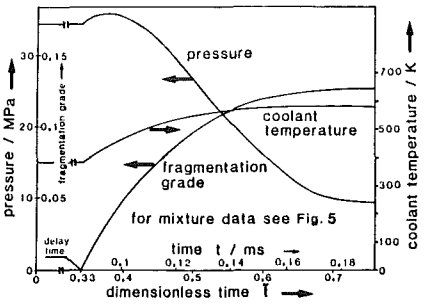

Fig. 4: Theoretical results of the steady state detonation model for a corium-water sample case

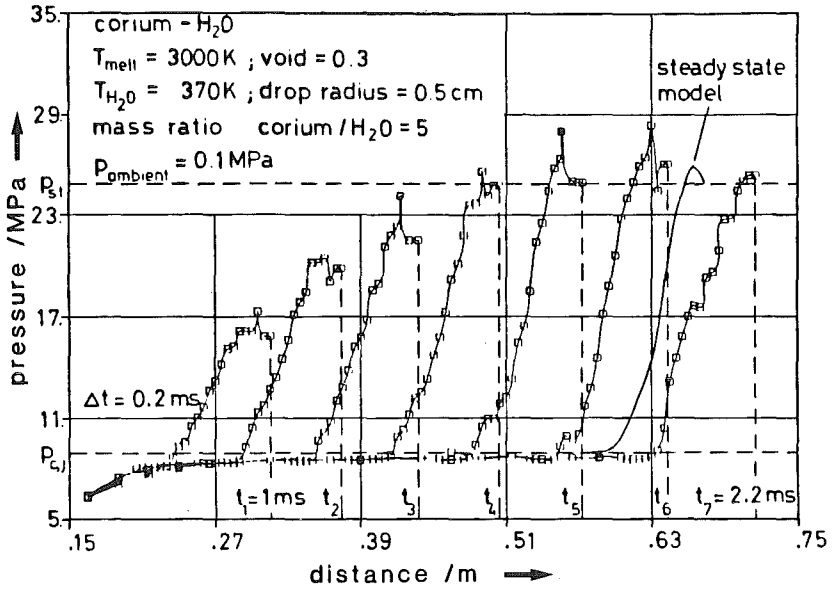

Fig. 5: Pressure development from the transient model and comparison to the steady state case from the steady state model ($P_{C,J}$ = Chapman-Jouguet pressure at the end of the steady state detonation wave, P_{st} = shock front pressure of the steady state case)

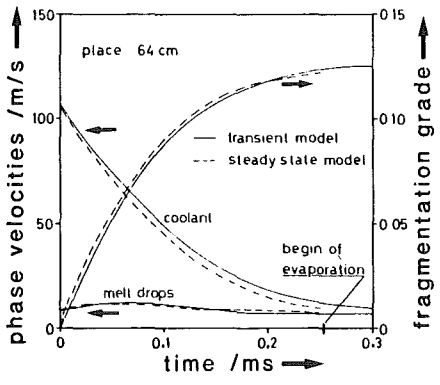

Fig. 6: Time development of the phase velocities and the fragmentation grade for both transient and the steady state model

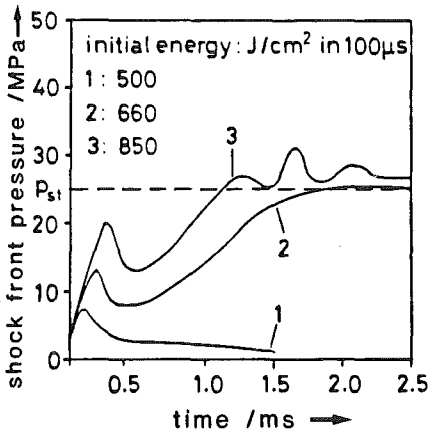

Fig. 7: Escalation behavior of the transient model for different values of the initial energy

CORE-CONCRETE INTERACTION: STATUS OF BETA EXPERIMENTAL PROGRAM

H. Alsmeyer

Kernforschungszentrum Karlsruhe
Federal Republic of Germany

ABSTRACT

The experimental BETA program is carried out at KfK with the principal goal to verify the existing computer codes on core concrete interaction. In BETA all the interaction processes during core melt/concrete contact are being studied, starting with very high melt temperatures of 2400 °C and following all the sequences until the melt is substantially frozen. The experiments at different interaction temperatures were specified following the requirements of the codes.

Tests in the early 84 show the reliable operation of the experimental facility. The experimental program starts with high temperature investigations of melt concrete interaction. The newest experimental results are discussed.

INTRODUCTION

Core melt down accident research in the FRG concentrates on risk assessment of nuclear power plants /1/. The dominant role of core concrete interaction on the possible overpressurization of the containment has led to the development of sophisticated computer codes such as KAVERN /2/, WECHSL /3/, and CORCON /4/. These codes calculate the core-concrete interaction, the energy fluxes, the generated gaseous and liquid products, crust formation, chemical reactions and melt front propagation. Verification of the codes was limited up to now on separate effect experiments or transient small scale experiments with reactor typical materials.

As the final step for code development and code verification, the BETA facility has been constructed as a large scale experiment. With closely connected experiments and pre- and post-test code calculations, the various processes during melt/concrete interaction and their models in the computer codes are studied in detail. At the end of the experimental BETA program, verified codes will be available to describe melt/concrete interaction during a hypothetical core melt down accident.

DESCRIPTION OF THE BETA-FACILITY

Following the needs of code verification, the BETA facility was constructed as a large melt facility with sustained heating of the simulated core melt in a concrete crucible (Fig. 1). All the interacting processes during melt/concrete contact will be investigated, starting with very high melt temperatures of more than 2000 °C, and following all the sequences until the melt is substantially frozen.

The principle idea is to investigate the different regimes which occur in the process of melt/concrete interaction with a sequence of experiments at different temperature levels, which are studied in BETA under controlled quasi steady conditions. The melt is heated internally in the BETA facility by induction heating with very high input power to keep the temperature of the melt constant, according to the need of a specific experiment. This approach has the advantage that the complex physical and chemical reactions can be elaborated in more detail and that the time scale approaches the real accident situation. Accordingly, heat flux and temperatures, melt fron penetration and most of the other relevant processes are simulated in a 1:1 scale, which is essential for the applicability of the experimental results to the real core melt down accident.

The main characteristics of the test facility are described in Ref. /5/. The melt consists of up to 300 kg steel and up to 300 kg oxidic phase contained in a concrete crucible of 38 cm inner diameter (Fig. 1). The concrete crucible (1) with the melt is enclosed by the induction coil (2) in its central part. The electric power supply feeding the coil, and its very large capacitor bank, is not shown here. The hood and offgas pipe (3) collect all gaseous products generated during melt/concrete interaction for physical and chemical analysis. On top of the crucible are both the reaction tank (4) to prepare the thermite generated melt, with an attached pouring spout, and a container (5) with dip-in measurement systems for melt analysis.

The most important measurements during the experiments are power input to the melt; temperatures, melt front position and moisture detectors in the crucible; temperatures of the melt; off-gas composition, and aerosol release.

FIRST EXPERIMENTAL RESULTS

The construction of the BETA facility was finished at the end of 1983. Operation began in February 1984. Three experiments, V0.1 to V0.3, have been conducted to test the equipment and measurement systems (Tab. 1). In experiment V0.1, the thermite melt generation and pouring device were successfully tested. The experiments V0.2 and V0.3 are the first sustained heating experiments and are similar to the experiments in the test matrix. They proved that the power input by induction heating is in accordance with the planned data and that continuous heating of a 300 kg steel melt with a maximum net input power of 1700 kW is achieved. Off-gas system and measurement systems were operated safely.

Test	Initial melt in crucible	Heating	Remarks
V0.1	300 kg steel	no	equipment tests,
V0.2	300 kg steel	400 kW	V0.2 and V0.3 similar to
V0.3	300 kg steel, 150 kg Al_2O_3	1700 kW	test matrix experiments
V1.1	20 kg steel	pulsed	failure of pouring control
V1.2	200 kg steel, 150 kg Al_2O_3	pulsed	influence of Lorentz-forces excluded
V1.3	300 kg steel, 150 kg Al_2O_3 + SiO_2	1000 kW	

Tab. 1: BETA experiment until August 1984.

The experimental series V1, which follows the equipment tests,is investigating the high temperature interaction of the liquid melt with the concrete. It should be mentioned that the experiments, up to now, use siliceous concrete crucibles only.

Some of the cross sections of BETA crucibles, which were cut after the test, are reproduced in Figs. 2a-b. The crucibles of the soustained heating experiments with 400 and 1000 kW power input, respectively, show a considerable difference in melt front propagation when compared to previous transient tests. Downward propagation is clearly dominant when the temperature of the melt is kept high over longer periods of time, while the sideward penetration is rather limited. This effect was observed also in experiment V0.3 with the very high power input of 1.7 MW, indicating that this behavior is valid for a wide temperature range of the melt. In earlier transient tests, melt front propagation is only some 5 cm in both the downward and sideward directions.

The influence of magnetic Lorentz-forces, resulting from induction heating, on melt front propagation was investigated experimentally and theoretically when the BETA facility was planned. This influence was found to be neglegible, compared with that of the gas agitation of the melt. However, because of the unexpected melt front shape, an additional experiment V1.2 was carried out in BETA to validate the experimental melt front results. With pulsed heating, at maximum input power, the melt was repeatedly heated in the crucible to high temperatures and then allowed to interact with the crucible with zero induction field. After a series of ten power cycles comparison of the melt shape with V0.2 shows no significant difference, and it was concluded that radial and axial penetration are not affected by the heating method.

A second inportant effect has been observed in the sustained heating experiments, which becomes most clearly visible in V1.3. This experiment, with a rather high sustained heating power of 1000 kW, began with oxidic and metallic melt in the crucible, with the metallic phase initially at the bottom. With the high gas release from the concrete the steel is entrained into the oxidic phase in fine droplets. After 5 to 6 minutes of interaction, an almost complete disperion of the metal into the oxide is observed, and no continuous steel phase exists which may be heated by the induction field. Therefore, the heating power drops to a low value, ending this high temperature experiment. The dispersion process is mainly influenced by the superficial gas velocity and the viscosity and density of the metal and the oxide. Therefore, it is strongly dependent on the temperature of the melt, and the inverse process of segregation must be considered when the liquid melt is at lower temperatures, with reduced gas flow rates, for longer times.

As discussed above, the heating power which is coupled to the melt in BETA contains important information of the constitution of the melt and is given in Figs. 3a-b. In experiment V0.2 nearly constant heating was achieved over some 40 minutes, with the exception of three power peeks between 1700 and 2100 sec, which were applied to test the equipment, and a short power failure at 600 sec. The experiment started with no oxidic phase. A closer inspection of the power curve shows a slight increase of the power over the first 600 sec. Probably, the metal undergoes a coarse mixing with molten silica and gas, resulting in a distribution of metal with a higher effective cylindrical surface more amenable to induction heating. As the oxidic melt mass grows, fine metallic particles produced by the entraining gas flow may be kept in the oxide, unable to be heated inductively because of their small sizes. Therefore, a slow decrease of input power results.

Power input during V1.3 (Fig. 3b), with a much higher gas release and the oxidic phase present from the beginning of the experiment, suggests a much faster transition to the fine distribution of the metal with a drastic reduction in power input. A similar behavior is observed in experiment V0.3.

Melt front propagation in the BETA experiments was evaluated from the failure time of thermocouples in the crucibles (Figs. 4a-b). It is seen that the

downward melt front propagation rate is nearly constant with time, indicating a quasi-steady experimental condition, and reaches from .18 mm/s for the 400 kW power input to 1.0 mm/s for the 1.7 MW power input in V0.3. The downward propagation velocity is approximately proportional to the power input, but is up to a factor of 2 higher than has been observed in earlier transient experiments. The corresponding maximum heat flux density is 4.4 MW/m^2. However, as seen from Fig. 4, the sideward penetration is limited to only a few centimeters. After some minutes of interaction, the radius of the cavity remains almost constant.

The gas and aerosol release are discussed below for the pulsed heating experiment V1.2. The aerosol measurements by extinction of a laser beam, are given in Fig. 5, which shows a series of aerosol peaks over a low base level. The initial peak of aerosols is observed with the first contact between the melt and the concrete, and is probably due to the fabrication of the crucible, which is cast in a greased mold for easier separation of concrete and mold. The other large peaks are due to the insertion of paper shrouded thermocouple lances into the melt, producing a significant amount of smoke by pyrolysis. Smaller peaks are from ceramic shielded thermocouple lances. It can be stated that the amount of aerosols produced directly from melt/concrete interaction is very low, in the range of some mg/m^3. This is confirmed by the visual observation with TV- and film cameras. Furthermore, temperature variations due to the power peaks in this experiment have no significant effect on aerosol release.

On-line measurements of gas concentration during this experiment are given in Fig. 6 in relative units of the mass spectrometer. The constant argon cover gas flow gives a time dependent concentration signal because of the varying contribution of the gas release from the concrete in response to the changing temperature of the melt. The most important gases are H_2, H_2O, and CO, while the amount of CO_2 is very small (lowest curve in Fig. 6). The release rates of H_2, CO_2 and CO follow the power peaks in the melt, and the gas increase is due to the higher melt front propagation at increased melt temperatures. Some of the peaks are due to the insertion of paper shrouded thermocouples, producing gases as well as aerosols. It is interesting to note that the release of water vapor is independent of power variation. Therefore, it is concluded that the detected vapor is released from the upper sidewalls of the crucible which are covered with splashed oxidic melt, while the water vapor bubbling through the liquid metal is completely reduced to hydrogen. Most of the CO_2 is reduced to CO by the steel. Due to the use of siliceous concrete, the most important gas is hydrogen. Future experiments with constant power input will allow more detailed gas analysis.

CONCLUSIONS

From the BETA experiments carried out so far, following preliminary conclusions may be drawn:

- Downward propagation of the metallic melt dominates for the high temperature melt/concrete interaction. Present modelling of heat transfer in the computer codes, based on earlier transient experiments, must be improved.

- Dispersion of the metallic into the oxidic phases is observed in the experiments with high gas release. The long-time stability of the dispersed materials and the possible influence on freezing processes needs further investigation.

- The gas released from the melt surface is mainly hydrogen for the siliceous type of concrete.

- The aerosol release from melt/concrete interaction is observed to be very low (some mg/m^3).

Further analysis of these phenomena is carried out in the ongoing BETA experiments in close cooperation with code verification, presently concentrating on the high temperature interaction. The subsequent experiments involving crust formation and solidification processes will complete code verification at the end of 1985.

Considering the implications of the preliminary BETA results with respect to the reactor situation, the following consequences may be derived: A faster downward propagation of the melt may occur while the melt is liquid. However, because of the higher heat transfer rates from the liquid melt, freezing processes in the melt will start earlier limiting the fast downward propagation. The reduced radial propagation of the melt may lead, for the German PWR, to a retarded sump water ingression, with the consequence of a later overpressurization of the containment. However, the containment atmosphere may be loaded by a relatively higher hydrogen content.

REFERENCES

/1/ Hassmann, K., Hosemann, J.P., "Influence of containment failure mode on the fission product term", ANS Annual Meeting, New Orleans, Louisiana, June 1984.

/2/ Schwarzott, W. et al, "Detaillierung von KAVERN und Modellentwicklung zur Gasabströmung aus der Schildgrube", Final Report, BMFT 150 379, KWU Erlangen, April 1983.

/3/ Reimann, W., Murfin, W.B., "The WECHSL-Code: A Computer Program for the Interaction of a Core Melt with Concrete", KfK 2890, 1981.

/4/ Cole, R.K., jr., et al., "CORCON-MOD2: A Computer Program for Analysis of Molten-Core Concrete Interactions", SAND84-1246, NUREG/CR-3920, 1984.

/5/ Alsmeyer, H., Peehs, M., Perinic, D., "Untersuchung der Wechselwirkung einer Kernschmelze mit Beton in der BETA-Versuchsanlage", PNS-Jahreskolloquium, Karlsruhe, Oktober 1982.

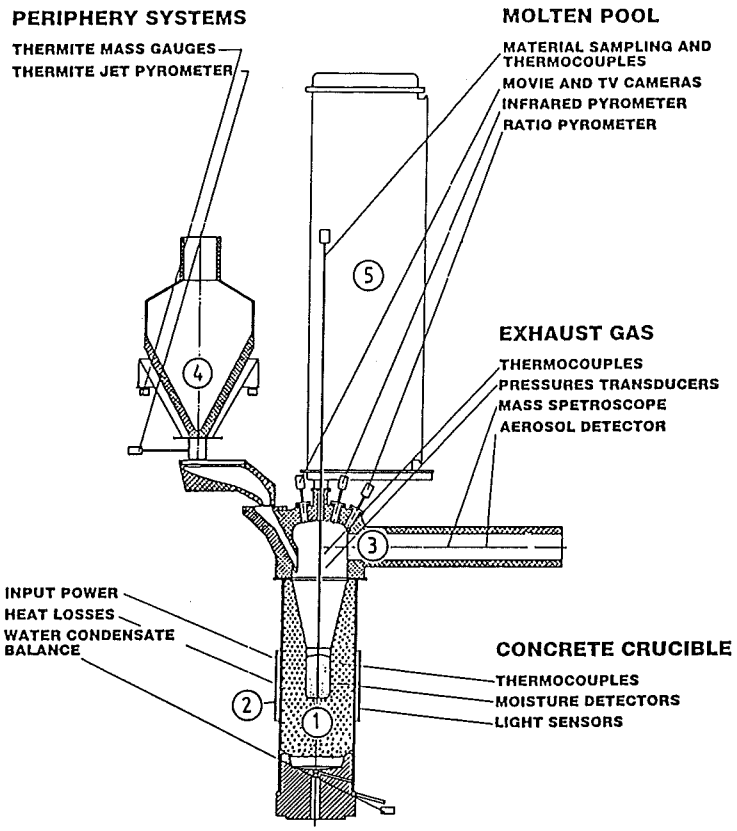

1 CONCRETE CRUCIBLE
2 INDUCTION COIL
3 OFFGAS SYSTEM
4 THERMITE REACTION TANK
5 CONTAINER FOR MEASUREMENT PROBES

Fig. 1 Schematic view of BETA facility.

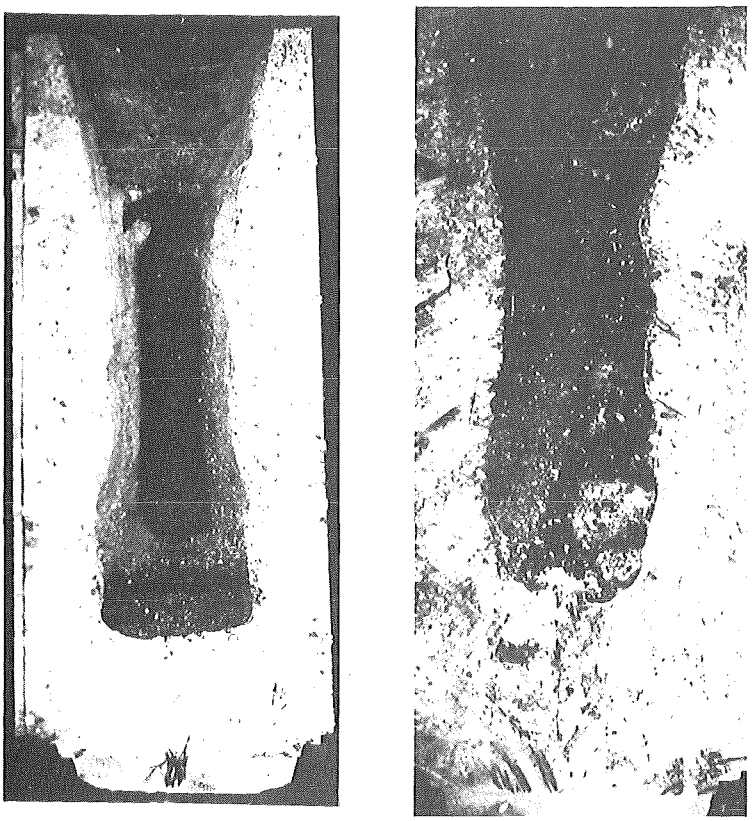

V0.2 V1.3

Fig. 2 Cross sections of BETA crucibles after test

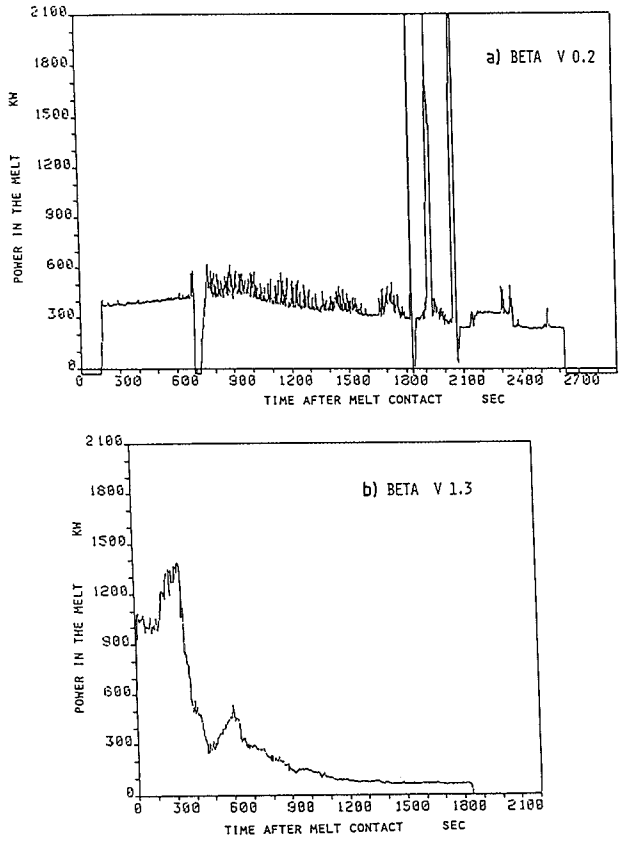

Fig. 3 a, b Power input during BETA experiments

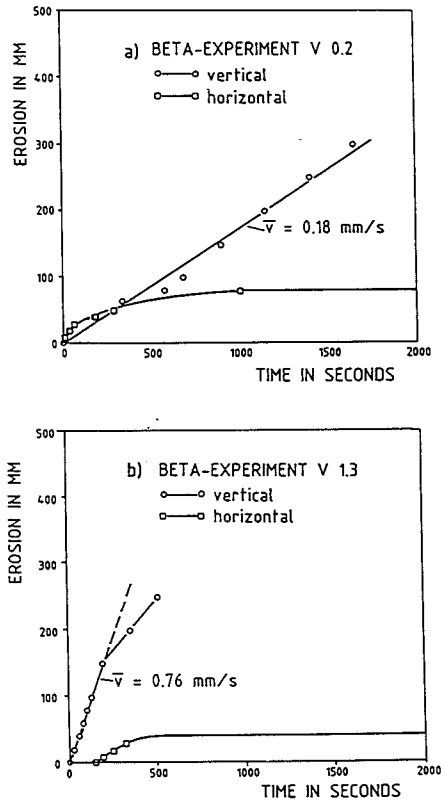

Fig. 4 a, b Horizontal and vertical erosion

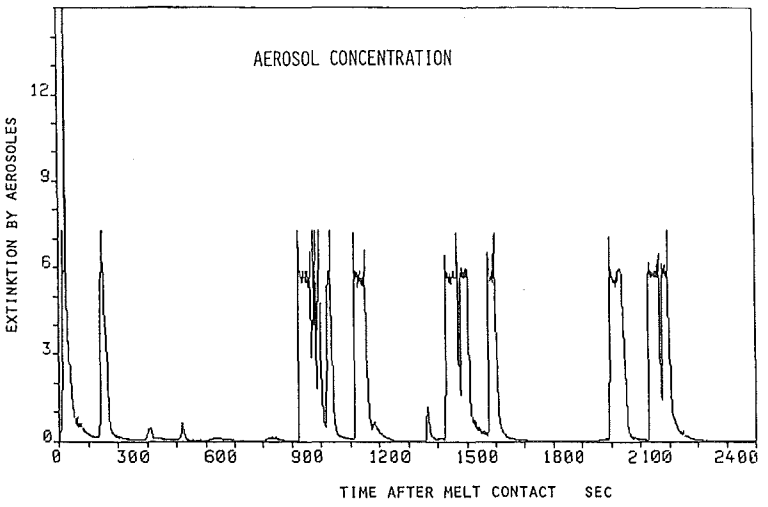

Fig. 5 Aerosol release during BETA experiment V1.2.

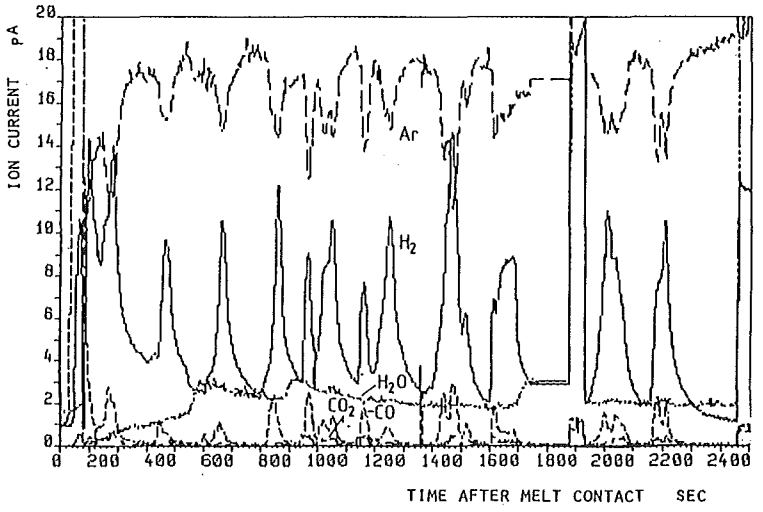

Fig. 6 Off-gas concentration of Ar, H_2O, H_2, CO_2, and CO during BETA experiment V1.2.

LARGE-SCALE MELT/MATERIAL INTERACTION EXPERIMENTS*

T. Y. Chu, J. E. Brockmann

Sandia National Laboratories
Albuquerque, New Mexico 87185, U.S.A.

ABSTRACT

The paper describes the design and performance of the Large-Scale Melt Facility (LMF) at Sandia National Laboratories. The facility is capable of producing up to 500 kg of core melt with super heat up to 150°K. The results of the first experiment carried out in the facility involving the interaction of 230 kg of a 70% UO_2-30% ZrO_2 melt and a magnesia crucible are also presented.

INTRODUCTION

Core melt/material interaction experiments are currently being carried out at SNLA to provide quantitative data for the validation of computer codes for severe reactor accident assessment. For the data to accurately reflect the thermal hydraulic phenomena involved the experiment must be carried out in large-scale and the facility must be designed to be flexible enough to accommodate a variety of test conditions. The LMF at Sandia is designed to meet these requirements. A description of the facility and a summary of some of the developmental studies are presented in the first part of the paper. More detailed descriptions can be found in references [1,2].

The second part of the paper reports the results of a core melt/magnesia interaction test. The purpose of the test is to assess the ability of magnesia bricks in mitigating or moderating core melt attack. Of interests are thermal and mechanical responses of the material as well as the amount of gas and aerosol generation.

LARGE SCALE MELT FACILITY (LMF)

Furnace and Test Chamber

The LMF consists of an induction furnace on a platform for melt preparation and a test chamber below for the interaction test, Figure 1. The furnace is approximately 1.5 m in diameter and 2.1 m high with a water cooled outer shell, Figure 2. The test chamber is 2.7 m in diameter and 2.4 m high, made of 1-cm-thick mild steel, with external girdling beams. The test chamber is mounted on tracks to allow both the furnace and the chamber to be serviced simultaneously. The melt is prepared in the furnace and tapped into the test chamber for experimentation.

*This work supported by the U.S. Nuclear Regulatory Commission and performed at Sandia Nat'l Labs. which is operated for the U.S. Dept. of Energy under Contract Number DE-AC04-76DP00789.

During operation the furnace is continuously purged with argon. The power supplied to the induction coil is coupled to a graphite susceptor. The power supply for the furnace operates at 1000 Hz with a maximum power of 280 kW. The maximum power deposition into the susceptor was experimentally determined to be 154 kW. The susceptor has an outside diameter of 56 cm and is 76 cm high. The melt crucible assembly is an upright cylinder with a hemispherical bottom; the overall height is 53.3 cm and the diameter is 34.2 cm. The crucible assembly fits into a cavity inside the graphite susceptor, the cavity is closed off by a graphite lid, Figure 2. An opening on the bottom of the susceptor allows the melt to be tapped from the bottom by explosively driven projectiles. Two methods are used. One is to use a self-forging fragment which is a slug of metal formed and driven by explosives. Another way is by firing two special slugs from a double barrel 12-gauge shotgun into the bottom of the melt crucible. The self-forging fragment is found to be more effective. A 200-kg melt can be released into the test chamber in less than one second.

The test chamber is designed to withstand an internal pressure of two atmospheres. It has a spring loaded relief port to prevent overpressurization. Two access doors allow the introduction of test objects up to 1.5 m in width and 2 m high. There are a number of ports on the side and top of the chamber to provide television and motion picture coverage of the test. There are also various instrumentation ports through the chamber wall for thermal, gas and aerosol instrumentations. Experiments are remotely operated from a control building about 100 m from the furnace platform. Up to 128 channels at 1.5 sec. intervals are available for data acquisition; the system is currently being upgraded to 200 channels at 0.5 sec. intervals.

MELT CHARGE AND CRUCIBLE ASSEMBLY

The charge material was a mixture of urania 70% by weight and the balance zirconia (stabilized by 12% yttria). The raw materials were in powder form with a typical packing density of about 30%. To increase the amount of charge in the crucible and, more importantly, to improve the thermal properties of the melt charge, the powders were hot pressed to approximately 80% of theoretical density. A typical charge billet was a cylinder about 30 cm diameter and 10 cm high weighing about 50 kg. Holes were drilled into the charge to accept temperature instrumentation. The bottom charge billet was machined to fit the spherical contour of the crucible bottom. The melting range of the melt charge was determined in two independent sets of experiments at Sandia to be between 2798 K (2525°C) and 2848 K (2575°C).

The melt crucible was actually an assembly of two vessels. This was because of the compatibility requirements. The melt crucible had to be able to withstand, concurrently, the diffusion of carbon from the susceptor on the outside and the possible attack of the melt from the inside. Material compatibility tests showed that none of the candidate materials, Ta, W, Ta-2 1/2W, and Ta-10W, could meet both requirements. Carbon diffusion was lowest in Ta-10W, about 1/3 that of other materials, but the tantalum in the Ta-10W alloy was found to be soluble in UO_2. Tungsten was the only material compatible with molten UO_2. Therefore, the crucible had to be a multi-walled structure with an 8-mm-thick Ta-10W vessel on the outside and a 1.6-mm-thick CVD (chemical vapor deposition) tungsten liner inside. Additional barrier were provided by a 3 mm of plasma-sprayed tungsten on the inside of the TA-10W vessel and a 2.5-mm-thick tungsten-powder packing between the liner and the outer vessel. The powder packing also helped to distribute the loading on the liner, Figure 3. Similarly, a 5-mm layer of UO2 powder was used between the melt charge billets and the tungsten liner to even out the loading resulting from the charge.

Instrumentation

The susceptor and the melt charge were instrumented with 21 type C (tungsten 5%-rhenium vs tungsten 26%-rhenium) thermocouples, 5 ultrasonic thermometers and 2 pyrometers. Thermocouples in the charge were installed at 5.1-cm radius and 14.0-cm radius at depths from 7.5 cm to 4.1 cm into the charge. Ultrasonic thermometers were installed at similar locations. The susceptor temperature was also monitored by thermocouples and ultrasonic thermometers, Figure 4. Of the two pyrometers, one monitors the susceptor temperature and the other monitors the charge temperature. The tungsten pyrometer well in the charge was placed along the central axis of the charge and reached to within 7.4 cm of the bottom of the melt crucible.

Thermal Modelling of the Charge-Crucible-Susceptor Assembly

Concurrent with the development of the melting technology was the development of a computer model of the charge-crucible-susceptor assembly to guide the control of the experiment. The power from the induction coil is deposited in the graphite susceptor, the energy is transferred through the crucible to heat the melt charge. Because of the low thermal diffusivity of the melt billet and the UO_2 powder surrounding it, the energy transfer between the crucible and the charge is quite slow. The highest safe operating temperature of the crucible as defined by the Ta-W-C phase diagram is 3100 K which is only approximately 250 K above the melting range of the melt. When the rate of energy deposition into the susceptor exceed the rate of energy transfer into the charge, the crucible will fail by melting. In addition, components of the refractory crucible often have residual stresss developed during manufacturing and are susceptible to cracking due to thermal stress in the range of 300 K to 1300 K. It is, therefore, very important to be able to control the rate of heating of the susceptor throughout the experiment.

A finite difference model of the charge-crucible-susceptor assembly was developed [3]. The model was first used to evaluate different design alternatives and later used to set the heating schedule for the experiments. The model takes full account of conduction and radiation heat transfer. Melting of the charge is modelled by an increase in specific heat of the charge and convection in the melt is approximated by an increase in the thermal conductivity of the molten charge. The amount of increase is estimated by standard natural convection correlations. The model is accurate to within 100 K as compared to experiments [3] up to charge melting. Because convection in the melt is only approximated by conduction, the details of the melt front progression cannot be accurately modelled. But reasonable estimates of total time for melting can be obtained.

MOLTEN CORE/MgO INTERACTION EXPERIMENT

Physical Assembly of the Test

The magnesia crucible was made of Harklase MgO bricks. The bottom was made of three layers of flats with a total thickness of 19.1 cm. The sidewall consisted of two layers of arch bricks with a total thickness of 22.9 cm. The resulting cavity was approximately circular with an average "diameter" of 36.2 cm and a depth of 66 cm. The bricks were supported below by a 1.3 cm steel plate. The entire brick assembly was contained inside of a 107x107-cm-square steel box 95 cm high. The space between the bricks and the box was filled with MgO powder. The bottom and the sidewall of the crucible were instrumented with thermocouples at depths ranging from 0.32 cm to 15.2 cm below the surface.

An 81.3-cm diameter shield was instrumented to measure the upward heat flux from the melt in the MgO crucible. It was mounted on a boom and was designed to be moved over the MgO crucible cavity after the tapping of the melt was completed. The shield was a sandwich structure; the top and bottom were made of 8-mm steel plates with a middle layer of alumina felt insulation. The lower plate was segmented with a 35.6-cm-diameter disk surrounded by a 19.7-cm-wide middle ring and an 24.8-cm-wide outer ring. The center disk was plasma sprayed with a layer of alumina. The segments were separated by 3 mm of alumina insulation. In addition, the shield was equipped with a number of heat flux gauges for local measurements.

The test chamber was extensively instrumented for aerosol measurements. Two main items of interest in aerosol measurements were the aerosol source term and the size distribution. The aerosol source term was obtained by mass balance measurements. The rate of change of the total suspended aerosol mass in the test chamber was the result of the balance between production, the source term, and depletion due to venting and deposition. Filter samplers and an aerosol photometer were used to measure aerosol concentration as a function of time from which the total rate of change of aerosol mass was calculated. To insure that the concentration measurements were representative, three fans were used for mixing and moving three times the chamber volume per minute. Deposition was measured by the use of deposition surfaces and deposition samplers. Cascade impactors and cyclones were used to collect aerosols for size distribution determination.

Results

Figure 5 shows the temperature history of the susceptor and the charge during the heating and melting phase of the experiment. The susceptor temperature was driven through a series of ramps and plateaus according to a predetermined heating schedule based on model calculations [3]. The plateaus were used for cross-checking temperature instruments and also to allow the interior temperature to catch up to the susceptor temperature. The middle curve on Figure 5 corresponds to the temperature 2.2 cm from the crucible inner wall; it lagged behind the susceptor by about one hour. The center of the charge showed a lag of about three hours. Sixteen and a half hours into the test, the center pyrometer showed a melting plateau at 2798 K (2525°C), it lasted for about one hour. Eighteen hours into the test, the first attempt to tap was made. For this experiment, a double barrel shotgun was used for tapping. Four attempts were made before the crucible was successfully tapped at 19:56 hr. Approximately 4.25 minutes were required to drain all the melt from the furnace into the MgO crucible. Because of the slow rate of melt release, the melt charge lost some of its superheat in transit. Video tape made during the test indicated that the charge was barely molten toward the end of the four minutes. Therefore, the present result should correspond to a case between that of a hot solid attack and a melt attack.

Shown in Figure 6a is the upper portion of the MgO crucible after the test. Cracks and some shallow (3 mm) surface spallations are evident. The cracks were found to be through the bricks. Most of the cracks were on the sidewall above the melt surface. In addition, diagonal cracks were observed at the corner of sidewall bricks, Figure 6b, where they meet the flat bricks making up the bottom of the crucible. This type of failure has been observed in previous smaller scale test using thermite generated melts. The crack pattern could be attributed to the two dimensional heat transfer effects due to the presence of the bottom bricks. A set of slits ranging from 0.3 mm to 3 mm wide and one brick deep, 6.4 cm, were located in the bottom of the crucible to observe gap penetration by the melt. Post-test examinations indicated that gaps as narrow

as 0.6 mm were penetrated by melt through the full depth of 6.4 cm. The gaps were not in all cases totally filled probably due to solidification as a result of the low superheat of the melt. There was no melt in any of the cracks within the brick. Despite the cracks and gap penetration there was no gross dislocation of the brick pattern and the crucible structure was essentially intact. Scanning electron microscope examinations were made of the melt brick interface. The interface appeared to be sharply defined with no evidence of melting (of the brick) or inter-diffusion of materials. In summary, there were no significant macro or micro alterations of the brick due to the melt interaction.

Gas generation measurements showed that very little gas was generated. There was no detectable amount of hydrogen due to the possible reaction of the melt and water in the bricks. Visually the aerosol generation appeared to be much less than that of melt/concrete interactions. The maximum aerosol concentration was 2 g/m^3 at about two minutes after tapping. The total aerosol generation was estimated to be 103 g and the source term was calculated to be less than 1 g/s. The aerosol size distribution was trimodal during the melt release. After the melt release, the two large modes no longer existed and the peak of the size distribution was then at 1 μm, see Fig. 7. The larger modes were probably caused by mechanical break-up of the melt during the melt release.

Typical temperature histories at different depths in the brick are shown in Figure 8. The thermocouples were within a circle of radius 4.45 cm around the center of the bottom of the crucible cavity. Thermocouple CR31 was installed in a crack between two bricks. It showed a little faster response, compared to the trend of the other thermocouples but there was no sharp increase in temperature that might have indicated a direct contact with the melt. This was consistent with the post-test observation of partially-filled gaps. Heat fluxes into the MgO bricks were obtained from in-depth temperature responses using inverse heat conduction calculations [4]. Results for the crucible bottom (downward heat flux) and the portion of the sidewall covered by the melt (sideward heat flux) are shown in Figure 9. In both cases, during melt release the surface fluxes were in the range of 20 W/cm^2. Twenty minutes later the downward heat flux decreased to about 5 W/cm^2 and the sideward heat flux decreased to about 3-4 W/cm^2. Heat fluxes into the sidewall above the melt also were in the range of 20 W/cm^2 during melt release but reduced to a value of 1.5-2.5 W/cm^2 20 minutes later. Heat fluxes into the instrument shield were monitored by heat flux gauges as well as by the temperature rise of the shield. Because the shield could only be moved over the pool after the tapping was completed, this heat flux data was not available until approximately five minutes after tapping. At this time, the heat flux as measured 33 cm above the pool was 36 W/cm^2; the flux decreased rather quickly to 3 W/cm^2 in five minutes.

From the above calculations and measurements, the upward heat flux from the melt can be obtained using radiation enclosure calculations. The result for the duration from 5.25 minutes to 11.75 minutes after tapping (or 1.0 to 7.5 minutes after completion of tapping as plotted) is shown in Figure 10. The net heat loss from the melt surface varied from 82 W/cm^2 to 13 W/cm^2. Twenty minutes after tapping the upward heat flux reduced to 3 W/cm^2.

SUMMARY

It appears from the present study that MgO is more resistant to core melt attack than concrete from thermal considerations as well as from gas and aerosol production considerations. While MgO bricks suffered cracking due to thermal stress, the overall integrity of structure was not seriously compromised.

REFERENCES

1. T.Y. Chu, et al, Large-Scale Molten Core/Magnesia Interaction Test, SAND83-1692, NUREG/CR-3438. In press.

2. T.Y. Chu, J.E. Brockmann and J.E. Gronager, "Large-Scale Melt Interaction Tests", Proceeding 11th Water Reactor Safety Research Information Meeting, Gaithersburg, Maryland, Oct. 24-28, 1983, Vol. 3 pp 188-203.

3. K.B. Sigurdson, T.Y. Chu, Thermal Analysis of Large Melt Furnace - Performance Evaluation of Susceptor-Crucible Design, SAND81-1262, NUREG/CR-3002 (Albuquerque, NM: Sandia National Laboratories, July, 1983).

4. J.V. Beck, B. Litkouhi and C.R. St. Clair, "EFficient Sequential Solution of Nonlinear Inverse Heat Conduction Problem," Numerical Heat Transfer, Vol. 5, 1982, pp 275-286.

5. E.R. Copus, "Sustained UO_2 Melts Using the Inductive Ring Susceptor Technique," Heat Transfer - Seattle 1983, AIChE Symposium Series 225, Vol. 79, 1983, pp 310-313.

6. E.R. Copus, Development of the Inductive Ring Susceptor Technique for Sustaining Oxide Melts, NUREG/CR-3043 (Albuquerque, NM: Sandia National Laboratories, Sept. 1983).

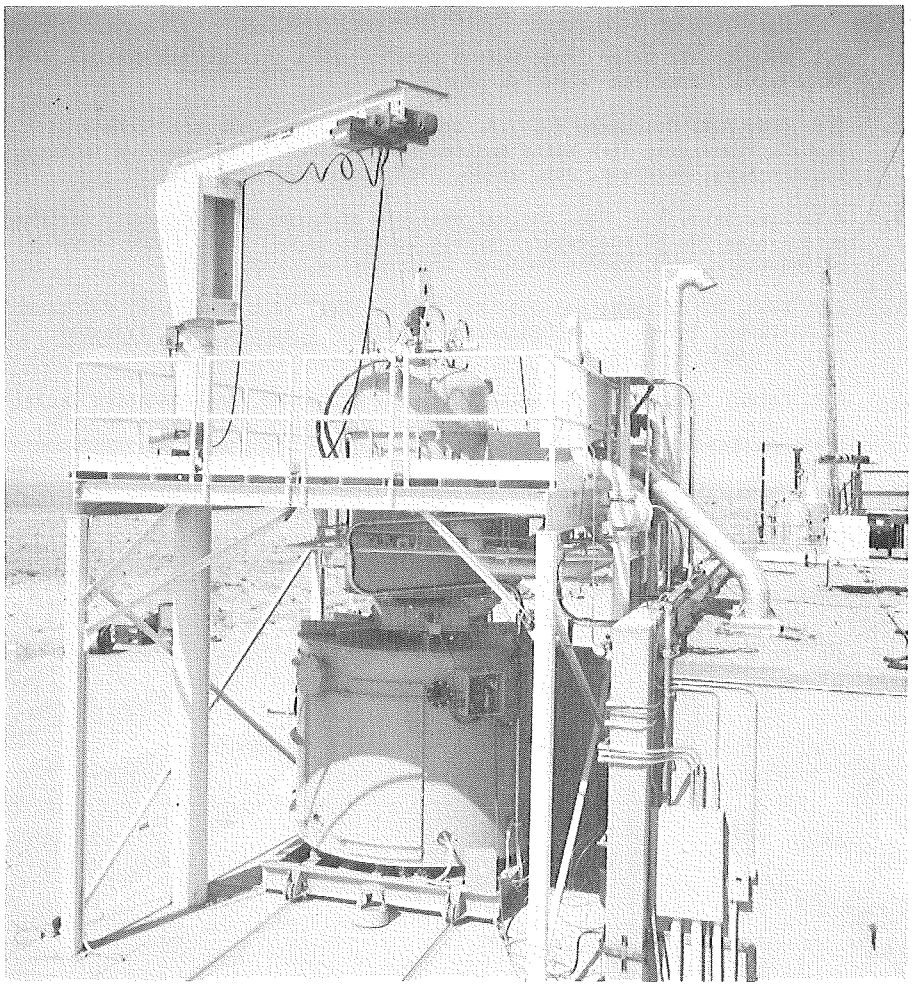

Figure 1 The Large-Scale Melt Facility

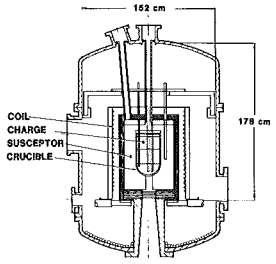

Figure 2 A Schematic of the LMF Furnace

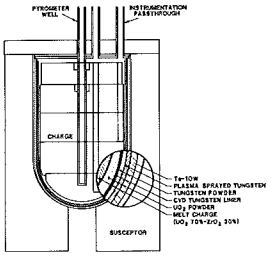

Figure 3 Charge/Crucible/ Susceptor Assembly

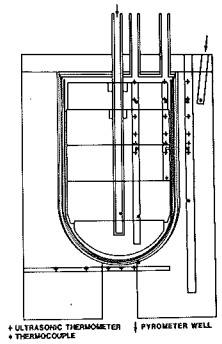

Figure 4 Schematic of Instrumentation Placement in the Charge and the Susceptor

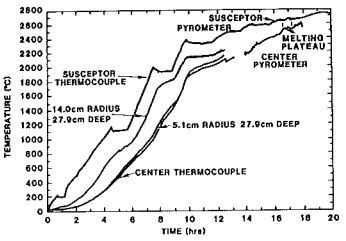

Figure 5 Susceptor and Charge Temperature During Test

Figure 6a MgO Brick Crucible After the Test

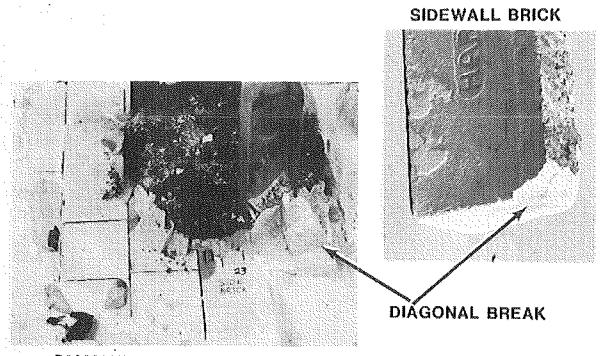

Figure 6b Example of Diagonal Break of the Sidewall Bricks

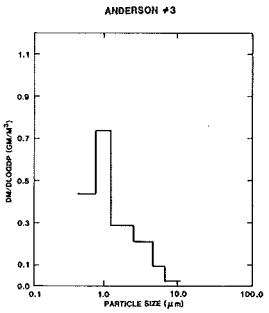

Figure 7 Aerosol Size Distribution 10.0 - 15.0 Min.

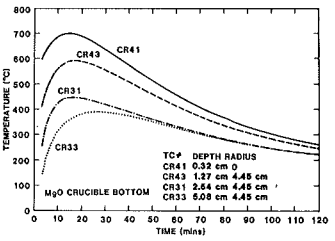

Figure 8 Thermal Response in the Bottom of the Crucible

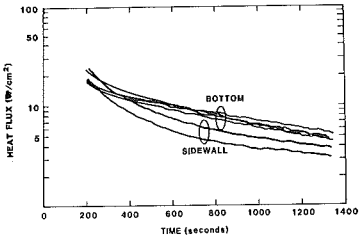

Figure 9 Surface Heat Flux on the Bottom of the MgO Crucible

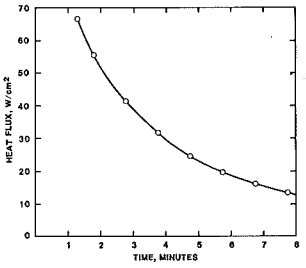

Figure 10 Heat Loss from the Top of the Melt

THE MELPROG MODEL FOR INTEGRATED MELT PROGRESSION ANALYSIS

J. E. Kelly, M. F. Young, J. L. Tomkins, P. J. Maudlin and W. J. Camp

Sandia National Laboratories
Albuquerque, NM 87185, U.S.A.

ABSTRACT

The in-vessel modules of the integrated LWR melt progression analysis code, MELPROG, are described. These in-vessel modules are being developed along with a reactor coolant system model and a containment response model to provide a detailed, best-estimate analysis tool for severe accident analysis in both BWR and PWR designs. The MELPROG code, which is designed to treat melt progression from accident inception up to and through melt ejection from the reactor vessel, consists of eight explicitly coupled modules: Fluids, Pin-Behavior, Structures, Debris Formation/Behavior, Radiation, Vapor Explosions, Fission Product Release and Transport, and Material Ejection. The first version of the code, which includes the first five modules, has been completed and tested on a simulation of an S1D accident. The results of that simulation are presented herein.

INTRODUCTION

Since the TMI-2 accident, renewed emphasis has been placed on improving our understanding of severe accidents in light water reactors (LWRs). One avenue of research has been to create detailed systems models for the response of the reactor core and vessel, the reactor coolant system (RCS) and the reactor containment. In this paper, we describe one such core/vessel response code, MELPROG, which is being developed at Sandia and Los Alamos National Laboratories as part of the USNRC and Foreign Partners' Severe Fuel Damage program.

The MELPROG code has evolved from efforts in the MIMAS project[1] at Los Alamos National Laboratory and the MELPROG project[2,3] at Sandia National Laboratories. The MIMAS project developed a computer code, MIMAS, which treats the thermal and hydrodynamic response of the reactor core region during a severe LWR accident. MIMAS consisted of modules for fluid dynamics, rod behavior, core-barrel and grid plate heating, and radiation heat transfer.

MIMAS was taken as the starting basis for an extended melt progression treatment in the MELPROG project. The goal of MELPROG is to be a best-estimate model for meltdown sequences and, in particular, to predict the fission product release and transport in a physically based manner. In order to do this, the transient behavior of the reactor core and components must be calculated. Consequently, the code must analyze all the various phenomena and the associated coupling between the phenomena for severe accident sequences.

MELPROG uses the fluid behavior, radiation, and rod behavior modules of MIMAS with only minor modifications. A debris module has been added to allow for detailed treatment of debris formation, dryout, melting, and relocation of debris. A complete thermomechanical response and failure module for structural components has been developed and added to the code. A stand-alone model to treat steam explosions, TEXAS[4], has been developed for later inclusion in the melt progression model. Work has begun on incorporating into the code a thermochemical behavior of fission product model and a melt ejection model. Finally, the code has been implicitly linked by the MIMAS project to the TRAC-PF1 RCS model developed at Los Alamos National Laboratory[5]. The resulting code is capable of analyzing the reactor core, vessel, and other components as well as the reactor coolant system.

The initial version of the code has been exercised on an S1D accident sequence for a simplified model of a Westinghouse PWR. This sequence involves a medium-size break in the cold leg with failure of the emergency core cooling system. The sequence was run from accident inception through core uncovering, clad oxidation, rod failure, debris bed formation, debris liquefaction, debris slumping through the grid plate and core support plate, debris interaction with the water in the lower plenum, debris quenching, dryout and remelt, and vessel failure by melt-through. This accident poses particular difficulties for any hydrodynamics treatment since coolant blowdown is via flashing and the debris-coolant interactions are very violent. In addition, it allows thorough exercise of all the other modules (and coupling between modules) in the initial code version; namely, the rod behavior, radiation, structures, and debris modules.

Both MIMAS and the complete in-vessel code, MELPROG, have been described in recent publications[1,2,3]. Herein we present only a brief summary of each module in the current code version in order to describe in detail the results of the S1D accident sequence.

DESCRIPTION OF MELPROG IN-VESSEL MODULES

The MELPROG code consists of modules which perform specific parts of the overall calculation. The current code consists of five in-vessel modules. These modules are explicitly coupled together to simplify the calculational procedure. The modeling of the reactor vessel is pseudo-two-dimensional (R-Z) in that the vessel is divided into axial nodes and radial rings which define two-dimensional cells. This means that the radial and axial locations of the various components and fuel rods can be modeled. However, in the current version the hydrodynamic solution is strictly one-dimensional (i.e. axial direction only).

The hydrodynamic equations are solved in the FLUIDS module. The current version of MELPROG uses a one-dimensional, three-field, semi-implicit model. The three fields are debris (i.e. solid and liquid fuel, clad, control rod, and failed structural materials), liquid coolant, and vapor (i.e. steam, hydrogen, fission product vapors, and aerosols). A four-field, two-dimensional version is currently under development for incorporation into MELPROG by Los Alamos National Laboratory[6]. This improved model will allow for recirculation effects and the separation of the debris field into liquid and solid components. For each field, mass, energy, and momentum equations are solved in order to calculate the volume fraction, temperature, and velocity of each field. Auxiliary continuity equations are also solved in order to account for

the hydrogen, fission product, and Zr masses. The numerical technique utilized is the stability-enhancing two-step method[7].

A detailed rod behavior module, PINS, which was developed as part of the MIMAS project, is used in MELPROG. This model uses a single representative rod for each radial ring in the core. The rods are noded axially according to the FLUIDS noding. Within a node a detailed model for radial heat transfer, chemical reactions, and mechanical response utilizing the REBEKA[8] and MATPRO[9] data bases is used to predict fuel and clad heat up and failure.

The thermomechanical analysis of structural components is calculated in the STRUCTURES module. One and two-dimensional heat transfer models have been constructed in the MELPROG project for the major generic structure types of a Westinghouse PWR. These models include conduction heat transfer, plate-out of materials on the structures, and melting or ablation of the structures. In addition, brittle and ductile failure models have been developed for these structures.

A simple debris bed formation model has been developed to allow bed formation in any cell. Once a bed has been formed, the DEBRIS module takes control of bed behavior from the FLUIDS module. The DEBRIS module utilizes a much finer finite difference mesh than the FLUIDS module. This allows detailed analysis of debris dryout, heat up, melting, relocation, and crusting, as well as crust remelt, within the debris bed. This detailed analysis is also needed to provide the heat transfer to supporting structures. Both decay heat and chemical (oxidation) heating are included in the modeling.

Radiation heat transfer is calculated in the RADIATION module which was developed as part of the MIMAS project and has been adapted and extended for inclusion in MELPROG. The current model is based on a combination of the net radiation enclosure method and a diffuse flux treatment between cells. Each cell in the two-dimensional grid is treated as a net enclosure with internal structures and contains an isotropic, homogeneous, absorbing/emitting medium. The cell boundaries are treated as black-body absorbers and emitters. The flux entering or leaving a cell is treated as diffuse. The structures within a cell are treated as diffuse emitters/absorbers/reflectors. Within a given cell, the treatment is three-dimensional (3-D view factors are used). Fluxes between cells are strictly two-dimensional (R-Z geometry). The model treats radiation between pins, gas, water, debris, and structures. Changing geometry during the core degradation process is accounted for by dynamic view factors within each cell.

TEST PROBLEM DESCRIPTION

In order to test the first version of MELPROG, an S1D sequence in a Westinghouse PWR was chosen as a calculational exercise. The intent of this effort was two-fold. First, while the various modules had been tested separately, the combined code and the coupling between modules had not been fully tested. Hence, this problem served to identify and resolve inconsistencies between modules. Second, the actual reactor vessel modeling process and running of the problem required certain simplifications which have identified specific areas which require improvement. It is important to note that the current calculation, while complex in itself, contains numerous modeling simplifications and, hence, the calculational results must be viewed as a demonstration exercise and not a quantitative assessment of this accident sequence.

In performing this simulation, the link to TRAC-PF1 was not utilized in order to avoid unnecessary complications. Instead, the RCS was represented by a set of upper-plenum pressure, liquid fraction, and temperature boundary conditions obtained from a RELAP5 calculation of this accident[10]. A simulated flow coastdown was used for the lower boundary condition. These simplifications have repercussions on the details of the calculated sequence, since no active feedback to the RCS hydraulics from in-vessel processes is included. However, the use of these boundary conditions presents no limitations on the exercise of individual modules, nor on the overall code itself. Since the exercise was in the nature of a code demonstration and evaluation, these simple boundary conditions were felt to be sufficient.

The S1D sequence involves a high pressure blowdown through a 66 - 102 mm diameter break with scram and pump trip. The upper plenum pressure behavior can be characterized as a sharp drop to saturation pressure over about a 50 second time span followed by continuous steam generation and slow pressure drop as water flashes out of the reactor. It was necessary to simulate voiding of the upper plenum by linearly decreasing the liquid fraction at the upper plenum boundary to zero in about 80 seconds. This rate of voiding was arbitrarily chosen and will have some influence on the timing of events during the accident sequence.

A schematic of the MELPROG nodalization model for this test problem is illustrated in Figure 1. The problem was set up with four radial rings and seven axial nodes (five in the core region and two in the lower plenum). Structures modeled were the vessel wall and vessel bottom head, the core barrel, the core support plate, support columns (not shown), and upper and lower core grid plates. For simplicity, neither the upper plenum (replaced by a pressure boundary) nor the downcomer were explicitly modeled. Also, instrument penetrations of the lower head were not treated in this calculation, although these may be included at the option of the code user.

TEST PROBLEM RESULTS

The results of this test problem are summarized in this section. In order to clarify the results, the details of the calculation have been divided according to the module in which they were calculated. Table I highlights the major events which occurred during the calculation in each of the in-vessel modules (except for the radiation module). This summary gives a good indication as to where and when various phenomena are being calculated. The main events in each module are discussed below.

As discussed above, the FLUIDS module is concerned with predicting the fluid dynamic behavior in the problem. In particular, it calculates the volume fraction, temperature, and velocity of each field as a function of time and space. Since the modeling is one-dimensional, only averaged quantities are calculated. Nevertheless, these quantities give a good indication of the accident sequence.

Of particular interest during this test sequence is the production and transport of vapor. Figure 2 shows the vapor volume fraction distribution during the accident sequence. (Note that the sum of the liquid, vapor, and debris volume fractions is always equal to 1.0 and the point Z=0 is at the bottom of the vessel.) Flashing of water to steam is predicted to begin relatively early in the sequence when the system pressure drops to the saturation pressure. Core uncovering begins shortly after flashing and at

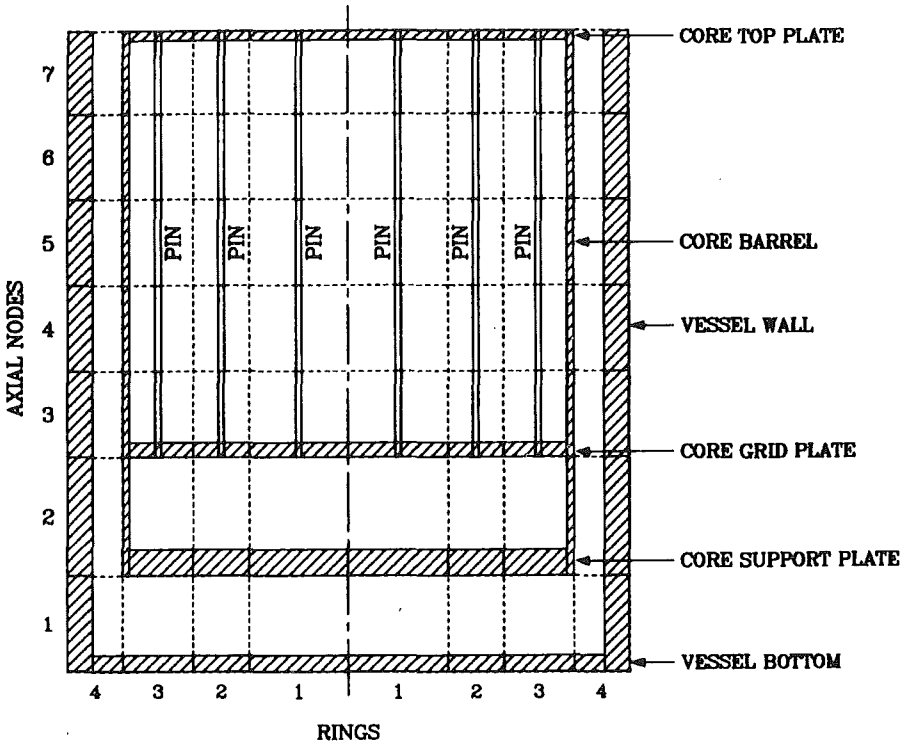

Figure 1: MELPROG Nodalizational for S1D Test Calculation

Table I: Summary of Important Events

TIME (s)	FLUIDS	PINS	DEBRIS	STRUCTURES
50	Flashing Begins			
135	Core Uncovering Begins			
400		Pin Ballooning Occurs		
560	Core 80% Uncovered	Pin Oxidation Begins		
800		Rods Embrittled		
815		Control Rod Failure Begins		
825	T_{max}=1700 K	Pin Melting Begins	Debris Bed Forms	T_{max}=800 K
900	Core 100% Uncovered	20% of Pins Failed	Debris Melting Begins	
1200	T_{max}=2220 K	45% of Pins Failed		T_{max}=1100 K
1900	T_{max}=2400 K	60% of Pins Failed	Melting and Compaction	Top Plate Fails
2300		72% of Pins Failed	Molten Pool Forms	Core Barrel Failure Begins
2700	T_{max}=2480 K			$T_{grid\ plate}$=1460 K
3200	T_{max}=2480 K	80% of Pins Failed	Debris 70% Molten	$T_{grid\ plate}$=1600 K
3375	Steam Spike Occurs		Debris Quenches	Grid Plate Fails
3380	Vessel Completely Dry		Bed Forms In Bottom	T_{head}=500 K
3400	T_{max}=2285 K	92% of Pins Failed	Debris Melting Begins	
3700	T_{max}=2500 K			T_{head}=520 K
4430	T_{max}=2450 K			T_{head}=650 K
6400	T_{max}=2720 K		Debris 63% Molten	T_{head}=1400 K
6900	T_{max}=2780 K		Debris 73% Molten	Vessel Bottom Head Fails

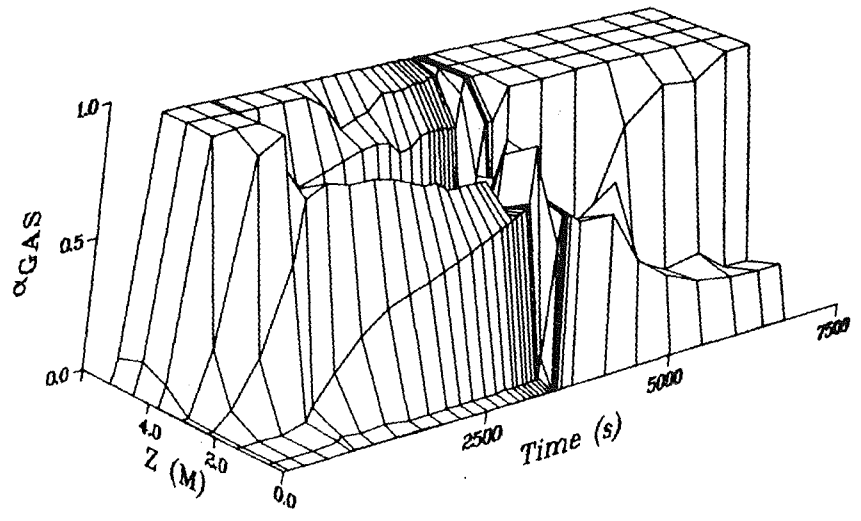

Figure 2: Vapor Volume Fraction Distribution During SID Test Calculation

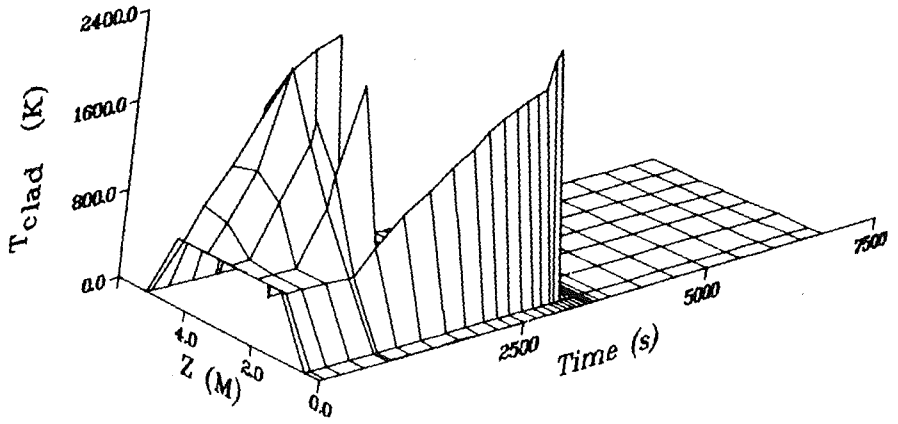

Figure 3: Clad Wall Temperature Distribution in Ring 1 During SID Test Calculation

560 s the core is 80% uncovered and the maximum steam temperature is 1100 K. The steam continues to heat and fuel pin oxidation begins shortly after this point. The water in the vessel continues to vaporize due to the depressurization and heat transfer and at 900 s the core is completely uncovered. From this point until later in the accident, the vapor behavior is benign as the water in the lower plenum slowly vaporizes. However, at 3375 s, grid plate failure leads to a debris-coolant interaction resulting in rapid vaporization and a steam spike. This event causes the code to run with an extremely small time step, typical for hydrodynamic codes under conditions of rapid phase change and shock generation. Following this event, with the debris generating heat and no water supply, the water in the lower head boils rapidly and is completely gone at 3380 s. After this point, the vapor is nearly stagnant and changes in its volume occur only due to the movement of debris.

As discussed above, the PINS module is responsible for predicting the fuel pin behavior. Specifically, in each core region ring, one representative fuel pin is modeled and its temperature distribution as function of time is calculated. When the representative pin in a given node is predicted to fail, all the pins in that node fail and their associated mass and energy are transferred into the debris field in FLUIDS.

In the test problem, the fuel pins begin to overheat as soon as core uncovering is initiated. Figure 3 illustrates the clad surface temperature distribution for the pin modeled in ring 1. (A value of 0 K for the temperature indicates that there are no pins at that location.) This figure shows the rapid heating of the pins as cooling is lost and as Zr oxidation occurs. Ballooning of the pin in the top of the core occurs at 400 s. Oxidation and subsequent rapid heating of the pin begin to occur at 560 s. The rods become embrittled at 800 s. At this point, a quench would shatter the pin. Melting of the zircalloy cladding begins at 815 s and the first pin failure occurs at 825 s. Following this point, pin failure occurs in other cells as the sequence continues. Pin failure can be seen by a sudden decrease in temperature to zero. At 1900 s, 60% of the pins have failed. The model continues to calculate the behavior of the remaining intact pin stubs until complete failure occurs.

As discussed above, the DEBRIS module is responsible for predicting the debris behavior after the debris is created. While FLUIDS calculates the average mass, temperature, and velocity of the debris on a one-dimensional basis, DEBRIS calculates detailed temperature and compositional distributions in the debris on a two-dimensional basis. This information is important for providing the correct heat flow to supporting structures such as the grid plate and vessel bottom head.

In the current problem, the debris formed by pin failure is predicted to move downward and freeze in the lower sections of the core. Hence, the debris does not move through the grid plate until grid plate failure begins. The debris accumulates on the grid plate and the first debris bed is formed at 825 s. At this point, the DEBRIS module begins to calculate. Core uncovering leads to bed dryout and the debris begins to overheat. Since there is steam production below the bed, Zr oxidation occurs in the bed. By 900 s, debris melting begins leading to some compaction of the bed. As pin failure continues, the resulting debris is added to the bed and the radial extent of the bed increases. The melting, relocation, and freezing of the debris in the bed lead to blockages in the bottom of the bed which effectively insulate the molten regions from the grid plate. At 2300 s, a molten pool is predicted to exist in the bed.

The downward heat flux from the bed to the grid ultimately results in grid plate failure at 3375 s. The debris then interacts with the water in the lower head to produce a steam spike and to fragment and quench some of the debris. However, most of the debris remains hot and the remaining water quickly boils away. By 3380 s, all of the debris is in the lower head where it continues to heat. Melting and relocation are predicted to occur. By the time the vessel bottom head fails, nearly 73% of the debris is molten.

The RADIATION module is responsible for predicting the radiative heat transport in the vessel. As such, it calculates the radiative energy exchanged between the various modules. Although major events can not be associated with this module, radiation heat transfer significantly affects the heat flow distribution and timing of events in the vessel. For example, the failure of the outer ring of pins is delayed relative to the inner rings due to the energy lost by these outer pins to the core barrel. Furthermore, the primary heat transfer mechanism to the core barrel and top grid plate is radiation. Radiation heat transfer also acts to cool the top surface of the debris bed and strongly impacts the heating of the steam. Another, important feature of this module is its ability to modify the view factors as structures and pins fail.

The STRUCTURES module is responsible for calculating the thermomechanical response of the structures in the problem. In each structure modeled, a detail heat transfer calculation is performed and, based on this, the mechanical response of the structure is determined.

Since there is little or no heat source in any structure, the temperature increase of a given structure is governed by the heat transfer from the vapor to the structure and by radiation heat transfer. This leads to a lag in the heating of the structures relative to the vapor and pins. As seen in Table I, the maximum temperature of any structure is 1000 K at 1200 s. Initially, the core barrel is the hottest structure. However, it is the top plate which mechanically fails first at 1900 s. Following this, sections of the core barrel begin to overheat and fail. The grid plate heat up is controlled by heating from the debris bed on top of it and from cooling by steam flow from below. Failure occurs at 3375 s due to melt through. At this point in the sequence, the lower vessel head is still at the saturation temperature and, hence, is relatively cold. Consequently, failure of the vessel by melting (and problem termination) does not occur until 6900 s.

On a integral basis, at the time of vessel bottom head failure, 486 kg of H_2 had been evolved which represents oxidation of approximately 50% of the zircalloy in the core. Approximately 106000 kg of molten debris would have been ejected which represents 73% of the core inventory. While these numbers and the timing of specific events are certainly not a best-estimate due to the simplifications involved, the results of this calculation demonstrate the potential capabilities of MELPROG.

SUMMARY

The performance of the modules in MELPROG for this S1D test problem calculation has demonstrated that the current code contains most of the features necessary to calculate a meltdown progression. The code is able to analyze in an integrated manner the important in-vessel phenomena anticipated for this accident sequence with the exception of fission product chemistry, which is currently being added. The code performed largely as designed for this test problem. The timing of events as well as the interaction of the

various modules seemed to be consistent. While the simplifications in the modeling of the reactor core and vessel mean that this particular calculation is not a best-estimate, it should be clear, that the major components for a best-estimate calculation currently exist in the code.

ACKNOWLEDGEMENT

This work was supported by the U.S. Nuclear Regulatory Commission and Foreign Partners' Severe Fuel Damage program and performed at Sandia National Laboratories which is operated for the U.S. Department of Energy under Contract Number DE-AC04-76DP00789.

REFERENCES

1. P. J. Maudlin et al., "A Damage Assessment of TMI-2," LA-UR-83-737 (1983).

2. W. J. Camp and J. B. Rivard, "Modeling of LWR Systems During Severe Accidents: The MELPROG Perspective," SAND83-1205 (1983).

3. M. F. Young et al.,"MELPROG Code Development and Methods," Proceedings, International Meeting on LWR Severe Accident Evaluation, Vol. 1, p. 2.8-1, Cambridge, MA (1983).

4. M. F. Young, "The TEXAS Code for Fuel-Coolant Interaction Analysis," Proceedings, LMFBR Safety Topical Meeting, Lyon, France, Vol. 3, p. 567 (1982).

5. "TRAC-PF1 An Advanced Best Estimate Code for PWR Analysis," Los Alamos National Laboratories preprint (1982).

6. S. Dearing, private communication.

7. J. H. Mahaffy, "A Stability Enhancing Two-Step Method for One-Dimensional Two-Phase Flow," LA-7951-MS (1980).

8. D. A. Powers and R. O. Meyer, NUREG-0630 (1980).

9. "MATPRO-Version 11 (Revision 1), A Handbook of Material Properties for Use in the Analysis of LWR Fuel Rod Behavior," NUREG/CR-0947, TREE-1280, Rev. 1 (1980).

10. S. M. Modro et al., Proceedings, International Meeting on Thermal Reactor Safety, Chicago, Ill., NUREG/CR-0027, Vol. 2, p. 839 (1982).

RESULTS OF THE IN-PILE DEGRADED CORE COOLABILITY EXPERIMENTS: DCC-1 AND DCC-2*

Kenneth R. Boldt, Paul A Kuenstler, Jr., and Theodore R. Schmidt

Sandia National Laboratories
Albuquerque, New Mexico 87185 USA

ABSTRACT

The results of DCC-1 and DCC-2, the first Degraded Core Coolability experiments in the USNRC's Severe Fuel Damage Program, are presented. The experiments evaluated the coolability of a fission-heated UO_2 debris bed in a water bath with pressure variable from 1 to 170 atmospheres. The 0.5-meter deep bed consisted of small-sized particulate with an average diameter of 0.4 mm for DCC-1 and large-sized particulate with an average diameter of 1.8 mm for DCC-2. DCC-1 evaluated deep bed behavior in the laminar coolability regime while DCC-2 examined coolability in the transition and turbulent flow regimes. The main results presented are the dryout heat flux dependence on pressure and the rate and method of quench of dry debris.

INTRODUCTION

DCC-1 and DCC-2 are the first two experiments in the USNRC-sponsored Degraded Core Coolability (DCC) Program being performed at Sandia National Laboratories. The DCC program is part of the NRC's Severe Fuel Damage (SFD) program established after the accident at TMI-2. The main objective of the DCC program is to verify, with a limited number of in-pile experiments, the accuracy of existing debris coolability models for predicting bed behavior in previously-untested SFD parameter regimes. The primary test matrix consists of three experiments of which the first two are reported here. Both experiments evaluated the coolability of a deep UO_2 debris bed in a pressurized water bath with pressure variable from 1 to 170 atmospheres. The beds were fission-heated in the Annular Core Research Reactor to simulate the internal heat generation from decay heat in an SFD accident. DCC-3, to be performed in mid-1985, will be a similar experiment with the addition of bed stratification and liquid injection to the bottom of the bed.

DCC-1 and DCC-2 differ primarily in their particle size distributions for the debris bed. DCC-1 contained a broad small-particle distribution simulating the expected debris from the interaction of molten fuel in a steam explosion. DCC-2 had a narrow, large-particle distribution simulating the rubble that would be expected from the quench of non-molten fuel. In addition to being prototypic of different accident scenarios, the DCC particle distributions were selected to span the range of coolability regimes. Figure 1 shows the

*This work was supported by the U.S. Nuclear Regulatory Commission and performed at Sandia National Laboratories which is operated for the U.S. Department of Energy under contract number DE-AC04-76DP00789.

predicted dryout heat flux as a function of particle diameter and bed porosity using the Lipinski zero-dimensional coolability model.[1]

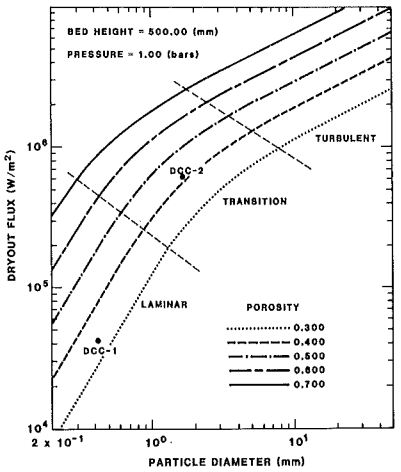

Figure 1 DCC Coolability Regimes

The graph is subdivided into the three general coolability regimes -- laminar, transition and turbulent. Mapping the DCC-1 and DCC-2 effective particle diameters and porosities onto this graph illustrates that the experiments are predominantly in the laminar and transition regimes, respectively. As pressure is increased, the tendency is for each experiment to become more turbulent.

EXPERIMENT DESCRIPTIONS

The DCC-1 and DCC-2 experiment packages (Figure 2) are nearly identical in design, assembly, and operation.[2] During operation, the experiment packages are located in the dry central cavity of the ACRR, utilizing all of the axial height of the reactor for irradiation of the debris bed. The bed has a diameter of 0.10 m, a height of about 0.50 m, and is contained in a insulated double-wall crucible. The crucible provides a near adiabatic boundary condition on the bed bottom and walls. The debris consists of coarse UO_2 particulate seeded with Gd_2O_3 to decrease thermal neutron sensitivity. The relative differences in the particle size distributions for DCC-1 and DCC-2 are shown in Figure 3. Predictions of dryout heat flux contained in this report use the effective (Fair-Hatch weighted) particle diameters with a shape factor correction (assumed a constant multiple of 0.78). The porosity achieved for the dry-packed DCC-1 bed was 34.5% and for DCC-2 was 38.4%. The total fuel mass in the debris beds was 27.0 kg and 24.0 kg, respectively.

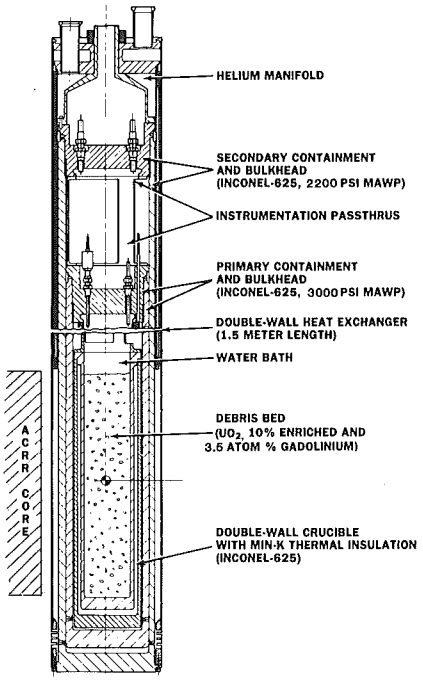

Figure 2 DCC Experiment Package

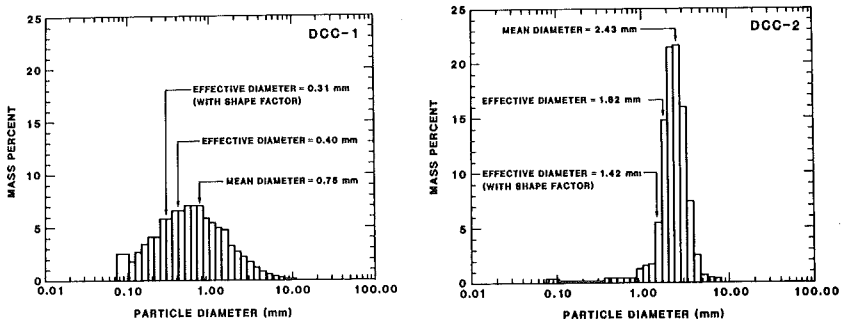

Figure 3 Particle Size Distributions for the DCC-1 and DCC-2 Debris Beds

As shown in Figure 2, the debris bed, crucible, and water bath are enclosed in the primary containment vessel. To evaluate the dryout heat flux at very high pressures (up to 170 atmospheres), the primary vessel was fabricated from Inconel 625 and extensively tested to withstand all expected normal and abnormal pressure environments. The primary containment vessel is a closed system with pressure adjusted by raising and lowering the saturation temperature of the water bath. Subsequently, most all of the experimental dryout points were obtained for a saturated pool with little or no subcooling. To prevent fission product release in the event of any primary boundary failure, a secondary containment vessel completely surrounds the primary vessel. A concentric-flow heat exchanger is attached to the secondary vessel. The manifold on the top of the heat exchanger routes cold helium gas down the outside of the secondary containment vessel and receives the return flow from the outer annulus of the package.

The main diagnostic instrumentation for determining bed conditions are sheathed thermocouples located at various radial and axial positions in the debris bed (Figure 4).

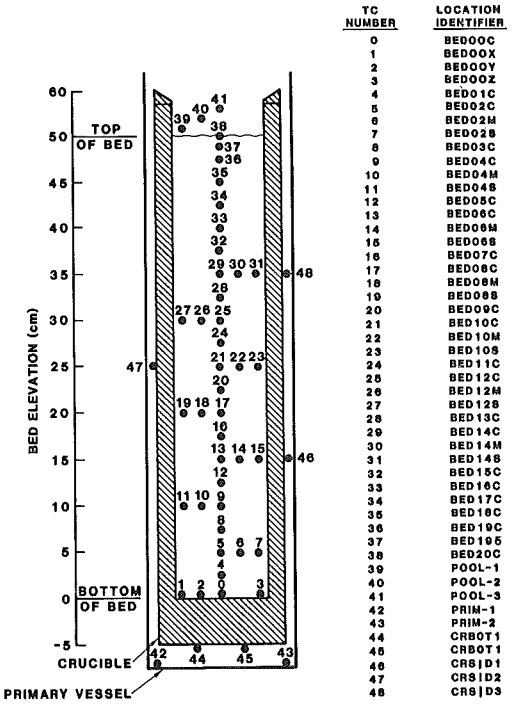

TC NUMBER	LOCATION IDENTIFIER
0	BED00C
1	BED00X
2	BED00Y
3	BED00Z
4	BED01C
5	BED03C
6	BED02M
7	BED02B
8	BED03C
9	BED04C
10	BED04M
11	BED04B
12	BED05C
13	BED06C
14	BED06M
15	BED06B
16	BED07C
17	BED08C
18	BED08M
19	BED08B
20	BED09C
21	BED10C
22	BED10M
23	BED10B
24	BED11C
25	BED12C
26	BED12M
27	BED12B
28	BED13C
29	BED14C
30	BED14M
31	BED14B
32	BED15C
33	BED16C
34	BED17C
35	BED18C
36	BED19C
37	BED19B
38	BED20C
39	POOL-1
40	POOL-2
41	POOL-3
42	PRIM-1
43	PRIM-2
44	CRBOT1
45	CRBOT1
46	CRBJD1
47	CRBJD2
48	CRBJD3

Figure 4 Thermocouple Locations for DCC Debris Beds

The extensive array of thermocouples was used to interpret subcooled, boiling, and dryout conditions in the bed. Pressure in the primary vessel was measured using pressure transducers and verified by the saturation temperature.

The DCC auxiliary systems and their interconnection to the experiment package are shown in Figure 5. The DCC debris bed is fission heated in the central irradiation cavity of the ACRR. Cooling lines are connected to the mobile helium cooling loop located outside of the reactor highbay. The flow from the loop to the package can be diverted to a heat exchanger in the liquid nitrogen tank to provide additional cooling capacity. Diagnostic instrumentation from the package is monitored by an HP-9845/HP-1000 computer-based data acquisition system. A separate HP-9845 computer-based data acquisition system is used to monitor cooling loop parameters for diagnostic and control functions.

EXPERIMENT OPERATION

Due primarily to the difference in particle size distributions, the DCC-1 and DCC-2 experiments exhibited considerably different dryout behavior.[3,4] A listing of the main features and operating history for both experiments are shown in Table I.

Table I. DCC-1 and DCC-2 Operating Summary

	DCC-1	DCC-2
Effective particle diameter	0.31 mm	1.42 mm
Total bed loading	27 kg	24 kg
Initial Bed porosity	34.5%	38.4%
Date performed	August, 1983	April, 1984
Days/hours of operation	9 d/116 hrs	8 d/91 hrs
Dryouts	49 total 35 incipient 14 forced	72 total 62 local 10 global
Extended dryouts and quench	4	6
Maximum temperature	1120 K	1350 K
Other observed phenomena	Superheat flashes	Low permeability zone

In DCC-1, dryouts were obtained in two general forms: incipient and forced. Incipient dryouts were achieved by taking small power steps from a boiling-bed condition. Figure 6 shows the temperature and power history for a typical incipient dryout in DCC-1. This particular dryout was performed at pressure of 0.62 MP with all of bed thermocouples indicating saturation temperature of $160^{o}C \pm 1^{o}C$. As shown in the figure, the dryout was first detected after the reactor power step to 19 kW. After observing the growth of the dry zone to a few more thermocouple positions, the dryout was terminated by reducing reactor power to 1 kW; quench behavior was observed. Following quench at one pressure, the experiment saturation pressure was changed to the next desired value by adjusting reactor heating and package cooling. In this manner the entire pressure curve was mapped.

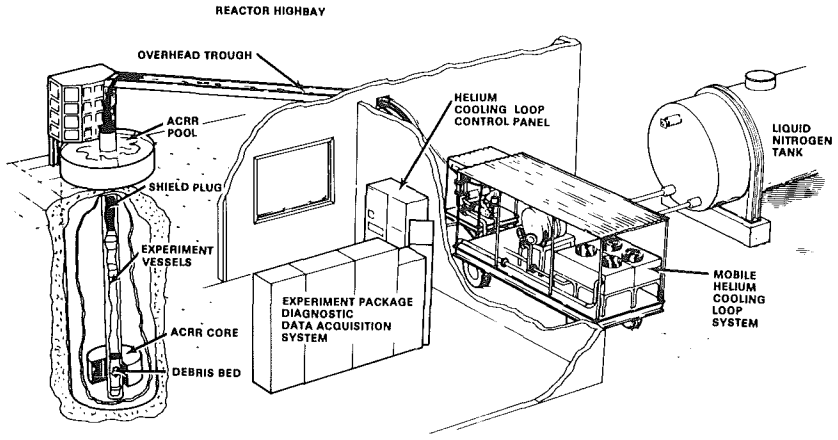

Figure 5 Overall Setup for In-Pile DCC Experiments

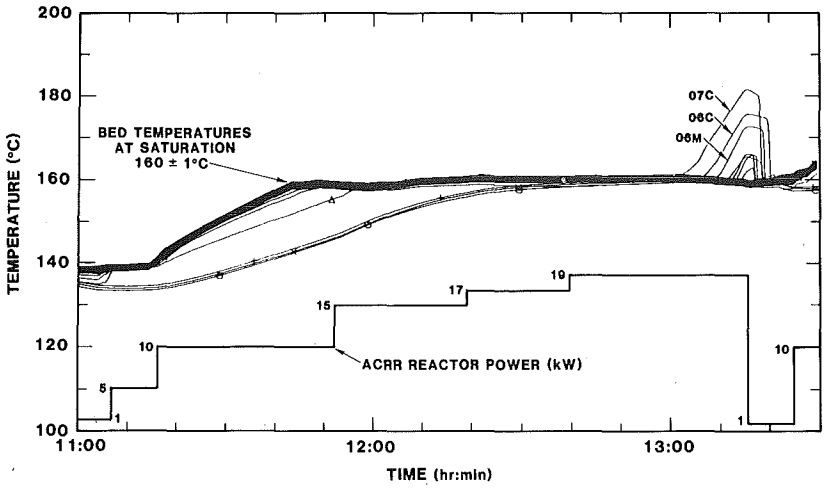

Figure 6 Typical DCC-1 Incipient Dryout Temperature and Power Histories

A few of the dryouts in DCC-1 were forced with rapid pressure drops or large power steps. When system pressure was reduced at a rapid rate (~4%/min), dryouts occurred even though the bed power was only a small fraction (down to 10%) of the incipient dryout value. Large power steps were performed from 1.2 to 40 times the dryout power. These steps were used to investigate the location of initial dryout as a function of power in excess of dryout and to attempt to disrupt the bed. One of the large power steps was extended to a maximum bed temperature of 850°C to observe quench behavior (Figure 7). About two-thirds of the bed was dried when the power was reduced to obtain near steady-state conditions. When the power was dropped to zero, the resulting quench was slow, and wetting occured at successive thermocouple levels without fingering.

In DCC-2 a quite different dryout behavior was apparent as compared to the incipient dryouts of DCC-1. The existence of local dryouts was identified early in the experiment operation. A local dryout is defined as a portion of the bed drying and increasing in temperature above saturation; however, the temperature reaches a steady-state value and the dry zone ceases to grow. Figure 8 shows the temperature history of a typical local dryout (DO#7) for DCC-2. With successively higher reactor powers, the local dryout obtained higher temperatures and grew in size, and a new steady-state condition was achieved. The local dryouts in DCC-2 are predicted to be caused by the existence of a low permeability zone in one side of the bed. The liquid flow through the remainder of the bed supplies sufficient coolant to maintain a stable local dry zone.

Global dryouts are those extending across the bed, cutting off the flow of coolant to the bottom of the bed. In DCC-2 global dryouts were obtained at about 1.5 times the local dryout power. Figure 8 shows a global dryout (DO#8) achieved for the same conditions as local dryout #7. In DO#8 the reactor power is increased until it becomes apparent that the local dryout has extended across the bed and is not approaching a steady-state condition.

Attempts to disrupt the low permeability zone were partially successful. With sudden large power steps to 3 W/g from a subcooled condition in the bed, sufficient vapor generation was induced to rearrange the debris particles. The resultant debris bed was more than 2 cm taller and had a porosity increase from 38.4% to 41.0%. Local dryouts were not eliminated; however, their initial location in the bed was lowered. Global dryouts as a function of pressure were evaluated for this post-disruption bed.

EXPERIMENT RESULTS

To date, the reduction of the data from the DCC-1 and DCC-2 experiments has focused on the determination of the dryout heat flux as a function of pressure. A primary input needed to determine the heat flux is the coupling factor between the reactor and the debris bed. Using adiabatic heatups performed throughout the experiments, the localized coupling factors were determined for the wet and dry conditions. Combining the measured coupling factors with neutronics and saturation calculations, local power densities were integrated to yield the total bed power at the point of dryout. Further analysis is expected to reduce the uncertainty associated with this method of bed power determination.

The dryout heat flux as a function of pressure for both experiments is shown in Figure 9. The data points are compared to predictions using the Lipinski zero-dimensional coolability model. Most of the dryout points shown in Figure

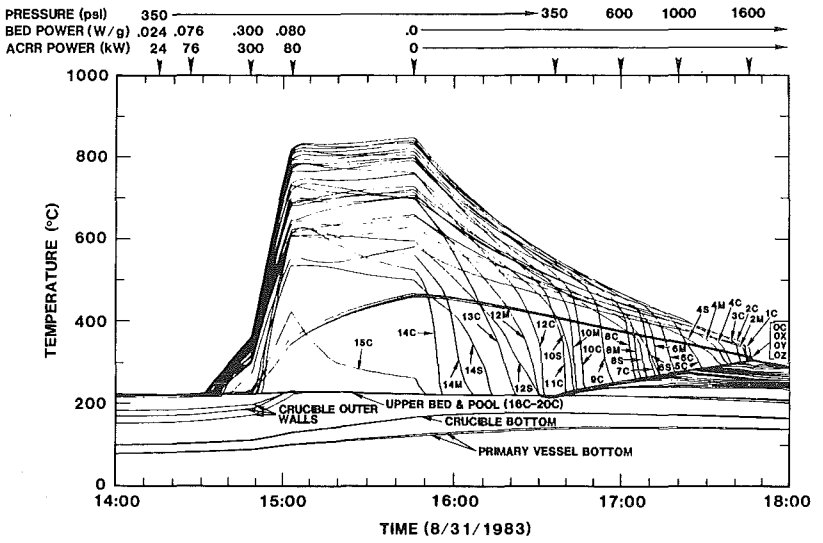

Figure 7 Temperature, Power and Pressure Histories for DCC-1 Extended Dryout and Quench

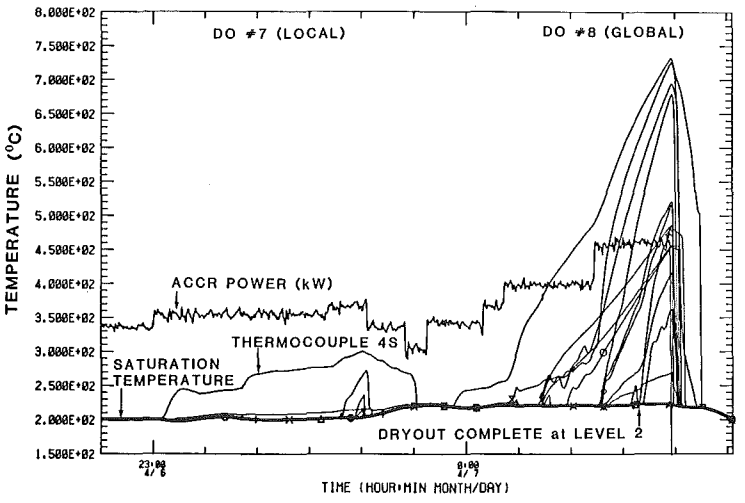

Figure 8 Temperature and Power Histories for DCC-2 Local and Global Dryouts

9 are uncertain by ±15%, primarily due to the uncertainty in the coupling factor. For DCC-1, the experimental and predicted dryout heat flux at one bar agree within experimental error; however, the pressure dependence of the data was much less than predicted. A factor of 6 was predicted for the ratio of the dryout heat flux at its maximum (~ 80 bars) and at 1 bar; whereas, only a factor of 2.5 was realized experimentally. For DCC-2 the agreement between predictions and the global dryout experimental results is better. The low pressure dryout data for DCC-2 could not be obtained due to pressurization of the primary vessel by non-condensable gas generation. Local dryouts for DCC-2 were obtained over the entire pressure range of interest with only those occurring after the bed disruption shown in the figure.

Quenches of extended dryouts in the two experiments were quite different in manner and rate. For DCC-1 quenches were slow (~2 hours for 1000 K fuel) and revealed a uniform quench front (i.e., no fingering was observed). The quench rate in DCC-2 was fast (~10 minutes for 1000 K fuel) with rewet occurring through the high permeability side of the bed and then extending to the low permeability side.

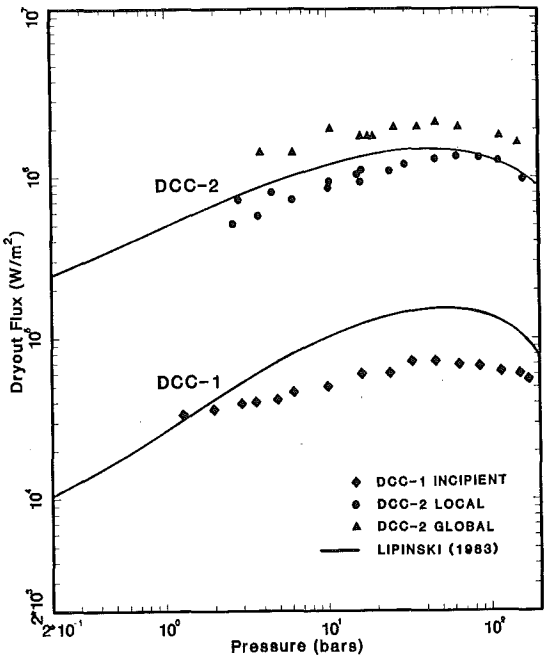

Figure 9 DCC-1 and DCC-2 Dryout Heat Flux Dependence on Pressure

SUMMARY

The first two in-pile experiments in the DCC program were performed and provide a data base for model verification in parameter ranges previously not investigated. The experiments were operated for a total of over 200 hours with 121 observed dryouts. DCC-1, designed to test the laminar flow region of dryout, displayed unexpected results. While the dryout fluxes at one atmosphere are approximately those predicted by the Lipinski model, the pressure dependence of the dryout data is not predicted accurately. The quench behavior of DCC-1 displayed a uniform quench front with quench times extending to hours. The DCC-2 dryout data conforms in magnitude and pressure dependence with the Lipinski model. In addition to "global" dryouts, in which the dry zone extends across the bed, "local" dryouts were observed. These are zones of lower than average permeability which dry out and achieve stable temperatures. The quench times in DCC-2 are only a few minutes long.

REFERENCES

1. R. J. Lipinski, A Model for Boiling and Dryout in Particle Beds," Sandia National Laboratories, NUREG/CR-2646, SAND82-0765, 1982.

2. E. D. Bergeron, K. R. Boldt, R. J. Lipinski, and P. A. Kuenstler, LWR Severe Core Damage Phenomenology Program Plan, Volume 2: LWR Degraded Core Coolability Program, SAND82-1115 (2 of 2), NUREG/CR-2725 (2 of 2), Sandia National Laboratories, Albuquerque, NM, November 1982.

3. K. R. Boldt, E. D. Bergeron, P. A. Kuenstler, and T. R. Schmidt, DCC-1 Experiment Report, Sandia National Laboratories (to be published).

4. K. R. Boldt, A. W. Reed, and E. D. Bergeron, DCC-2 Experiment Report, Sandia National Laboratories (to be published).

EXTENDED DRYOUT AND REWETTING OF PARTICULATE CORE DEBRIS BEDS*

L. Barleon, K. Thomauske, H. Werle

Kernforschungszentrum Karlsruhe
Postfach 3640, 7500 Karlsruhe, FRG

ABSTRACT

A knowledge of the behaviour of dry zones after dryout of particulate core debris beds is of importance because, if remelting occurs, attack on supporting structures is possible. Furthermore in the course of a reactor accident, temporarily dry zones may be envisaged, therefore rewetting behaviour is of interest. This topics have been studied experimentally out-of-pile with inductively-heated, water-cooled particle beds.

Studies of the location, size and temperature distribution of dry zones allow to check predictions of dryout models and to identify the main heat transfer process in dry zones. The rewetting behaviour of beds with small and large particles have been investigated and the rewetting velocity has been correlated with prediction based on available dryout models.

INTRODUCTION

Analysing Light Water Reactor degraded core accident sequences, the existence of high temperature core debris beds has to be considered [1,2]. This debris could be formed within the reactor vessel (in vessel) or in the reactor cavity (ex vessel) depending on the preceeding accident history.

A knowledge of the behaviour after dryout, namely the dry front propagation and the temperature profile within the dry zones is of importance especially for the in vessel case, because, if remelting of the fuel occurs, attack on and failure of supporting structures is possible. On the other side steam generated as a consequence of quenching dry debris bed by feeding in emergency cooling water could lead to pressure loadings on the primary system or on the containment building, which have to be quantified for reactor safety evaluations.

In this work, the beds were composed of small, spherical stainless steel particles and water was used as coolant. Small particles are characterized by capillary pressure being comparable to the hydrostatic pressure. Extended dryout, especially the location, size and temperature distribution of the dry zone and the variation of these parameters with time and power density (down to rewetting) was studied with volume-heated beds. In addition, transient rewetting was investigated starting with a dry bed of uniform temperature.

---

* Work performed within the Fast Breeder Project Karlsruhe

EXPERIMENTS AND RESULTS

VOLUMETRIC HEATING

Behaviour after dryout was studied with volumetrically heated beds of stainless steel spheres (diameter 150-710, 200-500 and 200-315 μ, bed height 16-20 cm) using water as coolant. The particles were contained in a double-wall, cylindrical glass vessel with a radial vacuum gap to minimize heat losses. The bed power is removed by a cooled bottom plate and a heat exchanger above the bed. Several dryout runs were performed with each bed. In each run the power was first increased stepwise beyond dryout and then decreased down to rewetting, allowing for stationary conditions at each power level. The experimental setup has been described in more detail previously [3].

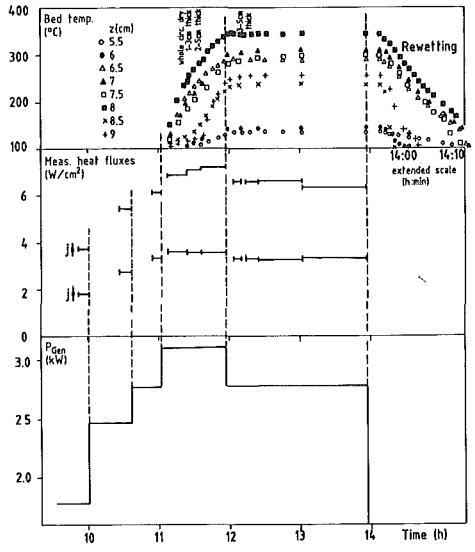

Fig. 1
Bed 83/10/18-11/19, SS 316L, 200-500 μ
ε=.395, H=20.0 cm, water, bottom cooled
Bed history

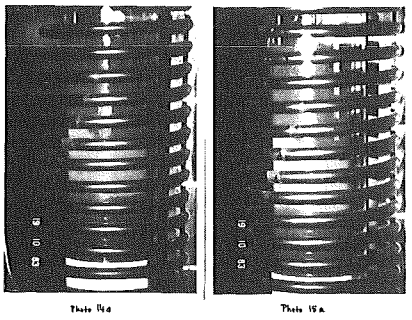

Fig. 2
Bed 83/10/18-11/19, 200-500 μ, ε =.395, water, bottom cooled, j ≈ 9 W/cm²
Stable dry zone

Cooled bottom

After reaching dryout, the temperatures in the dry zone increase very fast (Fig. 1). Within about 30 min the dry zone achieves its asymptotic size, which was generally between about 5 and 10 cm from the bottom. After further 30 min the asymptotic temperatures are established. Generally the maximum temperatures were very high, therefore the power had to be reduced to limit the temperatures to a tolerable value (≈ 500 °C). With few exceptions the dry zone extended radially over the whole bed, but the thickness at the circumference varied considerably (Fig. 2). Even when the dry zone extended radially over the whole bed, stable conditions (location, size and temperature of the dry zone; ratio of downward to upward heat flux) were maintained over several hours, indicating that the mass transport between the bottom and top wetted zone is very small. The dryout zone increases with power beyond dryout (Fig. 3), but there are only few data available because of the temperature limitation. The most surprising result is that once a dry zone has formed, it is extremely stable against power reducions (Fig. 3). Reducing the power to 50 % of that for initial dryout did not diminish the size of the dry zone and to achieve rewetting, the power had to be reduced to 30 % of the initial dryout power. Whereas the size of the dry zones is independent of the power, the temperature varies strongly with power (Fig. 4).

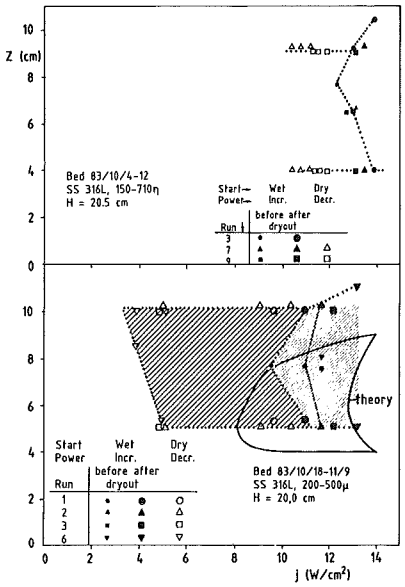

Fig. 3
Irreversibility of dry zones
Stainless steel particles, water, bottom cooled

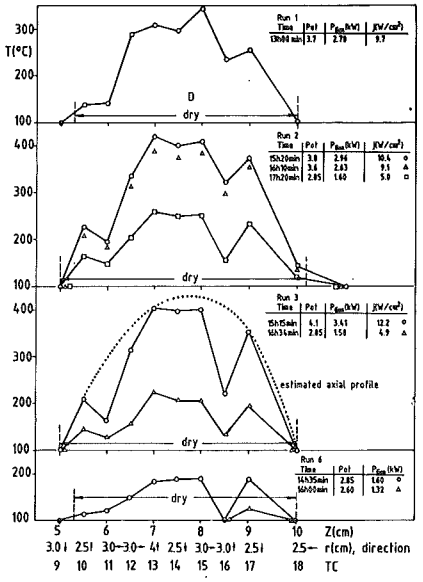

Fig. 4
Bed 83/10/18-11/19, SS 316L, 200-500μ, ε=.395, H=20.0 cm, water, bottom cooled
Steady state temperature distribution in dry zones

If conduction is the main heat transfer process in the dry zone, the axial temperature profile should be parabolic and the relation $\Delta T/D^2 = q/8\ \lambda_b$ should hold. ΔT is the difference between the maximum and the saturation temperature, D is the thickness of the dry zone, q the volumetric power density and λ_b is the conductivity of the dry (vapor-filled) zone. The experimental profile is approximately parabolic, although some fluctuations exist, which are probably due to different radial positions of the thermocouples. Using the relation above and stationary experimental data of q, ΔT and D (≈ 5 cm) one gets $\lambda_b \approx 6 \times 10^{-3}$ W/cmK.

At dryout, about 30 % of the power is transferred downward (Tab. 1). This is considerably more than is generated in the subcooled bottom layer (<1 cm at dryout), which confirms "downward boiling" caused by capillary forces [3].

Adiabatic bottom

After reaching initial dryout at about 6.6 W/cm² the power density was increased further to extend the dryout front before in the dry zone stable temperature conditions are established and temperatures above experimental limitations (500°C) are reached. By this way a dry zone with a rather constant thickness of 9 cm, which radially extended over the whole bed, could be obtained. Once established a well defined dry zone the power was stepwise reduced waiting at each power level several hours for stable conditions. Similar to the bottom cooled experiments the dry zone was very stable against power reductions. Rewetting and decreasing of the dry zone occurred only if the power was decreased below 40 % of the initial dryout power. The values of the initial dryout and rewetting are listed in Tab. 1.

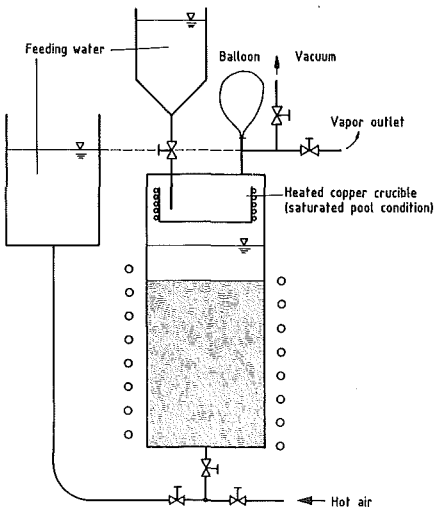

Fig. 5 Schematic experimental set up

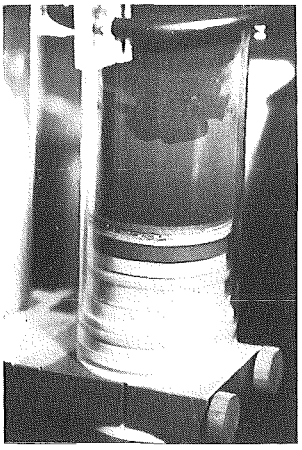

Fig. 6
Bed 84/5/25-29, SS 316L, 200-500 μ,
ε=.395, H=20.0 cm, water, T_o=260±60°
Shape of rewetting front

The heat conductivity of the dry zone determined from experimental values of q, ΔT and D is $\lambda_b \approx 8 \times 10^{-3}$ W/cmK, which is within the experimental error in agreement with the value for the bottom cooled experiments.

TRANSIENT REWETTING FROM TOP

The volume-heated experiments are not well suited for detailed rewetting studies because the initial conditions are very complex (dry zones are relatively small and complex in shape, large temperature gradients in dry zone). Therefore transient rewetting has been studied starting with dry beds of uniform temperature which are normally not heated during rewetting. The main goal was to study the shape of dry/wet interface and to determine the rewetting velocity.

Suitable, initial conditions are achieved by heating up inductively dry beds of stainless steel particles (200-500 μ diameter) in air or in vacuum. Again, more than 20 thermocouples were used to measure the bed temperature. The beds heated in vacuum were filled with steam at atmospheric pressure before initiating rewetting. The results of preliminary transient rewetting experiments were the same if the bed was initially filled with air or vapor. Therefore in the final experiments the beds were heated in air. Furthermore after reaching a certain temperature the inductive heating was stopped and hot air was blown from below through the bed to equalize local uniformities in the temperature (caused by inhomogeneities in the power density probably due to local variations in porosity and particle size), resulting in a temperature which is uniform within 10 % over the whole bed.The gas flow is interupted before rewetting is initiated. Rewetting is started by pouring saturated water from above on the heated crucible above the bed (Fig. 5). The heater vaporizes part of the impinging water, helps to sustain saturated conditions and also prevents disturbances of the bed surface by atomizing the jet of water poured into the vessel. Additional water is poured in during rewetting to keep the liquid level constant.

Preliminary tests indicated that the shape of the dry/wet interface is very sensitive to local inhomogeneities in porosity, particle size and temperature.

If the rewetting front is not uniform, the interpretation, especially the determination of the rewetting velocity, is difficult. In order to equalize at least the temperatures within the bed, the already mentioned additional heating with hot air was used in the final series.

Few minutes after starting rewetting the saturated water pool reached his final height of about 10 cm above the top of the bed. The first 2 to 3 cm of the bed were rewetted in about one minute. This depth corresponds to the region, where later on vapor channel formation was observed. Proceeding deeper the rewetting front velocity decreased to an asymptotic value. The shape of the rewetting front in this region was rather flat and did not show fingering (Fig. 6). This behaviour is in contrast to experiments with bigger particles where pronounced fingering was observed [4], resulting in rather high rewetting velocities.

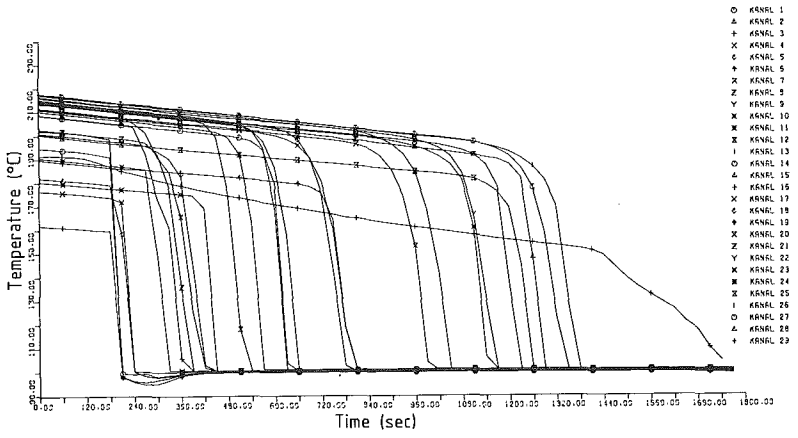

Fig. 7 Bed 84/8/14-31, SS 316L, 200-500μ, ε =.395, H=20.0 cm, water, T_o=200°
Time dependent temperature

In Fig. 7 the time dependent bed temperatures are plotted. For a given position within the bed the temperature decreases very slowly with time until the rewetting front approaches. Then the temperature drops down to the saturation point rather quickly. This behaviour indicates that in the dry zone the temperature front velocity is slower than the rewetting front velocity. Under this condition the involved rewetting heat flux j_{rew} may be evaluated from the rewetting front velocity u_{rew} by a simple correlation, which is a modification of the Landau equation [5]:

$$u_{rew} = \frac{j^{meas}_{rew}}{\rho_v \varepsilon h_v \Delta s + \rho_p (1-\varepsilon) c_p (T_o - T_s)}$$

where u_{rew} is the rewetting front velocity, ρ the density, ε the porosity of the bed, c the specific heat, T the temperature, h_v the heat of vaporization, Δs the change of saturation; v, p, o, s indicate vapor, particle, initial and saturation. Using this correlation we calculate from the measured rewetting front velocities the rewetting heat fluxes at different depths H_{rew} of the rewetting front in the bed. The results are plotted in the Fig. 8 together with theoretical results.

As a spin off of the transient rewetting experiments it was found out that if the liquid is not spreaded homogeneously over the bed surface the liquid will

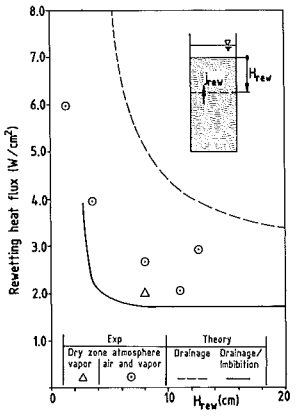

Fig. 8
Rewetting heat flux of a hot debris bed in dependence of the depth H_{rew} of the rewetting front, bed: SS 200-500µ ϕ, H = 20.0 cm T_o = 200 °C, water

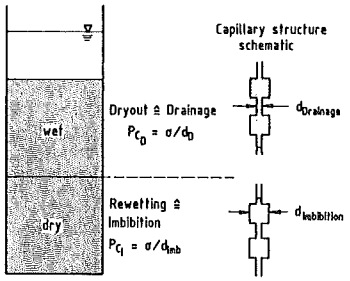

Fig. 9
Capillary effects for dryout and rewetting of particulate beds

penetrate on one side of the bed rather quickly whilst the produced vapor escape through the non-wetted part of the bed. This results in an about two times shorter overall rewetting time.

CALCULATION

The DEBRIS code [6] (version Oct. 82; cosinus of contact angle 0.8; Leverett function $J = (1/s-1)^{0.175}/\sqrt{5}$, s effective saturation) was used to calculate the bed behaviour up to and beyond dryout. Generally the experimental data for the upward and downward heat fluxes (for bottom cooling), the initial dryout heat flux and the location and size of the dry zones are in reasonable agreement with the predictions (Fig. 3, Tab. 1).

The available dryout models and also DEBRIS assume that bed behaviour is independent of the previous bed history, i.e. rewetting of a dry zone is predicted to occur at the same power as initial dryout. As discussed earlier this is not true for the beds investigated here.

A rewetting model based on DEBRIS and the following two assumptions is proposed:

1. The differences in the heat fluxes for dryout and rewetting are caused by different capillary pressures (Leverett functions) for drainage and imbibition. The difference in the capillary pressures can qualitatively be explained by modeling the particle bed by a capillary with varying diameter. For drainage the driving capillary pressure is determined by the smallest, for imbibition by the largest diameter of the capillary (Fig.9).
2. A bed with a dry zone behaves on power reductions similarly as a stratified bed (large variations of the saturation at the layer boundaries).

According to these assumptions, rewetting is described with DEBRIS and by replacing the normally used Leverett function for drainage J in the dry zone by that for imbibition. The Leverett function for imbibition is approximated by 0.7J. In this model the saturation decreases steeply at the boundary between the "wet" (J) and "dry" (0.7J) zone and rewetting is assumed when initial dryout of this "layered" bed is reached. According to this model the rewetting heat flux generally will depend on the location and size of the initial dry region.

For the volume heated experiments the volumetric power density q is the independent parameter. For the transient rewetting experiments (q = 0), the rewetting heat flux originates at the dry/wet interface. These experiments are

therefore modeled assuming bottom heating. To be consistent with volume heated experiments the whole dry zone is modeled, but the thickness of the dry zone has in this case no influence on the calculated rewetting heat flux. Because DEBRIS is a stationary code, the description of the transient rewetting experiments requires that the liquid mass transport to the wet/dry interface, which is necessary to generate the appropriate saturation in the initial dry zone, is taken into account by an iterative procedure.

Tab. 1: Dryout and rewetting heat fluxes for volumetric heating.

		Heat fluxes (W/cm²)					
		Experiment			Theory *)		
		Dryout		Rewetting	Dryout		Rewetting
		Down	Total	Total	Down	Total	Total
Bottom cooled	150-710μ, ε = .363, H=20.5 cm	≈4	10.8-12.3	≈4	3.9	12.9	8.1
	200-500μ, ε = .395, H=20.0 cm	≈4	9.7-11.0	-			
	200-315μ, ε = .400, H=16.0 cm	≈3	9.7-10.2	-			
Bottom adiabatic	200-500μ, ε = .395, H=20.0 cm		5.8-6.6	2.5		7.4	3.8

*) DEBRIS, Version Oct. 1982; cos θ = 0.8, Leverett J = $(s^{-1}-1)^{0.175}/\sqrt{5}$

Tab. 2: Conductivity λ_b of dry zones.

			λ_b (W/cmK)
Experiment	Cooled bottom		6×10^{-3}
	Adiabatic bottom		8×10^{-3}
Theory	Bruggemann [7]	$\varepsilon = \frac{\lambda_s-\lambda}{\lambda_s-\lambda_g}\left(\frac{\lambda_g}{\lambda_b}\right)$	5.4×10^{-3}
	Kämpf-Karsten [8]	$\lambda_b/\lambda_g = 1 - \frac{(1-\varepsilon)(1-\lambda_s/\lambda_g)}{\lambda_s/\lambda_g+(1-\varepsilon)^{1/3}(1-\lambda_s/\lambda_g)}$	1.8×10^{-3}
	Imura-Takegoshi [9]	$\lambda_b/\lambda_g = \Psi + \frac{1-\Psi}{\Phi+(1-\Phi)\lambda_g/\lambda_s}$; $\Psi=(\varepsilon-\Phi)/(1-\Phi)$; $\Phi = 0.3\cdot\varepsilon^{1.6}(\lambda_s/\lambda_g)^{-0.044}$	4.5×10^{-3}
	Kunii-Smith [10]	$\lambda_b/\lambda_g = 1+(1-\varepsilon)(1-\lambda_g/\lambda_s)+(1-\varepsilon)(1-\lambda_g/\lambda_s)^2\ \Omega/\omega$; $\omega = 0.5\frac{(1-\lambda_g/\lambda_s)^2\sin^2\beta}{\ln[\lambda_s/\lambda_g-(\lambda_s/\lambda_g-1)\cos\beta]-(1-\lambda_g/\lambda_s)(\cos\beta)}$; $\sin^2\beta = \frac{1-\varepsilon}{13.23(1-\varepsilon)-5.36}$, $\Omega = 0.666$	3.2×10^{-3}

ε = 0.40; stainless steel (500 K) λ_s = .171 W/cmK; steam (250°C) $\lambda_g = 3.81\times10^{-4}$ W/cmK
Indices: s solid, g gas, b bed.

Calculated results for volumetric heating using this rewetting model are compared in Fig. 3 and Tab. 1 with experiments. In agreement with the experiments, the size of the dry zone is predicted to stay constant if the heat flux is decreased below dryout and rewetting occurs at a power which is considerably lower than that for initial dryout. The transient rewetting experiments too are reasonably well described by the rewetting model. The prediction for both, the absolute values and the dependence of the rewetting heat flux on the position of the wet/dry interface, are in satisfactory agreement with the experiments (Fig. 8).

In Tab. 2 the heat conductivity of dry zones derived from the volumetric heating experiments is compared with theoretical predictions. The experimental data are within the range of predicted values, indicating that conduction is the main heat transfer process within dry zones.

CONCLUSIONS

For beds where the capillary pressure is comparable with the hydrostatic pressure, the rewetting heat flux is considerably smaller than the heat flux causing initial dryout of a wet bed. In addition, once a dry zone has formed, the size will not change if the power is varied between dryout and rewetting. This rewetting behaviour can reasonably well be described by a model based on the DEBRIS code and using the drainage and the imbibition Leverett function for the wet and dry zone, respectively.

From comparisons of experimentaly derived and theoretically predicted heat conductivities of dry zones it is concluded that conduction is the main heat transfer process.

REFERENCES

[1] R.S. Peckover: "Outline of PAHR problems related to licensing", Proc. Fifth Post Accident Heat Removal Exchange Meeting, Nuclear Research Center Karlsruhe, 1982.

[2] V.K. Dhir: "On the coolability of degraded LWR cores", Nucl. Safety 24, 319 (1983).

[3] L. Barleon, K. Thomauske, H. Werle: "Cooling of Debris Beds", Nucl. Technology 65, 67 (1984).

[4] T. Ginsberg, J. Klein, C.E. Schwarz, J. Klages: "Transient core debris bed heat removal experiments and analysis", Proc. Int. Meeting Thermal Nuclear Reactor Safety, Chicago, 1982.

[5] H.G. Landau: "Heat conduction in a melting solid", Quarterly of Appl. Math, 8, 1950.

[6] R.J. Lipinski: "A model for boiling and dryout in Particle beds", NUREG/CR-2646, 1982.

[7] D.A.G. Bruggeman: "Annalen der Physik", Bd. 24, 5. Folge, p. 636 (1935).

[8] H. Kämpf, G. Karsten: "Effects of different types of void volumes in the radial temperature distribution of fuel pins", Nucl. Applications and Technology 9, 288 (1970).

[9] S. Imura and E. Takegoshi: "Effects of gas pressure on the effective thermal conductivity of packed beds", Heat Transfer, Japan. Research, Oct. 13-26, 1974.

[10] D. Kunii and J.M. Smith: "Heat transfer characteristics in porous rocks", A.I.Ch.E. J16, 71-77 (1960).

Chapter 8
Containment Response

IMPROVING OUR UNDERSTANDING OF NUCLEAR POWER PLANT RESPONSE TO SEVERE ACCIDENTS: SUMMARY OF IDCOR RESULTS

M. H. Fontana, Director
National Industry Degraded Core Rulemaking Program (IDCOR)

A. R. Buhl, Vice President

Technology for Energy Corporation
Knoxville, Tennessee USA

ABSTRACT

The IDCOR program, funded by a nuclear industry consortium, developed a comprehensive, integrated position on the issues related to potential severe accidents in nuclear power reactors. This effort encompasses the following: how nuclear power plants proceed into severe accident conditions and how this may be prevented; plant behavior under severe accident conditions; effectiveness of containment systems in preventing fission product dispersal; length of time that containments function acceptably; the consequences of fission product release; operator actions to manage accidents; and mitigation features having sufficient potential value to warrant further consideration. The results of the IDCOR program show that present-generation plants complying with present NRC regulation are highly tolerant of severe accident conditions, constitute risks lower than previously perceived, and require no major backfits.

INTRODUCTION

The Industry Degraded Core Rulemaking (IDCOR) Program developed a comprehensive, integrated, well-documented, technically sound position on the issues related to potential severe accidents--i.e., accidents beyond the design basis--in nuclear power light water reactors. This program is an effort funded by a consortium of over 60 nuclear utilities, NSSS suppliers, and architect engineers, and is the basis for industry participation in the Nuclear Regulatory Commission (NRC) severe accident decision process.

IDCOR comprises a sequence of 52 analytical activities designed to identify key issues, develop the understanding of controlling phenomena and models to describe these issues, develop the necessary analytical methods,

apply the models and methods to perform best-estimate analyses of the severe accident behavior of a limited number of reference plants, and extend the findings as generically as possible. The results of these activities are reported in a Technical Summary Report[1] which summaries nearly forty in-depth reports which separately document the research, development, and evaluations performed by IDCOR on the major technical issues. An overview of the program, as of 1983, was published in Reference 2.

POLICY

IDCOR was guided by an overall policy that called for the review and use of existing information to the maximum extent possible, the enhancement of technical understanding and communication between the industry and NRC and among members of the industry, the use of best estimate rather than conservative analysis, and the use of an independent expert review process.

MAJOR ISSUES

Major issues that guided the IDCOR assessment were: how nuclear power plants proceed into severe accident conditions and how this may be prevented, plant behavior under severe accident conditions, effectiveness of containment systems in preventing fission product dispersal, length of time that containments function acceptably, the consequences of fission product release, operator actions to manage accidents, and mitigation features having sufficient potential value to warrant further consideration.

TECHNICAL APPROACH

The technical approach of the IDCOR Program utilized a logical structure of 24 technical tasks, subdivided into 52 subtasks, which are described in Reference 1. Specifically, the approach was to:

- Review in depth the existing base of information about severe accident behavior in nuclear power plants
- Identify the important phenomena involved
- Adopt and develop appropriate mathematical models, correlations, and assessment techniques
- Select a set of representative reference plant designs
- Identify the important accident sequences which can result in severe conditions if allowed to proceed unchecked
- Realistically characterize plant behavior in these accident sequences

- Identify and assess the opportunities for preventing these sequences, terminating their progress, or mitigating them
- Estimate consequences and relate results to safety goals and applicable deterministic criteria.

REFERENCE PLANT SELECTION

IDCOR analyzed the behavior of reference nuclear power plants under a relatively small number of key accident sequences. Four reference plants were chosen to represent the important characteristics of present-generation plants in the United States. These reference plants were Peach Bottom (General Electric BWR with Mark I pressure suppression containment), Grand Gulf (General Electric BWR with Mark III pressure suppression containment), Zion (Westinghouse PWR with a large dry containment system), and Sequoyah (Westinghouse PWR with an ice condenser containment). Additional plants were identified to represent those classes of plants different from the reference plants. These were Susquehanna (GE BWR with Mark II pressure suppression containment), Oconee (Babcock and Wilcox PWR), and Calvert Cliffs (Combustion Engineering PWR). Although in-depth analyses of these plants were not performed, analytical tools were developed for their analysis.

ACCIDENT SEQUENCE SELECTION

The IDCOR evaluations of existing PRAs showed that a relatively small number of accident sequences dominated public risk. The large number of remaining sequences have probabilities of occurrence and/or consequences such that their contribution to the total risk is negligible.

For the dominant sequences, the factors that most strongly affect risk are the probability of core damage, the capability of containment to perform its function, and the fission products available for release to the environment.

The sequences chosen for detailed analysis of plant response are representative of large classes of sequences with potential severe accident conditions. They were drawn from core damage dominant and risk dominant sequences as identified by prior PRAs. These sequences were chosen using the criteria that they (1) be physically realizable; (2) have traceability to reasonable initiating events; (3) be perceived as being important to risk; and (4) be representative of large classes of sequences. The probabilities of these sequences actually occurring are low. In general, the baseline analyses were performed for sequences with little or no operator intervention; in general, these are not the most probable cases, but tend to yield results which represent upper bounds of consequences.

The IDCOR Program did not separately identify nor evaluate accident sequences specific to large seismic events nor willful acts of sabotage. IDCOR did evaluate initiating accident events similar to those that could be

postulated to emanate from either seismic events or sabotage. The major way that seismically or saboteur induced accidents could differ from IDCOR results is to cause earlier failure of containment. However, IDCOR has examined the risks associated with containment bypass and impaired containment sequences.

CORE DAMAGE PREVENTION

Extensive efforts have been devoted to core damage prevention since the beginning of the nuclear industry, with increased efforts after the accident at Three Mile Island (TMI). All probabilistic risk assessments done to date indicate that core damage frequencies in modern nuclear power plants are low. IDCOR assessments show that some additional benefits can be gained by enhancing operator understanding and utilization of existing non-safety-related systems for achievement of these functions. However, there appears to be little benefit to be derived from major addition of equipment or from major operational changes.

SEVERE ACCIDENT PHENOMENA

The important phenomena affecting ultimate consequences are those that affect containment and provide the impetus for fission product dispersal. Those factors which could cause early containment failure are particularly important. Risk is greatly reduced if containment failure does not occur until long times--measured in terms of time for operator intervention to terminate the accident, for fission product attenuation, and for emergency response measures--after the start of the accident, if at all.

The major historical concerns about phenomena potentially affecting fission product release to the environment can be distilled into a few key issues: (1) steam explosions potentially threatening to containment through the action of pressure pulses, liquid slugs, or missiles; (2) containment overpressure due to rapid steam generation; (3) containment overpressure due to hydrogen generation and subsequent combustion; (4) bypass of containment by such factors as open valves, failures of separation between interfacing systems, and other sneak paths to the environment; (5) containment overpressure due to noncondensable gas; (6) melt-through of the containment basemat; (7) containment overtemperature and overpressure due to heat-up caused by the loss of heat removal capability; (8) containment failure; and (9) radionuclide release and transport.

IDCOR reviewed the existing information on these issues and assessed existing analytical models and codes, and significantly improved the understanding of these issues. New models were developed and incorporated into an integrated code for accident analyses called the Modular Accident Analysis Program (MAAP).

IDCOR conclusions on the key phenomena issues that underly the plant response analyses are:

1. The necessary conditions do not exist in LWRs to allow steam explosions sufficiently energetic to cause containment failure.

2. Rapid steam generation from core debris quenching is less than the capability of the primary system pressure relief values and of the containment.

3. The conditions for hydrogen detonation do not exist; hydrogen burns will not fail large containments and hydrogen control measure are in place in smaller containments, such as pressure suppression and ice condenser containments.

4. The probabilities of containment bypass, such as pre-existing impaired containment or interfacing systems LOCA, are small; nevertheless, these were analyzed.

5. Containment overpressure due to noncondensable gas generation is slow and does not cause early containment failure.

6. Melt-through of the concrete basemat would not occur if water can be supplied to the debris and appropriate power and heat sinks made operative; if the debris is allowed to run dry, basemat penetration would be slow and would always occur after the containment fails from high pressure or high temperature.

7. Containment overpressure or overtemperature due to heatup caused by loss of heat removal capability is very slow.

8. Containment failure, due either to overpressure or overtemperature, is likely to be a relatively small leak rather than a large break; therefore, the base case for analysis is a hole size in containment large enough to preclude further pressure buildup.

9. Radionuclide release and transport must take into consideration the chemical forms of the important fission products (CsI, CsOH, and TeO_2) which have lower volatilities than their constituent elements; the behavior of aerosols in the primary system and in containment, which tends to be dominated by gravitational settling and diffusiophoresis; and the potential for revaporization and relocation due to self heating of the fission products in poorly cooled areas of the primary systems. These effects are incorporated into the MAAP code which is used for the integrated plant analyses.

PLANT RESPONSE TO SEVERE ACCIDENTS

A major portion of IDCOR's resources was devoted to evaluation of the inherent margin of safety provided by existing containment designs under

severe accident conditions. Containment function is controlled by: (1) water for cooling the fuel debris, (2) power for and survival of essential equipment, (3) capability of removing heat from containment, and (4) containment integrity.

The IDCOR evaluations of plant response to severe accident conditions were conducted using the newly developed integrated Modular Accident Analysis Program (MAAP) for temperatures, pressures, material motions, and fission product transport throughout the systems within containment. The models in these codes are based upon a fundamental understanding of physical processes and are supported by the available body of experimental evidence.

Final assessments of accident sequence probabilities and offsite consequences are now underway and will be presented at the IDCOR/NRC technical interaction meeting to be held in November, 1984.

Peach Bottom Atomic Power Station (BWR Mark I)

The characteristics of BWR Mark I containment are shown in Figure 1. The containment has four regions modeled in MAAP: the primary system, the pedestal cavity, the drywell, and the wetwell, which contains the suppression pool.

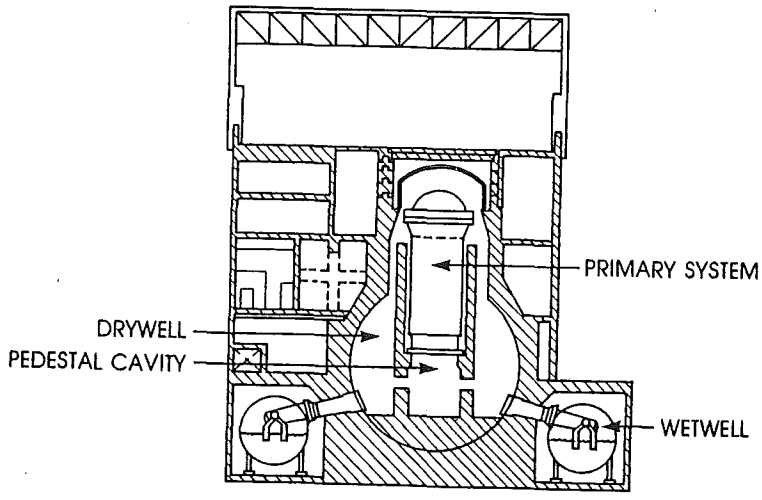

Figure 1. BWR Mark I Containment

The key accident sequences for BWR Mark I systems considered are transient with failure of heat removal (TW), anticipated transient with failure to scram (TC), station blackout (TQVW), and LOCA with failure of injection (S_1E). Each of these events pose potentially significant challenges to containment. However, many of the sequences provide ample opportunity to limit the amount of core damage or to preserve containment integrity. In addition, important system features significantly reduce the radionuclide release. Detailed descriptions of the thermal hydraulic and fission product behavior, and results are given in References 1 and 3.

A summary of results for Peach Bottom are given in Table 1, which presents the key sequences and event times, a general description of system failures and physical processes, and fission product release fractions.

Grand Gulf Nuclear Station (BWR Mark III)

Characteristics of the BWR Mark III containment are shown in Figure 2. The containment as modeled in MAAP has six regions: the primary system; the pedestal cavity; the drywell; the wetwell, which contains the suppression pool; and two outer containment regions, one below the refueling floor and one above it.

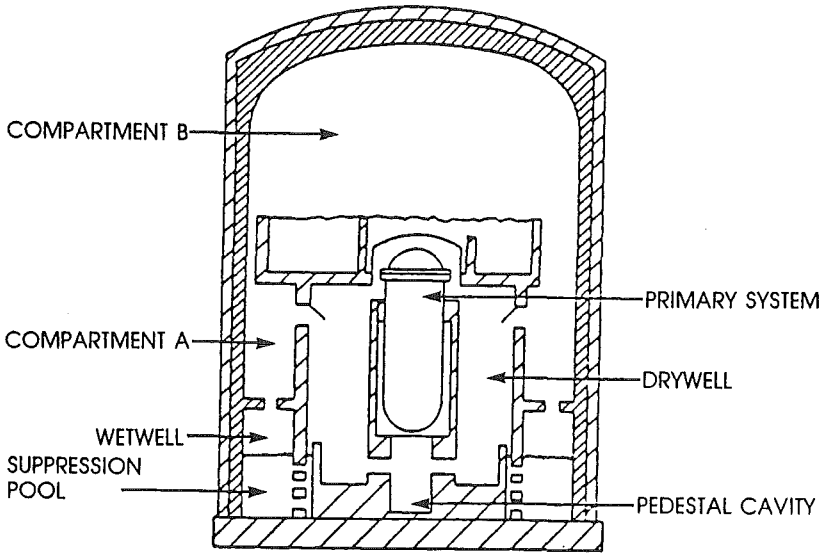

Figure 2. BWR Mark III Containment

Table 1
SUMMARY OF PEACH BOTTOM RESULTS

Results	TW	TC	TQVW	S_1E
Core uncovery, hr	34.0	1.3	8.4	1.1
Start of fuel melting, hr	39.0	3.0	11.4	2.5
Vessel failure, hr	40.0	3.9	12.4	3.4
Containment failure modes[b]	δ	τ	τ	τ
Containment failure, time, hr	32.0	13.0	18.0	24.0
Time of fission product release, hr.	42.0	13.0	19.0	24.0
Duration of release, hr	80.0	50.0	30.0	30.0
Fission product release fraction[a]				
Xe-Kr	1.0	1.0	1.0	1.0
I-Br, Cs-Rb	0.1[c]	0.03[d]	0.05[e]	0.01
Te-Sb	0.1[c]	0.07[d]	0.04[e]	0.01
Ba-Sr	9(-5)	5(-5)	5(-5)	2(-5)
Ru	4(-4)	2(-4)	2(-4)	6(-5)

[a]Numbers in parentheses are exponents of 10.

[b]Symbols:

δ - overpressure due to steam generation

τ - containment structural failure due to high temperature

[c]If CRD flow or drywell sprays are reestablished after vessel failure and before hour 65, these values are reduced to 0.03.

[d]Assumes wetwell venting at 115 psia, according to procedures. Also, if CRD flow or drywell sprays are reestablished before hour 30, these values are reduced to 0.01.

[e]If power can be restored before hour 30, these values reduce to less than 0.01.

The key accident sequences analyzed for the Grand Gulf plant were transient with failure of heat removal ($T_{23}QW$), anticipated transient with failure to scram ($T_{23}C$) LOCA with failure of injection (AE), and transient with failure of injection (T_1QUV). The response of the primary system and containment is influenced by the separation of the drywell and containment by the suppression pool, the pedestal and drywell configuration, and by the presence of igniters. Detailed descriptions of the thermal-hydraulic and fission product behavior and results are given in References 1 and 4.

Table 2 presents the key sequences and event times, a general description of system failures and physical processes, and fission product release fractions.

Zion Nuclear Station (Large Dry PWR)

Characteristics of the Zion PWR large dry containment are shown in Figure 3. The containment, as modeled in MAAP has four major regions: the upper compartment, the lower compartment, the annular compartment, and the reactor cavity.

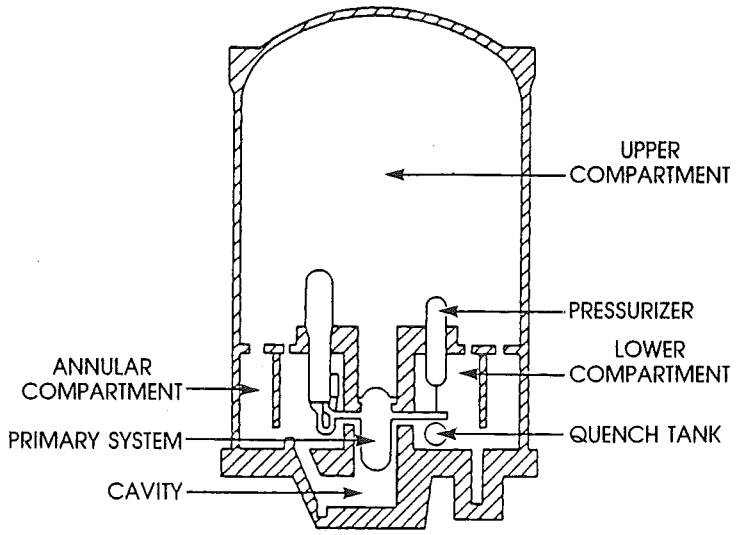

Figure 3. PWR Large Dry Containment

Table 2
SUMMARY OF GRAND GULF RESULTS

Results	$T_{23}QW$	$T_{23}C$	AE	T_1QUV
Core uncovery, hr	49.0	1.3	0.1	0.5
Start of fuel melting, hr	54.0	3.0	1.1	2.0
Vessel failure, hr	56.0	3.8	1.4	2.4
Containment failure modes[b]	δ	δ	ζ	ζ
Containment failure, time, hr	40.0	1.0	58.0	47.0
Time of fission product release, hr	50.0	3.0	58.0	47.0
Duration of release, hr	80.0	47.0	12.0	33.0
Fission product release fraction[a]				
Xe-Kr	1.0	1.0	1.0	1.0
I-Br, Cs-Rb	3(-4)	8(-4)	<1(-5)	7(-5)
Te-Sb	2(-4)	8(-4)	1(-5)	3(-5)
Ba-Sr	<1(-5)	<1(-5)	<1(-5)	<1(-5)
Ru	<1(-5)	<1(-5)	<1(-5)	<1(-5)

[a]Number in parentheses is exponent of 10

[b]symbols:

ζ - overpressure due to non-condensible gas generation

δ - overpressure due to steam generation

The key accident sequences considered for the large dry PWR plant which involve release to the environment are: station blackout (14-TE), station blackout with reactor coolant pump (RCP) seal LOCA (2-SE), station blackout with RCP seal LOCA and a pre-existing impaired containment (2-SE, impaired), and an interfacing LOCA (16-VL). In the interfacing LOCA sequence, fission product releases are to the auxiliary building, which significantly attenuates release to the environment. Large and small LOCAs with failure of recirculation do not fail containment because of action of the fan coolers and spray system. Detailed description of the thermal-hydraulic and fission product behavior, and results are given in References 1 and 5.

Table 3 presents the sequences and event times, a general description of system failures and physical processes, and fission product release fractions.

Sequoyah Nuclear Plant (PWR Ice Condenser)

Characteristics of the PWR ice condenser containment are shown in Figure 4. This containment, as modeled in MAAP, has five compartments: the upper compartment, the lower compartment, the annular compartment, the ice condenser, and the reactor cavity.

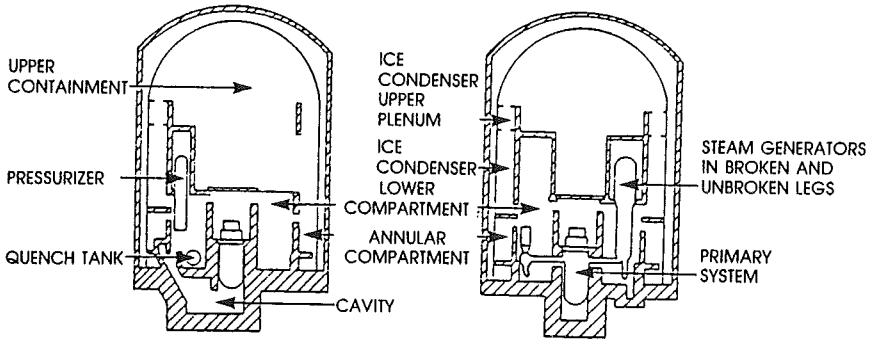

Figure 4. PWR Ice Condenser Containment

Table 3
SUMMARY OF ZION RESULTS

Results	14-TE	2-SE	2-SE (Impaired)	16-VL
Core uncovery, hr	2.3	2.2	2.2	20.0
Start of fuel melting, hr	3.1	3.0	3.0	~23.0
Vessel failure, hr	4.0	3.8	3.8	26.0
Containment failure modes[b]	ζ	ζ	β	--
Containment failure, time, hr	32.0	32.0	0.0	--
Time of fission product release hr	32.0	32.0	4.0	24.0
Duration of release, hr	13.0	13.0	7.0	4.0
Fission product release fraction[a]				
Xe-Kr	1.0	1.0	1.0	1.0
I-Br, Cs-Rb	2(-3)	2(-3)	1(-2)	8(-5)
Te-Sb	2(-5)	2(-5)	3(-4)	8(-5)
Ba-Sr	<1(-5)	<1(-5)	6(-4)	5(-5)
Ru	<1(-5)	<1(-5)	6(-5)	<1(-5)

[a]Numbers in parentheses are exponents of 10.
[b]Symbols:
ζ - overpressure due to non-condensible gas generation
β - failure to isolate containment in the event of an accident

The key accident sequences that could result in release to the environment are LOCA with failure of recirculation and sprays, with the drains between the upper and lower compartment blocked (S2HF-drains blocked); the same sequence with the drains open (S2HF-drain open); the same sequence with a pre-existing impaired containment assumed to be a 0.6 m (2 ft) hole; a station blackout ($T_1B_3MLB_{13}$); and an interfacing system LOCA (V). In the transient with loss of feedwater, large LOCA with failure of injection, small LOCA with failure of recirculation, and small LOCA with failure of injection, containment does not fail.

For only those key sequences which involve the release of fission products to the environment, Table 4 presents the sequences and event times, a general description of system failures and physical processes, and fission product release fractions.

Detailed description of thermal hydraulic and fission product behavior, and results and given in References 1 and 6.

CONCLUSIONS

The major conclusions of IDCOR result from generic research and development of the underlying physical phenomena and operational characteristics which influence plant behavior under severe accident conditions, and from specific evaluations of plant response to these severe accident driving forces for four reference plants covering the major characteristics of existing plants.

Although a limited set of specific areas of design dependency may warrant further assessment for individual plants, the severe accident conditions used to establish these conclusions are representative of the nature and types of events which could potentially challenge containment integrity; the conclusions regarding the major phenomena of importance to containment effectiveness are broadly applicable.

In summary, the IDCOR studies of the representative existing nuclear power plants show that they have a substantial capability to accommodate severe accidents. IDCOR calculated the fission product source terms for many important accident sequences in both boiling water reactor and pressurized water reactors, which are significantly below those predicted by previous evaluations. The technical results support a reduction in the current source terms used to license plants.

Because of the low probability of severe accidents in nuclear power plants that are designed, constructed, operated, and maintained in accordance with current regulations and because of the inherent capability of such plants to control the consequences of a wide spectrum of such accidents, we conclude that major design or operational changes are not warranted for potential severe accident conditions.

Table 4

SUMMARY OF SEQUOYAH RESULTS

Results	S_2HF (drains blocked)	S_2HF (drains) (open)	S_2HF (impared containment)	$T_1B_3MLB_{13}$	V
Core uncovery, hr	1.2	1.2	1.2	1.9	16.0
Start of fuel melting, hr	1.9	1.9	1.9	2.5	18.0
Vessel failure, hr	2.8	2.8	2.8	3.3	20.0
Ice depletion, hr	3.4	4.2	4.2	9.7	--
Containment failure mode[b]	ζ	δ	β	δ	--
Containment failure, time, hr	23.7	10.0	0.0	27.5	--
Time of fission product release hr	23.7	10.0	5.3	27.4	18.0
Duration of release, hr	6.0	6.0	5.0	4.0	4.0
Radionuclide release fraction[a]					
Xe-Kr	1.0	1.0	1.0	1.0	1.0
I-Br, Cs-Rb	6(-4)	7(-4)	2(-2)	4(-3)	1(-4)
Te-Sb	2(-4)	2(-4)	4(-3)	2(-3)	1(-4)
Ba-Sr	<1(-5)	<1(-5)	5(-4)	<1(-5)	<1(-5)
Ru	<1(-5)	<1(-5)	5(-4)	<1(-5)	<1(-5)

[a] Numbers in parentheses are exponents of 10.

[b] Symbols:

ζ - overpressure due to non-condensible gas generation

δ - overpressure due to steam generation

β - failure to isolate containment in the event of an accident

REFERENCES

1. IDCOR Technical Summary Report, Technology for Energy Corporation, available for Atomic Industrial Forum, to be published.

2. M. H. Fontana, The Industry Degraded Core Rulemaking Program: IDCOR--An Overview; Proceedings, International Meeting on Water Reactor Severe Accident Evaluation; Cambridge, MA, USA, August 28 - September 1, 1983.

3. Peach Bottom Atomic Power Station IDCOR Task 23.1 Integrated Containment Analysis, available from Atomic Industrial Forum; to be published.

4. Grand Gulf Nuclear Station IDCOR Task 23.1 Integrated Containment Analyses, available from Atomic Industrial Forum, to be published.

5. Zion Nuclear Generating Station IDCOR Task 23.1 Integrated Containment Analysis, available from Atomic Industrial Forum, to be published.

6. Sequoyah Nuclear Generating Station IDCOR Task 23.1 Integrated Containment Analysis, available from Atomic Industrial Forum, to be published.

ACKNOWLEDGEMENT

This paper is a summary of work done by IDCOR teams composed of many persons from many organizations. We acknowledge especially the following:

Dr. Hans Fauske, Dr. Robert Henry, Dr. Marc Kenton, and Dr. Jeff Gabor, Fauske Associates, Inc.; Mr. George Daebeler and Mr. Alan Marie, Philadelphia Electric Company; Mr. Mike Lloyd, Mid South Services, Inc.; Mr. George Klopp, Commonwealth Edison Company; and Mr. Frank Koontz and Mr. William Mims, Tennessee Valley Authority. Particular recognition is due Dr. Edward L. Fuller, of the Electric Power Research Institute, on assignment to the IDCOR Program at the Technology for Energy Corporation as Technical Manager for Phenomena and Plant Analyses.

ANALYSIS OF CONTAINMENT RESPONSE AFTER VESSEL FAILURE WITH CORIUM EJECTION INTO A REACTOR CAVITY

T. Ishigami, M. Nishi, H. Horii, K. Kobayashi,
K. Muramatsu and K. Soda

Japan Atomic Energy Research Institute
Tokai-mura, Naka-gun, Ibaraki-ken, JAPAN

ABSTRACT

An analysis of thermal hydraulic response in a PWR large dry containment after a pressure vessel failure with corium ejection into a reactor cavity was performed with severe accident analysis codes, THALES-CV developed at JAERI and MARCH1.0. The analysis covered important events and phenomena for several hours duration after the pressure vessel failure. Some differences between the calculated results with THALES-CV and MARCH1.0 were found for the behavior of the corium temperature and the concrete decomposition rate. These were caused by the differences of models in the two computer codes related to the configuration and the property of corium. Important parameters which influenced the thermal hydraulic response in the containment during the accident were identified through the sensitivity analyses with THALES-CV and MARCH1.0.

INTRODUCTION

In recent years, a severe accident analysis has drawn a considerable attention since the TMI-2 accident exhibited a fair amount of core destruction. It is well recognized that a nuclear reactor has a potential risk in itself and that probability of having an accident leading to a core melt still exists unless an adequate prevention or mitigation procedure is taken. In order to properly assess a reactor safety, a risk associated with a nuclear reactor must be quantified. The WASH-1400 /1/ was prepared for this purpose, and several Probabilistic Risk Assessment Programs have been planned and performed. However the present status of quantification of such a risk is still in the state of the art and a computer code to predict such a risk involves a lot of uncertainties due to lack of information on physical phenomena in a severe accident, and computer codes have not always been verified satisfactorily from experiments. This leads us to an alternative method for verification of a computer code, that is a comparison of calculated results among several computer codes with different models to identify important parameters which influence a risk of a severe accident.

This analysis focused on thermal hydraulic response in a PWR large dry containment after vessel failure with corium ejection into a cavity, which constituted a part of an international code comparison exercise organized by OECD/CSNI. Hence this analysis covered important events and phenomena lasting

several hours after a pressure vessel failure. The analysis was performed with severe accident analysis codes, THALES-CV developed at JAERI [2] and MARCH1.0 [3], including sensitivity analysis and comparison of calculated results with these two codes.

COMPUTER CODES

Severe accident analysis codes, THALES-CV and MARCH1.0, were used for the analysis. The THALES-CV code is one of the codes composing the THALES (Thermal Hydraulic Analysis of Loss-of-Coolant, Emergency Core Cooling, and Severe Core Damage) code system, under development at JAERI since 1981. THALES evaluates an overall physical phenomenon and fission product behavior during a severe accident of a nuclear reactor. THALES-CV is a computer code for evaluating pressure and temperature response in a containment vessel during severe accidents. A containment vessel is divided into several control volumes, and the containment pressure and the temperatures of liquid region and gas region in each control volume are evaluated. THALES-CV includes mass and heat transfer models which are required for the analysis of wide-range phenomena during severe accidents.

MARCH1.0 developed in U.S.A. is to evaluate an overall thermal hydraulic behavior in a water-cooled reactor during a core meltdown accident and has been used extensively in several institutions. For the present analysis, however, two subroutines were added to the code, one being to accommodate the initial thermal hydraulic conditions at vessel failure and the other being to give a decay heat level at the constant value of 30 MW as specified for the code comparison exercise. Also the composition of steel was changed from the composition used in MARCH1.0 to the specified one.

Major differences exist between the models in THALES-CV and MARCH1.0 regarding a configuration of corium dropped into water in the cavity at the instance when water in the cavity is vaporized and also regarding a property of corium. In THALES-CV, the configuration of corium is assumed to form a layer for heat transfer calculation between corium and water, while spherical shape is assumed in MARCH1.0. THALES-CV assumes corium to be one layer while MARCH1.0 assumes corium to be separated into an oxide layer and a metallic layer after corium-concrete interaction is initiated. Effect of the differences on the calculated results was investigated by comparing the THALES-CV results with the MARCH1.0 results.

ASSUMPTIONS AND INPUT DATA

This analysis focused on thermal hydraulic response in a PWR large dry containment after vessel failure with corium ejection into a cavity. In the analysis, the containment was assumed to be adiabatic and its integrity maintained during the accident. The total containment pressure at vessel failure was 0.4 MPa at initial with partial pressure of air 0.1 MPa and partial pressure of steam 0.3 MPa. Vessel and primary system pressure at vessel failure was also 0.4 MPa (low pressure) at inital, and therefore the mass and heat transfer from the primary system to the containment in a course of the accident was neglected. The corium ejection from a pressure vessel was assumed to take place instantaneously and to fall into a reactor cavity without scattering outside the cavity.

Base case input data for THALES-CV and MARCH1.0 used for the present analysis are given in Table I. These data include cavity/containment geometry and thermal hydraulic conditions at vessel failure, mass and temperature of corium at vessel failure, type of concrete and decay heat level assumed to be constant during the accident.

Table I Base Case Input Data for THALES-CV and MARCH1.0

Cavity/Containment Data	
Cavity	
Radius of Cavity	3.73 m
Mass of Water	65550 Kg
Water temperature	397 K
Containment	
Number of Compartment	1
Compartment Volume	80000 m^3
Floor Area	1329.7 m^2 (1394 m^2)*
Total Pressure at Vessel Failure	0.4 MPa
Temperature at Vessel Failure	407 K
Corium Data	
Mass of Corium	
Mass of UO_2	90000 Kg
Mass of Steel	22000 Kg Fe:85%, Cr:10%, Ni:5%
Mass of Zr (50% oxidation was assumed)	25859 Kg (22000 Kg)
Total Corium Mass	137859 Kg (calculated)
Temperature at Vessel Failure	2533 K
Concrete Data	
Density	2400 Kg/m^3
Contents	$CaCO_3$:80w%, $Ca(OH)_2$:15w%, SiO_2:1w%, H_2O:3w%, Al_2O_3: 1w%
Decay Heat Level	30 MW

Note : * Values in parentheses indicate data for MARCH1.0.

THALES-CV ANALYSIS

(1) Calculated Results for Base Case

Thermal hydraulic response in a PWR containment after vessel failure until 300 minutes was calculated with the THALES-CV code. Figure 1 shows the calculated pressure and temperature in a containment in the course of the accident, and Figure 2 shows the calculated corium temperature. In these figures, the time 0 corresponds to the time when a pressure vessel failed and corium was ejected. Physical processes calculated with the THALES-CV code are as follows. When a pressure vessel failed at time 0, corium was ejected from the pressure vessel into the reactor cavity and reacted with water in the cavity. The containment pressure rapidly increased with a violent steam generation. Corium temperature rapidly dropped to 600 K in the cavity water until all of the water in the cavity was vaporized. For that time decay heat in corium was balanced with the heat transferred from corium to water. For about ten minutes after the vaporization of water in the cavity was over in 33 minutes, pressure and temperature in the containment were kept to be almost constant. This is because corium temperature is low (less than 1000 K), which

results in the small heat transfer from corium to atmosphere. As the corium temperature began to rise, pressure and temperature in the containment also started to increase. The concrete decomposition was initiated at about 40 minutes after vessel failure. The calculated pressure and temperature in the containment reached 1.4 MPa and 900 K respectively in 300 minutes when the calculation was terminated.

(2) Sensitivity Analysis

In order to identify important parameters which would influence thermal hydraulic response in the containment, sensitvity analysis with THALES-CV was performed. The parameters selected for the sensitivity analysis are shown in Table II together with the ranges of the parameters.

It was found in the sensitivity analysis that the deviation among the calculated containment pressures was ± 30 % at the most for the parameters selected for this analysis. The parameters resulting in a relatively large deviation were heat transfer coefficient (H.T.C.) between corium and concrete, and radiative heat transfer rate from corium to atmosphere. Figures 3 and 4 show the effect of H.T.C. between corium and concrete on the containment pressure and total mass of concrete decomposition, respectively. When H.T.C. between corium and concrete was large, the containment pressure was lower than the base case, while the total mass of concrete deceomposition was about twice as much as the base case. It is because the radiation heat transferred from corium to atmosphere is reduced when the heat transferred from corium to concrete was increased. The corium temperature was found to be much lower than the base case when H.T.C. between corium and concrete was large.

The time interval for all water in the cavity to be vaporized varied considerably with the change of an amount of water in the cavity, the corium temperature at vessel failure, and H.T.C. between corium and water. It was found in the present analysis that the change of an amount of water in the cavity from 50 % to 300 % resulted in the time interval being varied from 5 minutes to 110 minutes.

The corium temperature and the total mass of concrete decomposition after water in the cavity was vaporized showed similar behavior for the parameters selected for this analysis. Therefore the corium temperature and the total

Table II Parameters Selected for the THALES-CV Sensitivity Analysis

Parameters	Low	Standard	High
Mass of Corium (Kg)	68929.5	137859	——
Relative Amount of Metal in the Mass of Corium	SV×1/2*	SV	——
Corium Temperature at Vessel Failure (K)	2033	2533	3033
Amount of Water in the Cavity (Kg)	32775	65550	131100
Concrete Decomposition Temperature (K)	——	796	1160
Concrete Decomposition Enthalpy (J/g)	——	1342	1653
H.T.C.** between Corium and Concrete (W/cm^2K)	0.001	0.01	0.1
Radiative Heat Transfer Rate from Corium to Atmosphere	SV×1/10	SV	SV×10
H.T.C. between Corium and Water (W/cm^2K)	0.05153	0.5153	5.153
Fraction of the Generated Gas Contributing to Metal-Gas Chemical Reactions	0.0	1.0	——

Note : * The acronym SV stands for the standard value.
** The acronym H.T.C. stands for heat transfer coefficient.

mass of concrete decomposition were almost determined by the time interval for all water in the cavity to be vaporized.

MARCH1.0 ANALYSIS

(1) Calculated Results for Base Case

Thermal hydraulic response in a PWR containment during the accident was calculated with the MARCH1.0 code. Figure 5 shows the calculated pressure and temperature in the containment in a course of the accident. Figure 6 shows the calculated temperatures of an oxide layer and a metallic layer of corium which is, in MARCH1.0, assumed to be separated into the two layers after corium-concrete interaction is initiated. When the vessel failed at time 0, corium was ejected into the reactor cavity and reacted with water in the cavity resulting in a violent steam and hydrogen generation and a rapid increase of the containment pressure. The corium temperature dropped to 700 K at the time when the water in the cavity was vaporized. All of the water in the cavity was vaporized in 17 minutes after vessel failure. Then the corium temperature began to rise and reached 1644 K in 67 minutes when a concrete decomposition was initiated. In 117 minutes, the temperature of the oxide layer of corium reached its melting point and gases generated by the concrete decomposition started to flow through the oxide layer. In 192 minutes, a metallic layer located in the upper layer of corium was overturned and moved to the lower layer with the density of the metallic layer being smaller than that of the oxide layer. Then the rate of concrete decomposition increased. The calculated pressure and temperature in the containment reached 1.5 MPa and 1100 K respectively in 290 minutes when the calculation was terminated.

(2) Sensitivity Analysis

Sensitivity analysis similar to the THALES-CV analysis was performed with the MARCH1.0 code. The parameters selected for the sensitivity analysis are shown in Table III together with the ranges of the parameters.

As in the THALES-CV calculation, the deviation among the calculated pressures and temperatures in the containment was ±30 % at the most for the parameters selected for this study. The parameters resulting in a relatively large deviation were an amount of water in the cavity and a particle diameter of corium. Figure 7 shows the effect of a particle diameter on the containment pressure. Some differences among the calculated results can be seen concerning the increase of containment pressure at the time immediately after vessel failure. The increase of pressure at the time immediately after vessel

Table III Parameters Selected for the MARCH1.0 Sensitivity Analysis

Parameters	Low	Standard	High
Mass of Corium (Kg)	67000	134000	——
Relative Amount of Steel in the Mass of Corium	SV×1/2	SV	——
Corium Temperature at Vessel Failure (K)	2033	2533	3033
Amount of Water in the Cavity (Kg)	32800	65550	131100
Radius of the Reactor Cavity (m)	2.5	3.73	4.0
H.T.C. between Corium and Concrete (W/cm^2K)	0.001	0.01	0.1
Particle Diameter of Corium (cm)	0.0254	2.54	25.4
Thermal Conductivity of Corium (W/mK)	0.692	3.46	17.3

failure is caused by the vaporization of water in the cavity resulted from corium-water interaction. Since MARCH1.0 assumes corium dropped into water in the cavity to take the form of spheres, the heat transfer area from corium to water becomes larger as the particle diameter is smaller. Thus the vaporization time of water in the cavity becomes shorter and the pressure increase becomes more rapid as the corium diameter is smaller, and vice versa.

The initiation time of corium-concrete interaction, namely the time when corium was separated into an oxide layer and a metallic layer in the MARCH1.0 model, was extremely sensitive to an amount of water in the cavity, a particle diameter of corium and the corium temperature at vessel failure. Figure 8 shows the effect of an amount of water in the cavity on corium temperature. When an amount of water in the cavity was large, the corium temperature was kept to be 460 K until the water in the cavity was vaporized, and then it began to rise. When an amount of water in the cavity was small, the water in the cavity was vaporized in a short time (less than one minute) and the corium temperature was kept to be high. Thus the initiation time of corium-concrete interaction varied from 0.6 minute to 180 minutes by changing the amount of water in the cavity from 50 % to 300 %.

As in the THALES-CV calculation, the corium temperature and the total mass of concrete decomposition after completion of water vaporization in the cavity showed similar behavior for the parameters selected for this analysis.

COMPARISON OF MARCH1.0 AND THALES-CV RESULTS

The calculated results with THALES-CV and MARCH1.0 was compared to investigate the effect of different models used in these codes on the thermal hydraulic response in the containment during the accident. Figure 9 shows the comparison of the calculated containment pressures with THALES-CV and MARCH1.0. The two calculated results agree well even though the MARCH1.0 result shows a little higher pressure than the THALES-CV result. This was caused by the difference in calculation of the system pressure. The system pressure was determined in THALES-CV so as to keep total system volume constant and the temperature was determined from mass and energy conservation, while MARCH1.0 determined the atmosphere temperature first so as to give total system enthalpy consisting of each enthalpy of air, steam, and water. Then the system pressure is determined according to the given temperature based on a thermal equilibrium model.

As for the corium temperature, the MARCH1.0 result was higher than the THALES-CV result for 200 minutes after vessel failure as shown in Figure 10. This is because heat transferred from corium to concrete estimated by THALES-CV is larger than by MARCH1.0 since radiation heat transferred from corium to concrete is considered in THALES-CV, not in MARCH1.0.

The MARCH result showed that the concrete decomposition rate increased rapidly at the time when a metallic layer located in the upper layer of corium was overturned and moved to the lower layer. On the other hand, the THALES-CV result showed an almost constant decomposition rate because THALES-CV assumed corium to be one layer.

CONCLUSION

Thermal hydraulic response in a PWR large dry containment after vessel failure with corium ejection into a reactor cavity was analyzed with the THALES-CV and MARCH1.0 codes. The conclusion obtained from the analysis is summarized as follows.

(1) The sensitivity analysis with the THALES-CV code and the MARCH1.0 code showed the deviation among the calculated containment pressures was ± 30 % for the parameters selected in this analysis. The relatively important parameters for pressure and temperature in the containment and event times were an amount of water in the cavity, corium to concrete heat transfer coefficient, corium to atmosphere radiation heat transfer rate, and a particle diameter of corium (in the MARCH1.0 code).

(2) Comparing the calculated results of thermal hydraulic response in the containment with THALES-CV and MARCH1.0, some differences were found for the corium temperature and the concrete decomposition rate. These were caused by the differences existing between the models in THALES-CV and MARCH1.0 related to the configuration of corium dropped into water in the cavity for the time when water in it is vaporized and the property of corium.

(3) It should be recognized that lack of experimental data results in large uncertainty in the present analysis such as the parameters identified to be important from the sensitivity analysis and the models related to the configuration and the property of corium. Therefore experimental investigations on physical phenomena associated with the parameters and the models are strongly recommended.

REFERENCES

/1/ "Reactor Safety Study : An Assessment of Accident Risks in U.S. Commercial Nuclear Power Plants," WASH-1400, NUREG-75/104 (1975).

/2/ Abe, K. et al., "Description of THALES-CV1 : A Computer Code for Evaluating Containment Temperature and Pressure during Core Meltdown Accident," JAERI-M 83-037 (1983).

/3/ Wooton, R. O. and Avci, H. I., "MARCH (Meltdown Accident Response CHaracteristics) Code Description and User's Manual," NUREG/CR-1711 (1980).

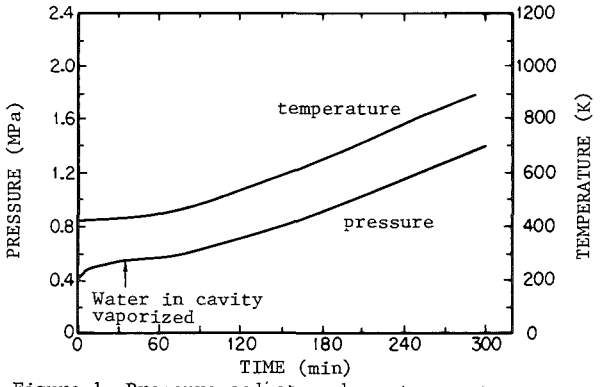

Figure 1 Pressure and atmosphere temperature in the containment calculated with THALES-CV.

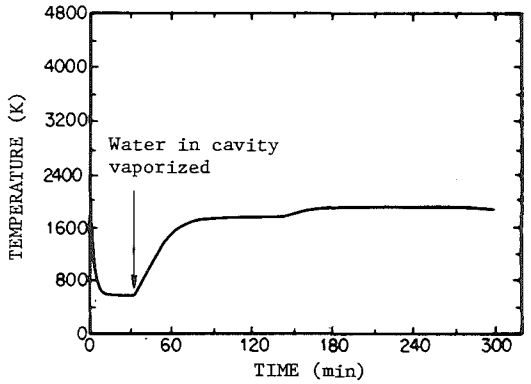

Figure 2 Corium temperature calculated with THALES-CV.

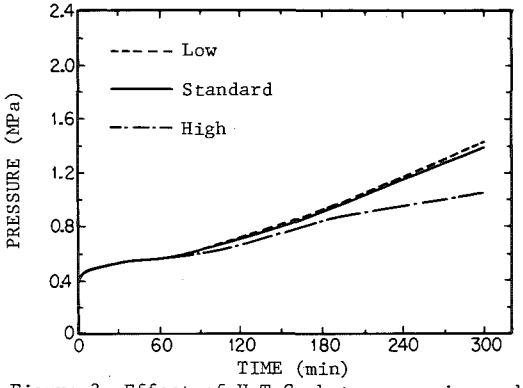

Figure 3 Effect of H.T.C. between corium and concrete on containment pressure.

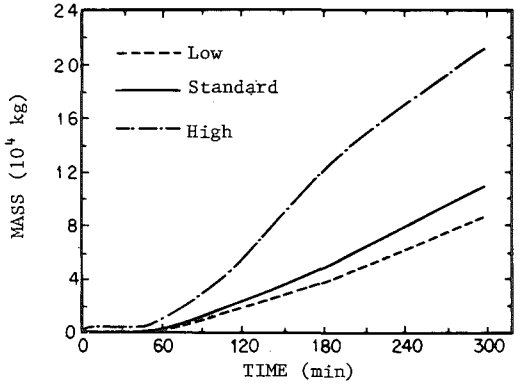

Figure 4 Effect of H.T.C. between corium and concrete on total mass of concrete decomposition.

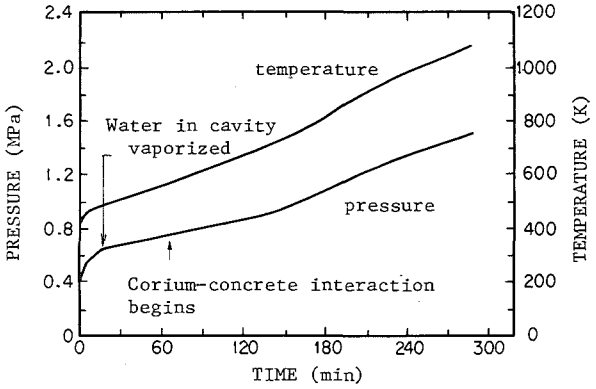

Figure 5 Pressure and atmosphere temperature in the containment calculated with MARCH1.0.

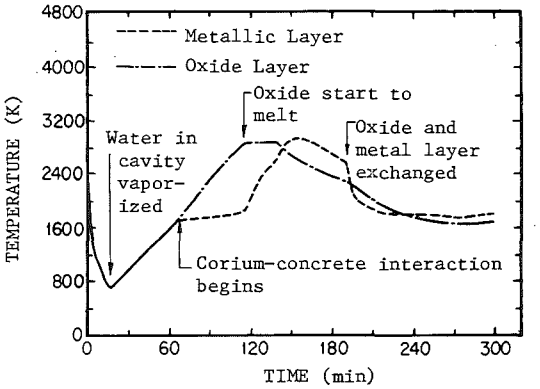

Figure 6 Corium temperature calculated with MARCH1.0.

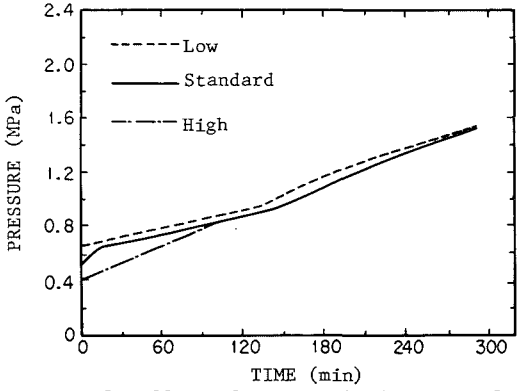

Figure 7 Effect of a particle diameter of corium on containment pressure.

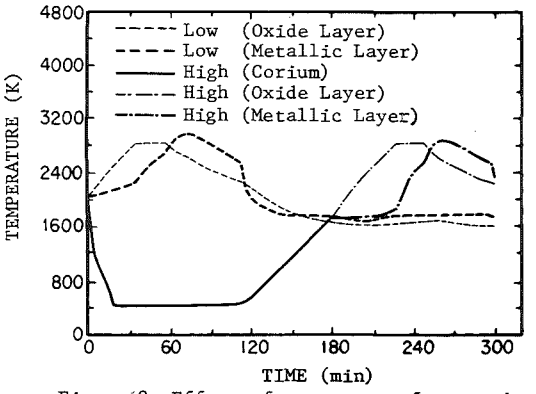

Figure 8 Effect of an amount of water in the cavity on corium temperature.

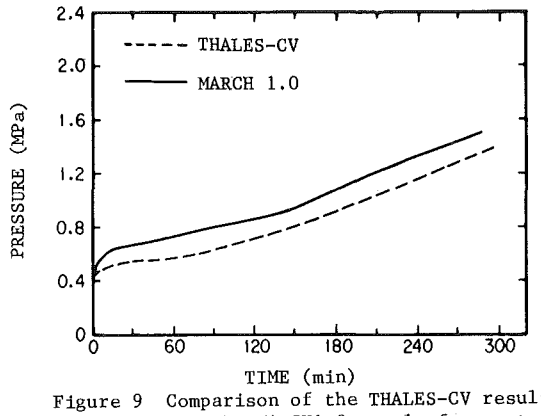

Figure 9 Comparison of the THALES-CV result and the MARCH1.0 result for containment pressure.

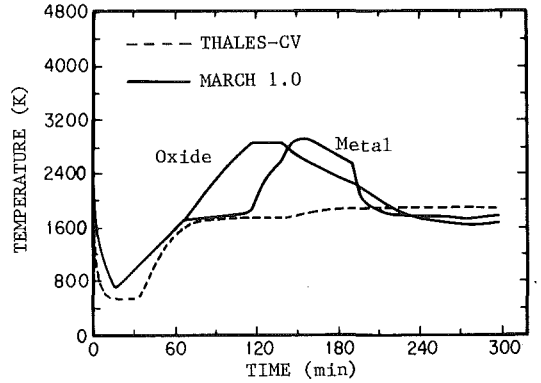

Figure 10 Comparison of the THALES-CV result and the MARCH1.0 result for corium temperature.

CONTAINMENT RESPONSE DURING POSTULATED SEVERE ACCIDENTS IN FIRST GENERATION OF SWEDISH BWR'S

Roland Blomquist, Studsvik Energiteknik AB, S-611 82 Nyköping, Sweden
Anders Enerholm, Royal Institute of Technology, S-100 44 Stockholm, Sweden
Johan Engström, OKG AB, Box 1746, S-111 87 Stockholm, Sweden
Ferenc Müller, Swedish State Power Board, S-162 87 Vällingby, Sweden
Gunnel Nordgren, Studsvik Energiteknik AB, S-611 82 Nyköping, Sweden

ABSTRACT

The purpose of the Swedish project RAMA (Reactor Accident Mitigation Analysis) is to provide the methods and tools for assessing the containment response and fission product release during a severe reactor accident. The analysis of the containment response is performed with MAAP (the Modular Accident Analysis Program), which evaluates the postulated accident from the initiating events to a permanently coolable state with or without containment failure. This paper presents and discusses results for Ringhals 1 and Oskarshamn 2. The calculations show that the time to containment failure for these reactors is in the order of days for the two sequences total blackout and large break LOCA followed by loss of core and containment cooling.

BACKGROUND

The RAMA (Reactor Accident Mitigation Analysis) project was established in the wake of the decision by the Swedish government that decided measures if any should be taken before 1989 at all Swedish nuclear power plants in order to further reduce the likelihood of radioactive releases that could be caused by severe accidents including core-meltdown. This applies especially to those releases that could cause long lasting land contamination. The purpose of the RAMA project is to provide methods and tools for the analysis of the source term and the containment response during a severe accident. The work is accordingly carried out in two working groups, one on the containment response and one on the source term. The task of the containment group is to evaluate temperature and pressure in the primary system and the containment during a severe accident. All twelve Swedish reactors will be analysed. As a first part of the work the thermal-hydraulic responses of the reactors Ringhals 1 and Oskarshamn 2 have been studied. This paper presents some results from the severe accident analysis of these reactors and the resulting impact on containment structures.

CONTAINMENTS LAYOUTS AND DATA

The containment configurations for Oskarshamn 2 (O2) and Ringhals 1 (R1) are depicted in Fig. 1. As can be seen the containments are similar. Characteristic features of these containments are the cylindrical condensation pool which covers the whole containment basemat and the vertical drain pipe from the compartment under the reactor pressure vessel to the suppression pool. The main data for the reactors and their containments are given in Table 1.

SEQUENCES ANALYSED

The following accident sequences have been analysed:

TB	Loss of AC power
AQUVW	Large LOCA, loss of all coolant injection and containment cooling

When the AC power is lost in the loss of AC power sequence the reactor is automatically shut down. Battery power vill be available for closing the containment isolation valves and later activate the automatic depressurization system (ADS).

For the large LOCA case, a high temperature signal from drywell initiates automatically shutdown of the reactor. The large LOCA is assumed to be a guillotine break in one of the main coolant loops and outflow of hot water and steam from both ends.

METHOD OF ANALYSIS

The analysis has been performed by using the MAAP (Modular Accident Analysis Program) computer program /1/ in which major pysical processes during an accident such as core heat up, clad oxidation, core melting, vessel melt-through, debris configuration and coolability etc. are modelled. The code evaluates the entire accident sequence from the initiating events to a permanently coolable state with or without containment failure. The program has been developed for IDCOR by Fauske and Associates Inc. (FAI) in two major versions, one for BWR's and one for PWR's. As a member of IDCOR, RAMA has gained access to the MAAP codes. Because of the differences between different reactor systems the original MAAP BWR code had to be modified for application to the ASEA-ATOM reactors Oskarshamn 2 and Ringhals 1. The modifications of the code were performed by FAI and concerned mainly the containment arrangement and the system functions.

CONTAINMENT RESPONSE

Loss of AC power.

The results of the studies for this sequence are summarized in Table 2. UO_2 accumulation in lower drywell and wetwell, drywell gas and suppression pool temperature and drywell pressure are shown in Figs. 2 to 4.

During the first part of the accident, water in the reactor vessel is boiled off by the decay heat. The steam produced is blown off to the suppression pool where it condenses. After about 30 min the top of the core is uncovered. The uncovered part of the core is overheated and melting of the core starts at about 2.5 hours Due to reaction between zirconium and steam hydrogen is produced. Vessel failure takes place at 3 to 4 hours, molten corium flows out and falls down to the lower drywell floor. The melt heats up the concrete floor and the concrete begins to melt. Also during this reaction some hydrogen is produced. The main part of the melt makes its way down to the suppression pool through the drainpipe in the floor. By melting through a steel door and electrical penetrations the melt may also flow down into the pool through these openings. Due to the considerable depth of the pool (6 m) the falling melt

fragments and the fragments solidifies. The debris ends up as a coolable layer on the bottom of the suppression pool. Since the pool is uncooled the pool temperature will increase due to latent and residual heat in the debris. After some time the pool begins to boil. The steam partial pressure in the containment increases. After 40 hours the total containment pressure is about 0.7 MPa. The containments of Ringhals 1 and Oskarshamn 2 is expected to remain essentially leaktight up to about 1.0 MPa. If the containment is not cooled this pressure will be reached after about 50 hours.

Large LOCA, loss of coolant injection and containment cooling.

This sequence has been analyzed for Oskarshamn 2 only. The results are summarized in Table 2. UO_2 accumulation in lower drywell and wetwell, drywell gas and suppression pool temperature and drywell pressure are shown in Figs. 5 to 7.

The large LOCA break area assumed results in a fast emptying of the reactor vessel. The core is completely uncovered within about 10 seconds. Compared to the loss of AC power case the start of core melting and vessel failure occurs about 1.5 hours earlier. The continuation of the accident is then quite similar to the loss of AC power sequence. The highest calculated gas temperature is somewhat higher, 260°C compared to 240°C. The total mass of hydrogen is somewhat less, 40 kg compared to 50 kg.

COMPARISONS WITH EARLIER CALCULATIONS

The results from the MAAP calculations have been compared with results from the FILTRA project, where the purpose was to design a filtered venting system for the Barsebäck reactors, which are identical to Oskarshamn 2. In the FILTRA analysis it was conservatively assumed that 50 % of the zircaloy in the core was oxidized, which corresponds to a hydrogen production of 750 kg. This leads to a somewhat faster pressurization and earlier failure of the containment. Otherwise the comparison showed a reasonably satisfactory agreement.

CONCLUSIONS

As the main part of the core debris end up in a coolable state in the suppression pool the risk for an early leakage from the containment caused by the melt itself is small. The main threat to the integrity of the containment is instead the combined influence on containment seals and penetrations from increased inside gas temperature and pressure.

The containment atmosphere is heated by energy emitted from the stream of molten corium, the frozen crust of core debris permanently resting on lower drywell floor and gasborne radioactive substances. According to Table 2 and Figs 3 and 6 the highest gas temperature is about 260°C.

The containment pressure increases as a result of steam partial pressure, hydrogen production during chemical reactions and increased containment gas temperature. If the containment cooling is not restored the pressure rises continuously and may reach 1.0 MPa after about 50 hours for the accident sequences studied.

REFERENCES

1 GABOR J R, HENRY R E
The MAAP-BWR Severe Accident Analysis Code. Proc. of International Meeting on Light Water Reactor Severe Accident Evaluation, Cambridge, Massachusetts, USA, Aug. 28 to Sept 1, 1983

Table 1. Reactor and containment data

	Oskarshamn 2	Ringhals 1
Thermal power	1700 MW	2270 MW
UO_2 mass	90 tons	130 tons
Drywell gas volume	4980 m^3	5460 m^3
Wetwell gas volume	2990 m^3	2830 m^3
Suppression pool volume	1930 m^3	2600 m^3

Table 2. Event times and important results

	Loss of AC power		Large LOCA, loss of core and containment cooling
Reactor	O2	R1	O2
Core uncovered	34 min	32 min	5.7 s
Start of core melt	2.5 h	2.6 h	1.1 h
Vessel failure	2.9 h	3.8 h	1.4 h
Time to containment pressure = 0.7 MPa	43 h	39 h	44 h
Peak drywell temperature	240°C	240°C	260°C
Total mass of hydrogen produced	50 kg	90 kg	40 kg
Penetration in the lower drywell concrete floor	0.21 m	0.24 m	0.23 m

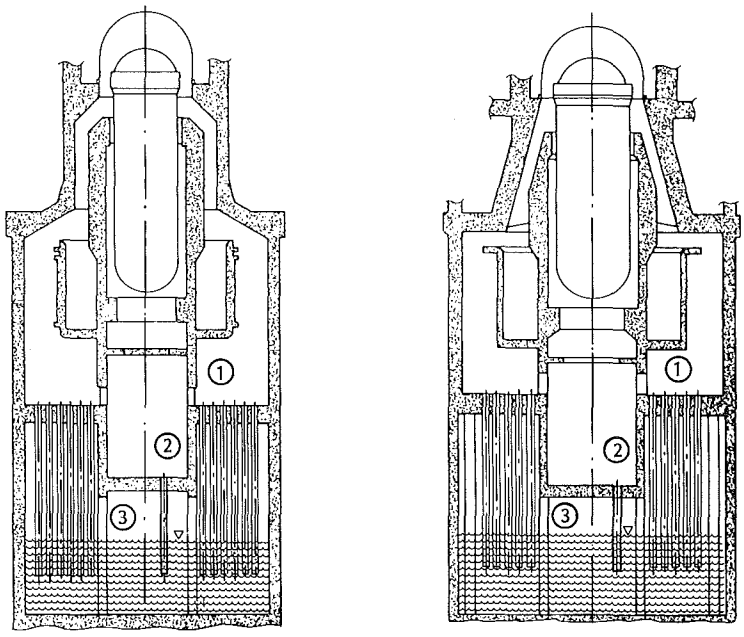

Oskarshamn 2 Ringhals 1

① Upper drywell
② Lower drywell
③ Wetwell

Fig 1. Oskarshamn 2 and Ringhals 1 containments

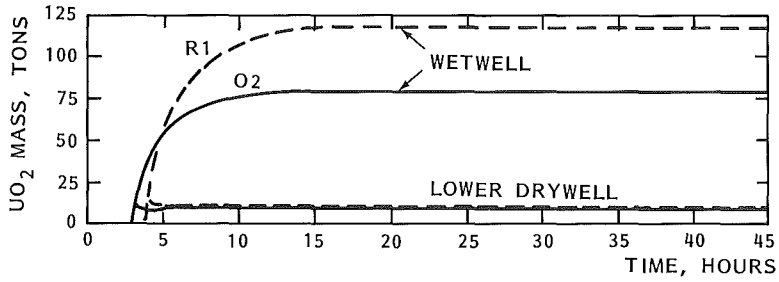

Fig 2. Loss of AC power. UO_2 accumulation in containment.

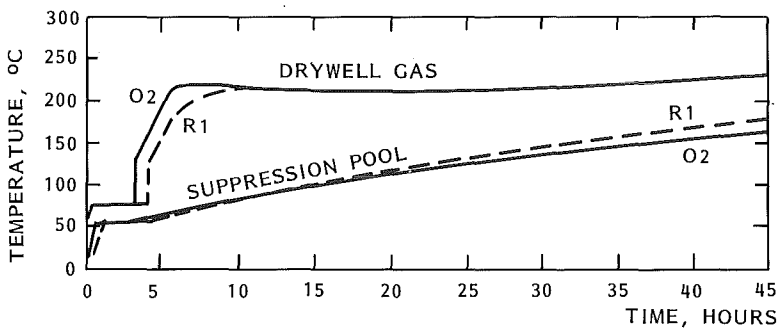

Fig 3. Loss of AC power. Temperature of drywell gas and suppression pool.

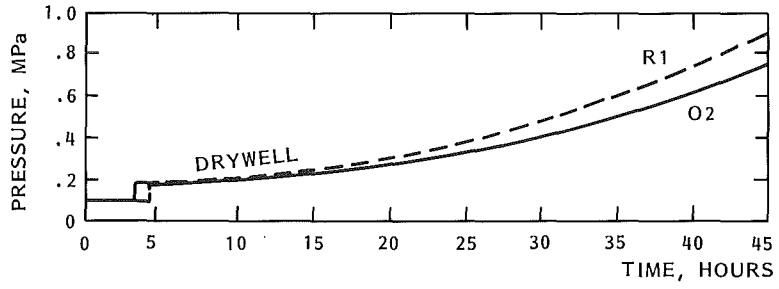

Fig 4. Loss of AC power. Drywell pressure.

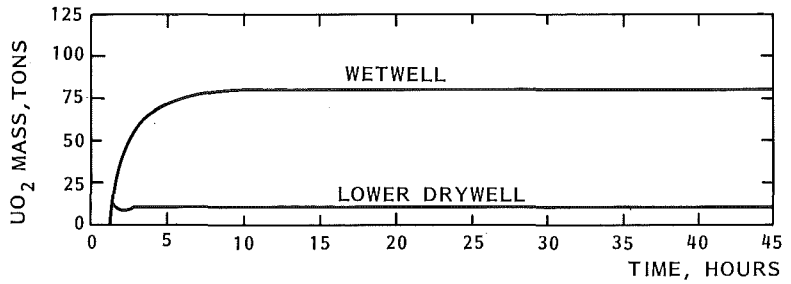

Fig 5. O2. Large LOCA, loss of core and containment cooling. UO_2 accumulation in containment.

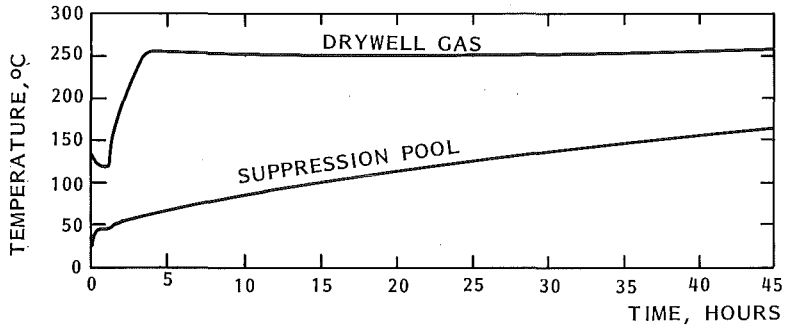

Fig 6. O2. Large LOCA, loss of core and containment cooling. Temperature of drywell gas and suppression pool.

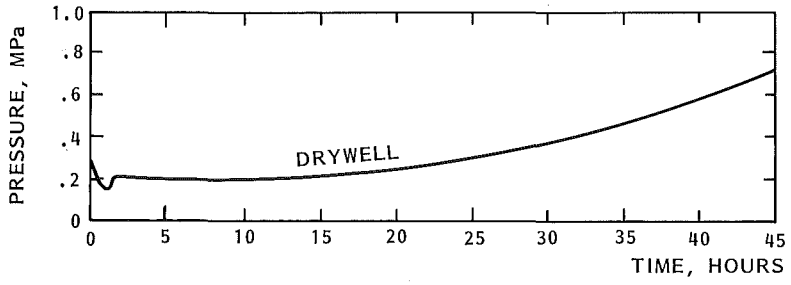

Fig 7. O2. Large LOCA, loss of core and containment cooling. Drywell pressure.

CONTAINMENT LOADING DURING SEVERE CORE DAMAGE ACCIDENTS

J. Fermandjian, J.M. Evrard, G. Cenerino

CEA/IPSN/DAS
B.P. 6 F-92260 Fontenay-aux-Roses (France)

Y. Berthion, G. Carvallo
CEA/IRDI/DEMT
B.P. 2 F-91190 Gif-sur-Yvette (France)

ABSTRACT

The paper assesses the reactor containment loading during a severe accident sequence for a 900 MWe PWR unit. Calculations are performed by using the JERICHO thermalhydraulics code concerning the following cases: dry cavity, flooded cavity with corium not cooled and flooded cavity with corium cooled.

INTRODUCTION

During the past several years, some work has been accomplished, in the field of the nuclear reactor safety, concerning the evaluation of hypothetical severe accidents on pressurized water reactors. These accidents involve core degradation and important fission product release from the fuel. The radiological consequences of such accidents are mainly linked to the residence time of the fission product in the reactor containment building (RCB). Indeed, fission product deposition, by settling on the floor and diffusion on the walls of the RCB, will reduce the amount of radioactive material which will be released to the environment if the containment fails.

Consequently, it is important to determine the mechanical behaviour of the RCB during the accident and the thermal-hydraulic conditions (especially, atmosphere moisture) in the RCB which influence the fission product behaviour. The JERICHO computer code has been developed in order to provide the thermal-hydraulics in the containment: gas pressure, gas and wall temperatures, atmosphere moisture, atmosphere composition and leakage rate.

The objective of the present paper is to study the influence of the state of the reactor cavity (dry or flooded) and of the corium coolability on the thermal-hydraulics in the containment in the case of an accident sequence involving core melting and subsequent containment basemat erosion.

DESCRIPTION OF THE JERICHO CODE [1], [2]

Since the objective of the JERICHO code is to analyse accidents evolution over several days, it was necessary to write a computer code with a rather simple modelization and a sophisticated numerical treatment. The containment volume is modelized in one compartment with two phases: gaseous atmosphere and sump water. Both phases are assumed to be homogeneous, in pressure equilibrium, but in thermal non-equilibrium. Containment atmosphere can be composed of oxygen, nitrogen, steam, hydrogen, carbon dioxide and carbon monoxide. The main physical phenomena are described below (also, see Figure 1).

Mass and Energy Sources

The JERICHO code provides the thermal-hydraulic conditions in the reactor containment building from the onset of the accident through the stages of blowdown, core heat-up, boiloff, core meltdown, pressure vessel bottom head failure and interaction of the molten debris with the concrete containment basemat. The energy and mass flowrates of the different gaseous species (H_2O, H_2, CO_2 and CO) entering the containment during the different phases of the accident are evaluated by various codes (described in [3]).

Besides, the following energy sources are taken into account :

- decay heat associated with fission products released into the containment. This energy, initially released in the gaseous phase, is rapidly transferred into the sump water in order to simulate the fission product deposition (the deposition rate being calculated by the AEROSOLS/B1 Code [3]),

- energy radiated by the corium surface during the corium-concrete interaction phase. The radiation generated by the corium surface is to a large extent stopped by the reactor cavity walls: it leads to the heat-up and the thermal degradation of the concrete, releasing steam and carbon dioxide,

- energy released from hydrogen and carbon monoxide burning.

Heat and Mass Transfer Between Atmosphere and Sump Water

At the surface of the sump water, convection occurs in thermal non-equilibrium and condensation if the liquid temperature is lower than the saturation temperature or evaporation in the opposite case. Steam condensation in the bulk gaseous phase and sump water boiling are also considered.

Heat and Mass Transfer Between Atmosphere and Structures

Heat and mass exchanges, between atmosphere and structures, occur by convection and condensation if the structure temperature is lower than the saturation temperature. In the JERICHO code, the condensation film is not modelized as a distinct system; the condensed water is assumed to reach the sump water instantaneously at the wall temperature.

Thermal Conduction in the Structures

Containment walls and internal structures are modelized as one-dimensional slab geometry heat sink. Each structure consists of only one material. In the case of concrete structures with a steel liner, a separate calculation is performed for the steel liner. The outside atmosphere and the ground are treated as sinks at constant temperature.

Containment Spray

In French 900 MWe PWR's, the containment spray system works either, in direct phase, from the storage tank, in common with emergency core cooling system, or, in its recirculation phase, from the sump water. In the second case, the liquid passes through heat exchanger in order to evacuate the decay heat in the long-term. The JERICHO code calculates the energy transferred to the heat exchanger and the inlet temperature of the spray water.

Leakage and Venting

From the containment design pressure, venting of the RCB is designed through a rough filtration device in order to reduce the radioactive release to the environment. The gas is assumed to be expanded isoenthalpic ant the flowrate is calculated from the SAINT-VENANT law. The containment leakages (natural containment leakage and containment isolation failure) are also modelized.

Hydrogen and Carbon Monoxide Combustion

The combustion of hydrogen and carbon monoxide becomes possible when each of these components exceeds a given volumetric concentration. More accurately, the flammability limit is determined in the ternary diagram (H_2+CO, H_2O+CO_2, air).

Hydrogen and carbon monoxide burning is modelized in two ways:
1) continuous burning as soon as the flammability limits are reached,
2) storage and instantaneously burning (deflagration) at input specified time.

Numerical Treatment

The evolution of gas components and liquid water mass and internal energy, as well as structure surface temperature, is governed by a system of first order non-linear differential equations. In order to modelize the engineered safety feature performance and some physical phenomena (fission product influence and leakage), some additional equations are considered. This system is solved by an ADAMS-PECE method. Gas and liquid temperatures, as well as gas component partial pressures, are obtained by solving a system of non-linear equations with a specific residues method.

ACCIDENT SEQUENCE DESCRIPTION

The accident sequence to be studied, on which the following study is based, is a break loss-of-coolant accident (2" diameter) with failure of both the emergency core cooling system and the containment spray system (S_2CD sequence according to the Reactor Safety Study terminology [4]). Note that, in this case, the containment building cooling is not operational. The reactor to be considered is a 900 MWe PWR unit with a large dry containment (Figure 2). The reactor building is a prestressed concrete containment with an internal steel liner (steel thickness = 6 mm, air gap = 0.5 mm). We present herein-after the successive stages of the accident and the corresponding containment response. The timing of the main events occurring throughout the accident is given below:

Time (minutes)	Events
0	Start of blowdown
0.8	Reactor scram (primary pressure less than 12.9 MPa)
0.8	Secondary circuit: feedwater and steam outlet shut-off
1.8	Auxiliary feedwater pumps start
4	Primary pumps stop (cavitation)
31	Core uncovery begins
47	Accumulator discharge
150	Fission product release starts
155	Core melting begins
175	Core slump
200	Reactor vessel dry
262	Bottom head fails
262	Corium-concrete interactions begins
622	Corium solidification
10,080 (7 days)	Containment floor melt-through

Primary Circuit Blowdown

The primary circuit depressurization initiates the reactor scram and the starting of the auxiliary steam generators feedwater supply system. Main pumps are stopped because of the cavitation. The primary circuit blowdown progresses and the core uncovery occurs at about 30 minutes. This stage has been computed by using the RELAP 4 Mod 6 code [5].

Core Heat-Up and Meltdown

The core uncovery involves its heat-up, enhanced by the zircaloy cladding oxidation by steam, which releases large amounts of energy and of hydrogen. During this stage, the primary circuit depressurization continues and the pressure falls below the accumulators pressure threshold (4.2 MPa): the accumulator water discharge temporary refloods the core. After this water is vaporized, the core melting process resumes: the most volatile fission products are released by the core. This stage comes to an end with the core slumping in the vessel bottom head (at 195 minutes). Some water is still present in the bottom head and its sudden contact with the melting core causes its rapid vaporization. The metallic components of the core are supposed to be oxidized and hydrogen is again released in the containment building. The computer code used here is a version of the BOIL 2 code [6], modified in order to calculate small break and transient accidents; moreover the decay heat and fission product release models have been markedly improved. According to a simplified evaluation, the bottom head rupture occurs after about one hour. This long delay is due to the low primary pressure, which does not lead to important mechanical stresses.

Concrete Basemat Ablation

The melting fuel and internal structures mixture (corium) falls down on the concrete basemat in the reactor activity. The concrete basemat is progressively eroded by a thermal degradation process: concrete is decomposed and free water, bound water and carbon dioxide are successively released.

Water and carbon dioxide are partially reduced into hydrogen and carbon monoxide when passing through the corium metallic layer. At the same time, large amounts of energy are radiated by the very hot (temperature decreasing from 2000°C to 1500°C) upper layer of the corium. The concrete ablation kinetics, as well as the gas masses released into the containment atmosphere, are highly dependent upon the composition of the concrete.

Main characteristics of a limestone concrete are presented in Table I. In the case of limestone concrete, the ablation rate is estimated to be 30 cm/h during the first hour of interaction, 18 cm/h thereafter and 2 cm/h after the solidification of the corium metallic layer in contact with the concrete basemat. It is to be noted that considerable uncertainties still exist in the knowledge of these phenomena and so we have simply adopted the approximate values currently accepted. With this hypothesis, the basemat rupture occurs at about 7 days (thickness of the concrete containment basemat: 4.2 m).

PRESENTATION OF THE JERICHO CALCULATIONS

After the vessel rupture, the corium forms a deep bed about 60-70 cm high, according to the amount of core and structures involved, and progressively ablates the concrete basemat. During the long period of time (several days) preceding the complete basemat pass-through, it is likely to set up or recover means of providing cooled water on the corium surface. Hence the problem of corium coolability is of primary importance as concerns the management of severe accidents. Three key-questions are to be answered: (a) what kind of interaction between the corium and water does occur, (b) does it bring to a stable coolable configuration and (c) what are the consequences on containment integrity ?

The molten corium and the water pool overlying it will probably be separated by a solid crust and a vapor film, which limit the heat transfer to rather low values. Yet crust dislocation by gas release and destabilization of the vapor film, with direct water-corium interaction, are likely to occur. These mechanisms could lead to a certain extent to corium fragmentation, but it is difficult to imagine the formation of a coolable debris bed in this way, according to the corium depth.

Nevertheless it is impossible up to now to answer the question of corium coolability, and the present paper is aimed only at addressing the third question, with arbitrary assumptions on coolability. It allows therefore to bracket the containment response during this stage of the accident, assuming the containment building cooling is not available.

To this end, three calculations were performed: dry cavity, flooded cavity with corium assumed being not coolable and flooded cavity with corium assumed being coolable.

Case 1 (dry cavity)

The first calculation concerns the study of the S_2CD sequence in which the reactor cavity is dry. In this case, the concrete basemat is heated to high temperatures before water vapor and gases are released from it. During the first hours, a considerable amount of the available energy in the core debris is therefore transferred to and stored in the concrete, leaving only a fraction of the energy to be transferred to the containment building atmosphere as steam and non condensible gases (mainly, carbon dioxide).

Case 2 (flooded cavity - corium not cooled)

The second calculation relates to the study of an accidental sequence similar to the preceding, except that the reactor cavity is flooded (for example, by recovery of the emergency core cooling system) after the beginning of the corium-concrete interaction. Therefore, the radiation heat generated by the corium surface does not heat up the reactor cavity walls but rather vaporizes the water poured into the reactor cavity.

Case 3 (flooded cavity - corium cooled)

For the third calculation, we assume that the cavity contains an unlimited amount of water to cool the debris to the extent that the core could not reheat and interact with concrete. After the core is brought into thermal equilibrium with the water (in 1 hour) and the rapid steam production and rapid pressure rise have occured, the decay heat in the core materials continues to boil water (at the rate of 400 kg/minute).

For the previous three cases, the sources, in kg, released (after 4 days) to the reactor containment building during the "corium-concrete interaction" are given in the following table:

	Case 1	Case 2	Case 3
Steam released to the RCB	34,128	573,873	1,303,010
Hydrogen released to the RCB	276	276	80
Carbon dioxide released to the RCB	74,437	41,125	
Carbon monoxide released to the RCB	4,338	4,338	

The main characteristics of the reactor containment building are presented in Table I and the different sources released into the containment throughout the accident (dry cavity) in Table II, among which the main sources are the two-phase water flow during the primary circuit depressurization and the carbon dioxide generated by the concrete basemat erosion.

RESULTS OBTAINED - DISCUSSION

Containment Atmosphere Pressure and Temperatures

The curves of pressure and average temperature of the gaseous and liquid phases (Figures 3, 4 and 5) show two peaks corresponding to the primary circuit depressurization and to the bottom head water vaporization when the core slumps. These pressure peaks reach respectively 0.20 and 0.28 MPa and so are far lower than the containment building design pressure (0.5 MPa). For case 3, the third peak (0.35 MPa) corresponds to the rapid steam production due to the thermal equilibrium between core and water (see previous section).

The containment atmosphere pressure exceeds the design pressure: after 6 days for case 1, after 3 days for case 2 and after 1 day for case 3.

When the containment design pressure is reached, the containment atmosphere temperatures are equal to 117°C, 131°C and 138°C for cases 1, 2 and 3 respectively.

Note that:

. the containment basemat is supposed to be penetrated by the corium after 7 days,

. the best-estimate assessments of the actual strength limits of reactor containment with an internal steel liner had led to the conclusion that the rupture occurs suddenly by fracture of prestressing cables at about 1.0 to 1.3 MPa leading to loss of containment integrity [7].

Therefore, the above-ground containment rupture occurs only for case 3, after 3 days. For case 2, the above-ground containment rupture and the base-mat rupture occur at about the same time (after 6-7 days).

The pressure and temperature increase rates are:

. 1.8 kPa per hour and 0.29°C per hour for case 1;
. 4.4 kPa per hour and 0.54°C per hour for case 2;
. 10.5 kPa per hour and 0.83°C per hour for case 3.

Containment Atmosphere Moisture

Figure 6 gives the containment atmosphere moisture versus time for case 1. This curve shows that the containment atmosphere is not always saturated during the first hours of the accident. Similar results have been obtained for cases 2 and 3.

Containment Atmosphere Composition

Figures 7, 8 and 9 give the atmosphere composition (O_2, N_2, H_2O, H_2, CO_2 and CO) as functions of time for cases 1, 2 and 3. These curves show clearly:

. the importance of steam and carbon dioxide for case 1,
. the importance of steam for cases 2 and 3.

When the containment design pressure of 0.5 MPa is reached, the atmosphere compositions are the following (%, in mass):

	Case 1	Case 2	Case 3
O_2	5.9	7.4	8.4
N_2	19.5	24.4	27.9
H_2O	23.4	44.9	63.1
H_2	0.5	0.6	0.6
CO_2	48.6	20.1	0
CO	2.1	2.6	0

Concerning the hydrogen combustion:
. For case 1, the hydrogen concentrations always exceed the flammability limits: hydrogen volume fraction more than 4% and steam volume fraction less than 60%.
. For cases 2 and 3, the steam volume fractions are higher than 60% after 3.5 days and 0.5 days respectively.

Energy Balance

For cases 1, 2 and 3, the energy balances after 4 days are the following (in % of energy injected into the reactor containment building):

	Case 1	Case 2	Case 3
Energy located in the concrete walls	23	21	19
Energy located in the internal structures	58	42	46
Energy located in the atmosphere	6	9	12
Energy located in the sump water	6	13	19
Energy transferred to the environment	7	5	4

Note the importance of the energy located in the internal structures.

Concerning the decay heat, after 4 days, 5.334 MW is still located in the corium (71.3%), 2.026 MW in the sump water (27.1%) and 0.118 MW in the gas phase (1.6%).

CONCLUSION

The JERICHO code has been developed in order to study the thermodynamic behavior inside the reactor containment building for the complete spectrum of accident sequences likely to occur on a PWR.

Sensitivity analyses performed with the JERICHO code on the S_2CD sequence (involving core melting and subsequent containment basemat erosion) have shown the importance of the state of the reactor cavity (dry or flooded) and of the corium coolability on the thermal-hydraulics in the containment.

For a dry cavity, the containment building failure is due to the basemat rupture, after 7 days. For a flooded cavity with corium not cooled, the basemat rupture and the above-ground containment rupture occur at the same time, after about 7 days. For a flooded cavity with corium cooled, the containment building failure is due to the steam overpressurization, at 3 days. For this case, if the containment building cooling is recovered the above-ground containment rupture will be prevented and the fission products will not be released to the environment.

A substantial buildup of combustible gases resulting from the corium-concrete interaction can be prevented if the core can be flooded with water. The formation of a coolable debris bed remains to be demonstrated. Nevertheless, in the long-term, the rates for corium penetration and for combustible gas production are expected to be lower compared with the dry cavity sequence, even if the coolability is not demonstrated.

In the near future, we intend to check the adequacy of the input data for the JERICHO code (in particular, mass and energy flowrates released into the reactor containment building during the corium-concrete interaction) and to validate the JERICHO code from analytical and integral experiments.

REFERENCES

[1] J. FERMANDJIAN, J.M. EVRARD, Y. BERTHION, G. LHIAUBET
JERICHO computer code: PWR containment response during severe accidents. Description and sensitivity analysis.
OECD-NEA-CSNI Specialist Meeting on Water Reactor Containment Safety.
Toronto, Canada - October 17-21, 1983.

[2] A. L'HOMME, P. PEPIN, Y. BERTHION, G. CARVALLO
Code de calcul réaliste du comportement thermodynamique et radiologique des enceintes de confinement des réacteurs PWR.
AMS Conference - Paris, France - July 1982.

[3] J. FERMANDJIAN, J.M. EVRARD, Y. BERTHION, G. LHIAUBET, M. LUCAS
Source term associated with two severe accidents in a 900 MWe PWR.
International Meeting on LWR Severe Accident Evaluation - Cambridge, USA
August 28 - September 1, 1983.

[4] Reactor Safety Study - An assessment of accident risks in U.S. commercial nuclear power plants.
WASH-1400 (NUREG-75/014), October 1975.

[5] RELAP 4 Mod 6. A computer program for transient thermal hydraulic analysis of nuclear reactors and related systems. User's manual.
EG & G, Idaho, Inc-Report CDAP TR 003, January 1978.

[6] R.O. WOOTON, H.I. AVCI
MARCH (Meltdown Accident Response CHaracteristics). Code description and user's manual. NUREG/CR.1711 (BMI-2064), October 1980.

[7] J. BROCHARD et al.
Study of the behavior of containment buildings of PWR-type reactor, until complete failure in case of LOCA.
6th International Conference on Structural Mechanics in Reactor Technology - Paris, France - August 17-21, 1981.

TABLE I - MAIN CHARACTERISTICS OF THE REACTOR CONTAINMENT BUILDING, OF THE PRIMARY COOLANT SYSTEM AND OF THE CORE

Reactor containment building		
Volume	49,900	m^3
Design pressure	0.5	MPa
Failure pressure estimate	1.0 - 1.3	MPa
Floor area	830	m^2
Total surface	50,000	m^2
Concrete composition		
$CaCO_3$	0.557	weight fraction
$Ca(OH)_2$	0.013	weight fraction
SiO_2	0.219	weight fraction
Free H_2O	0.038	weight fraction
Al_2O_3, Fe_2O_3 ...	0.173	weight fraction
Primary coolant system		
Mass of water (including accumulator tanks)	280,000	kg
Core		
Mass of UO_2 (fuel)	79,600	kg
Mass of Zr (fuel cladding)	18,200	kg
Mass of Fe, Ni, Cr (structure material)	4,600	kg
Mass of Ag, In, Cd (control rods)	1,900	kg
Mass of active fission products *	385	kg
Mass of inactive fission products *	1,260	kg
Mass of actinides *	580	kg

* *for fuel burn-up* { *1/3 11,000 MWd/MTU* ; *1/3 22,000 "* ; *1/3 33,000 "*

TABLE II - MASSES RELEASED TO THE REACTOR CONTAINMENT BUILDING (in kg) FOR THE REFERENCE CASE

Initial conditions	
Nitrogen	41,048
Oxygen	12,400
Steam	1,276
Blowdown *(from 0 to 31 min.)*	
Water - steam	129,914
Core heat-up_Boiloff_Core meltdown *(from 31 to 195 min)*	
Steam produced	129,825
Steam released from the break to the RCB	124,965
Hydrogen released from the break to the RCB	540
Core slumping and vessel failure *(from 195 to 262 min)*	
Steam produced	24,078
Steam released from the break to the RCB	21,683
Hydrogen released from the break to the RCB	266
Corium-concrete interaction *(from 262 min to 4 days)*	
Steam released to the RCB	34,128
Hydrogen released to the RCB	276
Carbon dioxide released to the RCB	74,437
Carbon monoxide released to the RCB	4,338
Sump water radiolysis *(after 4 days)*	
Hydrogen released to the RCB	80

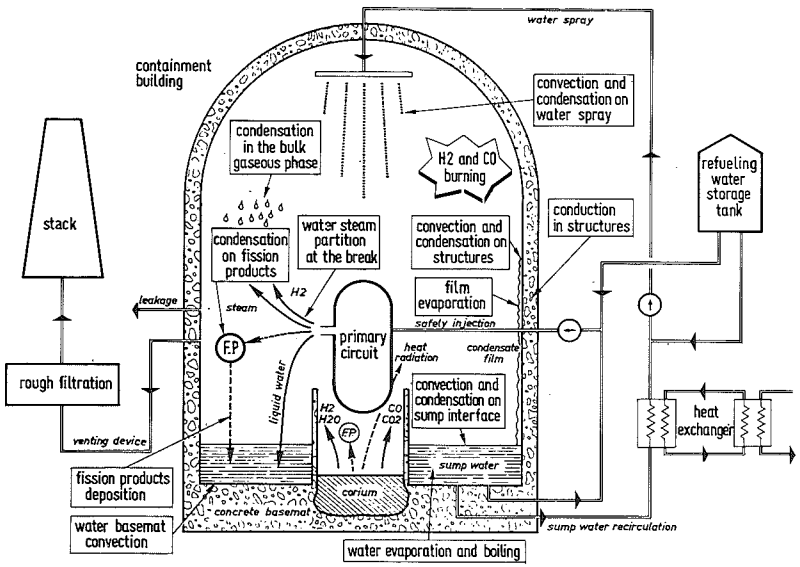

Fig.1_ DIAGRAM OF SYSTEMS AND PHYSICAL PHENOMENA IN THE JERICHO CODE

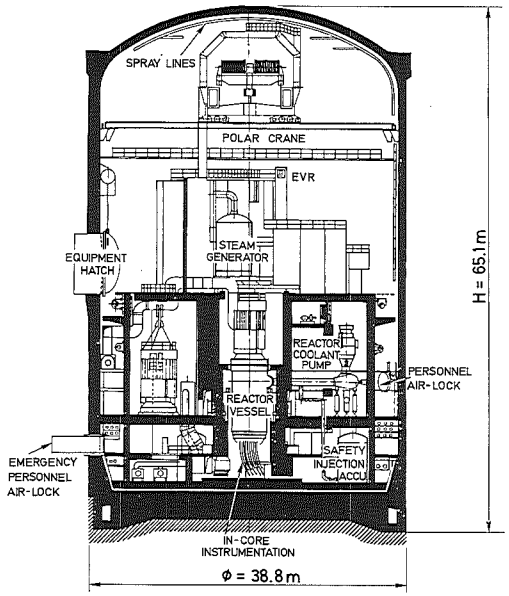

Fig.2 - REACTOR CONTAINMENT BUILDING LARGE DRY - 900 MWe

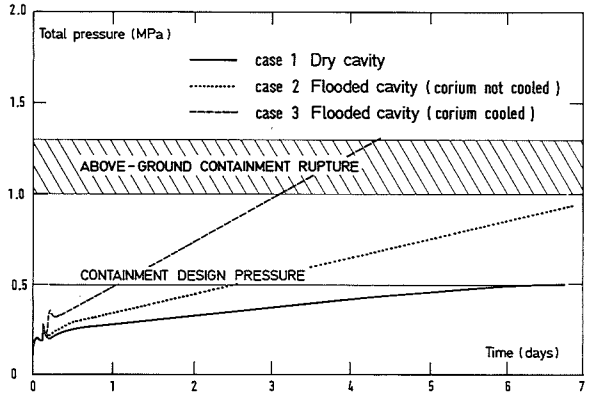

Fig. 3 _ CONTAINMENT BUILDING INTERNAL PRESSURE VERSUS TIME for S_2CD

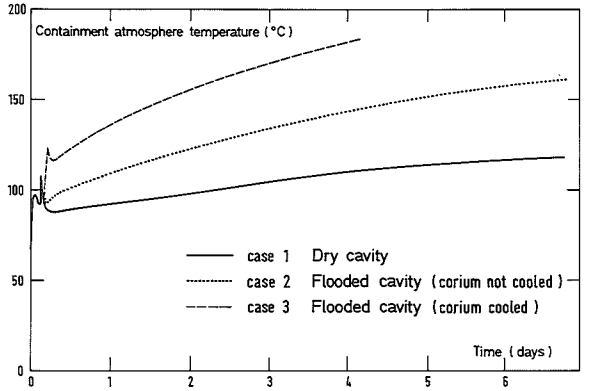

Fig. 4 _ CONTAINMENT BUILDING ATMOSPHERE TEMPERATURE VERSUS TIME for S_2CD

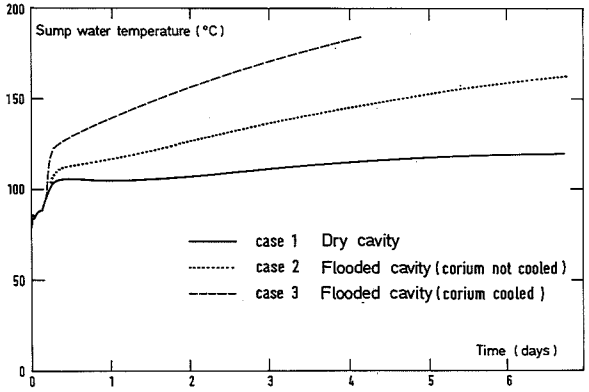

Fig.5 _ CONTAINMENT SUMP WATER TEMPERATURE VERSUS TIME for S_2CD

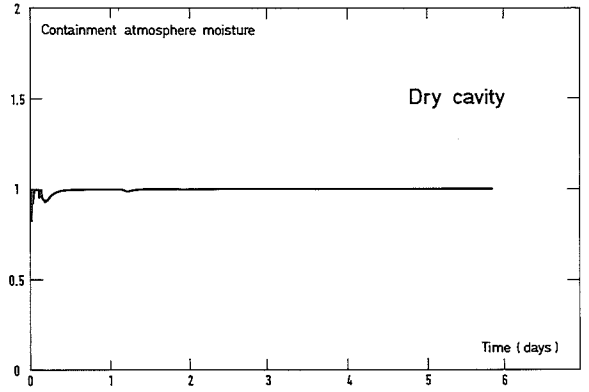

Fig. 6 _ CONTAINMENT BUILDING ATMOSPHERE MOISTURE VERSUS TIME for S_2CD

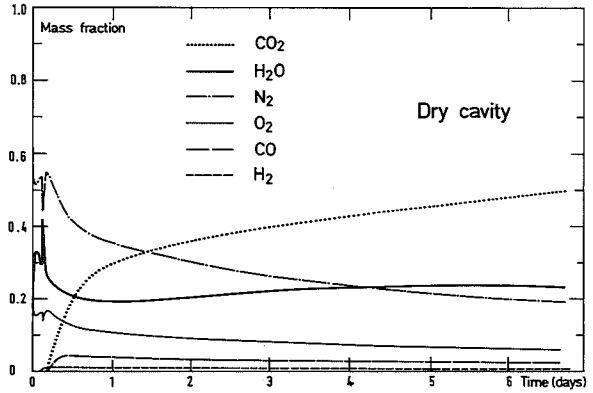

Fig. 7 _ ATMOSPHERE MASS COMPOSITION VERSUS TIME for S_2CD

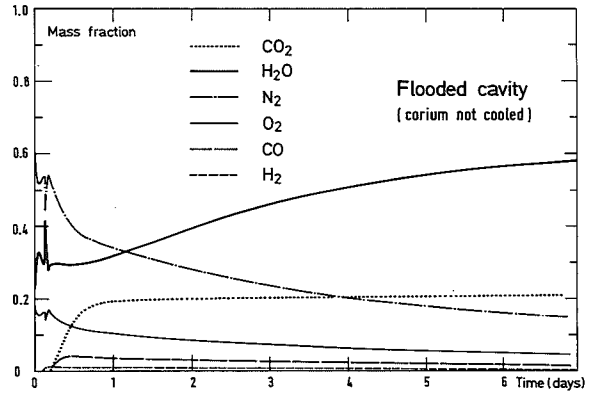

Fig. 8 _ ATMOSPHERE MASS COMPOSITION VERSUS TIME for S_2CD

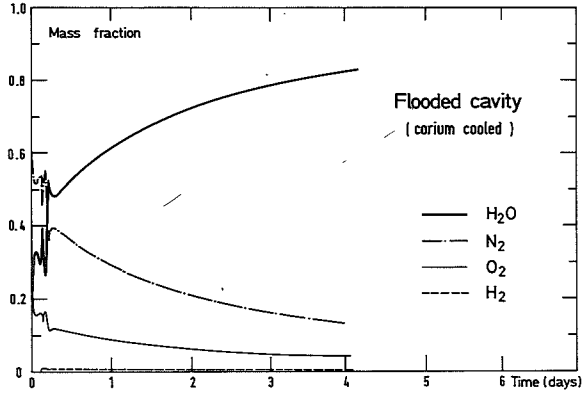

Fig. 9 _ ATMOSPHERE MASS COMPOSITION VERSUS TIME for S_2CD

STRUCTURAL INTEGRITY OF CANDU REACTOR'S VACUUM BUILDING

S.G. Krishnasamy and W.W. Koziak

Ontario Hydro
Toronto, Ontario, Canada, M8Z 5S4

ABSTRACT

The vacuum building of the negative pressure containment system is an important safety feature of the CANDU nuclear power plant. During a loss-of-coolant accident (LOCA), when the pressure in the reactor building reaches a preset value, the pressure relief valves (PRVs), which provide a pressure barrier between the reactor and vacuum building, open to allow flow into the vacuum building. This prevents the pressure in the reactor building from rising beyond the design value. The change of pressure in the vacuum building, from approximately 7 kPa to atmospheric, the high velocity at which the released gases or vapour enter the building, and the action of the dousing system, all apply considerable forces on the various structural components of the vacuum building. The program described in this paper, which is part of a comprehensive test plan coordinated by the Atomic Energy of Canada Ltd, comprises measurement of the pressure distribution in the main building, the wind velocity, movement of vacuum duct support and the forces on various critical components. An extensive analysis of the test data has been done to determine the integrity of the vacuum building under an emergency situation.

INTRODUCTION

The vacuum building of the negative pressure containment system is an important safety feature of the CANDU nuclear power plant (Figure 1). During a Loss-of-Coolant Accident (LOCA), gases and vapours from the reactor building would be safely transferred via pressure relief valves to the vacuum building. The vacuum building consists of a main vacuum chamber, a water storage tank, an upper vacuum chamber and a basement. The main vacuum chamber is the vessel formed by the perimeter wall, and the roof and floor slabs. The upper vacuum chamber, mounted centrally on the roof slab, contains sixteen suction pipes (or riser pipes) which run into the water storage tank. A walkway, situated just below the spray headers, provides access for maintenance. These parts of the vacuum building are shown in Figure 2.

In case of a LOCA, when the pressure in the reactor building reaches a preset value, the pressure relief valves (PRVs), which provide a pressure barrier between the reactor and vacuum buildings, open to allow flow into the vacuum building. This prevents the pressure in the reactor building from rising beyond the design value. During a LOCA the dousing system in the vacuum building is also activated, forcing the water from the storage tank, through the riser pipes, into the upper vacuum chamber. The water flowing through the upper chamber is released into the main vacuum chamber via spray headers, to condense and cool the vapours and gases that enter the vacuum building.

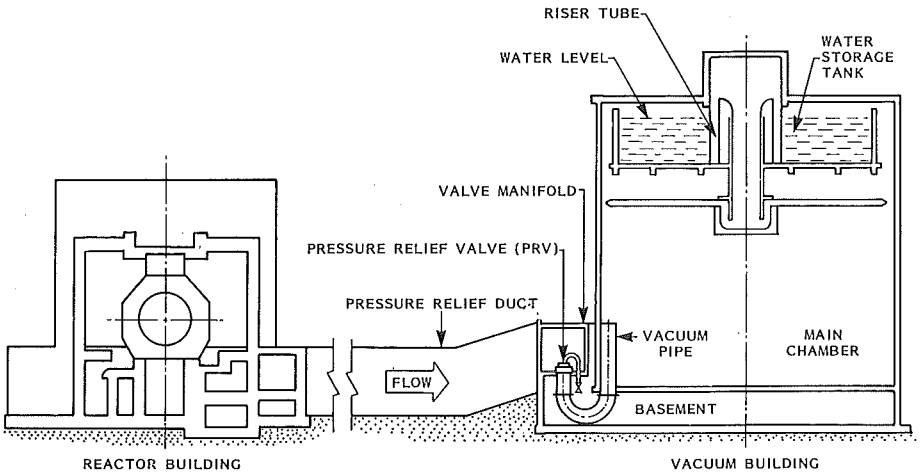

FIGURE 1

SCHEMATIC VIEW OF REACTOR BUILDING
AND EMERGENCY PRESSURE RELIEF SYSTEM

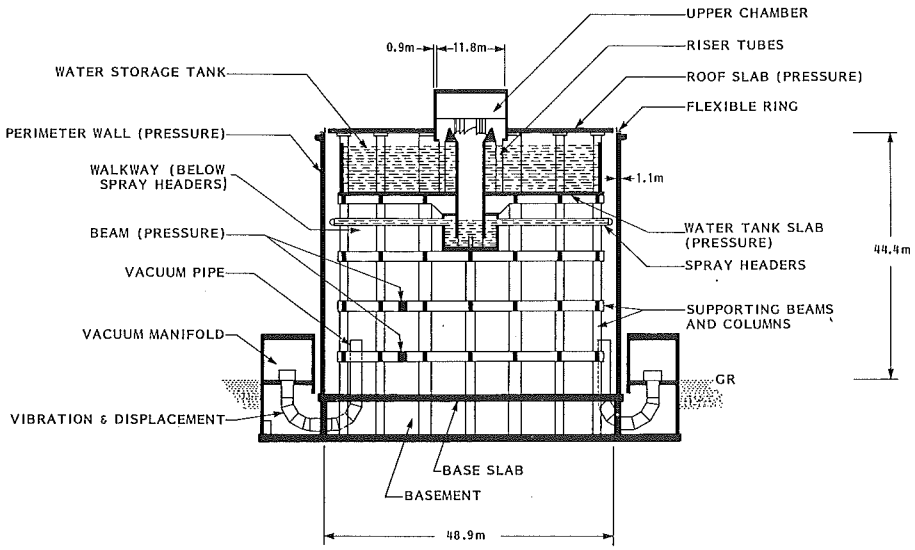

FIGURE 2

INTERNAL ARRANGEMENT OF THE VACUUM BUILDING
WITH MEASUREMENT LOCATIONS

The maximum change of pressure in the vacuum building, from approximately 7 kPa to atmospheric (approximately 100 kPa); the high velocity at which the released gases or vapours enter the building; and the action of the dousing system; all apply considerable forces on the various structural components of the vacuum building.

OBJECTIVE

The test program on the Bruce NGS 'B' vacuum building, before it was brought into service, was to confirm its structural integrity under a simulated emergency situation. The testing program described in this paper, which is part of a comprehensive test plan coordinated by the Atomic Energy of Canada Ltd [1], comprises measurement of the pressure distribution in the main building and the forces on various critical components.

TEST PROGRAM

In an emergency when the reactor building pressure increases by approximately 7 kPa, the sixteen self-actuating PRVs open and increase the main vacuum chamber pressure. A pressure rise of approximately 27 kPa in the main vacuum chamber activates the dousing system. For the blowthrough test program, a specially designed pneumatic system was used to open the pressure relief valves to the atmosphere instead of to the reactor building.

The test program was designed to measure, at locations indicated in Figure 2, the following parameters:

i) Pressure distribution along a horizontal axis on the underside of the roof slab, along a vertical axis on the inner face of the perimeter wall, on the underside of the water tank slab and at two levels in the main chamber.

ii) Strain and temperature on two riser pipes.

iii) Forces on the walkways and spray headers.

iv) Air velocity at three locations in the main vacuum chamber.

INSTRUMENTATION

Considering the hostile environment in which they had to function effectively the various measuring instruments described below were made rugged and compact, and in general had a high output signal. The supports for the various instruments and the conduits for routing the signal cables were also designed to withstand the forces generated during the blowthrough test. The instrument profiles were such that they would cause minimum obstruction to the air flow.

Static pressure distribution measurements were made at three locations (Figure 2) using solid state absolute pressure transducers. The pressure transducers were mounted on the roof, the water tank slabs, the perimeter wall and beem surfaces.

Specially designed anemometers were used for measuring the wind speed at three selected locations in the main vacuum chamber during the blow-through test. The anemometer type chosen for this project measures the drag force on a cylindrical rod, which then is converted into wind speed by proper calibration.

The cantilever beam gauges were designed to deform permanently by forces induced by wind pressure during the blowthrough test. Permanent deformations were then used to estimate the dynamic pressure on walkways and spray headers.

A LVDT (Linear Variable Differential Transformer) was used to measure the horizontal movement of one of the vacuum pipe supports.

Of the sixteen riser pipes, two were instrumented to measure strains in the axial and circumferential directions at four locations.

All the measuring instruments, except the strain gauges, were continuously monitored during the blowthrough test. The strain gauge signals were monitored using a multiplexer at the rate of 10 readings per second. The conditioned signals were stored in three tape recorders for further analysis.

The pressure transducers, anemometers, signal conditioners and data loggers were calibrated prior to the tests to minimize the instrument error. In the case of pressure transducer, strain gauges and anemometer the estimated maximum instrument error is ±1% and it is ±5% in the case of beam gauges.

BLOWTHROUGH TESTS SCHEDULE

The earlier tests in the series were scheduled to check instrument operation and calibration before the final "wet" blowthrough test. The following are the different tests carried out under this program.

1) Sixteen valve blowthrough test without dousing under partial vacuum (at 60kPa initially) or miniblowthrough test - intended as a calibration test.

2) Single valve blowthrough test without dousing - to measure PRV performance characteristics under prolonged choked flow conditions.

3) Sixteen valve blowthrough test without dousing or dry blowthrough test.

4) Sixteen valve blowthrough test with dousing or wet blowthrough test.

The blowthrough test without dousing was conducted because the pressure transducers used were not designed to operate in wet conditions. The details of the tests and other related information are given in Reference [2,3].

This paper deals primarily with the results of the dry and wet blowthrough tests.

RESULTS

A total of 40 data signals were monitored during each of the dry and wet blowthrough tests. Three magnetic tape recorders were used to store the data and on each tape a time signal was included as a reference. Time zero coincided with the activation of the PRV opening circuit. The pressure data were digitized at a rate of 8 per second and the airflow data at a rate of 200 per second. The type of signals, the recording mode, etc are listed in Table I.

TABLE I

DETAILS OF STRUCTURAL INTEGRITY MEASUREMENTS

No	Measurement Category	Location	Type of Transducer	No of Transducers and Spacing	Type of Monitoring
1	Pressure in main vacuum chamber	Perimeter wall surface	Absolute pressure transducer with specially designed mounting	5 - spaced vertically at 3 m intervals	continuous analog signal
		Bottom of the roof slab	"	2-one close to the perimeter wall and another near the water tank wall	"
		Bottom of water tank slab	"	3	"
		Beam surfaces at two levels	"	3 - at each level	"
2	Air speed in main vacuum building	Three locations at two levels	2 dimensional anemometers	1-at each location	"
3	Forces on structural components	Four locations on the circular walkways (catwalk)	Specially designed cantilever beam gauges	a set of 7 gauges at each location	self monitoring devices; no cabling necessary
4	Movement of vacuum duct	A typical support	Deflection Transducer (LVDT)	1	continuous analog signal
5	Strain in riser pipes	Two riser pipes	Strain gauges	16-8 on each of 2 riser pipes	digitized

Pressure in the Main Vacuum Building

Of the total 32 pressure measurements made at five different locations during the dry and wet blowthrough tests a typical one is plotted as a function of time in Figure 3. In each of these plots the pressure reading of one of the transducers on a beam, which was least affected by the jet flow, is included as a reference. The pressure difference relative to the reference value was calculated for each location. A typical plot of pressure difference values on the perimeter wall is shown in Figure 4. The maximum pressure differences at the roof slab, water tank slab and perimeter wall levels during dry and wet blowthrough test were about 4 kPa, 1.0 kPa and 1.5 kPa, and 4 kPa, 2.75 kPa and 1.5 kPa respectively.

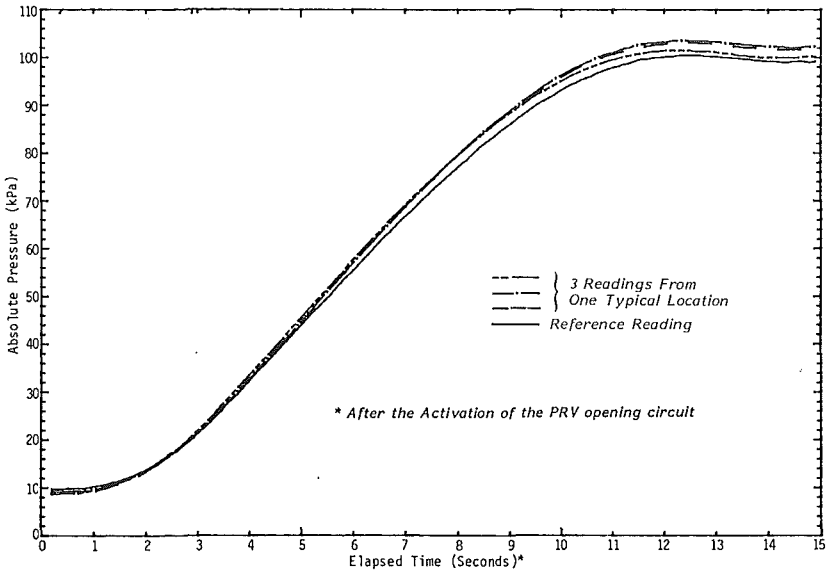

FIGURE 3

TYPICAL PRESSURE MEASUREMENTS (BLOWTHROUGH WITHOUT DOUSING)

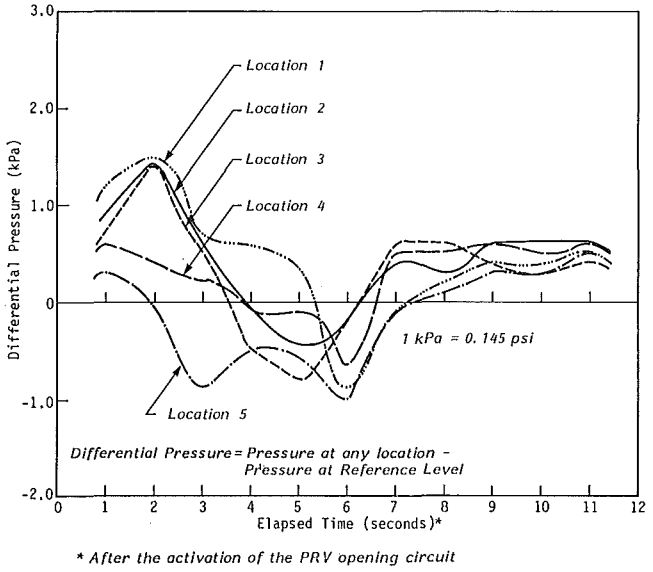

FIGURE 4

DIFFERENTIAL PRESSURE ON PERIMETER WALL
(BLOWTHROUGH WITH DOUSING)

TABLE II

AIRFLOW MEASUREMENT IN THE MAIN VACUUM BUILDING

Anemometer Location	Maximum Axial Wind Speed (m/s)	Time of Occurrence (seconds)*	Maximum Transverse Wind Speed (m/s)	Time of Occurrence (seconds)*
Location 1	85 (upwards)	1.1	130 (north west)	0.8
Location 2	45 (upwards)	1.2	75 (north east)	1.2
Location 3	40 (downwards)	1.6	60 (south east)	1.9 & 3.1

*After the activation of the PRV opening circuit

Airflow in the Main Vacuum Building

The air flow measurements were done during both dry and wet blowthrough tests. The wind speeds, both in the axial and transverse directions, for one of the three locations are shown as a function of time in Figure 5 and 6. The maximum axial velocities in the upward and downward directions were 85 m/s and 80 m/s, respectively. The maximum transverse velocity was about 130 m/s. The maximum axial-upward velocity occurred about 1.1 s after the activation of the PRV opening circuit while the maximum transverse velocity occurred after about 0.8 s. The velocity measurements at the three locations are shown in Table II. Unexpectedly, the transverse speeds are consistently greater than axial speeds.

Blowthrough Wind Loads on Walkways and Spray Headers

The wind pressures on walkways and on spray headers were measured at four selected locations on the radial catwalk for each of the dry and wet blowthrough tests. The pressures on the beam gauges for both tests were calculated from the permanent deflection of the mechanical gauges. The maximum pressures on catwalk members and spray headers during wet and dry tests were approximately 6.3 kPa and 4.1 kPa, respectively. It was observed that all the beam gauges deflected downwards indicating a predominantly downward force.

Stresses on Riser Pipes

Both axial and circumferential strains were measured at four diametrically opposite locations on each of the two riser pipes. The maximum axial and circumferential stresses were about 20680 kPa and 14480 kPa, respectively. This is small compared to the yield strength of the material.

Movement of Vacuum Duct Support

The maximum horizontal movement of a typical support measured during the wet blowthrough test was less than 1 mm and occurred about three seconds after the test initiation.

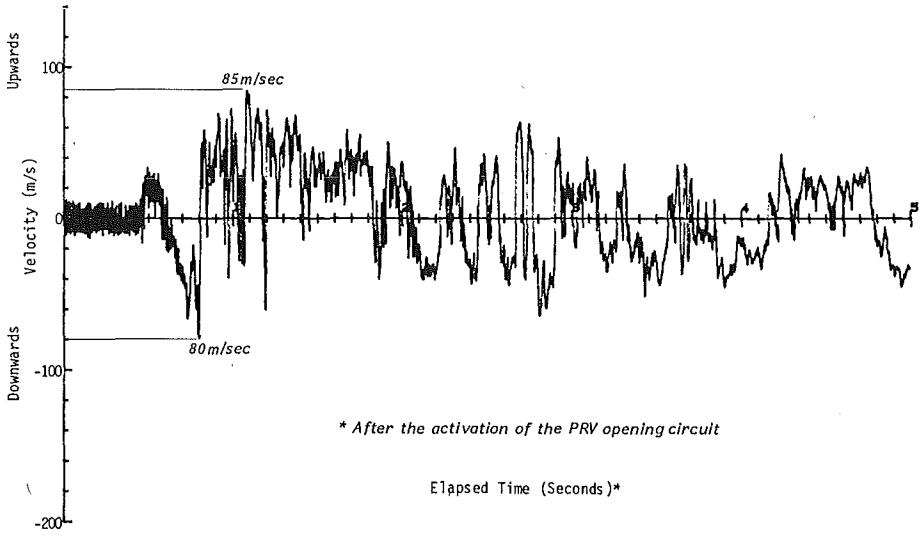

FIGURE 5
TYPICAL AXIAL AIRFLOW MEASUREMENT
(BLOWTHROUGH WITH DOUSING)

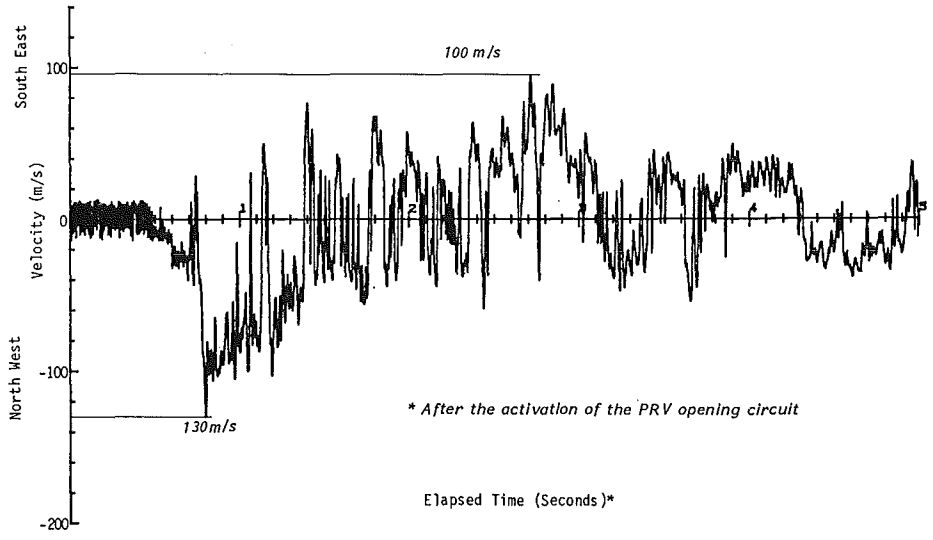

FIGURE 6
TYPICAL TRANSVERSE AIRFLOW MEASUREMENT
(BLOWTHROUGH WITH DOUSING)

TABLE III

SOME IMPORTANT MEASUREMENTS DURING BLOWTHROUGH TESTS

No	Component and/or Location	Type of Measurement	Maximum	Type of Blowthrough Test
1	Roof Slab Bottom	Pressure	Differ. Pressure = 4 kPa = 4 kPa	Without dousing With dousing
2	Water Tank Slab	Pressure	Differ. Pressure = 1 kPa = 2.75 kPa	Without dousing With dousing
3	Perimeter Wall	Pressure	Differ. Pressure = 1.5 kPa = 1.5 kPa	Without dousing With dousing
4	Wind Measurement			
	Location 1	Air Speed	85 m/s Axial Up 130 m/s Transverse	With dousing
	Location 2	Air Speed	45 m/s Axial Up 75 m/s Transverse	With dousing
	Location 3	Air Speed	40 m/s Axial Down 60 m/s Transverse	With dousing
5	Walkway and Spray Header	Pressure	6.3 kPa 4.1 kPa	Without dousing With dousing
6	Riser Pipes	Stress Calculated from Measured Strain	20680 kPa Axial 14050 kPa Circumferential	With dousing

DISCUSSIONS AND CONCLUSIONS

Measurements of pressure, air velocity and flow force were made during blowthrough tests in the CANDU system's vacuum building in order to assess the response of its structural components to postulated LOCA conditions.

The pressure variation, as a function of time at all the measurement locations in the main vacuum building, was relatively smooth. The difference between the various pressure readings at any one location were not considered significant.

The air speed in the axial direction was less than the corresponding transverse speed. The beam-column grid in the building may have been responsible for the observed flow.

The measurements on the service platform and spray headers show that these structures were subjected to relatively low pressures with resultant downward forces exceeding the upward forces.

Water flow induced stresses in the riser pipes during the wet blowthrough test were not significant.

Measurements are summarized in Table III.

The results from these tests confirm that the design assumptions for the vacuum building are reasonably conservative.

REFERENCES

1. H.W. Stokes, M.R. Khan, S. Krishnasamy, W.W. Koziak and T. Bukhanov, "16 PRV Blowthrough Test at Bruce 'B' GS." Proceedings of the 1984 International Containment Design Conference, Toronto, Ontario, Canada, June 1984.

2. S.G. Krishnasamy, "Structural Integrity of the Vacuum Building for the Bruce Nuclear Generating Station (Sixteen Valve Blowthrough Test)", Ontario Hydro Research Division Report No 83-204-K, Dec. 30, 1983.

3. W.W. Koziak, "Bruce NGS 'B' - Containment Commissioning Test", CSNI Specialist Meeting on Water Reactor Containment Safety, Toronto, Ontario, Canada, October 1983.

RECENT PROGRESS ON NRC-SUPPORTED HYDROGEN RESEARCH*

by

Marshall Berman
Sandia National Laboratories
Albuquerque, New Mexico, USA

and

John T. Larkins
United States Nuclear Regulatory Commission
Washington, DC, USA

ABSTRACT

The United States Nuclear Regulatory Commission has been supporting a research program to study the impact of hydrogen combustion on nuclear reactor safety. The objective of that program is to quantify the threat to containment survival posed by the mechanical and thermal loads resulting from hydrogen combustion. The program also addresses the potential sources of hydrogen for postulated severe accidents, the evaluation of proposed mitigation systems for reducing the threat from hydrogen, and the impact of combustion on the survival and functioning of safety equipment. This paper will be limited to discussing recent progress in understanding several forms of hydrogen combustion including ordinary deflagrations, accelerated flames, detonations, and diffusion flames.

DIFFUSION FLAMES

A diffusion flame may occur under various conditions during hypothetical reactor accidents. Such flames may autoignite as hot steam:hydrogen mixtures leave the primary system through a break or stuck-open valve. They might also be ignited accidentally or deliberately elsewhere in containment, and flash back to a point near the exiting mixture. Diffusion flame plumes might also form above the suppression pool in a BWR. The primary threat from these flames is the high thermal load applied to neighboring safety equipment and to containment penetration seals, including penetrations through the drywell wall. Recent research [1] has shown that such flames can be very stable, even for steam mole fractions as high as 80%, Figure 1. Current research is addressing the applicability of small-scale systems to predicting large-scale reactor situations. Models are being developed to predict the spatial and temporal heat fluxes associated with these flames. Work sponsored by other organizations (e.g., EPRI, HCOG) is being used to support this model development effort.

---

* This work was supported by the United States Nuclear Regulatory Commission and performed at Sandia National Laboratories which is operated for the U. S. Department of Energy under contract number DE-AC04-76DP00789.

DEFLAGRATIONS

Many experiments have been conducted around the world to measure hydrogen:air:steam flammability limits, pressure rises and flame speeds. Figure 2 [2] illustrates the ternary flammability limits that have been measured for such mixtures. The limits widen with increasing temperature on the hydrogen-lean side, but narrow with increasing initial temperature on the rich side. Precombustion gas motion has also been shown to affect these limits [3,4]. Figure 3 shows that the peak pressure resulting from combustion of lean hydrogen mixtures depends strongly on the pre-burn gas motion, vessel geometry and location of ignition source. For mixtures richer than about 10% hydrogen, the dependence on these parameters decreases significantly, and hydrogen concentration becomes the major determinant of peak pressure. For lean mixtures, pre-burn gas motion tends to increase flame speed and, consequently, increases the degree of combustion completeness. This can be seen by comparing experimentally measured flame speeds for the "fans off" (Figure 4) and "fans on" (Figure 5) cases. The effects of aerosols on combustion is a current research topic. There is also some preliminary evidence of a scale effect in burning limits (seen in EPRI tests at the Nevada Test Site) especially with respect to the location of the ignition source.

DETONATIONS

Significant progress has been made in determining the initial and boundary conditions for the initiation and self-sustained propagation of a detonation wave. The detonation cell width, which can be measured experimentally, has been shown to be an important fundamental length scale that characterizes the chemical rate processes. A knowledge of the cell width permits the detonation limits to be prescribed. The critical energy for direct initiation of a detonation wave in a given mixture can also be estimated from the cell width and the equilibrium Chapman-Jouguet detonation states. The critical tube diameter or the critical channel width for the continued propagation of a confined detonation transmitting suddenly into an unconfined region has also been shown to be directly proportional to the cell width. Thus, recent research on hydrogen-air detonations has been centered around the measurement of this fundamental cell width, not only for hydrogen-air mixtures, but for CO_2-H_2-air as well as steam-H_2-air mixtures. Figure 6 shows the detonation cell width as a function of hydrogen concentration in air with and without the addition of carbon dioxide. Attention is also devoted to the development of theories and empirical correlations to link the cell width data to the dynamic detonation parameters of practical interest (i.e., detonation limits, initiation energies, critical tube diameters, transition to detonation, etc.). Detonations have been observed at hydrogen concentrations as lean as 13.5% in air, much less than the 18% limit that has been frequently reported in other references.

The initiation of detonations is as important as detonation propagation for some reactor safety situations. Prevailing scientific opinion recognizes two distinct methods for initiating detonations: direct initiation (by explosives) and DDT (deflagration-to-detonation transition) occurring in confined geometries. Recent experiments in Germany, Norway, and the U.S. indicate that a third mechanism is possible, especially at large scales. A sudden, spontaneous transition to detonation can occur when an energetic source of sufficient size is present. This source could be a hot flame jet, or a turbulent burning region (e.g., in the vicinity of a fan, or when the flame encounters an obstacle).

ACCELERATED FLAMES (High-Speed Deflagrations)

Under appropriate initial and boundary conditions (e.g., strong ignition sources, geometrical confinement, the presence of turbulence-inducing obstacles) H_2-air deflagrations can accelerate rapidly to very high flame speeds and may even transit to detonation. Because of the dense distribution of equipment in some reactor regions, high-speed deflagrations are of great practical significance. Research on high-speed deflagrations has focused on establishment of the acceleration rate and the maximum flame speed attainable under different boundary conditions and hydrogen concentrations. Figure 7 shows the maximum steady state turbulent deflagration speed as a function of H_2 content. These flame speeds are obtained in circular tubes (5 and 15 cm in diameter) and with repeated (one diameter spacing) circular orifice plates of blockage ratio BR = 0.4 as turbulence-inducing obstacles. The flame speed increases sharply at hydrogen concentrations just exceeding 13%; transition-to-detonation results near a concentration of 25% hydrogen. The corresponding overpressures associated with these high-speed deflagrations are shown in Figure 8. Transverse venting has been shown to be very effective in limiting flame accelerations in lean H_2-air mixtures. For example, for 12.7% H_2, the deflagration accelerated rapidly to almost 200 m/sec in an obstacle-filled rectangular channel, Figure 9. However, with only 8% venting on the top ceiling of the channel, the flame acceleration has virtually disappeared. Recent large-scale experiments at Sandia have not demonstrated such a dramatic effect of venting.

Current research is aimed at establishing scaling laws for flame acceleration and transverse venting in large-scale field experiments at Sandia. The important problem of formulating criteria for the transition from these high-speed deflagrations to detonations is also receiving considerable attention.

MODEL DEVELOPMENT

Several computer codes have been developed to analyze the probability and consequences of various forms of combustion. The HECTR code is used to predict the transport, mixing and combustion of hydrogen during reactor accidents, for ordinary deflagrations [5]. The Vortex Dynamics code is used to study flame acceleration under certain conditions [6]. The CONCHAS-SPRAY code is also being used for studies of flame acceleration and diffusion flames [7]. The CSQ code [8] calculates the spatial and temporal dynamic pressures that can result from detonations in containment geometries.

CONCLUSIONS

Figure 10 illustrates the various forms of combustion that depend on the rate of burning. Much progress has been made in understanding the upper and lower extremes of this region, i.e., ordinary deflagrations and detonations. Work is proceeding to complete our understanding of those phenomena, and improve our ability to predict the intermediate regime of complex deflagrations and accelerated flames.

REFERENCES

1. Proceedings of the Second International Conference on the Impact of Hydrogen on Water Reactor Safety, Oct. 3-7, 1982, NUREG/CP-0038, EPRI RP 1932-35, SAND82-2456, Albuquerque, NM. Session V: J. E. Shepherd, O. B. Crump, "Steam:Hydrogen Flame Jet Experiments," p. 843.

2. M. Berman and J. C. Cummings, "The Hydrogen Problem in LWRs," NUCLEAR SAFETY, Vol. 25, No. 1, January-February 1984.

3. Several papers in Ref. 1, Sessions V and VI are appropriate, e.g., H. Tamm et al., "A Review of Recent WNRE Experiments on Hydrogen Combustion," p. 633.

4. Steve Hall, United Kingdom Atomic Energy Authority, Private Communications.

5. Ref. 1, p. 827, A. L. Camp et al., "HECTR: A Computer Code for Modelling the Response to Hydrogen Burns in Containment."

6. Ref. 1, p. 915, W. T. Ashurst and P. K. Barr, "Discrete Vortex Simulation of Flame Acceleration Due to Obstacle-Generated Turbulent Flow."

7. L. D. Cloutman, J. K. Dukowicz, J. D. Ramshaw, A. A. Amsden, "CONCHAS-SPRAY: A Computer Code for Reactive Flows with Fuel Sprays," LANL Report LA-9294-MS, May 1982.

8. R. K. Byers, "CSQ Calculations of H_2 Detonations in Zion and Sequoyah," NUREG/CR-2385, SAND81-2216, Albuquerque, NM, July 1982.

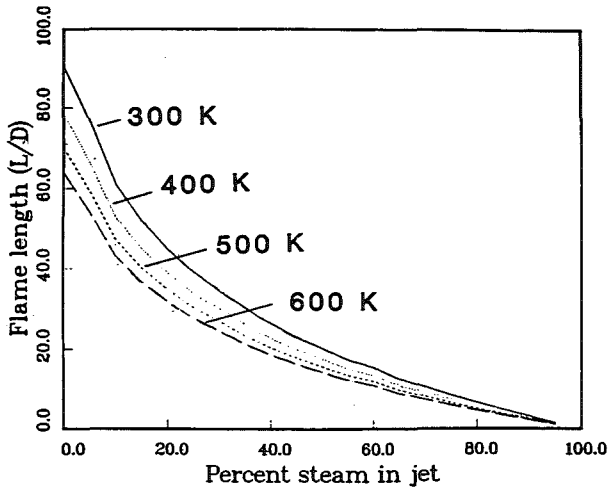

Figure 1. Flame lengths for H_2:steam mixtures for various exit temperatures

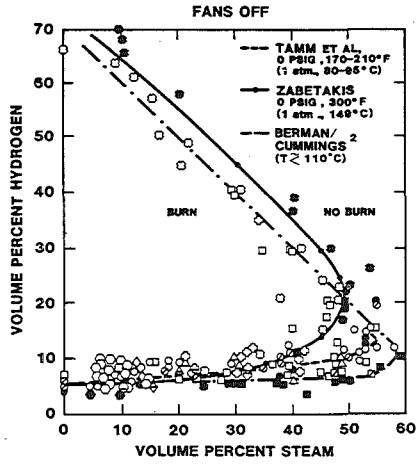

	FITS	WHITESHELL	TVA	FENWAL	LLNL	WHITESHELL	BM
BURN	□	○	△	◇	⬡	○	○
NO BURN	■	●	▲	◆	⬢	●	●
MARGINAL	⊠	⊘	⧋	⟐	⊖	⊖	—
T_0	110°C	80-95°C	-	60-100°C	Test	83°C	149°C
P	1 atm	1 atm	-	1.4 atm	1.1-2.8 atm	~0.9-1.0 atm	1 atm

Figure 2. Flammability limits for Hydrogen: Air: Steam mixtures with fans off. [FITS=Fully Instrumented Test System (Sandia National Laboratories); WHITESHELL=Whiteshell Nuclear Research Establishment (Canada); TVA=Tennessee Valley Authority; FENWAL=Fenwal, Inc.; LLNL=Lawrence Livermore National Laboratory; BM=Bureau of Mines.] See Reference 2.

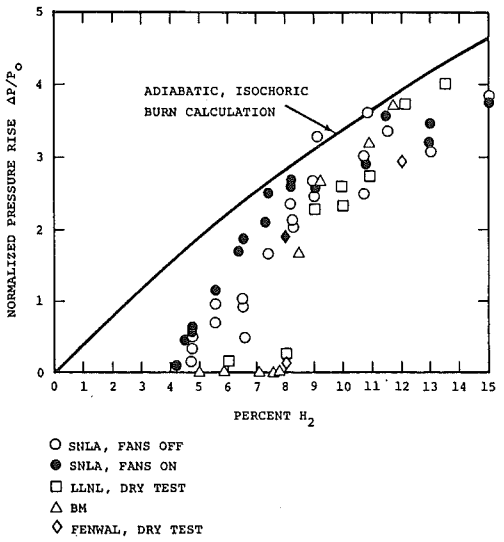

Figure 3. Peak pressure vs. initial H_2 concentration, Sandia National Laboratories-Albuquerque (SNLA), Lawrence Livermore National Laboratory (LLNL), Bureau of Mines (BM), and Fenwal data, (Reference 1).

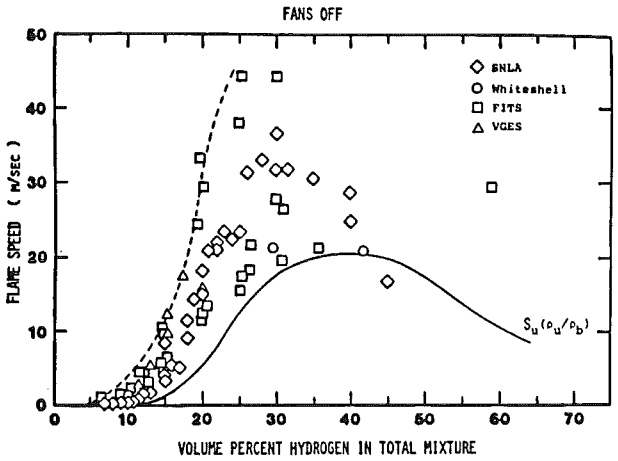

Figure 4. Flame speeds (laboratory frame) for dry hydrogen:air mixtures, fans off, (S_u = Laminar burning velocity, ρ_u = unburned gas density, and ρ_b = burned gas density). See Reference 2.

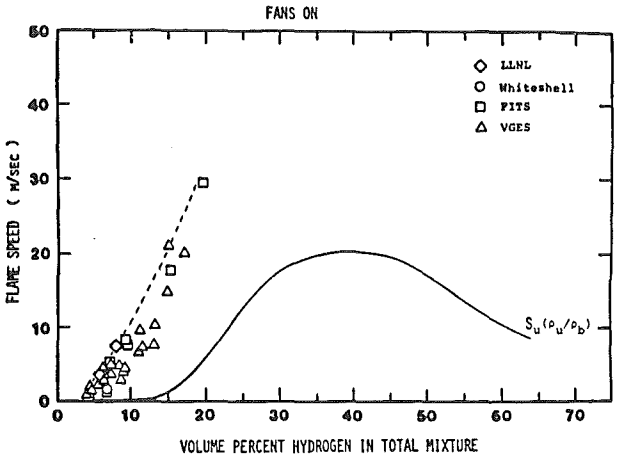

Figure 5. Flame speeds (laboratory frame) for dry hydrogen:air mixtures, fans on, (S_u = Laminar burning velocity, ρ_u = unburned gas density, and ρ_b = burned gas density). See Reference 2.

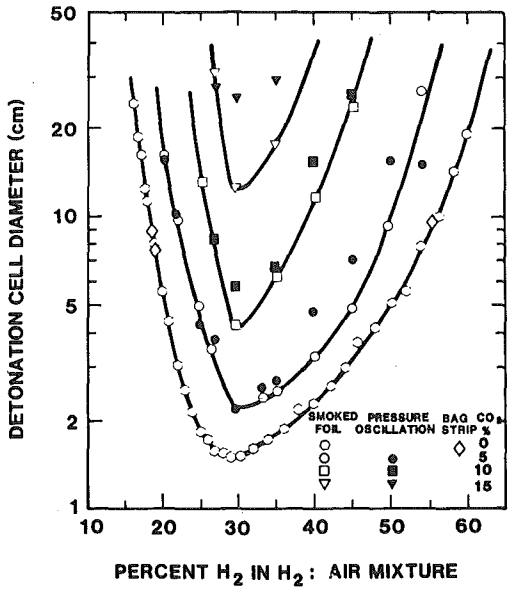

Figure 6. Detonation Cell Diameter measurements for various Hydrogen : Air: CO_2 Mixtures.

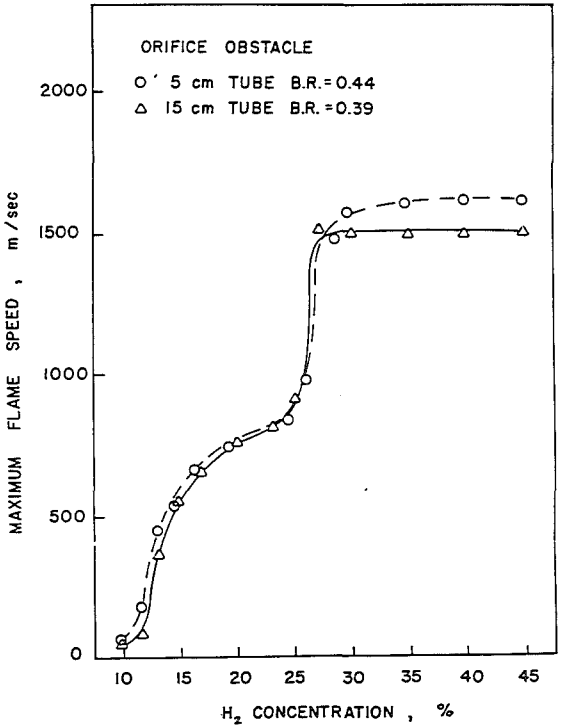

Figure 7. Maximum steady-state turbulent deflagration speeds for small-scale experiments.

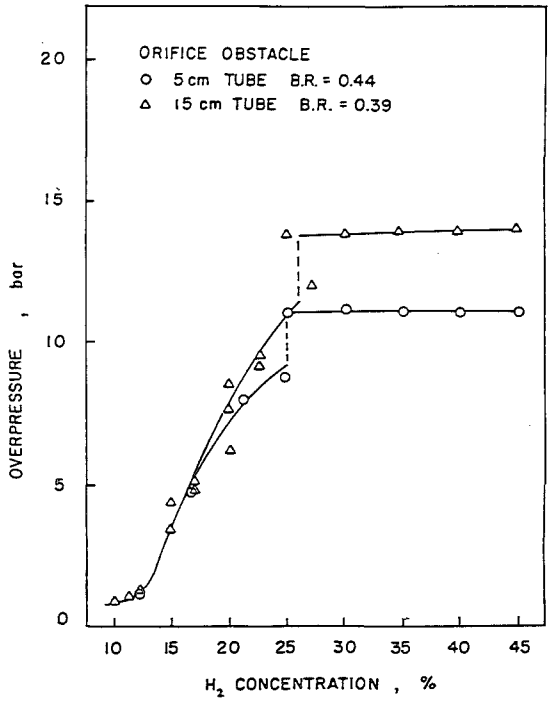

Figure 8. Pressures associated with high-speed deflagrations.

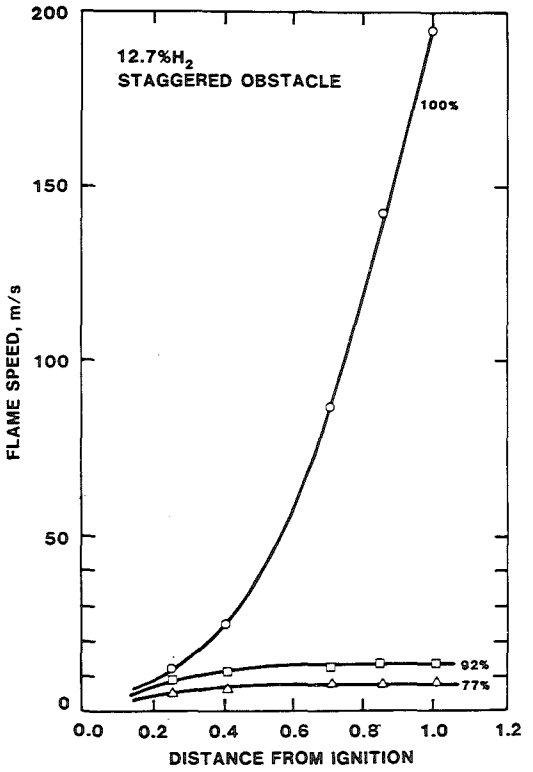

Figure 9. Flame speed profiles for 12.7% H_2:air mixture under various degrees of confinement.

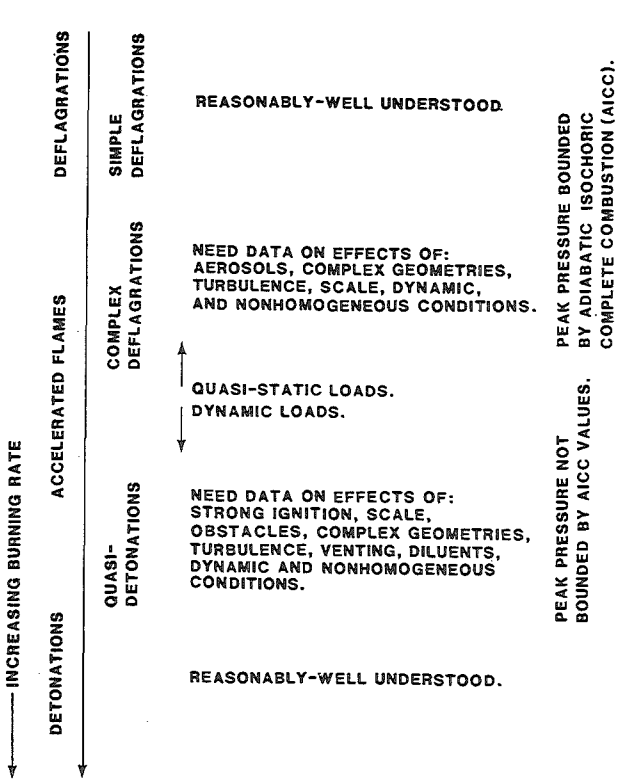

Figure 10. Combustion Phenomena.

Scaling Problems Associated to the Extrapolation of Containment Experiments

H. Karwat

Technische Universität München
D-8046 Garching, FRG

Abstract

Similarity considerations are of utmost importance to back-up the interpretation of experimental results obtained from downscaled experimental test rigs. The availability of adequate computer codes which describe transient events was considered to be sufficient once the codes have been assessed by those experimental results. However all codes, in particular the "advanced codes" require empirical correlations derived from downscaled basic experiments to amend the necessary constitutive equations. Therefore the codes have to be analysed with respect to possible sensitivities of the applied equation system with respect to linear dimensions and operational parameters. Phase separation and jet expansion processes are in particular sus-pect to be described by empiricism which may be dimension-dependent. Resulting inherent distortions of the simulation are addressed and proposals for possible improvements are given.

Introduction

Similarity laws and scaling criteria are very important for the interpretation of experimental observations obtained from downscaled models. In the field of containment related research three facilities have been utilized to perform experiments, the CVTR, the Battelle Frankfurt test facility and the HDR-test facility. None of these facilities are geometrically similar replica of existing PWR-containments nor are they similar amongst each other. The availability of a computer code to describe the involved physical processes and the actually existing geometric structures of a containment is essential to understand and interprete experimental observations. On the other hand the validity of code calculations is demonstrated by a comparison of calculated results with experimental results obtained from the test rigs. The same code is then considered to be adequate for the design of full size containments for light-water cooled reactors.

Fig. 1 makes an attempt to illustrate the interrelations between analytical tools, experimental facilities, the design of nuclear power plant systems and the various engineering tasks. Within the lefthand circuit codes serve the experimental activities and are verified by appropriate measurements, while within the right-hand circuit the same codes are used to design full-size prototype equipment mostly following specific code application guidance from rules and licensing requirements.

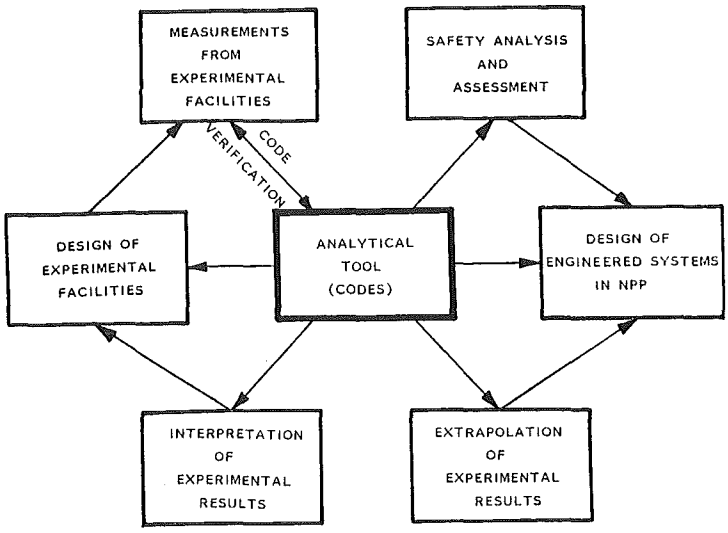

FIG.1 INTERRELATIONS BETWEEN VARIOS ENGINEERING TASKS AND ANALYTICAL TOOLS (CODES)

The most important physical phenomena to be predicted by codes to properly design containment systems are

- -subcompartment pressurisation in the vicinity of an assumed rupture
- -jet impingement forces caused by the rupture
- -maximum containment pressure (design pressure)
- -the long term temperature evolution within the containment.

These tasks require the availability of sophisticated thermo-hydraulic codes to simulate the involved fluid-dynamic and heat exchange processes with the high accuracy anticipated within national reactor safety rules and guidelines.
In general, fluiddynamic design analyses to define loads (overall pressure, subcompartment pressure differences and temperatures) are nowadays performed applying codes based on the volume-averaging lumped parameter concept (COFLOW /1/, CONTEMPT /2/, DDIFF /3/, TRAP /4/, etc.) which offer a variety of empirical options to cope with the heterogeneous reality of the 2phase-2component flows. Three containments systems have been available which yielded extensive experimental data for code verification purposes:

- -The decommissioned CVTR containment (heat transfer only) /7/
- -The Battelle-Frankfurt Containment (BFC) Model /5/
- -The decommissioned HDR reactor containment /6/.

All experiments to study the pressurisation process under design basis accident conditions have been performed within the BFC and HDR facilities. The free volume of BFC is approx. 1/100, of HDR approx. 1/7 that of a full size PWR containment. Valuable experimental evidence has been obtained from the BFC experiments which is documented and assessed within numerous reports (e.g. /8 -10/). Confirmative experiments within HDR should serve to demonstrate the applica-

bility of the BFC findings to another containment, different in construction and free volume (factor 15 - 20).

General Scaling Aspects

The term "scaling" is in general understood in a broad sense covering all differences existing between a real full-size industrial plant (e.g. a nuclear power plant system) and a corresponding experimental facility. An experimental facility may differ in geometric dimensions and shape, in arrangements and availability of components, in the mode of operation (e.g. nuclear vs. electrical heating) or even in the applied test fluid (e.g. Freon vs. water).

All these differences have the potential to distort an experimental observation precluding its direct and immediate application for the design or operation of full-size plants. An extrapolation procedure is necessary which requires good understanding of the experiment and the involved processes to the largest possible extent.

The term distortion may be defined as a partial or total suppression of physical processes (sometimes also called physical phenomena) observed by only changing the size (geometric dimensions) or the shape (arrangement of components) of the test rigs, although the same experiment whith an identical goal is performed in both facilities. Furthermore such distortions may also be caused by differences in the mode of operation of the test rigs considered or by the use of different materials. In this connection it will be a central question to what degree the analytical tools are able to simulate these distortions without a facility-dependent tuning.

In the field of emergency core cooling and primary system blowdown an overview about the present scaling principles for nuclear reactor systems has been given by Nahavandi /11/. Three types of possible scaling principles have been derived from a fundamental consideration of the conservation equations for mass, momentum and energy for a homogeneous two-phase flow (3 equation system):

1. time-reducing scaling
2. time-preserving scaling
3. idealized time-preserving modeling procedures.

The latter method requires the availability of a mathematical description of the physical process which can be applied to full size prototype facilities as well as to downscaled experimental test rigs in an equivalent unrestricted manner. In an earlier study /12/ we came also to the general conclusion that small scaled reactor safety experiments can be best understood by the use of sophisticated two-phase flow models. However, the accuracy of measurements, specifically those of important boundary conditions has been identified to be a limiting factor for the overall agreement between analysis and experiment. Heterogeneity of the fluid, thermo-dynamic nonequilibrium and unsufficient treatment of flow resistances for irregularly shaped flow paths have been supposed to be influencial on the achievable accuracy of containment code predictions in terms of local pressure differences and temperature fields. In so far it was not supprising that the expected confirmation of conclusions drawn earlier from a large number of analyses for BFC experiments concerning achievable predictive accuracies has not been found for the first HDR containment experiments. A lack of geometric simularity between both experimental test rigs and the highly empirical concept to cope with local flow phenomena may be reasons for this finding. In this context it appears necessary to analyse the frequently used lumped parameter codes with respect to their inherent dependence on dimensional effects. For the following considerations it is assumed that a prototype containment is represented by an experimental model designed in strictly geometric similarity to the prototype.

Dimensional Analysis of COFLOW

The lumped parameter code COFLOW is extensively used for the design of PWR containment systems while the analyses of experimental results for many years served the verification of this code. The code is described in detail within references /1;13/. It is based on continuity equations for vapor, water, air, transportable water droplets within the gas/vapor - phase and energy - as well as a momentum balance between adjacent nodes. The set of ordinary differential equations can easily be transformed into a set of partial differential equations. The vapor - balance may serve as an example for the following dimensional analysis of the basic COFLOW equations.

Vapor balance combined with the evaporation rate related to a sub-volume V

$$\frac{\partial}{\partial t}\left(\varrho_D \frac{V_G}{V}\right) + \frac{\partial}{\partial x}\left(\varrho_D \frac{V_G}{V} W\right) =$$

$$= -\varrho_D^2 \frac{V_G}{V} \frac{d}{dt}\left(\frac{1}{\varrho_D}\right) - \varrho_D \varrho_W \frac{V_W}{V} \frac{d}{dt}\left(\frac{1}{\varrho_W}\right) - \sum\left(\frac{G \varrho_D V_G}{V M_B}\right) \qquad (1)$$

$$- \sum\left(\frac{G}{V} \frac{\varrho_D V_{WG}}{M_B}\right)$$

Defining for each involved variable a dimensionless ratio

$$\frac{\text{Variable}_{\text{Prototype}}}{\text{Variable}_{\text{Modell}}} = \text{Variable}^* \quad \left(\text{e.g.} \frac{V_{\text{Prototype}}}{V_{\text{Modell}}} = V^*\right)$$

and replacing within equation (1) each variable by the product $V_{\text{Prototype}} = V_{\text{Model}}\ V^*$ yields the following equation

$$\frac{\partial}{\partial t' t^*}\left(\varrho_D' \varrho_D^* \frac{V_G' V_G^*}{V' V^*}\right) + \frac{\partial}{\partial x' \partial x^*}\left(\varrho_D' \varrho_D^* \frac{V_G' V_G^*}{V' V^*} W' W^*\right) =$$

$$= -\varrho_D'^2 \varrho_D^{*2} \frac{V_G' V_G^*}{V' V^*} \frac{d}{dt' dt^*}\left(\frac{1}{\varrho_D' \varrho_D^*}\right) - \qquad (2)$$

$$\varrho_D' \varrho_D^*\ \varrho_W' \varrho_W^* \frac{V_W' V_W^*}{V' V^*} \frac{d}{dt' dt^*}\left(\frac{1}{\varrho_W' \varrho_W^*}\right)$$

$$- \sum\left(\frac{G' G^* \varrho_D' \varrho_D^* V_G' V_G^*}{V' V^* M_B' M_B^*}\right) - \sum\left(\frac{G' G^* \varrho_D' \varrho_D^* V_{WG}' V_{WG}^*}{V' V^* M_B' M_B^*}\right)$$

Assuming that for all variables the ratios "variable*" remain independent from space within the described control volume and assuming in particular that it may be justified to keep the time ratio t* = constant for the entire transient we are allowed to rearrange equation (2) into

$$\frac{\partial}{\partial t'}\left(\rho_D' V_G'\right) + \frac{W^* t^*}{x^*}\frac{\partial}{\partial x'}\left(\rho_D' V_G' w'\right) =$$

$$\rho_D'^2 V_G' \frac{d}{dt}\left(\frac{1}{\rho_D'}\right) - \frac{V_W^*}{V_G^*}\rho_D' \rho_W' V_{WG}' \frac{d}{dt}\left(\frac{1}{\rho_W'}\right)$$

$$- \sum \frac{G^* t^*}{M_B^*}\left(V_G' \frac{\rho_D' G'}{M_B'}\right) - \sum \frac{V_W^*}{V_G^*}\frac{G^* t^*}{M_B^*}\left(V_{WG}' \frac{\rho_D' G'}{M_B'}\right) \qquad (3)$$

with $K_1^* = \frac{W^* t^*}{x^*}$ $K_2^* = \frac{V_W^*}{V_G^*}$ $K_3^* = \frac{G^* t^*}{M_B^*} = \frac{W^* t^*}{L^*}$ $K_4^* = \frac{\rho_{WG}^*}{\rho_W^*} K_3$

Equations (3) and (1) will describe identical processes within the prototype and the model if for a geometrically similar experimental model the ratios of the dimensionless groups K^*_1 to K^*_4 would become equal to 1.
Of particular interest for containment pressurisation processes may be the balance for water entrained within the gas phase. Droplet deposition into the sump water phase of a considered sub-volume is assumed to follow the empirical equation

$$G_{sep} = C_{WA} \cdot G_{WG} + \sqrt{2gH'}\,\rho_W \cdot V_{WG} \cdot \frac{F_Z}{V}$$

The transformed partial differential equation for the density of entrained water within the gas phase finally will be

$$\frac{\partial}{\partial t'}\left(\rho_{WG}'\right) + K_1^* \frac{\partial}{\partial x'}\left(\rho_{WG}' W'\right) =$$

$$- \sum \left(K_5^* \frac{C_{WA}' \rho_{WG}' G'}{M_B'}\right) - K_6^* \sqrt{2gH'}\,\frac{\rho_{WG}'}{H'} +$$

$$\frac{K_Z^*}{K_2^*}\frac{\rho_D'^2 V_G' \rho_{WG}'}{V_W' \rho_W'}\frac{d}{dt'}\left(\frac{1}{\rho_D'}\right) + K_7^* \frac{\rho_D' \rho_{WG}'}{V_W'}\frac{d}{dt}\left(\frac{1}{\rho_W'}\right) \qquad (5)$$

$$+ \sum \left(\frac{K_7^* K_3^*}{K_2^*}\frac{\rho_{WG}' V_G' \rho_D' G'}{\rho_W' V_W' M_B'}\right) + \sum \left(K_7^* K_4^* \frac{\rho_{WG}'^2 V_G' \rho_D G'}{\rho_W^2 V_W' M_B'}\right)$$

yielding additional dimensionless parameter combinations. At the end we obtain a set of 17 similarity groups listed within table 1. A more detailed analysis of all basic equations involved within the COFLOW-model can be found in /14/.

Additional similarity requirements have been found originating from the activation of the optional model within COFLOW which describes the dynamic components of compartment internal pressure drop /13/. Work in this connex however is still in progress. Hence, the following discussion is strictly limited to fundamental questions of the lumped parameter code simulation in the vicinity of the two-phase flow discharge.

	K_1	K_1^*		K_1	K_1^*
MASS - BALANCES (AIR, VAPOR, WATER)	$K_1 = \frac{W \cdot t}{X}$	$S^{-1/3}$	ENERGY - BALANCE	$K_8 = \frac{W^2}{h_D}$	1
	$K_2 = \frac{V_W}{V_G}$	?		$K_9 = \frac{\varrho_L \cdot h_L}{\varrho_D \cdot h_D}$	1
	$K_3 = K_1 \cdot \frac{X}{L}$	L^{*-1}		$K_{10} = K_8 \frac{\varrho_L}{\varrho_D}$	1
	$K_4 = K_3 \frac{\varrho_{WG}}{\varrho_W}$	$\varrho_{WG}^* \cdot L^{*-1}$		$K_{11} = \frac{h_W \cdot \varrho_W}{h_D \cdot \varrho_D}$	1
ENTRAINMENT MODEL	$K_5 = K_3 \cdot C_{WA}$	$C_{WA}^* \cdot L^{*-1}$		$K_{12} = \frac{h_W \varrho_W}{h_D \varrho_D} \cdot \frac{V}{V_G}$	1 (?)
	$K_6 = \sqrt{\frac{G}{H}} \cdot t$	$H^{*-1/2}$		$K_{13} = \frac{p}{h_D \varrho_D} \cdot \frac{V}{V_G}$	1 (?)
	$K_7 = \frac{\varrho_D}{\varrho_W}$	1		$K_{14} = \frac{Q \cdot t}{h_D \varrho_D X} \cdot \frac{V}{V_G}$	$Q^* S^{-1/3}$ (?)
MOMENTUM BALANCE	$K_{15} = \frac{G \cdot t}{W}$	1			
	$K_{16} = \frac{P \cdot t}{X \cdot W \cdot \varrho_B}$	$\varrho_B^{*-1} \cdot S^{-1/3}$			
	$K_{17} = \frac{\xi \cdot W \cdot t}{\varrho_B}$	$\xi^* \cdot \varrho_B^{*-1}$			

$$S = \frac{V_{TOTAL,PROTOTYPE}}{V_{TOTAL,MODEL}} = V_{TOTAL}^*$$

$$K_1^* = \frac{K_{PROTOTYPE}}{K_{MODEL}}$$

Tabelle I Dimensionless Similarity Groups for the COFLOW-code for Geometrically Similar Experimental Models.

The groups K_1 to K_4 result from the steam, water and air balances, groups K_5 to K_7 from the droplet entrainment model, K_8 to K_{14} from the energy balance and K_{15} to K_{17} from the momentum equation.

One should take note that the groups K_2, K_3, K_6 and K_{12} to K_{14} express some empirical committments with respect to the adopted discretisation scheme (nodalisation). In this context L represents the distance between node centers of the momentum balance while V is linked to the subvolume of the node representative for the mass- and energy balances (superimposed mesh-scheme). H describes the height of a control volume to which the empirical droplet deposition equation applies. These parameters (L,V and H) do not necessarily follow the general geometric hardware scaling between model and prototype expressed by the linear ratio $x^* = S^{1/3}$ (geometric similarity provided), they normally are considered as optional to the code user.

Discussion of the Dimensionless Groups

Containment experiments have been performed so far under a "time preserving operating condition"

$$\frac{V_{Prototype}}{V_{Model}} = \frac{\text{Energy Addition}_{Prototype}}{\text{Energy Addition}_{Model}} = S$$

which can be easily deduced from the first law of thermodynamics to yield for all components under favourable circumstances

$$t^* = \dot{P}_i^* = \varrho_i^* = h_i^* = 1$$

as a good approximation. In this respect the free volume V of the entire containment served as the important scaling parameter.
An idealized geometric similar scaling principle is shown in fig. 2 for the compartment where the local mass- and energy release into the containment may occur. To obtain equal relative energy addition requires $D_{rupture}$ to be scaled proportional

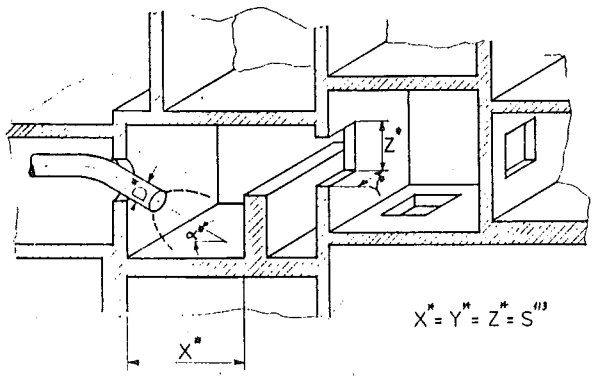

Fig. 2 Idealized Scaling Scheme for Compartmented Containments

to $S^{1/2}$, if the properties of the pressurized water discharged into the containment are identical (as usually aimed for). With respect to the local pressurisation process we find as important local boundary condition W* = 1 at least in the vicinity of the discharging two-phase jet.

For the formation of local pressure differences a similarity consideration has to originate from this definable and reproducible boundary condition.
The column K_i^* within table I illustrates for which similarity groups a value of unity (1) may be expected. The question marks (?) indicate the implications of the applied nodalisation concept. They may be disregarded if model and prototype would be nodalized with an identical scheme, otherwise the implications should be discussed in more detail.
Of particular importance are the ratios K_3^* to K_6^* which are derived from the applied droplet entrainment model and the ratios K_{16}^* and K_{17}^* which are representative for the momentum equation governed by the density ϱ_B of the massflow and the flow resistance empirics.
The flow density ϱ_B again is coupled to the droplet density ϱ_{WG} by the expression

$$\varphi_B = \varphi_{WG} + \varphi_L + \varphi_D$$

linking the above mentioned groups closely together. From the K_i^* ratios in table I the sensitivity of the code results with respect to the formation of local pressure differences on the purely empirical corrective constants C_{WA} and φ becomes evident and some more fundamental treatment of the process within the code is highly recommended if model -or scaling- dependent errors are to be limited. While the operating boundary condition $W^* = 1$ allows the simplifying conclusion that a similar velocity field may exist around the discharge-nozzle, K_1^* indicates a distortion with respect to the available linear dimensions when or where ever a two-phase jet will hit a structure. Thus, associated local thermal and mechanical nonequilibrium processes may be distorted, although several more recent fundamental studies concerning the behaviour of two-phase jets (e.g. /15,16/) suppose a linear relationship between the diameter of the jet orifice and the necessary distance for a jet to decay its pressure field to ambient conditions. In so far downscaling of $D_{rupture}$ by $S^{1/2}$ to a certain extent would compensate the distortion expected from the K1* conditions. However, a quantitative assessment of the jet expansion behaviour and the associated entrainment of water during such experiments necessitates the development and/or application of highly sophisticated advanced codes (e.g. COBRA-NC) at least to describe the flow within the compartment of energy release. At the present stage of this work only qualitative indications can be given for which areas of the COFLOW-simulation (and other lumped-parameter code concepts) scaling-related distortions may be expected.

Similarity conditions for flow fields further downstream from the compartment of rupture are of course burdened by the uncertainty which exists for the compartment of rupture itself. From an engineering point of view more detailed considerations in this respect would be of secondary importance unless correct predictions of the component distribution (air, vapor, water) within the entire containment are of specific interest. This is certainly not the case for the short term pressurisation period. Therefore K_i^*-ratios within table I should only be considered as informative for the local pressurisation process in the vicinity of the simulated rupture. Respecting this limitation the lack of geometric similarity of the available containment experimental facilities may also become a less stringent additional problem not yet fully covered by nowadays simulation procedures.

Maximum total containment pressure will be reached towards the end of energy release from the primary system. At this time internal flow velocities will decay and the main similarity groups of interest will be K_9, and K_{11} to K_{14}. K_{14} shows the well known effect of an increase of heat losses to structures of downscaled experimental models. This is caused by an increase of the ratio surface/volume proportional to $S^{1/3}$. The other dimensionless groups may be of some interest if thermal nonequilibrium between the phases had to be taken into account (for the present study complete equilibrium was assumed).
For long term natural convection processes (e.g. the distribution of hydrogen and/or fission products) K_{14} may be again an important similarity group together with K_{15}, K_{16} and K_{17}. However additional studies deem necessary to more precisely define the most important operating and boundary conditions common to the experimental model and the prototype facility in this direction. Therefore no further discussion of similarity requirements for this area seem appropriate within the present paper.

Conclusions

An attempt has been made to analyse the basic equations of the lumped parameter code COFLOW with respect to possible inherent distortions related to its experimental verification on basis of downscaled test results. In specific the local pressurisation process in the vicinity of the energy release point is suspect to be largely influenced by the particular characteristics of the experimental set-up entering into the primitive empiricism by which flow resistance and water entrainment are analytically simulated. In this context nodalisation concepts may also play an important role if different for the simulation of model and prototype. It is expected that these effects may increase the uncertainty margins of code predictions for the containment-related fluiddynamics well above the 15-20% assessed from the analyses of earlier BFC-tests /10/ for local dynamic pressurisation. The lack of geometric similarity between model and prototype containments and the impossibility to predict or influence the shape of a fracture of a recirculation line might aggrevate the problem. However, the application of advanced containment codes like COBRA-NC for well defined experimental conditions of a rupture compartment seems inevitable and promising to allow quantification of space-effects and influences associated to the heterogeneity of the two component-twophase-flow not amenable to lumped parameter simulation.
The development of maximum overall containment pressure is likely to be only slightly distorted by scaling due to an increased heat exchange with structures which may be conservatively neglected for design purpose code application. The assessment of long term containment experiments may deserve further studies concerning possible scaling related distortion if full understanding of experimental evidence should be warranted (e.g. in the field of hydrogen behaviour).

Nomenclature:

C	constant	-
F	flow area	m^2
G	massflow rate	kg/s
H	height of Control volume	m
h	specific enthalpy	kJ/kg
K	dimensionless group	-
L	node length	m
M	mass	kg
P	pressure	N/m^2
q	heat flux	W/m^2
s	scaling factor	-
t	time	s
V	node volume	m^3
W	speed	m/s
x,y,z,	coordinates of space	m
ρ	density	kg/m^3_4
ζ	resistance function	kg/m^4

Indices

D	steam phase
B	in motion
W	water phase
G	gas phase
L	air
sep in	separation
WG	entrained water
Z	node

References:

/1/ Mansfeld, G.: Zum instationären Druckaufbau in Volldrucksicherheitsbehältern wassergekühlter Kernreaktoren nach einem Kühlmittelverlustunfall, Dissertation TU München, Juli 1977
/2/ CONTEMPT 4/MOD 3, A Multicompartment Containment System Analysis Program, NUREG/GR-2558, December 1982
/3/ DDIFF-Code-Topical Report; Standard-Problem Subcompartment Analysis, CENPD-141 Combustion Engineering 1974
/4/ Stubbe, E.J; et. al. TRAP: Computer Codes for the Evaluation of Pressure Transients in Containments; Proc. ENS/ANS Int. Meeting Reactor Safety, Brussels 1978; Vol.III p. 2168
/5/ Die Containment Versuchsanlage (C- und D-Versuche), Battelle Bericht RS 50-21-1 (GERRSR-328), Oct. 1978
/6/ Wolf, L.; et. al. Overwiew of the HDR-Containment Tests, NUREG/CP-0048 (1983), Vol. 3 p. 258-324
/7/ Bingham, G.E. et. al. Simulated Design Basis Accident Tests of the Carolinas Virginia Tube Reactor (CVTR) Containment USAEC-Report IN-1325, Oct. 1969
/8/ Kanzleiter, T.; Modell-Containment Versuche, Abschlußbericht Battelle Bericht BF-RS-50-01, December 1980
/9/ Karwat, H., Bewertung der experimentellen und analytischen Untersuchungen zum Verhalten von Volldrucksicherheitsbehältern und Empfehlungen von Anschlußaktivitäten, GRS-A573, März 1981
/10/ Karwat, H., Experimental Verification of FRG Full-Pressure Containment Concepts, IAEA-CN-39/32 in "Current Nuclear Power Plant Safety Issues", Vol. III, Wien 1981
/11/ Nahavandi, A. N. et. al., Scaling Laws for Modeling Nuclear Reactor Systems, Nucl. Sci. Engng. 72 (1979), S. 75-83
/12/ Karwat, H., Analytical Simulations in the Field of Two-Phase Flow: A Promising Scaling Law for the Interpretation of Experiments; Nucl. Technology 46 (1979) p. 546-558.
/13/ Hellings, G., Mansfeld, G.; COFLOW - Ein Rechenmodell zur Ermittlung des instationären Druckaufbaus in Volldrucksicherheitsbehältern wassergekühlter Kernreaktoren (Programmbeschreibung), GRS-A-254, Dezember 1978.
/14/ Karwat, H., Skalierungseinflüsse bei der Übertragung von Ergebnissen experimenteller Untersuchungen zum Containment Verhalten, TU München, Interner Bericht, 1984.
/15/ Yano, T. et. al.; An experimental Study of Blowdown Thrust and Jet Forces by 6-inch Pipe under BWR LOCA, Thermal Hydraulics of Nuclear Reactors, Vol.II, Santa Barbara Jan. 1983 (ANS) p. 761-768.
/16/ Epstein, M. et. al.; One Dimensional Modeling of Two Phase Jet Expansion and Jet Impingement; Thermal Hydraulics of Nuclear Reactors Vol. II, Santa Barbara 1983 (ANS) p. 769-777.

SCALING ASPECTS OF SUBCOMPARTMENT ANALYSIS

K. Almenas* and Un-Chul Lee

University of Maryland, College Park, MD 20742

Traiforos, S. A.

Bechtel Power Corporation, Gaithersburg, MD.

ABSTRACT

Comparison of pressure differences measured during the HDR and Battele Frankfurt Containment tests have shown that the traditional energy density/volume scaling approach is inadequate. Additional factors are important such as absolute compartment size, relative complexity of compartment geometry, density and size of internal structures, average drop size of suspended water and extent of departure from equilibrium conditions. Relevant scaling methodology is reviewed and its applicability to subcompartment scaling is assessed. Several new dimensionless indexes characterizing compartment geometry flow channel geometry and departure from equilibrium conditions are defined.

INTRODUCTION

Several recent studies have demonstrated that the modeling of short term pressure transients between zones of a containment during a loss-of-coolant accident is inadequate [1,2]. This is true for experiment to model [2,3], and even for model to model [4] comparisons.

A successful calculation of pressure gradients within a network of compartments subjected to a two-phase blowdown fluid, requires the specification of flow resistances, evaluation of local fluid densities, consideration of energy transfer to structures and the determination of droplet to vapor relative velocities. Until recently experimental data has been limited and this basically two-phase flow problem has been analyzed using simplified, usually homogenous computational models. The broadening of the relevant data base by the addition of the HDR containment test results [2,5] has demonstrated the limitations of such models. The physical processes which

*Work performed under NRC Grant NRCG-04-84-004

determine the transfer of the air-steam-droplet mixture between compartments are complex. It is doubtful that integral experiments like the HDR test series can adequately resolve the various issues raised. For a quantitative resolution, carefully designed, separate effect tests are required. However, appropriate separate effect tests can not be designed before the scaling aspects of such facilities are fully understood.

DIFFERENCES BETWEEN PIPE AND COMPARTMENT HYDRAULICS

The design of scaled experimental facilities for thermal-hydraulic tests is an established sub-discipline. An extensive literature on various scaling aspects exist. Relevant recent information can be found in references [6 to 8]. Many of the approaches developed in the listed references can be adapted to scaling of subcompartment facilities. However, this can not be done uncritically.

The focus of interest for most of the reactor safety related thermal-hydraulic experiments to date have been the primary and secondary coolant systems. In order to emphasize this characteristic, the term "pipe hydraulics" is applied to this broad subject. It is appreciated, that this is not correct at all times. The reactor downcommer, head and the steam generator dome are not realy 'pipes'. Nevertheless, the primary and secondary systems flow geometries are dominated by pipes.

The point to note is that for primary and secondary system hydraulics this is, for the most part, applicable. For flow in and between compartments it is <u>not</u>. In fact, ideas and models developed for pipe flow and uncritically transferred to flow between compartments can under circumstances make understanding more difficult. It is thus imperative to draw a clear distinction between flow problems encountered in pipes on the one hand and compartments on the other.

The three main differences are:

(1) Pipe flow geometry is regular and well defined. Compartment flow geometry is highly irregular. Compartments are filled with structures, have blind corners and highly irregular shapes. In a practical sense there are definite limits beyond which compartment flow geometry can not be defined.

(2) The flow profile in a pipe is for the most part regular. Parameters as average velocity, average density average void fraction all have well defined and measurable physical meanings. None of this is true for compartment flow. In a compartment strong internal circulation flows can be present. Velocities can vary from nearly zero in blind corners to sonic velocities at the edge of an expanding blowdown plume. Not only the magnitude but also the direction of the fluid velocity is ill defined.

(3) In the primary system and parts of the secondary system the fluid is dense, either single phase liquid or dominated by the liquid phase. Two-phase flow regimes are then resonably well defined and relative vapor liquid velocities can be described with universal empirical relationships. In compartment flow the dominating fluid is vapor-air. The liquid phase can make up half the mass and inertia but will usually comprise less than 1% by volume. The relative liquid-vapor velocity then can not be defined without additional knowledge regarding droplet size and population distribution.

Additional differences can be listed. Thus for example, in pipe flow the cross sectional flow area, the frictional and heat-transfer surfaces all have a fixed analytical interrelationship. This is not true for compartment flow. In fact, for compartment flow it is an important to establish the nature of the heat-transfer surface (i.e. concrete, thin or thick metal) as the total available surface area [10]. Linear dimensions characterizing a compartment can be related to the volume of the compartment, to the available surface area, to the flow channels within it, the opening leading out of it or to the diameter of structures. In scaling these distinctions must be kept clearly in mind, and a length to diameter relationship established for pipe hydraulics will usually have little relevance when applied in an uncritical manner to compartment flow.

SCALING APPROACHES

Scaling of experimental facilities for containment tests is a new field and it is premature to propose a definitive classification system. Nevertheless, in order to gain an overview of the subject, an initial categorization is helpful. The following categories are recognized in this survey:

1. Pipe hydraulics scaling. This is the classical scaling approach used for designing primary and secondary system scaled facilities. The distinction between pipe and compartment hydraulics are described in the previous chapter.

2. Code based scaling. The general and special purpose thermal-hydraulic codes employed in nuclear reactor system safety analysis calculations presently represent more then just indispensable computational tools. They are also a compendium of information assembled by groups of interdisciplinary specialists. As such they can become objects of investigation in their own right. In a recent study Karwat [11] has deduced subcompartment scaling laws based on the COFLOW [12] code..

3. Phenomenoglogical scaling. The two previous categories represent integral scaling approaches. It is probable that for separate effect tests such methods can provide only general guidelines. Separate effects tests are designed to measure specific parameters or the influence of certain physical mechanism. In that case scaling based on the mechanism in question becomes important.

PIPE HYDRAULICS SCALING

Reviews of pipe hydraulic scaling are presented in refs 8 and 9. The methodology developed has direct applicability. Some of the derived results can also be utilized if the parameters are interpreted appropriately.

The method is based on the definition of dimensionless ratios for all relevant parameters. For example:

$$L^t = \frac{L_M}{L_P} \quad ; \quad P^t = \frac{P_M}{P_P} \quad ; \quad \text{etc.} \tag{1}$$

Assume that the basic balance equations refer to the scaled facility. That is, they are expressed in terms of Lm, Pm, tm, etc. These variables are substituted by the product obtained from the ratios given by 1. The equations are then rearranged to yield the original relationships, but in terms of prototype parameters. This creates a set of dimensionless groups which define the basic scaling requirements.

For compartment hydraulics application it is preferable to arrange the dimensionless groups of the momentum balance in a different manner then quoted in the listed references.

$$\rho_M \frac{\partial u_M}{\partial t_M} + \rho_M u_M \frac{\partial u_M}{\partial x_M} = - \frac{\partial P_M}{\partial x_M} - \xi_M \rho_M u_M^2 - g \rho_M \tag{2}$$

After substitution of $U_M = U^t u_P$; $t_M = t^t t_P$ etc. we have:

$$\left(\frac{\rho^t u^t}{t^t}\right) \rho_P \frac{\partial u_P}{\partial t_P} + \left(\frac{\rho^t u^t}{x^t}\right) \rho_P u_P \frac{\partial u_P}{\partial x_P} = - \left(\frac{P^t}{x^t}\right) \frac{\partial P_P}{\partial x_P} - \left(\xi^t \rho^t u^{t2}\right) \xi_P \rho_P u_P^2 - \left(g \rho^t\right) \rho_P \tag{3}$$

The 5 bracketed coefficeints of eq 3 can be reduced to a set of 4 by appropriate division. In pipe thermal hydraulics the fluid usually has a high density and inertial effects (term 1) are important. Eq 3 is then multiplied by $(t^t/\rho^t u^t)$ setting the coefficent of the first term to 1. The remaining coefficients then express the relationship which must be preserved to assure identical inertial effects. One requirement is that in order to preserve identical model and prototype pressures, both length and velocity must be conserved. This can be done in a limited way for pipe thermal hydraulics and leads to 'long thin' scaling geometries exemplified by the semiscale facility [13]. For compartment scaling such an approach is impractical. Since the fluids have a lower density inertial effects are not as important. However, pressure is of primary importance and the amount of its distortion must be known. It is preferable then to multiply eq 3 by (x^t/P^t). This leads to the following four dimensionless groups:

$$\left(\frac{\rho u L}{t P}\right) \rho_P \frac{\partial u_P}{\partial t_P} + \left(\frac{\rho u^2}{P}\right) \rho_P u_P \frac{\partial u_P}{\partial x_P} = - \frac{\partial P_P}{\partial x_P} - \left(\frac{\xi \rho u^2}{P}\right) \xi_P \rho_P u_P^2 - \left(\frac{g \rho L}{P}\right) \rho_P \tag{4}$$

Where the superscript is dropped and x is replaced by its integral value. All of the dimensionless groups including two sets arising from the momentum balance are shown in table I. On the right hand side of the table the conditions are listed which must be met if state functions are to be preserved undistorted between the model and prototype. The linear scaling factor is defined as:

$$\lambda = L^{*} = \left(\frac{L_M}{L_P}\right) = \left(\frac{V_M}{V_P}\right)^{1/3} \qquad (5)$$

λ is thus a dimension characterizing the volume. Preservation of time and state leads to the requirement (term 2) that power input be scaled volumetrically; that is $\dot{P}_M = \lambda^3$. Note that the average flow velocity in the model will be reduced by a factor of λ (term 1). Since fluid state is preserved, temperatures and surface fluxes will also be identical. As shown in term 4, this leads to the distortion of surface energy transfer terms by $1/\lambda$. Note that for this scaling scheme it is impossible to keep all events synchronous. Interial effects will occur earlier by a factor of λ^{-2}.

A final note. The presented methodology provides a useful framework. However, in case of compartment thermo-hydraulics it is not to be taken too literaly. As noted previously, the L, U, ρ parameters which for pipe hydraulics have a well defined meaning are not well defined in compartment flow and in fact are subject to multiple interpretations..

PHENOMENOLOGICAL SCALING

The last scaling category is by its very nature the least systematic. A whole range of physical phenomena such as deentrainment and entrainment of drops, acceleration of a two phase mixture contribute to an integral parameter like the compartment pressure. Seperate effect tests will likely focus upon the elucidation of such phenomena. They will then have to concern themselves with specifically targeted scaling problems.

In this section an initial survey of potential phenomenological scaling approaches is made. The list will probably expand as additional phenomena are considered and also possibly, it will be pared down as redundant and not very useful criteria are dropped. At this point no attempt at ranking is made.

As for the previous section, scaling criteria are best represented in terms of dimensionless groupings. Table II lists the dimensionless numbers as well as the scaling ratios for isochronic, same fluid at same state scaling. They will be surveyed by considering their origin and purpose.

NCI , A_F and A_T

The first group of 3 are taken from ref 2. The numbers were defined for an analysis of Battele-Frankfurt and HDR subcompartment pressure difference data. It was shown in [2[that in terms of traditional comparative indexes (i.e. energy addition rate per compartment volume or per flow opening

area) the two sets of experiments were quite comparable. Matter of fact, the Battele-Frankfurt experimental parameter range usually bracketed the corresponding range of the HDR experiments. Nevertheless, the results of the two test series did not overlap and formed two quite distinct groups of data. It was then necessary to devise indexes which would quantify the geometric differences of the two facilities. The three indexes are:

The Normalized Compartment Complexity Index-NCI

$$NCI = \frac{A_{ST}}{6 V^{2/3}}$$

defines the ratio of all structural surface areas (including walls and internal equipment) to the surface area of an empty cube having the same volume as the compartment in question, NCI is thus equal to one for an empty cube and grows as the compartment geometry becomes more complex or as internal equipment is added.

The Total Flow Area Ratio - FT

$$FT = \frac{\sum A_{F,d}}{V^{2/3}}$$

where the numerator represents a summation over the junctions of the compartment. FT is thus the ratio of the total flow area to the cross sectional area of an equivalent volume cube.

The Largest Flow Area Ratio - FL

$$FL = \frac{A_{F,MAX}}{V^{2/3}}$$

To maintain equivalency between model and prototye, a scaling scheme which modifies compartment linear distances by λ, should modify both structural diameter and flow opening diameters D_F by λ as well. However, other scaling considerations conflict with this requirement. Thus in order to assume equal flow opening vapor velocities D_F has to be scaled by a $\lambda^{3/2}$ factor. For downscaled experiments this would lead to a distortion of F_T and F_L by a factor of λ. This means that for the scaled facility the influence of the opening on the flow field within the compartment would be less. The potential intensity and complexity of internal flow fields would be reduced.

We_{ST} The Weber number is a classical index representing a ratio of inertial and surface tension forces. Traditionally it is used to correlate drop and bubble properties. In refs [14] and [15[the number has been redefined by equating the linear dimension to the diameter of internal structures. Most structures within a containment consist of pipes, reinforcing bars, stairs railings and other elongated shapes which can be reasonably well characterized by a typical diameter D_{ST} and a length L proportional to the characteristic linear length of a compartment. The structural We number then becomes proportional to the inertial and surface tension force subjecting

a liquid flow deposited on the structure. In the noted references it is used to correlate effective deentrainment rate within a compartment. If it is desired to maintain this index unchanged structural diameters would have to be scaled by a factor of λ^2 .

FR_L

In ref 8 this index is used to correlate entrainment in pipes or vessels for which a small break occurs above a liquid level. The linear dimension L_{FL} is then the distance from the center to the opening to the liquid surface. For containment scaling the index is likely to be relevant only in a negative sense. That is, under actual containment conditions entrainment from liquid pooled at the floor of the containment is likely to be negligible. That is FR_L will be quite small. However, if care is not taken, for downscaled facilities will be decreased sufficiently that FR_L increases and entrainment from this mechanism becomes important.

D_R and S_L

The next two dimensionless groups, called the Drag Coefficient and Slip ratio numbers are derived from the droplet momentum balance equation. They determine whether the suspended liquid will be accelerated to the same velocity during flow between compartments.

For circular openings the spatial derivative of the drop velocity can be approximated by:

$$\frac{dU_\delta}{dr} = \frac{0.75\, C_D\, \rho_g}{\delta\, \rho_\delta}\left(\frac{U_{VF}}{8f^2 U_\delta} - 1\right)\left|\frac{U_{VF}}{8f^2} - U_\delta\right| \qquad (6)$$

Where the fluid is asumed to be incompressible, f is a dimensionless distance along a radius vector.

Eq 6 can be used to establish the flow geometry and drop size relationships which will assure identical drop acceleration rates. Utilizing the techniques summarized in refs 7 and 8, the dimensionless groups listed in table II are obtained. The D_R number is thus seen to represent a ratio of the opening diameter and the effective (drag modified) droplet diameter. If droplet size could be controlled, potentially this number could be kept unchanged for different opening diameters. Unfortunately this is not feasible.. The D_R number then implies that drop acceleration rates can not be reproduced for different opening sizes.

Me_δ , Me_r and T_e

The last group of numbers serve as indexes measuring departure from equilibrium. They are defined by first evaluating the time required to reach equilibrium at a constant approach rate. For example, in case of mechanical equilibrium:

$$\frac{\Delta U}{d(\Delta U)/dt} = \Delta t_{Me} \qquad (7)$$

Where for dispersed flow $\Delta U = (U_g - U_\delta)$. Note that

both of these time constants assume that the rate of approach to equilibrium remains constant. This is not the case, of course. Both Δu and ΔT represent driving potentials thus the actual rate decreases as equilibrium is approached. The defined Δt values thus represent times which are proportional to actual equilibration time intervals. The dimensionless numbers shown in table II are obtained by dividing eq's 7 by a characteristic transit time: $\Delta t_{TR} = \frac{L_{re}}{u}$

The nonequilibrium indexes depend strongly on drop diameter. This dependence is also reflected in the circumstance that based on the relative drop-to-vapor flow conditions two mechanical nonequilibrium indexes are required. Between laminar and fully developed flow the drag coefficient changes not only in magnitude, but assumes a different functional dependence.

All of the nonequilibrium indexes show a scale dependence. Thus for facilities which preserve pressure differences the maximum flow opening velocities must be equal for model and prototype. This implies that departure from equilibrium will increase as the facility becomes smaller. For Te and Me_5 the distortion will be equal to λ, for Me_7 it will be larger and approach λ^2.

NOMENCLATURE

A	-Area	Nu	Nusselt Number
Cd	-drag coefficient	P	Pressure
D	-diameter	P	Power rate
$\mathcal{D}$	-drop diameter	q	heat flux
f	-friction factor	Q	volumetric en. gen.
g	-accel. of grav.	t	time
h	-enthalpy	u	velocity
k	-conductivity	v	volume
K	-head loss coeff	w	mass flow rate
L	-length		
α	-void fraction	μ	-viscosity (kg/ms)
Δ	-main difference	ξ	-friction and head loss group $\left(\frac{f}{D_H} + \frac{K}{L}\right)$

Subscripts

C	compartment	M	model
D	drop	P	Prototype
F	flow opening	Pl	pool
g	gas - vapor + air	ST	structure
h	hydraulic	T	Total
l	liquid	TR	transit
		w	wall

REFERENCES

1. Karwat, H., "Problems of Scaling and Extrapolation of Experimental Results in the Area of Fluiddynamics and Associated Heat Transfer Related to Reactor Safety", Univ. of munich (Nov. 1983).

2. Almenas, K., "Comparison of Experimental and Calculated Pressure Differences in the HDR Containment" PHDR Arbeitsbericht Nr. 3/388/83 (Aug. 1983).

3. Wolf, L., Valencia,L. and Kanzleiter, T. "Overview of the HDR-Containment Tests", 11th Reactor Safety Research Meeting, NUREG/CP.0048 (Oct. 1984).

4. Burkett, M.W. et al. "Comparison of BEACON and COMPARE Reactor Cavity Subcompartment Analysis" NUREG/CR-3305 (1984).

5. "Statusbericht des Projektes HDR-Sicheheitsprogram" Nr 3.388/83 (Aug. 1983).

6. Larson, T.K., Anderson, J. L. and D.J. Shimeck, "Scaling Criteria and an Assessment of Semiscale MOD-3 Scaling for Small Break LOCA", EGG M-21082 (Sept. 1982).

7. Ishii, M. and Kataoka, I. "Scaling Criteria for LWR's under Single Phase and Two-phase Natural Circulation" Joint NRC/ANS Meeting. Bethesda, MD. (Sept. 1982).

8. Zuber, N. "Problems in Modeling of Small Break LOCA" NUREG 0724 (Oct. 1980).

9. Nahavandi, A.N., et.al."Scaling Laws for Modeling Nuclear Reactor Systems," Nucl. Sc. and Eng. Vol 72 (1979).

10. Almenas, K., "Comparison of Measured and Calculated Heat Transfer Coefficients for the HDR Containment Experiments", PHDR-Arbeitsbericht Nr. 3.364/83 (March 1983).

11. Karwat, H. "Skalierungseinflüsse bei der Ubertragung von Ergebnissen aus experimentellen Untersuchungen zum Containmentverhalten" (To be published).

12. Hellings, G. and Mansfeld, G. "COFLOW-Ein Rechenmodell zur Ermittlung des instationären Druckaufbaus" GRS-A-254.(Dec. 1978).

13. Patton, M.L. "Semiscale Mod-3 Test Program and System Description" TREE-NUREG-1335 (July 1978).

14. Dallman, J.C. and Kirchner, W.L., "De-Entrainment onVertical Elements in Air Droplet Cross Flow", ASME Paper 80-WA/HT46.

15. Traiforos, S.A. and Almenas, K., "Liquid Suspension in Subcompartment Analysis: Adv. in Cont. Design and Analysis ASME/ANS Conf. (Portland 1982).

Table I

Pipe Hydraulics Scaling Methodology

Bal eq.	Description	Dimensionless Group		State Conserving Scaling	
				N_M/N_P	Scaling condition
Mass	1) Mass Flux term. (Also energy)	$\left(\frac{ut}{L}\right)$		1.	$u_M = \lambda$
En.	2) Volumetric en. source term	$\left(\frac{t\dot{Q}}{\rho h}\right)$		1.	$\dot{Q}_M = \dot{Q}_P$ $\dot{P}_M = \lambda^3$
	3) Pressure work term	$\left(\frac{P\rho}{h}\right)$		1.	$P_M = P_P$ $\rho_M = \rho_P$
	4) Energy transfer term	$\left(\frac{t\dot{q}}{D_H \rho h}\right)$		$1/\lambda$	
Mom.	5) Inertial term	1. *	$\left(\frac{\rho u L}{t P}\right)^{**}$	λ^2	$t = \frac{1}{\lambda^2}$ inertial effects
	6) Pressure gradient	$\left(\frac{Pt}{\rho L u}\right)$	1.	1.	
	7) Momentum dissipation term	$\left(\frac{f}{D_H} + \frac{K}{L}\right)(ut)$	$\left(\frac{f}{D_H} + \frac{K}{L}\right)\left(\frac{\rho u^2 L}{P}\right)$	1.	$\left(\frac{f}{D_H} + \frac{K}{L}\right) = \frac{1}{\lambda}$
	8) Gravitational term	$\left(\frac{gt}{u}\right)$	$\left(\frac{g\rho L}{P}\right)$	λ	

* Inertial preserving scaling

** Pressure Preserving scaling

Table II

Dimensionless Scaling Groups:

Phenomenological Scaling

	Description	Dimensionless Group	(N_M/N_P)
NCI	Normalized Compartment Complexity Index	$\frac{A_{ST}}{6\,V^{2/3}}$	$1.$ to $>\lambda$
F_T	Total flow area ratio	$\frac{\sum_j A_{F,j}}{V^{2/3}}$	$1.$ to $>\lambda$
F_L	Largest flow area ratio	$\frac{A_{F,MAX}}{V^{2/3}}$	$1.$ to $>\lambda$
We_{ST}	Structural Weber Number	$\frac{u^2 D_{ST} \rho_g}{\sigma}$	$1.$ to λ
Fr	Overflow Froude number	$\frac{u_{VF}}{\sqrt{g L_{TL}}}\sqrt{\frac{\rho_g}{\Delta\rho}}$	$1/\lambda^{1/2}$
D_R	Drag Coefficient number	$\frac{C_D f D_F}{\mathcal{D}}\left(\frac{\rho_g}{\rho_{\mathcal{D}}}\right)$	$\sim \lambda^{3/2}$
S_L	Slip ratio number	$\frac{\pi u_{VF}}{4 f^2 u_D}$	$> 1.$
Re_S	Mech. eq. number Stokes flow	$\frac{\rho_e \mathcal{D}^2 u_g}{18\,\mu\, L_{TR}}$	$1.$ to $1/\lambda$
Re_T	Mech. eq. number Turb. flow	$\frac{3.3\,\rho_e \mathcal{D}\, u_g}{\rho_g \cdot \Delta u\, L_{TR}}$	$>1.$ to $>\frac{1}{\lambda}$
Te	Thermal eq. number	$\frac{c_p \mathcal{D}^2 \rho_e u_g}{k\, Nu\, L_{TR}}$	$>1.$ to $>\frac{1}{\lambda}$

TESTING AND ANALYSIS OF CONTAINMENT MODELS

Thomas E. Blejwas

Sandia National Laboratories
Albuquerque, New Mexico 87185, U.S.A.

ABSTRACT

To better understand the structural and leakage behavior of U.S. containments during severe accidents, Sandia National Laboratories is testing and analyzing scale models of containment structures. The quasi-static pneumatic pressurization of models of steel containments of 1/32 scale has been completed and testing of a 1/8 scale steel model is now beginning (September 1984). By comparing results of analyses (conducted by Sandia and others) with the experimental data, methods for analyzing the structural behavior of containments are being qualified. Leakage data is being obtained during tests of the larger models that have operable equipment hatches. The leakage will be correlated with measured and predicted distortions of the sealing surfaces.

INTRODUCTION

Sandia National Laboratories is conducting the Containment Safety Margins Program for the U. S. Nuclear Regulatory Commission. The objective of the program is to qualify methods for predicting the behavior of containment structures during severe (beyond design basis) accidents. The program is one of three programs at Sandia in the area of containment integrity during severe accidents. Whereas, individual penetrations and seals will be tested in the other programs, models of containment structures with a variety of penetrations and other details are being tested in the Containment Safety Margins Program. Four models of about 1/32 the size of hybrid steel containments have been tested; testing of a 1/8 size steel model is beginning; and a 1/6 size concrete model has been conceptually designed and is being acquired. The experimental data from the model tests are being compared with analyses performed at Sandia and elsewhere; the capabilities of the methods for predicting structural response are being evaluated. Data for the leakage through equipment hatch representations on the larger model tests will be correlated with measured and analytically predicted distortions of the sealing surfaces. The data will be combined with results from the other programs on penetration behavior during severe accident conditions. Also, the model tests and analyses will be used to determine important boundary conditions for testing of full-size penetrations (e.g. personnel locks) in one of the companion programs.

Descriptions of the first three tests with small steel containment models have been previously reported [1, 2]. The results from the test and analysis of the fourth small model (a shell with representations of major penetrations) were more recently presented at a workshop [3]. Analyses and plans for testing the 1/8th size steel model and conceptual plans for a 1/6th size reinforced concrete model were also presented [4, 5, 6]. In this paper the small steel model results will be reviewed and conclusions drawn; updated analyses and recently completed preparations for testing the 1/8th size steel model will be described; the conceptual design for the reinforced concrete model will be reviewed; and progress on the concrete model project will be reported.

*Work supported by the U. S. Nuclear Regulatory Commission, Office of Nuclear Regulatory Research, and performed at Sandia National Laboratories which is operated for the U. S. Department of Energy under Contract Number DE-AC04-76DP00789.

SMALL STEEL MODELS

Review of Tests and Analyses

Four steel containment models about 1/32 the size of U. S. hybrid steel containments (often used for PWR ice-condenser or BWR Mark III suppression systems) were tested between December 1982 and December 1983. The configurations for the models are shown in Figure 1. The models were pressurized with nitrogen gas in a quasi-static manner until a rupture or significant leakage occurred. The high temperatures of severe accidents were not represented in the tests, i.e., testing was at near ambient temperature.

The first model, a clean shell configuration, was tested to check out the testing hardware and software. Complete rupture occurred when pressure was being raised from 0.90 MPa (130 psig) to 0.93 MPa (135 psig). However, because of time constraints during this check-out test, the model did not fully stabilize at the lower pressures; failure at a lower pressure may have occurred if full stabilization were allowed. Maximum circumferential membrane strains were about 20% at rupture. A second clean shell configuration that was fully instrumented was tested. This model started leaking through a crack near an improperly repaired weld at 0.76 MPa (110 psig). The maximum circumferential strain at the onset of leakage was about 7%. Comparisons with analytical predictions [1] show good agreement except that the pressure for gross membrane yielding was over estimated by about 10 percent. (A resolution of the difference may not be available until more testing is completed.) The welding and repair techniques used for the model were not representative of procedures used in actual containments and no inference of cracking and leaking of actual containments can be made from the test results.

A single ring-reinforced shell model was tested twice. During the first pressurization, the model developed leaks at 0.83 MPa (120 psig) when the maximum membrane strain was about 3%. Again, the leaks were due to improper weld repairs in the very thin (1.2 mm) model material. The model was repaired and retested. However, because the model material had yielded and was allowed to stand for about three weeks between tests, the material properties were changed by strain aging . (Strain aging causes an apparent raising of the yield plateau for some steels when they are yielded and allowed to stand). During the second testing, significant reyielding of the model was not observed until just before complete rupture at 0.97 MPa (140 psig). Comparisons of experimental data and analytical predictions for the first pressurization [1, 3] show good correlation. However, the analytical model did not include the relatively large amount of brazing material used to attach the stiffeners, because the brazes had through thickness radial cracks in numerous locations. If full or partial credit had been given to the braze material, the pressure at which gross membrane yielding occurred would have been slightly overpredicted. The analysis and experiment with the ring model both show a very smooth behavior after yielding at the wall and ring, which occur at about the same pressure level.

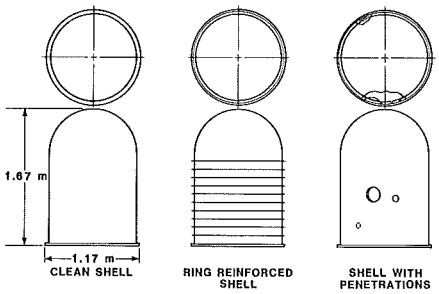

Figure 1. 1/32 Scale Steel Models

The testing of a single model with penetrations completed the experiments with small models. Until recently, the results of this test have received limited dissemination [3]. However, the results are being presented at a specialty conference [7] at the same time as this meeting. The penetration model included simple representations of an equipment hatch and two personnel airlocks. The penetrations were of fully welded construction, that is, they were not operable. The shell was not thickened around the penetrations, i.e., the ASME area-replacement rule was not used. During initial stages of testing, the cover on the equipment hatch that was concave inward buckled in a snap-through manner when pressure in the model was raised from 0.28 MPa (40 psig) to 0.34 MPa (50 psig). In a finite element analysis, buckling of the hatch cover was calculated to occur at 0.52 MPa (76 psig).

After the buckling of the cover plate, the model was depressurized and quickly modified with the addition of a thick flat plate to the outside of the sleeve of the equipment-hatch representation. The model was then slowly repressurized in steps to 0.83 MPa (120 psig). Shortly after the model was photographed (Figure 2) and about 1/2 hour after pressure was raised to 0.83 MPa, the model failed completely. The circumferential membrane strain in areas away from penetrations was about 15% at rupture. Based upon the location of fragments and observations during rupture, failure of the model initiated on the side of the model with two penetrations. One of the many fracture surfaces passed between the two penetrations. Therefore, the failure of the model may have initiated near the penetrations. However, the model was so highly strained in free-field areas, that a small flaw or slightly thinner area may also have been the location of failure initiation.

A comparison of the experimental and calculated (pre-experiment) strains for a location about three inches from the equipment hatch sleeve (three o'clock position) is presented in Figure 3. The major and minor principal strains from two points in an analysis are plotted with sets of principal major and minor strains from two strain gage rosettes. The analytical results were obtained using the MARC finite element code with a mesh representing a 45 degree segment of the model with the modified equipment hatch. More details of the analysis will be available in references [3 and 7]. A second comparison of experimental and analytical results for a location just below the six o'clock position of the equipment hatch sleeve is presented in Figure 4. Strains from a single rosette and the two closest integration points in the finite element model are shown. The two sets of comparisons are representative of the range of differences between the experiment and analysis. The onset of yielding was generally overpredicted for all locations, although pressures corresponding to higher strains were both under and over estimated depending upon the location. In areas of very high strain gradients, such as near penetrations, the finite size of the strain gages (generally 0.32 to 0.64 cm) makes direct comparisons unreliable.

Conclusions from Small Steel Model Experiments

The comparisons between experimental results and analytical predictions has been generally good for the small model experiments. However, several areas require further investigation. Explanations for the general overprediction of the pressure at which yielding occurs are being investigated by Sandia. The testing of the 1/8th size model will provide additional data on yielding under multi-axial loading. Comparisons of analytical predictions and experimental data in some areas, particularly those with high strain gradients, are not always satisfactory. Resolution of differences will await the testing of the large model. The large steel model will be heavily instrumented in selected areas of high strain gradients and the larger model makes gage size less critical. Sandia has also obtained analytical predictions from outside organizations using codes other than MARC. Comparisons of all the analyses with the experimental data are planned.

Based upon the experiment with the ring reinforced model and related analyses, the smearing of the effect of the stiffeners is a reasonable analytical procedure. Prior to the testing of the ring reinforced model, analyses with finite strain and geometric nonlinear

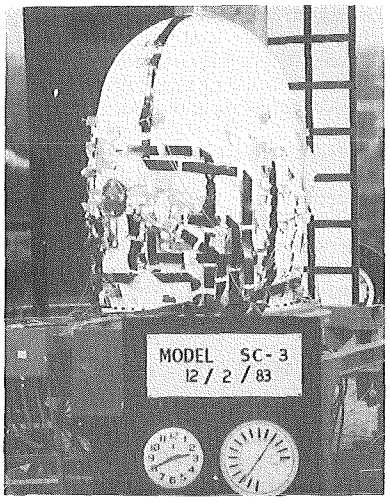

Figure 2. Penetration Model at 0.83 MPa (120 psig)

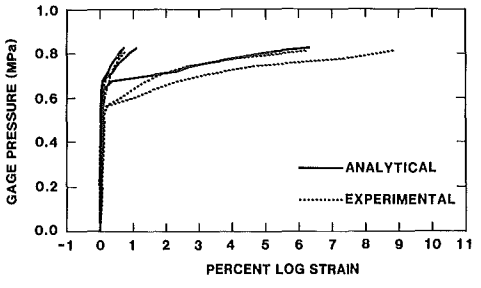

Figure 3. First Comparison of Strains Near Equipment Hatch

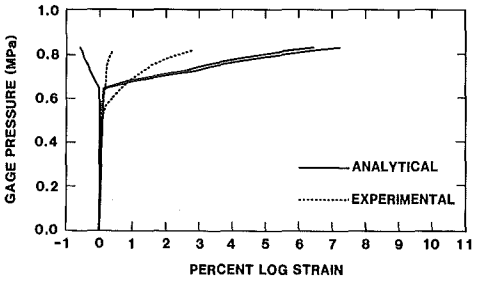

Figure 4. Second Comparison of Strains Near Equipment Hatch

capabilities indicated that the rings would yield at pressures close to those for which the cylinder wall yielded and that the rings and wall would move outward with increased pressure in a smooth manner (with little noticeable bending). The qualitative behavior of the model was as predicted. The behavior of ring stiffeners will be further studied on the large steel model that has relatively thinner and wider stiffeners.

Penetrations do not necessarily cause early failures of containment shells. In the testing of the model with penetrations, strains in the free field of the cylinder wall of about 15% were reached before failure. By comparison, the first clean shell model ruptured when maximum circumferential strains were only somewhat higher (20%). (Both levels can be considered very high strains; the presence of a small flaw may lead to rupture at such levels.) Although stress concentrations around penetrations are very high during elastic response, a general smoothing of strains was observed both experimentally and analytically as plastic flow occurs.

LARGE STEEL MODEL

Description of the Model

A large steel model, about 1/8th the size of typical U. S. hybrid steel containments, was designed and fabricated for Sandia by Chicago Bridge and Iron Co. Dimensions and features of the model are shown in Figure 5. The shell of the upper structure (shown in white in Figure 6) has a design pressure of 0.28 MPa (40 psig) and was fabricated from A516 steel, a material that is used in many steel containments and for liners in concrete containments. The bottom torospherical head serves as a test fixture and is not representative of actual containments.

Instrumentation

The large steel model has been instrumented for measuring structural and leakage behavior at pressures several times the design pressure. The structural instrumentation includes over 700 high elongation strain gages (capable of measuring strains of up to 20%), over 40 displacement transducers and nearly 40 thermocouples. Ten resistance temperature detectors and a high accuracy pressure transducer will record the gas state inside the model for leak rate estimates. An acoustic emission system will be used to locate the sources of any leakage.

The distortion of penetrations are of particular interest because of the possible effect upon leakage. Because preliminary analyses have indicated that leakage due to the distortion of the sealing surfaces of the equipment hatch is probable, the hatches are heavily instrumented. In Figure 7, the open hatch is shown with numerous strain gages on the surrounding shell, the sleeve and the cover. The photo was taken before the cover was closed and displacement transducers were mounted to measure relative motion of the sealing surfaces. A single "O" ring was placed in a groove in the sealing surface prior to closure.

Areas around other penetrations, such as the non-operable personnel lock representation shown in Figure 8, have been heavily instrumented with strain gages. Information on distortion of penetrations that are operable in actual containments will be used to plan future tests of actual full size penetrations, which are to be conducted in a companion program.

The area around a constrained pipe penetration has been instrumented with both strain gages and displacement transducers. The displacement transducers, which are mounted on a free standing interior structure that doesn't move during pressurization, measure the total movement of a point on the shell. The constraint on the pipe penetrations is intended to bound the restraint on pipes in actual containments. (Many pipes through containment walls are limited in their outward movement by various types of pipe supports and restraints).

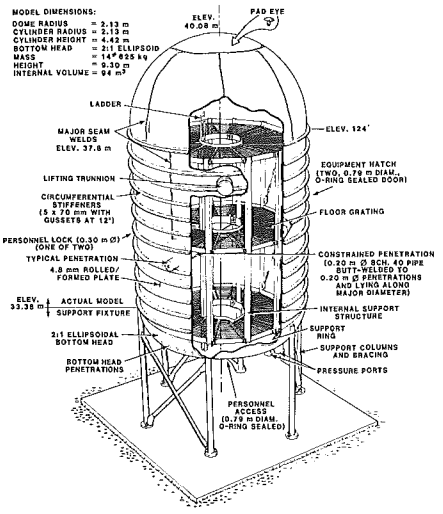

Figure 5. Large Steel Model

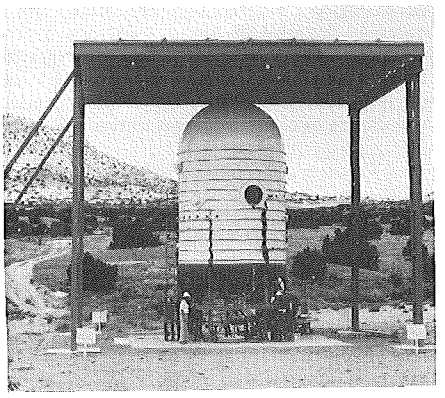

Figure 6. Large Steel Model with Open Equipment Hatch

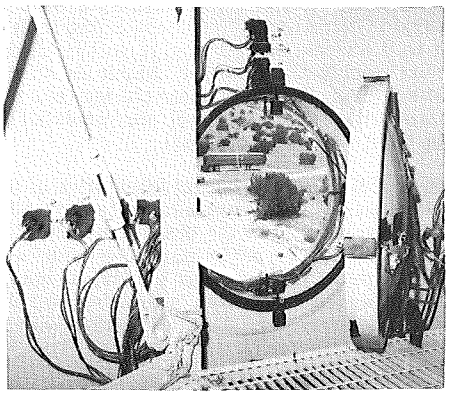

Figure 7. Equipment Hatch with Installed Strain Gages

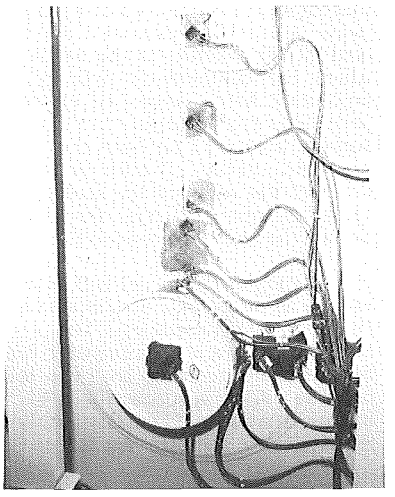

Figure 8. Strain Gages around Personnel Lock Representation

The steel model will be pressurized in slowly applied steps and data will be taken at each step via a computer controlled data acquisition system. Photogrammetric data from cameras located at three locations around the model will be used to determine global displacements. In addition, a coordinate determination system, which uses data from three theodolites in bunkers about 80 meters from the model, will be used to measure displacements of specific targets placed on the outside of the model. One of the theodolite bunkers is shown in the left side of Figure 9.

Test Plans and Expected Results

The model will be pressurized with nitrogen gas from a computer operated controller, shown in Figure 9. Temperature in the model will be held at slightly above ambient. If the model begins to leak, the pressure controller can maintain pressure while data is recorded and can increase pressure as commanded. Testing will be halted if the leakage due to local tearing or distortions in sealing surfaces exceeds equipment capabilities (the equivalent of at least 200 percent per day at 1.4 MPa or 200 psig). If the maximum free-field membrane strains in the model are less than about six percent when severe leakage occurs, the model may be modified to allow further pressurization. However, present plans do not include pressurizing the model to a global rupture. An actual U. S. steel containment is surrounded by a concrete shield wall that would alter the response to pressure when the radial displacements of the shell are about five to six percent of the cylindrical radius. The model will be pressurized to at least a comparable level, if possible.

Preliminary analyses of the model [3, 7] indicate that the containment shell would have a global pressure capability of about 1.7 MPa (250 psig). Local strains near the thickened sections around penetrations are predicted to exceed the maximum strains achieved in uniaxial test specimens (about 20%) at about 1.55 MPa (225 psig). Analyses of the equipment hatch area of the model have been recently updated because of inaccuracies in those previously reported [3, 7]. The more recent analysis also includes a more accurate representation of the shell stiffeners. The updated results are qualitatively similar to the earlier ones. Specifically, at a pressure level near those for which the containment cylinder yields globally (about 1.3 MPa) the sleeve of the equipment hatch begins to distort significantly, that is, the sleeve begins to become noticeably oval in shape. In Figure 10 the change in diameter of the sleeve at the sealing surface is plotted for both the meridional (3 to 9 o'clock) and vertical (6 to 12 o'clock) positions. Above 1.3 MPa the diameter change quickly approaches a magnitude on the order of the width of the sealing surface (about 3 cm). If the diameter change does not cause excessive leakage, the local strains (primarily due to bending) are predicted to exceed the ultimate uniaxial strain of the material at 1.40 MPa (200 psig).

Testing of the model will begin in September 1984. In a manner representative of the testing of actual U. S. containments, the model will first be pressurized to 0.32 MPa (115% of design pressure). The pressure will then be reduced to the design pressure, 0.28 MPa (40 psig), and an integrated leak rate test (ILRT) will be performed. The model will be tested and repaired until the leakage is less than 0.1 percent mass per day at design pressure. After a successful ILRT, the model will be depressurized and data from all the instrumentation will be thoroughly checked. If necessary, low pressure testing will be repeated until the data acquisition system performs satisfactorily.

Testing at pressures significantly above design pressure will be conducted in steps of 14 to 140 kPa (2 to 20 psi). Smaller steps will be taken as predicted global yielding is approached and while the model responds plastically. As discussed previously, if leakage occurs before sufficient structural response has been obtained, the model may be repaired and retested. The entire test program will require at least one to two months.

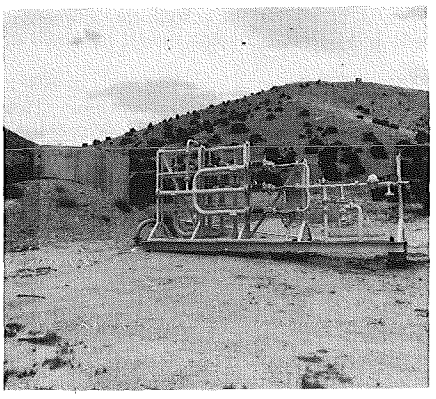

Figure 9. Theodolite Bunker and Pressure Controller

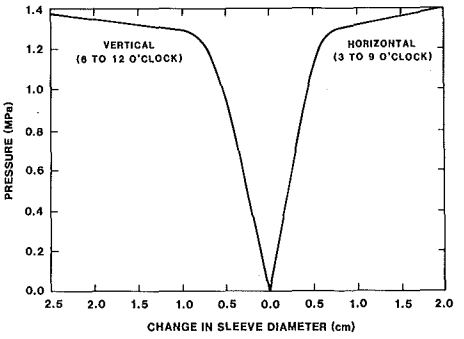

Figure 10. Deformation of Equipment Hatch Sleeve at the Sealing Surface

REINFORCED CONCRETE MODEL

Following the testing of the large steel model, the model will be removed and a model of a reinforced concrete (R/C) containment will be constructed at the same site. The model will be approximately 1/6th the size of typical U. S. R/C containments. A drawing of the planned model is shown in Figure 11.

The conceptual design of the R/C model has been completed and requests for proposals from prospective contractors have been placed. By the time of this conference, the proposals will have been received by Sandia and review will begin. After the contract is awarded, a series of small tests will be performed to ensure that a high quality model can be constructed and that the behavior of certain key components, e.g., liner-stud-concrete anchorage, are representative of actual containments. Construction of the model is expected to begin in 1985 and testing will occur in 1986. However, a reliable schedule will not be available until input from contractors is received.

The concrete model will have the following features:

1. 1/6 scale
2. #3 rebar as major reinforcement
3. 1.6 mm (1/16 inch) thick steel liner with stud attachments
4. Two operating equipment hatches with seals
5. Two personnel lock representations
6. Restrained pipe penetrations
7. Other pipe penetrations
8. Thickened liner sections around penetrations
9. A "flat" basemat
10. A hemispherical dome
11. Diagonal seismic rebar that is scaled from actual containments
12. A design pressure of 0.32 MPa (46 psig)

Details of reinforcement are specified to be typical of that in actual containments. A possible reinforcing plan for the cylindrical wall and basemat of the model is shown in Figure 12.

The equipment hatches in the model will receive particular attention. Two equipment hatch penetrations and three covers are planned for the model. A pressure unseating cover will be used on the exterior of one of the penetrations until leakage becomes excessive. The cover will then be replaced by a pressure seating cover on the model interior.

LONG RANGE PLANS

The testing planned through the end of 1986 is for quasi-static pressurization of the large steel and reinforced concrete containment models. Although a prestressed concrete model is not presently planned, attempts will be made to extend the information learned to this third type of containment. Tests of walls of panels that are similar to the wall of the R/C model will be tested in a like manner to panel tests (sponsored by the Electric Power Research Institute) of full size wall panels from prestressed containments [8]. Comparisons of all results may provide additional insight into both reinforced and prestressed concrete containment behavior.

Testing for the years beyond 1986 may include the seismic response of containments and the response to dynamic internal pressurization. Particular attention is being given to tests that will represent the behavior of containments during accidents that are initiated by an extreme seismic event.

ACKNOWLEDGEMENTS

The various components of work described herein are being conducted or directed by Sandia staff members, D. S. Horschel, L. N. Koenig, L. D. Lambert, P. E. Matson, D. B. Clauss and J. Jung. Dr. W. A. von Riesemann is the responsible Sandia supervisor and Dr. J. F. Costello is the NRC program manager. The work of these people is gratefully acknowledged.

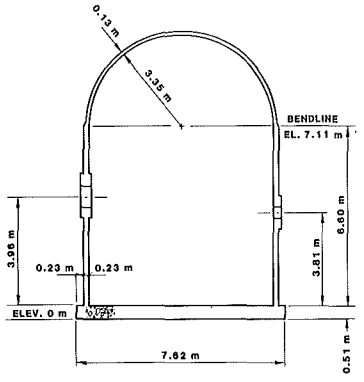

Figure 11. Conceptual Drawing of Reinforced Concrete Model

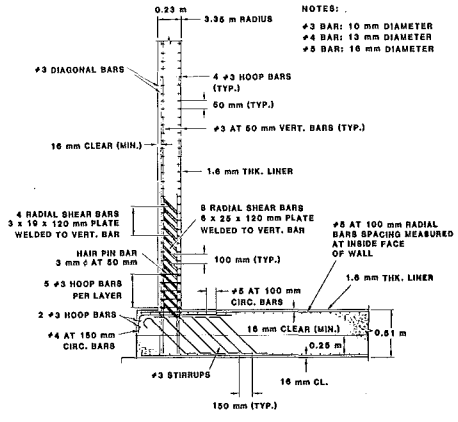

Figure 12. Reinforcement at the Cylinder-Wall and Basemat Junction

REFERENCES

1. Blejwas, T. E. and von Riesemann, W. A., "Pneumatic Pressure Tests of Steel Containments - Recent Developments", Nuclear Engineering and Design, Vol. 79, No. 2, May 1984.

2. Blejwas, T. E., "Containment Integrity Program, Recent Results and Plans", Proceedings of the International Meeting on Light Water Reactor Severe Accident Evaluation, American Nuclear Society, ANL Order 700085, 1983.

3. Horschel, D. S., "Experimental and Analytical Results of Steel Containment Tests," Proceedings of the 2nd Workshop on Containment Integrity, NUREG/CP-0056, to be published.

4. Clauss, D. B., "Analysis of a 1:8 Scale Steel Containment Model Subject to Internal Static Pressurization," Proceedings of the 2nd Workshop on Containment Integrity, NUREG/CP-0056, to be published.

5. Koenig, L. N., "Proceedings and Objectives for Testing a 1/8 Scale Model of Steel Containment," Proceedings of the 2nd Workshop on Containment Integrity, NUREG/CP-0056, to be published.

6. Jung, J. "Plans for a 1/6th Scale Reinforced Concrete Containment Model," Proceedings of the 2nd Workshop on Containment Integrity, NUREG/CP-0056, to be published.

7. Horschel, D. S. and Clauss, D. B., "The Response of Steel Containment Models to Internal Pressurization," Proceedings of the ASCE Specialty Conference on Structural Engineering in Nuclear Facilities, Raleigh, North Carolina, September 10-17, 1984, to be published.

8. Schultz, D. M., Hanson, N. W., "Full Scale Leak-Rate Tests of Concrete Containment Wall Elements," Proceedings of the 2nd Workshop on Containment Integrity, NUREG/CP-0056, to be published.

PWR CONTAINMENT BEHAVIOUR BEYOND THE DESIGN CONDITIONS

R. Avet-Flancard and B. Barbe'

Commissariat à l'Energie Atomique
Institut de Protection et de Sûreté Nucléaire
Boîte Postale n° 6
92260 Fontenay-aux-Roses, FRANCE

J-L. Costaz and J. Dulac

Electricité de France
Service Etudes et Projets Thermiques et Nucléaires
12-14, Avenue Dutrievoz
69628 Villeurbanne - Cedex, FRANCE

ABSTRACT

Studies on the behaviour of reactor containments under off-design conditions have been conducted in France on both 900 MW Pressurized Water Reactors (PWR) with metallined containments and 1300 MW Pressurized Water Reactors with dual concrete wall containments.

The results show that :

- 900 MW PWR containments should keep their integrity until failure since the risks of metal liner tearing are low,
- The behaviour of 1300 MW PWR containments is governed by the transverse carcking of the concrete which, due to the resulting leakage rate, tends to control internal pressure to a value less than collapse pressure,
- Mechanical penetrations exhibit a mechanical strength which is well above containment collapse pressure.

INTRODUCTION

French 900 and 1300 MW PWR containments are designed to withstand a design basis accident (complete rupture of the largest pipe in the main primary circuit). This load configuration is conditioned by temperature and pressure and pressure variations conservatively calculated to bound those potentially

reached during the plausible accidents considered in plant design.

However, it was considered beneficial from the safety standpoint to examine containment behaviour under conditions in excess of design.

These studies, jointly conducted by the French Atomic Energy Commission and Electricité de France, were intentionally limited to a gradual pressure and temperature rise above design basis accident conditions (0.03 MPa/hour for pressure and 2°C/hour for temperature from 0.4 MPa and 140°C). They aim to estimate margins to loss of integrity or containment collapse and more generally to define the scenario leading to collapse : concrete cracking, reinforcing steel rupture zones, any tearing of the metal liner, leakage rate caused by concrete cracking, strength of mechanical or electrical penetrations...

This document summarizes the main results obtained for metal-lined 900 MW PWR containments and for 1300 MW PWR containments with dual concrete walls.

STUDY PROGRAM

Studies focus on two main areas :

- containment behaviour,
- containment mechanical penetration behaviour.

Containment behaviour :

a) Mechanical behaviour

900 MW and 1300 MW PWR containments are considered as axisymmetrical structures, without defects or penetrations, and a complete thermal/mechanical calculation is performed for both containments up to the collapse point, with due allowance for concrete and rebar steel non-linear behavioural laws.

These calculations were preceded by a "test case" study : calculations by four different computer codes conducted by different design offices relating to a limited area of the containment and aiming to provide knowledge of the accuracy to be expected from such non-linear calculations when applied to prestressed concrete.

b) Concrete cracking and leakage rate

French 1300 MW PWR containments have dual concrete walls instead of metal liners. When cracks spread across the concrete of the inner containment wall, the wall starts to leak and its mechanical strength is dependent on this leak, which tends to reduce internal pressure. Thorough analysis is made of the distribution and opening of cracks in a containment wall (calculations + mockup) and its associated leakage rate.

Penetration strength :

When the collapse mechanism of each containment is known, an assessment has to be made to find out whether the mechanical penetrations constitute weak points.

RESULTS

900 MW PWR containments :

a) "Test case" study

This analysis, which related to a limited containments area (barrel to base mat junction zone) made it possible to determine the state of the art for concrete structure elastic/plastic calculations and to highlight the inadequacies of the concrete behavioural models in order to specify result uncertainties (four codes were used). These calculations, which included modelling of all the containment load-bearing elements (finite element modelling with non-linear behavioural laws) showed :

- good agreement on final collapse (between 1.15 and 1.3 MPa gage). The latter is related to the rupture of the barrel horizontal prestress cables and the final mechanism is simple.

- however, there is wider scatter affecting the intermediate concrete cracking mechanisms. The influence of the concrete behavioural models is direct and accuracy is lower (for example transverse barrel cracks appear between 0.6 an 1K1 MPa gage).

b) Mechanical strength of 900 MW PWR containments

After a critical examination of the above test calculations, a complete study of this metal-lined containment was conducted and led to the following conclusions :

- final collapse is due to rupture of the barrel horizontal prestress cables and (almost simultaneously) of the dome prestress cables at an internal pressure of about 1.2 MPa.

- metal liner deformation is still moderate just before collapse (less than a few %). This suggests that the risks of liner tearing in the zones free of discontinuities are low. Therefore, if no tear appears in the area of the penetrations and if the liner exhibits no initial defects, these containments would remain leaktight right up to the end. Intermediate concrete cracking mechanisms are less important and do not have a direct effect on collapse.

1300 MW PWR containments :

a) Mechanical strength of 1300 MW PWR containments

A complete calculation along the same lines for a containment of this design showed that behavioural was very different from the 900 MW containments. This containment consists of a dual concrete wall without a metal liner and with provision for leakage recovery in the space between the containment walls and the filters.

- During the first hours after the Design Basis Accident, leaktightness is provided by a concrete layer (highly compressed because of heat shock) on the inner face of the inner containment wall.

- However, transverse concrete cracks appear over a large area of the dome at internal gage pressures of about 0.6 MPa and 0.75 MPa in the barrel zone free of discontinuities. This results in leakage through the crack lattice, which tends to offset the steam production in the containment due to the accident. A straightforward mechanical study is inadequate in this case and it is necessary to analyse the possible distribution of the cracks, their opening and related leakage, the recovery of this leakage in the inter-wall space or the possible rise of containment pressure... Containment mechanical strength and the entire accident scenario depend on leakage rate.

b) Concrete cracking and leakage rate

This study involves the detection of cracks and monitoring of their growth, depth and opening with the rise in containment pressure.

. As regards cracking, calculations show that this is highly sensitive both to the steel-to-concrete average bonding value and to the criterion for the rupture of concrete subjected to tensile loads.

. On a practical basis, if it is assumed that there is a regular array of vertical cracks, the associated minimum leakage rate rapidly becomes very high when these cracks open under the effect of internal pressure.

. To confirm the validity of this calculation, a 1/10 containment local mockup (barrel) showed that cracking was at first regular and that collapse was preceded by the occurrence of several large cracks close to which all the deformations are concentrated.

. Development of the calculational model is continuing based on closer comparison with the test results acquired by the above mockup which is built in a concrete representation of the PALUEL containment.

Penetration strength :

In reality, containments are not axisymmetrical structures without defects or penetrations. The aim of these studies is to find out whether the existence of these discontinuities (equipment hatch opening etc) does not constitute a series of weak points which risk the premature collapse of the containment.

- Equipment hatch opening : An initial buckling analysis shows that, if this metal shell does not exhibit any initial defects, its strength is guaranteed above 1.2 MPa (900 MW PWR containment collapse pressure) without risk of instability.

- Personnel hatch : A complete finite element calculation of this hatch with geometrical and mechanical non-linearities shows that at a pressure of 1.2 MPa part of the structure is plastified, but that corresponding deformations are slight and the hatch as a whole remained perfectly stable. Mockups were also built to ascertain the strength of the windows and inflatable seals and demonstrated their good performance.

CONCLUSION

Pending final conclusions, it can be stated that the behaviour of the 900 MW PWR metal-lined containments is very different from that of 1300 MW PWR containments with dual concrete walls and cannot be covered by the same type of study. 900 MW PWR containments exhibit purely mechanical behaviour in that they probably remain leaktight right up to the end, whereas the behaviour of the 1300 MW PWR containments is much more complex and is largely dependent on concrete cracking and associated leakage.

A containment depressurization system is currently being studied in France, which would cover both cases. The study will determine the pressure above which the system should enter into service in each possible scenario.

THE EFFECT OF FAN-INDUCED TURBULENCE ON THE COMBUSTION OF HYDROGEN-AIR MIXTURES

R.K. Kumar and H. Tamm
Systems Analysis Branch
Whiteshell Nuclear Research Establishment
Atomic Energy of Canada Limited
Pinawa, Manitoba ROE 1LO Canada

ABSTRACT

The effect of fan-induced turbulence on the combustion of hydrogen-air mixtures has been studied in a 2.3-m diameter sphere over a hydrogen concentration range of 4 to 42% (by volume). Two fans were used to produce the turbulence, which was measured at various locations by hot-wire anemometry.

For low hydrogen concentrations ($\leq$ 7%), turbulence increases the rate and extent of combustion; for large turbulence intensities the extent of combustion approaches 100%, and combustion times are reduced by factors of 8 to 10 from those observed under quiescent conditions. At high hydrogen concentrations, the effect of turbulence on combustion time is less pronounced than at low hydrogen concentrations. Flame-generated turbulence has a significant effect on the combustion rate.

1. INTRODUCTION

The possible combustion of hydrogen-air-steam mixtures is an important concern in certain postulated loss-of-coolant accidents in nuclear reactors. The factors influencing combustion in reactor containment buildings must be known in order to predict hydrogen combustion behaviour when potential sources of ignition are present.

One factor that significantly affects combustion in reactor containment buildings is turbulence, such as that produced by fans or by the combustion process itself. The factor that governs the rate of flame propagation or the rate of combustion when turbulence is present is the turbulent burning velocity. Whereas the laminar burning velocity is a fundamental physico-chemical property of the combustible mixture, the turbulent burning velocity depends strongly on the flow itself. However, a correlation exists in most cases between the turbulent and laminar burning velocities and the parameters governing the nature of the turbulence. The turbulent burning velocity, S_t, may be expressed as:

$$S_t/S_u = f(u'/S_u, l, L)$$

where S_u is the laminar burning velocity, u' is the turbulent intensity, and l and L represent the microscopic and integral scales of turbulence, respectively. Numerous correlations of the above type have been proposed by several researchers, and a detailed account of several of these is given in Reference 1. Even though such correlations may be used to predict combustion behaviour in large systems, experimental work is required to verify their applicability.

Although turbulent combustion has been studied extensively, the work to date has dealt primarily with small systems. Results of some large-scale methane-air combustion experiments in the presence of fan turbulence, described in Reference 2, are not directly applicable to hydrogen-air systems because of the special nature of hydrogen. Furthermore, the experimental results were qualitative in that turbulent intensities were not measured. The results were reported in terms of the peak pressure versus fan speed or blade tip Reynolds number.

Since the laminar burning velocity of hydrogen-air mixtures increases with hydrogen concentration, up to 42%, it may be expected that the effect of turbulence on the burning velocity should diminish as the hydrogen concentration is increased, because the ratio S_t/S_u depends upon u'/S_u. The effect of turbulence is large for mixtures with small burning velocities and increases with the intensity of the turbulence. Recent work by Abdel- Gayed and Bradley [3] shows that this is true for most fuel-air mixtures.

Recent investigations by the present authors [4] have shown that combustion of hydrogen-air and hydrogen-steam-air mixtures is greatly influenced by turbulence at low hydrogen concentrations. At low hydrogen concentrations, turbulence increased the extent of combustion and the resulting pressure rise, and increased the rate of combustion by a factor of five to six. At high hydrogen concentrations, the rate of combustion increased only marginally. However, these present observations were qualitative because the fan turbulence was not characterized.

Experiments have therefore been done in a 2.3-m diameter sphere to relate these effects to the amount of turbulence. This paper discusses the results.

2. DESCRIPTION OF THE TEST FACILITY AND INSTRUMENTATION

2.1 Test Facility

The Containment Test Facility (CTF) consists of three major components that may be interconnected: a sphere, a cylindrical duct and a vertical cylinder. The sphere alone was used for this series of experiments. It has three large openings and several smaller ones. The smaller openings are used for mounting instruments and probes. The sphere is insulated and trace-heated with steam, and its temperature can be maintained constant as desired (up to about 135°C). Two fans driven by variable-speed air motors are mounted diametrically opposite each other in the sphere, as shown in Figure 1.

2.2 Instrumentation

Figure 1 also shows the CTF instrumentation. Transient pressures in the sphere during combustion were measured by four piezoelectric transducers, with a rise-time of 2 μs, and a Kulite semiconductor transducer with a similar rise-time. The Kulite transducer provided highly reliable measurements over the entire range of pressures encountered. A Rosemount pressure transmitter with a response time of 0.2 s was used for monitoring the pressure during introduction of gases into the sphere. The response of

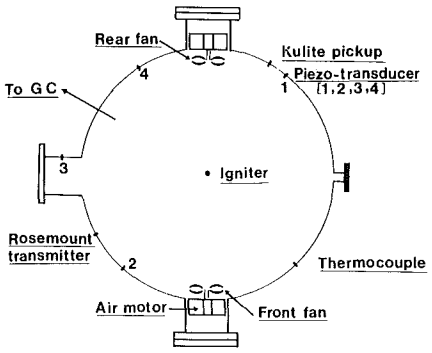

Figure 1. Arrangement of Fans and Instrumentation in the Sphere

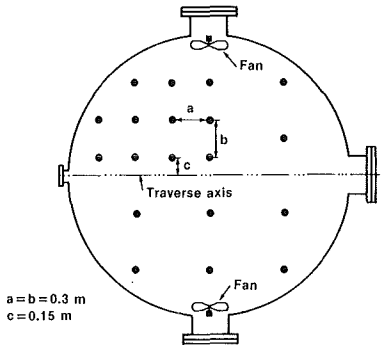

Figure 2. Location of the Measurement Points in the Sphere

the Rosemount transmitter was acceptable for hydrogen concentrations between 5% and 10%, and the indicated pressure was close to that of the Kulite transducer. A fine-wire (0.075 mm diameter), Type S thermocouple was used to measure the transient temperature of the gases close to the wall of the sphere.

Two of the piezoelectric transducers were recess-mounted and coated with RTV-108 for thermal protection. The other two piezoelectric transducers were mounted flush with the inner wall of the vessel.

The signals from all the transducers were processed by an analog-to-digital converter with a scan time of 1.5 ms. A two-channel transient recorder that could record 4000 data points with a maximum sampling rate of 2 MHz was also used to record transient pressures.

The gases in the sphere were analyzed, before and after combustion, using a gas chromatograph.

3. RESULTS AND DISCUSSION

3.1 Measurement of Turbulence in the Sphere

Ideally, it is preferable to have homogenous and isotropic turbulence, to facilitate comparison with theoretical predictions. This would permit measurements at a single point during the experiment, and could be accomplished by laser-Doppler anemometry. However, homogeneous turbulence is difficult to achieve in a real situation, and turbulence parameters tend to vary spatially. Since spatial measurement of turbulence was not possible during combustion, it was decided to carry out detailed turbulence measurements in the sphere at certain fan speeds and then to carry out combustion experiments later at these same fan speeds.

Since the flow field produced by the fans is strongly three-dimensional, a TSI (Thermo Systems Incorporated) 1294 three-dimensional hot-film probe was used for the measurements. The probe was operated with three TSI 1050 research anemometers. Each sensor was calibrated separately over a range of velocities from 1 to 15 m/s with flows normal to the sensor.

Figure 2 shows a schematic of the measurement grid used. The probe was traversed manually by moving the arm on which the probe was mounted. Detailed measurements were made in one quarter of the horizontal diametral plane. The flow field produced by the fans was assumed to be symmetric about the fan axis, although measurements indicated that true symmetry did not exist. Velocities at corresponding points differed by as much as 30%, especially at low velocity values.

Figures 3 to 5 show the root-mean-square velocity (u') plotted against the distance from the fan axis, for three fan speeds. As can be seen, the r.m.s. velocities decrease with fan speed. Except at low fan speeds, the highest r.m.s. velocities are observed along the fan axis. It should be noted that the measured r.m.s. velocities are high, as high as 50% of the time-averaged velocities in many cases. This is mainly due to the confinement of the gas in the sphere. In large unconfined volumes, the situation would be somewhat different. The flow entering the fan would be less likely

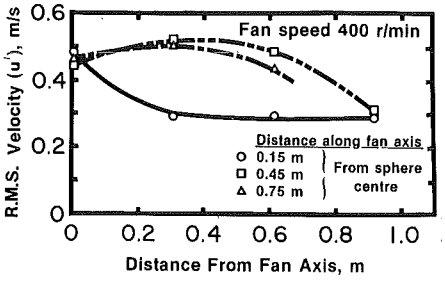

Figure 3. Turbulent Intensity in the Sphere with a Fan Speed of 400 r/min

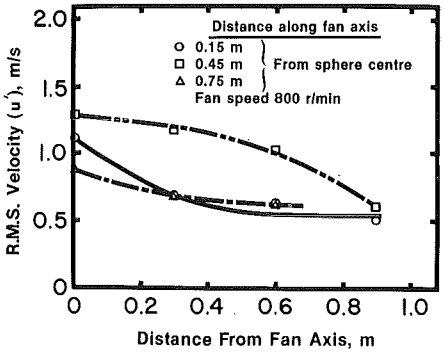

Figure 4. Turbulent Intensity in the Sphere with a Fan Speed of 800 r/min

to be influenced by the flow field at the fan exit. In confined volumes, however, circulatory flow is set up in the vicinity of the fan and there is short-circuiting. The flow at the fan entry itself is highly turbulent, which causes high turbulence at the fan exit.

Even though no single characteristic turbulent velocity exists in the sphere, due to the complicated flow patterns, it is useful to think of a single r.m.s. velocity that is characteristic of the turbulence. It should be noted that the r.m.s. velocity at any point is related to the average kinetic energy for an entire spectrum of eddy sizes. A space averaging of these average kinetic energies can be defined as:

$$E' = \frac{\sum_{i=1}^{n} E_i}{n}$$

where E_i is the local kinetic energy associated with each point in space, and n is the number of points. E' is used in the calculation of a single characteristic turbulent intensity $\bar{u}'$, expressed as follows:

$$\bar{u}' = \left[\frac{\sum_{i=1}^{n} u'^2}{n} \right]^{1/2}$$

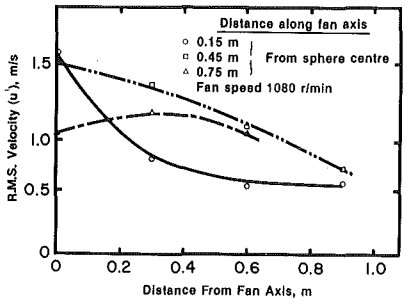

Figure 5. Turbulent Intensity in the Sphere with a Fan Speed of 1080 r/min

A plot of the space-averaged r.m.s. velocity versus fan speed is shown in Figure 6. For the range of speeds investigated, u' appears to be a linear function of the rotational speed of the fan.

Another important quantity in determining the turbulent burning velocity of a combustible mixture is the scale of turbulence, which depends upon the r.m.s. velocity u' and the auto-correlation coefficient, ρ.

In a generally three-dimensional flow field it is difficult to compute the fluctuating velocity components directly and to find their auto-correlation coefficients. Therefore, no attempt was made in these measurements to resolve the components directly and obtain auto-correlation coefficients. The effective velocity measured by each sensor was correlated with itself. Although this does not provide an accurate value for ρ, it is sufficient to give a rough measure of the scale of turbulence. Knowing the scale and turbulent intensity permits calculation of the turbulent burning velocity, via a suitable correlation [1].

3.2 Combustion Experiments

All the combustion experiments described were conducted at 100°C, and near atmospheric pressure. The mixtures were ignited centrally and the fans were activated 1 to 2 min prior to ignition.

Figure 7 compares pressure-time traces obtained with a low (5%) hydrogen concentration, for three fan speeds. Without turbulence, the extent of combustion is very small, less than 10% of the hydrogen [4]. The corresponding pressure rise is also small. However, with the lowest fan speed the pressure rise is appreciable, and nearly 60% of the hydrogen is burned. Furthermore, the combustion time is short, around 2 s, compared with 6 s under quiescent conditions. As the fan speed is increased from 400 to 1050 r/min, the peak pressure increases from 60 kPa to 105 kPa. The rate of combustion also increases by a factor of 3 to 4. The fraction burned increases from 60 to 100% as the fan speed is increased. At high fan speeds, the turbulent intensities are large and the flame front is fragmented and transported in the sphere in almost all directions, before the effects of buoyancy can be felt. This results in complete combustion. For example, at 1050 r/min the highest turbulent intensity measured is of the order of 1.6 m/s, and with central ignition we therefore expect the flame speed to be of this magnitude. The expected combustion time would be around 0.7 s. The observed combustion time is 0.86 s, roughly in agreement with the expected value.

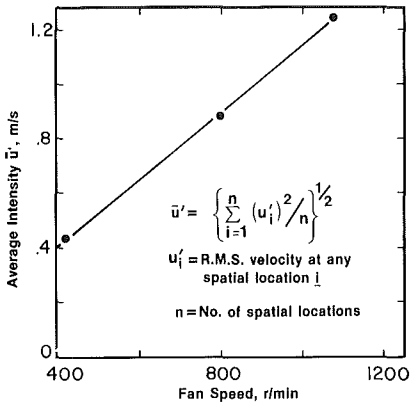

Figure 6. Average Turbulent Intensity in the Sphere

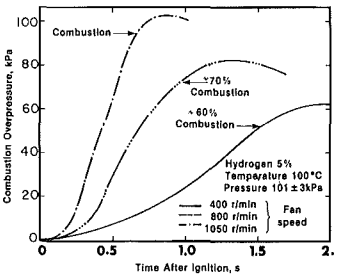

Figure 7. Effect of Turbulence on Combustion for 5% Hydrogen in Air

The present finding that turbulence has a strong effect for low-burning-velocity mixtures agrees with that of Abdel-Gayed and Bradley [3]. The experiments clearly demonstrate that even low-level turbulence has a strong effect on combustion. However, a 4% hydrogen-air mixture did not ignite in the presence of turbulence.

The situation is somewhat different at high hydrogen concentrations. At these concentrations, the ratio u'/S_u is small and the influence of turbulence is also small. Figure 8 shows the pressure transients observed at a high (20%) hydrogen concentration, for three fan speeds. The effect of turbulence on the combustion time and the peak pressure is reduced significantly.

The variation of the combustion peak pressure with hydrogen concentration for various fan speeds is shown in Figure 9. The peak pressures for all fan speeds and hydrogen concentrations lie between the theoretical adiabatic limit and the experimental quiescent limit. At 400 r/min, corresponding to low turbulent intensities in the sphere, peak pressures are close to the quiescent combustion values for hydrogen concentrations greater than 10%. This is reasonable, because $u'/S_u \approx 1$ and combustion is not greatly influenced by turbulence at low turbulence levels. Furthermore, peak pressures at a fan speed of 1050 r/min are close to the adiabatic pressures, in general agreement with earlier combustion experiments in the sphere [4]. The only difference between combustion at 1050 r/min and under quiescent conditions is the level of turbulence, which alters the rate of combustion and the time to peak pressure. This indicates that the observed pressure differences between quiescent and theoretical adiabatic combustion are mainly due to radiative losses from the system.

Figure 10 shows the time to peak pressure plotted as a function of hydrogen concentration for various fan speeds. It is clear that the rate of combustion and thus the total time are both strongly influenced by the level of turbulence in the sphere, and depend upon the initial hydrogen concentration. At low hydrogen concentrations, combustion times under turbulent conditions are an order of magnitude shorter than the corresponding laminar values; at high hydrogen concentrations this effect is only half as large.

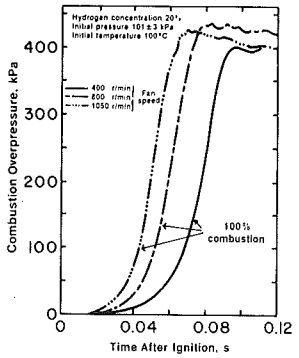

Figure 8. Effect of Turbulence on Combustion for 20% Hydrogen in Air

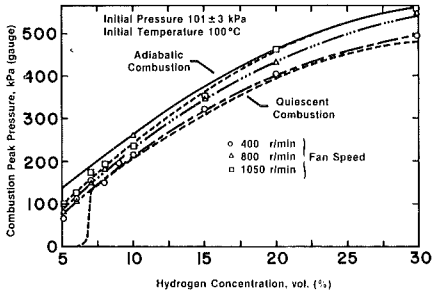

Figure 9. Variation of Combustion Peak Pressure with Hydrogen Concentration

3.3 Theoretical Considerations

Theoretical calculation of the pressure transients, for a given vessel geometry, depends upon the turbulent burning velocity S_t. An extensive literature survey done by Andrews et al. [1] shows that the ratio S_t/S_u depends upon the quantity u'/S_u. Although complicated relationships between S_t/S_u and u'/S_u have been proposed, the simpler ones take the form

$$S_t/S_u = \left[1 + B(u'/S_u)^m\right]^n$$

where B, m and n are constants. The earliest correlation, based on a continuously wrinkled laminar flame, was by Damköhler [5], with $B = m = n = 1$, and is used here.

It has been noted by Karlovitz et al. [6] that the flame itself generates turbulence when propagating in a strongly turbulent medium. The flame-generated turbulence diffuses upstream of the flame and should be added to the burning velocity. The turbulent velocity should be modified to include this, as follows

$$S_t = S_u + u' + u''$$

where u" is the flame-generated turbulence and is given by

$$u'' = S_u(\rho_u/\rho_b - 1)/\sqrt{3}$$

The flame-generated turbulence exists only when the initial turbulence is strong, and is zero for laminar or mildly turbulent flame propagation. Since u" depends on S_u, its effect is minimal at low hydrogen concentrations, where the laminar burning velocities are small.

For comparison with experiment, calculations were performed assuming that the flame propagates as a smooth spherical front in an adiabatic enclosure. The laminar burning velocities used were those of Liu and MacFarlane [7].

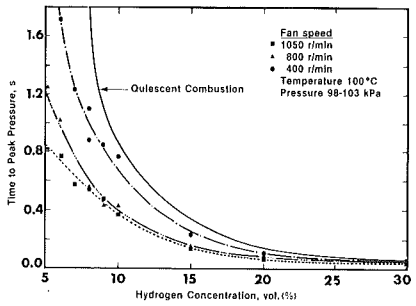

Figure 10. Variation of Combustion Times with Hydrogen Concentration

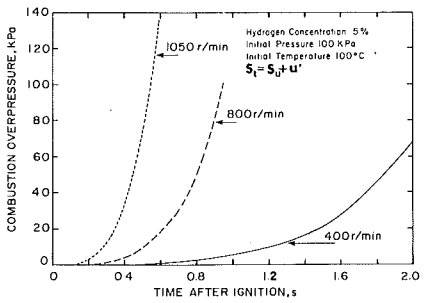

Figure 11. Calculated Pressure Transients at 5% Hydrogen in Air

Figure 11 shows the calculated pressure transients for mixtures containing 5% hydrogen, for various fan speeds. Since S_u is very small at these concentrations, the flame-generated turbulence is also very small compared to the fan-induced turbulent intensity. Hence, the flame-generated turbulence was not included in the calculation. As expected, the adiabatic model slightly overpredicts the peak pressures. Of more direct interest is the comparison of combustion times. Comparing Figures 11 and 7, it is seen that the calculated combustion times (times to peak pressure) are less than those observed. This may be due to the assumption of uniform turbulent intensity, whereas the measurements show a lower intensity towards the centre of the sphere. The discrepancy between the observed and calculated values may also be due to the assumption of no heat loss from the system. In reality, heat losses from the system reduce the flame speed, due to cooling of the gases, and slow the rate of pressure rise. Spatial variation of the turbulent intensity and mean velocity distort the assumed spherical symmetry of the flame. Nevertheless, for the highest fan speed employed (1050 r/min), the predicted and measured times of 0.6 s and 0.9 s, respectively, agree reasonably well. For the lower fan speeds, incomplete combustion may upset the predictions, since the calculations assume that the extent of combustion is spatially uniform.

Finally, Figure 12 shows the theoretical predictions for a mixture containing 20% hydrogen. Since in this case S_u is large, the calculations have been carried out with and without flame-generated turbulence. Without flame-generated turbulence, the calculated combustion times are greater than those measured. Even for the highest fan speed, the calculated combustion time is greater than the experimentally observed value for combustion with a fan speed of only 400 r/min. For example, at 1050 r/min, the calculated combustion time is 0.103 s, whereas the combustion time observed at 400 r/min is about 0.09 s. This clearly shows that flame-generated turbulence must be affecting the rate of combustion. The results calculated with flame-generated turbulence added to the initial turbulence are shown by chained lines in Figure 12. It is clear from the figure that flame-generated turbulence alters the combustion times by almost a factor of two, although the calculations show a faster rate of pressure rise. The measured pressure-time curve lies between the transients predicted with and without flame-generated turbulence. This is reasonable, since inclusion of flame-generated turbulence establishes an upper bound for the rate of pressure rise for normal combustion.

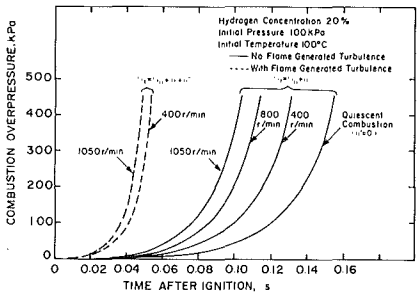

Figure 12. Calculated Pressure Transients for 20% Hydrogen in Air

4. CONCLUSIONS

The following conclusions can be drawn from these experiments:

1. For low hyrogen concentrations ($\leq$ 7%), turbulence increases the rate and extent of combustion. With large turbulent intensities, the extent of combustion approaches 100%. Furthermore, combustion times are much shorter (by factors of 8 to 10) than those for quiescent combustion.

2. At high hydrogen concentrations, the combustion rate increases with increasing turbulence, but the effects of turbulence are less pronounced than at low hydrogen concentrations.

3. Flame-generated turbulence has a significant effect on the combustion rate, and establishes an upper bound for the rate of pressure rise, for purposes of reactor safety assessment.

ACKNOWLEDGEMENTS

This work was partially funded by the AECL/Ontario Hydro CANDEV program.

REFERENCES

1. Andrews, G.E., Bradley, D., and Lwakabamba, S.B., "Turbulence and Turbulent Flame Propagation - A Critical Appraisal," Combust. Flame 24, 285 - 304, (1975).

2. Harris, G.F.P., "The Effect of Vessel Size and Degree of Turbulence on Gas Phase Explosion Pressures in Closed Vessels," Combust. Flame, 11, 17 - 25 (1967).

3. Abdel-Gayed, R.G. and Bradley, D., "Dependence of Turbulent Burning Velocity on Turbulent Reynolds Number and Ratio of Laminar Burning Velocity to R.M.S. Turbulent Velocity," in: "Sixteenth Symposium (International) on Combustion," pp. 1725 - 1735, The Combustion Institute, Pittsburgh, PA, (1977).

4. Kumar, R.K., Tamm, H., and Harrison, W.C., "Studies of Hydrogen Combustion in an Intermediate-Scale Test Facility," Atomic Energy of Canada Limited Report, AECL-7814 (1984).

5. Damköhler, G., "Influence of Turbulence on the Velocity of Flame in Gas Mixtures," Z. Elektrochem. 46, 601-626 (1940). English translation, NACA-TM-1112 (1947).

6. Liu, D.D.S. and MacFarlane R., "Laminar Burning Velocities of Hydrogen-Air and Hydrogen-Air-Steam Flames," Combust. Flame 49, 59-71 (1983).

7. Karlovitz, B., Denniston, Jr., D.W., and Wells, F.E., "Turbulent Flames," J. Chem. Phys. 19, 541-547 (1951).

ANALYSIS AND PREDICTION OF JET LOADS

Karsten Fischer and Wolfgang Häfner

Battelle-Institut e.V.
Am Roemerhof 35, D-6000 Frankfurt
West Germany

ABSTRACT

An empirical model for the estimation of jet forces on containment structures is presented. The model calculates the pressure distribution on an impingement plate, using the geometrical data of the break opening and plate distance as well as the thermodynamic data of the discharging fluid. Development and verification of the model was performed on the basis of Battelle (RS 50) and HDR (RS 123) experiments. The model can be applied for discharges of subcooled and saturated water, two-phase flow and pure steam.

INTRODUCTION

Containment structures and components must be designed to withstand hypothetical jet loads due to pipe breaks in the primary loop. The methods which are currently used in routine practice for to calculate jet force distributions /1, 2/ are very simple approximations and do not in general take into account the thermodynamic state of the discharging coolant. Numerical simulation calculations are too costly for routine applications.

The German Federal Ministry for Research and Technology (BMFT) sponsored a project to analyze the available experimental data on jet force distributions. The basic physical effects of the two-phase jet hydrodynamics were investigated by applying the two-dimensional numerical code K-FIX to some selected cases. The results of the experimental analysis and the numerical calculations lead to the development of an empirical model for jet force calculations, which is well suited for routine applications.

ANALYSIS OF EXPERIMENTAL DATA

Figures 1 and 2 show the experimental arrangement for the jet impingement tests. Data from the following experiments were inspected: KWU (BMFT-project RS 93), Battelle (BMFT-project RS 50), HDR (BMFT-project RS 123), Grenoble (project JERICHO), Japan (MIKT-experiments). The following results were found:

a) For discharge of steam or saturated water, the pressure profiles can be represented by a single Gaussian (Fig. 3)

$$p(r) = p_o \, e^{-\frac{r^2}{2\sigma_o^2}}$$

where p_o is the pressure (above ambient pressure), r is the radial coordinate perpendicular to the jet axis, and σ_o is the width parameter.

b) For discharge of subcooled water there appears an additional spiky pressure peak in the center of the profile; this profile can be represented by linear combination of two Gaussians (Fig. 4)

$$p(r) = p_o \, e^{-\frac{r^2}{2\sigma_o^2}} + p_1 \, e^{-\frac{r^2}{2\sigma_1^2}}$$

where the second term represents the additional pressure spike and can be visualized as the contribution of a jet core consisting of pure water.

Other profiles with off-center maximum pressure were observed. However, these profiles were not considered in a special manner because such a treatment would be very complicated and unnecessary from a safety viewpoint; instead, they too were represented by equivalent single Gaussians for further investigations. The formation of such profiles is governed by shock wave effects, as was shown by similar single-phase gas dynamical experiments elsewhere.

NUMERICAL SIMULATION

The numerical calculations with K-FIX(2D) lead to the following results:

a) During discharge of steam and saturated water there exist approximately homogeneous phase distributions and thermodynamic equilibrium.

b) During discharge of subcooled water there exists a considerable delay in evaporation. The pressure distribution is influenced by a locally variable evaporation rate, the difference between water and steam velocities is large.

c) The empirical models for the evaporation process currently in use do not sufficiently take into account the influence of the local distribution of nucleation sites.

In figure 5 a pressure profile calculated with K-FIX is shown in comparison with experimental data of the HDR-experiment V 42. In this case, a steam discharge occurred, and the experimental data are well reproduced by the numerical code.

Figure 6 shows the comparison for a case with discharge of subcooled water.

EMPIRICAL MODEL FOR CALCULATING PRESSURE PROFILES

The model parameters p_o, σ_o, p_1 and σ_1 are determined empirically (Fig. 7). For the steam part of the jet, a theory of Lamkin et al. /3/ is used to calculate the width parameter σ_o. This theory is modified in such a way that the water evaporating in the free jet region is taken into account. The water part of the pressure profile is calculated by the empirical relations

$$p_1 = p_{stag} e^{-a}$$

and

$$\sigma_1 = (1 + 0.611(1-e^{-b}))R_M$$

where p_{stag} is the stagnation pressure in the break opening and R_M is the break radius. The coefficients a and b depend on geometrical conditions and thermodynamic parameters of the fluid. The remaining parameter of the pressure profile, p_o, is calculated from a stationary momentum balance.

The empirical model equations are constructed in such a way that the limiting cases of pure steam or cold water discharge are represented reasonably. The model can be applied for quasi-stationary conditions; the thermodynamic conditions in the break opening (pressure, temperature, density and velocity) must be known.

Figure 9 shows a comparison between a pressure profile calculated by the present empirical model and a simpler correlation /2/, together with experimental data from RS 50. In this case a subcooling of 20 ^{o}C exists in the break opening. The central pressure spike is represented well by the empirical model curve.

CONCLUSIONS

An empirical model for calculating pressure profiles was developed, taking into account geometrical and thermodynamical parameters. The model was verified against the available experimental data (Fig. 5, 8, 9). Especially the pressure spikes caused by subcooled discharge are represented well by the model. It is suited for use on small computers (e. g. PDP 11) for routine applications.

ACKNOWLEDGEMENTS

The authors are indebted to J. R. Travis and B. A. Kashiwa from the Los Alamos National Laboratory for supporting the K-FIX applications; to Ph. Gully from the centre d`Études Nucléaires de Grenoble and to K. Kitade from the Mitsubishi Atomic Power Industries, Inc., for supplying jet force data.

LITERATURE

/1/ F.J. Moody, ASME Symp. Non-Equilibrium Two-Phase Flow, Houston 1975, p. 27-36

/2/ W. Kastner, H. Lochner, KWU-Bericht RE23/053/75, Erlangen 1979

/3/ D.E. Lamkin et al., Report NUREG/CR-1511, Los Alamos 1980

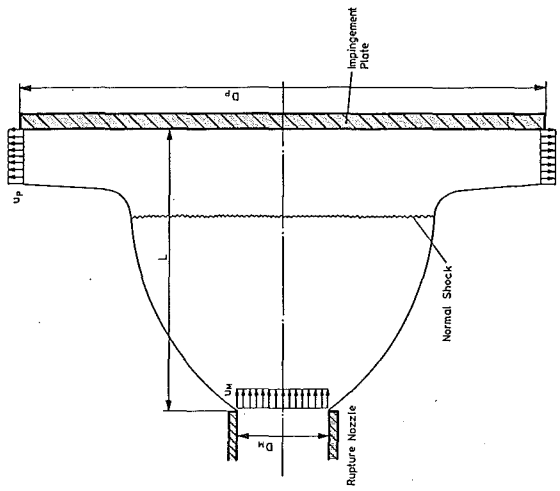

Figure 2 : Jet impingement of a highly underexpanded compressible free jet

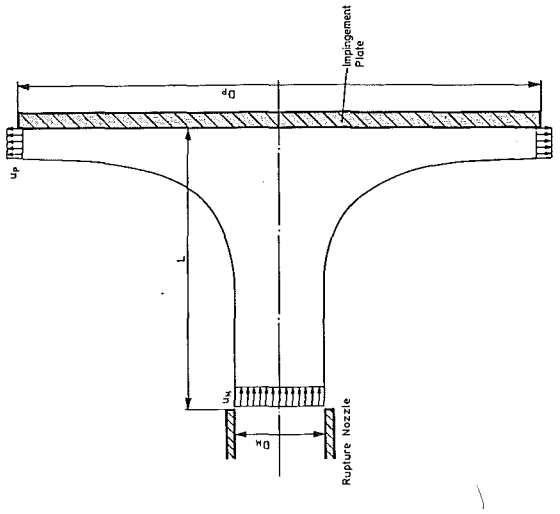

Figure 1 : Jet impingement of an incompressible free jet

Battelle

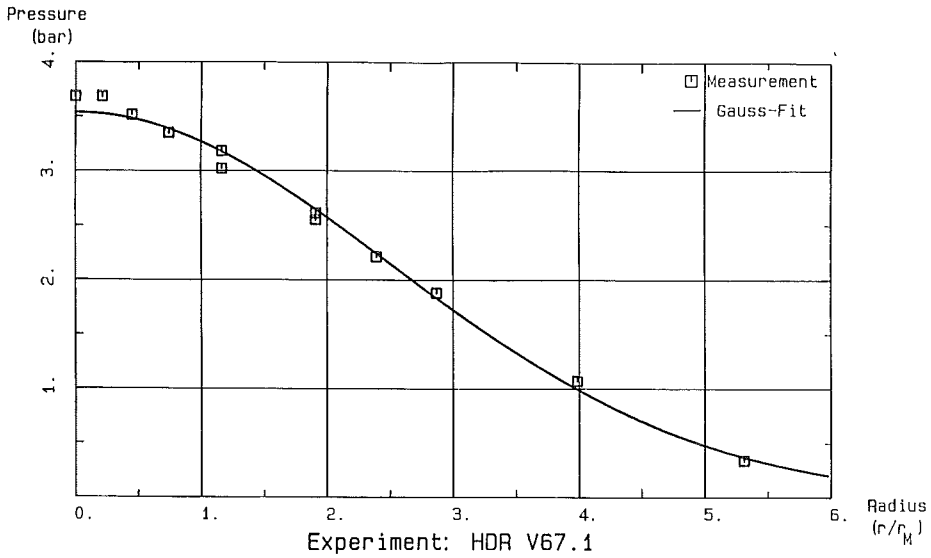

Experiment: HDR V67.1

Pressure profile, represented by a single Gaussian

Figure 3: Timestep # 7 t=700.00ms

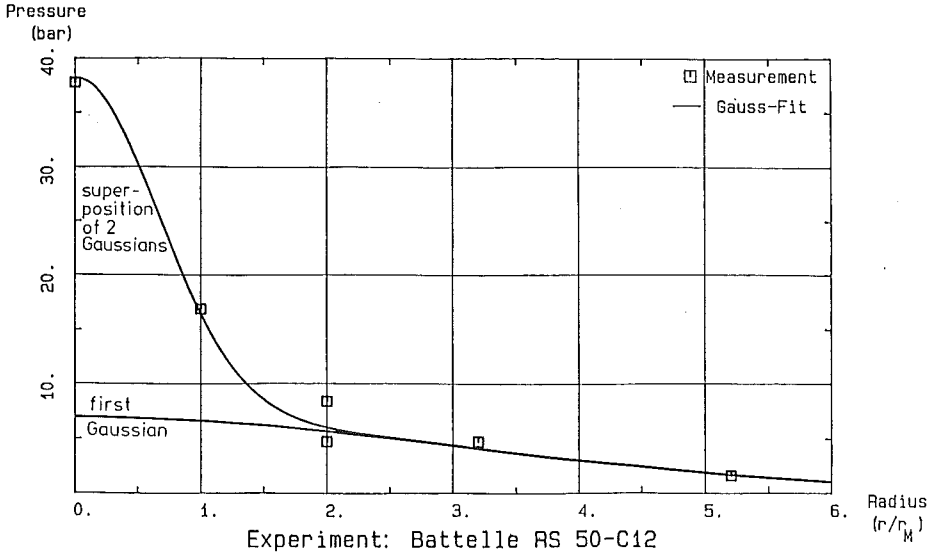

Experiment: Battelle RS 50-C12

Pressure profile, represented by superposition of 2 Gaussians

Figure 4: Timestep # 16 t=24.38ms

Battelle

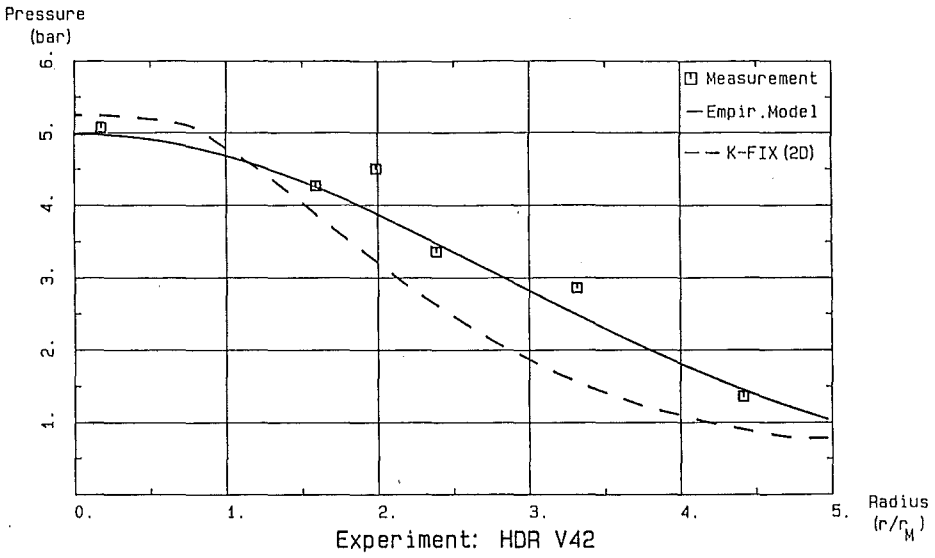

Experiment: HDR V42

Radial pressure profile during discharge of steam

Figure 5: Timestep # 11 t=55.00ms

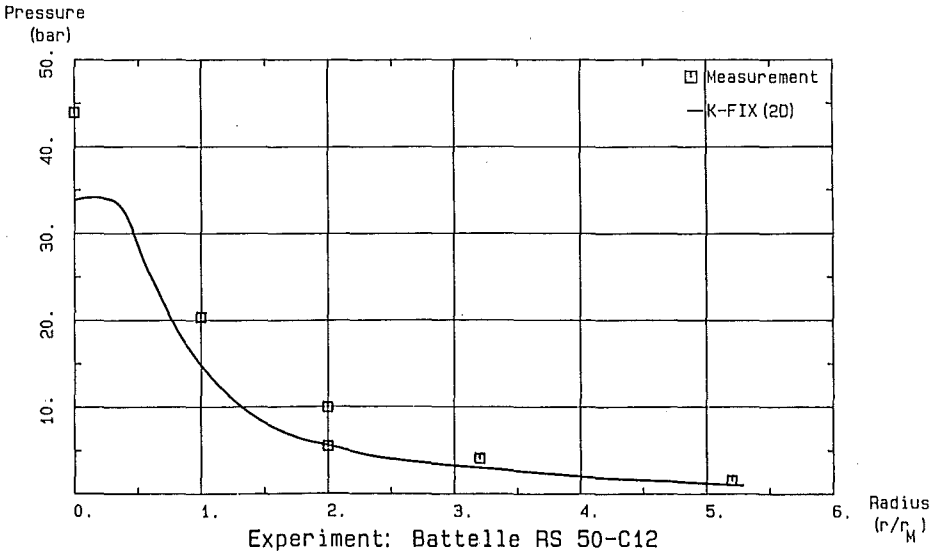

Experiment: Battelle RS 50-C12

Radial pressure profile during discharge of subcooled water

Figure 6: Timestep # 8 t=14.38ms

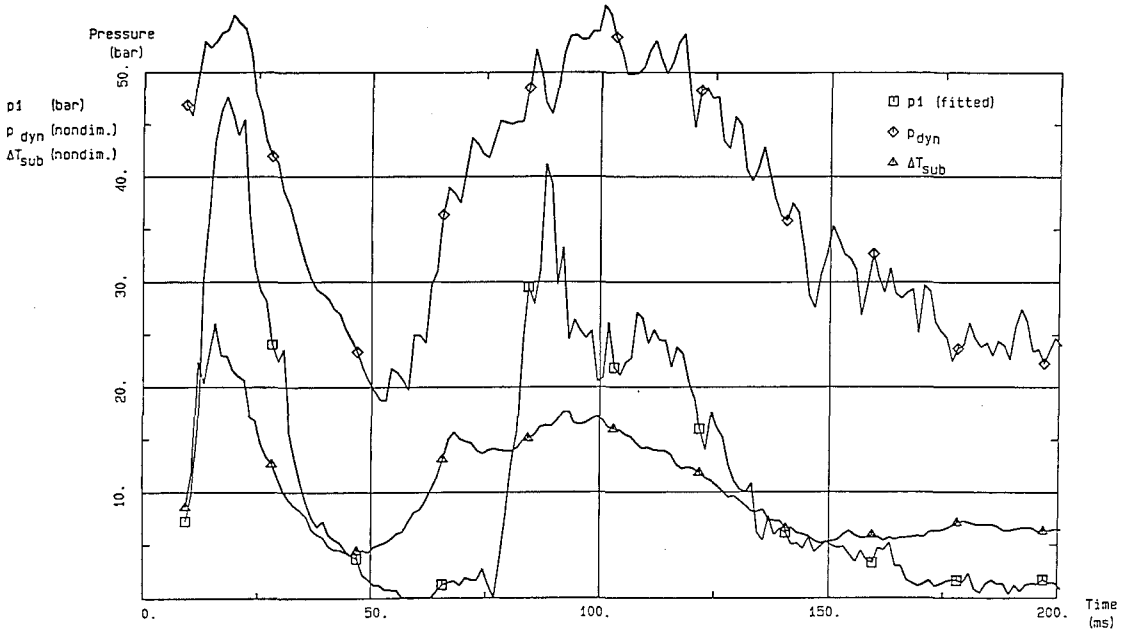

Experiment: Battelle RS 50-C12
Interrelation between core pressure partial p1 and
Figure 7: subcooling ΔT and dynamic pressure p_{dyn}

Battelle

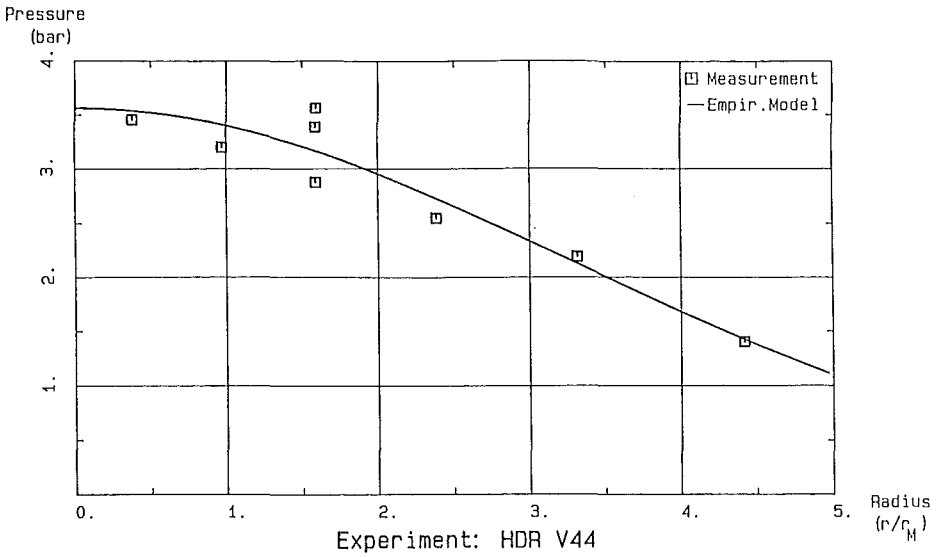

Experiment: HDR V44

Radial pressure profile during discharge of steam

Figure 8: Timestep # 11 t=55.00ms

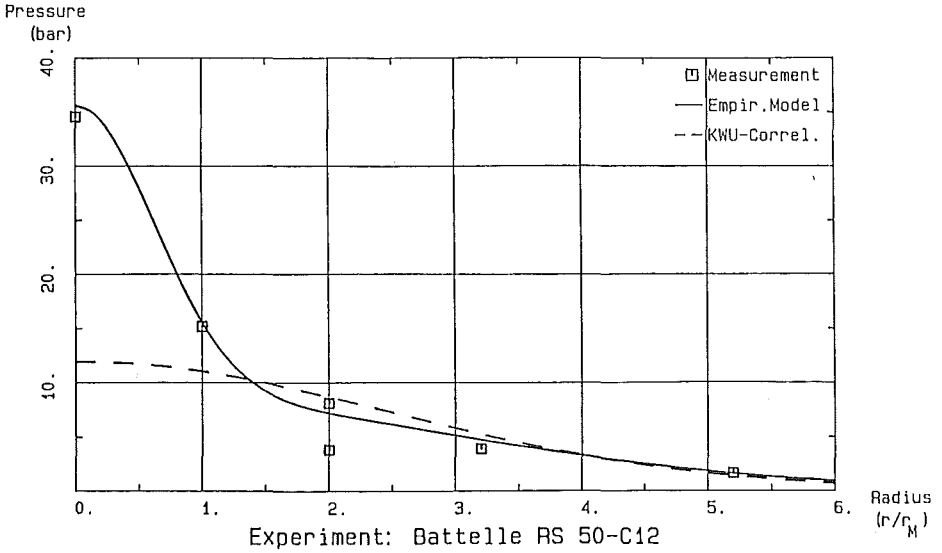

Experiment: Battelle RS 50-C12

Radial pressure profile during discharge of subcooled water

Figure 9: Timestep # 64 t=84.37ms

BEHAVIOR OF CONTAINMENT AND STRUCTURES DURING BLOWDOWN AND OTHER TESTS AT THE HDR PLANT

K. Müller, G. Katzenmeier

Project HDR Safety Programm
Kernforschungszentrum Karlsruhe
Postfach 3640
D-7500 Karlsruhe 1
West-Germany

ABSTRACT

The HDR-safety program includes various experiments to study the component behavior under accidental loads as Blowdown, earthquake, containment over pressure, thermal shock etc.

The construction of the HDR facility for test purposes will be briefly described and the measured loads discussed. The functional behavior of test equipment as valves during blowdown as well as the response of the containment shell to blowdown loads will be discussed. Examples of the effects of blowdown tests on the facility concrete structure and different equipment parts of the mechanical and electrical installations will be shown in load diagrams and illustrated by colour prints.

Furthermore, graphic information will be given about experimental and theoretical studies concerning crack growth under cyclic thermal shock on an RPV-nozzle. Other figures shown the effects of a real quillotine pipe break NW 300 in the HDR-plant under operating conditions.

TESTS ON THE HDR-FACILITY

The HDR is a former test reactor for demonstrating nuclear steam superheating.

Its external form is not typical for current light water reactors, as a comparison with a German 1300 MW_e reactor plant clearly shows (Fig. 1).

Nevertheless, the atypical geometry produces loss of coolant accident loads on the containment that would be comparably greater to those that would be expected in a modern nuclear power plant.

The containment, consisting of approximately 50 compartments of various volumes, the crane, elevator, and electric equipment are conceptually typical of the state of the art in reactor safety technology in 1966.

The realism of the large-scale experiments performed at HDR allows the primary goal of reactor safety research, namely the transfer of experimental results to commercial reactor plants, to be achieved to large extent.

The components of interest include:

- feed water check valves and steam isolation valves of nominally 200 mm, 350 mm, and 500 mm in pipe diameter.
- pipe systems up to NW 500
- reactor pressure vessel (12 m high, 3 m i.d.) with nozzles up to NW 450
- core barrel (7.5 m high, 2.6 m i.d.)

. steel shell containment (60 m high, 20 m i.d.)

. reactor building, including concrete internals and surrounding soil.

These components are either full-size of nearly full-size when compared with the dimensions of their counterparts in a 1300 MW_e light water reactor. Of particular importance is the fact that the components are included in realistic plant configurations and therefore to a great extent allow HDR experiments to address specific reactor applications (Fig. 2).

The loads wich are exerted include:

- Conditions close to operating conditions and test conditions.
  .. Boiling water reactor conditions
  .. Pressurized water reactor conditions (110 bar, 310°C)
  .. Hydro pressure tests (143 bar, 50°C)

- Accident conditions
  .. Fire
  .. Loss-of-Coolant accident (blowdown)
  .. Emergency cooling ("cyclic" thermal shock)
  .. Earthquake
  .. Impulsive type loads (e.g., airplane crash, explosion).

The survey diagram in Fig. 3 shows the load cases with the characteristic parameters as realized in the HDR, compared with the characteristic parameters employed as a design basis for nuclear power plants.

LOAD EFFECTS TO CONTAINEMENT STRUCTURES

The HDR structures and components are affected by:

. Static loads

- pressure
- temperature fields
- humidity

. Dynamic loads

- pressure waves
- temperature waves (steam front)
- jet impingement loads
- reaction forces in pipe supports

The long term static loads

. deform plastic components
. dissolve smooth stairway coatings
. force oil out of valve bodies
. corrode unprotected electrical contacts and relays
. cause metal structures to rust

Static temperature loads act primarily in the containment dome.

The dynamic loads affect

. ventilation ducts
. insulation of Vessel and piping
. doors/hatches
. cover plates and block walls
. lamps/cable channels/telephons
. coatings

The following conclusions can be drawn from the HDR tests run so far:

- the HDR components can withstand the induced loads and test conditions without safety-relevant weakening.

- concrete structures have up to now been damaged mostly from thermal shock effects; differential pressures or jet forces resulted in no significant structural loading.

- extensive damage has been limited to the individual blowdown compartments and the main pressure wave propagation paths.

- the severe dispersion of glass wool throughout the facility indicates the potential difficulties of decontamination following a serious accident.

- practical experience on the design and installation of blowdown-resistant equipment has been gained at HDR, as well as experience with the load-carrying capability of components as pipes and valves etc. under overload conditions.

FUTURE PLANS ON HDR

In Phase II of the HDR Safety Program (1984 - 1987) experiments are planned with loads clearly severer than tho se applied in Phase I. A summary of the experiments planned is given in the table in Fig. 4. On the one hand, tests will be conducted to enlarge and supplement studies already conducted Phase I, including

- further Containment Blowdown Tests to clarify existing differences between measurements and calculations with respect to differential pressures

- Reactor Pressu re Vessel Internals Blowdown Tests with simulations of small breaks (0.1 F) and longer break opening time

- Cyckic Thermal Shock Tests with deeper cracks and extensive non-destructive testing

- "Earthquake Tests" with an extremely large excentric mass shaker.

The shaker, with some 50 t of rotating mass, will be able to cause the whole building to vibrate strongly in accordance with the maximum European and American seismic criteria, with vibrations extending clearly into the non-linear range.

On the other hand, some experiments are planned on new topics:

- Temperatur stratification tests in pipes and vessel - injection of cold water emergency coolant test
- Pipe failure tests
- Reactor building impact tests
- Fire protection tests.

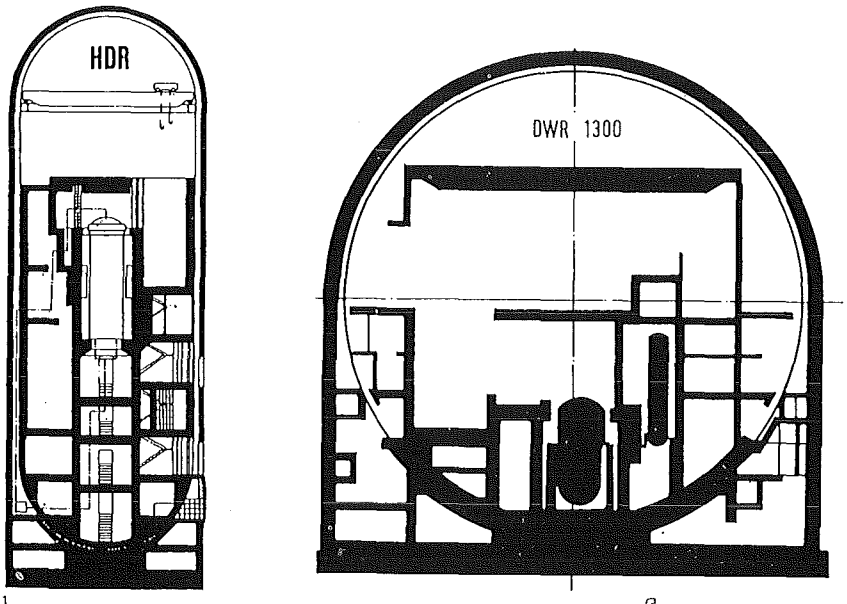

CONTAINMENT (HDR-DWR1300) Fig. 1

Components:
① Containment
② Reactor pressure vessel (RPV)
③ RPV-Internals
④ Piping system for cooling
⑤ Crane
⑥ Material lock
⑦ Flood water storage tank
⑧ Reactorbuilding
⑨ Soil
⑩ Fuel element storage room

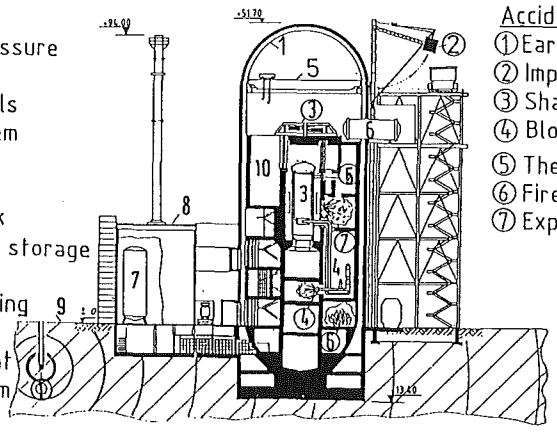

Accident simulations:
① Earthquake
② Impulsive type loads
③ Shaker
④ Blowdown
⑤ Thermal shocking
⑥ Fire
⑦ Explosion

HDR-Testfacility and applicated accident simulations Fig. 2

Load	Characteristic Data			
	HDR-Tests		PWR/BWR-Design	
BWR-Operation	70 bar 285°C 220°C			
PWR-Operation	110 bar, 310°C		160 bar, 350°C	
Blowdown RPV-J	Breaknozzle NW 200, Length 4,5/1,3m	Rupture Opening time 3ms	Nozzle NW 500-800 Length 0m	Rupture Opening time 15ms
Cont Valve	NW 450/350 DIV: NW 500 SRV: NW 200/350		Div: NW 450/700 SRV: NW 350/450	
Earthquake	Simulation: (Shaker, Snapback, Blast) b max= 410cm/s² at 19Hz = 12cm/s² at 4Hz		(KNK II/KFK) b= 100cm/s²	
Thermal Shock	K_I 0 to K_{IC} (20-310°C) Crack propagation 0-1/4W		$K_I < K_{IC}$ (20-310°C) Crack propagation 1/4W	

Parameter HDR-Test/PWR/BWR Design Fig. 3

	TEST CATEGORY	ABBREV.
SP 1000/2000	• Cyclic Thermal Shock (Crack Propagation)	THES/ THEZ
	• RPV Emergency Cooling Tests (to penetration)	NOTS/ NOTZ
	• Pipe Failure Tests (to penetration)	RORV
	• Pipe Blowdown with Valve (Plastification)	RORB
SP 3000	• Temperature Stratification (Cold Water Injection)	TEMB/ TEMR
	• Blowdown with RPV Internals	RBE
	• Blowdown in Containment	CON
SP 4000	• Shaker Tests (High-Level to Plastification)	SHAG/ SHAM
	• Ambient Noise	RAU
	• Impact Tests (Aircraft Impact)	STO
SP 5000	• Containment Leak Rate Tests-Cold	LEK
	• Decommissioning Tests in Containment	ZER
	• Fire Protection	BRA

PHDR Test Categories, Phase II 1984-1987 Fig. 4